CLM5 Documentation

Feb 12, 2019

CONTENTS

February 2018

Technical Description of version 5.0 of the Community Land Model (CLM)

Coordinating Lead Authors

David Lawrence, Rosie Fisher, Charles Koven, Keith Oleson, Sean Swenson, Mariana Vertenstein

Lead Authors

Ben Andre, Gordon Bonan, Bardan Ghimire, Leo van Kampenhout, Daniel Kennedy, Erik Kluzek, Ryan Knox, Peter Lawrence, Fang Li, Hongyi Li, Danica Lombardozzi, Yaqiong Lu, Justin Perket, William Riley, William Sacks, Mingjie Shi, Will Wieder, Chonggang Xu

Contributing Authors

Ashehad Ali, Andrew Badger, Gautam Bisht, Patrick Broxton, Michael Brunke, Jonathan Buzan, Martyn Clark, Tony Craig, Kyla Dahlin, Beth Drewniak, Louisa Emmons, Josh Fisher, Mark Flanner, Pierre Gentine, Jan Lenaerts, Sam Levis, L. Ruby Leung, William Lipscomb, Jon Pelletier, Daniel M. Ricciuto, Ben Sanderson, Jacquelyn Shuman, Andrew Slater, Zachary Subin, Jinyun Tang, Ahmed Tawfik, Quinn Thomas, Simone Tilmes, Francis Vitt, Xubin Zeng

LIST OF FIGURES

LIST OF TABLES

ACKNOWLEDGEMENTS

CHAPTER 1

INTRODUCTION

The purpose of this document is to fully describe the biogeophysical and biogeochemical parameterizations and numerical implementation of version 5.0 of the Community Land Model (CLM5.0). Scientific justification and evaluation of these parameterizations can be found in the referenced scientific papers (*References*). This document and the CLM5.0 User's Guide together provide the user with the scientific description and operating instructions for CLM.

1.1 Model History

1.1.1 Inception of CLM

The early development of the Community Land Model can be described as the merging of a community-developed land model focusing on biogeophysics and a concurrent effort at NCAR to expand the NCAR Land Surface Model (NCAR LSM, *Bonan 1996*) to include the carbon cycle, vegetation dynamics, and river routing. The concept of a community-developed land component of the Community Climate System Model (CCSM) was initially proposed at the CCSM Land Model Working Group (LMWG) meeting in February 1996. Initial software specifications and development focused on evaluating the best features of three existing land models: the NCAR LSM (*Bonan 1996, 1998*) used in the Community Climate Model (CCM3) and the initial version of CCSM; the Institute of Atmospheric Physics, Chinese Academy of Sciences land model (IAP94) (*Dai and Zeng 1997*); and the Biosphere-Atmosphere Transfer Scheme (BATS) (*Dickinson et al. 1993*) used with CCM2. A scientific steering committee was formed to review the initial specifications of the design provided by Robert Dickinson, Gordon Bonan, Xubin Zeng, and Yongjiu Dai and to facilitate further development. Steering committee members were selected so as to provide guidance and expertise in disciplines not generally well-represented in land surface models (e.g., carbon cycling, ecological modeling, hydrology, and river routing) and included scientists from NCAR, the university community, and government laboratories (R. Dickinson, G. Bonan, X. Zeng, Paul Dirmeyer, Jay Famiglietti, Jon Foley, and Paul Houser).

The specifications for the new model, designated the Common Land Model, were discussed and agreed upon at the June 1998 CCSM Workshop LMWG meeting. An initial code was developed by Y. Dai and was examined in March 1999 by Mike Bosilovich, P. Dirmeyer, and P. Houser. At this point an extensive period of code testing was initiated. Keith Oleson, Y. Dai, Adam Schlosser, and P. Houser presented preliminary results of offline 1-dimensional testing at the June 1999 CCSM Workshop LMWG meeting. Results from more extensive offline testing at plot, catchment, and large scale (up to global) were presented by Y. Dai, A. Schlosser, K. Oleson, M. Bosilovich, Zong-Liang Yang, Ian Baker, P. Houser, and P. Dirmeyer at the LMWG meeting hosted by COLA (Center for Ocean-Land-Atmosphere Studies) in November 1999. Field data used for validation included sites adopted by the Project for Intercomparison of

Land-surface Parameterization Schemes (*Henderson-Sellers et al. 1993*) (Cabauw, Valdai, Red-Arkansas river basin) and others [FIFE (*Sellers et al. 1988*), BOREAS (*Sellers et al. 1995*), HAPEX-MOBILHY (*André et al. 1986*), ABRACOS (*Gash et al. 1996*), Sonoran Desert (*Unland et al. 1996*), GSWP (*Dirmeyer et al. 1999*)]. Y. Dai also presented results from a preliminary coupling of the Common Land Model to CCM3, indicating that the land model could be successfully coupled to a climate model.

Results of coupled simulations using CCM3 and the Common Land Model were presented by X. Zeng at the June 2000 CCSM Workshop LMWG meeting. Comparisons with the NCAR LSM and observations indicated major improvements to the seasonality of runoff, substantial reduction of a summer cold bias, and snow depth. Some deficiencies related to runoff and albedo were noted, however, that were subsequently addressed. Z.-L. Yang and I. Baker demonstrated improvements in the simulation of snow and soil temperatures. Sam Levis reported on efforts to incorporate a river routing model to deliver runoff to the ocean model in CCSM. Soon after the workshop, the code was delivered to NCAR for implementation into the CCSM framework. Documentation for the Common Land Model is provided by *Dai et al. (2001)* while the coupling with CCM3 is described in *Zeng et al. (2002)*. The model was introduced to the modeling community in *Dai et al. (2003)*.

1.1.2 CLM2

Concurrent with the development of the Common Land Model, the NCAR LSM was undergoing further development at NCAR in the areas of carbon cycling, vegetation dynamics, and river routing. The preservation of these advancements necessitated several modifications to the Common Land Model. The biome-type land cover classification scheme was replaced with a plant functional type (PFT) representation with the specification of PFTs and leaf area index from satellite data (*Oleson and Bonan 2000*; *Bonan et al. 2002a, b*). This also required modifications to parameterizations for vegetation albedo and vertical burying of vegetation by snow. Changes were made to canopy scaling, leaf physiology, and soil water limitations on photosynthesis to resolve deficiencies indicated by the coupling to a dynamic vegetation model. Vertical heterogeneity in soil texture was implemented to improve coupling with a dust emission model. A river routing model was incorporated to improve the fresh water balance over oceans. Numerous modest changes were made to the parameterizations to conform to the strict energy and water balance requirements of CCSM. Further substantial software development was also required to meet coding standards. The resulting model was adopted in May 2002 as the Community Land Model (CLM2) for use with the Community Atmosphere Model (CAM2, the successor to CCM3) and version 2 of the Community Climate System Model (CCSM2).

K. Oleson reported on initial results from a coupling of CCM3 with CLM2 at the June 2001 CCSM Workshop LMWG meeting. Generally, the CLM2 preserved most of the improvements seen in the Common Land Model, particularly with respect to surface air temperature, runoff, and snow. These simulations are documented in *Bonan et al. (2002a)*. Further small improvements to the biogeophysical parameterizations, ongoing software development, and extensive analysis and validation within CAM2 and CCSM2 culminated in the release of CLM2 to the community in May 2002.

Following this release, Peter Thornton implemented changes to the model structure required to represent carbon and nitrogen cycling in the model. This involved changing data structures from a single vector of spatially independent sub-grid patches to one that recognizes three hierarchical scales within a model grid cell: land unit, snow/soil column, and PFT. Furthermore, as an option, the model can be configured so that PFTs can share a single soil column and thus "compete" for water. This version of the model (CLM2.1) was released to the community in February 2003. CLM2.1, without the compete option turned on, produced only round off level changes when compared to CLM2.

1.1.3 CLM3

CLM3 implemented further software improvements related to performance and model output, a re-writing of the code to support vector-based computational platforms, and improvements in biogeophysical parameterizations to correct deficiencies in the coupled model climate. Of these parameterization improvements, two were shown to have a noticeable impact on simulated climate. A variable aerodynamic resistance for heat/moisture transfer from ground to canopy air that depends on canopy density was implemented. This reduced unrealistically high surface temperatures in semi-arid regions. The second improvement added stability corrections to the diagnostic 2-m air temperature calculation which reduced biases in this temperature. Competition between PFTs for water, in which PFTs share a single soil

column, is the default mode of operation in this model version. CLM3 was released to the community in June 2004. *Dickinson et al. (2006)* describe the climate statistics of CLM3 when coupled to CCSM3.0. *Hack et al. (2006)* provide an analysis of selected features of the land hydrological cycle. *Lawrence et al. (2007)* examine the impact of changes in CLM3 hydrological parameterizations on partitioning of evapotranspiration (ET) and its effect on the timescales of ET response to precipitation events, interseasonal soil moisture storage, soil moisture memory, and land-atmosphere coupling. *Qian et al. (2006)* evaluate CLM3's performance in simulating soil moisture content, runoff, and river discharge when forced by observed precipitation, temperature and other atmospheric data.

1.1.4 CLM3.5

Although the simulation of land surface climate by CLM3 was in many ways adequate, most of the unsatisfactory aspects of the simulated climate noted by the above studies could be traced directly to deficiencies in simulation of the hydrological cycle. In 2004, a project was initiated to improve the hydrology in CLM3 as part of the development of CLM version 3.5. A selected set of promising approaches to alleviating the hydrologic biases in CLM3 were tested and implemented. These included new surface datasets based on Moderate Resolution Imaging Spectroradiometer (MODIS) products, new parameterizations for canopy integration, canopy interception, frozen soil, soil water availability, and soil evaporation, a TOPMODEL-based model for surface and subsurface runoff, a groundwater model for determining water table depth, and the introduction of a factor to simulate nitrogen limitation on plant productivity. *Oleson et al. (2008a)* show that CLM3.5 exhibits significant improvements over CLM3 in its partitioning of global ET which result in wetter soils, less plant water stress, increased transpiration and photosynthesis, and an improved annual cycle of total water storage. Phase and amplitude of the runoff annual cycle is generally improved. Dramatic improvements in vegetation biogeography result when CLM3.5 is coupled to a dynamic global vegetation model. *Stöckli et al. (2008)* examine the performance of CLM3.5 at local scales by making use of a network of long-term ground-based ecosystem observations [FLUXNET (*Baldocchi et al. 2001*)]. Data from 15 FLUXNET sites were used to demonstrate significantly improved soil hydrology and energy partitioning in CLM3.5. CLM3.5 was released to the community in May, 2007.

1.1.5 CLM4

The motivation for the next version of the model, CLM4, was to incorporate several recent scientific advances in the understanding and representation of land surface processes, expand model capabilities, and improve surface and atmospheric forcing datasets (*Lawrence et al. 2011*). Included in the first category are more sophisticated representations of soil hydrology and snow processes. In particular, new treatments of soil column-groundwater interactions, soil evaporation, aerodynamic parameters for sparse/dense canopies, vertical burial of vegetation by snow, snow cover fraction and aging, black carbon and dust deposition, and vertical distribution of solar energy for snow were implemented. Major new capabilities in the model include a representation of the carbon-nitrogen cycle (CLM4CN, see next paragraph for additional information), the ability to model land cover change in a transient mode, inclusion of organic soil and deep soil into the existing mineral soil treatment to enable more realistic modeling of permafrost, an urban canyon model to contrast rural and urban energy balance and climate (CLMU), and an updated biogenic volatile organic compounds (BVOC) model. Other modifications of note include refinement of the global PFT, wetland, and lake distributions, more realistic optical properties for grasslands and croplands, and an improved diurnal cycle and spectral distribution of incoming solar radiation to force the model in land-only mode.

Many of the ideas incorporated into the carbon and nitrogen cycle component of CLM4 derive from the earlier development of the land-only ecosystem process model Biome-BGC (Biome BioGeochemical Cycles), originating at the Numerical Terradynamic Simulation Group (NTSG) at the University of Montana, under the guidance of Prof. Steven Running. Biome-BGC itself is an extension of an earlier model, Forest-BGC (*Running and Coughlan, 1988*; *Running and Gower, 1991*), which simulates water, carbon, and, to a limited extent, nitrogen fluxes for forest ecosystems. Forest-BGC was designed to be driven by remote sensing inputs of vegetation structure, and so used a diagnostic (prescribed) leaf area index, or, in the case of the dynamic allocation version of the model (*Running and Gower, 1991*), prescribed maximum leaf area index.

Biome-BGC expanded on the Forest-BGC logic by introducing a more mechanistic calculation of leaf and canopy

---

scale photosynthesis (*Hunt and Running, 1992*), and extending the physiological parameterizations to include multiple woody and non-woody vegetation types (*Hunt et al. 1996*; *Running and Hunt, 1993*). Later versions of Biome-BGC introduced more mechanistic descriptions of belowground carbon and nitrogen cycles, nitrogen controls on photosynthesis and decomposition, sunlit and shaded canopies, vertical gradient in leaf morphology, and explicit treatment of fire and harvest disturbance and regrowth dynamics (*Kimball et al. 1997*; *Thornton, 1998*; *Thornton et al. 2002*; *White et al. 2000*). Biome-BGC version 4.1.2 (*Thornton et al. 2002*) provided a point of departure for integrating new biogeochemistry components into CLM4.

CLM4 was released to the community in June, 2010 along with the Community Climate System Model version 4 (CCSM4). CLM4 is used in CCSM4, CESM1, CESM1.1, and remains available as the default land component model option for coupled simulations in CESM1.2.

1.1.6 CLM4.5

The motivations for the development of CLM4.5 were similar to those for CLM4: incorporate several recent scientific advances in the understanding and representation of land surface processes, expand model capabilities, and improve surface and atmospheric forcing datasets.

Specifically, several parameterizations were revised to reflect new scientific understanding and in an attempt to reduce biases identified in CLM4 simulations including low soil carbon stocks especially in the Arctic, excessive tropical GPP and unrealistically low Arctic GPP, a dry soil bias in Arctic soils, unrealistically high LAI in the tropics, a transient 20th century carbon response that was inconsistent with observational estimates, and several other more minor problems or biases.

The main modifications include updates to canopy processes including a revised canopy radiation scheme and canopy scaling of leaf processes, co-limitations on photosynthesis, revisions to photosynthetic parameters (*Bonan et al. 2011*), temperature acclimation of photosynthesis, and improved stability of the iterative solution in the photosynthesis and stomatal conductance model (*Sun et al. 2012*). Hydrology updates included modifications such that hydraulic properties of frozen soils are determined by liquid water content only rather than total water content and the introduction of an ice impedance function, and other corrections that increase the consistency between soil water state and water table position and allow for a perched water table above icy permafrost ground (*Swenson et al. 2012*). A new snow cover fraction parameterization is incorporated that reflects the hysteresis in fractional snow cover for a given snow depth between accumulation and melt phases (*Swenson and Lawrence, 2012*). The lake model in CLM4 was replaced with a completely revised and more realistic lake model (*Subin et al. 2012a*). A surface water store was introduced, replacing the wetland land unit and permitting prognostic wetland distribution modeling. The surface energy fluxes are calculated separately (*Swenson and Lawrence, 2012*) for snow-covered, water-covered, and snow/water-free portions of vegetated and crop land units, and snow-covered and snow-free portions of glacier land units. Globally constant river flow velocity is replaced with variable flow velocity based on mean grid cell slope. A vertically resolved soil biogeochemistry scheme is introduced with base decomposition rates modified by soil temperature, water, and oxygen limitations and also including vertical mixing of soil carbon and nitrogen due to bioturbation, cryoturbation, and diffusion (*Koven et al. 2013*). The litter and soil carbon and nitrogen pool structure as well as nitrification and denitrification that were modified based on the Century model. Biological fixation was revised to distribute fixation more realistically over the year (*Koven et al. 2013*). The fire model was replaced with a model that includes representations of natural and anthropogenic triggers and suppression as well as agricultural, deforestation, and peat fires (*Li et al. 2012a,b*; *Li et al. 2013a*). The biogenic volatile organic compounds model is updated to MEGAN2.1 (*Guenther et al. 2012*).

Additions to the model include a methane production, oxidation, and emissions model (*Riley et al. 2011a*) and an extension of the crop model to include interactive fertilization, organ pools (*Drewniak et al. 2013*), and irrigation (*Sacks et al. 2009*). Elements of the Variable Infiltration Capacity (VIC) model are included as an alternative optional runoff generation scheme (*Li et al. 2011*). There is also an option to run with a multilayer canopy (*Bonan et al. 2012*). Multiple urban density classes, rather than the single dominant urban density class used in CLM4, are modeled in the urban land unit. Carbon (^{13}C and ^{14}C) isotopes are enabled (*Koven et al. 2013*). Minor changes include a switch of the C3 Arctic grass and shrub phenology from stress deciduous to seasonal deciduous and a change in the glacier bare ice

albedo to better reflect recent estimates. Finally, the carbon and nitrogen cycle spinup is accelerated and streamlined with a revised spinup method, though the spinup timescale remains long.

Finally, the predominantly low resolution input data for provided with CLM4 to create CLM4 surface datasets is replaced with newer and higher resolution input datasets where possible (see section 2.3.3 for details). The default meteorological forcing dataset provided with CLM4 (*Qian et al. 2006*) is replaced with the 1901-2010 CRUNCEP forcing dataset (see Chapter 33) for CLM4.5, though users can also still use the *Qian et al. (2006)* dataset or other alternative forcing datasets.

CLM4.5 was released to the community in June 2013 along with the Community Earth System Model version 1.2 (CESM1.2).

1.1.7 CLM5.0

Developments for CLM5.0 build on the progress made in CLM4.5. Most major components of the model have been updated with particularly notable changes made to soil and plant hydrology, snow density, river modeling, carbon and nitrogen cycling and coupling, and crop modeling. Much of the focus of development centered on a push towards more mechanistic treatment of key processes, in addition to more comprehensive and explicit representation of land use and land-cover change. Prior versions of CLM included relatively few options for physics parameterizations or structure. In CLM5, where new parameterizations or model decisions were made, in most cases, the CLM4.5 parameterization was maintained so that users could switch back and forth between different parameterizations via namelist control where appropriate or desirable. Throughout the CLM5 Technical Descpription, in general only the default parameterization for any given process is described. Readers are referred to the CLM4.5 or CLM4 Technical Descriptions for detailed descriptions of non-default parameterizations.

The hydrology updates include the introduction of a dry surface layer-based soil evaporation resistance parameterization *(Swenson and Lawrence, 2014)* and a revised canopy interception parameterization. Canopy interception is now divided into liquid and solid phases, with the intercepted snow subject to unloading events due to wind or above-freezing temperatures. The snow-covered fraction of the canopy is used within the canopy radiation and surface albedo calculation. Instead of applying a spatially uniform soil thickness, soil thickness can vary in space *(Brunke et al. 2016* and *Swenson and Lawrence, 2015)* and is set to values within a range of 0.4m to 8.5m depth, derived from a spatially explicit soil thickness data product *(Pelletier et al., 2016)*. The explicit treatment of soil thickness allows for the deprecation of the unconfined aquifer parameterization used in CLM4.5, which is replaced with a zero flux boundary condition and explicit modeling of both the saturated and unsaturated zones. The default model soil layer resolution is increased, especially within the top 3m, to more explicitly represent active layer thickness within the permafrost zone. Rooting profiles were used inconsistently in CLM4.5 with *Zeng (2001)* profiles used for water and *Jackson et al. (1996)* profiles used for carbon inputs. For CLM5, the Jackson et al. (1996) rooting profiles are used for both water and carbon. Roots are deepened for the broadleaf evergreen tropical tree and broadleaf deciduous tropical tree types. Finally, an adaptive time-stepping solution to the Richard's equation is introduced, which improves the accuracy and stability of the numerical soil water solution. The River Transport Model (RTM) is replaced with the Model for Scale Adaptive River Transport (MOSART, *Li et al., 2013b)* in which surface runoff is routed across hillslopes and then discharged along with subsurface runoff into a tributary subnetwork before entering the main channel.

Several changes are included that are mainly targeted at improving the simulation of surface mass balance over ice sheets. The fresh snow density parameterization is updated to more realistically capture temperature effects and to additionally account for wind effects on new snow density *(van Kampenhout et al., 2017)*. The maximum number of snow layers and snow amount is increased from 5 layers and 1m snow water equivalent to 12 layers and 10m snow water equivalent to allow for the formation of firn in regions of persistent snow-cover (e.g., glaciers and ice sheets) *(van Kampenhout et al., 2017)*. The CISM2 ice sheet model is included for Greenland by default. The ice sheet does not evolve for typical configurations, but ice sheet evolution can be turned on by choosing an appropriate compset. The introduction in CLM5 of the capability to dynamically adjust landunit weights means that a glacier can initiate, grow, shrink, or disappear during a simulation when ice evolution is active. That is, there are two-way feedbacks between CLM and CISM. Multiple elevation classes (10 elevation classes by default) and associated temperature, rain/snow partitioning, and downwelling longwave downscaling are used for glacier landunits to account for the strong topographic elevation heterogeneity over glaciers and ice sheets.

A plant hydraulic stress routine is introduced which explicitly models water transport through the vegetation according to a simple hydraulic framework (Kennedy et al., to be submitted). The water supply equations are used to solve for vegetation water potential forced by transpiration demand and a set of layer-by-layer soil water potentials. Stomatal conductance, therefore, is a function of prognostic leaf water potential. Water stress is calculated as the ratio of attenuated stomatal conductance to maximum stomatal conductance. An emergent feature of the plant hydraulics is soil hydraulic redistribution. In CLM5, maximum stomatal conductance is obtained from the Medlyn conductance model *(Medlyn et al., 2011)*, rather than the Ball-Berry stomatal conductance model that was utilized in CLM4.5 and prior versions of the model. The Medlyn stomatal conductance model is preferred mainly for it's more realistic behavior at low humidity levels *(Rogers et al., 2017)*. The stress deciduous vegetation phenology trigger is augmented with a antecedent precipitation requirement *(Dahlin et al. 2015)*.

Plant nutrient dynamics are substantially updated to resolve several deficiencies with the CLM4 and CLM4.5 nutrient cycling representation. The Fixation and Update of Nitrogen (FUN) model based on the work of *Fisher et al. (2010)*, *Brzostek et al. (2014)*, and *Shi et al. (2016)* is incorporated. The concept of FUN is that in most cases, N uptake requires the expenditure of energy in the form of carbon, and further, that there are numerous potential sources of N in the environment which a plant may exchange for carbon. The ratio of carbon expended to N acquired is therefore the cost, or exchange rate, of N acquisition. FUN calculates the rate of symbiotic N fixation, with this N passed straight to the plant, not the mineral N pool. Separately, CLM5 also calculates rates of symbiotic (or free living) N fixation as a function of evapotranspiration *(Cleveland et al. 1999)*, which is added to the soil inorganic ammonium (NH_4^+) pool. The static plant carbon:nitrogen (C:N) ratios utilized in CLM4 and CLM4.5 are replaced with variable plant C:N ratios which allows plants to adjust their C:N ratio, and therefore their leaf nitrogen content, with the cost of N uptake *(Ghimire et al. 2016)*. The implementation of a flexible C:N ratio means that the model no longer relies on instantaneous downregulation of potential photosynthesis rates based on soil mineral nitrogen availability to represent nutrient limitation. Furthermore, stomatal conductance is now based on the N-limited photosynthesis rather than on potential photosynthesis. Finally, the Leaf Use of Nitrogen for Assimilation (LUNA, *Xu et al., 2012* and *Ali et al., 2016)* model is incorporated. The LUNA model calculates photosynthetic capacity based on optimization of the use of leaf nitrogen under different environmental conditions such that light capture, carboxylation, and respiration are co-limiting.

CLM5 applies a fixed allocation scheme for woody vegetation. The decision to use a fixed allocation scheme in CLM5, rather than a dynamic NPP-based allocation scheme, as was used in CLM4 and CLM4.5, was driven by the fact that observations indicate that biomass saturates with increasing productivity, in contrast to the behavior in CLM4 and CLM4.5 where biomass continuously increases with increasing productivity *(Negron-Juarez et al., 2015)*. Soil carbon decomposition processes are unchanged in CLM5, but a new metric for apparent soil carbon turnover times *(Koven et al., 2017)* suggested parameter changes that produce a weak intrinsic depth limitation on soil carbon turnover rates (rather than the strong depth limitaiton in CLM4.5) and that the thresholds for soil moisture limitation on soil carbon turnover rates in dry soils should be set at a wetter soil moisture level than that used in CLM4.5.

Representation of human management of the land (agriculture, wood harvest) is augmented in several ways. The CLM4.5 crop model is extended to operate globally through the addition of rice and sugarcane as well as tropical varieties of corn and soybean *(Badger and Dirmeyer, 2015* and *Levis et al., 2016)*. These crop types are added to the existing temperate corn, temperature soybean, spring wheat, and cotton crop types. Fertilization rates and irrigation equipped area updated annually based on crop type and geographic region through an input dataset. The irrigation trigger is updated. Additional minor changes include crop phenological triggers that vary by latitude for selected crop types, grain C and N is now removed at harvest to a 1-year product pool with the carbon for the next season's crop seed removed from the grain carbon at harvest. Through the introduction of the capability to dynamically adjust landunit weights during a simulation, the crop model can now be run coincidentally with prescribed land use, which significantly expands the capabilities of the model. Mass-based rather than area-based wood harvest is applied. Several heat stress indices for both urban and rural areas are calculated and output by default *(Buzan et al., 2015)*. A more sophisticated and realistic building space heating and air conditioning submodel that prognoses interior building air temperature and includes more realistic space heating and air conditioning wasteheat factors is incorporated.

The fire model is the same as utilized in CLM4.5 except that a modified scheme is used to estimate the dependence of fire occurrence and spread on fuel wetness for non-peat fires outside cropland and tropical closed forests *(Li and Lawrence, 2017)* and the dependence of agricultural fires on fuel load is removed.

Included with the release of CLM5.0 is a functionally supported version of the Functionally-Assembled Terrestrial Ecosystem Simulator (FATES, *Fisher et al., 2015*). A major motivation of FATES is to allow the prediction of biome boundaries directly from plant physiological traits via their competitive interactions. FATES is a cohort model of vegetation competition and co-existence, allowing a representation of the biosphere which accounts for the division of the land surface into successional stages, and for competition for light between height structured cohorts of representative trees of various plant functional types. FATES is not active by default in CLM5.0.

Note that the classical dynamic global vegetation model (CLM-DGVM) that has been available within CLM4 and CLM4.5 remains available, though it is largely untested. The technical description of the CLM-DGVM can be found within the CLM4.5 Technical Description (*Oleson et al. 2013)*.

During the course of the development of CLM5.0, it became clear that the increasing complexity of the model combined with the increasing number and range of model development projects required updates to the underlying CLM infrastructure. Many such software improvements are included in CLM5 including a partial transition to an object-oriented modular software structure. Many hard coded model parameters have been extracted into either the parameter file or the CLM namelist, which allows users to more readily calibrate the model for use at specific locations or to conduct parameter sensitivity studies. As part of the effort to increase the scientific utility of the code, in most instances older generation parameterizations (i.e., the parameterizations available in CLM4 or CLM4.5) are retained under namelist switches, allowing the user to revert to CLM4.5 from the same code base or to revert individual parameterizations where the old parameterizations are compatible with the new code. Finally, multiple vertical soil layer structures are defined and it is relatively easy to add additional structures.

1.2 Biogeophysical and Biogeochemical Processes

Biogeophysical and biogeochemical processes are simulated for each subgrid land unit, column, and plant functional type (PFT) independently and each subgrid unit maintains its own prognostic variables (see section 2.1.1 for definitions of subgrid units). The same atmospheric forcing is used to force all subgrid units within a grid cell. The surface variables and fluxes required by the atmosphere are obtained by averaging the subgrid quantities weighted by their fractional areas. The processes simulated include (Figure 1.1):

1. Surface characterization including land type heterogeneity and ecosystem structure (Chapter 2)

2. Absorption, reflection, and transmittance of solar radiation (Chapter 3, 4)

3. Absorption and emission of longwave radiation (Chapter 4)

4. Momentum, sensible heat (ground and canopy), and latent heat (ground evaporation, canopy evaporation, transpiration) fluxes (Chapter 5)

5. Heat transfer in soil and snow including phase change (Chapter 6)

6. Canopy hydrology (interception, throughfall, and drip) (Chapter 7)

7. Soil hydrology (surface runoff, infiltration, redistribution of water within the column, sub-surface drainage, groundwater) (Chapter 7)

8. Snow hydrology (snow accumulation and melt, compaction, water transfer between snow layers) (Chapter 8)

9. Stomatal physiology, photosythetic capacity, and photosynthesis (Chapters 9 and 10)

10. Plant hydraulics (Chapter 11)

11. Lake temperatures and fluxes (Chapter 12)

12. Glacier processes (Chapter 13)

13. River routing and river flow (Chapter 14)

14. Urban energy balance and climate (Chapter 15)

15. Vegetation carbon and nitrogen allocation (Chapter 19)

16. Vegetation phenology (Chapter 20)

17. Plant respiration (Chapter 17)

18. Soil and litter carbon decomposition (Chapter 21)

19. Fixation and uptake of nitrogen (Chapter 18)

20. External nitrogen cycling including deposition, denitrification, leaching, and losses due to fire (Chapter 22)

21. Plant mortality (Chapter 23)

22. Fire ignition, suppression, spread, and emissions, including natural, deforestation, and agricultural fire (Chapter 24)

23. Methane production, oxidation, and emissions (Chapter 25)

24. Crop dynamics, irrigation, and fertilization (Chapter 26)

25. Land cover and land use change including wood harvest (Chapter 27)

26. Biogenic volatile organic compound emissions (Chapter 30)

27. Dust mobilization and deposition (Chapter 31)

28. Carbon isotope fractionation (Chapter 32)
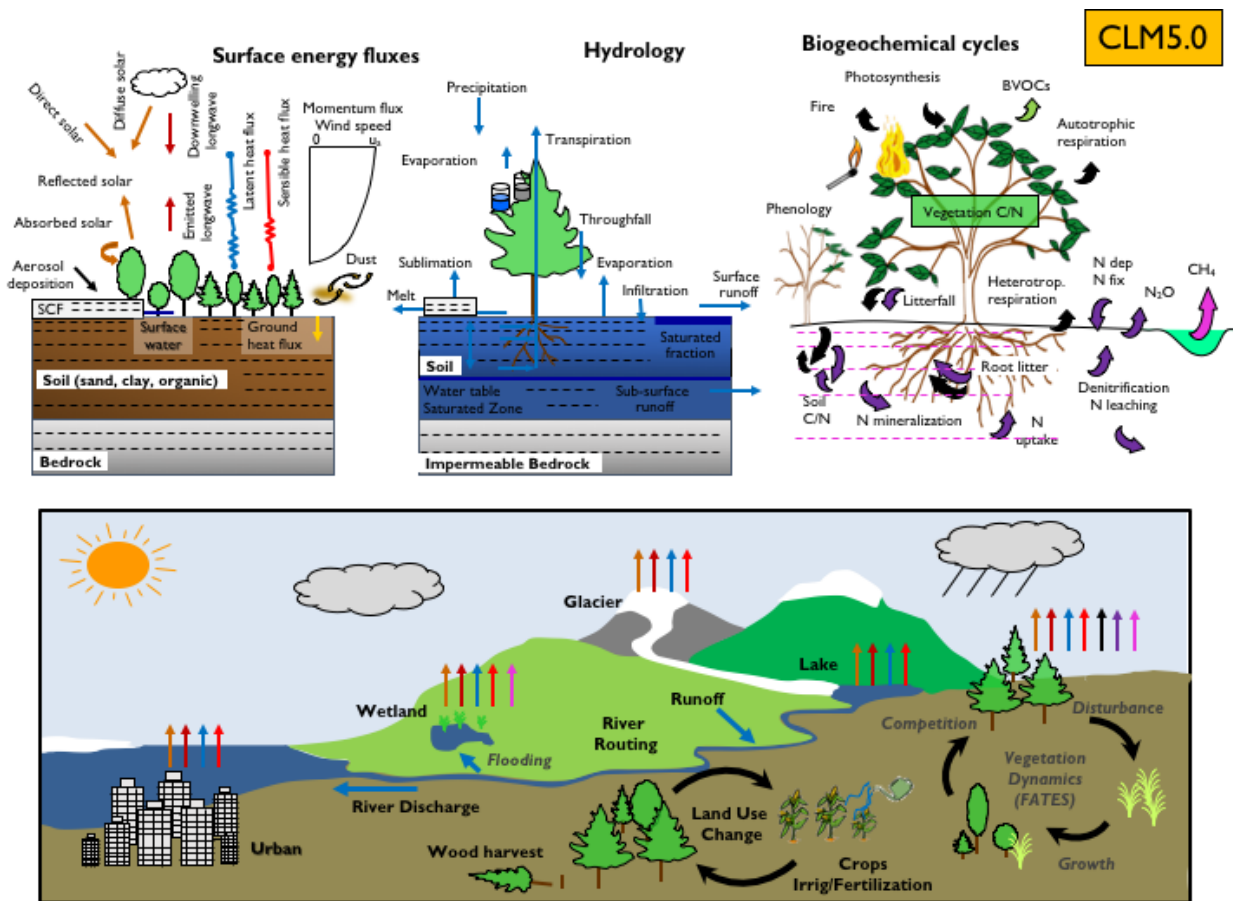
Figure 1.1: Land biogeophysical, biogeochemical, and landscape processes simulated by CLM (adapted from *Lawrence et al. (2011)* for CLM5.0).

CHAPTER 2

SURFACE CHARACTERIZATION, VERTICAL DISCRETIZATION, AND MODEL INPUT REQUIREMENTS

2.1 Surface Characterization

2.1.1 Surface Heterogeneity and Data Structure

Spatial land surface heterogeneity in CLM is represented as a nested subgrid hierarchy in which grid cells are composed of multiple land units, snow/soil columns, and PFTs (Figure 2.1). Each grid cell can have a different number of land units, each land unit can have a different number of columns, and each column can have multiple PFTs. The first subgrid level, the land unit, is intended to capture the broadest spatial patterns of subgrid heterogeneity. The current land units are glacier, lake, urban, vegetated, and crop (when the crop model option is turned on). The land unit level can be used to further delineate these patterns. For example, the urban land unit is divided into density classes representing the tall building district, high density, and medium density urban areas.

The second subgrid level, the column, is intended to capture potential variability in the soil and snow state variables within a single land unit. For example, the vegetated land unit could contain several columns with independently evolving vertical profiles of soil water and temperature. Similarly, the managed vegetation land unit can be divided into two columns, irrigated and non-irrigated. The default snow/soil column is represented by 25 layers for ground (with up to 20 of these layers classified as soil layers and the remaining layers classified as bedrock layers) and up to 10 layers for snow, depending on snow depth. The central characteristic of the column subgrid level is that this is where the state variables for water and energy in the soil and snow are defined, as well as the fluxes of these components within the soil and snow. Regardless of the number and type of PFTs occupying space on the column, the column physics operates with a single set of upper boundary fluxes, as well as a single set of transpiration fluxes from multiple soil levels. These boundary fluxes are weighted averages over all PFTs. Currently, for lake and vegetated land units, a single column is assigned to each land unit. The crop land unit is split into irrigated and unirrigated columns with a single crop occupying each column. The urban land units have five columns (roof, sunlit walls and shaded walls, and pervious and impervious canyon floor) (Oleson et al. 2010b). The glacier land unit is separated into up to 10 elevation classes.
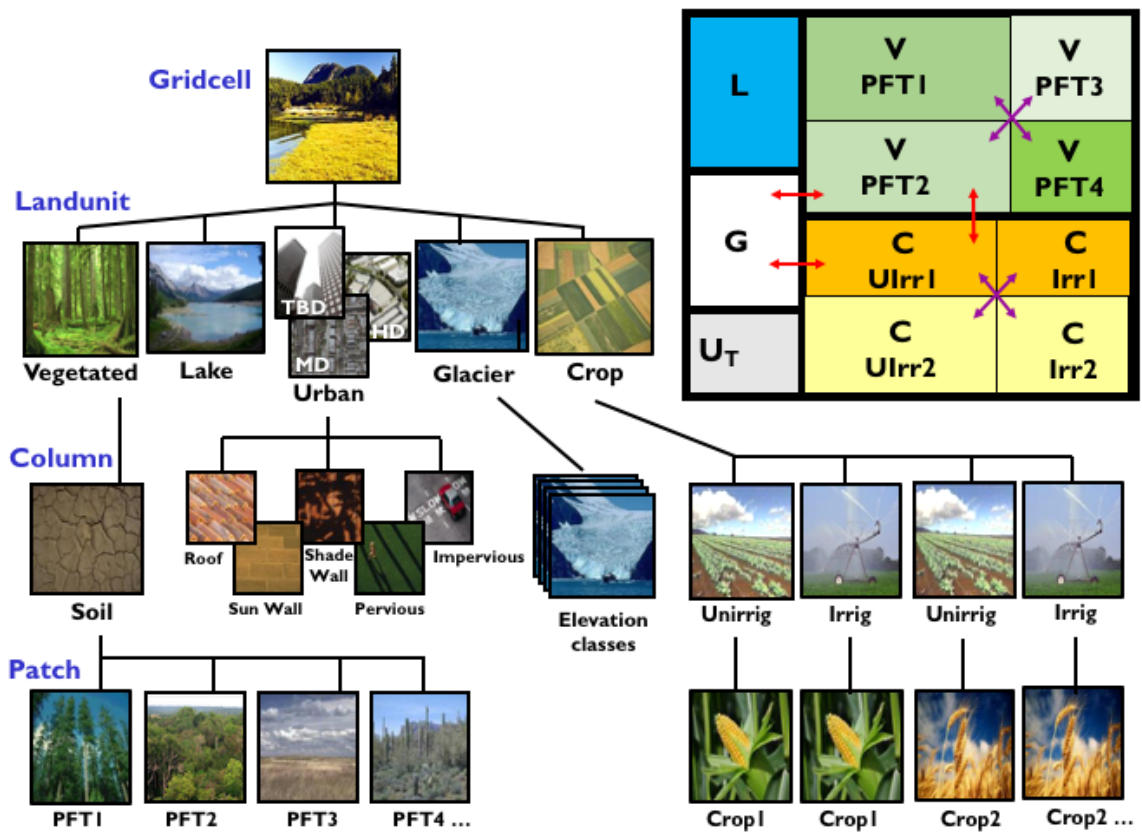
Figure 2.1: Configuration of the CLM subgrid hierarchy. Box in upper right shows hypothetical subgrid distribution for a single grid cell. Note that the Crop land unit is only used when the model is run with the crop model active. Abbreviations: TBD – Tall Building District; HD – High Density; MD – Medium Density, G – Glacier, L – Lake, U – Urban, C – Crop, V – Vegetated, PFT – Plant Functional Type, Irr – Irrigated, UIrr – Unirrigated. Red arrows indicate allowed land unit transitions. Purple arrows indicate allowed patch-level transitions.

The third subgrid level is referred to as the patch level. Patches can be PFTs or bare ground on the vegetated land unit and crop functional types (CFTs) on the crop land unit. The patch level is intended to capture the biogeophysical and biogeochemical differences between broad categories of plants in terms of their functional characteristics. On the vegetated land unit, up to 16 possible PFTs that differ in physiology and structure may coexist on a single column. All fluxes to and from the surface are defined at the PFT level, as are the vegetation state variables (e.g. vegetation temperature and canopy water storage). On the crop land unit, typically, different crop types can be represented on each crop land unit column (see Chapter 26 for details).

In addition to state and flux variable data structures for conserved components at each subgrid level (e.g., energy, water, carbon), each subgrid level also has a physical state data structure for handling quantities that are not involved in conservation checks (diagnostic variables). For example, the urban canopy air temperature and humidity are defined through physical state variables at the land unit level, the number of snow layers and the soil roughness lengths are defined as physical state variables at the column level, and the leaf area index and the fraction of canopy that is wet are defined as physical state variables at the PFT level.

The standard configuration of the model subgrid hierarchy is illustrated in Figure 2.1. Here, only four PFTs are shown associated with the single column beneath the vegetated land unit but up to sixteen are possible. The crop land unit is present only when the crop model is active.

Note that the biogeophysical processes related to soil and snow require PFT level properties to be aggregated to the column level. For example, the net heat flux into the ground is required as a boundary condition for the solution of snow/soil temperatures (Chapter 6). This column level property must be determined by aggregating the net heat flux from all PFTs sharing the column. This is generally accomplished in the model by computing a weighted sum of the desired quantity over all PFTs whose weighting depends on the PFT area relative to all PFTs, unless otherwise noted in the text.

2.1.2 Vegetation Composition

Vegetated surfaces are comprised of up to 15 possible plant functional types (PFTs) plus bare ground (Table 2.1). An additional PFT is added if the irrigation model is active and six additional PFTs are added if the crop model is active (Chapter 26). These plant types differ in leaf and stem optical properties that determine reflection, transmittance, and absorption of solar radiation (Table 3.1), root distribution parameters that control the uptake of water from the soil (Table 11.1), aerodynamic parameters that determine resistance to heat, moisture, and momentum transfer (Table 5.1), and photosynthetic parameters that determine stomatal resistance, photosynthesis, and transpiration (Table 9.1, Table 9.2). The composition and abundance of PFTs within a grid cell can either be prescribed as time-invariant fields (e.g., using the present day dataset described in section 21.3.3) or can evolve with time if the model is run in transient landcover mode (Chapter 27).

Table 2.1: Plant functional types

Plant functional type	Acronym
Needleleaf evergreen tree – temperate	NET Temperate
Needleleaf evergreen tree - boreal	NET Boreal
Needleleaf deciduous tree – boreal	NDT Boreal
Broadleaf evergreen tree – tropical	BET Tropical
Broadleaf evergreen tree – temperate	BET Temperate
Broadleaf deciduous tree – tropical	BDT Tropical
Broadleaf deciduous tree – temperate	BDT Temperate
Broadleaf deciduous tree – boreal	BDT Boreal
Broadleaf evergreen shrub - temperate	BES Temperate
Broadleaf deciduous shrub – temperate	BDS Temperate
Broadleaf deciduous shrub – boreal	BDS Boreal
C_3 arctic grass	•
C_3 grass	•
C_4 grass	•
C_3 Unmanaged Rainfed Crop	UCrop UIrr
[1]C_3 Unmanaged Irrigated Crop	UCrop Irr
[2]Managed Rainfed Unirrigated Crops	Crop UIrr
[2]Managed Irrigated Crops	Crop Irr

[1]Only used if irrigation is active (Chapter 26). [2]Only used if crop model is active (see Chapter 26 for list of represented crops).

2.1.3 Vegetation Structure

Vegetation structure is defined by leaf and stem area indices (L, S) and canopy top and bottom heights (z_{top}, z_{bot}). Separate leaf and stem area indices and canopy heights are prescribed or calculated for each PFT. Daily leaf and stem area indices are obtained from griddeddatasets of monthly values (section 2.3.3). Canopy top and bottom heights for trees are from ICESat (*Simard et al. (2011)*). Canopy top and bottom heights for short vegetation are obtained from gridded datasets but are invariant in space and time and were obtained from PFT-specific values (*Bonan et al. (2002a)*) (Table 2.2). When the biogeochemistry model is active, vegetation state (LAI, SAI, canopy top and bottom heights) are calculated prognostically (see Chapter 20).

Table 2.2: Plant functional type canopy top and bottom heights

Plant functional type	z_{top}	z_{bot}
BES Temperate	0.5	0.1
BDS Temperate	0.5	0.1
BDS Boreal	0.5	0.1
C_3 arctic grass	0.5	0.01
C_3 grass	0.5	0.01
C_4 grass	0.5	0.01
UCrop UIrr	0.5	0.01
UCrop Irr	0.5	0.01
Crop UIrr	0.5	0.01
Crop Irr	0.5	0.01

2.1.4 Phenology and vegetation burial by snow

When the biogeochemistry model is inactive, leaf and stem area indices (m^2 leaf area m^{-2} ground area) are updated daily by linearly interpolating between monthly values. Monthly PFT leaf area index values are developed from the 1-km MODIS-derived monthly grid cell average leaf area index of *Myneni et al. (2002)*, as described in *Lawrence and Chase (2007)*. Stem area ndex is calculated from the monthly PFT leaf area index using the methods of *Zeng et al. (2002)*. The leaf and stem area indices are adjusted for vertical burying by snow (*Wang and Zeng 2009*) as

$$A = A^*(1 - f_{veg}^{sno}) \tag{2.1}$$

where A is the leaf or stem area before adjustment for snow, A is the remaining exposed leaf or stem area, f_{veg}^{sno} is the vertical fraction of vegetation covered by snow

$$
\begin{aligned}
f_{veg}^{sno} &= \frac{z_{sno} - z_{bot}}{z_{top} - z_{bot}} && \text{for tree and shrub} \\
f_{veg}^{sno} &= \frac{\min\left(z_{sno}, z_c\right)}{z_c} && \text{for grass and crop}
\end{aligned}
\tag{2.2}
$$

where $z_{sno} - z_{bot} \geq 0$, $0 \leq f_{veg}^{sno} \leq 1$, z_{sno} is the depth of snow (m) (Chapter 8), and $z_c = 0.2$ is the snow depth when short vegetation is assumed to be completely buried by snow (m). For numerical reasons, exposed leaf and stem area are set to zero if less than 0.05. If the sum of exposed leaf and stem area is zero, then the surface is treated as snow-covered ground.

2.2 Vertical Discretization

2.2.1 Soil Layers

The soil column can be discretized into an arbitrary number of layers. The default vertical discretization (Table 2.3) uses $N_{levgrnd} = 25$ layers, of which $N_{levsoi} = 20$ are hydrologically and biogeochemically active. The deepest 5 layers are only included in the thermodynamical calculations (*Lawrence et al. 2008*) described in Chapter 6.

The layer structure of the soil is described by the node depth, z_i (m), the thickness of each layer, Δz_i (m), and the depths at the layer interfaces $z_{h, i}$ (m).

Table 2.3: Soil layer structure

Layer	z_i	Δz_i	$z_{h,i}$
1	0.010	0.020	0.020
2	0.040	0.040	0.060
3	0.090	0.060	0.120
4	0.160	0.080	0.200
5	0.260	0.120	0.320
6	0.400	0.160	0.480
7	0.580	0.200	0.680
8	0.800	0.240	0.920
9	1.060	0.280	1.200
10	1.360	0.320	1.520
11	1.700	0.360	1.880
12	2.080	0.400	2.280
13	2.500	0.440	2.720
14	2.990	0.540	3.260
15	3.580	0.640	3.900
16	4.270	0.740	4.640
17	5.060	0.840	5.480
18	5.950	0.940	6.420
19	6.940	1.040	7.460
20	8.030	1.140	8.600
21	9.795	2.390	10.990
22	13.328	4.676	15.666
23	19.483	7.635	23.301
24	28.871	11.140	34.441
25	41.998	15.115	49.556

Layer node depth (z_i), thickness (Δz_i), and depth at layer interface ($z_{h,i}$) for default soil column. All in meters.

2.2.2 Depth to Bedrock

The hydrologically and biogeochemically active portion of the soil column can be restricted to a thickness less than that of the maximum soil depth. By providing a depth-to-bedrock dataset, which may vary spatially, the number of layers used in the hydrologic and biogeochemical calculations, $N_{bedrock}$, may be specified, subject to the constraint $N_{bedrock} \leq N_{levsoi}$. The default depth-to-bedrock values are from *Pelletier et al. [2016]*.

2.3 Model Input Requirements

2.3.1 Atmospheric Coupling

The current state of the atmosphere (Table 2.4) at a given time step is used to force the land model. This atmospheric state is provided by an atmospheric model in coupled mode or from an observed dataset in land-only mode (Chapter 33). The land model then initiates a full set of calculations for surface energy, constituent, momentum, and radiative fluxes. The land model calculations are implemented in two steps. The land model proceeds with the calculation of surface energy, constituent, momentum, and radiative fluxes using the snow and soil hydrologic states from the previous time step. The land model then updates the soil and snow hydrology calculations based on these fluxes. These fields are passed to the atmosphere (Table 2.5). The albedos sent to the atmosphere are for the solar zenith angle at the next time step but with surface conditions from the current time step.

Table 2.4: Atmospheric input to land model

Field	variable name	units
[1]Reference height	z'_{atm}	m
Atmosphere model's surface height	$z_{surf,atm}$	m
Zonal wind at z_{atm}	u_{atm}	m s^{-1}
Meridional wind at z_{atm}	v_{atm}	m s^{-1}
Potential temperature	$\overline{\theta_{atm}}$	K
Specific humidity at z_{atm}	q_{atm}	kg kg^{-1}
Pressure at z_{atm}	P_{atm}	Pa
Temperature at z_{atm}	T_{atm}	K
Incident longwave radiation	$L_{atm}\downarrow$	W m^{-2}
[2]Liquid precipitation	q_{rain}	mm s^{-1}
[2]Solid precipitation	q_{sno}	mm s^{-1}
Incident direct beam visible solar radiation	$S_{atm}\downarrow_{vis}^{\mu}$	W m^{-2}
Incident direct beam near-infrared solar radiation	$S_{atm}\downarrow_{nir}^{\mu}$	W m^{-2}
Incident diffuse visible solar radiation	$S_{atm}\downarrow_{vis}$	W m^{-2}
Incident diffuse near-infrared solar radiation	$S_{atm}\downarrow_{nir}$	W m^{-2}
Carbon dioxide (CO_2) concentration	c_a	ppmv
[3]Aerosol deposition rate	D_{sp}	kg m^{-2} s^{-1}
[4]Nitrogen deposition rate	NF_{ndep_sminn}	g (N) m^{-2} yr^{-1}
[5]Lightning frequency	I_l	flash km^{-2} hr^{-1}

[1]The atmospheric reference height received from the atmospheric model z'_{atm} is assumed to be the height above the surface as defined by the roughness length z_0 plus displacement height d. Thus, the reference height used for flux computations (Chapter 5) is $z_{atm} = z'_{atm} + z_0 + d$. The reference heights for temperature, wind, and specific humidity ($z_{atm,\,h}$, $z_{atm,\,m}$, $z_{atm,\,w}$) are required. These are set equal to z_{atm} .

[2]CAM provides convective and large-scale liquid and solid precipitation, which are added to yield total liquid precipitation q_{rain} and solid precipitation q_{sno} . However, in CLM5, the atmosphere's partitioning into liquid and solid precipitation is ignored. Instead, CLM repartitions total precipitation using a linear ramp. For most landunits, this ramp generates all snow below $0C$, all rain above $2C$, and a mix of rain and snow for intermediate temperatures. For glaciers, the end points of the ramp are $-2C$ and $0C$, respectively. Changes to the phase of precipitation are accompanied by a sensible heat flux (positive or negative) to conserve energy.

[3]There are 14 aerosol deposition rates required depending on species and affinity for bonding with water; 8 of these are dust deposition rates (dry and wet rates for 4 dust size bins, $D_{dst,\,dry1}$, $D_{dst,\,dry2}$, $D_{dst,\,dry3}$, $D_{dst,\,dry4}$, $D_{dst,\,wet1}$, $D_{dst,\,wet2}$, $D_{dst,wet3}$, $D_{dst,wet4}$), 3 are black carbon deposition rates (dry and wet hydrophilic and dry hydrophobic rates, $D_{bc,\,dryhphil}$, $D_{bc,\,wethphil}$, $D_{bc,\,dryhphob}$), and 3 are organic carbon deposition rates (dry and wet hydrophilic and dry hydrophobic rates, $D_{oc,\,dryhphil}$, $D_{oc,\,wethphil}$, $D_{oc,\,dryhphob}$). These fluxes are computed interactively by the atmospheric model (when prognostic aerosol representation is active) or are prescribed from a time-varying (annual cycle or transient), globally-gridded deposition file defined in the namelist (see the CLM4.5 User's Guide). Aerosol deposition rates were calculated in a transient 1850-2009 CAM simulation (at a resolution of 1.9x2.5x26L) with interactive chemistry (troposphere and stratosphere) driven by CCSM3 20th century sea-surface temperatures and emissions (*Lamarque et al. 2010*) for short-lived gases and aerosols; observed concentrations were specified for methane, N_2O, the ozone-depleting substances (CFCs) ,and CO_2. The fluxes are used by the snow-related parameterizations (Chapters 3 and 8).

[4]The nitrogen deposition rate is required by the biogeochemistry model when active and represents the total deposition of mineral nitrogen onto the land surface, combining deposition of NO$_y$ and NH$_x$. The rate is supplied either as a time-invariant spatially-varying annual mean rate or time-varying for a transient simulation. Nitrogen deposition rates were calculated from the same CAM chemistry simulation that generated the aerosol deposition rates.

[5]Climatological 3-hourly lightning frequency at ~1.8º resolution is provided, which was calculated via bilinear interpolation from 1995-2011 NASA LIS/OTD grid product v2.2 (http://ghrc.msfc.nasa.gov) 2-hourly, 2.5º lightning

frequency data. In future versions of the model, lightning data may be obtained directly from the atmosphere model.

Density of air (ρ_{atm}) (kg m^{-3}) is also required but is calculated directly from $\rho_{atm} = \frac{P_{atm} - 0.378 e_{atm}}{R_{da} T_{atm}}$ where P_{atm} is atmospheric pressure (Pa), e_{atm} is atmospheric vapor pressure (Pa), R_{da} is the gas constant for dry air (J kg^{-1} K^{-1}) (Table 2.7), and T_{atm} is the atmospheric temperature (K). The atmospheric vapor pressure e_{atm} is derived from atmospheric specific humidity q_{atm} (kg kg^{-1}) as $e_{atm} = \frac{q_{atm} P_{atm}}{0.622 + 0.378 q_{atm}}$.

The O$_2$ partial pressure (Pa) is required but is calculated from molar ratio and the atmospheric pressure P_{atm} as $o_i = 0.209 P_{atm}$.

Table 2.5: Land model output to atmospheric model

Field	Variable name	units
[1]Latent heat flux	$\lambda_{vap} E_v + \lambda E_g$	W m^{-2}
Sensible heat flux	$H_v + H_g$	W m^{-2}
Water vapor flux	$E_v + E_g$	mm s^{-1}
Zonal momentum flux	τ_x	kg m^{-1} s^{-2}
Meridional momentum flux	τ_y	kg m^{-1} s^{-2}
Emitted longwave radiation	$L \uparrow$	W m^{-2}
Direct beam visible albedo	$I \uparrow_{vis}^{\mu}$	•
Direct beam near-infrared albedo	$I \uparrow_{nir}^{\mu}$	•
Diffuse visible albedo	$I \uparrow_{vis}$	•
Diffuse near-infrared albedo	$I \uparrow_{nir}$	•
Absorbed solar radiation	$\vec{S}$	W m^{-2}
Radiative temperature	T_{rad}	K
Temperature at 2 meter height	T_{2m}	K
Specific humidity at 2 meter height	q_{2m}	kg kg^{-1}
Wind speed at 10 meter height	u_{10m}	m s^{-1}
Snow water equivalent	W_{sno}	m
Aerodynamic resistance	r_{am}	s m^{-1}
Friction velocity	u_*	m s^{-1}
[2]Dust flux	F_j	kg m^{-2} s^{-1}
Net ecosystem exchange	NEE	kgCO$_2$ m^{-2} s^{-1}

[1]λ_{vap} is the latent heat of vaporization (J kg^{-1}) (Table 2.7) and λ is either the latent heat of vaporization λ_{vap} or latent heat of sublimation λ_{sub} (J kg^{-1}) (Table 2.7) depending on the liquid water and ice content of the top snow/soil layer (section 5.4).

[2]There are $j = 1, \ldots, 4$ dust transport bins.

2.3.2 Initialization

Initialization of the land model (i.e., providing the model with initial temperature and moisture states) depends on the type of run (startup or restart) (see the CLM4.5 User's Guide). A startup run starts the model from either initial conditions that are set internally in the Fortran code (referred to as arbitrary initial conditions) or from an initial conditions dataset that enables the model to start from a spun up state (i.e., where the land is in equilibrium with the simulated climate). In restart runs, the model is continued from a previous simulation and initialized from a restart file that ensures that the output is bit-for-bit the same as if the previous simulation had not stopped. The fields that are

required from the restart or initial conditions files can be obtained by examining the code. Arbitrary initial conditions are specified as follows.

Soil points are initialized with surface ground temperature T_g and soil layer temperature T_i , for $i = 1, \ldots, N_{levgrnd}$, of 274 K, vegetation temperature T_v of 283 K, no snow or canopy water ($W_{sno} = 0$, $W_{can} = 0$), and volumetric soil water content $\theta_i = 0.15$ mm^3 mm^{-3} for layers $i = 1, \ldots, N_{levsoi}$ and $\theta_i = 0.0$ mm^3 mm^{-3} for layers $i = N_{levsoi} + 1, \ldots, N_{levgrnd}$. placeLake temperatures (T_g and T_i) are initialized at 277 K and $W_{sno} = 0$.

Glacier temperatures ($T_g = T_{snl+1}$ and T_i for $i = snl + 1, \ldots, N_{levgrnd}$ where snl is the negative of the number of snow layers, i.e., snl ranges from –5 to 0) are initialized to 250 K with a snow water equivalent $W_{sno} = 1000$ mm, snow depth $z_{sno} = \frac{W_{sno}}{\rho_{sno}}$ (m) where $\rho_{sno} = 250$ kg m^{-3} is an initial estimate for the bulk density of snow, and $\theta_i = 1.0$ for $i = 1, \ldots, N_{levgrnd}$. The snow layer structure (e.g., number of snow layers snl and layer thickness) is initialized based on the snow depth (section 6.1). The snow liquid water and ice contents (kg m^{-2}) are initialized as $w_{liq, i} = 0$ and $w_{ice, i} = \Delta z_i \rho_{sno}$, respectively, where $i = snl + 1, \ldots, 0$ are the snow layers, and Δz_i is the thickness of snow layer i (m). The soil liquid water and ice contents are initialized as $w_{liq, i} = 0$ and $w_{ice, i} = \Delta z_i \rho_{ice} \theta_i$ for $T_i \leq T_f$, and $w_{liq, i} = \Delta z_i \rho_{liq} \theta_i$ and $w_{ice, i} = 0$ for $T_i > T_f$, where ρ_{ice} and ρ_{liq} are the densities of ice and liquid water (kg m^{-3}) (Table 2.7), and T_f is the freezing temperature of water (K) (Table 2.7). All vegetated and glacier land units are initialized with water stored in the unconfined aquifer and unsaturated soil $W_a = 4000$ mm and water table depth z_∇ at five meters below the soil column.

2.3.3 Surface Data

Required surface data for each land grid cell are listed in Table 2.6 and include the glacier, lake, and urban fractions of the grid cell (vegetated and crop occupy the remainder), the fractional cover of each plant functional type (PFT), monthly leaf and stem area index and canopy top and bottom heights for each PFT, soil color, soil texture, soil organic matter density, maximum fractional saturated area, slope, elevation, biogenic volatile organic compounds (BVOCs) emissions factors, population density, gross domestic production, peat area fraction, and peak month of agricultural burning. Optional surface data include crop irrigation and managed crops. All fields are aggregated to the model's grid from high-resolution input datasets (Table 2.6) that are obtained from a variety of sources described below.

Table 2.6: Surface data required for CLM and their base spatial resolution

Surface Field	Resolution
Percent glacier	0.05º
Percent lake and lake depth	0.05º
Percent urban	0.05º
Percent plant functional types (PFTs)	0.05º
Monthly leaf and stem area index	0.5º
Canopy height (top, bottom)	0.5º
Soil color	0.5º
Percent sand, percent clay	0.083º
Soil organic matter density	0.083º
Maximum fractional saturated area	0.125º
Elevation	1km
Slope	1km
Biogenic Volatile Organic Compounds	0.5º
Crop Irrigation	0.083º
Managed crops	0.5º
Population density	0.5º
Gross domestic production	0.5º
Peat area fraction	0.5º
Peak month of agricultural waste burning	0.5º

At the base spatial resolution of 0.05º, the percentage of each PFT is defined with respect to the vegetated portion of the grid cell and the sum of the PFTs is 100%. The percent lake, glacier, and urban at their base resolution are specified with respect to the entire grid cell. The surface dataset creation routines re-adjust the PFT percentages to ensure that the sum of all land cover types in the grid cell sum to 100%. A minimum threshold of 0.1% of the grid cell by area is required for urban areas.

The percentage glacier mask was derived from vector data of global glacier and ice sheet spatial coverage. Vector data for glaciers (ice caps, icefields and mountain glaciers) were taken from the first globally complete glacier inventory, the Randolph Glacier Inventory version 1.0 (RGIv1.0: *Arendt et al. 2012*). Vector data for the Greenland Ice Sheet were provided by Frank Paul and Tobias Bolch (University of Zurich: *Rastner et al. 2012*). Antarctic Ice Sheet data were provided by Andrew Bliss (University of Alaska) and were extracted from the Scientific Committee on Antarctic Research (SCAR) Antarctic Digital Database version 5.0. Floating ice is only provided for the Antarctic and does not include the small area of Arctic ice shelves. High spatial resolution vector data were then processed to determine the area of glacier, ice sheet and floating ice within 30-second grid cells globally. The 30-second glacier, ice sheet and Antarctic ice shelf masks were subsequently draped over equivalent-resolution GLOBE topography (Global Land One-km Base Elevation Project, Hastings et al. 1999) to extract approximate ice-covered elevations of ice-covered regions. Grid cells flagged as land-ice in the mask but ocean in GLOBE (typically, around ice sheets at high latitudes) were designated land-ice with an elevation of 0 meters. Finally, the high-resolution mask/topography datasets were aggregated and processed into three 3-minute datasets: 3-minute fractional areal land ice coverage (including both glaciers and ice sheets); 3-minute distributions of areal glacier fractional coverage by elevation and areal ice sheet fractional coverage by elevation. Ice fractions were binned at 100 meter intervals, with bin edges defined from 0 to 6000 meters (plus one top bin encompassing all remaining high-elevation ice, primarily in the Himalaya). These distributions by elevation are used to divide each glacier land unit into columns based on elevation class.

When running with the CISM ice sheet model, CISM dictates glacier areas and elevations in its domain, overriding the values specified by CLM's datasets. In typical CLM5 configurations, this means that CISM dictates glacier areas and elevations over Greenland.

Percent lake and lake depth are area-averaged from the 90-second resolution data of *Kourzeneva (2009, 2010)* to the 0.05º resolution using the MODIS land-mask. Percent urban is derived from LandScan 2004, a population density dataset derived from census data, nighttime lights satellite observations, road proximity and slope (*Dobson et al. 2000*) as described by *Jackson et al. (2010)* at 1km resolution and aggregated to 0.05º. A number of urban radiative, thermal, and morphological fields are also required and are obtained from *Jackson et al. (2010)*. Their description can be found in Table 3 of the Community Land Model Urban (CLMU) technical note (*Oleson et al. 2010b*).

Percent PFTs are derived from MODIS satellite data as described in *Lawrence and Chase (2007)* (section 21.3.3). Prescribed PFT leaf area index is derived from the MODIS satellite data of *Myneni et al. (2002)* using the de-aggregation methods described in *Lawrence and Chase (2007)* (section 2.2.3). Prescribed PFT stem area index is derived from PFT leaf area index phenology combined with the methods of *Zeng et al. (2002)*. Prescribed canopy top and bottom heights are from *Bonan (1996)* as described in *Bonan et al. (2002b)*. If the biogeochemistry model is active, it supplies the leaf and stem area index and canopy top and bottom heights dynamically, and the prescribed values are ignored.

Soil color determines dry and saturated soil albedo (section 3.2). Soil colors are from *Lawrence and Chase (2007)*.

The soil texture and organic matter content determine soil thermal and hydrologic properties (sections 6.3 and 7.4.1). The International Geosphere-Biosphere Programme (IGBP) soil dataset (Global Soil Data Task 2000) of 4931 soil mapping units and their sand and clay content for each soil layer were used to create a mineral soil texture dataset *(Bonan et al. 2002b)*. Soil organic matter data is merged from two sources. The majority of the globe is from ISRIC-WISE (*Batjes, 2006*). The high latitudes come from the 0.25º version of the Northern Circumpolar Soil Carbon Database (*Hugelius et al. 2012*). Both datasets report carbon down to 1m depth. Carbon is partitioned across the top seven CLM4 layers (∼1m depth) as in *Lawrence and Slater (2008)*.

The maximum fractional saturated area ($f_{\max}$) is used in determining surface runoff and infiltration (section 7.3). Maximum fractional saturated area at 0.125º resolution is calculated from 1-km compound topographic indices (CTIs) based on the USGS HYDRO1K dataset (*Verdin and Greenlee 1996*) following the algorithm in *Niu et al. (2005)*. $f_{\max}$ is the ratio between the number of 1-km pixels with CTIs equal to or larger than the mean CTI and the total number

of pixels in a 0.125° grid cell. See section 7.3.1 and *Li et al. (2013b)* for further details. Slope and elevation are also obtained from the USGS HYDRO1K 1-km dataset (*Verdin and Greenlee 1996*). Slope is used in the surface water parameterization (section 7.2.2), and elevation is used to calculate the grid cell standard deviation of topography for the snow cover fraction parameterization (section 8.1).

Biogenic Volatile Organic Compounds emissions factors are from the Model of Emissions of Gases and Aerosols from Nature version 2.1 (MEGAN2.1; *Guenther et al. 2012*).

The default list of PFTs includes an unmanaged crop treated as a second C3 grass (Table 2.1). The unmanaged crop has grid cell fractional cover assigned from MODIS satellite data (*Lawrence and Chase (2007)*). A managed crop option uses grid cell fractional cover from the present-day crop dataset of *Ramankutty and Foley (1998)* (CLM4CNcrop). Managed crops are assigned in the proportions given by *Ramankutty and Foley (1998)* without exceeding the area previously assigned to the unmanaged crop. The unmanaged crop continues to occupy any of its original area that remains and continues to be handled just by the CN part of CLM4CNcrop. The managed crop types (corn, soybean, and temperate cereals) were chosen based on the availability of corresponding algorithms in AgroIBIS (*Kucharik et al. 2000*; *Kucharik and Brye 2003*). Temperate cereals include wheat, barley, and rye here. All temperate cereals are treated as summer crops (like spring wheat, for example) at this time. Winter cereals (such as winter wheat) may be introduced in a future version of the model.

To allow crops to coexist with natural vegetation in a grid cell and be treated by separate models (i.e., CLM4.5BGCcrop versus the Dynamic Vegetation version (CLM4.5BGCDV)), we separate the vegetated land unit into a naturally vegetated land unit and a human managed land unit. PFTs in the naturally vegetated land unit share one soil column and compete for water (default CLM setting). PFTs in the human managed land unit do not share soil columns and thus permit for differences in land management between crops.

CLM includes the option to irrigate cropland areas that are equipped for irrigation. The application of irrigation responds dynamically to climate (see Chapter 26). In CLM, irrigation is implemented for the C3 generic crop only. When irrigation is enabled, the cropland area of each grid cell is divided into an irrigated and unirrigated fraction according to a dataset of areas equipped for irrigation (*Siebert et al. (2005)*). The area of irrigated cropland in each grid cell is given by the smaller of the grid cell's total cropland area, according to the default CLM4 dataset, and the grid cell's area equipped for irrigation. The remainder of the grid cell's cropland area (if any) is then assigned to unirrigated cropland. Irrigated and unirrigated crops are placed on separate soil columns, so that irrigation is only applied to the soil beneath irrigated crops.

Several input datasets are required for the fire model (*Li et al. 2013a*) including population density, gross domestic production, peat area fraction, and peak month of agricultural waste burning. Population density at 0.5° resolution for 1850-2100 combines 5-min resolution decadal population density data for 1850–1980 from the Database of the Global Environment version 3.1 (HYDEv3.1) with 0.5° resolution population density data for 1990, 1995, 2000, and 2005 from the Gridded Population of the World version 3 dataset (GPWv3) (CIESIN, 2005). Gross Domestic Production (GDP) per capita in 2000 at 0.5° is from *Van Vuuren et al. (2006)*, which is the base-year GDP data for IPCC-SRES and derived from country-level World Bank's World Development Indicators (WDI) measured in constant 1995 US$ (*World Bank, 2004*) and the UN Statistics Database (*UNSTAT, 2005*). The peatland area fraction at 0.5° resolution is derived from three vector datasets: peatland data in Indonesia and Malaysian Borneo (*Olson et al. 2001*); peatland data in Canada (*Tarnocai et al. 2011*); and bog, fen and mire data in boreal regions (north of 45°N) outside Canada provided by the Global Lakes and Wetlands Database (GLWD) (*Lehner and Döll, 2004*). The climatological peak month for agricultural waste burning is from *van der Werf et al. (2010)*.

2.3.4 Adjustable Parameters and Physical Constants

Values of certain adjustable parameters inherent in the biogeophysical or biogeochemical parameterizations have either been obtained from the literature or calibrated based on comparisons with observations. These are described in the text. Physical constants, generally shared by all of the components in the coupled modeling system, are presented in Table 2.7.

Table 2.7: Physical constants

description	name	value	units
Pi	π	3.14159265358979323846	
Acceleration of gravity	g	9.80616	m s^{-2}
Standard pressure	P_{std}	101325	Pa
Stefan-Boltzmann constant	σ	5.67×10^{-8}	W m^{-2} K^{-4}
Boltzmann constant	κ	1.38065×10^{-23}	J K^{-1} molecule^{-1}
Avogadro's number	N_A	6.02214×10^{26}	molecule kmol^{-1}
Universal gas constant	R_{gas}	$N_A \kappa$	J K^{-1} kmol^{-1}
Molecular weight of dry air	MW_{da}	28.966	kg kmol^{-1}
Dry air gas constant	R_{da}	R_{gas}/MW_{da}	J K^{-1} kg^{-1}
Molecular weight of water vapor	MW_{wv}	18.016	kg kmol^{-1}
Water vapor gas constant	R_{wv}	R_{gas}/MW_{wv}	J K^{-1} kg^{-1}
Von Karman constant	k	0.4	-
Freezing temperature of fresh water	T_f	273.15	K
Density of liquid water	ρ_{liq}	1000	kg m^{-3}
Density of ice	ρ_{ice}	917	kg m^{-3}
Specific heat capacity of dry air	C_p	1.00464×10^3	J kg^{-1} K^{-1}
Specific heat capacity of water	C_{liq}	4.188×10^3	J kg^{-1} K^{-1}
Specific heat capacity of ice	C_{ice}	2.11727×10^3	J kg^{-1} K^{-1}
Latent heat of vaporization	λ_{vap}	2.501×10^6	J kg^{-1}
Latent heat of fusion	L_f	3.337×10^5	J kg^{-1}
Latent heat of sublimation	λ_{sub}	$\lambda_{vap} + L_f$	J kg^{-1}
[1] "Thermal conductivity of water"	λ_{liq}	0.57	W m^{-1} K^{-1}
[1] "Thermal conductivity of ice"	λ_{ice}	2.29	W m^{-1} K^{-1}
[1] "Thermal conductivity of air"	λ_{air}	0.023 W m^{-1} K^{-1}	
Radius of the earth	R_e	6.37122	$\times 10^6$ m

[1]Not shared by other components of the coupled modeling system.

CHAPTER 3

SURFACE ALBEDOS

3.1 Canopy Radiative Transfer

Radiative transfer within vegetative canopies is calculated from the two-stream approximation of *Dickinson (1983)* and *Sellers (1985)* as described by *Bonan (1996)*

$$-\bar{\mu}\frac{dI\uparrow}{d\left(L+S\right)} + \left[1-\left(1-\beta\right)\omega\right]I\uparrow -\omega\beta I\downarrow = \omega\bar{\mu}K\beta_0 e^{-K(L+S)} \tag{3.1}$$

$$\bar{\mu}\frac{dI\downarrow}{d\left(L+S\right)} + \left[1-\left(1-\beta\right)\omega\right]I\downarrow -\omega\beta I\uparrow = \omega\bar{\mu}K\left(1-\beta_0\right)e^{-K(L+S)} \tag{3.2}$$

where $I\uparrow$ and $I\downarrow$ are the upward and downward diffuse radiative fluxes per unit incident flux, $K = G\left(\mu\right)/\mu$ is the optical depth of direct beam per unit leaf and stem area, μ is the cosine of the zenith angle of the incident beam, $G\left(\mu\right)$ is the relative projected area of leaf and stem elements in the direction $\cos^{-1}\mu$, $\bar{\mu}$ is the average inverse diffuse optical depth per unit leaf and stem area, ω is a scattering coefficient, β and β_0 are upscatter parameters for diffuse and direct beam radiation, respectively, L is the exposed leaf area index, and S is the exposed stem area index (section 2.1.4). Given the direct beam albedo $\alpha_{g,\Lambda}^{\mu}$ and diffuse albedo $\alpha_{g,\Lambda}$ of the ground (section 3.2), these equations are solved to calculate the fluxes, per unit incident flux, absorbed by the vegetation, reflected by the vegetation, and transmitted through the vegetation for direct and diffuse radiation and for visible ($< 0.7\mu$m) and near-infrared ($\geq 0.7\mu$m) wavebands. The absorbed radiation is partitioned to sunlit and shaded fractions of the canopy. The optical parameters $G\left(\mu\right)$, $\bar{\mu}$, ω, β, and β_0 are calculated based on work in *Sellers (1985)* as follows.

The relative projected area of leaves and stems in the direction $\cos^{-1}\mu$ is

$$G\left(\mu\right) = \phi_1 + \phi_2\mu \tag{3.3}$$

where $\phi_1 = 0.5 - 0.633\chi_L - 0.33\chi_L^2$ and $\phi_2 = 0.877\left(1-2\phi_1\right)$ for $-0.4 \leq \chi_L \leq 0.6$. χ_L is the departure of leaf angles from a random distribution and equals +1 for horizontal leaves, 0 for random leaves, and –1 for vertical leaves.

The average inverse diffuse optical depth per unit leaf and stem area is

$$\bar{\mu} = \int_0^1 \frac{\mu'}{G\left(\mu'\right)}d\mu' = \frac{1}{\phi_2}\left[1 - \frac{\phi_1}{\phi_2}\ln\left(\frac{\phi_1+\phi_2}{\phi_1}\right)\right] \tag{3.4}$$

where μ' is the direction of the scattered flux.

The optical parameters ω, β, and β_0, which vary with wavelength (Λ), are weighted combinations of values for vegetation and snow, using the canopy snow-covered fraction $f_{can,\,sno}$ (Chapter 7). The optical parameters are

$$\omega_\Lambda = \omega_\Lambda^{veg}\left(1 - f_{can,\,sno}\right) + \omega_\Lambda^{sno} f_{can,\,sno} \tag{3.5}$$

$$\omega_\Lambda\beta_\Lambda = \omega_\Lambda^{veg}\beta_\Lambda^{veg}\left(1 - f_{can,\,sno}\right) + \omega_\Lambda^{sno}\beta_\Lambda^{sno} f_{can,\,sno} \tag{3.6}$$

$$\omega_\Lambda\beta_{0,\,\Lambda} = \omega_\Lambda^{veg}\beta_{0,\,\Lambda}^{veg}\left(1 - f_{can,\,sno}\right) + \omega_\Lambda^{sno}\beta_{0,\,\Lambda}^{sno} f_{can,\,sno} \tag{3.7}$$

The snow and vegetation weights are applied to the products $\omega_\Lambda\beta_\Lambda$ and $\omega_\Lambda\beta_{0,\,\Lambda}$ because these products are used in the two-stream equations. If there is no snow on the canopy, this reduces to

$$\omega_\Lambda = \omega_\Lambda^{veg} \tag{3.8}$$

$$\omega_\Lambda\beta_\Lambda = \omega_\Lambda^{veg}\beta_\Lambda^{veg} \tag{3.9}$$

$$\omega_\Lambda\beta_{0,\,\Lambda} = \omega_\Lambda^{veg}\beta_{0,\,\Lambda}^{veg}. \tag{3.10}$$

For vegetation, $\omega_\Lambda^{veg} = \alpha_\Lambda + \tau_\Lambda$. α_Λ is a weighted combination of the leaf and stem reflectances ($\alpha_\Lambda^{leaf}, \alpha_\Lambda^{stem}$)

$$\alpha_\Lambda = \alpha_\Lambda^{leaf} w_{leaf} + \alpha_\Lambda^{stem} w_{stem} \tag{3.11}$$

where $w_{leaf} = L/\left(L + S\right)$ and $w_{stem} = S/\left(L + S\right)$. τ_Λ is a weighted combination of the leaf and stem transmittances ($\tau_\Lambda^{leaf}, \tau_\Lambda^{stem}$)

$$\tau_\Lambda = \tau_\Lambda^{leaf} w_{leaf} + \tau_\Lambda^{stem} w_{stem}. \tag{3.12}$$

The upscatter for diffuse radiation is

$$\omega_\Lambda^{veg}\beta_\Lambda^{veg} = \frac{1}{2}\left[\alpha_\Lambda + \tau_\Lambda + \left(\alpha_\Lambda - \tau_\Lambda\right)\cos^2\bar\theta\right] \tag{3.13}$$

where $\bar\theta$ is the mean leaf inclination angle relative to the horizontal plane (i.e., the angle between leaf normal and local vertical) (*Sellers (1985)*). Here, $\cos\bar\theta$ is approximated by

$$\cos\bar\theta = \frac{1 + \chi_L}{2} \tag{3.14}$$

Using this approximation, for vertical leaves ($\chi_L = -1, \bar\theta = 90^\circ$), $\omega_\Lambda^{veg}\beta_\Lambda^{veg} = 0.5\left(\alpha_\Lambda + \tau_\Lambda\right)$, and for horizontal leaves ($\chi_L = 1, \bar\theta = 0^\circ$) , $\omega_\Lambda^{veg}\beta_\Lambda^{veg} = \alpha_\Lambda$, which agree with both *Dickinson (1983)* and *Sellers (1985)*. For random (spherically distributed) leaves ($\chi_L = 0, \bar\theta = 60^\circ$), the approximation yields $\omega_\Lambda^{veg}\beta_\Lambda^{veg} = 5/8\alpha_\Lambda + 3/8\tau_\Lambda$ whereas the approximate solution of *Dickinson (1983)* is $\omega_\Lambda^{veg}\beta_\Lambda^{veg} = 2/3\alpha_\Lambda + 1/3\tau_\Lambda$. This discrepancy arises from the fact that a spherical leaf angle distribution has a true mean leaf inclination $\bar\theta \approx 57$ *(Campbell and Norman 1998)* in equation , while $\bar\theta = 60$ in equation . The upscatter for direct beam radiation is

$$\omega_\Lambda^{veg}\beta_{0,\,\Lambda}^{veg} = \frac{1 + \bar\mu K}{\bar\mu K} a_s\left(\mu\right)_\Lambda \tag{3.15}$$

where the single scattering albedo is

$$\begin{aligned} a_s\left(\mu\right)_\Lambda &= \frac{\omega_\Lambda^{veg}}{2}\int_0^1\frac{\mu' G(\mu)}{\mu G(\mu') + \mu' G(\mu)}d\mu'\\ &= \frac{\omega_\Lambda^{veg}}{2}\frac{G(\mu)}{\min(\mu\phi_2 + G(\mu), 1e-6)}\left[1 - \frac{\mu\phi_1}{\min(\mu\phi_2 + G(\mu), 1e-6)}\ln\left(\frac{\mu\phi_1 + \min(\mu\phi_2 + G(\mu), 1e-6)}{\mu\phi_1}\right)\right]. \end{aligned} \tag{3.16}$$

Note here the restriction on $\mu\phi_2 + G\left(\mu\right)$. We have seen cases where small values can cause unrealistic single scattering albedo associated with the log calculation, thereby eventually causing a negative soil albedo.

The upward diffuse fluxes per unit incident direct beam and diffuse flux (i.e., the surface albedos) are

$$I\uparrow_\Lambda^\mu = \frac{h_1}{\sigma} + h_2 + h_3 \tag{3.17}$$

$$I \uparrow_\Lambda = h_7 + h_8. \tag{3.18}$$

The downward diffuse fluxes per unit incident direct beam and diffuse radiation, respectively, are

$$I \downarrow_\Lambda^\mu = \frac{h_4}{\sigma} e^{-K(L+S)} + h_5 s_1 + \frac{h_6}{s_1} \tag{3.19}$$

$$I \downarrow_\Lambda = h_9 s_1 + \frac{h_{10}}{s_1}. \tag{3.20}$$

With reference to Figure 4.1, the direct beam flux transmitted through the canopy, per unit incident flux, is $e^{-K(L+S)}$, and the direct beam and diffuse fluxes absorbed by the vegetation, per unit incident flux, are

$$\vec{I}_\Lambda^\mu = 1 - I \uparrow_\Lambda^\mu - (1 - \alpha_{g,\Lambda}) I \downarrow_\Lambda^\mu - \left(1 - \alpha_{g,\Lambda}^\mu \right) e^{-K(L+S)} \tag{3.21}$$

$$\vec{I}_\Lambda = 1 - I \uparrow_\Lambda - (1 - \alpha_{g,\Lambda}) I \downarrow_\Lambda . \tag{3.22}$$

These fluxes are partitioned to the sunlit and shaded canopy using an analytical solution to the two-stream approximation for sunlit and shaded leaves *(Dai et al. 2004)*, as described by *Bonan et al. (2011)*. The absorption of direct beam radiation by sunlit leaves is

$$\vec{I}_{sun,\Lambda}^\mu = (1 - \omega_\Lambda) \left[1 - s_2 + \frac{1}{\bar{\mu}} (a_1 + a_2) \right] \tag{3.23}$$

and for shaded leaves is

$$\vec{I}_{sha,\Lambda}^\mu = \vec{I}_\Lambda^\mu - \vec{I}_{sun,\Lambda}^\mu \tag{3.24}$$

with

$$a_1 = \frac{h_1}{\sigma} \left[\frac{1 - s_2^2}{2K} \right] + h_2 \left[\frac{1 - s_2 s_1}{K + h} \right] + h_3 \left[\frac{1 - s_2/s_1}{K - h} \right] \tag{3.25}$$

$$a_2 = \frac{h_4}{\sigma} \left[\frac{1 - s_2^2}{2K} \right] + h_5 \left[\frac{1 - s_2 s_1}{K + h} \right] + h_6 \left[\frac{1 - s_2/s_1}{K - h} \right]. \tag{3.26}$$

For diffuse radiation, the absorbed radiation for sunlit leaves is

$$\vec{I}_{sun,\Lambda} = \left[\frac{1 - \omega_\Lambda}{\bar{\mu}} \right] (a_1 + a_2) \tag{3.27}$$

and for shaded leaves is

$$\vec{I}_{sha,\Lambda} = \vec{I}_\Lambda - \vec{I}_{sun,\Lambda} \tag{3.28}$$

with

$$a_1 = h_7 \left[\frac{1 - s_2 s_1}{K + h} \right] + h_8 \left[\frac{1 - s_2/s_1}{K - h} \right] \tag{3.29}$$

$$a_2 = h_9 \left[\frac{1 - s_2 s_1}{K + h} \right] + h_{10} \left[\frac{1 - s_2/s_1}{K - h} \right]. \tag{3.30}$$

The parameters h_1–h_{10}, σ, h, s_1, and s_2 are from *Sellers (1985)* [note the error in h_4 in *Sellers (1985)*]:

$$b = 1 - \omega_\Lambda + \omega_\Lambda \beta_\Lambda \tag{3.31}$$

$$c = \omega_\Lambda \beta_\Lambda \tag{3.32}$$

$$d = \omega_\Lambda \bar{\mu} K \beta_{0,\Lambda} \tag{3.33}$$

$$f = \omega_\Lambda \bar{\mu} K \left(1 - \beta_{0,\Lambda}\right) \tag{3.34}$$

$$h = \frac{\sqrt{b^2 - c^2}}{\bar{\mu}} \tag{3.35}$$

$$\sigma = \left(\bar{\mu} K\right)^2 + c^2 - b^2 \tag{3.36}$$

$$u_1 = b - c \Big/ \alpha_{g,\Lambda}^\mu \text{ or } u_1 = b - c/\alpha_{g,\Lambda} \tag{3.37}$$

$$u_2 = b - c\alpha_{g,\Lambda}^\mu \text{ or } u_2 = b - c\alpha_{g,\Lambda} \tag{3.38}$$

$$u_3 = f + c\alpha_{g,\Lambda}^\mu \text{ or } u_3 = f + c\alpha_{g,\Lambda} \tag{3.39}$$

$$s_1 = \exp\left\{-\min\left[h\left(L + S\right), 40\right]\right\} \tag{3.40}$$

$$s_2 = \exp\left\{-\min\left[K\left(L + S\right), 40\right]\right\} \tag{3.41}$$

$$p_1 = b + \bar{\mu} h \tag{3.42}$$

$$p_2 = b - \bar{\mu} h \tag{3.43}$$

$$p_3 = b + \bar{\mu} K \tag{3.44}$$

$$p_4 = b - \bar{\mu} K \tag{3.45}$$

$$d_1 = \frac{p_1 \left(u_1 - \bar{\mu} h\right)}{s_1} - p_2 \left(u_1 + \bar{\mu} h\right) s_1 \tag{3.46}$$

$$d_2 = \frac{u_2 + \bar{\mu} h}{s_1} - \left(u_2 - \bar{\mu} h\right) s_1 \tag{3.47}$$

$$h_1 = -dp_4 - cf \tag{3.48}$$

$$h_2 = \frac{1}{d_1} \left[\left(d - \frac{h_1}{\sigma} p_3\right) \frac{\left(u_1 - \bar{\mu} h\right)}{s_1} - p_2 \left(d - c - \frac{h_1}{\sigma} \left(u_1 + \bar{\mu} K\right)\right) s_2 \right] \tag{3.49}$$

$$h_3 = \frac{-1}{d_1} \left[\left(d - \frac{h_1}{\sigma} p_3\right) \left(u_1 + \bar{\mu} h\right) s_1 - p_1 \left(d - c - \frac{h_1}{\sigma} \left(u_1 + \bar{\mu} K\right)\right) s_2 \right] \tag{3.50}$$

$$h_4 = -fp_3 - cd \tag{3.51}$$

$$h_5 = \frac{-1}{d_2} \left[\left(\frac{h_4 \left(u_2 + \bar{\mu} h\right)}{\sigma s_1}\right) + \left(u_3 - \frac{h_4}{\sigma} \left(u_2 - \bar{\mu} K\right)\right) s_2 \right] \tag{3.52}$$

$$h_6 = \frac{1}{d_2} \left[\frac{h_4}{\sigma} \left(u_2 - \bar{\mu} h\right) s_1 + \left(u_3 - \frac{h_4}{\sigma} \left(u_2 - \bar{\mu} K\right)\right) s_2 \right] \tag{3.53}$$

$$h_7 = \frac{c \left(u_1 - \bar{\mu} h\right)}{d_1 s_1} \tag{3.54}$$

$$h_8 = \frac{-c \left(u_1 + \bar{\mu} h\right) s_1}{d_1} \tag{3.55}$$

$$h_9 = \frac{u_2 + \bar{\mu} h}{d_2 s_1} \tag{3.56}$$

$$h_{10} = \frac{-s_1 \left(u_2 - \bar{\mu} h\right)}{d_2}. \tag{3.57}$$

Plant functional type optical properties (Table 3.1) for trees and shrubs are from *Dorman and Sellers (1989)*. Leaf and stem optical properties (VIS and NIR reflectance and transmittance) were derived for grasslands and crops from full optical range spectra of measured optical properties (*Asner et al. 1998*). Optical properties for intercepted snow (Table 3.2) are from *Sellers et al. (1986)*.

Table 3.1: Plant functional type optical properties

Plant Functional Type	χ_L	α_{vis}^{leaf}	α_{nir}^{leaf}	α_{vis}^{stem}	α_{nir}^{stem}	τ_{vis}^{leaf}	τ_{nir}^{leaf}	τ_{vis}^{stem}	τ_{nir}^{stem}
NET Temperate	0.01	0.07	0.35	0.16	0.39	0.05	0.10	0.001	0.001
NET Boreal	0.01	0.07	0.35	0.16	0.39	0.05	0.10	0.001	0.001
NDT Boreal	0.01	0.07	0.35	0.16	0.39	0.05	0.10	0.001	0.001
BET Tropical	0.10	0.10	0.45	0.16	0.39	0.05	0.25	0.001	0.001
BET temperate	0.10	0.10	0.45	0.16	0.39	0.05	0.25	0.001	0.001
BDT tropical	0.01	0.10	0.45	0.16	0.39	0.05	0.25	0.001	0.001
BDT temperate	0.25	0.10	0.45	0.16	0.39	0.05	0.25	0.001	0.001
BDT boreal	0.25	0.10	0.45	0.16	0.39	0.05	0.25	0.001	0.001
BES temperate	0.01	0.07	0.35	0.16	0.39	0.05	0.10	0.001	0.001
BDS temperate	0.25	0.10	0.45	0.16	0.39	0.05	0.25	0.001	0.001
BDS boreal	0.25	0.10	0.45	0.16	0.39	0.05	0.25	0.001	0.001
C_3 arctic grass	-0.30	0.11	0.35	0.31	0.53	0.05	0.34	0.120	0.250
C_3 grass	-0.30	0.11	0.35	0.31	0.53	0.05	0.34	0.120	0.250
C_4 grass	-0.30	0.11	0.35	0.31	0.53	0.05	0.34	0.120	0.250
C_3 Crop	-0.30	0.11	0.35	0.31	0.53	0.05	0.34	0.120	0.250
Temp Corn	-0.50	0.11	0.35	0.31	0.53	0.05	0.34	0.120	0.250
Spring Wheat	-0.50	0.11	0.35	0.31	0.53	0.05	0.34	0.120	0.250
Temp Soybean	-0.50	0.11	0.35	0.31	0.53	0.05	0.34	0.120	0.250
Cotton	-0.50	0.11	0.35	0.31	0.53	0.05	0.34	0.120	0.250
Rice	-0.50	0.11	0.35	0.31	0.53	0.05	0.34	0.120	0.250
Sugarcane	-0.50	0.11	0.35	0.31	0.53	0.05	0.34	0.120	0.250
Tropical Corn	-0.50	0.11	0.35	0.31	0.53	0.05	0.34	0.120	0.250
Tropical Soybean	-0.50	0.11	0.35	0.31	0.53	0.05	0.34	0.120	0.250

Table 3.2: Intercepted snow optical properties

Parameter	vis	nir
ω^{sno}	0.8	0.4
β^{sno}	0.5	0.5
β_0^{sno}	0.5	0.5

3.2 Ground Albedos

The overall direct beam $\alpha_{g,\Lambda}^{\mu}$ and diffuse $\alpha_{g,\Lambda}$ ground albedos are weighted combinations of "soil" and snow albedos

$$\alpha_{g,\Lambda}^{\mu} = \alpha_{soi,\Lambda}^{\mu} \left(1 - f_{sno}\right) + \alpha_{sno,\Lambda}^{\mu} f_{sno} \tag{3.58}$$

$$\alpha_{g,\Lambda} = \alpha_{soi,\Lambda} \left(1 - f_{sno}\right) + \alpha_{sno,\Lambda} f_{sno} \tag{3.59}$$

where f_{sno} is the fraction of the ground covered with snow (section 8.1).

$\alpha_{soi,\Lambda}^{\mu}$ and $\alpha_{soi,\Lambda}$ vary with glacier, lake, and soil surfaces. Glacier albedos are from *Paterson (1994)*

$$\alpha_{soi,vis}^{\mu} = \alpha_{soi,vis} = 0.6$$

$$\alpha_{soi,nir}^{\mu} = \alpha_{soi,nir} = 0.4.$$

Unfrozen lake albedos depend on the cosine of the solar zenith angle μ

$$\alpha_{soi,\Lambda}^{\mu} = \alpha_{soi,\Lambda} = 0.05 \left(\mu + 0.15\right)^{-1}. \tag{3.60}$$

Frozen lake albedos are from NCAR LSM (*Bonan 1996*)

$$\alpha^{\mu}_{soi,\,vis} = \alpha_{soi,\,vis} = 0.60$$

$$\alpha^{\mu}_{soi,\,nir} = \alpha_{soi,\,nir} = 0.40.$$

As in NCAR LSM (*Bonan 1996*), soil albedos vary with color class

$$\alpha^{\mu}_{soi,\,\Lambda} = \alpha_{soi,\,\Lambda} = (\alpha_{sat,\,\Lambda} + \Delta) \le \alpha_{dry,\,\Lambda} \tag{3.61}$$

where Δ depends on the volumetric water content of the first soil layer θ_1 (section 7.3) as $\Delta = 0.11 - 0.40\theta_1 > 0$, and $\alpha_{sat,\,\Lambda}$ and $\alpha_{dry,\,\Lambda}$ are albedos for saturated and dry soil color classes (Table 3.3).

CLM soil colors are prescribed so that they best reproduce observed MODIS local solar noon surface albedo values at the CLM grid cell following the methods of *Lawrence and Chase (2007)*. The soil colors are fitted over the range of 20 soil classes shown in Table 3.3 and compared to the MODIS monthly local solar noon all-sky surface albedo as described in *Strahler et al. (1999)* and *Schaaf et al. (2002)*. The CLM two-stream radiation model was used to calculate the model equivalent surface albedo using climatological monthly soil moisture along with the vegetation parameters of PFT fraction, LAI, and SAI. The soil color that produced the closest all-sky albedo in the two-stream radiation model was selected as the best fit for the month. The fitted monthly soil colors were averaged over all snow-free months to specify a representative soil color for the grid cell. In cases where there was no snow-free surface albedo for the year, the soil color derived from snow-affected albedo was used to give a representative soil color that included the effects of the minimum permanent snow cover.

Table 3.3: Dry and saturated soil albedos

Color Class	Dry vis	Dry nir	Saturated vis	Saturated nir	Color Class	Dry vis	Dry nir	Saturated vis	Saturated nir
1	0.36	0.61	0.25	0.50	11	0.24	0.37	0.13	0.26
2	0.34	0.57	0.23	0.46	12	0.23	0.35	0.12	0.24
3	0.32	0.53	0.21	0.42	13	0.22	0.33	0.11	0.22
4	0.31	0.51	0.20	0.40	14	0.20	0.31	0.10	0.20
5	0.30	0.49	0.19	0.38	15	0.18	0.29	0.09	0.18
6	0.29	0.48	0.18	0.36	16	0.16	0.27	0.08	0.16
7	0.28	0.45	0.17	0.34	17	0.14	0.25	0.07	0.14
8	0.27	0.43	0.16	0.32	18	0.12	0.23	0.06	0.12
9	0.26	0.41	0.15	0.30	19	0.10	0.21	0.05	0.10
10	0.25	0.39	0.14	0.28	20	0.08	0.16	0.04	0.08

3.2.1 Snow Albedo

Snow albedo and solar absorption within each snow layer are simulated with the Snow, Ice, and Aerosol Radiative Model (SNICAR), which incorporates a two-stream radiative transfer solution from *Toon et al. (1989)*. Albedo and the vertical absorption profile depend on solar zenith angle, albedo of the substrate underlying snow, mass concentrations of atmospheric-deposited aerosols (black carbon, mineral dust, and organic carbon), and ice effective grain size (r_e), which is simulated with a snow aging routine described in section 3.2.3. Representation of impurity mass concentrations within the snowpack is described in section 8.4. Implementation of SNICAR in CLM is also described somewhat by *Flanner and Zender (2005)* and *Flanner et al. (2007)*.

The two-stream solution requires the following bulk optical properties for each snow layer and spectral band: extinction optical depth (τ), single-scatter albedo (ω), and scattering asymmetry parameter (g). The snow layers used for radiative calculations are identical to snow layers applied elsewhere in CLM, except for the case when snow mass is greater than zero but no snow layers exist. When this occurs, a single radiative layer is specified to have the column

snow mass and an effective grain size of freshly-fallen snow (section 3.2.3). The bulk optical properties are weighted functions of each constituent k, computed for each snow layer and spectral band as

$$\tau = \sum_1^k \tau_k \tag{3.62}$$

$$\omega = \frac{\sum_1^k \omega_k \tau_k}{\sum_1^k \tau_k} \tag{3.63}$$

$$g = \frac{\sum_1^k g_k \omega_k \tau_k}{\sum_1^k \omega_k \tau_k} \tag{3.64}$$

For each constituent (ice, two black carbon species, two organic carbon species, and four dust species), ω, g, and the mass extinction cross-section ψ (m^2 kg$_{-1}$) are computed offline with Mie Theory, e.g., applying the computational technique from *Bohren and Huffman (1983)*. The extinction optical depth for each constituent depends on its mass extinction cross-section and layer mass, w_k (kgm^{-1}) as

$$\tau_k = \psi_k w_k \tag{3.65}$$

The two-stream solution (*Toon et al. (1989)*) applies a tri-diagonal matrix solution to produce upward and downward radiative fluxes at each layer interface, from which net radiation, layer absorption, and surface albedo are easily derived. Solar fluxes are computed in five spectral bands, listed in Table 3.4. Because snow albedo varies strongly across the solar spectrum, it was determined that four bands were needed to accurately represent the near-infrared (NIR) characteristics of snow, whereas only one band was needed for the visible spectrum. Boundaries of the NIR bands were selected to capture broad radiative features and maximize accuracy and computational efficiency. We partition NIR (0.7-5.0 μ m) surface downwelling flux from CLM according to the weights listed in Table 3.4, which are unique for diffuse and direct incident flux. These fixed weights were determined with offline hyperspectral radiative transfer calculations for an atmosphere typical of mid-latitude winter (*Flanner et al. (2007)*). The tri-diagonal solution includes intermediate terms that allow for easy interchange of two-stream techniques. We apply the Eddington solution for the visible band (following *Wiscombe and Warren 1980*) and the hemispheric mean solution ((*Toon et al. (1989)*) for NIR bands. These choices were made because the Eddington scheme works well for highly scattering media, but can produce negative albedo for absorptive NIR bands with diffuse incident flux. Delta scalings are applied to τ, ω, and g (*Wiscombe and Warren 1980*) in all spectral bands, producing effective values (denoted with *) that are applied in the two-stream solution

$$\tau^* = \left(1 - \omega g^2\right) \tau \tag{3.66}$$

$$\omega^* = \frac{\left(1 - g^2\right) \omega}{1 - g^2 \omega} \tag{3.67}$$

$$g^* = \frac{g}{1 + g} \tag{3.68}$$

Table 3.4: Spectral bands and weights used for snow radiative transfer

Spectral band	Direct-beam weight	Diffuse weight
Band 1: 0.3-0.7μm (visible)	(1.0)	(1.0)
Band 2: 0.7-1.0μm (near-IR)	0.494	0.586
Band 3: 1.0-1.2μm (near-IR)	0.181	0.202
Band 4: 1.2-1.5μm (near-IR)	0.121	0.109
Band 5: 1.5-5.0μm (near-IR)	0.204	0.103

Under direct-beam conditions, singularities in the radiative approximation are occasionally approached in spectral bands 4 and 5 that produce unrealistic conditions (negative energy absorption in a layer, negative albedo, or total absorbed flux greater than incident flux). When any of these three conditions occur, the Eddington approximation is

attempted instead, and if both approximations fail, the cosine of the solar zenith angle is adjusted by 0.02 (conserving incident flux) and a warning message is produced. This situation occurs in only about 1 in 10^6 computations of snow albedo. After looping over the five spectral bands, absorption fluxes and albedo are averaged back into the bulk NIR band used by the rest of CLM.

Soil albedo (or underlying substrate albedo), which is defined for visible and NIR bands, is a required boundary condition for the snow radiative transfer calculation. Currently, the bulk NIR soil albedo is applied to all four NIR snow bands. With ground albedo as a lower boundary condition, SNICAR simulates solar absorption in all snow layers as well as the underlying soil or ground. With a thin snowpack, penetrating solar radiation to the underlying soil can be quite large and heat cannot be released from the soil to the atmosphere in this situation. Thus, if the snowpack has total snow depth less than 0.1 m ($z_{sno} < 0.1$) and there are no explicit snow layers, the solar radiation is absorbed by the top soil layer. If there is a single snow layer, the solar radiation is absorbed in that layer. If there is more than a single snow layer, 75% of the solar radiation is absorbed in the top snow layer, and 25% is absorbed in the next lowest snow layer. This prevents unrealistic soil warming within a single timestep.

The radiative transfer calculation is performed twice for each column containing a mass of snow greater than 1×10^{-30} kgm^{-2} (excluding lake and urban columns); once each for direct-beam and diffuse incident flux. Absorption in each layer i of pure snow is initially recorded as absorbed flux per unit incident flux on the ground ($S_{sno,\,i}$), as albedos must be calculated for the next timestep with unknown incident flux. The snow absorption fluxes that are used for column temperature calculations are

$$S_{g,\,i} = S_{sno,\,i}\left(1 - \alpha_{sno}\right) \tag{3.69}$$

This weighting is performed for direct-beam and diffuse, visible and NIR fluxes. After the ground-incident fluxes (transmitted through the vegetation canopy) have been calculated for the current time step (sections 3.1 and 4.1), the layer absorption factors

($S_{g,\,i}$) are multiplied by the ground-incident fluxes to produce solar absorption (W m^{-2}) in each snow layer and the underlying ground.

3.2.2 Snowpack Optical Properties

Ice optical properties for the five spectral bands are derived offline and stored in a namelist-defined lookup table for online retrieval (see CLM5.0 User's Guide). Mie properties are first computed at fine spectral resolution (470 bands), and are then weighted into the five bands applied by CLM according to incident solar flux, $I^{\downarrow}(\lambda)$. For example, the broadband mass-extinction cross section ($\bar{\psi}$) over wavelength interval λ_1 to λ_2 is

$$\bar{\psi} = \frac{\int_{\lambda_1}^{\lambda_2} \psi\left(\lambda\right) I^{\downarrow}\left(\lambda\right) \mathrm{d}\lambda}{\int_{\lambda_1}^{\lambda_2} I^{\downarrow}\left(\lambda\right) \mathrm{d}\lambda} \tag{3.70}$$

Broadband single-scatter albedo ($\bar{\omega}$) is additionally weighted by the diffuse albedo for a semi-infinite snowpack (α_{sno})

$$\bar{\omega} = \frac{\int_{\lambda_1}^{\lambda_2} \omega(\lambda) I^{\downarrow}(\lambda) \alpha_{sno}(\lambda) \mathrm{d}\lambda}{\int_{\lambda_1}^{\lambda_2} I^{\downarrow}(\lambda) \alpha_{sno}(\lambda) \mathrm{d}\lambda} \tag{3.71}$$

Inclusion of this additional albedo weight was found to improve accuracy of the five-band albedo solutions (relative to 470-band solutions) because of the strong dependence of optically-thick snowpack albedo on ice grain single-scatter albedo (*Flanner et al. (2007)*). The lookup tables contain optical properties for lognormal distributions of ice particles over the range of effective radii: 30μm $< r_e < 1500\mu$m, at 1 μ m resolution. Single-scatter albedos for the end-members of this size range are listed in Table 3.5.

Optical properties for black carbon are described in *Flanner et al. (2007)*. Single-scatter albedo, mass extinction cross-section, and asymmetry parameter values for all snowpack species, in the five spectral bands used, are listed in Table 3.5, Table 3.6, and Table 3.7. These properties were also derived with Mie Theory, using various published

sources of indices of refraction and assumptions about particle size distribution. Weighting into the five CLM spectral bands was determined only with incident solar flux, as in equation .

Table 3.5: Single-scatter albedo values used for snowpack impurities and ice

Species	Band 1	Band 2	Band 3	Band 4	Band 5
Hydrophilic black carbon	0.516	0.434	0.346	0.276	0.139
Hydrophobic black carbon	0.288	0.187	0.123	0.089	0.040
Hydrophilic organic carbon	0.997	0.994	0.990	0.987	0.951
Hydrophobic organic carbon	0.963	0.921	0.860	0.814	0.744
Dust 1	0.979	0.994	0.993	0.993	0.953
Dust 2	0.944	0.984	0.989	0.992	0.983
Dust 3	0.904	0.965	0.969	0.973	0.978
Dust 4	0.850	0.940	0.948	0.953	0.955
Ice ($r_e = 30\ \mu$ m)	0.9999	0.9999	0.9992	0.9938	0.9413
Ice ($r_e = 1500\ \mu$ m)	0.9998	0.9960	0.9680	0.8730	0.5500

Table 3.6: Mass extinction values ($m^2\ kg^{-1}$) used for snowpack impurities and ice

Species	Band 1	Band 2	Band 3	Band 4	Band 5
Hydrophilic black carbon	25369	12520	7739	5744	3527
Hydrophobic black carbon	11398	5923	4040	3262	2224
Hydrophilic organic carbon	37774	22112	14719	10940	5441
Hydrophobic organic carbon	3289	1486	872	606	248
Dust 1	2687	2420	1628	1138	466
Dust 2	841	987	1184	1267	993
Dust 3	388	419	400	397	503
Dust 4	197	203	208	205	229
Ice ($r_e = 30\ \mu$ m)	55.7	56.1	56.3	56.6	57.3
Ice ($r_e = 1500\ \mu$ m)	1.09	1.09	1.09	1.09	1.1

Table 3.7: Asymmetry scattering parameters used for snowpack impurities and ice.

Species	Band 1	Band 2	Band 3	Band 4	Band 5
Hydrophilic black carbon	0.52	0.34	0.24	0.19	0.10
Hydrophobic black carbon	0.35	0.21	0.15	0.11	0.06
Hydrophilic organic carbon	0.77	0.75	0.72	0.70	0.64
Hydrophobic organic carbon	0.62	0.57	0.54	0.51	0.44
Dust 1	0.69	0.72	0.67	0.61	0.44
Dust 2	0.70	0.65	0.70	0.72	0.70
Dust 3	0.79	0.75	0.68	0.63	0.67
Dust 4	0.83	0.79	0.77	0.76	0.73
Ice ($r_e = 30\mu$m)	0.88	0.88	0.88	0.88	0.90
Ice ($r_e = 1500\mu$m)	0.89	0.90	0.90	0.92	0.97

3.2.3 Snow Aging

Snow aging is represented as evolution of the ice effective grain size (r_e). Previous studies have shown that use of spheres which conserve the surface area-to-volume ratio (or specific surface area) of ice media composed of more

complex shapes produces relatively small errors in simulated hemispheric fluxes (e.g., *Grenfell and Warren 1999*). Effective radius is the surface area-weighted mean radius of an ensemble of spherical particles and is directly related to specific surface area (SSA) as $r_e = 3/\left(\rho_{ice}SSA\right)$, where ρ_{ice} is the density of ice. Hence, r_e is a simple and practical metric for relating the snowpack microphysical state to dry snow radiative characteristics.

Wet snow processes can also drive rapid changes in albedo. The presence of liquid water induces rapid coarsening of the surrounding ice grains (e.g., *Brun 1989*), and liquid water tends to refreeze into large ice clumps that darken the bulk snowpack. The presence of small liquid drops, by itself, does not significantly darken snowpack, as ice and water have very similar indices of refraction throughout the solar spectrum. Pooled or ponded water, however, can significantly darken snowpack by greatly reducing the number of refraction events per unit mass. This influence is not currently accounted for.

The net change in effective grain size occurring each time step is represented in each snow layer as a summation of changes caused by dry snow metamorphism ($dr_{e,dry}$), liquid water-induced metamorphism ($dr_{e,wet}$), refreezing of liquid water, and addition of freshly-fallen snow. The mass of each snow layer is partitioned into fractions of snow carrying over from the previous time step (f_{old}), freshly-fallen snow (f_{new}), and refrozen liquid water (f_{rfz}), such that snow r_e is updated each time step t as

$$r_e\left(t\right) = \left[r_e\left(t-1\right) + dr_{e,dry} + dr_{e,wet}\right]f_{old} + r_{e,0}f_{new} + r_{e,rfz}f_{rfrz} \tag{3.72}$$

Here, the effective radius of freshly-fallen snow ($r_{e,0}$) is based on a simple linear temperature-relationship. Below -30 degrees Celsius, a minimum value is enforced of 54.5 μ m (corresponding to a specific surface area of 60 m^2 kg^{-1}). Above 0 degrees Celsius, a maximum value is enforced of 204.5 μ m. Between -30 and 0 a linear ramp is used.

The effective radius of refrozen liquid water ($r_{e,rfz}$) is set to 1000μ m.

Dry snow aging is based on a microphysical model described by *Flanner and Zender (2006)*. This model simulates diffusive vapor flux amongst collections of ice crystals with various size and inter-particle spacing. Specific surface area and effective radius are prognosed for any combination of snow temperature, temperature gradient, density, and initial size distribution. The combination of warm snow, large temperature gradient, and low density produces the most rapid snow aging, whereas aging proceeds slowly in cold snow, regardless of temperature gradient and density. Because this model is currently too computationally expensive for inclusion in climate models, we fit parametric curves to model output over a wide range of snow conditions and apply these parameters in CLM. The functional form of the parametric equation is

$$\frac{dr_{e,dry}}{dt} = \left(\frac{dr_e}{dt}\right)_0 \left(\frac{\eta}{\left(r_e - r_{e,0}\right) + \eta}\right)^{1/\kappa} \tag{3.73}$$

The parameters $\left(\frac{dr_e}{dt}\right)_0$, η, and κ are retrieved interactively from a lookup table with dimensions corresponding to snow temperature, temperature gradient, and density. The domain covered by this lookup table includes temperature ranging from 223 to 273 K, temperature gradient ranging from 0 to 300 K m^{-1}, and density ranging from 50 to 400 kg m^{-3}. Temperature gradient is calculated at the midpoint of each snow layer n, using mid-layer temperatures (T_n) and snow layer thicknesses (dz_n), as

$$\left(\frac{dT}{dz}\right)_n = \frac{1}{dz_n}abs\left[\frac{T_{n-1}dz_n + T_ndz_{n-1}}{dz_n + dz_{n-1}} + \frac{T_{n+1}dz_n + T_ndz_{n+1}}{dz_n + dz_{n+1}}\right] \tag{3.74}$$

For the bottom snow layer ($n = 0$), T_{n+1} is taken as the temperature of the top soil layer, and for the top snow layer it is assumed that $T_{n-1} = T_n$.

The contribution of liquid water to enhanced metamorphism is based on parametric equations published by *Brun (1989)*, who measured grain growth rates under different liquid water contents. This relationship, expressed in terms of $r_e(\mu m)$ and subtracting an offset due to dry aging, depends on the mass liquid water fraction f_{liq} as

$$\frac{dr_e}{dt} = \frac{10^{18}C_1f_{liq}^3}{4\pi r_e^2} \tag{3.75}$$

The constant C_1 is 4.22×10^{-13}, and: $f_{liq} = w_{liq}/\left(w_{liq} + w_{ice}\right)$(Chapter 8).

In cases where snow mass is greater than zero, but a snow layer has not yet been defined, r_e is set to $r_{e,0}$. When snow layers are combined or divided, r_e is calculated as a mass-weighted mean of the two layers, following computations of other state variables (section 8.7). Finally, the allowable range of r_e, corresponding to the range over which Mie optical properties have been defined, is 30-1500μ m.

3.3 Solar Zenith Angle

The CLM uses the same formulation for solar zenith angle as the Community Atmosphere Model. The cosine of the solar zenith angle μ is

$$\mu = \sin \phi \sin \delta - \cos \phi \cos \delta \cos h \tag{3.76}$$

where h is the solar hour angle (radians) (24 hour periodicity), δ is the solar declination angle (radians), and ϕ is latitude (radians) (positive in Northern Hemisphere). The solar hour angle h (radians) is

$$h = 2\pi d + \theta \tag{3.77}$$

where d is calendar day ($d = 0.0$ at 0Z on January 1), and θ is longitude (radians) (positive east of the Greenwich meridian).

The solar declination angle δ is calculated as in *Berger (1978a,b)* and is valid for one million years past or hence, relative to 1950 A.D. The orbital parameters may be specified directly or the orbital parameters are calculated for the desired year. The required orbital parameters to be input by the user are the obliquity of the Earth ε (degrees, $-90° < \varepsilon < 90°$), Earth's eccentricity e ($0.0 < e < 0.1$), and the longitude of the perihelion relative to the moving vernal equinox $\tilde{\omega}$ ($0° < \tilde{\omega} < 360°$) (unadjusted for the apparent orbit of the Sun around the Earth (*Berger et al. 1993*)). The solar declination δ (radians) is

$$\delta = \sin^{-1} \left[\sin (\varepsilon) \sin (\lambda) \right] \tag{3.78}$$

where ε is Earth's obliquity and λ is the true longitude of the Earth.

The obliquity of the Earth ε (degrees) is

$$\varepsilon = \varepsilon * + \sum_{i=1}^{i=47} A_i \cos \left(f_i t + \delta_i \right) \tag{3.79}$$

where $\varepsilon*$ is a constant of integration (Table 3.8), A_i , f_i , and δ_i are amplitude, mean rate, and phase terms in the cosine series expansion (*Berger (1978a,b)*, and $t = t_0 - 1950$ where t_0 is the year. The series expansion terms are not shown here but can be found in the source code file shr_orb_mod.F90.

The true longitude of the Earth λ (radians) is counted counterclockwise from the vernal equinox ($\lambda = 0$ at the vernal equinox)

$$\lambda = \lambda_m + \left(2e - \frac{1}{4}e^3 \right) \sin (\lambda_m - \tilde{\omega}) + \frac{5}{4}e^2 \sin 2 (\lambda_m - \tilde{\omega}) + \frac{13}{12}e^3 \sin 3 (\lambda_m - \tilde{\omega}) \tag{3.80}$$

where λ_m is the mean longitude of the Earth at the vernal equinox, e is Earth's eccentricity, and $\tilde{\omega}$ is the longitude of the perihelion relative to the moving vernal equinox. The mean longitude λ_m is

$$\lambda_m = \lambda_{m0} + \frac{2\pi (d - d_{ve})}{365} \tag{3.81}$$

where $d_{ve} = 80.5$ is the calendar day at vernal equinox (March 21 at noon), and

$$\lambda_{m0} = 2 \left[\left(\frac{1}{2}e + \frac{1}{8}e^3 \right) (1 + \beta) \sin \tilde{\omega} - \frac{1}{4}e^2 \left(\frac{1}{2} + \beta \right) \sin 2\tilde{\omega} + \frac{1}{8}e^3 \left(\frac{1}{3} + \beta \right) \sin 3\tilde{\omega} \right] \tag{3.82}$$

where $\beta = \sqrt{1 - e^2}$. Earth's eccentricity e is

$$e = \sqrt{(e^{\cos})^2 + (e^{\sin})^2}$$ (3.83)

where

$$\begin{aligned} e^{\cos} &= \sum_{j=1}^{19} M_j \cos{(g_j t + B_j)}, \\ e^{\sin} &= \sum_{j=1}^{19} M_j \sin{(g_j t + B_j)} \end{aligned}$$ (3.84)

are the cosine and sine series expansions for e, and M_j , g_j , and B_j are amplitude, mean rate, and phase terms in the series expansions (*Berger (1978a,b)*). The longitude of the perihelion relative to the moving vernal equinox $\tilde{\omega}$ (degrees) is

$$\tilde{\omega} = \Pi \frac{180}{\pi} + \psi$$ (3.85)

where Π is the longitude of the perihelion measured from the reference vernal equinox (i.e., the vernal equinox at 1950 A.D.) and describes the absolute motion of the perihelion relative to the fixed stars, and ψ is the annual general precession in longitude and describes the absolute motion of the vernal equinox along Earth's orbit relative to the fixed stars. The general precession ψ (degrees) is

$$\psi = \frac{\tilde{\psi} t}{3600} + \zeta + \sum_{i=1}^{78} F_i \sin{\left(f_i' t + \delta_i' \right)}$$ (3.86)

where $\tilde{\psi}$ (arcseconds) and ζ (degrees) are constants (Table 3.8), and F_i , f_i' , and δ_i' are amplitude, mean rate, and phase terms in the sine series expansion (*Berger (1978a,b)*)). The longitude of the perihelion Π (radians) depends on the sine and cosine series expansions for the eccentricity e as follows:

$$\Pi = \begin{cases} 0 & \text{for } -1 \times 10^{-8} \le e^{\cos} \le 1 \times 10^{-8} \text{ and } e^{\sin} = 0 \\ 1.5\pi & \text{for } -1 \times 10^{-8} \le e^{\cos} \le 1 \times 10^{-8} \text{ and } e^{\sin} < 0 \\ 0.5\pi & \text{for } -1 \times 10^{-8} \le e^{\cos} \le 1 \times 10^{-8} \text{ and } e^{\sin} > 0 \\ \tan^{-1} \left[\frac{e^{\sin}}{e^{\cos}} \right] + \pi & \text{for } e^{\cos} < -1 \times 10^{-8} \\ \tan^{-1} \left[\frac{e^{\sin}}{e^{\cos}} \right] + 2\pi & \text{for } e^{\cos} > 1 \times 10^{-8} \text{ and } e^{\sin} < 0 \\ \tan^{-1} \left[\frac{e^{\sin}}{e^{\cos}} \right] & \text{for } e^{\cos} > 1 \times 10^{-8} \text{ and } e^{\sin} \ge 0 \end{cases} .$$ (3.87)

The numerical solution for the longitude of the perihelion $\tilde{\omega}$ is constrained to be between 0 and 360 degrees (measured from the autumn equinox). A constant 180 degrees is then added to $\tilde{\omega}$ because the Sun is considered as revolving around the Earth (geocentric coordinate system) (*Berger et al. 1993*)).

Table 3.8: Orbital parameters

Parameter	
$\varepsilon*$	23.320556
$\tilde{\psi}$ (arcseconds)	50.439273
ζ (degrees)	3.392506

CHAPTER 4

RADIATIVE FLUXES

The net radiation at the surface is $\left(\vec{S}_v + \vec{S}_g\right) - \left(\vec{L}_v + \vec{L}_g\right)$, where $\vec{S}$ is the net solar flux absorbed by the vegetation ("v") and the ground ("g") and $\vec{L}$ is the net longwave flux (positive toward the atmosphere) (W m^{-2}).

4.1 Solar Fluxes

Figure 4.1 illustrates the direct beam and diffuse fluxes in the canopy.

$I \uparrow_\Lambda^\mu$ and $I \uparrow_\Lambda$ are the upward diffuse fluxes, per unit incident direct beam and diffuse flux (section 3.1). $I \downarrow_\Lambda^\mu$ and $I \downarrow_\Lambda$ are the downward diffuse fluxes below the vegetation per unit incident direct beam and diffuse radiation (section 3.1). The direct beam flux transmitted through the canopy, per unit incident flux, is $e^{-K(L+S)}$. $\vec{I}_\Lambda^\mu$ and $\vec{I}_\Lambda$ are the fluxes absorbed by the vegetation, per unit incident direct beam and diffuse radiation (section 3.1). $\alpha_{g,\Lambda}^\mu$ and $\alpha_{g,\Lambda}$ are the direct beam and diffuse ground albedos (section 3.2). L and S are the exposed leaf area index and stem area index (section 2.1.4). K is the optical depth of direct beam per unit leaf and stem area (section 3.1).

For clarity, terms involving $T^{n+1} - T^n$ are not shown in (c).

The total solar radiation absorbed by the vegetation and ground is

$$\vec{S}_v = \sum_\Lambda S_{atm} \downarrow_\Lambda^\mu \vec{I}_\Lambda^\mu + S_{atm} \downarrow_\Lambda \vec{I}_\Lambda \tag{4.1}$$

$$\vec{S}_g = \sum_\Lambda S_{atm} \downarrow_\Lambda^\mu e^{-K(L+S)} \left(1 - \alpha_{g,\Lambda}^\mu\right) + \\ \left(S_{atm} \downarrow_\Lambda^\mu I \downarrow_\Lambda^\mu + S_{atm} \downarrow_\Lambda I \downarrow_\Lambda\right) \left(1 - \alpha_{g,\Lambda}\right) \tag{4.2}$$

where $S_{atm} \downarrow_\Lambda^\mu$ and $S_{atm} \downarrow_\Lambda$ are the incident direct beam and diffuse solar fluxes (W m^{-2}). For non-vegetated surfaces, $e^{-K(L+S)} = 1$, $\vec{I}_\Lambda^\mu = \vec{I}_\Lambda = 0$, $I \downarrow_\Lambda^\mu = 0$, and $I \downarrow_\Lambda = 1$, so that

$$\vec{S}_g = \sum_\Lambda S_{atm} \downarrow_\Lambda^\mu \left(1 - \alpha_{g,\Lambda}^\mu\right) + S_{atm} \downarrow_\Lambda \left(1 - \alpha_{g,\Lambda}\right) \\ \vec{S}_v = 0 \tag{4.3}$$

Solar radiation is conserved as

$$\sum_\Lambda \left(S_{atm} \downarrow_\Lambda^\mu + S_{atm} \downarrow_\Lambda\right) = \left(\vec{S}_v + \vec{S}_g\right) + \sum_\Lambda \left(S_{atm} \downarrow_\Lambda^\mu I \uparrow_\Lambda^\mu + S_{atm} \downarrow_\Lambda I \uparrow_\Lambda\right) \tag{4.4}$$
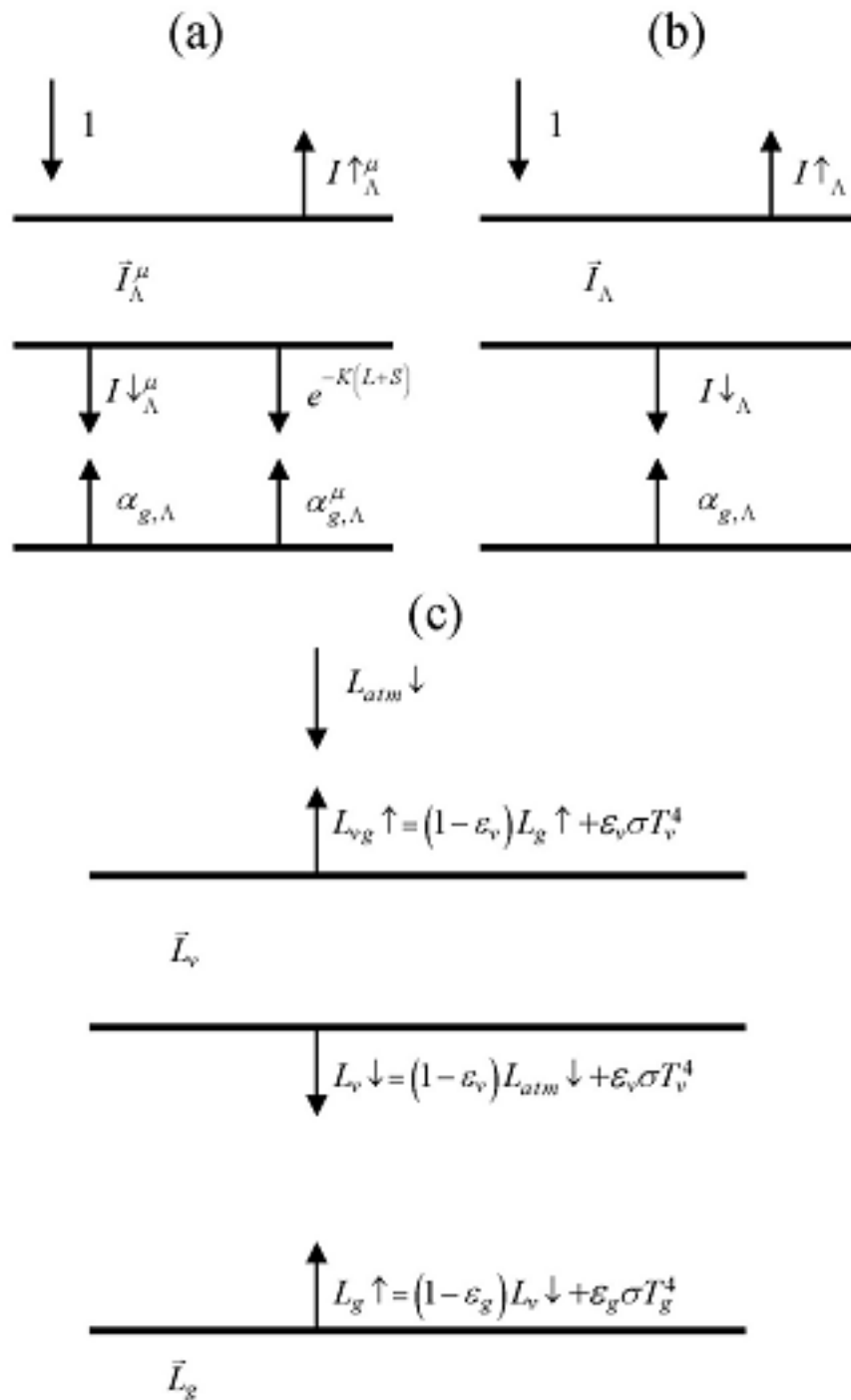
Figure 4.1: Schematic diagram of (a) direct beam radiation, (b) diffuse solar radiation, and (c) longwave radiation absorbed, transmitted, and reflected by vegetation and ground.

where the latter term in parentheses is reflected solar radiation.

Photosynthesis and transpiration depend non-linearly on solar radiation, via the light response of stomata. The canopy is treated as two leaves (sunlit and shaded) and the solar radiation in the visible waveband (< 0.7 µm) absorbed by the vegetation is apportioned to the sunlit and shaded leaves (section 3.1). The absorbed photosynthetically active (visible waveband) radiation averaged over the sunlit canopy (per unit plant area) is

$$\phi^{sun} = \left(\vec{I}^{\mu}_{sun,vis} S_{atm} \downarrow^{\mu}_{vis} + \vec{I}_{sun,vis} S_{atm} \downarrow_{vis} \right) \Big/ L^{sun} \tag{4.5}$$

and the absorbed radiation for the average shaded leaf (per unit plant area) is

$$\phi^{sha} = \left(\vec{I}^{\mu}_{sha,vis} S_{atm} \downarrow^{\mu}_{vis} + \vec{I}_{sha,vis} S_{atm} \downarrow_{vis} \right) \Big/ L^{sha} \tag{4.6}$$

with L^{sun} and L^{sha} the sunlit and shaded plant area index, respectively. The sunlit plant area index is

$$L^{sun} = \frac{1 - e^{-K(L+S)}}{K} \tag{4.7}$$

and the shaded leaf area index is $L^{sha} = (L + S) - L^{sun}$. In calculating L^{sun},

$$K = \frac{G(\mu)}{\mu} \tag{4.8}$$

where $G(\mu)$ and μ are parameters in the two-stream approximation (section 3.1).

The model uses the two-stream approximation to calculate radiative transfer of direct and diffuse radiation through a canopy that is differentiated into leaves that are sunlit and those that are shaded (section 3.1). The two-stream equations are integrated over all plant area (leaf and stem area) in the canopy. The model has an optional (though not supported) multi-layer canopy, as described by *Bonan et al. (2012)*. The multi-layer model is only intended to address the non-linearity of light profiles, photosynthesis, and stomatal conductance in the plant canopy.

In the multi-layer canopy, canopy-integrated radiative fluxes are calculated from the two-stream approximation. The model additionally derives the light profile with depth in the canopy by taking the derivatives of the absorbed radiative fluxes with respect to plant area index ($L' = L + S$) and evaluating them incrementally through the canopy with cumulative plant area index (x). The terms $d\vec{I}^{\mu}_{sun,\Lambda}(x) \big/ dL'$ and $d\vec{I}_{sun,\Lambda}(x) \big/ dL'$ are the direct beam and diffuse solar radiation, respectively, absorbed by the sunlit fraction of the canopy (per unit plant area) at a depth defined by the cumulative plant area index x; $d\vec{I}^{\mu}_{sha,\Lambda}(x) \big/ dL'$ and $d\vec{I}_{sha,\Lambda}(x) \big/ dL'$ are the corresponding fluxes for the shaded fraction of the canopy at depth x. These fluxes are normalized by the sunlit or shaded fraction at depth x, defined by $f_{sun} = \exp(-Kx)$, to give fluxes per unit sunlit or shaded plant area at depth x.

4.2 Longwave Fluxes

The net longwave radiation (W m^{-2}) (positive toward the atmosphere) at the surface is

$$\vec{L} = L \uparrow - L_{atm} \downarrow \tag{4.9}$$

where $L \uparrow$ is the upward longwave radiation from the surface and $L_{atm} \downarrow$ is the downward atmospheric longwave radiation (W m^{-2}). The radiative temperature T_{rad} (K) is defined from the upward longwave radiation as

$$T_{rad} = \left(\frac{L \uparrow}{\sigma} \right)^{1/4} \tag{4.10}$$

where σ is the Stefan-Boltzmann constant (Wm^{-2} K^{-4}) (Table 2.7). With reference to Figure 4.1, the upward longwave radiation from the surface to the atmosphere is

$$\begin{aligned} L \uparrow = &\ \delta_{veg} L_{vg} \uparrow + (1 - \delta_{veg})(1 - \varepsilon_g) L_{atm} \downarrow + \\ &\ (1 - \delta_{veg}) \varepsilon_g \sigma \left(T_g^n \right)^4 + 4 \varepsilon_g \sigma \left(T_g^n \right)^3 \left(T_g^{n+1} - T_g^n \right) \end{aligned} \tag{4.11}$$

where $L_{vg} \uparrow$ is the upward longwave radiation from the vegetation/soil system for exposed leaf and stem area $L + S \geq 0.05$, δ_{veg} is a step function and is zero for $L + S < 0.05$ and one otherwise, ε_g is the ground emissivity, and T_g^{n+1} and T_g^n are the snow/soil surface temperatures at the current and previous time steps, respectively (*Soil and Snow Temperatures*).

For non-vegetated surfaces, the above equation reduces to

$$L \uparrow = (1 - \varepsilon_g) L_{atm} \downarrow + \varepsilon_g \sigma \left(T_g^n\right)^4 + 4\varepsilon_g \sigma \left(T_g^n\right)^3 \left(T_g^{n+1} - T_g^n\right) \tag{4.12}$$

where the first term is the atmospheric longwave radiation reflected by the ground, the second term is the longwave radiation emitted by the ground, and the last term is the increase (decrease) in longwave radiation emitted by the ground due to an increase (decrease) in ground temperature.

For vegetated surfaces, the upward longwave radiation from the surface reduces to

$$L \uparrow = L_{vg} \uparrow + 4\varepsilon_g \sigma \left(T_g^n\right)^3 \left(T_g^{n+1} - T_g^n\right) \tag{4.13}$$

where

$$
\begin{aligned}
L_{vg} \uparrow =\ & (1 - \varepsilon_g)(1 - \varepsilon_v)(1 - \varepsilon_v) L_{atm} \downarrow \\
& + \varepsilon_v \left[1 + (1 - \varepsilon_g)(1 - \varepsilon_v)\right] \sigma \left(T_v^n\right)^3 \left[T_v^n + 4\left(T_v^{n+1} - T_v^n\right)\right] \\
& + \varepsilon_g (1 - \varepsilon_v) \sigma \left(T_g^n\right)^4 \\
=\ & (1 - \varepsilon_g)(1 - \varepsilon_v)(1 - \varepsilon_v) L_{atm} \downarrow \\
& + \varepsilon_v \sigma \left(T_v^n\right)^4 \\
& + \varepsilon_v (1 - \varepsilon_g)(1 - \varepsilon_v) \sigma \left(T_v^n\right)^4 \\
& + 4\varepsilon_v \sigma \left(T_v^n\right)^3 \left(T_v^{n+1} - T_v^n\right) \\
& + 4\varepsilon_v (1 - \varepsilon_g)(1 - \varepsilon_v) \sigma \left(T_v^n\right)^3 \left(T_v^{n+1} - T_v^n\right) \\
& + \varepsilon_g (1 - \varepsilon_v) \sigma \left(T_g^n\right)^4
\end{aligned}
\tag{4.14}
$$

where ε_v is the vegetation emissivity and T_v^{n+1} and T_v^n are the vegetation temperatures at the current and previous time steps, respectively (*Momentum, Sensible Heat, and Latent Heat Fluxes*). The first term in the equation above is the atmospheric longwave radiation that is transmitted through the canopy, reflected by the ground, and transmitted through the canopy to the atmosphere. The second term is the longwave radiation emitted by the canopy directly to the atmosphere. The third term is the longwave radiation emitted downward from the canopy, reflected by the ground, and transmitted through the canopy to the atmosphere. The fourth term is the increase (decrease) in longwave radiation due to an increase (decrease) in canopy temperature that is emitted by the canopy directly to the atmosphere. The fifth term is the increase (decrease) in longwave radiation due to an increase (decrease) in canopy temperature that is emitted downward from the canopy, reflected from the ground, and transmitted through the canopy to the atmosphere. The last term is the longwave radiation emitted by the ground and transmitted through the canopy to the atmosphere.

The upward longwave radiation from the ground is

$$L_g \uparrow = (1 - \varepsilon_g) L_v \downarrow + \varepsilon_g \sigma \left(T_g^n\right)^4 \tag{4.15}$$

where $L_v \downarrow$ is the downward longwave radiation below the vegetation

$$L_v \downarrow = (1 - \varepsilon_v) L_{atm} \downarrow + \varepsilon_v \sigma \left(T_v^n\right)^4 + 4\varepsilon_v \sigma \left(T_v^n\right)^3 \left(T_v^{n+1} - T_v^n\right). \tag{4.16}$$

The net longwave radiation flux for the ground is (positive toward the atmosphere)

$$\vec{L}_g = \varepsilon_g \sigma \left(T_g^n\right)^4 - \delta_{veg} \varepsilon_g L_v \downarrow - (1 - \delta_{veg}) \varepsilon_g L_{atm} \downarrow. \tag{4.17}$$

The above expression for $\vec{L}_g$ is the net longwave radiation forcing that is used in the soil temperature calculation (*Soil and Snow Temperatures*). Once updated soil temperatures have been obtained, the term $4\varepsilon_g \sigma \left(T_g^n\right)^3 \left(T_g^{n+1} - T_g^n\right)$ is added to $\vec{L}_g$ to calculate the ground heat flux (section 5.4)

The net longwave radiation flux for vegetation is (positive toward the atmosphere)

$$\vec{L}_v = \left[2 - \varepsilon_v \left(1 - \varepsilon_g\right)\right] \varepsilon_v \sigma \left(T_v\right)^4 - \varepsilon_v \varepsilon_g \sigma \left(T_g^n\right)^4 - \varepsilon_v \left[1 + \left(1 - \varepsilon_g\right)\left(1 - \varepsilon_v\right)\right] L_{atm} \downarrow. \tag{4.18}$$

These equations assume that absorptivity equals emissivity. The emissivity of the ground is

$$\varepsilon_g = \varepsilon_{soi} \left(1 - f_{sno}\right) + \varepsilon_{sno} f_{sno} \tag{4.19}$$

where $\varepsilon_{soi} = 0.96$ for soil, 0.97 for glacier, $\varepsilon_{sno} = 0.97$, and f_{sno} is the fraction of ground covered by snow (section 8.1). The vegetation emissivity is

$$\varepsilon_v = 1 - e^{-(L+S)/\bar{\mu}} \tag{4.20}$$

where L and S are the leaf and stem area indices (section 2.1.4) and $\bar{\mu} = 1$ is the average inverse optical depth for longwave radiation.

CHAPTER 5

MOMENTUM, SENSIBLE HEAT, AND LATENT HEAT FLUXES

The zonal τ_x and meridional τ_y momentum fluxes (kg m^{-1} s^{-2}), sensible heat flux H (W m^{-2}), and water vapor flux E (kg m^{-2} s^{-1}) between the atmosphere at reference height $z_{atm,\,x}$ (m) [where x is height for wind (momentum) (m), temperature (sensible heat) (h), and humidity (water vapor) (w); with zonal and meridional winds u_{atm} and v_{atm} (m s^{-1}), potential temperature θ_{atm} (K), and specific humidity q_{atm} (kg kg^{-1})] and the surface [with u_s , v_s , θ_s , and q_s] are

$$\tau_x = -\rho_{atm}\frac{(u_{atm} - u_s)}{r_{am}} \tag{5.1}$$

$$\tau_y = -\rho_{atm}\frac{(v_{atm} - v_s)}{r_{am}} \tag{5.2}$$

$$H = -\rho_{atm}C_p\frac{(\theta_{atm} - \theta_s)}{r_{ah}} \tag{5.3}$$

$$E = -\rho_{atm}\frac{(q_{atm} - q_s)}{r_{aw}}. \tag{5.4}$$

These fluxes are derived in the next section from Monin-Obukhov similarity theory developed for the surface layer (i.e., the nearly constant flux layer above the surface sublayer). In this derivation, u_s and v_s are defined to equal zero at height $z_{0m} + d$ (the apparent sink for momentum) so that r_{am} is the aerodynamic resistance (s m^{-1}) for momentum between the atmosphere at height $z_{atm,\,m}$ and the surface at height $z_{0m} + d$. Thus, the momentum fluxes become

$$\tau_x = -\rho_{atm}\frac{u_{atm}}{r_{am}} \tag{5.5}$$

$$\tau_y = -\rho_{atm}\frac{v_{atm}}{r_{am}}. \tag{5.6}$$

Likewise, θ_s and q_s are defined at heights $z_{0h} + d$ and $z_{0w} + d$ (the apparent sinks for heat and water vapor, respectively

r_{aw} are the aerodynamic resistances (s m^{-1}) to sensible heat and water vapor transfer between the atmosphere at heights $z_{atm,\,h}$ and $z_{atm,\,w}$ and the surface at heights $z_{0h} + d$ and $z_{0w} + d$, respectively. The specific heat capacity of air C_p (J kg^{-1} K^{-1}) is a constant (Table 2.7). The atmospheric potential temperature used here is

$$\theta_{atm} = T_{atm} + \Gamma_d z_{atm,\,h} \tag{5.7}$$

where T_{atm} is the air temperature (K) at height $z_{atm,\,h}$ and $\Gamma_d = 0.0098$ K m^{-1} is the negative of the dry adiabatic lapse rate [this expression is first-order equivalent to $\theta_{atm} = T_{atm} \left(P_{srf}/P_{atm}\right)^{R_{da}/C_p}$ (*Stull 1988*), where P_{srf} is the surface pressure (Pa), P_{atm} is the atmospheric pressure (Pa), and R_{da} is the gas constant for dry air (J kg^{-1} K^{-1}) (Table 2.7)]. By definition, $\theta_s = T_s$. The density of moist air (kg m^{-3}) is

$$\rho_{atm} = \frac{P_{atm} - 0.378 e_{atm}}{R_{da} T_{atm}} \tag{5.8}$$

where the atmospheric vapor pressure e_{atm} (Pa) is derived from the atmospheric specific humidity q_{atm}

$$e_{atm} = \frac{q_{atm} P_{atm}}{0.622 + 0.378 q_{atm}}. \tag{5.9}$$

5.1 Monin-Obukhov Similarity Theory

The surface vertical kinematic fluxes of momentum $\overline{u'w'}$ and $\overline{v'w'}$ (m^2 s$_{-2}$), sensible heat $\overline{\theta'w'}$ (K m s $^{-1}$), and latent heat $\overline{q'w'}$ (kg kg^{-1} m s^{-1}), where u', v', w', θ', and q' are zonal horizontal wind, meridional horizontal wind, vertical velocity, potential temperature, and specific humidity turbulent fluctuations about the mean, are defined from Monin-Obukhov similarity applied to the surface layer. This theory states that when scaled appropriately, the dimensionless mean horizontal wind speed, mean potential temperature, and mean specific humidity profile gradients depend on unique functions of $\zeta = \frac{z-d}{L}$ (*Zeng et al. 1998*) as

$$\frac{k\,(z-d)}{u_*} \frac{\partial\,|u|}{\partial z} = \phi_m\left(\zeta\right) \tag{5.10}$$

$$\frac{k\,(z-d)}{\theta_*} \frac{\partial \theta}{\partial z} = \phi_h\left(\zeta\right) \tag{5.11}$$

$$\frac{k\,(z-d)}{q_*} \frac{\partial q}{\partial z} = \phi_w\left(\zeta\right) \tag{5.12}$$

where z is height in the surface layer (m), d is the displacement height (m), L is the Monin-Obukhov length scale (m) that accounts for buoyancy effects resulting from vertical density gradients (i.e., the atmospheric stability), k is the von Karman constant (Table 2.7), and $|u|$ is the atmospheric wind speed (m s^{-1}). ϕ_m , ϕ_h , and ϕ_w are universal (over any surface) similarity functions of ζ that relate the constant fluxes of momentum, sensible heat, and latent heat to the mean profile gradients of $|u|$, θ , and q in the surface layer. In neutral conditions, $\phi_m = \phi_h = \phi_w = 1$. The velocity (i.e., friction velocity) u (m s^{-1}), temperature θ (K), and moisture q (kg kg^{-1}) scales are

$$u_*^2 = \sqrt{\left(\overline{u'w'}\right)^2 + \left(\overline{v'w'}\right)^2} = \frac{|\tau|}{\rho_{atm}} \tag{5.13}$$

$$\theta_* u_* = -\overline{\theta'w'} = -\frac{H}{\rho_{atm} C_p} \tag{5.14}$$

$$q_* u_* = -\overline{q'w'} = -\frac{E}{\rho_{atm}} \tag{5.15}$$

where $|\tau|$ is the shearing stress (kg m^{-1} s^{-2}), with zonal and meridional components $\overline{u'w'} = -\frac{\tau_x}{\rho_{atm}}$ and $\overline{v'w'} = -\frac{\tau_y}{\rho_{atm}}$, respectively, H is the sensible heat flux (W m^{-2}) and E is the water vapor flux (kg m^{-2} s^{-1}).

The length scale L is the Monin-Obukhov length defined as

$$L = -\frac{u_*^3}{k\left(\frac{g}{\overline{\theta_{v,\,atm}}}\right)\theta_v'w'} = \frac{u_*^2 \overline{\theta_{v,\,atm}}}{kg\theta_{v*}} \tag{5.16}$$

where g is the acceleration of gravity (m s^{-2}) (Table 2.7), and $\overline{\theta_{v,atm}} = \overline{\theta_{atm}} (1 + 0.61 q_{atm})$ is the reference virtual potential temperature. $L > 0$ indicates stable conditions. $L < 0$ indicates unstable conditions. $L = \infty$ for neutral conditions. The temperature scale θ_{v*} is defined as

$$\theta_{v*} u_* = \left[\theta_* \left(1 + 0.61 q_{atm} \right) + 0.61 \overline{\theta_{atm}} q_* \right] u_* \tag{5.17}$$

where $\overline{\theta_{atm}}$ is the atmospheric potential temperature.

Following *Panofsky and Dutton (1984)*, the differential equations for $\phi_m (\zeta)$, $\phi_h (\zeta)$, and $\phi_w (\zeta)$ can be integrated formally without commitment to their exact forms. Integration between two arbitrary heights in the surface layer z_2 and z_1 ($z_2 > z_1$) with horizontal winds $|u|_1$ and $|u|_2$, potential temperatures θ_1 and θ_2, and specific humidities q_1 and q_2 results in

$$|u|_2 - |u|_1 = \frac{u_*}{k} \left[\ln \left(\frac{z_2 - d}{z_1 - d} \right) - \psi_m \left(\frac{z_2 - d}{L} \right) + \psi_m \left(\frac{z_1 - d}{L} \right) \right] \tag{5.18}$$

$$\theta_2 - \theta_1 = \frac{\theta_*}{k} \left[\ln \left(\frac{z_2 - d}{z_1 - d} \right) - \psi_h \left(\frac{z_2 - d}{L} \right) + \psi_h \left(\frac{z_1 - d}{L} \right) \right] \tag{5.19}$$

$$q_2 - q_1 = \frac{q_*}{k} \left[\ln \left(\frac{z_2 - d}{z_1 - d} \right) - \psi_w \left(\frac{z_2 - d}{L} \right) + \psi_w \left(\frac{z_1 - d}{L} \right) \right]. \tag{5.20}$$

The functions $\psi_m (\zeta)$, $\psi_h (\zeta)$, and $\psi_w (\zeta)$ are defined as

$$\psi_m (\zeta) = \int_{z_{0m}/L}^{\zeta} \frac{\left[1 - \phi_m (x) \right]}{x} dx \tag{5.21}$$

$$\psi_h (\zeta) = \int_{z_{0h}/L}^{\zeta} \frac{\left[1 - \phi_h (x) \right]}{x} dx \tag{5.22}$$

$$\psi_w (\zeta) = \int_{z_{0w}/L}^{\zeta} \frac{\left[1 - \phi_w (x) \right]}{x} dx \tag{5.23}$$

where z_{0m}, z_{0h}, and z_{0w} are the roughness lengths (m) for momentum, sensible heat, and water vapor, respectively.

Defining the surface values

$$|u|_1 = 0 \text{ at } z_1 = z_{0m} + d,$$

$$\theta_1 = \theta_s \text{ at } z_1 = z_{0h} + d, \text{ and}$$

$$q_1 = q_s \text{ at } z_1 = z_{0w} + d,$$

and the atmospheric values at $z_2 = z_{atm,x}$

$$|u|_2 = V_a = \sqrt{u_{atm}^2 + v_{atm}^2 + U_c^2} \geq 1, \tag{5.24}$$

$$\theta_2 = \theta_{atm}, \text{ and}$$

$$q_2 = q_{atm},$$

the integral forms of the flux-gradient relations are

$$V_a = \frac{u_*}{k} \left[\ln \left(\frac{z_{atm,m} - d}{z_{0m}} \right) - \psi_m \left(\frac{z_{atm,m} - d}{L} \right) + \psi_m \left(\frac{z_{0m}}{L} \right) \right] \tag{5.25}$$

$$\theta_{atm} - \theta_s = \frac{\theta_*}{k} \left[\ln \left(\frac{z_{atm,h} - d}{z_{0h}} \right) - \psi_h \left(\frac{z_{atm,h} - d}{L} \right) + \psi_h \left(\frac{z_{0h}}{L} \right) \right] \tag{5.26}$$

$$q_{atm} - q_s = \frac{q_*}{k} \left[\ln \left(\frac{z_{atm,\,w} - d}{z_{0w}} \right) - \psi_w \left(\frac{z_{atm,\,w} - d}{L} \right) + \psi_w \left(\frac{z_{0w}}{L} \right) \right]. \tag{5.27}$$

The constraint $V_a \geq 1$ is required simply for numerical reasons to prevent H and E from becoming small with small wind speeds. The convective velocity U_c accounts for the contribution of large eddies in the convective boundary layer to surface fluxes as follows

$$U_c = \left\{ \begin{array}{ll} 0 & \zeta \geq 0 \quad \text{(stable)} \\ \beta w_* & \zeta < 0 \quad \text{(unstable)} \end{array} \right\} \tag{5.28}$$

where w_* is the convective velocity scale

$$w_* = \left(\frac{-gu\overline{\theta_{v*}} z_i}{\theta_{v,\,atm}} \right)^{1/3}, \tag{5.29}$$

$z_i = 1000$ is the convective boundary layer height (m), and $\beta = 1$.

The momentum flux gradient relations are (*Zeng et al. 1998*)

$$\begin{array}{lll} \phi_m\left(\zeta\right) = 0.7 k^{2/3} \left(-\zeta\right)^{1/3} & \text{for } \zeta < -1.574 & \text{(very unstable)} \\ \phi_m\left(\zeta\right) = \left(1 - 16\zeta\right)^{-1/4} & \text{for } -1.574 \leq \zeta < 0 & \text{(unstable)} \\ \phi_m\left(\zeta\right) = 1 + 5\zeta & \text{for } 0 \leq \zeta \leq 1 & \text{(stable)} \\ \phi_m\left(\zeta\right) = 5 + \zeta & \text{for } \zeta > 1 & \text{(very stable)}. \end{array} \tag{5.30}$$

The sensible and latent heat flux gradient relations are (*Zeng et al. 1998*)

$$\begin{array}{lll} \phi_h\left(\zeta\right) = \phi_w\left(\zeta\right) = 0.9 k^{4/3} \left(-\zeta\right)^{-1/3} & \text{for } \zeta < -0.465 & \text{(very unstable)} \\ \phi_h\left(\zeta\right) = \phi_w\left(\zeta\right) = \left(1 - 16\zeta\right)^{-1/2} & \text{for } -0.465 \leq \zeta < 0 & \text{(unstable)} \\ \phi_h\left(\zeta\right) = \phi_w\left(\zeta\right) = 1 + 5\zeta & \text{for } 0 \leq \zeta \leq 1 & \text{(stable)} \\ \phi_h\left(\zeta\right) = \phi_w\left(\zeta\right) = 5 + \zeta & \text{for } \zeta > 1 & \text{(very stable)}. \end{array} \tag{5.31}$$

To ensure continuous functions of $\phi_m\left(\zeta\right)$, $\phi_h\left(\zeta\right)$, and $\phi_w\left(\zeta\right)$, the simplest approach (i.e., without considering any transition regimes) is to match the relations for very unstable and unstable conditions at $\zeta_m = -1.574$ for $\phi_m\left(\zeta\right)$ and $\zeta_h = \zeta_w = -0.465$ for $\phi_h\left(\zeta\right) = \phi_w\left(\zeta\right)$ (*Zeng et al. 1998*). The flux gradient relations can be integrated to yield wind profiles for the following conditions:

Very unstable $(\zeta < -1.574)$

$$V_a = \frac{u_*}{k} \left\{ \left[\ln \frac{\zeta_m L}{z_{0m}} - \psi_m\left(\zeta_m\right) \right] + 1.14 \left[\left(-\zeta\right)^{1/3} - \left(-\zeta_m\right)^{1/3} \right] + \psi_m\left(\frac{z_{0m}}{L} \right) \right\} \tag{5.32}$$

Unstable $(-1.574 \leq \zeta < 0)$

$$V_a = \frac{u_*}{k} \left\{ \left[\ln \frac{z_{atm,\,m} - d}{z_{0m}} - \psi_m\left(\zeta\right) \right] + \psi_m\left(\frac{z_{0m}}{L} \right) \right\} \tag{5.33}$$

Stable $(0 \leq \zeta \leq 1)$

$$V_a = \frac{u_*}{k} \left\{ \left[\ln \frac{z_{atm,\,m} - d}{z_{0m}} + 5\zeta \right] - 5\frac{z_{0m}}{L} \right\} \tag{5.34}$$

Very stable $(\zeta > 1)$

$$V_a = \frac{u_*}{k} \left\{ \left[\ln \frac{L}{z_{0m}} + 5 \right] + \left[5 \ln \zeta + \zeta - 1 \right] - 5\frac{z_{0m}}{L} \right\} \tag{5.35}$$

where

$$\psi_m\left(\zeta\right) = 2 \ln \left(\frac{1+x}{2} \right) + \ln \left(\frac{1+x^2}{2} \right) - 2 \tan^{-1} x + \frac{\pi}{2} \tag{5.36}$$

and

$$x = (1 - 16\zeta)^{1/4} \, .$$

The potential temperature profiles are:

Very unstable $(\zeta < -0.465)$

$$\theta_{atm} - \theta_s = \frac{\theta_*}{k} \left\{ \left[\ln \frac{\zeta_h L}{z_{0h}} - \psi_h \left(\zeta_h \right) \right] + 0.8 \left[\left(-\zeta_h \right)^{-1/3} - \left(-\zeta \right)^{-1/3} \right] + \psi_h \left(\frac{z_{0h}}{L} \right) \right\} \tag{5.37}$$

Unstable $(-0.465 \leq \zeta < 0)$

$$\theta_{atm} - \theta_s = \frac{\theta_*}{k} \left\{ \left[\ln \frac{z_{atm,\, h} - d}{z_{0h}} - \psi_h \left(\zeta \right) \right] + \psi_h \left(\frac{z_{0h}}{L} \right) \right\} \tag{5.38}$$

Stable $(0 \leq \zeta \leq 1)$

$$\theta_{atm} - \theta_s = \frac{\theta_*}{k} \left\{ \left[\ln \frac{z_{atm,\, h} - d}{z_{0h}} + 5\zeta \right] - 5 \frac{z_{0h}}{L} \right\} \tag{5.39}$$

Very stable $(\zeta > 1)$

$$\theta_{atm} - \theta_s = \frac{\theta_*}{k} \left\{ \left[\ln \frac{L}{z_{0h}} + 5 \right] + \left[5 \ln \zeta + \zeta - 1 \right] - 5 \frac{z_{0h}}{L} \right\} \, . \tag{5.40}$$

The specific humidity profiles are:

Very unstable $(\zeta < -0.465)$

$$q_{atm} - q_s = \frac{q_*}{k} \left\{ \left[\ln \frac{\zeta_w L}{z_{0w}} - \psi_w \left(\zeta_w \right) \right] + 0.8 \left[\left(-\zeta_w \right)^{-1/3} - \left(-\zeta \right)^{-1/3} \right] + \psi_w \left(\frac{z_{0w}}{L} \right) \right\} \tag{5.41}$$

Unstable $(-0.465 \leq \zeta < 0)$

$$q_{atm} - q_s = \frac{q_*}{k} \left\{ \left[\ln \frac{z_{atm,\, w} - d}{z_{0w}} - \psi_w \left(\zeta \right) \right] + \psi_w \left(\frac{z_{0w}}{L} \right) \right\} \tag{5.42}$$

Stable $(0 \leq \zeta \leq 1)$

$$q_{atm} - q_s = \frac{q_*}{k} \left\{ \left[\ln \frac{z_{atm,\, w} - d}{z_{0w}} + 5\zeta \right] - 5 \frac{z_{0w}}{L} \right\} \tag{5.43}$$

Very stable $(\zeta > 1)$

$$q_{atm} - q_s = \frac{q_*}{k} \left\{ \left[\ln \frac{L}{z_{0w}} + 5 \right] + \left[5 \ln \zeta + \zeta - 1 \right] - 5 \frac{z_{0w}}{L} \right\} \tag{5.44}$$

where

$$\psi_h \left(\zeta \right) = \psi_w \left(\zeta \right) = 2 \ln \left(\frac{1 + x^2}{2} \right) \, . \tag{5.45}$$

Using the definitions of u_*, θ_*, and q_*, an iterative solution of these equations can be used to calculate the surface momentum, sensible heat, and water vapor flux using atmospheric and surface values for $|u|$, θ, and q except that L depends on u_*, θ_*, and q_*. However, the bulk Richardson number

$$R_{iB} = \frac{\theta_{v,\, atm} - \theta_{v,\, s}}{\theta_{v,\, atm}} \frac{g \left(z_{atm,\, m} - d \right)}{V_a^2} \tag{5.46}$$

is related to ζ (*Arya 2001*) as

$$R_{iB} = \zeta \left[\ln \left(\frac{z_{atm,\,h} - d}{z_{0h}} \right) - \psi_h \left(\zeta \right) \right] \left[\ln \left(\frac{z_{atm,\,m} - d}{z_{0m}} \right) - \psi_m \left(\zeta \right) \right]^{-2}. \tag{5.47}$$

Using $\phi_h = \phi_m^2 = \left(1 - 16\zeta \right)^{-1/2}$ for unstable conditions and $\phi_h = \phi_m = 1 + 5\zeta$ for stable conditions to determine $\psi_m \left(\zeta \right)$ and $\psi_h \left(\zeta \right)$, the inverse relationship $\zeta = f \left(R_{iB} \right)$ can be solved to obtain a first guess for ζ and thus L from

$$\begin{array}{llll} \zeta = \frac{R_{iB} \ln \left(\frac{z_{atm,\,m} - d}{z_{0m}} \right)}{1 - 5 \min \left(R_{iB}, 0.19 \right)} & 0.01 \leq \zeta \leq 2 & \text{for } R_{iB} \geq 0 \text{ (neutral or stable)} \\ \zeta = R_{iB} \ln \left(\frac{z_{atm,\,m} - d}{z_{0m}} \right) & -100 \leq \zeta \leq -0.01 & \text{for } R_{iB} < 0 \text{ (unstable)} \end{array}. \tag{5.48}$$

Upon iteration (section 5.3.2), the following is used to determine ζ and thus L

$$\zeta = \frac{\left(z_{atm,\,m} - d \right) kg\theta_{v*}}{u_*^2 \theta_{v,\,atm}} \tag{5.49}$$

where

$$\begin{array}{ll} 0.01 \leq \zeta \leq 2 & \text{for } \zeta \geq 0 \text{ (neutral or stable)} \\ -100 \leq \zeta \leq -0.01 & \text{for } \zeta < 0 \text{ (unstable)} \end{array}.$$

The difference in virtual potential air temperature between the reference height and the surface is

$$\theta_{v,\,atm} - \theta_{v,\,s} = \left(\theta_{atm} - \theta_s \right) \left(1 + 0.61 q_{atm} \right) + 0.61 \overline{\theta_{atm}} \left(q_{atm} - q_s \right). \tag{5.50}$$

The momentum, sensible heat, and water vapor fluxes between the surface and the atmosphere can also be written in the form

$$\tau_x = -\rho_{atm} \frac{\left(u_{atm} - u_s \right)}{r_{am}} \tag{5.51}$$

$$\tau_y = -\rho_{atm} \frac{\left(v_{atm} - v_s \right)}{r_{am}} \tag{5.52}$$

$$H = -\rho_{atm} C_p \frac{\left(\theta_{atm} - \theta_s \right)}{r_{ah}} \tag{5.53}$$

$$E = -\rho_{atm} \frac{\left(q_{atm} - q_s \right)}{r_{aw}} \tag{5.54}$$

where the aerodynamic resistances (s m^{-1}) are

$$r_{am} = \frac{V_a}{u_*^2} = \frac{1}{k^2 V_a} \left[\ln \left(\frac{z_{atm,\,m} - d}{z_{0m}} \right) - \psi_m \left(\frac{z_{atm,\,m} - d}{L} \right) + \psi_m \left(\frac{z_{0m}}{L} \right) \right]^2 \tag{5.55}$$

$$r_{ah} = \frac{\theta_{atm} - \theta_s}{\theta_* u_*} = \frac{1}{k^2 V_a} \left[\ln \left(\frac{z_{atm,\,m} - d}{z_{0m}} \right) - \psi_m \left(\frac{z_{atm,\,m} - d}{L} \right) + \psi_m \left(\frac{z_{0m}}{L} \right) \right] \left[\ln \left(\frac{z_{atm,\,h} - d}{z_{0h}} \right) - \psi_h \left(\frac{z_{atm,\,h} - d}{L} \right) + \psi_h \left(\frac{z_{0h}}{L} \right) \right] \tag{5.56}$$

$$r_{aw} = \frac{q_{atm} - q_s}{q_* u_*} = \frac{1}{k^2 V_a} \left[\ln \left(\frac{z_{atm,\,m} - d}{z_{0m}} \right) - \psi_m \left(\frac{z_{atm,\,m} - d}{L} \right) + \psi_m \left(\frac{z_{0m}}{L} \right) \right] \left[\ln \left(\frac{z_{atm,\,w} - d}{z_{0w}} \right) - \psi_w \left(\frac{z_{atm,\,w} - d}{L} \right) + \psi_w \left(\frac{z_{0w}}{L} \right) \right]. \tag{5.57}$$

A 2-m height "screen" temperature is useful for comparison with observations

$$T_{2m} = \theta_s + \frac{\theta_*}{k} \left[\ln \left(\frac{2 + z_{0h}}{z_{0h}} \right) - \psi_h \left(\frac{2 + z_{0h}}{L} \right) + \psi_h \left(\frac{z_{0h}}{L} \right) \right] \tag{5.58}$$

where for convenience, "2-m" is defined as 2 m above the apparent sink for sensible heat $(z_{0h} + d)$. Similarly, a 2-m height specific humidity is defined as

$$q_{2m} = q_s + \frac{q_*}{k} \left[\ln\left(\frac{2 + z_{0w}}{z_{0w}}\right) - \psi_w\left(\frac{2 + z_{0w}}{L}\right) + \psi_w\left(\frac{z_{0w}}{L}\right) \right]. \tag{5.59}$$

Relative humidity is

$$RH_{2m} = \min\left(100, \frac{q_{2m}}{q_{sat}^{T_{2m}}} \times 100\right) \tag{5.60}$$

where $q_{sat}^{T_{2m}}$ is the saturated specific humidity at the 2-m temperature T_{2m} (section 5.5).

A 10-m wind speed is calculated as (note that this is not consistent with the 10-m wind speed calculated for the dust model as described in Chapter 31)

$$u_{10m} = \left\{ \begin{array}{ll} V_a & z_{atm,\,m} \leq 10 \\ V_a - \frac{u_*}{k}\left[\ln\left(\frac{z_{atm,\,m}-d}{10+z_{0m}}\right) - \psi_m\left(\frac{z_{atm,\,m}-d}{L}\right) + \psi_m\left(\frac{10+z_{0m}}{L}\right)\right] & z_{atm,\,m} > 10 \end{array} \right\} \tag{5.61}$$

5.2 Sensible and Latent Heat Fluxes for Non-Vegetated Surfaces

Surfaces are considered non-vegetated for the surface flux calculations if leaf plus stem area index $L + S < 0.05$ (section 2.1.4). By definition, this includes bare soil and glaciers. The solution for lakes is described in Chapter 12. For these surfaces, the surface may be exposed to the atmosphere, snow covered, and/or surface water covered, so that the sensible heat flux H_g (W m^{-2}) is, with reference to Figure 5.1,

$$H_g = (1 - f_{sno} - f_{h2osfc})\,H_{soil} + f_{sno}H_{snow} + f_{h2osfc}H_{h2osfc} \tag{5.62}$$

where $(1 - f_{sno} - f_{h2osfc})$, f_{sno}, and f_{h2osfc} are the exposed, snow covered, and surface water covered fractions of the grid cell. The individual fluxes based on the temperatures of the soil T_1, snow T_{snl+1}, and surface water T_{h2osfc} are

$$H_{soil} = -\rho_{atm}C_p\frac{(\theta_{atm} - T_1)}{r_{ah}} \tag{5.63}$$

$$H_{sno} = -\rho_{atm}C_p\frac{(\theta_{atm} - T_{snl+1})}{r_{ah}} \tag{5.64}$$

$$H_{h2osfc} = -\rho_{atm}C_p\frac{(\theta_{atm} - T_{h2osfc})}{r_{ah}} \tag{5.65}$$

where ρ_{atm} is the density of atmospheric air (kg m^{-3}), C_p is the specific heat capacity of air (J kg^{-1} K^{-1}) (Table 2.7), θ_{atm} is the atmospheric potential temperature (K), and r_{ah} is the aerodynamic resistance to sensible heat transfer (s m^{-1}).

The water vapor flux E_g (kg m^{-2} s^{-1}) is, with reference to Figure 5.2,

$$E_g = (1 - f_{sno} - f_{h2osfc})\,E_{soil} + f_{sno}E_{snow} + f_{h2osfc}E_{h2osfc} \tag{5.66}$$

$$E_{soil} = -\frac{\rho_{atm}\left(q_{atm} - q_{soil}\right)}{r_{aw} + r_{soil}} \tag{5.67}$$

$$E_{sno} = -\frac{\rho_{atm}\left(q_{atm} - q_{sno}\right)}{r_{aw}} \tag{5.68}$$

$$E_{h2osfc} = -\frac{\rho_{atm}\left(q_{atm} - q_{h2osfc}\right)}{r_{aw}} \tag{5.69}$$

where q_{atm} is the atmospheric specific humidity (kg kg^{-1}), q_{soil}, q_{sno}, and q_{h2osfc} are the specific humidities (kg kg^{-1}) of the soil, snow, and surface water, respectively, r_{aw} is the aerodynamic resistance to water vapor transfer (s m^{-1}), and r_{soi} is the soil resistance to water vapor transfer (s m^{-1}). The specific humidities of the snow q_{sno} and surface water q_{h2osfc} are assumed to be at the saturation specific humidity of their respective temperatures

$$q_{sno} = q_{sat}^{T_{snl+1}} \qquad (5.70)$$

$$q_{h2osfc} = q_{sat}^{T_{h2osfc}} \qquad (5.71)$$

The specific humidity of the soil surface q_{soil} is assumed to be proportional to the saturation specific humidity

$$q_{soil} = \alpha_{soil} q_{sat}^{T_1} \qquad (5.72)$$

where $q_{sat}^{T_1}$ is the saturated specific humidity at the soil surface temperature T_1 (section 5.5). The factor α_{soil} is a function of the surface soil water matric potential ψ as in *Philip (1957)*

$$\alpha_{soil} = \exp\left(\frac{\psi_1 g}{1 \times 10^3 R_{wv} T_1}\right) \qquad (5.73)$$

where R_{wv} is the gas constant for water vapor (J kg^{-1} K^{-1}) (Table 2.7), g is the gravitational acceleration (m s^{-2}) (Table 2.7), and ψ_1 is the soil water matric potential of the top soil layer (mm). The soil water matric potential ψ_1 is

$$\psi_1 = \psi_{sat,1} s_1^{-B_1} \geq -1 \times 10^8 \qquad (5.74)$$

where $\psi_{sat,1}$ is the saturated matric potential (mm) (section 7.3.1), B_1 is the *Clapp and Hornberger (1978)* parameter (section 7.3.1), and s_1 is the wetness of the top soil layer with respect to saturation. The surface wetness s_1 is a function of the liquid water and ice content

$$s_1 = \frac{1}{\Delta z_1 \theta_{sat,1}} \left[\frac{w_{liq,1}}{\rho_{liq}} + \frac{w_{ice,1}}{\rho_{ice}} \right] \qquad 0.01 \leq s_1 \leq 1.0 \qquad (5.75)$$

where Δz_1 is the thickness of the top soil layer (m), ρ_{liq} and ρ_{ice} are the density of liquid water and ice (kg m^{-3}) (Table 2.7), $w_{liq,1}$ and $w_{ice,1}$ are the mass of liquid water and ice of the top soil layer (kg m^{-2}) (Chapter 7), and $\theta_{sat,1}$ is the saturated volumetric water content (i.e., porosity) of the top soil layer (mm^3 mm^{-3}) (section 7.3.1). If $q_{sat}^{T_1} > q_{atm}$ and $q_{atm} > q_{soil}$, then $q_{soil} = q_{atm}$ and $\frac{dq_{soil}}{dT} = 0$. This prevents large increases (decreases) in q_{soil} for small increases (decreases) in soil moisture in very dry soils.

The resistance to water vapor transfer occurring within the soil matrix r_{soil} (s m^{-1}) is

$$r_{soil} = \frac{DSL}{D_v \tau} \qquad (5.76)$$

where DSL is the thickness of the dry surface layer (m), D_v is the molecular diffusivity of water vapor in air (m^2 s^{-2}) and τ (*unitless*) describes the tortuosity of the vapor flow paths through the soil matrix (*Swenson and Lawrence 2014*).

The thickness of the dry surface layer is given by

$$DSL = \begin{array}{ll} D_{max} \frac{(\theta_{init}-\theta_1)}{(\theta_{init}-\theta_{air})} & \theta_1 < \theta_{init} \\ 0 & \theta_1 \geq \theta_{init} \end{array} \qquad (5.77)$$

where D_{max} is a parameter specifying the length scale of the maximum DSL thickness (default value = 15 mm), θ_{init} (mm^3 mm^{-3}) is the moisture value at which the DSL initiates, θ_1 (mm^3 mm^{-3}) is the moisture value of the top model soil layer, and θ_{air} (mm^3 mm^{-3}) is the 'air dry' soil moisture value (*Dingman 2002*):

$$\theta_{air} = \Phi \left(\frac{\Psi_{sat}}{\Psi_{air}}\right)^{\frac{1}{B_1}} . \qquad (5.78)$$

where Φ is the porosity (mm^3 mm^{-3}), Ψ_{sat} is the saturated soil matric potential (mm), $\Psi_{air} = 10^7$ mm is the air dry matric potential, and B_1 is a function of soil texture (section 7.3.1).

The soil tortuosity is

$$\tau = \Phi_{air}^2 \left(\frac{\Phi_{air}}{\Phi} \right)^{\frac{3}{B_1}} \tag{5.79}$$

where Φ_{air} (mm^3 mm^{-3}) is the air filled pore space

$$\Phi_{air} = \Phi - \theta_{air} . \tag{5.80}$$

D_v depends on temperature

$$D_v = 2.12 \times 10^{-5} \left(\frac{T_1}{T_f} \right)^{1.75} . \tag{5.81}$$

where T_1 (K) is the temperature of the top soil layer and T_f (K) is the freezing temperature of water (Table 2.7).

The roughness lengths used to calculate r_{am} , r_{ah} , and r_{aw} are $z_{0m} = z_{0m, g}$, $z_{0h} = z_{0h, g}$, and $z_{0w} = z_{0w, g}$. The displacement height $d = 0$. The momentum roughness length is $z_{0m, g} = 0.01$ for soil, glaciers, and $z_{0m, g} = 0.0024$ for snow-covered surfaces ($f_{sno} > 0$). In general, z_{0m} is different from z_{0h} because the transfer of momentum is affected by pressure fluctuations in the turbulent waves behind the roughness elements, while for heat and water vapor transfer no such dynamical mechanism exists. Rather, heat and water vapor must be transferred by molecular diffusion across the interfacial sublayer. The following relation from *Zilitinkevich (1970)* is adopted by *Zeng and Dickinson 1998*

$$z_{0h, g} = z_{0w, g} = z_{0m, g} e^{-a(u_* z_{0m, g}/v)^{0.45}} \tag{5.82}$$

where the quantity $u z_{0m, g}/v$ is the roughness Reynolds number (and may be interpreted as the Reynolds number of the smallest turbulent eddy in the flow) with the kinematic viscosity of air $v = 1.5 \times 10^{-5}$ m^2 s^{-1} and $a = 0.13$.

The numerical solution for the fluxes of momentum, sensible heat, and water vapor flux from non-vegetated surfaces proceeds as follows:

1. An initial guess for the wind speed V_a is obtained from (5.24) assuming an initial convective velocity $U_c = 0$ m s^{-1} for stable conditions ($\theta_{v, atm} - \theta_{v, s} \geq 0$ as evaluated from (5.50)) and $U_c = 0.5$ for unstable conditions ($\theta_{v, atm} - \theta_{v, s} < 0$).

2. An initial guess for the Monin-Obukhov length L is obtained from the bulk Richardson number using (5.46) and (5.48).

3. The following system of equations is iterated three times:

4. Friction velocity u_* ((5.32), (5.33), (5.34), (5.35))

5. Potential temperature scale θ_* ((5.37) , (5.38), (5.39), (5.40))

6. Humidity scale q_* ((5.41), (5.42), (5.43), (5.44))

7. Roughness lengths for sensible $z_{0h, g}$ and latent heat $z_{0w, g}$ ((5.82))

8. Virtual potential temperature scale θ_{v*} ((5.17))

9. Wind speed including the convective velocity, V_a ((5.24))

10. Monin-Obukhov length L ((5.49))

11. Aerodynamic resistances r_{am} , r_{ah} , and r_{aw} ((5.55), (5.56), (5.57))

12. Momentum fluxes τ_x , τ_y ((5.5), (5.6))

13. Sensible heat flux H_g ((5.62))

5.2. Sensible and Latent Heat Fluxes for Non-Vegetated Surfaces

14. Water vapor flux E_g ((5.66))

15. 2-m height air temperature T_{2m} and specific humidity q_{2m} ((5.58) , (5.59))

The partial derivatives of the soil surface fluxes with respect to ground temperature, which are needed for the soil temperature calculations (section 6.1) and to update the soil surface fluxes (section 5.4), are

$$\frac{\partial H_g}{\partial T_g} = \frac{\rho_{atm} C_p}{r_{ah}} \tag{5.83}$$

$$\frac{\partial E_g}{\partial T_g} = \frac{\beta_{soi} \rho_{atm}}{r_{aw}} \frac{dq_g}{dT_g} \tag{5.84}$$

where

$$\frac{dq_g}{dT_g} = (1 - f_{sno} - f_{h2osfc}) \alpha_{soil} \frac{dq_{sat}^{T_{soil}}}{dT_{soil}} + f_{sno} \frac{dq_{sat}^{T_{sno}}}{dT_{sno}} + f_{h2osfc} \frac{dq_{sat}^{T_{h2osfc}}}{dT_{h2osfc}}. \tag{5.85}$$

The partial derivatives $\frac{\partial r_{ah}}{\partial T_g}$ and $\frac{\partial r_{aw}}{\partial T_g}$, which cannot be determined analytically, are ignored for $\frac{\partial H_g}{\partial T_g}$ and $\frac{\partial E_g}{\partial T_g}$.

5.3 Sensible and Latent Heat Fluxes and Temperature for Vegetated Surfaces

In the case of a vegetated surface, the sensible heat H and water vapor flux E are partitioned into vegetation and ground fluxes that depend on vegetation T_v and ground T_g temperatures in addition to surface temperature T_s and specific humidity q_s . Because of the coupling between vegetation temperature and fluxes, Newton-Raphson iteration is used to solve for the vegetation temperature and the sensible heat and water vapor fluxes from vegetation simultaneously using the ground temperature from the previous time step. In section 5.3.1, the equations used in the iteration scheme are derived. Details on the numerical scheme are provided in section 5.3.2.

5.3.1 Theory

The air within the canopy is assumed to have negligible capacity to store heat so that the sensible heat flux H between the surface at height $z_{0h} + d$ and the atmosphere at height $z_{atm, h}$ must be balanced by the sum of the sensible heat from the vegetation H_v and the ground H_g

$$H = H_v + H_g \tag{5.86}$$

where, with reference to Figure 5.1,

$$H = -\rho_{atm} C_p \frac{(\theta_{atm} - T_s)}{r_{ah}} \tag{5.87}$$

$$H_v = -\rho_{atm} C_p (T_s - T_v) \frac{(L + S)}{r_b} \tag{5.88}$$

$$H_g = (1 - f_{sno} - f_{h2osfc}) H_{soil} + f_{sno} H_{snow} + f_{h2osfc} H_{h2osfc} , \tag{5.89}$$

where

$$H_{soil} = -\rho_{atm} C_p \frac{(T_s - T_1)}{r'_{ah}} \tag{5.90}$$

$$H_{sno} = -\rho_{atm} C_p \frac{(T_s - T_{snl+1})}{r'_{ah}} \tag{5.91}$$

$$H_{h2osfc} = -\rho_{atm} C_p \frac{(T_s - T_{h2osfc})}{r'_{ah}} \tag{5.92}$$

where ρ_{atm} is the density of atmospheric air (kg m^{-3}), C_p is the specific heat capacity of air (J kg^{-1} K^{-1}) (Table 2.7), θ_{atm} is the atmospheric potential temperature (K), and r_{ah} is the aerodynamic resistance to sensible heat transfer (s m^{-1}).

Here, T_s is the surface temperature at height $z_{0h} + d$, also referred to as the canopy air temperature. L and S are the exposed leaf and stem area indices (section 2.1.4), r_b is the leaf boundary layer resistance (s m^{-1}), and r'_{ah} is the aerodynamic resistance (s m^{-1}) to heat transfer between the ground at height z'_{0h} and the canopy air at height $z_{0h} + d$.

Equations (5.86) - (5.89) can be solved for the canopy air temperature T_s

$$T_s = \frac{c_a^h \theta_{atm} + c_g^h T_g + c_v^h T_v}{c_a^h + c_g^h + c_v^h} \tag{5.93}$$

where

$$c_a^h = \frac{1}{r_{ah}} \tag{5.94}$$

$$c_g^h = \frac{1}{r'_{ah}} \tag{5.95}$$

$$c_v^h = \frac{(L+S)}{r_b} \tag{5.96}$$

are the sensible heat conductances from the canopy air to the atmosphere, the ground to canopy air, and leaf surface to canopy air, respectively (m s^{-1}).

When the expression for T_s is substituted into equation (5.88), the sensible heat flux from vegetation H_v is a function of θ_{atm}, T_g, and T_v

$$H_v = -\rho_{atm} C_p \left[c_a^h \theta_{atm} + c_g^h T_g - \left(c_a^h + c_g^h \right) T_v \right] \frac{c_v^h}{c_a^h + c_v^h + c_g^h}. \tag{5.97}$$

Similarly, the expression for T_s can be substituted into equation to obtain the sensible heat flux from ground H_g

$$H_g = -\rho_{atm} C_p \left[c_a^h \theta_{atm} + c_v^h T_v - \left(c_a^h + c_v^h \right) T_g \right] \frac{c_g^h}{c_a^h + c_v^h + c_g^h}. \tag{5.98}$$

The air within the canopy is assumed to have negligible capacity to store water vapor so that the water vapor flux E between the surface at height $z_{0w} + d$ and the atmosphere at height $z_{atm,\,w}$ must be balanced by the sum of the water vapor flux from the vegetation E_v and the ground E_g

$$E = E_v + E_g \tag{5.99}$$

where, with reference to Figure 5.2,

$$E = -\rho_{atm} \frac{(q_{atm} - q_s)}{r_{aw}} \tag{5.100}$$

$$E_v = -\rho_{atm} \frac{\left(q_s - q_{sat}^{T_v} \right)}{r_{total}} \tag{5.101}$$

$$E_g = (1 - f_{sno} - f_{h2osfc}) E_{soil} + f_{sno} E_{snow} + f_{h2osfc} E_{h2osfc}, \tag{5.102}$$

where

$$E_{soil} = -\rho_{atm} \frac{(q_s - q_{soil})}{r'_{aw} + r_{soil}} \tag{5.103}$$

5.3. Sensible and Latent Heat Fluxes and Temperature for Vegetated Surfaces
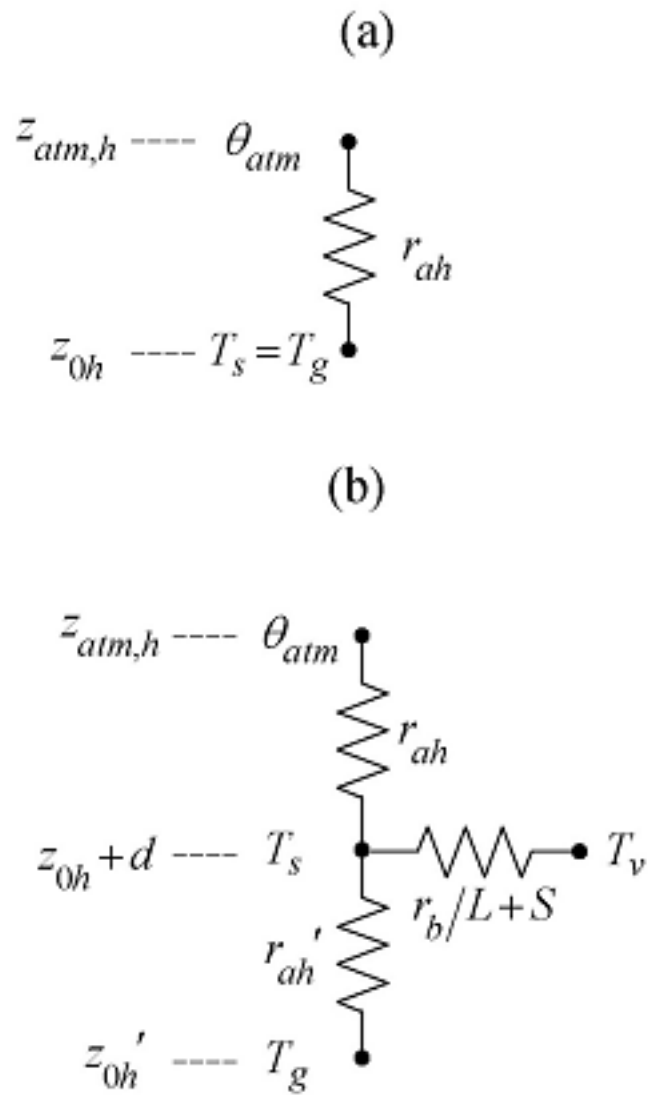
Figure 5.1: Figure Schematic diagram of sensible heat fluxes for (a) non-vegetated surfaces and (b) vegetated surfaces.
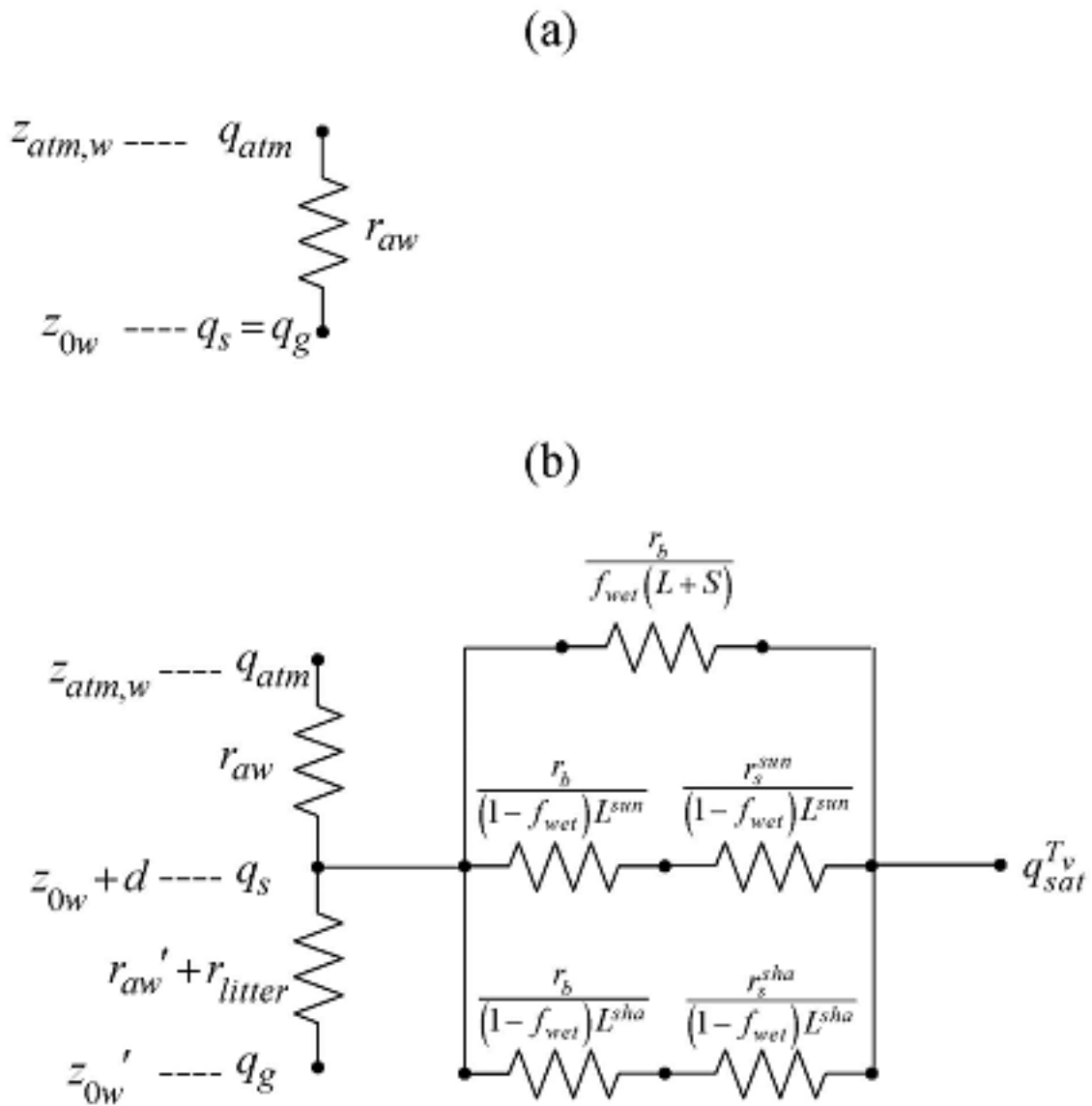
Figure 5.2: Figure Schematic diagram of water vapor fluxes for (a) non-vegetated surfaces and (b) vegetated surfaces.

$$E_{sno} = -\rho_{atm} \frac{(q_s - q_{sno})}{r'_{aw} + r_{soil}}$$ (5.104)

$$E_{h2osfc} = -\rho_{atm} \frac{(q_s - q_{h2osfc})}{r'_{aw} + r_{soil}}$$ (5.105)

where q_{atm} is the atmospheric specific humidity (kg kg^{-1}), r_{aw} is the aerodynamic resistance to water vapor transfer (s m^{-1}), $q_{sat}^{T_v}$ (kg kg^{-1}) is the saturation water vapor specific humidity at the vegetation temperature (section 5.5), q_g , q_{sno} , and q_{h2osfc} are the specific humidities of the soil, snow, and surface water (section 5.2), r'_{aw} is the aerodynamic resistance (s m^{-1}) to water vapor transfer between the ground at height z_{0w} and the canopy air at height $z_{0w} + d$, and r_{soil} ((5.76)) is a resistance to diffusion through the soil (s m^{-1}). r_{total} is the total resistance to water vapor transfer from the canopy to the canopy air and includes contributions from leaf boundary layer and sunlit and shaded stomatal resistances r_b , r_s^{sun} , and r_s^{sha} (Figure 5.2). The water vapor flux from vegetation is the sum of water vapor flux from wetted leaf and stem area E_v^w (evaporation of water intercepted by the canopy) and transpiration from dry leaf surfaces E_v^t

$$E_v = E_v^w + E_v^t.$$ (5.106)

Equations (5.99) - (5.102) can be solved for the canopy specific humidity q_s

$$q_s = \frac{c_a^w q_{atm} + c_g^w q_g + c_v^w q_{sat}^{T_v}}{c_a^w + c_v^w + c_g^w}$$ (5.107)

where

$$c_a^w = \frac{1}{r_{aw}}$$ (5.108)

$$c_v^w = \frac{(L + S)}{r_b} r''$$ (5.109)

$$c_g^w = \frac{1}{r'_{aw} + r_{soil}}$$ (5.110)

are the water vapor conductances from the canopy air to the atmosphere, the leaf to canopy air, and ground to canopy air, respectively. The term r'' is determined from contributions by wet leaves and transpiration and limited by available water and potential evaporation as

$$r'' = \begin{cases} \min \left(f_{wet} + r''_{dry}, \ \frac{E_v^{w,pot} r''_{dry} + \frac{W_{can}}{\Delta t}}{E_v^{w,pot}} \right) & E_v^{w,pot} > 0, \ \beta_t > 0 \\ \min \left(f_{wet}, \ \frac{E_v^{w,pot} r''_{dry} + \frac{W_{can}}{\Delta t}}{E_v^{w,pot}} \right) & E_v^{w,pot} > 0, \ \beta_t \leq 0 \\ 1 & E_v^{w,pot} \leq 0 \end{cases}$$ (5.111)

where f_{wet} is the fraction of leaves and stems that are wet (section 7.1), W_{can} is canopy water (kg m^{-2}) (section 7.1), Δt is the time step (s), and β_t is a soil moisture function limiting transpiration (Chapter 9). The potential evaporation from wet foliage per unit wetted area is

$$E_v^{w,pot} = -\frac{\rho_{atm} \left(q_s - q_{sat}^{T_v} \right)}{r_b}.$$ (5.112)

The term r''_{dry} is

$$r''_{dry} = \frac{f_{dry} r_b}{L} \left(\frac{L^{sun}}{r_b + r_s^{sun}} + \frac{L^{sha}}{r_b + r_s^{sha}} \right)$$ (5.113)

where f_{dry} is the fraction of leaves that are dry (section 7.1), L^{sun} and L^{sha} are the sunlit and shaded leaf area indices (section 4.1), and r_s^{sun} and r_s^{sha} are the sunlit and shaded stomatal resistances (s m^{-1}) (Chapter 9).

When the expression for q_s is substituted into equation (5.101), the water vapor flux from vegetation E_v is a function of q_{atm}, q_g, and $q_{sat}^{T_v}$

$$E_v = -\rho_{atm} \left[c_a^w q_{atm} + c_g^w q_g - \left(c_a^w + c_g^w \right) q_{sat}^{T_v} \right] \frac{c_v^w}{c_a^w + c_v^w + c_g^w}. \tag{5.114}$$

Similarly, the expression for q_s can be substituted into (5.84) to obtain the water vapor flux from the ground beneath the canopy E_g

$$E_g = -\rho_{atm} \left[c_a^w q_{atm} + c_v^w q_{sat}^{T_v} - \left(c_a^w + c_v^w \right) q_g \right] \frac{c_g^w}{c_a^w + c_v^w + c_g^w}. \tag{5.115}$$

The aerodynamic resistances to heat (moisture) transfer between the ground at height z_{0h}' (z_{0w}') and the canopy air at height $z_{0h} + d$ ($z_{0w} + d$) are

$$r_{ah}' = r_{aw}' = \frac{1}{C_s U_{av}} \tag{5.116}$$

where

$$U_{av} = V_a \sqrt{\frac{1}{r_{am} V_a}} = u_* \tag{5.117}$$

is the magnitude of the wind velocity incident on the leaves (equivalent here to friction velocity) (m s^{-1}) and C_s is the turbulent transfer coefficient between the underlying soil and the canopy air. C_s is obtained by interpolation between values for dense canopy and bare soil (*Zeng et al. 2005*)

$$C_s = C_{s,\,bare} W + C_{s,\,dense} (1 - W) \tag{5.118}$$

where the weight W is

$$W = e^{-(L+S)}. \tag{5.119}$$

The dense canopy turbulent transfer coefficient (*Dickinson et al. 1993*) is

$$C_{s,\,dense} = 0.004 \ . \tag{5.120}$$

The bare soil turbulent transfer coefficient is

$$C_{s,\,bare} = \frac{k}{a} \left(\frac{z_{0m,\,g} U_{av}}{\upsilon} \right)^{-0.45} \tag{5.121}$$

where the kinematic viscosity of air $\upsilon = 1.5 \times 10^{-5}$ m^2 s^{-1} and $a = 0.13$.

The leaf boundary layer resistance r_b is

$$r_b = \frac{1}{C_v} \left(U_{av} / d_{leaf} \right)^{-1/2} \tag{5.122}$$

where $C_v = 0.01$ ms$^{-1/2}$ is the turbulent transfer coefficient between the canopy surface and canopy air, and d_{leaf} is the characteristic dimension of the leaves in the direction of wind flow (Table 5.1).

The partial derivatives of the fluxes from the soil beneath the canopy with respect to ground temperature, which are needed for the soil temperature calculations (section 6.1) and to update the soil surface fluxes (section 5.4), are

$$\frac{\partial H_g}{\partial T_g} = \frac{\rho_{atm} C_p}{r_{ah}'} \frac{c_a^h + c_v^h}{c_a^h + c_v^h + c_g^h} \tag{5.123}$$

$$\frac{\partial E_g}{\partial T_g} = \frac{\rho_{atm}}{r_{aw}' + r_{soil}} \frac{c_a^w + c_v^w}{c_a^w + c_v^w + c_g^w} \frac{dq_g}{dT_g}. \tag{5.124}$$

5.3. Sensible and Latent Heat Fluxes and Temperature for Vegetated Surfaces

The partial derivatives $\frac{\partial r'_{ah}}{\partial T_g}$ and $\frac{\partial r'_{aw}}{\partial T_g}$, which cannot be determined analytically, are ignored for $\frac{\partial H_g}{\partial T_g}$ and $\frac{\partial E_g}{\partial T_g}$.

The roughness lengths used to calculate r_{am} , r_{ah} , and r_{aw} from (5.55), (5.56), and (5.57) are $z_{0m} = z_{0m,\,v}$, $z_{0h} = z_{0h,\,v}$, and $z_{0w} = z_{0w,\,v}$. The vegetation displacement height d and the roughness lengths are a function of plant height and adjusted for canopy density following *Zeng and Wang (2007)*

$$z_{0m,\,v} = z_{0h,\,v} = z_{0w,\,v} = \exp\left[V \ln\left(z_{top} R_{z0m}\right) + (1 - V) \ln\left(z_{0m,\,g}\right)\right] \tag{5.125}$$

$$d = z_{top} R_d V \tag{5.126}$$

where z_{top} is canopy top height (m) (Table 2.2), R_{z0m} and R_d are the ratio of momentum roughness length and displacement height to canopy top height, respectively (Table 5.1), and $z_{0m,\,g}$ is the ground momentum roughness length (m) (section 5.2). The fractional weight V is determined from

$$V = \frac{1 - \exp\left\{-\beta \min\left[L + S, (L + S)_{cr}\right]\right\}}{1 - \exp\left[-\beta \left(L + S\right)_{cr}\right]} \tag{5.127}$$

where $\beta = 1$ and $(L + S)_{cr} = 2$ (m^2 m^{-2}) is a critical value of exposed leaf plus stem area for which z_{0m} reaches its maximum.

Table 5.1: Plant functional type aerodynamic parameters

Plant functional type	R_{z0m}	R_d	d_{leaf} (m)
NET Temperate	0.055	0.67	0.04
NET Boreal	0.055	0.67	0.04
NDT Boreal	0.055	0.67	0.04
BET Tropical	0.075	0.67	0.04
BET temperate	0.075	0.67	0.04
BDT tropical	0.055	0.67	0.04
BDT temperate	0.055	0.67	0.04
BDT boreal	0.055	0.67	0.04
BES temperate	0.120	0.68	0.04
BDS temperate	0.120	0.68	0.04
BDS boreal	0.120	0.68	0.04
C_3 arctic grass	0.120	0.68	0.04
C_3 grass	0.120	0.68	0.04
C_4 grass	0.120	0.68	0.04
Crop R	0.120	0.68	0.04
Crop I	0.120	0.68	0.04
Corn R	0.120	0.68	0.04
Corn I	0.120	0.68	0.04
Temp Cereal R	0.120	0.68	0.04
Temp Cereal I	0.120	0.68	0.04
Winter Cereal R	0.120	0.68	0.04
Winter Cereal I	0.120	0.68	0.04
Soybean R	0.120	0.68	0.04
Soybean I	0.120	0.68	0.04

5.3.2 Numerical Implementation

Canopy energy conservation gives

$$-\vec{S}_v + \vec{L}_v\left(T_v\right) + H_v\left(T_v\right) + \lambda E_v\left(T_v\right) = 0 \tag{5.128}$$

where $\overrightarrow{S}_v$ is the solar radiation absorbed by the vegetation (section 4.1), $\overrightarrow{L}_v$ is the net longwave radiation absorbed by vegetation (section 4.2), and H_v and λE_v are the sensible and latent heat fluxes from vegetation, respectively. The term λ is taken to be the latent heat of vaporization λ_{vap} (Table 2.7).

$\overrightarrow{L}_v$, H_v , and λE_v depend on the vegetation temperature T_v . The Newton-Raphson method for finding roots of non-linear systems of equations can be applied to iteratively solve for T_v as

$$\Delta T_v = \frac{\overrightarrow{S}_v - \overrightarrow{L}_v - H_v - \lambda E_v}{\frac{\partial \overrightarrow{L}_v}{\partial T_v} + \frac{\partial H_v}{\partial T_v} + \frac{\partial \lambda E_v}{\partial T_v}} \tag{5.129}$$

where $\Delta T_v = T_v^{n+1} - T_v^n$ and the subscript "n" indicates the iteration.

The partial derivatives are

$$\frac{\partial \overrightarrow{L}_v}{\partial T_v} = 4\varepsilon_v\sigma \left[2 - \varepsilon_v \left(1 - \varepsilon_g\right)\right] T_v^3 \tag{5.130}$$

$$\frac{\partial H_v}{\partial T_v} = \rho_{atm}C_p \left(c_a^h + c_g^h\right) \frac{c_v^h}{c_a^h + c_v^h + c_g^h} \tag{5.131}$$

$$\frac{\partial \lambda E_v}{\partial T_v} = \lambda\rho_{atm} \left(c_a^w + c_g^w\right) \frac{c_v^w}{c_a^w + c_v^w + c_g^w} \frac{dq_{sat}^{T_v}}{dT_v}. \tag{5.132}$$

The partial derivatives $\frac{\partial r_{ah}}{\partial T_v}$ and $\frac{\partial r_{aw}}{\partial T_v}$, which cannot be determined analytically, are ignored for $\frac{\partial H_v}{\partial T_v}$ and $\frac{\partial \lambda E_v}{\partial T_v}$. However, if ζ changes sign more than four times during the temperature iteration, $\zeta = -0.01$. This helps prevent "flip-flopping" between stable and unstable conditions. The total water vapor flux E_v , transpiration flux E_v^t , and sensible heat flux H_v are updated for changes in leaf temperature as

$$E_v = -\rho_{atm} \left[c_a^w q_{atm} + c_g^w q_g - \left(c_a^w + c_g^w\right) \left(q_{sat}^{T_v} + \frac{dq_{sat}^{T_v}}{dT_v}\Delta T_v\right)\right] \frac{c_v^w}{c_a^w + c_v^w + c_g^w} \tag{5.133}$$

$$E_v^t = -r_{dry}^{''}\rho_{atm} \left[c_a^w q_{atm} + c_g^w q_g - \left(c_a^w + c_g^w\right) \left(q_{sat}^{T_v} + \frac{dq_{sat}^{T_v}}{dT_v}\Delta T_v\right)\right] \frac{c_v^h}{c_a^w + c_v^w + c_g^w} \tag{5.134}$$

$$H_v = -\rho_{atm}C_p \left[c_a^h\theta_{atm} + c_g^hT_g - \left(c_a^h + c_g^h\right) \left(T_v + \Delta T_v\right)\right] \frac{c_v^h}{c_a^h + c_v^h + c_g^h}. \tag{5.135}$$

The numerical solution for vegetation temperature and the fluxes of momentum, sensible heat, and water vapor flux from vegetated surfaces proceeds as follows:

1. Initial values for canopy air temperature and specific humidity are obtained from

$$T_s = \frac{T_g + \theta_{atm}}{2} \tag{5.136}$$

$$q_s = \frac{q_g + q_{atm}}{2}. \tag{5.137}$$

2. An initial guess for the wind speed V_a is obtained from (5.24) assuming an initial convective velocity $U_c = 0$ m s^{-1} for stable conditions ($\theta_{v, atm} - \theta_{v, s} \geq 0$ as evaluated from (5.50)) and $U_c = 0.5$ for unstable conditions ($\theta_{v, atm} - \theta_{v, s} < 0$).

3. An initial guess for the Monin-Obukhov length L is obtained from the bulk Richardson number using equation and (5.46) and (5.48).

4. Iteration proceeds on the following system of equations:

5. Friction velocity u_* ((5.32), (5.33), (5.34), (5.35))

5.3. Sensible and Latent Heat Fluxes and Temperature for Vegetated Surfaces

6. Ratio $\frac{\theta_*}{\theta_{atm}-\theta_s}$ ((5.37) , (5.38), (5.39), (5.40))

7. Ratio $\frac{q_*}{q_{atm}-q_s}$ ((5.41), (5.42), (5.43), (5.44))

8. Aerodynamic resistances r_{am} , r_{ah} , and r_{aw} ((5.55), (5.56), (5.57))

9. Magnitude of the wind velocity incident on the leaves U_{av} ((5.117))

10. Leaf boundary layer resistance r_b ((5.136))

11. Aerodynamic resistances r'_{ah} and r'_{aw} ((5.116))

12. Sunlit and shaded stomatal resistances r_s^{sun} and r_s^{sha} (Chapter 9)

13. Sensible heat conductances c_a^h , c_g^h , and c_v^h ((5.94), (5.95), (5.96))

14. Latent heat conductances c_a^w , c_v^w , and c_g^w ((5.108), (5.109), (5.110))

15. Sensible heat flux from vegetation H_v ((5.97))

16. Latent heat flux from vegetation λE_v ((5.101))

17. If the latent heat flux has changed sign from the latent heat flux computed at the previous iteration ($\lambda E_v^{n+1} \times \lambda E_v^n < 0$), the latent heat flux is constrained to be 10% of the computed value. The difference between the constrained and computed value ($\Delta_1 = 0.1\lambda E_v^{n+1} - \lambda E_v^{n+1}$) is added to the sensible heat flux later.

18. Change in vegetation temperature ΔT_v ((5.129)) and update the vegetation temperature as $T_v^{n+1} = T_v^n + \Delta T_v$. T_v is constrained to change by no more than 1ºK in one iteration. If this limit is exceeded, the energy error is

$$\Delta_2 = \overrightarrow{S}_v - \overrightarrow{L}_v - \frac{\partial \overrightarrow{L}_v}{\partial T_v}\Delta T_v - H_v - \frac{\partial H_v}{\partial T_v}\Delta T_v - \lambda E_v - \frac{\partial \lambda E_v}{\partial T_v}\Delta T_v \qquad (5.138)$$

where $\Delta T_v = 1$ or -1. The error Δ_2 is added to the sensible heat flux later.

1. Water vapor flux E_v ((5.133))

2. Transpiration E_v^t ((5.134) if $\beta_t > 0$, otherwise $E_v^t = 0$)

3. The water vapor flux E_v is constrained to be less than or equal to the sum of transpiration E_v^t and the water available from wetted leaves and stems $W_{can}/\Delta t$. The energy error due to this constraint is

$$\Delta_3 = \max\left(0, \; E_v - E_v^t - \frac{W_{can}}{\Delta t}\right). \qquad (5.139)$$

The error $\lambda \Delta_3$ is added to the sensible heat flux later.

1. Sensible heat flux H_v (:eq:''). The three energy error terms, Δ_1 , Δ_2 , and $\lambda\Delta_3$ are also added to the sensible heat flux.

2. The saturated vapor pressure e_i (Chapter 9), saturated specific humidity $q_{sat}^{T_v}$ and its derivative $\frac{dq_{sat}^{T_v}}{dT_v}$ at the leaf surface (section 5.5), are re-evaluated based on the new T_v .

3. Canopy air temperature T_s ((5.93))

4. Canopy air specific humidity q_s ((5.107))

5. Temperature difference $\theta_{atm} - \theta_s$

6. Specific humidity difference $q_{atm} - q_s$

7. Potential temperature scale $\theta_* = \frac{\theta_*}{\theta_{atm}-\theta_s} (\theta_{atm} - \theta_s)$ where $\frac{\theta_*}{\theta_{atm}-\theta_s}$ was calculated earlier in the iteration

8. Humidity scale $q_* = \frac{q_*}{q_{atm}-q_s} (q_{atm} - q_s)$ where $\frac{q_*}{q_{atm}-q_s}$ was calculated earlier in the iteration

9. Virtual potential temperature scale θ_{v*} ((5.17))

10. Wind speed including the convective velocity, V_a ((5.24))

11. Monin-Obukhov length L ((5.49))

12. The iteration is stopped after two or more steps if $\tilde{\Delta} T_v < 0.01$ and $\left| \lambda E_v^{n+1} - \lambda E_v^n \right| < 0.1$ where $\tilde{\Delta} T_v = \max \left(\left| T_v^{n+1} - T_v^n \right|, \left| T_v^n - T_v^{n-1} \right| \right)$, or after forty iterations have been carried out.

13. Momentum fluxes τ_x , τ_y ((5.5), (5.6))

14. Sensible heat flux from ground H_g ((5.89))

15. Water vapor flux from ground E_g ((5.102))

16. 2-m height air temperature T_{2m} , specific humidity q_{2m} , relative humidity RH_{2m} ((5.58) , (5.59), (5.60))

5.4 Update of Ground Sensible and Latent Heat Fluxes

The sensible and water vapor heat fluxes derived above for bare soil and soil beneath canopy are based on the ground surface temperature from the previous time step T_g^n and are used as the surface forcing for the solution of the soil temperature equations (section 6.1). This solution yields a new ground surface temperature T_g^{n+1} . The ground sensible and water vapor fluxes are then updated for T_g^{n+1} as

$$H_g' = H_g + \left(T_g^{n+1} - T_g^n \right) \frac{\partial H_g}{\partial T_g} \tag{5.140}$$

$$E_g' = E_g + \left(T_g^{n+1} - T_g^n \right) \frac{\partial E_g}{\partial T_g} \tag{5.141}$$

where H_g and E_g are the sensible heat and water vapor fluxes derived from equations and for non-vegetated surfaces and equations and for vegetated surfaces using T_g^n . One further adjustment is made to H_g' and E_g' . If the soil moisture in the top snow/soil layer is not sufficient to support the updated ground evaporation, i.e., if $E_g' > 0$ and $f_{evap} < 1$ where

$$f_{evap} = \frac{\left(w_{ice,\,snl+1} + w_{liq,\,snl+1} \right) / \Delta t}{\sum_{j=1}^{npft} \left(E_g' \right)_j (wt)_j} \leq 1, \tag{5.142}$$

an adjustment is made to reduce the ground evaporation accordingly as

$$E_g'' = f_{evap} E_g'. \tag{5.143}$$

The term $\sum_{j=1}^{npft} \left(E_g' \right)_j (wt)_j$ is the sum of E_g' over all evaporating PFTs where $\left(E_g' \right)_j$ is the ground evaporation from the jth PFT on the column, $(wt)_j$ is the relative area of the jth PFT with respect to the column, and $npft$ is the number of PFTs on the column. $w_{ice,\,snl+1}$ and $w_{liq,\,snl+1}$ are the ice and liquid water contents (kg m^{-2}) of the top snow/soil layer (Chapter 7). Any resulting energy deficit is assigned to sensible heat as

$$H_g'' = H_g + \lambda \left(E_g' - E_g'' \right). \tag{5.144}$$

The ground water vapor flux E_g'' is partitioned into evaporation of liquid water from snow/soil q_{seva} (kgm^{-2} s^{-1}), sublimation from snow/soil ice q_{subl} (kg m^{-2} s^{-1}), liquid dew on snow/soil q_{sdew} (kg m^{-2} s^{-1}), or frost on snow/soil q_{frost} (kg m^{-2} s^{-1}) as

$$q_{seva} = \max \left(E_{sno}'' \frac{w_{liq,\,snl+1}}{w_{ice,\,snl+1} + w_{liq,\,snl+1}}, 0 \right) \qquad E_{sno}'' \geq 0,\, w_{ice,\,snl+1} + w_{liq,\,snl+1} > 0 \tag{5.145}$$

$$q_{subl} = E_{sno}'' - q_{seva} \qquad E_{sno}'' \geq 0 \tag{5.146}$$

$$q_{sdew} = \left| E_{sno}'' \right| \qquad E_{sno}'' < 0 \text{ and } T_g \geq T_f \tag{5.147}$$

$$q_{frost} = |E''_{sno}| \qquad E''_{sno} < 0 \text{ and } T_g < T_f. \tag{5.148}$$

The loss or gain in snow mass due to q_{seva}, q_{subl}, q_{sdew}, and q_{frost} on a snow surface are accounted for during the snow hydrology calculations (Chapter 8). The loss of soil and surface water due to q_{seva} is accounted for in the calculation of infiltration (section 7.2.3), while losses or gains due to q_{subl}, q_{sdew}, and q_{frost} on a soil surface are accounted for following the sub-surface drainage calculations (section 7.5).

The ground heat flux G is calculated as

$$G = \vec{S}_g - \vec{L}_g - H_g - \lambda E_g \tag{5.149}$$

where $\vec{S}_g$ is the solar radiation absorbed by the ground (section 4.1), $\vec{L}_g$ is the net longwave radiation absorbed by the ground (section 4.2)

$$\vec{L}_g = L_g \uparrow - \delta_{veg} \varepsilon_g L_v \downarrow - (1 - \delta_{veg}) \varepsilon_g L_{atm} \downarrow + 4\varepsilon_g \sigma \left(T_g^n\right)^3 \left(T_g^{n+1} - T_g^n\right), \tag{5.150}$$

where

$$L_g \uparrow = \varepsilon_g \sigma \left[(1 - f_{sno} - f_{h2osfc}) \left(T_1^n\right)^4 + f_{sno} \left(T_{sno}^n\right)^4 + f_{h2osfc} \left(T_{h2osfc}^n\right)^4 \right] \tag{5.151}$$

and H_g and λE_g are the sensible and latent heat fluxes after the adjustments described above.

When converting ground water vapor flux to an energy flux, the term λ is arbitrarily assumed to be

$$\lambda = \left\{ \begin{array}{ll} \lambda_{sub} & \text{if } w_{liq,\,snl+1} = 0 \text{ and } w_{ice,\,snl+1} > 0 \\ \lambda_{vap} & \text{otherwise} \end{array} \right\} \tag{5.152}$$

where λ_{sub} and λ_{vap} are the latent heat of sublimation and vaporization, respectively (J (kg^{-1}) (Table 2.7). When converting vegetation water vapor flux to an energy flux, λ_{vap} is used.

The system balances energy as

$$\vec{S}_g + \vec{S}_v + L_{atm} \downarrow - L \uparrow - H_v - H_g - \lambda_{vap} E_v - \lambda E_g - G = 0. \tag{5.153}$$

5.5 Saturation Vapor Pressure

Saturation vapor pressure e_{sat}^T (Pa) and its derivative $\frac{de_{sat}^T}{dT}$, as a function of temperature T (ºC), are calculated from the eighth-order polynomial fits of *Flatau et al. (1992)*

$$e_{sat}^T = 100 \left[a_0 + a_1 T + \cdots + a_n T^n\right] \tag{5.154}$$

$$\frac{de_{sat}^T}{dT} = 100 \left[b_0 + b_1 T + \cdots + b_n T^n\right] \tag{5.155}$$

where the coefficients for ice are valid for $-75\,^\circ\text{C} \le T < 0\,^\circ\text{C}$ and the coefficients for water are valid for $0\,^\circ\text{C} \le T \le 100\,^\circ\text{C}$ (Table 5.2 and Table 5.3). The saturated water vapor specific humidity q_{sat}^T and its derivative $\frac{dq_{sat}^T}{dT}$ are

$$q_{sat}^T = \frac{0.622 e_{sat}^T}{P_{atm} - 0.378 e_{sat}^T} \tag{5.156}$$

$$\frac{dq_{sat}^T}{dT} = \frac{0.622 P_{atm}}{\left(P_{atm} - 0.378 e_{sat}^T\right)^2} \frac{de_{sat}^T}{dT}. \tag{5.157}$$

Table 5.2: Coefficients for e_{sat}^{T}

	water	ice
a_0	6.11213476	6.11123516
a_1	$4.44007856 \times 10^{-1}$	$5.03109514 \times 10^{-1}$
a_2	$1.43064234 \times 10^{-2}$	$1.88369801 \times 10^{-2}$
a_3	$2.64461437 \times 10^{-4}$	$4.20547422 \times 10^{-4}$
a_4	$3.05903558 \times 10^{-6}$	$6.14396778 \times 10^{-6}$
a_5	$1.96237241 \times 10^{-8}$	$6.02780717 \times 10^{-8}$
a_6	$8.92344772 \times 10^{-11}$	$3.87940929 \times 10^{-10}$
a_7	$-3.73208410 \times 10^{-13}$	$1.49436277 \times 10^{-12}$
a_8	$2.09339997 \times 10^{-16}$	$2.62655803 \times 10^{-15}$

Table 5.3: Coefficients for $\frac{de_{sat}^{T}}{dT}$

	water	ice
b_0	$4.44017302 \times 10^{-1}$	$5.03277922 \times 10^{-1}$
b_1	$2.86064092 \times 10^{-2}$	$3.77289173 \times 10^{-2}$
b_2	$7.94683137 \times 10^{-4}$	$1.26801703 \times 10^{-3}$
b_3	$1.21211669 \times 10^{-5}$	$2.49468427 \times 10^{-5}$
b_4	$1.03354611 \times 10^{-7}$	$3.13703411 \times 10^{-7}$
b_5	$4.04125005 \times 10^{-10}$	$2.57180651 \times 10^{-9}$
b_6	$-7.88037859 \times 10^{-13}$	$1.33268878 \times 10^{-11}$
b_7	$-1.14596802 \times 10^{-14}$	$3.94116744 \times 10^{-14}$
b_8	$3.81294516 \times 10^{-17}$	$4.98070196 \times 10^{-17}$

CHAPTER 6

SOIL AND SNOW TEMPERATURES

The first law of heat conduction is

$$F = -\lambda \nabla T \qquad (6.1)$$

where F is the amount of heat conducted across a unit cross-sectional area in unit time (W m^{-2}), λ is thermal conductivity (W m^{-1} K^{-1}), and ∇T is the spatial gradient of temperature (K m^{-1}). In one-dimensional form

$$F_z = -\lambda \frac{\partial T}{\partial z} \qquad (6.2)$$

where z is in the vertical direction (m) and is positive downward and F_z is positive upward. To account for non-steady or transient conditions, the principle of energy conservation in the form of the continuity equation is invoked as

$$c \frac{\partial T}{\partial t} = -\frac{\partial F_z}{\partial z} \qquad (6.3)$$

where c is the volumetric snow/soil heat capacity (J m^{-3} K^{-1}) and t is time (s). Combining equations and yields the second law of heat conduction in one-dimensional form

$$c \frac{\partial T}{\partial t} = \frac{\partial}{\partial z} \left[\lambda \frac{\partial T}{\partial z} \right]. \qquad (6.4)$$

This equation is solved numerically to calculate the soil, snow, and surface water temperatures for a fifteen-layer soil column with up to five overlying layers of snow and a single surface water layer with the boundary conditions of h as the heat flux into the top soil, snow, and surface water layers from the overlying atmosphere (section 6.1) and zero heat flux at the bottom of the soil column. The temperature profile is calculated first without phase change and then readjusted for phase change (section 6.2).

6.1 Numerical Solution

The soil column is discretized into 25 layers (section 2.2) where $N_{levgrnd} = 25$ is the number of soil layers (Table 2.3).

The overlying snow pack is modeled with up to five layers depending on the total snow depth. The layers from top to bottom are indexed in the Fortran code as $i = -4, -3, -2, -1, 0$, which permits the accumulation or ablation of snow

at the top of the snow pack without renumbering the layers. Layer $i = 0$ is the snow layer next to the soil surface and layer $i = snl + 1$ is the top layer, where the variable snl is the negative of the number of snow layers. The number of snow layers and the thickness of each layer is a function of snow depth z_{sno} (m) as follows.

$$\left\{ \begin{array}{l} snl = -1 \\ \Delta z_0 = z_{sno} \end{array} \right\} \qquad \text{for } 0.01 \leq z_{sno} \leq 0.03$$

$$\left\{ \begin{array}{l} snl = -2 \\ \Delta z_{-1} = z_{sno}/2 \\ \Delta z_0 = \Delta z_{-1} \end{array} \right\} \qquad \text{for } 0.03 < z_{sno} \leq 0.04$$

$$\left\{ \begin{array}{l} snl = -2 \\ \Delta z_{-1} = 0.02 \\ \Delta z_0 = z_{sno} - \Delta z_{-1} \end{array} \right\} \qquad \text{for } 0.04 < z_{sno} \leq 0.07$$

$$\left\{ \begin{array}{l} snl = -3 \\ \Delta z_{-2} = 0.02 \\ \Delta z_{-1} = (z_{sno} - 0.02)/2 \\ \Delta z_0 = \Delta z_{-1} \end{array} \right\} \qquad \text{for } 0.07 < z_{sno} \leq 0.12$$

$$\left\{ \begin{array}{l} snl = -3 \\ \Delta z_{-2} = 0.02 \\ \Delta z_{-1} = 0.05 \\ \Delta z_0 = z_{sno} - \Delta z_{-2} - \Delta z_{-1} \end{array} \right\} \qquad \text{for } 0.12 < z_{sno} \leq 0.18$$

$$\left\{ \begin{array}{l} snl = -4 \\ \Delta z_{-3} = 0.02 \\ \Delta z_{-2} = 0.05 \\ \Delta z_{-1} = (z_{sno} - \Delta z_{-3} - \Delta z_{-2})/2 \\ \Delta z_0 = \Delta z_{-1} \end{array} \right\} \qquad \text{for } 0.18 < z_{sno} \leq 0.29$$

$$\left\{ \begin{array}{l} snl = -4 \\ \Delta z_{-3} = 0.02 \\ \Delta z_{-2} = 0.05 \\ \Delta z_{-1} = 0.11 \\ \Delta z_0 = z_{sno} - \Delta z_{-3} - \Delta z_{-2} - \Delta z_{-1} \end{array} \right\} \qquad \text{for } 0.29 < z_{sno} \leq 0.41$$

$$\left\{ \begin{array}{l} snl = -5 \\ \Delta z_{-4} = 0.02 \\ \Delta z_{-3} = 0.05 \\ \Delta z_{-2} = 0.11 \\ \Delta z_{-1} = (z_{sno} - \Delta z_{-4} - \Delta z_{-3} - \Delta z_{-2})/2 \\ \Delta z_0 = \Delta z_{-1} \end{array} \right\} \qquad \text{for } 0.41 < z_{sno} \leq 0.64$$

$$\left\{ \begin{array}{l} snl = -5 \\ \Delta z_{-4} = 0.02 \\ \Delta z_{-3} = 0.05 \\ \Delta z_{-2} = 0.11 \\ \Delta z_{-1} = 0.23 \\ \Delta z_0 = z_{sno} - \Delta z_{-4} - \Delta z_{-3} - \Delta z_{-2} - \Delta z_{-1} \end{array} \right\} \qquad \text{for } 0.64 < z_{sno}$$

The node depths, which are located at the midpoint of the snow layers, and the layer interfaces are both referenced from the soil surface and are defined as negative values

$$z_i = z_{h,\,i} - 0.5\Delta z_i \qquad i = snl + 1, \ldots, 0 \tag{6.5}$$

$$z_{h,\,i} = z_{h,\,i+1} - \Delta z_{i+1} \qquad i = snl, \ldots, -1. \tag{6.6}$$

Note that $z_{h,0}$, the interface between the bottom snow layer and the top soil layer, is zero. Thermal properties (i.e., temperature T_i [K]; thermal conductivity λ_i [W m^{-1} K^{-1}]; volumetric heat capacity c_i [J m^{-3} K^{-1}]) are defined for soil layers at the node depths (Figure 6.1) and for snow layers at the layer midpoints. When present, snow occupies a fraction of a grid cell's area, therefore snow depth represents the thickness of the snowpack averaged over only the snow covered area. The grid cell average snow depth is related to the depth of the snow covered area as $\bar{z}_{sno} = f_{sno}z_{sno}$. By default, the grid cell average snow depth is written to the history file.

The heat flux F_i (W m^{-2}) from layer i to layer $i+1$ is

$$F_i = -\lambda\left[z_{h,\,i}\right]\left(\frac{T_i - T_{i+1}}{z_{i+1} - z_i}\right) \tag{6.7}$$

where the thermal conductivity at the interface $\lambda\left[z_{h,\,i}\right]$ is

$$\lambda\left[z_{h,\,i}\right] = \begin{cases} \frac{\lambda_i\lambda_{i+1}(z_{i+1}-z_i)}{\lambda_i(z_{i+1}-z_{h,\,i})+\lambda_{i+1}(z_{h,\,i}-z_i)} & i = snl+1, \ldots, N_{levgrnd} - 1 \\ 0 & i = N_{levgrnd} \end{cases}. \tag{6.8}$$

These equations are derived, with reference to Figure 6.1, assuming that the heat flux from i (depth z_i) to the interface between i and $i+1$ (depth $z_{h,\,i}$) equals the heat flux from the interface to $i+1$ (depth z_{i+1}), i.e.,

$$-\lambda_i\frac{T_i - T_m}{z_{h,\,i} - z_i} = -\lambda_{i+1}\frac{T_m - T_{i+1}}{z_{i+1} - z_{h,\,i}} \tag{6.9}$$

where T_m is the temperature at the interface of layers i and $i+1$.

Shown are three soil layers, $i-1$, i, and $i+1$. The thermal conductivity λ, specific heat capacity c, and temperature T are defined at the layer node depth z. T_m is the interface temperature. The thermal conductivity $\lambda\left[z_h\right]$ is defined at the interface of two layers

z_h. The layer thickness is Δz. The heat fluxes F_{i-1} and F_i are defined as positive upwards.

The energy balance for the ith layer is

$$\frac{c_i\Delta z_i}{\Delta t}\left(T_i^{n+1} - T_i^n\right) = -F_{i-1} + F_i \tag{6.10}$$

where the superscripts n and $n+1$ indicate values at the beginning and end of the time step, respectively, and Δt is the time step (s). This equation is solved using the Crank-Nicholson method, which combines the explicit method with fluxes evaluated at n (F_{i-1}^n, F_i^n) and the implicit method with fluxes evaluated at $n+1$ (F_{i-1}^{n+1}, F_i^{n+1})

$$\frac{c_i\Delta z_i}{\Delta t}\left(T_i^{n+1} - T_i^n\right) = \alpha\left(-F_{i-1}^n + F_i^n\right) + (1-\alpha)\left(-F_{i-1}^{n+1} + F_i^{n+1}\right) \tag{6.11}$$

where $\alpha = 0.5$, resulting in a tridiagonal system of equations

$$r_i = a_iT_{i-1}^{n+1} + b_iT_i^{n+1} + c_iT_{i+1}^{n+1} \tag{6.12}$$

where a_i, b_i, and c_i are the subdiagonal, diagonal, and superdiagonal elements in the tridiagonal matrix and r_i is a column vector of constants. When surface water is present, the equation for the top soil layer has an additional term representing the surface water temperature; this results in a four element band-diagonal system of equations.

For the top soil layer $i = 1$, top snow layer $i = snl+1$, or surface water layer, the heat flux from the overlying atmosphere h (W m^{-2}, defined as positive into the surface) is

$$h^{n+1} = -\alpha F_{i-1}^n - (1-\alpha) F_{i-1}^{n+1}. \tag{6.13}$$

The energy balance for these layers is then

$$\frac{c_i\Delta z_i}{\Delta t}\left(T_i^{n+1} - T_i^n\right) = h^{n+1} + \alpha F_i^n + (1-\alpha) F_i^{n+1}. \tag{6.14}$$
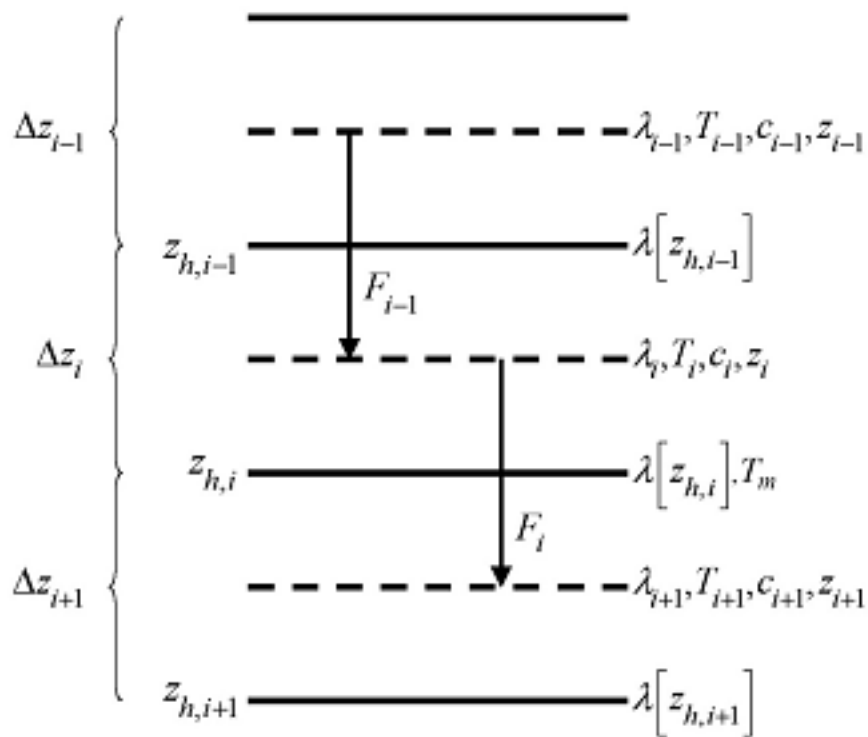
Figure 6.1: Schematic diagram of numerical scheme used to solve for soil temperature.

The heat flux h at $n + 1$ may be approximated as follows

$$h^{n+1} = h^n + \frac{\partial h}{\partial T_i}\left(T_i^{n+1} - T_i^n\right).$$ (6.15)

The resulting equations are then

$$\begin{aligned}\frac{c_i \Delta z_i}{\Delta t}\left(T_i^{n+1} - T_i^n\right) = & \ h^n + \frac{\partial h}{\partial T_i}\left(T_i^{n+1} - T_i\right)\\ & -\alpha\frac{\lambda[z_{h,\,i}]\left(T_i^n - T_{i+1}^n\right)}{z_{i+1} - z_i} - (1-\alpha)\frac{\lambda[z_{h,\,i}]\left(T_i^{n+1} - T_{i+1}^{n+1}\right)}{z_{i+1} - z_i}\end{aligned}$$ (6.16)

For the top snow layer, $i = snl + 1$, the coefficients are

$$a_i = 0$$ (6.17)

$$b_i = 1 + \frac{\Delta t}{c_i \Delta z_i}\left[(1-\alpha)\frac{\lambda[z_{h,\,i}]}{z_{i+1} - z_i} - \frac{\partial h}{\partial T_i}\right]$$ (6.18)

$$c_i = -(1-\alpha)\frac{\Delta t}{c_i \Delta z_i}\frac{\lambda[z_{h,\,i}]}{z_{i+1} - z_i}$$ (6.19)

$$r_i = T_i^n + \frac{\Delta t}{c_i \Delta z_i}\left[h_{sno}^n - \frac{\partial h}{\partial T_i}T_i^n + \alpha F_i\right]$$ (6.20)

where

$$F_i = -\lambda[z_{h,\,i}]\left(\frac{T_i^n - T_{i+1}^n}{z_{i+1} - z_i}\right).$$ (6.21)

The heat flux into the snow surface from the overlying atmosphere h is

$$h = \vec{S}_{sno} - \vec{L}_{sno} - H_{sno} - \lambda E_{sno}$$ (6.22)

where $\vec{S}_{sno}$ is the solar radiation absorbed by the top snow layer (section 3.2.1), $\vec{L}_{sno}$ is the longwave radiation absorbed by the snow (positive toward the atmosphere) (section 4.2), H_{sno} is the sensible heat flux from the snow (Chapter 5), and λE_{sno} is the latent heat flux from the snow (Chapter 5). The partial derivative of the heat flux h with respect to temperature is

$$\frac{\partial h}{\partial T} = -\frac{\partial \vec{L}}{\partial T} - \frac{\partial H}{\partial T} - \frac{\partial \lambda E}{\partial T}$$ (6.23)

where the partial derivative of the net longwave radiation is

$$\frac{\partial \vec{L}}{\partial T} = 4\varepsilon_g \sigma (T^n)^3$$ (6.24)

and the partial derivatives of the sensible and latent heat fluxes are given by equations and for non-vegetated surfaces, and by equations and for vegetated surfaces. σ is the Stefan-Boltzmann constant (W m^{-2} K^{-4}) (Table 2.7) and ε_g is the ground emissivity (section 4.2). For purposes of computing h and $\frac{\partial h}{\partial T_g}$, the term λ is arbitrarily assumed to be

$$\lambda = \left\{\begin{array}{ll}\lambda_{sub} & \text{if } w_{liq,\,snl+1} = 0 \text{ and } w_{ice,\,snl+1} > 0\\ \lambda_{vap} & \text{otherwise}\end{array}\right\}$$ (6.25)

where λ_{sub} and λ_{vap} are the latent heat of sublimation and vaporization, respectively (J kg^{-1}) (Table 2.7), and $w_{liq,\,snl+1}$ and $w_{ice,\,snl+1}$ are the liquid water and ice contents of the top snow/soil layer, respectively (kg m^{-2}) (Chapter 7).

For the top soil layer, $i = 1$, the coefficients are

$$a_i = -f_{sno}(1-\alpha)\frac{\Delta t}{c_i \Delta z_i}\frac{\lambda[z_{h,\,i-1}]}{z_i - z_{i-1}}$$ (6.26)

$$b_i = 1 + (1 - \alpha) \frac{\Delta t}{c_i \Delta z_i} \left[f_{sno} \frac{\lambda [z_{h,\,i-1}]}{z_i - z_{i-1}} + \frac{\lambda [z_{h,\,i}]}{z_{i+1} - z_i} \right] - (1 - f_{sno}) \frac{\Delta t}{c_i \Delta z_i} \frac{\partial h}{\partial T} \tag{6.27}$$

$$c_i = -(1 - \alpha) \frac{\Delta t}{c_i \Delta z_i} \frac{\lambda [z_{h,\,i}]}{z_{i+1} - z_i} \tag{6.28}$$

$$r_i = T_i^n + \frac{\Delta t}{c_i \Delta z_i} \left[(1 - f_{sno}) \left(h_{soil}^n - \frac{\partial h}{\partial T} T_i^n \right) + \alpha \left(F_i - f_{sno} F_{i-1} \right) \right] \tag{6.29}$$

The heat flux into the soil surface from the overlying atmosphere h is

$$h = \vec{S}_{soil} - \vec{L}_{soil} - H_{soil} - \lambda E_{soil} \tag{6.30}$$

It can be seen that when no snow is present ($f_{sno} = 0$), the expressions for the coefficients of the top soil layer have the same form as those for the top snow layer.

The surface snow/soil layer temperature computed in this way is the layer-averaged temperature and hence has somewhat reduced diurnal amplitude compared with surface temperature. An accurate surface temperature is provided that compensates for this effect and numerical error by tuning the heat capacity of the top layer (through adjustment of the layer thickness) to give an exact match to the analytic solution for diurnal heating. The top layer thickness for $i = snl + 1$ is given by

$$\Delta z_{i*} = 0.5 \left[z_i - z_{h,\,i-1} + c_a \left(z_{i+1} - z_{h,\,i-1} \right) \right] \tag{6.31}$$

where c_a is a tunable parameter, varying from 0 to 1, and is taken as 0.34 by comparing the numerical solution with the analytic solution (*Z.-L. Yang 1998, unpublished manuscript*). Δz_{i*} is used in place of Δz_i for $i = snl + 1$ in equations -. The top snow/soil layer temperature computed in this way is the ground surface temperature T_g^{n+1} .

The boundary condition at the bottom of the snow/soil column is zero heat flux, $F_i = 0$, resulting in, for $i = N_{levgrnd}$,

$$\frac{c_i \Delta z_i}{\Delta t} \left(T_i^{n+1} - T_i^n \right) = \alpha \frac{\lambda [z_{h,\,i-1}] \left(T_{i-1}^n - T_i^n \right)}{z_i - z_{i-1}} + (1 - \alpha) \frac{\lambda [z_{h,\,i-1}] \left(T_{i-1}^{n+1} - T_i^{n+1} \right)}{z_i - z_{i-1}} \tag{6.32}$$

$$a_i = -(1 - \alpha) \frac{\Delta t}{c_i \Delta z_i} \frac{\lambda [z_{h,\,i-1}]}{z_i - z_{i-1}} \tag{6.33}$$

$$b_i = 1 + (1 - \alpha) \frac{\Delta t}{c_i \Delta z_i} \frac{\lambda [z_{h,\,i-1}]}{z_i - z_{i-1}} \tag{6.34}$$

$$c_i = 0 \tag{6.35}$$

$$r_i = T_i^n - \alpha \frac{\Delta t}{c_i \Delta z_i} F_{i-1} \tag{6.36}$$

where

$$F_{i-1} = -\frac{\lambda [z_{h,\,i-1}]}{z_i - z_{i-1}} \left(T_{i-1}^n - T_i^n \right) . \tag{6.37}$$

For the interior snow/soil layers, $snl + 1 < i < N_{levgrnd}$, excluding the top soil layer,

$$\frac{c_i \Delta z_i}{\Delta t} \left(T_i^{n+1} - T_i^n \right) = -\alpha \frac{\lambda [z_{h,\,i}] \left(T_i^n - T_{i+1}^n \right)}{z_{i+1} - z_i} + \alpha \frac{\lambda [z_{h,\,i-1}] \left(T_{i-1}^n - T_i^n \right)}{z_i - z_{i-1}} \tag{6.38}$$

$$a_i = -(1 - \alpha) \frac{\Delta t}{c_i \Delta z_i} \frac{\lambda [z_{h,\,i-1}]}{z_i - z_{i-1}} \tag{6.39}$$

$$b_i = 1 + (1 - \alpha) \frac{\Delta t}{c_i \Delta z_i} \left[\frac{\lambda [z_{h,\,i-1}]}{z_i - z_{i-1}} + \frac{\lambda [z_{h,\,i}]}{z_{i+1} - z_i} \right] \tag{6.40}$$

$$c_i = -(1-\alpha)\frac{\Delta t}{c_i \Delta z_i}\frac{\lambda\left[z_{h,\,i}\right]}{z_{i+1}-z_i} \tag{6.41}$$

$$r_i = T_i^n + \alpha\frac{\Delta t}{c_i \Delta z_i}\left(F_i - F_{i-1}\right) + \frac{\Delta t}{c_i \Delta z_i}\vec{S}_{g,i}. \tag{6.42}$$

where $\vec{S}_{g,i}$ is the absorbed solar flux in layer i (section 3.2.1).

When surface water exists, the following top soil layer coefficients are modified

$$b_i = 1 + (1-\alpha)\frac{\Delta t}{c_i \Delta z_i}\left[f_{h2osfc}\frac{\lambda_{h2osfc}}{z_i - z_{h2osfc}} + f_{sno}\frac{\lambda[z_{h,\,i-1}]}{z_i - z_{i-1}} + \frac{\lambda[z_{h,\,i}]}{z_{i+1}-z_i}\right] \\ - (1 - f_{sno} - f_{h2osfc})\frac{\Delta t}{c_i \Delta z_i}\frac{\partial h}{\partial T} \tag{6.43}$$

$$r_i = T_i^n + \frac{\Delta t}{c_i \Delta z_i}\left[\begin{array}{l}(1 - f_{sno} - f_{h2osfc})\left(h_{soil}^n - \frac{\partial h}{\partial T}T_i^n\right) \\ +\alpha\left(F_i - f_{sno}F_{i-1} + f_{h2osfc}\frac{\lambda_{h2osfc}}{z_1 - z_{h2osfc}}\left(T_1 - T_{h2osfc}\right)\right)\end{array}\right] \tag{6.44}$$

$$d_i = -f_{h2osfc}\left(1-\alpha\right)\frac{\Delta t}{c_i \Delta z_i}\left[\frac{\lambda_{h2osfc}}{z_i - z_{h2osfc}}\right] \tag{6.45}$$

where d_i is an additional coefficient representing the heat flux from the surface water layer. The surface water layer coefficients are

$$a_{h2osfc} = 0 \tag{6.46}$$

$$b_{h2osfc} = 1 + \frac{\Delta t}{c_{h2osfc}\Delta z_{h2osfc}}\left[(1-\alpha)\frac{\lambda_{h2osfc}}{z_1 - z_{h2osfc}} - \frac{\partial h}{\partial T}\right] \tag{6.47}$$

$$c_{h2osfc} = -(1-\alpha)\frac{\Delta t}{c_{h2osfc}\Delta z_{h2osfc}}\frac{\lambda_{h2osfc}}{z_1 - z_{h2osfc}} \tag{6.48}$$

$$r_{h2osfc} = T_{h2osfc}^n + \frac{\Delta t}{c_i \Delta z_i}\left[h_{h2osfc}^n - \frac{\partial h}{\partial T}T_{h2osfc}^n + \alpha\frac{\lambda_{h2osfc}}{z_1 - z_{h2osfc}}\left(T_1 - T_{h2osfc}\right)\right] \tag{6.49}$$

6.2 Phase Change

6.2.1 Soil and Snow Layers

Upon update, the snow/soil temperatures are evaluated to determine if phase change will take place as

$$T_i^{n+1} > T_f \text{ and } w_{ice,\,i} > 0 \qquad i = snl + 1, \ldots, N_{levgrnd} \qquad \text{melting} \tag{6.50}$$

$$\begin{aligned}T_i^{n+1} &< T_f \text{ and } w_{liq,\,i} > 0 & i = snl + 1, \ldots, 0 \\ T_i^{n+1} &< T_f \text{ and } w_{liq,\,i} > w_{liq,\,\max,\,i} & i = 1, \ldots, N_{levgrnd}\end{aligned} \qquad \text{freezing} \tag{6.51}$$

where T_i^{n+1} is the soil layer temperature after solution of the tridiagonal equation set, $w_{ice,\,i}$ and $w_{liq,\,i}$ are the mass of ice and liquid water (kg m^{-2}) in each snow/soil layer, respectively, and T_f is the freezing temperature of water (K) (Table 2.7). For the freezing process in soil layers, the concept of supercooled soil water from *Niu and Yang (2006)* is adopted. The supercooled soil water is the liquid water that coexists with ice over a wide range of temperatures below freezing and is implemented through a freezing point depression equation

$$w_{liq,\,\max,\,i} = \Delta z_i \theta_{sat,\,i}\left[\frac{10^3 L_f\left(T_f - T_i\right)}{gT_i\psi_{sat,\,i}}\right]^{-1/B_i} \qquad T_i < T_f \tag{6.52}$$

where $w_{liq,\,\max,\,i}$ is the maximum liquid water in layer i (kg m^{-2}) when the soil temperature T_i is below the freezing temperature T_f, L_f is the latent heat of fusion (J kg^{-1}) (Table 2.7), g is the gravitational acceleration (m s^{-2}) (Table

2.7), and $\psi_{sat,i}$ and B_i are the soil texture-dependent saturated matric potential (mm) and *Clapp and Hornberger (1978)* exponent (section 7.3).

For the special case when snow is present (snow mass $W_{sno} > 0$) but there are no explicit snow layers ($snl = 0$) (i.e., there is not enough snow present to meet the minimum snow depth requirement of 0.01 m), snow melt will take place for soil layer $i = 1$ if the soil layer temperature is greater than the freezing temperature ($T_1^{n+1} > T_f$).

The rate of phase change is assessed from the energy excess (or deficit) needed to change T_i to freezing temperature, T_f . The excess or deficit of energy H_i (W m^{-2}) is determined as follows

$$
H_i = \left\{ \begin{array}{ll} \frac{\partial h}{\partial T}\left(T_f - T_i^n\right) - \frac{c_i \Delta z_i}{\Delta t}\left(T_f - T_i^n\right) & i = snl + 1 \\ \left(1 - f_{sno} - f_{h2osfc}\right)\frac{\partial h}{\partial T}\left(T_f - T_i^n\right) - \frac{c_i \Delta z_i}{\Delta t}\left(T_f - T_i^n\right) & i = 1 \\ -\frac{c_i \Delta z_i}{\Delta t}\left(T_f - T_i^n\right) & i \neq \{1, snl + 1\} \end{array} \right\}. \tag{6.53}
$$

If the melting criteria is met (6.50) and $H_m = \frac{H_i \Delta t}{L_f} > 0$, then the ice mass is readjusted as

$$
w_{ice,i}^{n+1} = w_{ice,i}^n - H_m \geq 0 \qquad i = snl + 1, \ldots, N_{levgrnd}. \tag{6.54}
$$

If the freezing criteria is met (6.51) and $H_m < 0$, then the ice mass is readjusted for $i = snl + 1, \ldots, 0$ as

$$
w_{ice,i}^{n+1} = \min\left(w_{liq,i}^n + w_{ice,i}^n, w_{ice,i}^n - H_m\right) \tag{6.55}
$$

and for $i = 1, \ldots, N_{levgrnd}$ as

$$
w_{ice,i}^{n+1} = \left\{ \begin{array}{ll} \min\left(w_{liq,i}^n + w_{ice,i}^n - w_{liq,\max,i}^n, w_{ice,i}^n - H_m\right) & w_{liq,i}^n + w_{ice,i}^n \geq w_{liq,\max,i}^n \\ 0 & w_{liq,i}^n + w_{ice,i}^n < w_{liq,\max,i}^n \end{array} \right\}. \tag{6.56}
$$

Liquid water mass is readjusted as

$$
w_{liq,i}^{n+1} = w_{liq,i}^n + w_{ice,i}^n - w_{ice,i}^{n+1} \geq 0. \tag{6.57}
$$

Because part of the energy H_i may not be consumed in melting or released in freezing, the energy is recalculated as

$$
H_{i*} = H_i - \frac{L_f\left(w_{ice,i}^n - w_{ice,i}^{n+1}\right)}{\Delta t} \tag{6.58}
$$

and this energy is used to cool or warm the snow/soil layer (if $|H_{i*}| > 0$) as

$$
T_i^{n+1} = \left\{ \begin{array}{ll} T_f + \frac{\Delta t}{c_i \Delta z_i} H_{i*} \Big/ \left(1 - \frac{\Delta t}{c_i \Delta z_i}\frac{\partial h}{\partial T}\right) & i = snl + 1 \\ T_f + \frac{\Delta t}{c_i \Delta z_i} H_{i*} \Big/ \left(1 - \left(1 - f_{sno} - f_{h2osfc}\right)\frac{\Delta t}{c_i \Delta z_i}\frac{\partial h}{\partial T}\right) & i = 1 \\ T_f + \frac{\Delta t}{c_i \Delta z_i} H_{i*} & i \neq \{1, snl + 1\} \end{array} \right\}. \tag{6.59}
$$

For the special case when snow is present ($W_{sno} > 0$), there are no explicit snow layers ($snl = 0$), and $\frac{H_1 \Delta t}{L_f} > 0$ (melting), the snow mass W_{sno} (kg m^{-2}) is reduced according to

$$
W_{sno}^{n+1} = W_{sno}^n - \frac{H_1 \Delta t}{L_f} \geq 0. \tag{6.60}
$$

The snow depth is reduced proportionally

$$
z_{sno}^{n+1} = \frac{W_{sno}^{n+1}}{W_{sno}^n} z_{sno}^n. \tag{6.61}
$$

Again, because part of the energy may not be consumed in melting, the energy for the surface soil layer $i = 1$ is recalculated as

$$
H_{1*} = H_1 - \frac{L_f\left(W_{sno}^n - W_{sno}^{n+1}\right)}{\Delta t}. \tag{6.62}
$$

If there is excess energy ($H_{1*} > 0$), this energy becomes available to the top soil layer as

$$H_1 = H_{1*}. \tag{6.63}$$

The ice mass, liquid water content, and temperature of the top soil layer are then determined from (6.54), (6.57), and (6.59) using the recalculated energy from (6.63). Snow melt M_{1S} (kg m^{-2} s^{-1}) and phase change energy $E_{p,1S}$ (W m^{-2}) for this special case are

$$M_{1S} = \frac{W_{sno}^n - W_{sno}^{n+1}}{\Delta t} \geq 0 \tag{6.64}$$

$$E_{p,1S} = L_f M_{1S}. \tag{6.65}$$

The total energy of phase change E_p (W m^{-2}) for the snow/soil column is

$$E_p = E_{p,1S} + \sum_{i=snl+1}^{N_{levgrnd}} E_{p,i} \tag{6.66}$$

where

$$E_{p,i} = L_f \frac{\left(w_{ice,i}^n - w_{ice,i}^{n+1}\right)}{\Delta t}. \tag{6.67}$$

The total snow melt M (kg m^{-2} s^{-1}) is

$$M = M_{1S} + \sum_{i=snl+1}^{i=0} M_i \tag{6.68}$$

where

$$M_i = \frac{\left(w_{ice,i}^n - w_{ice,i}^{n+1}\right)}{\Delta t} \geq 0. \tag{6.69}$$

The solution for snow/soil temperatures conserves energy as

$$G - E_p - \sum_{i=snl+1}^{i=N_{levgrnd}} \frac{c_i \Delta z_i}{\Delta t} \left(T_i^{n+1} - T_i^n\right) = 0 \tag{6.70}$$

where G is the ground heat flux (section 5.4).

6.2.2 Surface Water

Phase change of surface water takes place when the surface water temperature, T_{h2osfc}, becomes less than T_f. The energy available for freezing is

$$H_{h2osfc} = \frac{\partial h}{\partial T}\left(T_f - T_{h2osfc}^n\right) - \frac{c_{h2osfc}\Delta z_{h2osfc}}{\Delta t}\left(T_f - T_{h2osfc}^n\right) \tag{6.71}$$

where c_{h2osfc} is the volumetric heat capacity of water, and Δz_{h2osfc} is the depth of the surface water layer. If $H_m = \frac{H_{h2osfc}\Delta t}{L_f} > 0$ then H_m is removed from surface water and added to the snow column as ice

$$H_{h2osfc}^{n+1} = H_{h2osfc}^n - H_m \tag{6.72}$$

$$w_{ice,0}^{n+1} = w_{ice,0}^n + H_m \tag{6.73}$$

The snow depth is adjusted to account for the additional ice mass

$$\Delta z_{sno} = \frac{H_m}{\rho_{ice}} \tag{6.74}$$

If H_m is greater than W_{sfc}, the excess heat $\frac{L_f(H_m - W_{sfc})}{\Delta t}$ is used to cool the snow layer.

6.3 Soil and Snow Thermal Properties

The thermal properties of the soil are assumed to be a weighted combination of the mineral and organic properties of the soil (*Lawrence and Slater 2008*). The soil layer organic matter fraction $f_{om,i}$ is

$$f_{om,i} = \rho_{om,i}/\rho_{om,\max}. \tag{6.75}$$

Soil thermal conductivity λ_i (W m^{-1} K^{-1}) is from *Farouki (1981)*

$$\lambda_i = \left\{ \begin{array}{ll} K_{e,i}\lambda_{sat,i} + (1 - K_{e,i})\lambda_{dry,i} & S_{r,i} > 1 \times 10^{-7} \\ \lambda_{dry,i} & S_{r,i} \leq 1 \times 10^{-7} \end{array} \right\} \qquad i = 1, \ldots, N_{levsoi} \tag{6.76}$$

$$\lambda_i = \lambda_{bedrock} \qquad\qquad i = N_{levsoi} + 1, \ldots N_{levgrnd}$$

where $\lambda_{sat,i}$ is the saturated thermal conductivity, $\lambda_{dry,i}$ is the dry thermal conductivity, $K_{e,i}$ is the Kersten number, $S_{r,i}$ is the wetness of the soil with respect to saturation, and $\lambda_{bedrock} = 3$ W m^{-1} K^{-1} is the thermal conductivity assumed for the deep ground layers (typical of saturated granitic rock; *Clauser and Huenges 1995*). For glaciers,

$$\lambda_i = \left\{ \begin{array}{ll} \lambda_{liq,i} & T_i \geq T_f \\ \lambda_{ice,i} & T_i < T_f \end{array} \right\} \tag{6.77}$$

where λ_{liq} and λ_{ice} are the thermal conductivities of liquid water and ice, respectively (Table 2.7). The saturated thermal conductivity $\lambda_{sat,i}$ (W m^{-1} K^{-1}) depends on the thermal conductivities of the soil solid, liquid water, and ice constituents

$$\lambda_{sat} = \lambda_s^{1-\theta_{sat}} \lambda_{liq}^{\frac{\theta_{liq}}{\theta_{liq}+\theta_{ice}}\theta_{sat}} \lambda_{ice}^{\theta_{sat}\left(1-\frac{\theta_{liq}}{\theta_{liq}+\theta_{ice}}\right)} \tag{6.78}$$

where the thermal conductivity of soil solids $\lambda_{s,i}$ varies with the sand, clay, and organic matter content

$$\lambda_{s,i} = (1 - f_{om,i})\lambda_{s,\min,i} + f_{om,i}\lambda_{s,om} \tag{6.79}$$

where the mineral soil solid thermal conductivity $\lambda_{s,\min,i}$ is

$$\lambda_{s,\min,i} = \frac{8.80\ (\%sand)_i + 2.92\ (\%clay)_i}{(\%sand)_i + (\%clay)_i}, \tag{6.80}$$

and $\lambda_{s,om} = 0.25$ W m^{-1} K^{-1} (*Farouki 1981*). $\theta_{sat,i}$ is the volumetric water content at saturation (porosity) (section 7.3.1).

The thermal conductivity of dry soil is

$$\lambda_{dry,i} = (1 - f_{om,i})\lambda_{dry,\min,i} + f_{om,i}\lambda_{dry,om} \tag{6.81}$$

where the thermal conductivity of dry mineral soil $\lambda_{dry,\min,i}$ (W m^{-1} K^{-1}) depends on the bulk density $\rho_{d,i} = 2700\,(1 - \theta_{sat,i})$ (kg m^{-3}) as

$$\lambda_{dry,\min,i} = \frac{0.135\rho_{d,i} + 64.7}{2700 - 0.947\rho_{d,i}} \tag{6.82}$$

and $\lambda_{dry,om} = 0.05$ W m^{-1} K^{-1} (*Farouki 1981*) is the dry thermal conductivity of organic matter. The Kersten number $K_{e,i}$ is a function of the degree of saturation S_r and phase of water

$$K_{e,i} = \left\{ \begin{array}{ll} \log(S_{r,i}) + 1 \geq 0 & T_i \geq T_f \\ S_{r,i} & T_i < T_f \end{array} \right\} \tag{6.83}$$

where

$$S_{r,i} = \left(\frac{w_{liq,i}}{\rho_{liq}\Delta z_i} + \frac{w_{ice,i}}{\rho_{ice}\Delta z_i}\right)\frac{1}{\theta_{sat,i}} = \frac{\theta_{liq,i} + \theta_{ice,i}}{\theta_{sat,i}} \leq 1. \tag{6.84}$$

Thermal conductivity λ_i (W m^{-1} K^{-1}) for snow is from *Jordan (1991)*

$$\lambda_i = \lambda_{air} + \left(7.75 \times 10^{-5} \rho_{sno,\, i} + 1.105 \times 10^{-6} \rho_{sno,\, i}^2\right) \left(\lambda_{ice} - \lambda_{air}\right) \tag{6.85}$$

where λ_{air} is the thermal conductivity of air (Table 2.7) and $\rho_{sno,\, i}$ is the bulk density of snow (kg m^{-3})

$$\rho_{sno,\, i} = \frac{w_{ice,\, i} + w_{liq,\, i}}{\Delta z_i}. \tag{6.86}$$

The volumetric heat capacity c_i (J m^{-3} K^{-1}) for soil is from *de Vries (1963)* and depends on the heat capacities of the soil solid, liquid water, and ice constituents

$$c_i = c_{s,\, i}\left(1 - \theta_{sat,\, i}\right) + \frac{w_{ice,\, i}}{\Delta z_i} C_{ice} + \frac{w_{liq,\, i}}{\Delta z_i} C_{liq} \tag{6.87}$$

where C_{liq} and C_{ice} are the specific heat capacities (J kg^{-1} K^{-1}) of liquid water and ice, respectively (Table 2.7). The heat capacity of soil solids $c_{s,i}$ (J m^{-3} K^{-1}) is

$$c_{s,i} = (1 - f_{om,i})c_{s,\min,i} + f_{om,i}c_{s,om} \tag{6.88}$$

where the heat capacity of mineral soil solids $c_{s,\min,\, i}$ (J m^{-3} K^{-1}) is

$$
\begin{aligned}
c_{s,\min,\, i} &= \left(\frac{2.128\ (\%sand)_i + 2.385\ (\%clay)_i}{(\%sand)_i + (\%clay)_i}\right) \times 10^6 &\qquad i = 1, \ldots, N_{levsoi} \\
c_{s,\,\min,i} &= c_{s,\,bedrock} &\qquad i = N_{levsoi} + 1, \ldots, N_{levgrnd}
\end{aligned}
\tag{6.89}
$$

where $c_{s,bedrock} = 2 \times 10^6$ J m^{-3} K^{-1} is the heat capacity of bedrock and $c_{s,om} = 2.5 \times 10^6$ J m^{-3} K^{-1} (*Farouki 1981*) is the heat capacity of organic matter. For glaciers and snow

$$c_i = \frac{w_{ice,\, i}}{\Delta z_i} C_{ice} + \frac{w_{liq,\, i}}{\Delta z_i} C_{liq}. \tag{6.90}$$

For the special case when snow is present ($W_{sno} > 0$) but there are no explicit snow layers ($snl = 0$), the heat capacity of the top layer is a blend of ice and soil heat capacity

$$c_1 = c_1^* + \frac{C_{ice} W_{sno}}{\Delta z_1} \tag{6.91}$$

where c_1^* is calculated from (6.87) or (6.90).

CHAPTER 7

HYDROLOGY

The model parameterizes interception, throughfall, canopy drip, snow accumulation and melt, water transfer between snow layers, infiltration, evaporation, surface runoff, sub-surface drainage, redistribution within the soil column, and groundwater discharge and recharge to simulate changes in canopy water $\Delta W_{can,\,liq}$, canopy snow water $\Delta W_{can,\,sno}$ surface water ΔW_{sfc}, snow water ΔW_{sno}, soil water $\Delta w_{liq,\,i}$, and soil ice $\Delta w_{ice,\,i}$, and water in the unconfined aquifer ΔW_a (all in kg m^{-2} or mm of H$_2$O) (Figure 7.1).

The total water balance of the system is

$$
\begin{aligned}
&\Delta W_{can,\,liq} + \Delta W_{can,\,sno} + \Delta W_{sfc} + \Delta W_{sno}+ \\
&\sum_{i=1}^{N_{levsoi}} \left(\Delta w_{liq,\,i} + \Delta w_{ice,\,i} \right) + \Delta W_a = \left(\begin{array}{l} q_{rain} + q_{sno} - E_v - E_g - q_{over} \\ -q_{h2osfc} - q_{drai} - q_{rgwl} - q_{snwcp,ice} \end{array} \right) \Delta t
\end{aligned}
\tag{7.1}
$$

where q_{rain} is the liquid part of precipitation, q_{sno} is the solid part of precipitation, E_v is ET from vegetation (Chapter 5), E_g is ground evaporation (Chapter 5), q_{over} is surface runoff (section 7.2.1), q_{h2osfc} is runoff from surface water storage (section 7.2.1), q_{drai} is sub-surface drainage (section 7.5), q_{rgwl} and $q_{snwcp,ice}$ are liquid and solid runoff from glaciers and lakes, and runoff from other surface types due to snow capping (section 7.6) (all in kg m^{-2} s^{-1}), N_{levsoi} is the number of soil layers (note that hydrology calculations are only done over soil layers 1 to N_{levsoi}; ground levels $N_{levsoi} + 1$ to $N_{levgrnd}$ are currently hydrologically inactive; *(Lawrence et al. 2008)* and Δt is the time step (s).

7.1 Canopy Water

Liquid precipitation is either intercepted by the canopy, falls directly to the snow/soil surface (throughfall), or drips off the vegetation (canopy drip). Solid precipitation is treated similarly, with the addition of unloading of previously intercepted snow. Interception by vegetation is divided between liquid and solid phases $q_{intr,\,liq}$ and $q_{intr,\,ice}$ (kg m^{-2} s^{-1})

$$
q_{intr,\,liq} = f_{pi,\,liq}\, q_{rain}
\tag{7.2}
$$

$$
q_{intr,\,ice} = f_{pi,\,ice}\, q_{sno}
\tag{7.3}
$$

where $f_{pi,\,liq}$ and $f_{pi,\,ice}$ are the fractions of intercepted precipitation of rain and snow, respectively

$$
f_{pi,\,liq} = \alpha_{liq}\, tanh\,(L + S)
\tag{7.4}
$$
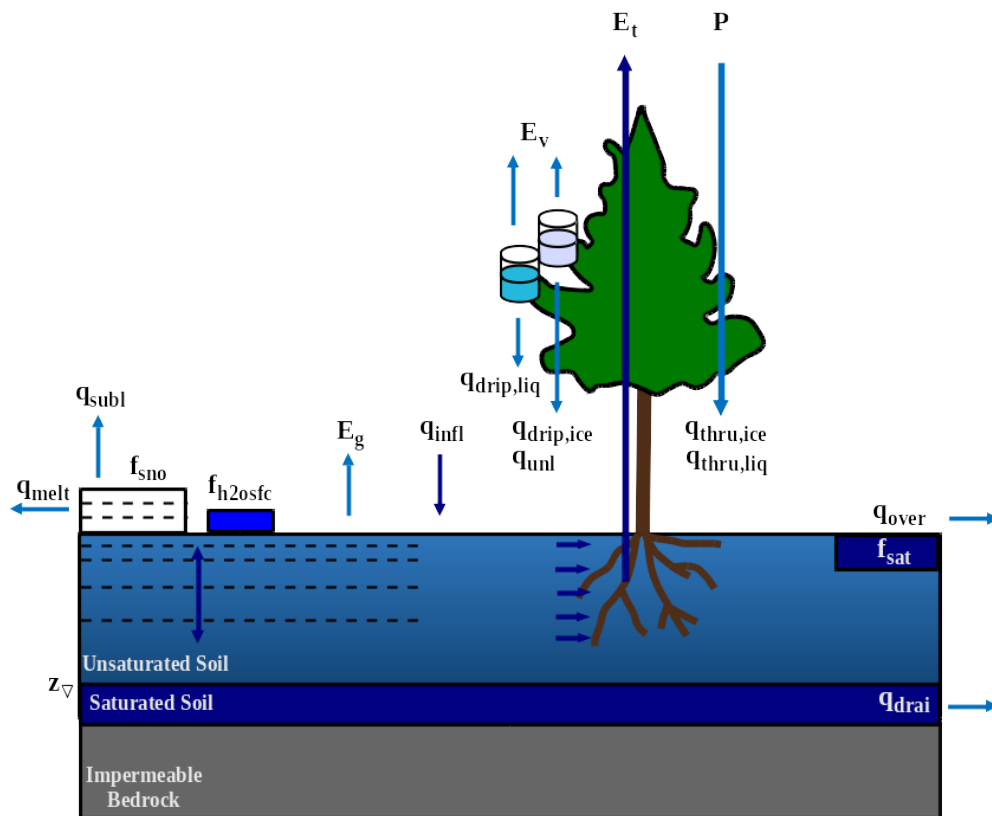
Figure 7.1: Hydrologic processes represented in CLM.

$$f_{pi,\,ice} = \alpha_{sno} \left\{ 1 - \exp\left[-0.5 \left(L + S \right) \right] \right\} , \tag{7.5}$$

and L and S are the exposed leaf and stem area index, respectively (section 2.1.4), and the α's scale the fractional area of a leaf that collects water (*Lawrence et al. 2007*). Default values of α_{liq} and α_{sno} are set to 1. Throughfall (kg m^{-2} s^{-1}) is also divided into liquid and solid phases, reaching the ground (soil or snow surface) as

$$q_{thru,\,liq} = q_{rain} \left(1 - f_{pi,\,liq} \right) \tag{7.6}$$

$$q_{thru,\,ice} = q_{sno} \left(1 - f_{pi,\,ice} \right) \tag{7.7}$$

Similarly, the liquid and solid canopy drip fluxes are

$$q_{drip,\,liq} = \frac{W_{can,\,liq}^{intr} - W_{can,\,liq}^{max}}{\Delta t} \geq 0 \tag{7.8}$$

$$q_{drip,\,ice} = \frac{W_{can,\,sno}^{intr} - W_{can,\,sno}^{max}}{\Delta t} \geq 0 \tag{7.9}$$

where

$$W_{can,liq}^{intr} = W_{can,liq}^{n} + q_{intr,\,liq}\Delta t \geq 0 \tag{7.10}$$

and

$$W_{can,sno}^{intr} = W_{can,sno}^{n} + q_{intr,\,ice}\Delta t \geq 0 \tag{7.11}$$

are the the canopy liquid water and snow water equivalent after accounting for interception, $W_{can,\,liq}^{n}$ and $W_{can,\,sno}^{n}$ are the canopy liquid and snow water from the previous time step, and $W_{can,\,liq}^{max}$ and $W_{can,\,snow}^{max}$ (kg m^{-2} or mm of H$_2$O) are the maximum amounts of liquid water and snow the canopy can hold. They are defined by

$$W_{can,\,liq}^{max} = p_{liq} \left(L + S \right) \tag{7.12}$$

$$W_{can,\,sno}^{max} = p_{sno} \left(L + S \right). \tag{7.13}$$

The maximum storage of liquid water is $p_{liq} = 0.1$ kg m^{-2} (*Dickinson et al. 1993*), and that of snow is $p_{sno} = 6$ kg m^{-2}, consistent with reported field measurements (*Pomeroy et al. 1998*).

Canopy snow unloading from wind speed u and above-freezing temperatures are modeled from linear fluxes and e-folding times similar to *Roesch et al. (2001)*

$$q_{unl,\,wind} = \frac{uW_{can,sno}}{1.56 \times 10^5 \text{ m}} \tag{7.14}$$

$$q_{unl,\,temp} = \frac{W_{can,sno}(T - 270 \text{ K})}{1.87 \times 10^5 \text{ K s}} > 0 \tag{7.15}$$

$$q_{unl,\,tot} = \min \left(q_{unl,\,wind} + q_{unl,\,temp}, W_{can,\,sno} \right) \tag{7.16}$$

The canopy liquid water and snow water equivalent are updated as

$$W_{can,\,liq}^{n+1} = W_{can,liq}^{n} + q_{intr,\,liq} - q_{drip,\,liq}\Delta t - E_v^{liq}\Delta t \geq 0 \tag{7.17}$$

and

$$W_{can,\,sno}^{n+1} = W_{can,sno}^{n} + q_{intr,\,ice} - \left(q_{drip,\,ice} + q_{unl,\,tot} \right) \Delta t - E_v^{ice}\Delta t \geq 0 \tag{7.18}$$

where E_v^{liq} and E_v^{ice} are partitioned from the stem and leaf surface evaporation E_v^w (Chapter 5) based on the vegetation temperature T_v (K) (Chapter 5) and its relation to the freezing temperature of water T_f (K) (Table 2.7)

$$E_v^{liq} = \left\{ \begin{array}{ll} E_v^w & T_v > T_f \\ 0 & T_v \leq T_f \end{array} \right\} \tag{7.19}$$

$$E_v^{ice} = \left\{ \begin{array}{ll} 0 & T_v > T_f \\ E_v^w & T_v \leq T_f \end{array} \right\}. \tag{7.20}$$

The total rate of liquid and solid precipitation reaching the ground is then

$$q_{grnd,liq} = q_{thru,liq} + q_{drip,liq} \tag{7.21}$$

$$q_{grnd,ice} = q_{thru,ice} + q_{drip,ice} + q_{unl,tot}. \tag{7.22}$$

Solid precipitation reaching the soil or snow surface, $q_{grnd,ice}\Delta t$, is added immediately to the snow pack (Chapter 8). The liquid part, $q_{grnd,liq}\Delta t$ is added after surface fluxes (Chapter 5) and snow/soil temperatures (Chapter 6) have been determined.

The wetted fraction of the canopy (stems plus leaves), which is required for surface flux (Chapter 5) calculations, is (*Dickinson et al.1993*)

$$f_{wet} = \left\{ \begin{array}{ll} \left[\frac{W_{can}}{p_{liq}(L+S)}\right]^{2/3} \leq 1 & L+S > 0 \\ 0 & L+S = 0 \end{array} \right\} \tag{7.23}$$

while the fraction of the canopy that is dry and transpiring is

$$f_{dry} = \left\{ \begin{array}{ll} \frac{(1-f_{wet})L}{L+S} & L+S > 0 \\ 0 & L+S = 0 \end{array} \right\}. \tag{7.24}$$

Similarly, the snow-covered fraction of the canopy is used for surface alebdo when intercepted snow is present (Chapter 3)

$$f_{can,sno} = \left\{ \begin{array}{ll} \left[\frac{W_{can,sno}}{p_{sno}(L+S)}\right]^{3/20} \leq 1 & L+S > 0 \\ 0 & L+S = 0 \end{array} \right\}. \tag{7.25}$$

7.2 Surface Runoff, Surface Water Storage, and Infiltration

The moisture input at the grid cell surface ,$q_{liq,0}$, is the sum of liquid precipitation reaching the ground and melt water from snow (kg m^{-2} s^{-1}). The moisture flux is then partitioned between surface runoff, surface water storage, and infiltration into the soil.

7.2.1 Surface Runoff

The simple TOPMODEL-based (*Beven and Kirkby 1979*) runoff model (SIMTOP) described by *Niu et al. (2005)* is implemented to parameterize runoff. A key concept underlying this approach is that of fractional saturated area f_{sat} , which is determined by the topographic characteristics and soil moisture state of a grid cell. The saturated portion of a grid cell contributes to surface runoff, q_{over} , by the saturation excess mechanism (Dunne runoff)

$$q_{over} = f_{sat}\, q_{liq,0} \tag{7.26}$$

The fractional saturated area is a function of soil moisture

$$f_{sat} = f_{max}\, \exp\left(-0.5 f_{over} z_\nabla\right) \tag{7.27}$$

where f_{max} is the potential or maximum value of f_{sat} , f_{over} is a decay factor (m^{-1}), and z_∇ is the water table depth (m) (section 7.5). The maximum saturated fraction, f_{max}, is defined as the value of the discrete cumulative distribution function (CDF) of the topographic index when the grid cell mean water table depth is zero. Thus, f_{max} is the percent of pixels in a grid cell whose topographic index is larger than or equal to the grid cell mean topographic index. It should be calculated explicitly from the CDF at each grid cell at the resolution that the model is run. However,

because this is a computationally intensive task for global applications, $f_{\max}$ is calculated once at 0.125° resolution using the 1-km compound topographic indices (CTIs) based on the HYDRO1K dataset (*Verdin and Greenlee 1996*) from USGS following the algorithm in *Niu et al. (2005)* and then area-averaged to the desired model resolution (section 2.3.3). Pixels with CTIs exceeding the 95 percentile threshold in each 0.125° grid cell are excluded from the calculation to eliminate biased estimation of statistics due to large CTI values at pixels on stream networks. For grid cells over regions without CTIs such as Australia, the global mean $f_{\max}$ is used to fill the gaps. See *Li et al. (2013b)* for additional details. The decay factor f_{over} for global simulations was determined through sensitivity analysis and comparison with observed runoff to be 0.5 m^{-1}.

7.2.2 Surface Water Storage

A surface water store has been added to the model to represent wetlands and small, sub-grid scale water bodies. As a result, the wetland land unit has been removed as of CLM4.5. The state variables for surface water are the mass of water W_{sfc} (kg m^{-2}) and temperature T_{h2osfc} (Chapter 6). Surface water storage and outflow are functions of fine spatial scale elevation variations called microtopography. The microtopography is assumed to be distributed normally around the grid cell mean elevation. Given the standard deviation of the microtopographic distribution, σ_{micro} (m), the fractional area of the grid cell that is inundated can be calculated. Surface water storage, $Wsfc$, is related to the height (relative to the grid cell mean elevation) of the surface water, d, by

$$W_{sfc} = \frac{d}{2}\left(1 + erf\left(\frac{d}{\sigma_{micro}\sqrt{2}}\right)\right) + \frac{\sigma_{micro}}{\sqrt{2\pi}}e^{\frac{-d^2}{2\sigma^2_{micro}}} \qquad (7.28)$$

where erf is the error function. For a given value of W_{sfc}, (7.28) can be solved for d using the Newton-Raphson method. Once d is known, one can determine the fraction of the area that is inundated as

$$f_{h2osfc} = \frac{1}{2}\left(1 + erf\left(\frac{d}{\sigma_{micro}\sqrt{2}}\right)\right) \qquad (7.29)$$

No global datasets exist for microtopography, so the default parameterization is a simple function of slope

$$\sigma_{micro} = (\beta + \beta_0)^\eta \qquad (7.30)$$

where β is the topographic slope, $\beta_0 = (\sigma_{\max})^{\frac{1}{\eta}}$ determines the maximum value of σ_{micro}, and η is an adjustable parameter. Default values in the model are $\sigma_{\max} = 0.4$ and $\eta = -3$.

If the spatial scale of the microtopography is small relative to that of the grid cell, one can assume that the inundated areas are distributed randomly within the grid cell. With this assumption, a result from percolation theory can be used to quantify the fraction of the inundated portion of the grid cell that is interconnected

$$\begin{aligned} f_{connected} &= (f_{h2osfc} - f_c)^\mu & f_{h2osfc} &> f_c \\ f_{connected} &= 0 & f_{h2osfc} &\leq f_c \end{aligned} \qquad (7.31)$$

where f_c is a threshold below which no single connected inundated area spans the grid cell and μ is a scaling exponent. Default values of f_c and μ are 0.4 and 0.14, respectively. When the inundated fraction of the grid cell surpasses f_c, the surface water store acts as a linear reservoir

$$q_{out,h2osfc} = k_{h2osfc}\, f_{connected}\,(Wsfc - Wc)\frac{1}{\Delta t} \qquad (7.32)$$

where $q_{out,h2osfc}$ is the surface water runoff, k_{h2osfc} is a constant, Wc is the amount of surface water present when $f_{h2osfc} = f_c$, and Δt is the model time step. The linear storage coefficent $k_{h2osfc} = \sin(\beta)$ is a function of grid cell mean topographic slope where β is the slope in radians.

7.2.3 Infiltration

The surface moisture flux remaining after surface runoff has been removed,

$$q_{in,surface} = (1 - f_{sat})\, q_{liq,0} \qquad (7.33)$$

is divided into inputs to surface water ($q_{in,\,h2osfc}$) and the soil $q_{in,soil}$. If $q_{in,soil}$ exceeds the maximum soil infiltration capacity (kg m^{-2} s^{-1}),

$$q_{infl,\,\max} = (1 - f_{sat})\,\Theta_{ice}k_{sat} \tag{7.34}$$

where Θ_{ice} is an ice impedance factor (section 7.3.1), infiltration excess (Hortonian) runoff is generated

$$q_{infl,\,excess} = \max\left(q_{in,soil} - (1 - f_{h2osfc})\,q_{\inf l,\max},0\right) \tag{7.35}$$

and transferred from $q_{in,soil}$ to $q_{in,h2osfc}$. After evaporative losses have been removed, these moisture fluxes are

$$q_{in,\,h2osfc} = f_{h2osfc}q_{in,surface} + q_{infl,excess} - q_{evap,h2osfc} \tag{7.36}$$

and

$$q_{in,soil} = (1 - f_{h2osfc})\,q_{in,surface} - q_{\inf l,excess} - (1 - f_{sno} - f_{h2osfc})\,q_{evap,soil}. \tag{7.37}$$

The balance of surface water is then calculated as

$$\Delta W_{sfc} = (q_{in,h2osfc} - q_{out,h2osfc} - q_{drain,h2osfc})\,\Delta t. \tag{7.38}$$

Bottom drainage from the surface water store

$$q_{drain,h2osfc} = \min\left(f_{h2osfc}q_{\inf l,\max}, \frac{W_{sfc}}{\Delta t}\right) \tag{7.39}$$

is then added to $q_{in,soil}$ giving the total infiltration into the surface soil layer

$$q_{infl} = q_{in,soil} + q_{drain,h2osfc} \tag{7.40}$$

Infiltration q_{infl} and explicit surface runoff q_{over} are not allowed for glaciers.

7.3 Soil Water

Soil water is predicted from a multi-layer model, in which the vertical soil moisture transport is governed by infiltration, surface and sub-surface runoff, gradient diffusion, gravity, and canopy transpiration through root extraction (Figure 7.1).

For one-dimensional vertical water flow in soils, the conservation of mass is stated as

$$\frac{\partial \theta}{\partial t} = -\frac{\partial q}{\partial z} - e \tag{7.41}$$

where θ is the volumetric soil water content (mm^3 of water / mm^{-3} of soil), t is time (s), z is height above some datum in the soil column (mm) (positive upwards), q is soil water flux (kg m^{-2} s^{-1} or mm s^{-1}) (positive upwards), and e is a soil moisture sink term (mm of water mm^{-1} of soil s^{-1}) (ET loss). This equation is solved numerically by dividing the soil column into multiple layers in the vertical and integrating downward over each layer with an upper boundary condition of the infiltration flux into the top soil layer q_{infl} and a zero-flux lower boundary condition at the bottom of the soil column (sub-surface runoff is removed later in the timestep, section 7.5).

The soil water flux q in equation can be described by Darcy's law *(Dingman 2002)*

$$q = -k\frac{\partial \psi_h}{\partial z} \tag{7.42}$$

where k is the hydraulic conductivity (mm s^{-1}), and ψ_h is the hydraulic potential (mm). The hydraulic potential is

$$\psi_h = \psi_m + \psi_z \tag{7.43}$$

where ψ_m is the soil matric potential (mm) (which is related to the adsorptive and capillary forces within the soil matrix), and ψ_z is the gravitational potential (mm) (the vertical distance from an arbitrary reference elevation to a point in the soil). If the reference elevation is the soil surface, then $\psi_z = z$. Letting $\psi = \psi_m$, Darcy's law becomes

$$q = -k \left[\frac{\partial (\psi + z)}{\partial z} \right] . \tag{7.44}$$

Equation (7.44) can be further manipulated to yield

$$q = -k \left[\frac{\partial (\psi + z)}{\partial z} \right] = -k \left(\frac{\partial \psi}{\partial z} + 1 \right) . \tag{7.45}$$

Substitution of this equation into equation (7.41), with $e = 0$, yields the Richards equation *(Dingman 2002)*

$$\frac{\partial \theta}{\partial t} = \frac{\partial}{\partial z} \left[k \left(\frac{\partial \psi}{\partial z} + 1 \right) \right] . \tag{7.46}$$

In practice (Section 7.3.2), changes in soil water content are predicted from (7.41) using finite-difference approximations for (7.46).

7.3.1 Hydraulic Properties

The hydraulic conductivity k_i (mm s^{-1}) and the soil matric potential ψ_i (mm) for layer i vary with volumetric soil water θ_i and soil texture. As with the soil thermal properties (section 6.3) the hydraulic properties of the soil are assumed to be a weighted combination of the mineral properties, which are determined according to sand and clay contents based on work by *Clapp and Hornberger (1978)* and *Cosby et al. (1984)*, and organic properties of the soil (*Lawrence and Slater 2008*).

The hydraulic conductivity is defined at the depth of the interface of two adjacent layers $z_{h,\,i}$ (Figure 7.2) and is a function of the saturated hydraulic conductivity $k_{sat} [z_{h,\,i}]$, the liquid volumetric soil moisture of the two layers θ_i and θ_{i+1} and an ice impedance factor Θ_{ice}

$$k [z_{h,\,i}] = \begin{cases} \Theta_{ice} k_{sat} [z_{h,\,i}] \left[\frac{0.5(\theta_i + \theta_{i+1})}{0.5(\theta_{sat,\,i} + \theta_{sat,\,i+1})} \right]^{2B_i+3} & 1 \leq i \leq N_{levsoi} - 1 \\ \Theta_{ice} k_{sat} [z_{h,\,i}] \left(\frac{\theta_i}{\theta_{sat,\,i}} \right)^{2B_i+3} & i = N_{levsoi} \end{cases} . \tag{7.47}$$

The ice impedance factor is a function of ice content, and is meant to quantify the increased tortuosity of the water flow when part of the pore space is filled with ice. *Swenson et al. (2012)* used a power law form

$$\Theta_{ice} = 10^{-\Omega F_{ice}} \tag{7.48}$$

where $\Omega = 6$ and $F_{ice} = \frac{\theta_{ice}}{\theta_{sat}}$ is the ice-filled fraction of the pore space.

Because the hydraulic properties of mineral and organic soil may differ significantly, the bulk hydraulic properties of each soil layer are computed as weighted averages of the properties of the mineral and organic components. The water content at saturation (i.e. porosity) is

$$\theta_{sat,i} = (1 - f_{om,i})\theta_{sat,\mathrm{min},i} + f_{om,i}\theta_{sat,om} \tag{7.49}$$

where $f_{om,i}$ is the soil organic matter fraction, $\theta_{sat,om} = 0.9$ (*Farouki 1981*; *Letts et al. 2000*) is the porosity of organic matter and the porosity of the mineral soil $\theta_{sat,\mathrm{min},i}$ is

$$\theta_{sat,\mathrm{min},i} = 0.489 - 0.00126(\%sand)_i . \tag{7.50}$$

The exponent B_i is

$$B_i = (1 - f_{om,i})B_{\mathrm{min},i} + f_{om,i}B_{om} \tag{7.51}$$

where $B_{om} = 2.7$ (*Letts et al. 2000*) and

$$B_{\min,i} = 2.91 + 0.159(\%clay)_i. \tag{7.52}$$

The soil matric potential (mm) is defined at the node depth z_i of each layer i (Figure 7.2)

$$\psi_i = \psi_{sat,i} \left(\frac{\theta_i}{\theta_{sat,i}} \right)^{-B_i} \geq -1 \times 10^8 \qquad 0.01 \leq \frac{\theta_i}{\theta_{sat,i}} \leq 1 \tag{7.53}$$

where the saturated soil matric potential (mm) is

$$\psi_{sat,i} = (1 - f_{om,i})\psi_{sat,\min,i} + f_{om,i}\psi_{sat,om} \tag{7.54}$$

where $\psi_{sat,om} = -10.3$ mm (*Letts et al. 2000*) is the saturated organic matter matric potential and the saturated mineral soil matric potential $\psi_{sat,\min,i}$ is

$$\psi_{sat,\min,i} = -10.0 \times 10^{1.88 - 0.0131(\%sand)_i}. \tag{7.55}$$

The saturated hydraulic conductivity, $k_{sat}[z_{h,i}]$ (mm s^{-1}), for organic soils ($k_{sat,om}$) may be two to three orders of magnitude larger than that of mineral soils ($k_{sat,\min}$). Bulk soil layer values of k_{sat} calculated as weighted averages based on f_{om} may therefore be determined primarily by the organic soil properties even for values of f_{om} as low as 1 %. To better represent the influence of organic soil material on the grid cell average saturated hydraulic conductivity, the soil organic matter fraction is further subdivided into "connected" and "unconnected" fractions using a result from percolation theory (*Stauffer and Aharony 1994*, *Berkowitz and Balberg 1992*). Assuming that the organic and mineral fractions are randomly distributed throughout a soil layer, percolation theory predicts that above a threshold value $f_{om} = f_{threshold}$, connected flow pathways consisting of organic material only exist and span the soil space. Flow through these pathways interacts only with organic material, and thus can be described by $k_{sat,om}$. This fraction of the grid cell is given by

$$\begin{aligned} f_{perc} &= N_{perc}(f_{om} - f_{threshold})^{\beta^{perc}} f_{om} & f_{om} \geq f_{threshold} \\ f_{perc} &= 0 & f_{om} < f_{threshold} \end{aligned} \tag{7.56}$$

where $\beta^{perc} = 0.139$, $f_{threshold} = 0.5$, and $N_{perc} = (1 - f_{threshold})^{-\beta^{perc}}$. In the unconnected portion of the grid cell, $f_{uncon} = (1 - f_{perc})$, the saturated hydraulic conductivity is assumed to correspond to flow pathways that pass through the mineral and organic components in series

$$k_{sat,uncon} = f_{uncon} \left(\frac{(1 - f_{om})}{k_{sat,\min}} + \frac{(f_{om} - f_{perc})}{k_{sat,om}} \right)^{-1}. \tag{7.57}$$

where saturated hydraulic conductivity for mineral soil depends on soil texture (*Cosby et al. 1984*) as

$$k_{sat,\min}[z_{h,i}] = 0.0070556 \times 10^{-0.884 + 0.0153(\%sand)_i}. \tag{7.58}$$

The bulk soil layer saturated hydraulic conductivity is then computed as

$$k_{sat}[z_{h,i}] = f_{uncon,i}k_{sat,uncon}[z_{h,i}] + (1 - f_{uncon,i})k_{sat,om}[z_{h,i}]. \tag{7.59}$$

7.3.2 Numerical Solution

With reference to Figure 7.2, the equation for conservation of mass (equation (7.41)) can be integrated over each layer as

$$\int_{-z_{h,i}}^{-z_{h,i-1}} \frac{\partial \theta}{\partial t} dz = -\int_{-z_{h,i}}^{-z_{h,i-1}} \frac{\partial q}{\partial z} dz - \int_{-z_{h,i}}^{-z_{h,i-1}} e\, dz. \tag{7.60}$$

Note that the integration limits are negative since z is defined as positive upward from the soil surface. This equation can be written as

$$\Delta z_i \frac{\partial \theta_{liq,i}}{\partial t} = -q_{i-1} + q_i - e_i \qquad (7.61)$$

where q_i is the flux of water across interface $z_{h,i}$, q_{i-1} is the flux of water across interface $z_{h,i-1}$, and e_i is a layer-averaged soil moisture sink term (ET loss) defined as positive for flow out of the layer (mm s^{-1}). Taking the finite difference with time and evaluating the fluxes implicitly at time $n+1$ yields

$$\frac{\Delta z_i \Delta \theta_{liq,i}}{\Delta t} = -q_{i-1}^{n+1} + q_i^{n+1} - e_i \qquad (7.62)$$

where $\Delta \theta_{liq,i} = \theta_{liq,i}^{n+1} - \theta_{liq,i}^{n}$ is the change in volumetric soil liquid water of layer i in time Δt and Δz_i is the thickness of layer i (mm).

The water removed by transpiration in each layer e_i is a function of the total transpiration E_v^t (Chapter 5) and the effective root fraction $r_{e,i}$

$$e_i = r_{e,i} E_v^t. \qquad (7.63)$$

Shown are three soil layers, $i-1$, i, and $i+1$. The soil matric potential ψ and volumetric soil water θ_{liq} are defined at the layer node depth z. The hydraulic conductivity $k\left[z_h\right]$ is defined at the interface of two layers z_h. The layer thickness is Δz. The soil water fluxes q_{i-1} and q_i are defined as positive upwards. The soil moisture sink term e (ET loss) is defined as positive for flow out of the layer.

Note that because more than one plant functional type (PFT) may share a soil column, the transpiration E_v^t is a weighted sum of transpiration from all PFTs whose weighting depends on PFT area as

$$E_v^t = \sum_{j=1}^{npft} \left(E_v^t\right)_j (wt)_j \qquad (7.64)$$

where $npft$ is the number of PFTs sharing a soil column, $\left(E_v^t\right)_j$ is the transpiration from the jth PFT on the column, and $(wt)_j$ is the relative area of the jth PFT with respect to the column. The effective root fraction $r_{e,i}$ is also a column-level quantity that is a weighted sum over all PFTs. The weighting depends on the per unit area transpiration of each PFT and its relative area as

$$r_{e,i} = \frac{\sum_{j=1}^{npft} \left(r_{e,i}\right)_j \left(E_v^t\right)_j (wt)_j}{\sum_{j=1}^{npft} \left(E_v^t\right)_j (wt)_j} \qquad (7.65)$$

where $\left(r_{e,i}\right)_j$ is the effective root fraction for the jth PFT

$$\begin{aligned} \left(r_{e,i}\right)_j &= \frac{(r_i)_j (w_i)_j}{(\beta_t)_j} & (\beta_t)_j &> 0 \\ \left(r_{e,i}\right)_j &= 0 & (\beta_t)_j &= 0 \end{aligned} \qquad (7.66)$$

and $(r_i)_j$ is the fraction of roots in layer i (Chapter 9), $(w_i)_j$ is a soil dryness or plant wilting factor for layer i (Chapter 9), and $(\beta_t)_j$ is a wetness factor for the total soil column for the jth PFT (Chapter 9).

The soil water fluxes in (7.62),, which are a function of $\theta_{liq,i}$ and $\theta_{liq,i+1}$ because of their dependence on hydraulic conductivity and soil matric potential, can be linearized about θ using a Taylor series expansion as

$$q_i^{n+1} = q_i^n + \frac{\partial q_i}{\partial \theta_{liq,i}} \Delta \theta_{liq,i} + \frac{\partial q_i}{\partial \theta_{liq,i+1}} \Delta \theta_{liq,i+1} \qquad (7.67)$$

$$q_{i-1}^{n+1} = q_{i-1}^n + \frac{\partial q_{i-1}}{\partial \theta_{liq,i-1}} \Delta \theta_{liq,i-1} + \frac{\partial q_{i-1}}{\partial \theta_{liq,i}} \Delta \theta_{liq,i}. \qquad (7.68)$$
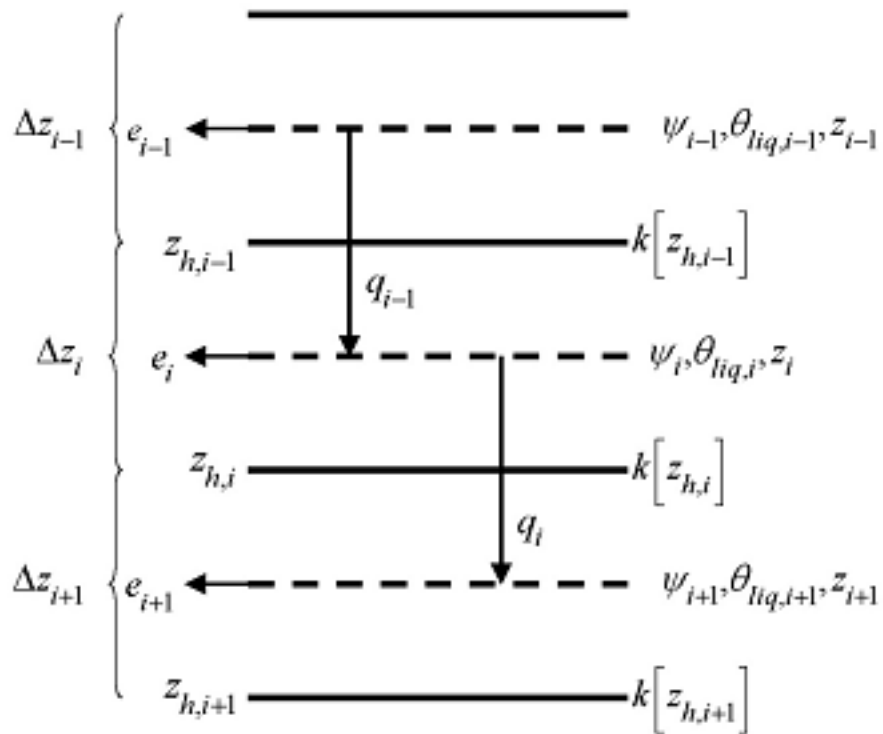
7.3. Soil Water

Figure 7.2: Schematic diagram of numerical scheme used to solve for soil water fluxes.

Substitution of these expressions for q_i^{n+1} and q_{i-1}^{n+1} into (7.62) results in a general tridiagonal equation set of the form

$$r_i = a_i \Delta\theta_{liq,\,i-1} + b_i \Delta\theta_{liq,\,i} + c_i \Delta\theta_{liq,\,i+1} \tag{7.69}$$

where

$$a_i = -\frac{\partial q_{i-1}}{\partial\theta_{liq,\,i-1}} \tag{7.70}$$

$$b_i = \frac{\partial q_i}{\partial\theta_{liq,\,i}} - \frac{\partial q_{i-1}}{\partial\theta_{liq,\,i}} - \frac{\Delta z_i}{\Delta t} \tag{7.71}$$

$$c_i = \frac{\partial q_i}{\partial\theta_{liq,\,i+1}} \tag{7.72}$$

$$r_i = q_{i-1}^n - q_i^n + e_i. \tag{7.73}$$

The tridiagonal equation set is solved over $i = 1, \ldots, N_{levsoi}$.

The finite-difference forms of the fluxes and partial derivatives in equations (7.70) - (7.73) can be obtained from equation as

$$q_{i-1}^n = -k\left[z_{h,\,i-1}\right]\left[\frac{(\psi_{i-1} - \psi_i) + (z_i - z_{i-1})}{z_i - z_{i-1}}\right] \tag{7.74}$$

$$q_i^n = -k\left[z_{h,\,i}\right]\left[\frac{(\psi_i - \psi_{i+1}) + (z_{i+1} - z_i)}{z_{i+1} - z_i}\right] \tag{7.75}$$

$$\frac{\partial q_{i-1}}{\partial\theta_{liq,i-1}} = -\left[\frac{k\left[z_{h,\,i-1}\right]}{z_i - z_{i-1}}\frac{\partial\psi_{i-1}}{\partial\theta_{liq,i-1}}\right] - \frac{\partial k\left[z_{h,\,i-1}\right]}{\partial\theta_{liq,i-1}}\left[\frac{(\psi_{i-1} - \psi_i) + (z_i - z_{i-1})}{z_i - z_{i-1}}\right] \tag{7.76}$$

$$\frac{\partial q_{i-1}}{\partial\theta_{liq,i}} = \left[\frac{k\left[z_{h,\,i-1}\right]}{z_i - z_{i-1}}\frac{\partial\psi_i}{\partial\theta_{liq,i}}\right] - \frac{\partial k\left[z_{h,\,i-1}\right]}{\partial\theta_{liq,i}}\left[\frac{(\psi_{i-1} - \psi_i) + (z_i - z_{i-1})}{z_i - z_{i-1}}\right] \tag{7.77}$$

$$\frac{\partial q_i}{\partial\theta_{liq,i}} = -\left[\frac{k\left[z_{h,\,i}\right]}{z_{i+1} - z_i}\frac{\partial\psi_i}{\partial\theta_{liq,i}}\right] - \frac{\partial k\left[z_{h,\,i}\right]}{\partial\theta_{liq,i}}\left[\frac{(\psi_i - \psi_{i+1}) + (z_{i+1} - z_i)}{z_{i+1} - z_i}\right] \tag{7.78}$$

$$\frac{\partial q_i}{\partial\theta_{liq,i+1}} = \left[\frac{k\left[z_{h,\,i}\right]}{z_{i+1} - z_i}\frac{\partial\psi_{i+1}}{\partial\theta_{liq,i+1}}\right] - \frac{\partial k\left[z_{h,\,i}\right]}{\partial\theta_{liq,i+1}}\left[\frac{(\psi_i - \psi_{i+1}) + (z_{i+1} - z_i)}{z_{i+1} - z_i}\right]. \tag{7.79}$$

The derivatives of the soil matric potential at the node depth are derived from (7.53)

$$\frac{\partial\psi_{i-1}}{\partial\theta_{liq,\,i-1}} = -B_{i-1}\frac{\psi_{i-1}}{\theta_{i-1}} \tag{7.80}$$

$$\frac{\partial\psi_i}{\partial\theta_{liq,\,i}} = -B_i\frac{\psi_i}{\theta_i} \tag{7.81}$$

$$\frac{\partial\psi_{i+1}}{\partial\theta_{liq,\,i+1}} = -B_{i+1}\frac{\psi_{i+1}}{\theta_{i+1}} \tag{7.82}$$

with the constraint $0.01\,\theta_{sat,\,i} \le \theta_i \le \theta_{sat,\,i}$.

The derivatives of the hydraulic conductivity at the layer interface are derived from (7.47)

$$\frac{\partial k[z_{h,\,i-1}]}{\partial\theta_{liq,\,i-1}} = \frac{\partial k[z_{h,\,i-1}]}{\partial\theta_{liq,\,i}} = (2B_{i-1} + 3)\,\overline{\Theta}_{ice}\,k_{sat}\left[z_{h,\,i-1}\right]\left[\frac{\overline{\theta}_{liq}}{\overline{\theta}_{sat}}\right]^{2B_{i-1}+2}\left(\frac{0.5}{\overline{\theta}_{sat}}\right) \tag{7.83}$$

where $\overline{\Theta}_{ice} = \Theta(\overline{\theta}_{ice})$ (7.48), $\overline{\theta}_{ice} = 0.5\,(\theta_{ice\,i-1} + \theta_{ice\,i})$, $\overline{\theta}_{liq} = 0.5\,(\theta_{liq\,i-1} + \theta_{liq\,i})$, and $\overline{\theta}_{sat} = 0.5\,(\theta_{sat,\,i-1} + \theta_{sat,\,i})$

and

$$\frac{\partial k[z_{h,\,i}]}{\partial\theta_{liq,\,i}} = \frac{\partial k[z_{h,\,i}]}{\partial\theta_{liq,\,i+1}} = (2B_i + 3)\,\overline{\Theta}_{ice}\,k_{sat}\left[z_{h,\,i}\right]\left[\frac{\overline{\theta}_{liq}}{\overline{\theta}_{sat}}\right]^{2B_i+2}\left(\frac{0.5}{\overline{\theta}_{sat}}\right). \tag{7.84}$$

where $\overline{\theta}_{liq} = 0.5\,(\theta_i + \theta_{i+1})$, $\overline{\theta}_{sat} = 0.5\,(\theta_{sat,\,i} + \theta_{sat,\,i+1})$.

Equation set for layer $i = 1$

For the top soil layer ($i = 1$), the boundary condition is the infiltration rate (section 7.2.1), $q_{i-1}^{n+1} = -q_{infl}^{n+1}$, and the water balance equation is

$$\frac{\Delta z_i \Delta \theta_{liq, i}}{\Delta t} = q_{infl}^{n+1} + q_i^{n+1} - e_i. \tag{7.85}$$

After grouping like terms, the coefficients of the tridiagonal set of equations for $i = 1$ are

$$a_i = 0 \tag{7.86}$$

$$b_i = \frac{\partial q_i}{\partial \theta_{liq, i}} - \frac{\Delta z_i}{\Delta t} \tag{7.87}$$

$$c_i = \frac{\partial q_i}{\partial \theta_{liq, i+1}} \tag{7.88}$$

$$r_i = q_{infl}^{n+1} - q_i^n + e_i. \tag{7.89}$$

Equation set for layers $i = 2, \ldots, N_{levsoi} - 1$

The coefficients of the tridiagonal set of equations for $i = 2, \ldots, N_{levsoi} - 1$ are

$$a_i = -\frac{\partial q_{i-1}}{\partial \theta_{liq, i-1}} \tag{7.90}$$

$$b_i = \frac{\partial q_i}{\partial \theta_{liq, i}} - \frac{\partial q_{i-1}}{\partial \theta_{liq, i}} - \frac{\Delta z_i}{\Delta t} \tag{7.91}$$

$$c_i = \frac{\partial q_i}{\partial \theta_{liq, i+1}} \tag{7.92}$$

$$r_i = q_{i-1}^n - q_i^n + e_i. \tag{7.93}$$

Equation set for layer $i = N_{levsoi}$

For the lowest soil layer ($i = N_{levsoi}$), a zero-flux bottom boundary condition is applied ($q_i^n = 0$) and the coefficients of the tridiagonal set of equations for $i = N_{levsoi}$ are

$$a_i = -\frac{\partial q_{i-1}}{\partial \theta_{liq, i-1}} \tag{7.94}$$

$$b_i = \frac{\partial q_i}{\partial \theta_{liq, i}} - \frac{\partial q_{i-1}}{\partial \theta_{liq, i}} - \frac{\Delta z_i}{\Delta t} \tag{7.95}$$

$$c_i = 0 \tag{7.96}$$

$$r_i = q_{i-1}^n + e_i. \tag{7.97}$$

Adaptive Time Stepping

The length of the time step is adjusted in order to improve the accuracy and stability of the numerical solutions. The difference between two numerical approximations is used to estimate the temporal truncation error, and then the step size Δt_{sub} is adjusted to meet a user-prescribed error tolerance *[Kavetski et al., 2002]*. The temporal truncation error is estimated by comparing the flux obtained from the first-order Taylor series expansion (q_{i-1}^{n+1} and q_i^{n+1}, equations (7.67) and (7.68)) against the flux at the start of the time step (q_{i-1}^n and q_i^n). Since the tridiagonal solution already provides an estimate of $\Delta\theta_{liq,i}$, it is convenient to compute the error for each of the i layers from equation (7.62) as

$$\epsilon_i = \left[\frac{\Delta\theta_{liq,i}\Delta z_i}{\Delta t_{sub}} - \left(q_{i-1}^n - q_i^n + e_i \right) \right] \frac{\Delta t_{sub}}{2} \tag{7.98}$$

and the maximum absolute error across all layers as

$$\epsilon_{crit} = \max\left(|\epsilon_i| \right) \qquad 1 \leq i \leq nlevsoi \quad . \tag{7.99}$$

The adaptive step size selection is based on specified upper and lower error tolerances, τ_U and τ_L. The solution is accepted if $\epsilon_{crit} \leq \tau_U$ and the procedure repeats until the adaptive sub-stepping spans the full model time step (the sub-steps are doubled if $\epsilon_{crit} \leq \tau_L$, i.e., if the solution is very accurate). Conversely, the solution is rejected if $\epsilon_{crit} > \tau_U$. In this case the length of the sub-steps is halved and a new solution is obtained. The halving of substeps continues until either $\epsilon_{crit} \leq \tau_U$ or the specified minimum time step length is reached.

Upon solution of the tridiagonal equation set, the liquid water contents are updated as follows

$$w_{liq,i}^{n+1} = w_{liq,i}^n + \Delta\theta_{liq,i}\Delta z_i \qquad i = 1, \ldots, N_{levsoi}. \tag{7.100}$$

The volumetric water content is

$$\theta_i = \frac{w_{liq,i}}{\Delta z_i \rho_{liq}} + \frac{w_{ice,i}}{\Delta z_i \rho_{ice}}. \tag{7.101}$$

7.4 Frozen Soils and Perched Water Table

When soils freeze, the power-law form of the ice impedance factor (section 7.3.1) can greatly decrease the hydraulic conductivity of the soil, leading to nearly impermeable soil layers. When unfrozen soil layers are present above relatively ice-rich frozen layers, the possibility exists for perched saturated zones. Lateral drainage from perched saturated regions is parameterized as a function of the thickness of the saturated zone

$$q_{drai,perch} = k_{drai,perch} \left(z_{frost} - z_{\nabla,perch} \right) \tag{7.102}$$

where $k_{drai,perch}$ depends on topographic slope and soil hydraulic conductivity,

$$k_{drai,perch} = 10^{-5} \sin(\beta) \left(\frac{\sum_{i=N_{perch}}^{i=N_{frost}} \Theta_{ice,i} k_{sat}\left[z_i \right] \Delta z_i}{\sum_{i=N_{perch}}^{i=N_{frost}} \Delta z_i} \right) \tag{7.103}$$

where Θ_{ice} is an ice impedance factor, β is the mean grid cell topographic slope in radians, z_{frost} is the depth to the frost table, and $z_{\nabla,perch}$ is the depth to the perched saturated zone. The frost table z_{frost} is defined as the shallowest frozen layer having an unfrozen layer above it, while the perched water table $z_{\nabla,perch}$ is defined as the depth at which the volumetric water content drops below a specified threshold. The default threshold is set to 0.9. Drainage from the perched saturated zone $q_{drai,perch}$ is removed from layers N_{perch} through N_{frost}, which are the layers containing $z_{\nabla,perch}$ and, z_{frost} respectively.

7.5 Lateral Sub-surface Runoff

Lateral sub-surface runoff occurs when saturated soil moisture conditions exist within the soil column. Sub-surface runoff is

$$q_{drai} = \Theta_{ice} K_{baseflow} tan\left(\beta\right) \Delta z_{sat}^{N_{baseflow}} \; , \tag{7.104}$$

where $K_{baseflow}$ is a calibration parameter, β is the topographic slope, the exponent $N_{baseflow} = 1$, and Δz_{sat} is the thickness of the saturated portion of the soil column.

The saturated thickness is

$$\Delta z_{sat} = z_{bedrock} - z_\nabla, \tag{7.105}$$

where the water table z_∇ is determined by finding the irst soil layer above the bedrock depth (section 2.2.2) in which the volumetric water content drops below a specified threshold. The default threshold is set to 0.9.

The specific yield, S_y , which depends on the soil properties and the water table location, is derived by taking the difference between two equilibrium soil moisture profiles whose water tables differ by an infinitesimal amount

$$S_y = \theta_{sat}\left(1 - \left(1 + \frac{z_\nabla}{\Psi_{sat}}\right)^{\frac{-1}{B}}\right) \tag{7.106}$$

where B is the Clapp-Hornberger exponent. Because S_y is a function of the soil properties, it results in water table dynamics that are consistent with the soil water fluxes described in section 7.3.

After the above calculations, two numerical adjustments are implemented to keep the liquid water content of each soil layer ($w_{liq, i}$) within physical constraints of $w_{liq}^{min} \leq w_{liq, i} \leq \left(\theta_{sat, i} - \theta_{ice, i}\right)\Delta z_i$ where $w_{liq}^{min} = 0.01$ (mm). First, beginning with the bottom soil layer $i = N_{levsoi}$, any excess liquid water in each soil layer ($w_{liq, i}^{excess} = w_{liq, i} - \left(\theta_{sat, i} - \theta_{ice, i}\right)\Delta z_i \geq 0$) is successively added to the layer above. Any excess liquid water that remains after saturating the entire soil column (plus a maximum surface ponding depth $w_{liq}^{pond} = 10$ kg m^{-2}), is added to drainage q_{drai} . Second, to prevent negative $w_{liq, i}$, each layer is successively brought up to $w_{liq, i} = w_{liq}^{min}$ by taking the required amount of water from the layer below. If this results in $w_{liq, N_{levsoi}} < w_{liq}^{min}$, then the layers above are searched in succession for the required amount of water ($w_{liq}^{min} - w_{liq, N_{levsoi}}$) and removed from those layers subject to the constraint $w_{liq, i} \geq w_{liq}^{min}$. If sufficient water is not found, then the water is removed from W_t and q_{drai} .

The soil surface layer liquid water and ice contents are then updated for dew q_{sdew} , frost q_{frost} , or sublimation q_{subl} (section 5.4) as

$$w_{liq, 1}^{n+1} = w_{liq, 1}^{n} + q_{sdew}\Delta t \tag{7.107}$$

$$w_{ice, 1}^{n+1} = w_{ice, 1}^{n} + q_{frost}\Delta t \tag{7.108}$$

$$w_{ice, 1}^{n+1} = w_{ice, 1}^{n} - q_{subl}\Delta t. \tag{7.109}$$

Sublimation of ice is limited to the amount of ice available.

7.6 Runoff from glaciers and snow-capped surfaces

All surfaces are constrained to have a snow water equivalent $W_{sno} \leq W_{cap} = 10,000$ kg m^{-2}. For snow-capped columns, any addition of mass at the top (precipitation, dew/riping) is balanced by an equally large mass flux at the bottom of the snow column. This so-called capping flux is separated into solid $q_{snwcp,ice}$ and liquid $q_{snwcp,liq}$ runoff terms. The partitioning of these phases is based on the phase ratio in the bottom snow layer at the time of the capping, such that phase ratio in this layer is unaltered.

The $q_{snwcp,ice}$ runoff is sent to the River Transport Model (RTM) (Chapter 11) where it is routed to the ocean as an ice stream and, if applicable, the ice is melted there.

For snow-capped surfaces other than glaciers and lakes the $q_{snwcp,liq}$ runoff is assigned to the glaciers and lakes runoff term q_{rgwl} (e.g. $q_{rgwl} = q_{snwcp,liq}$). For glacier surfaces the runoff term q_{rgwl} is calculated from the residual of the water balance

$$q_{rgwl} = q_{grnd,ice} + q_{grnd,liq} - E_g - E_v - \frac{\left(W_b^{n+1} - W_b^n\right)}{\Delta t} - q_{snwcp,ice} \tag{7.110}$$

where W_b^n and W_b^{n+1} are the water balances at the beginning and ending of the time step defined as

$$W_b = W_{can} + W_{sno} + \sum_{i=1}^{N} \left(w_{ice,i} + w_{liq,i}\right). \tag{7.111}$$

Currently, glaciers are non-vegetated and $E_v = W_{can} = 0$. The contribution of lake runoff to q_{rgwl} is described in section 12.6.3. The runoff term q_{rgwl} may be negative for glaciers and lakes, which reduces the total amount of runoff available to the river routing model (Chapter 14).

CHAPTER 8

SNOW HYDROLOGY

The parameterizations for snow are based primarily on *Anderson (1976)*, *Jordan (1991)*, and *Dai and Zeng (1997)*. The snowpack can have up to twelve layers. These layers are indexed in the Fortran code as $i = -11, -10, ..., -1, 0$ where layer $i = 0$ is the snow layer next to the top soil layer and layer $i = -11$ is the top layer of a twelve-layer snow pack. Since the number of snow layers varies according to the snow depth, we use the notation $snl + 1$ to describe the top layer of snow for the variable layer snow pack, where snl is the negative of the number of snow layers. Refer to Figure 8.1 for an example of the snow layer structure for a three layer snow pack.

Shown are three snow layers, $i = -2$, $i = -1$, and $i = 0$. The layer node depth is z, the layer interface is z_h, and the layer thickness is Δz.

The state variables for snow are the mass of water $w_{liq,i}$ (kg m^{-2}), mass of ice $w_{ice,i}$ (kg m^{-2}), layer thickness Δz_i (m), and temperature T_i (Chapter 6). The water vapor phase is neglected. Snow can also exist in the model without being represented by explicit snow layers. This occurs when the snowpack is less than a specified minimum snow depth ($z_{sno} < 0.01$ m). In this case, the state variable is the mass of snow W_{sno} (kg m^{-2}).

Section 8.1 describes the calculation of fractional snow covered area, which is used in the surface albedo calculation (Chapter 3) and the surface flux calculations (Chapter 5). The following two sections (8.2 and 8.3) describe the ice and water content of the snow pack assuming that at least one snow layer exists. Section 8.4 describes how black and organic carbon and mineral dust particles are represented within snow, including meltwater flushing. See Section 8.5 for a description of how a snow layer is initialized.

8.1 Snow Covered Area Fraction

The fraction of the ground covered by snow, f_{sno}, is based on the method of *Swenson and Lawrence (2012)*. Because the processes governing snowfall and snowmelt differ, changes in f_{sno} are calculated separately for accumulation and depletion. When snowfall occurs, f_{sno} is updated as

$$f_{sno}^{n+1} = 1 - ((1 - \tanh(k_{accum}q_{sno}\Delta t))(1 - f_{sno}^n))$$

(8.1)

where k_{accum} is a constant whose default value is 0.1, $q_{sno}\Delta t$ is the amount of new snow, f_{sno}^{n+1} is the updated snow covered fraction (SCF), and f_{sno}^n is the SCF from the previous time step.
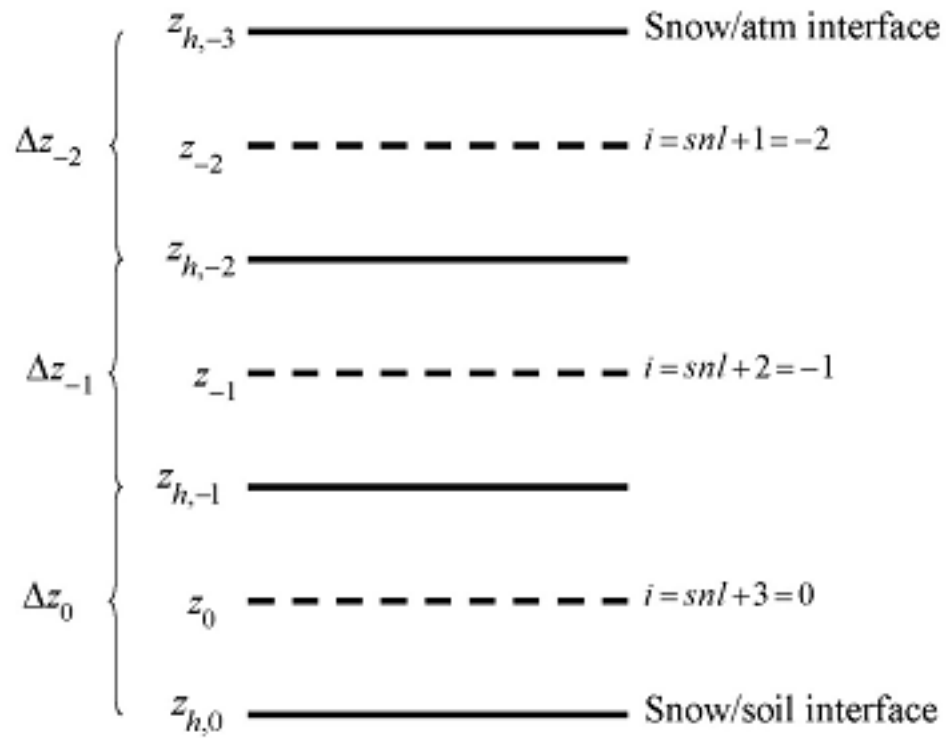
Figure 8.1: Example of three layer snow pack ($snl = -3$).

When snow melt occurs, f_{sno} is calculated from the depletion curve

$$f_{sno} = 1 - \left(\frac{\cos^{-1}(2R_{sno} - 1)}{\pi}\right)^{N_{melt}} \tag{8.2}$$

where R_{sno} is the ratio of W_{sno} to the maximum accumulated snow $W_{\max}$, and N_{melt} is a parameter that depends on the topographic variability within the grid cell. Whenever W_{sno} reaches zero, $W_{\max}$ is reset to zero. The depletion curve shape parameter is defined as

$$N_{melt} = \frac{200}{\min(10, \sigma_{topo})} \tag{8.3}$$

The standard deviation of the elevation within a grid cell, σ_{topo}, is calculated from a high resolution DEM (a 1km DEM is used for CLM). Note that *glacier_mec* columns (section 13.4) are treated differently in this respect, as they already account for the subgrid topography in a grid cell in their own way. Therefore, in each *glacier_mec* column very flat terrain is assumed, implemented as $N_{melt} = 10$.

8.2 Ice Content

The conservation equation for mass of ice in snow layers is

$$\frac{\partial w_{ice, i}}{\partial t} = \left\{\begin{array}{ll} f_{sno}\, q_{ice, i-1} - \frac{(\Delta w_{ice, i})_p}{\Delta t} & i = snl + 1 \\ -\frac{(\Delta w_{ice, i})_p}{\Delta t} & i = snl + 2, \ldots, 0 \end{array}\right\} \tag{8.4}$$

where $q_{ice, i-1}$ is the rate of ice accumulation from precipitation or frost or the rate of ice loss from sublimation (kg m^{-2} s^{-1}) in the top layer and $(\Delta w_{ice, i})_p / \Delta t$ is the change in ice due to phase change (melting rate) (section 6.2). The term $q_{ice, i-1}$ is computed in two steps as

$$q_{ice, i-1} = q_{grnd, ice} + (q_{frost} - q_{subl}) \tag{8.5}$$

where $q_{grnd, ice}$ is the rate of solid precipitation reaching the ground (section 7.1) and q_{frost} and q_{subl} are gains due to frost and losses due to sublimation, respectively (sectio 5.4). In the first step, immediately after $q_{grnd, ice}$ has been determined after accounting for interception (section 7.1), a new snow depth z_{sno} (m) is calculated from

$$z_{sno}^{n+1} = z_{sno}^{n} + \Delta z_{sno} \tag{8.6}$$

where

$$\Delta z_{sno} = \frac{q_{grnd, ice}\Delta t}{f_{sno}\rho_{sno}} \tag{8.7}$$

and ρ_{sno} is the bulk density of newly fallen snow (kg m^{-3}), which parameterized by a temperature-dependent and a wind-dependent term:

$$\rho_{sno} = \rho_T + \rho_w. \tag{8.8}$$

The temperature dependent term is given by (*van Kampenhout et al. (2017)*)

$$\rho_T = \left\{\begin{array}{ll} 50 + 1.7\,(17)^{1.5} & T_{atm} > T_f + 2 \\ 50 + 1.7\,(T_{atm} - T_f + 15)^{1.5} & T_f - 15 < T_{atm} \le T_f + 2 \\ -3.833\,(T_{atm} - T_f) - 0.0333\,(T_{atm} - T_f)^2 & T_{atm} \le T_f - 15 \end{array}\right\} \tag{8.9}$$

where T_{atm} is the atmospheric temperature (K), and T_f is the freezing temperature of water (K) (Table 2.7). When 10 m wind speed W_{atm} is greater than 0.1 m^{-1}, snow density increases due to wind-driven compaction according to *van Kampenhout et al. 2017*

$$\rho_w = 266.861 \left(\frac{1 + \tanh(\frac{W_{atm}}{5})}{2}\right)^{8.8} \tag{8.10}$$

which is added to the temperature-dependent term (cf. equation (8.8)).

The mass of snow W_{sno} is

$$W_{sno}^{n+1} = W_{sno}^n + q_{grnd,ice}\Delta t. \tag{8.11}$$

The ice content of the top layer and the layer thickness are updated as

$$w_{ice,snl+1}^{n+1} = w_{ice,snl+1}^n + q_{grnd,ice}\Delta t \tag{8.12}$$

$$\Delta z_{snl+1}^{n+1} = \Delta z_{snl+1}^n + \Delta z_{sno}. \tag{8.13}$$

In the second step, after surface fluxes and snow/soil temperatures have been determined (Chapters 5 and 6), $w_{ice,snl+1}$ is updated for frost or sublimation as

$$w_{ice,snl+1}^{n+1} = w_{ice,snl+1}^n + f_{sno}\left(q_{frost} - q_{subl}\right)\Delta t. \tag{8.14}$$

If $w_{ice,snl+1}^{n+1} < 0$ upon solution of equation , the ice content is reset to zero and the liquid water content $w_{liq,snl+1}$ is reduced by the amount required to bring $w_{ice,snl+1}^{n+1}$ up to zero.

The snow water equivalent W_{sno} is capped to not exceed 10,000 kg m^{-2}. If the addition of q_{frost} were to result in $W_{sno} > 10,000$ kg m^{-2}, the frost term q_{frost} is instead added to the ice runoff term $q_{snwcp,ice}$ (section 7.6).

8.3 Water Content

The conservation equation for mass of water in snow layers is

$$\frac{\partial w_{liq,i}}{\partial t} = (q_{liq,i-1} - q_{liq,i}) + \frac{(\Delta w_{liq,i})_p}{\Delta t} \tag{8.15}$$

where $q_{liq,i-1}$ is the flow of liquid water into layer i from the layer above, $q_{liq,i}$ is the flow of water out of layer i to the layer below, $(\Delta w_{liq,i})_p \big/ \Delta t$ is the change in liquid water due to phase change (melting rate) (section 6.2). For the top snow layer only,

$$q_{liq,i-1} = f_{sno}\left(q_{grnd,liq} + (q_{sdew} - q_{seva})\right) \tag{8.16}$$

where $q_{grnd,liq}$ is the rate of liquid precipitation reaching the snow (section 7.1), q_{seva} is the evaporation of liquid water and q_{sdew} is the liquid dew (section 5.4). After surface fluxes and snow/soil temperatures have been determined (Chapters 5 and 6), $w_{liq,snl+1}$ is updated for the liquid precipitation reaching the ground and dew or evaporation as

$$w_{liq,snl+1}^{n+1} = w_{liq,snl+1}^n + f_{sno}\left(q_{grnd,liq} + q_{sdew} - q_{seva}\right)\Delta t. \tag{8.17}$$

When the liquid water within a snow layer exceeds the layer's holding capacity, the excess water is added to the underlying layer, limited by the effective porosity $(1 - \theta_{ice})$ of the layer. The flow of water is assumed to be zero ($q_{liq,i} = 0$) if the effective porosity of either of the two layers ($1 - \theta_{ice,i}$ and $1 - \theta_{ice,i+1}$) is less than $\theta_{imp} = 0.05$, the water impermeable volumetric water content. Thus, water flow between layers, $q_{liq,i}$, for layers $i = snl + 1, \ldots, 0$, is initially calculated as

$$q_{liq,i} = \frac{\rho_{liq}\left[\theta_{liq,i} - S_r\left(1 - \theta_{ice,i}\right)\right]f_{sno}\Delta z_i}{\Delta t} \geq 0 \tag{8.18}$$

where the volumetric liquid water $\theta_{liq,i}$ and ice $\theta_{ice,i}$ contents are

$$\theta_{ice,i} = \frac{w_{ice,i}}{f_{sno}\Delta z_i\rho_{ice}} \leq 1 \tag{8.19}$$

$$\theta_{liq,\,i} = \frac{w_{liq,\,i}}{f_{sno}\Delta z_i \rho_{liq}} \le 1 - \theta_{ice,\,i}, \tag{8.20}$$

and $S_r = 0.033$ is the irreducible water saturation (snow holds a certain amount of liquid water due to capillary retention after drainage has ceased (*Anderson (1976)*)). The water holding capacity of the underlying layer limits the flow of water $q_{liq,\,i}$ calculated in equation , unless the underlying layer is the surface soil layer, as

$$q_{liq,\,i} \le \frac{\rho_{liq}\left[1 - \theta_{ice,\,i+1} - \theta_{liq,\,i+1}\right]\Delta z_{i+1}}{\Delta t} \qquad i = snl + 1, \dots, -1. \tag{8.21}$$

The liquid water content $w_{liq,\,i}$ is updated as

$$w_{liq,\,i}^{n+1} = w_{liq,\,i}^{n} + (q_{i-1} - q_i)\,\Delta t. \tag{8.22}$$

Equations - are solved sequentially from top ($i = snl + 1$) to bottom ($i = 0$) snow layer in each time step. The total flow of liquid water reaching the soil surface is then $q_{liq,\,0}$ which is used in the calculation of surface runoff and infiltration (sections 7.2.1 and 7.2.3).

8.4 Black and organic carbon and mineral dust within snow

Particles within snow originate from atmospheric aerosol deposition (D_{sp} in Table 2.3 (kg m^{-2} s^{-1}) and influence snow radiative transfer (sections 3.2.1, 3.2.2, and 3.2.3). Particle masses and mixing ratios are represented with a simple mass-conserving scheme. The model maintains masses of the following eight particle species within each snow layer: hydrophilic black carbon, hydrophobic black carbon, hydrophilic organic carbon, hydrophobic organic carbon, and four species of mineral dust with the following particle sizes: 0.1-1.0, 1.0-2.5, 2.5-5.0, and 5.0-10.0 μm. Each of these species has unique optical properties (Table 3.5) and meltwater removal efficiencies (Table 8.1).

The black carbon and organic carbon deposition rates described in Table 2.3 are combined into four categories as follows

$$D_{bc,\,hphil} = D_{bc,\,dryhphil} + D_{bc,\,wethphil} \tag{8.23}$$

$$D_{bc,\,hphob} = D_{bc,\,dryhphob} \tag{8.24}$$

$$D_{oc,\,hphil} = D_{oc,\,dryhphil} + D_{oc,\,wethphil} \tag{8.25}$$

$$D_{oc,\,hphob} = D_{oc,\,dryhphob} \tag{8.26}$$

Deposited particles are assumed to be instantly mixed (homogeneously) within the surface snow layer and are added after the inter-layer water fluxes are computed (section 8.3) so that some aerosol is in the top layer after deposition and is not immediately washed out before radiative calculations are done. Particle masses are then redistributed each time step based on meltwater drainage through the snow column (section 8.3) and snow layer combination and subdivision (section 8.7). The change in mass of each of the particle species $\Delta m_{sp,\,i}$ (kg m^{-2}) is

$$\Delta m_{sp,\,i} = \left[k_{sp}\left(q_{liq,\,i-1}c_{sp,\,i-1} - q_{liq,\,i}c_i\right) + D_{sp}\right]\Delta t \tag{8.27}$$

where k_{sp} is the meltwater scavenging efficiency that is unique for each species (Table 8.1), $q_{liq,\,i-1}$ is the flow of liquid water into layer i from the layer above, $q_{liq,\,i}$ is the flow of water out of layer i into the layer below (kg m^{-2} s^{-1}) (section 8.3), $c_{sp,\,i-1}$ and $c_{sp,\,i}$ are the particle mass mixing ratios in layers $i-1$ and i (kg kg^{-1}), D_{sp} is the atmospheric deposition rate (zero for all layers except layer $snl + 1$), and Δt is the model time step (s). The particle mass mixing ratio is

$$c_i = \frac{m_{sp,\,i}}{w_{liq,\,i} + w_{ice,\,i}}. \tag{8.28}$$

Values of k_{sp} are partially derived from experiments published by *Conway et al. (1996)*. Particles masses are re-distributed proportionately with snow mass when layers are combined or divided, thus conserving particle mass within

---

the snow column. The mass of particles carried out with meltwater through the bottom snow layer is assumed to be permanently lost from the snowpack, and is not maintained within the model.

Table 8.1: Meltwater scavenging efficiency for particles within snow

Species	k_{sp}
Hydrophilic black carbon	0.20
Hydrophobic black carbon	0.03
Hydrophilic organic carbon	0.20
Hydrophobic organic carbon	0.03
Dust species 1 (0.1-1.0 μm)	0.02
Dust species 2 (1.0-2.5 μm)	0.02
Dust species 3 (2.5-5.0 μm)	0.01
Dust species 4 (5.0-10.0 μm)	0.01

8.5 Initialization of snow layer

If there are no existing snow layers ($snl + 1 = 1$) but $z_{sno} \geq 0.01$ m after accounting for solid precipitation q_{sno}, then a snow layer is initialized ($snl = -1$) as follows

$$
\begin{aligned}
\Delta z_0 &= z_{sno} \\
z_o &= -0.5 \Delta z_0 \\
z_{h,-1} &= -\Delta z_0 \\
T_0 &= \min \left(T_f, T_{atm} \right) \\
w_{ice,0} &= W_{sno} \\
w_{liq,0} &= 0
\end{aligned}
. \tag{8.29}
$$

8.6 Snow Compaction

Snow compaction is initiated after the soil hydrology calculations [surface runoff (section 7.2.1), infiltration (section 7.2.3), soil water (section 7.3)] are complete. Currently, there are four processes included that lead to snow compaction:

1. destructive metamorphism of new snow (crystal breakdown due to wind or thermodynamic stress)

2. snow load or compaction by overburden pressure

3. melting (changes in snow structure due to melt-freeze cycles plus changes in crystals due to liquid water)

4. drifting snow compaction.

The total fractional compaction rate for each snow layer $C_{R,i}$ (s^{-1}) is the sum of multiple compaction processes

$$
C_{R,i} = \frac{1}{\Delta z_i} \frac{\partial \Delta z_i}{\partial t} = C_{R1,i} + C_{R2,i} + C_{R3,i} + C_{R4,i} + C_{R5,i}. \tag{8.30}
$$

Compaction is not allowed if the layer is saturated

$$
1 - \left(\frac{w_{ice,i}}{f_{sno} \Delta z_i \rho_{ice}} + \frac{w_{liq,i}}{f_{sno} \Delta z_i \rho_{liq}} \right) \leq 0.001 \tag{8.31}
$$

or if the ice content is below a minimum value ($w_{ice,i} \leq 0.1$).

The snow layer thickness after compaction is

$$
\Delta z_i^{n+1} = \Delta z_i^n \left(1 + C_{R,i} \Delta t \right). \tag{8.32}
$$

8.6.1 Destructive metamorphism

Compaction as a result of destructive metamorphism $C_{R1,\,i}$ (s^{-1}) is temperature dependent (*Anderson (1976)*)

$$C_{R1,\,i} = \left[\frac{1}{\Delta z_i}\frac{\partial \Delta z_i}{\partial t}\right]_{metamorphism} = -c_3 c_1 c_2 \exp\left[-c_4\left(T_f - T_i\right)\right] \tag{8.33}$$

where $c_3 = 2.777 \times 10^{-6}$ (s^{-1}) is the fractional compaction rate for $T_i = T_f$, $c_4 = 0.04$ K^{-1}, and

$$
\begin{aligned}
c_1 &= 1 & \frac{w_{ice,\,i}}{f_{sno}\Delta z_i} &\leq 175 \text{ kg m}^{-3} \\
c_1 &= \exp\left[-0.046\left(\frac{w_{ice,\,i}}{f_{sno}\Delta z_i} - 175\right)\right] & \frac{w_{ice,\,i}}{f_{sno}\Delta z_i} &> 175 \text{ kg m}^{-3} \\
c_2 &= 2 & \frac{w_{liq,\,i}}{f_{sno}\Delta z_i} &> 0.01 \\
c_2 &= 1 & \frac{w_{liq,\,i}}{f_{sno}\Delta z_i} &\leq 0.01
\end{aligned}
\tag{8.34}
$$

where $w_{ice,\,i}/\left(f_{sno}\Delta z_i\right)$ and $w_{liq,\,i}/\left(f_{sno}\Delta z_i\right)$ are the bulk densities of liquid water and ice (kg m^{-3}).

8.6.2 Overburden pressure compaction

The compaction rate as a result of overburden $C_{R2,\,i}$ (s^{-1}) is a linear function of the snow load pressure $P_{s,\,i}$ (kg m^{-2}) (*Anderson (1976)*):

$$C_{R2,\,i} = \left[\frac{1}{\Delta z_i}\frac{\partial \Delta z_i}{\partial t}\right]_{overburden} = -\frac{P_{s,\,i}}{\eta} \tag{8.35}$$

The snow load pressure $P_{s,\,i}$ is calculated for each layer as the sum of the ice $w_{ice,\,i}$ and liquid water contents $w_{liq,\,i}$ of the layers above plus half the ice and liquid water contents of the layer being compacted

$$P_{s,\,i} = \frac{w_{ice,\,i} + w_{liq,\,i}}{2} + \sum_{j=snl+1}^{j=i-1}\left(w_{ice,\,j} + w_{liq,\,j}\right). \tag{8.36}$$

Variable η in (8.35) is a viscosity coefficient (kg s m^{-2}) that varies with density and temperature as

$$\eta = f_1 f_2 \eta_0 \frac{\rho_i}{c_\eta} \exp\left[a_\eta\left(T_f - T_i\right) + b_\eta \rho_i\right] \tag{8.37}$$

with constant factors $\eta_0 = 7.62237 \times 10^6$ kg s^{-1} m^{-2}, $a_\eta = 0.1$ K^{-1}, $b_\eta = 0.023$ m^3 kg^{-1}, and $c_\eta = 450$ kg m^{-3} (*van Kampenhout et al. (2017)*). Further, factor f_1 accounts for the presence of liquid water (*Vionnet et al. (2012)*):

$$f_1 = \frac{1}{1 + 60\frac{w_{\text{liq},\,i}}{\rho_{\text{liq}}\Delta z_i}}. \tag{8.38}$$

Factor f_2 originally accounts for the presence of angular grains, but since grain shape is not modelled f_2 is fixed to the value 4.

8.6.3 Compaction by melt

The compaction rate due to melting $C_{R3,\,i}$ (s^{-1}) is taken to be the ratio of the change in snow ice mass after the melting to the mass before melting

$$C_{R3,\,i} = \left[\frac{1}{\Delta z_i}\frac{\partial \Delta z_i}{\partial t}\right]_{melt} = -\frac{1}{\Delta t}\max\left(0, \frac{W_{sno,\,i}^n - W_{sno,\,i}^{n+1}}{W_{sno,\,i}^n}\right) \tag{8.39}$$

and melting is identified during the phase change calculations (section 6.2). Because snow depth is defined as the average depth of the snow covered area, the snow depth must also be updated for changes in f_{sno} when W_{sno} has changed.

$$C_{R4,\,i} = \left[\frac{1}{\Delta z_i} \frac{\partial \Delta z_i}{\partial t} \right]_{fsno} = -\frac{1}{\Delta t} \max \left(0, \frac{f_{sno,\,i}^{n} - f_{sno,\,i}^{n+1}}{f_{sno,\,i}^{n}} \right) \tag{8.40}$$

8.6.4 Compaction by drifting snow

Crystal breaking by drifting snow leads to higher snow densities at the surface. This process is particularly important on ice sheets, where destructive metamorphism is slow due to low temperatures but high wind speeds (katabatic winds) are prevailing. Therefore a drifting snow compaction parametrization was introduced, based on (*Vionnet et al. (2012)*).

$$C_{R5,\,i} = \left[\frac{1}{\Delta z_i} \frac{\partial \Delta z_i}{\partial t} \right]_{drift} = -\frac{\rho_{\max} - \rho_i}{\tau_i}. \tag{8.41}$$

Here, $\rho_{\max} = 350$ kg m^{-3} is the upper limit to which this process is active, and τ_i is a timescale which is depth dependent:

$$\tau_i = \frac{\tau}{\Gamma_{\mathrm{drift}}^{i}} \quad , \quad \Gamma_{\mathrm{drift}}^{i} = \max \left[0, S_{\mathrm{I}}^{i} \exp(-z_i/0.1) \right]. \tag{8.42}$$

Here, τ is a characteristic time scale for drifting snow compaction and is empirically set to 48 h, and z_i is a pseudo-depth which takes into account previous hardening of snow layers above the current layer: $z_i = \sum_j \Delta z_j \cdot (3.25 - S_{\mathrm{I}}^{j})$. The driftability index S_{I} reflects how well snow can be drifted and depends on the mobility of the snow as well as the 10 m wind speed:

$$\begin{aligned} S_{\mathrm{I}} &= -2.868 \exp(-0.085 U) + 1 + M_{\mathrm{O}} \\ M_{\mathrm{O}} &= -0.069 + 0.66 F(\rho) \end{aligned} \tag{8.43}$$

The latter equation (for the mobility index M_{O}) is a simplification from the original paper by removing the dependency on grain size and assuming spherical grains (see *van Kampenhout et al. (2017)*).

8.7 Snow Layer Combination and Subdivision

After the determination of snow temperature including phase change(Chapter 6), snow hydrology (Chapter 8), and the compaction calculations (section 8.6) , the number of snow layers is adjusted by either combining or subdividing layers. The combination and subdivision of snow layers is based on *Jordan (1991)*.

8.7.1 Combination

If a snow layer has nearly melted or if its thickness Δz_i is less than the prescribed minimum thickness $\Delta z_{\min}$ (Table 8.2), the layer is combined with a neighboring layer. The overlying or underlying layer is selected as the neighboring layer according to the following rules

1. If the top layer is being removed, it is combined with the underlying layer

2. If the underlying layer is not snow (i.e., it is the top soil layer), the layer is combined with the overlying layer

3. If the layer is nearly completely melted, the layer is combined with the underlying layer

4. If none of the above rules apply, the layer is combined with the thinnest neighboring layer.

A first pass is made through all snow layers to determine if any layer is nearly melted ($w_{ice,\,i} \leq 0.1$). If so, the remaining liquid water and ice content of layer i is combined with the underlying neighbor $i + 1$ as

$$w_{liq,\,i+1} = w_{liq,\,i+1} + w_{liq,\,i} \tag{8.44}$$

$$w_{ice,\,i+1} = w_{ice,\,i+1} + w_{ice,\,i}. \tag{8.45}$$

This includes the snow layer directly above the top soil layer. In this case, the liquid water and ice content of the melted snow layer is added to the contents of the top soil layer. The layer properties, T_i, $w_{ice,\,i}$, $w_{liq,\,i}$, Δz_i, are then re-indexed so that the layers above the eliminated layer are shifted down by one and the number of snow layers is decremented accordingly.

At this point, if there are no explicit snow layers remaining ($snl = 0$), the snow water equivalent W_{sno} and snow depth z_{sno} are set to zero, otherwise, W_{sno} and z_{sno} are re-calculated as

$$W_{sno} = \sum_{i=snl+1}^{i=0} (w_{ice,\,i} + w_{liq,\,i}) \tag{8.46}$$

$$z_{sno} = \sum_{i=snl+1}^{i=0} \Delta z_i. \tag{8.47}$$

If the snow depth $0 < z_{sno} < 0.01$ m or the snow density $\frac{W_{sno}}{f_{sno}z_{sno}} < 50$ kg/m3, the number of snow layers is set to zero, the total ice content of the snowpack $\sum_{i=snl+1}^{i=0} w_{ice,\,i}$ is assigned to W_{sno}, and the total liquid water $\sum_{i=snl+1}^{i=0} w_{liq,\,i}$ is assigned to the top soil layer. Otherwise, the layers are combined according to the rules above.

When two snow layers are combined (denoted here as 1 and 2), their thickness combination (c) is

$$\Delta z_c = \Delta z_1 + \Delta z_2, \tag{8.48}$$

their mass combination is

$$w_{liq,\,c} = w_{liq,\,1} + w_{liq,\,2} \tag{8.49}$$

$$w_{ice,\,c} = w_{ice,\,1} + w_{ice,\,2}, \tag{8.50}$$

and their temperatures are combined as

$$T_c = T_f + \frac{h_c - L_f w_{liq,\,c}}{C_{ice}w_{ice,\,c} + C_{liq}w_{liq,\,c}} \tag{8.51}$$

where $h_c = h_1 + h_2$ is the combined enthalpy h_i of the two layers where

$$h_i = (C_{ice}w_{ice,\,i} + C_{liq}w_{liq,\,i})(T_i - T_f) + L_f w_{liq,\,i}. \tag{8.52}$$

In these equations, L_f is the latent heat of fusion (J kg^{-1}) and C_{liq} and C_{ice} are the specific heat capacities (J kg^{-1} K^{-1}) of liquid water and ice, respectively (Table 2.7). After layer combination, the node depths and layer interfaces (Figure 8.1) are recalculated from

$$z_i = z_{h,\,i} - 0.5\Delta z_i \qquad i = 0,\dots,snl+1 \tag{8.53}$$

$$z_{h,\,i-1} = z_{h,\,i} - \Delta z_i \qquad i = 0,\dots,snl+1 \tag{8.54}$$

where Δz_i is the layer thickness.

Table 8.2: Minimum and maximum thickness of snow layers (m)

Layer	$\Delta z_{\min}$	N_l	N_u	$(\Delta z_{\max})_l$	$(\Delta z_{\max})_u$
1 (top)	0.010	1	>1	0.03	0.02
2	0.015	2	>2	0.07	0.05
3	0.025	3	>3	0.18	0.11
4	0.055	4	>4	0.41	0.23
5	0.115	5	>5	0.88	0.47
6	0.235	6	>6	1.83	0.95
7	0.475	7	>7	3.74	1.91
8	0.955	8	>8	7.57	3.83
9	1.915	9	>9	15.24	7.67
10	3.835	10	>10	30.59	15.35
11	7.675	11	>11	61.30	30.71
12 (bottom)	15.355	12	•	•	•

The maximum snow layer thickness, $\Delta z_{\max}$, depends on the number of layers, N_l and N_u (section 8.7.2).

8.7.2 Subdivision

The snow layers are subdivided when the layer thickness exceeds the prescribed maximum thickness $\Delta z_{\max}$ with lower and upper bounds that depend on the number of snow layers (Table 8.2). For example, if there is only one layer, then the maximum thickness of that layer is 0.03 m, however, if there is more than one layer, then the maximum thickness of the top layer is 0.02 m. Layers are checked sequentially from top to bottom for this limit. If there is only one snow layer and its thickness is greater than 0.03 m (Table 8.2), the layer is subdivided into two layers of equal thickness, liquid water and ice contents, and temperature. If there is an existing layer below the layer to be subdivided, the thickness Δz_i, liquid water and ice contents, $w_{liq,\,i}$ and $w_{ice,\,i}$, and temperature T_i of the excess snow are combined with the underlying layer according to equations -. If there is no underlying layer after adjusting the layer for the excess snow, the layer is subdivided into two layers of equal thickness, liquid water and ice contents. The vertical snow temperature profile is maintained by calculating the slope between the layer above the splitting layer (T_1) and the splitting layer (T_2) and constraining the new temperatures (T_2^{n+1}, T_3^{n+1}) to lie along this slope. The temperature of the lower layer is first evaluated from

$$T_3' = T_2^n - \left(\frac{T_1^n - T_2^n}{(\Delta z_1^n + \Delta z_2^n)/2} \right) \left(\frac{\Delta z_2^{n+1}}{2} \right),\tag{8.55}$$

then adjusted as,

$$\begin{aligned} T_3^{n+1} &= T_2^n & T_3' \geq T_f \\ T_2^{n+1} &= T_2^n + \left(\frac{T_1^n - T_2^n}{(\Delta z_1 + \Delta z_2^n)/2} \right) \left(\frac{\Delta z_2^{n+1}}{2} \right) & T_3' < T_f \end{aligned}\tag{8.56}$$

where here the subscripts 1, 2, and 3 denote three layers numbered from top to bottom. After layer subdivision, the node depths and layer interfaces are recalculated from equations and .

CHAPTER 9

STOMATAL RESISTANCE AND PHOTOSYNTHESIS

9.1 Summary of CLM5.0 updates relative to the CLM4.5

We describe here the complete photosynthesis and stomatal conductance parameterizations that appear in CLM5.0. Corresponding information for CLM4.5 appeared in the CLM4.5 Technical Note (*Oleson et al. 2013*).

CLM5 includes the following new changes to photosynthesis and stomatal conductance:

- Default stomatal conductance calculation uses the Medlyn conductance model

- $V_{c,max}$ and J_{max} at 25 $^{\circ}$C: are now prognostic, and predicted via optimality by the LUNA model (Chapter 10)

- Leaf N concentration and the fraction of leaf N in Rubisco used to calculate V_{cmax25} are determined by the LUNA model (Chapter 10)

- Water stress is applied by the hydraulic conductance model (Chapter 11)

9.2 Introduction

Leaf stomatal resistance, which is needed for the water vapor flux (Chapter 5), is coupled to leaf photosynthesis similar to Collatz et al. (*1991*, *1992*). These equations are solved separately for sunlit and shaded leaves using average absorbed photosynthetically active radiation for sunlit and shaded leaves [ϕ^{sun}, ϕ^{sha} W m^{-2} (section 4.1)] to give sunlit and shaded stomatal resistance (r_s^{sun}, r_s^{sha} s m^{-1}) and photosynthesis (A^{sun}, A^{sha} µmol CO$_2$ m^{-2} s^{-1}). Canopy photosynthesis is $A^{sun}L^{sun} + A^{sha}L^{sha}$, where L^{sun} and L^{sha} are the sunlit and shaded leaf area indices (section 4.1). Canopy conductance is $\frac{1}{r_b+r_s^{sun}}L^{sun} + \frac{1}{r_b+r_s^{sha}}L^{sha}$, where r_b is the leaf boundary layer resistance (section 5.3).

9.3 Stomatal resistance

CLM5 calculates stomatal conductance using the Medlyn stomatal conductance model (*Medlyn et al. 2011*). Previous versions of CLM calculated leaf stomatal resistance is using the Ball-Berry conductance model as described by *Collatz et al. (1991)* and implemented in global climate models (*Sellers et al. 1996*). The Medlyn model calculates stomatal conductance (i.e., the inverse of resistance) based on net leaf photosynthesis, the vapor pressure deficit, and the CO_2 concentration at the leaf surface. Leaf stomatal resistance is:

$$\frac{1}{r_s} = g_s = g_o + 1.6(1 + \frac{g_1}{\sqrt{D}})\frac{A_n}{c_s/P_{atm}} \tag{9.1}$$

where r_s is leaf stomatal resistance (s m^2 μmol^{-1}), g_o is the minimum stomatal conductance (μ mol m^{-2} s^{-1}), A_n is leaf net photosynthesis (μmol CO_2 m^{-2} s^{-1}), c_s is the CO_2 partial pressure at the leaf surface (Pa), P_{atm} is the atmospheric pressure (Pa), and D is the vapor pressure deficit at the leaf surface (kPa). g_1 is a plant functional type dependent parameter (Table 9.1) and are the same as those used in the CABLE model (*de Kauwe et al. 2015*).

The value for $g_o = 100$ μ mol m^{-2} s^{-1} for C$_3$ and C$_4$ plants. Photosynthesis is calculated for sunlit (A^{sun}) and shaded (A^{sha}) leaves to give r_s^{sun} and r_s^{sha}. Additionally, soil water influences stomatal resistance through plant hydraulic stress, detailed in the *Plant Hydraulics* chapter.

Resistance is converted from units of s m^2 μ mol^{-1} to s m^{-1} as: 1 s m^{-1} = $1 \times 10^{-9} R_{gas} \frac{\theta_{atm}}{P_{atm}}$ μ mol^{-1} m^2 s, where R_{gas} is the universal gas constant (J K^{-1} kmol^{-1}) (Table 2.7) and θ_{atm} is the atmospheric potential temperature (K).

Table 9.1: Plant functional type (PFT) stomatal conductance parameters.

PFT	g_1
NET Temperate	2.35
NET Boreal	2.35
NDT Boreal	2.35
BET Tropical	4.12
BET temperate	4.12
BDT tropical	4.45
BDT temperate	4.45
BDT boreal	4.45
BES temperate	4.70
BDS temperate	4.70
BDS boreal	4.70
C$_3$ arctic grass	2.22
C$_3$ grass	5.25
C$_4$ grass	1.62
Temperate Corn	1.79
Spring Wheat	5.79
Temperate Soybean	5.79
Cotton	5.79
Rice	5.79
Sugarcane	1.79
Tropical Corn	1.79
Tropical Soybean	5.79

9.4 Photosynthesis

Photosynthesis in C$_3$ plants is based on the model of *Farquhar et al. (1980)*. Photosynthesis in C$_4$ plants is based on the model of *Collatz et al. (1992)*. *Bonan et al. (2011)* describe the implementation, modified here. In its simplest

form, leaf net photosynthesis after accounting for respiration (R_d) is

$$A_n = \min\left(A_c, A_j, A_p\right) - R_d. \tag{9.2}$$

The RuBP carboxylase (Rubisco) limited rate of carboxylation A_c (μ mol CO_2 m^{-2} s^{-1}) is

$$A_c = \begin{cases} \frac{V_{c\,\max}(c_i - \Gamma)}{c_i + K_c(1 + o_i/K_o)} & \text{for C}_3 \text{ plants} \\ V_{c\,\max} & \text{for C}_4 \text{ plants} \end{cases} \qquad c_i - \Gamma \geq 0. \tag{9.3}$$

The maximum rate of carboxylation allowed by the capacity to regenerate RuBP (i.e., the light-limited rate) A_j (μ mol CO_2 m^{-2} s^{-1}) is

$$A_j = \begin{cases} \frac{J_x(c_i - \Gamma)}{4c_i + 8\Gamma} & \text{for C}_3 \text{ plants} \\ \alpha(4.6\phi) & \text{for C}_4 \text{ plants} \end{cases} \qquad c_i - \Gamma \geq 0. \tag{9.4}$$

The product-limited rate of carboxylation for C$_3$ plants and the PEP carboxylase-limited rate of carboxylation for C$_4$ plants A_p (μ mol CO_2 m^{-2} s^{-1}) is

$$A_p = \begin{cases} 3T_p & \text{for C}_3 \text{ plants} \\ k_p \frac{c_i}{P_{atm}} & \text{for C}_4 \text{ plants} \end{cases}. \tag{9.5}$$

In these equations, c_i is the internal leaf CO_2 partial pressure (Pa) and $o_i = 0.20P_{atm}$ is the O_2 partial pressure (Pa). K_c and K_o are the Michaelis-Menten constants (Pa) for CO_2 and O_2. Γ (Pa) is the CO_2 compensation point. $V_{c\,\max}$ is the maximum rate of carboxylation (μmol m^{-2} s^{-1}, Chapter 10) and J_x is the electron transport rate (μmol m^{-2} s^{-1}). T_p is the triose phosphate utilization rate (μmol m^{-2} s^{-1}), taken as $T_p = 0.167V_{c\,\max}$ so that $A_p = 0.5V_{c\,\max}$ for C$_3$ plants (as in *Collatz et al. 1992*). For C$_4$ plants, the light-limited rate A_j varies with ϕ in relation to the quantum efficiency ($\alpha = 0.05$ mol CO_2 mol^{-1} photon). ϕ is the absorbed photosynthetically active radiation (W m^{-2}) (section 4.1) , which is converted to photosynthetic photon flux assuming 4.6 μ mol photons per joule. k_p is the initial slope of C$_4$ CO_2 response curve.

For C$_3$ plants, the electron transport rate depends on the photosynthetically active radiation absorbed by the leaf. A common expression is the smaller of the two roots of the equation

$$\Theta_{PSII}J_x^2 - \left(I_{PSII} + J_{\max}\right)J_x + I_{PSII}J_{\max} = 0 \tag{9.6}$$

where $J_{\max}$ is the maximum potential rate of electron transport (μmol m^{-2} s^{-1}, Chapter 10), I_{PSII} is the light utilized in electron transport by photosystem II (μmol m^{-2} s^{-1}), and Θ_{PSII} is a curvature parameter. For a given amount of photosynthetically active radiation absorbed by a leaf (ϕ, W m^{-2}), converted to photosynthetic photon flux density with 4.6 μmol J^{-1}, the light utilized in electron transport is

$$I_{PSII} = 0.5\Phi_{PSII}(4.6\phi) \tag{9.7}$$

where Φ_{PSII} is the quantum yield of photosystem II, and the term 0.5 arises because one photon is absorbed by each of the two photosystems to move one electron. Parameter values are $\Theta_{PSII} = 0.7$ and $\Phi_{PSII} = 0.85$. In calculating A_j (for both C$_3$ and C$_4$ plants), $\phi = \phi^{sun}$ for sunlit leaves and $\phi = \phi^{sha}$ for shaded leaves.

The model uses co-limitation as described by *Collatz et al. (1991, 1992)*. The actual gross photosynthesis rate, A, is given by the smaller root of the equations

$$\begin{aligned} \Theta_{cj}A_i^2 - \left(A_c + A_j\right)A_i + A_cA_j &= 0 \\ \Theta_{ip}A^2 - \left(A_i + A_p\right)A + A_iA_p &= 0 \end{aligned}. \tag{9.8}$$

Values are $\Theta_{cj} = 0.98$ and $\Theta_{ip} = 0.95$ for C$_3$ plants; and $\Theta_{cj} = 0.80$ and $\Theta_{ip} = 0.95$ for C$_4$ plants. A_i is the intermediate co-limited photosynthesis. $A_n = A - R_d$.

The parameters K_c, K_o, and Γ depend on temperature. Values at 25 $^\circ$ C are $K_{c25} = 404.9 \times 10^{-6}P_{atm}$, $K_{o25} = 278.4 \times 10^{-3}P_{atm}$, and $\Gamma_{25} = 42.75 \times 10^{-6}P_{atm}$. $V_{c\,\max}$, $J_{\max}$, T_p, k_p, and R_d also vary with temperature.

9.4. Photosynthesis

$J_{\max 25}$ at 25 °C: is calculated by the LUNA model (Chapter 10)

Parameter values at 25 °C are calculated from $V_{c\,\max}$ at 25 °C:, including: $T_{p25} = 0.167 V_{c\,\max 25}$, and $R_{d25} = 0.015 V_{c\,\max 25}$ (C$_3$) and $R_{d25} = 0.025 V_{c\,\max 25}$ (C$_4$).

For C$_4$ plants, $k_{p25} = 20000\ V_{c\,\max 25}$.

However, when the biogeochemistry is active (the default mode), R_{d25} is calculated from leaf nitrogen as described in (Chapter 17)

The parameters $V_{c\,\max 25}$, $J_{\max 25}$, T_{p25}, k_{p25}, and R_{d25} are scaled over the canopy for sunlit and shaded leaves (section 9.5). In C$_3$ plants, these are adjusted for leaf temperature, T_v (K), as:

$$
\begin{aligned}
V_{c\,\max} &= V_{c\,\max 25}\, f\,(T_v)\, f_H\,(T_v) \\
J_{\max} &= J_{\max 25}\, f\,(T_v)\, f_H\,(T_v) \\
T_p &= T_{p25}\, f\,(T_v)\, f_H\,(T_v) \\
R_d &= R_{d25}\, f\,(T_v)\, f_H\,(T_v) \\
K_c &= K_{c25}\, f\,(T_v) \\
K_o &= K_{o25}\, f\,(T_v) \\
\Gamma &= \Gamma_{25}\, f\,(T_v)
\end{aligned}
\tag{9.9}
$$

$$
f\,(T_v) = \exp\left[\frac{\Delta H_a}{298.15 \times 0.001 R_{gas}} \left(1 - \frac{298.15}{T_v} \right) \right]
\tag{9.10}
$$

and

$$
f_H\,(T_v) = \frac{1 + \exp\left(\frac{298.15 \Delta S - \Delta H_d}{298.15 \times 0.001 R_{gas}} \right)}{1 + \exp\left(\frac{\Delta S T_v - \Delta H_d}{0.001 R_{gas} T_v} \right)}.
\tag{9.11}
$$

Table 9.2 lists parameter values for ΔH_a and ΔH_d. ΔS is calculated separately for $V_{c\,\max}$ and J_{max} to allow for temperature acclimation of photosynthesis (see equation (9.15)), and ΔS is 490 J mol^{-1} K^{-1} for R_d (*Bonan et al. 2011*, *Lombardozzi et al. 2015*). Because T_p as implemented here varies with $V_{c\,\max}$, T_p uses the same temperature parameters as $V_{c\,\max}$. For C$_4$ plants,

$$
\begin{aligned}
V_{c\,\max} &= V_{c\,\max 25} \left[\frac{Q_{10}^{(T_v - 298.15)/10}}{f_H(T_v) f_L(T_v)} \right] \\
f_H\,(T_v) &= 1 + \exp\left[s_1\,(T_v - s_2) \right] \\
f_L\,(T_v) &= 1 + \exp\left[s_3\,(s_4 - T_v) \right]
\end{aligned}
\tag{9.12}
$$

with $Q_{10} = 2$, $s_1 = 0.3 \text{K}^{-1}$ $s_2 = 313.15$ K, $s_3 = 0.2 \text{K}^{-1}$, and $s_4 = 288.15$ K. Additionally,

$$
R_d = R_{d25} \left\{ \frac{Q_{10}^{(T_v - 298.15)/10}}{1 + \exp\left[s_5\,(T_v - s_6) \right]} \right\}
\tag{9.13}
$$

with $Q_{10} = 2$, $s_5 = 1.3$ K^{-1} and $s_6 = 328.15$K, and

$$
k_p = k_{p25}\, Q_{10}^{(T_v - 298.15)/10}
\tag{9.14}
$$

with $Q_{10} = 2$.

Table 9.2: Temperature dependence parameters for C3 photosynthesis.

Parameter	ΔH_a (J mol^{-1})	ΔH_d (J mol^{-1})
$V_{c\,\max}$	72000	200000
$J_{\max}$	50000	200000
T_p	72000	200000
R_d	46390	150650
K_c	79430	–
K_o	36380	–
Γ	37830	–

In the model, acclimation is implemented as in *Kattge and Knorr (2007)*. In this parameterization, $V_{c\,max}$ and J_{max} vary with the plant growth temperature. This is achieved by allowing ΔS to vary with growth temperature according to

$$
\begin{aligned}
\Delta S &= 668.39 - 1.07(T_{10} - T_f) & \text{for } V_{c\,max} \\
\Delta S &= 659.70 - 0.75(T_{10} - T_f) & \text{for } J_{max}
\end{aligned}
\tag{9.15}
$$

The effect is to cause the temperature optimum of $V_{c\,max}$ and J_{max} to increase with warmer temperatures. Additionally, the ratio $J_{max\,25}/V_{c\,max\,25}$ at 25 ºC decreases with growth temperature as

$$
J_{max\,25}/V_{c\,max\,25} = 2.59 - 0.035(T_{10} - T_f).
\tag{9.16}
$$

In these acclimation functions, T_{10} is the 10-day mean air temperature (K) and T_f is the freezing point of water (K). For lack of data, T_p acclimates similar to $V_{c\,max}$. Acclimation is restricted over the temperature range $T_{10} - T_f \geq 11$ºC and $T_{10} - T_f \leq 35$ºC.

9.5 Canopy scaling

When LUNA is on, the $V_{c\,max\,25}$ for sun leaves is scaled to the shaded leaves $J_{max\,25}$, T_{p25}, k_{p25}, and R_{d25} scale similarly.

$$
\begin{aligned}
V_{c\,max\,25sha} &= V_{c\,max\,25sha}\frac{i_{v,sha}}{i_{v,sun}} \\
J_{max\,25sha} &= J_{max\,25sun}\frac{i_{v,sha}}{i_{v,sun}} \\
T_{psha} &= T_{psun}\frac{i_{v,sha}}{i_{v,sun}}
\end{aligned}
\tag{9.17}
$$

Where $i_{v,sun}$ and $i_{v,sha}$ are the leaf-to-canopy scaling coefficients of the twostream radiation model, calculated as

$$
\begin{aligned}
i_{v,sun} &= \frac{(1 - e^{-(k_{n,ext}+k_{b,ext})*lai_e})/(k_{n,ext} + k_{b,ext})}{f_{sun} * lai_e} \\
i_{v,sha} &= \frac{(1 - e^{-(k_{n,ext}+k_{b,ext})*lai_e})/(k_{n,ext} + k_{b,ext})}{(1 - f_{sun}) * lai_e}
\end{aligned}
\tag{9.18}
$$

k_{n,ext} is the extinction coefficient for N through the canopy (0.3). k_{b,ext} is the direct beam extinction coefficient calculated in the surface albedo routine, and f_{sun} is the fraction of sunlit leaves, both derived from Chapter 3.

When LUNA is off, scaling defaults to the mechanism used in CLM4.5.

9.6 Numerical implementation

The CO_2 partial pressure at the leaf surface, c_s (Pa), and the vapor pressure at the leaf surface, e_s (Pa), needed for the stomatal resistance model in equation (9.1), and the internal leaf CO_2 partial pressure c_i (Pa), needed for the photosynthesis model in equations (9.2)-(9.4), are calculated assuming there is negligible capacity to store CO_2 and water vapor at the leaf surface so that

$$
A_n = \frac{c_a - c_i}{(1.4r_b + 1.6r_s)\,P_{atm}} = \frac{c_a - c_s}{1.4r_b P_{atm}} = \frac{c_s - c_i}{1.6r_s P_{atm}}
\tag{9.19}
$$

and the transpiration fluxes are related as

$$
\frac{e_a - e_i}{r_b + r_s} = \frac{e_a - e_s}{r_b} = \frac{e_s - e_i}{r_s}
\tag{9.20}
$$

where r_b is leaf boundary layer resistance (s m^2 μ mol^{-1}) (section 5.3), the terms 1.4 and 1.6 are the ratios of diffusivity of CO_2 to H_2O for the leaf boundary layer resistance and stomatal resistance, $c_a = CO_2 \left(\text{mol mol}^{-1}\right)$, P_{atm} is the atmospheric CO_2 partial pressure (Pa) calculated from CO_2 concentration (ppmv), e_i is the saturation vapor pressure (Pa) evaluated at the leaf temperature T_v , and e_a is the vapor pressure of air (Pa). The vapor pressure of air in the plant canopy e_a (Pa) is determined from

$$e_a = \frac{P_{atm}q_s}{0.622} \tag{9.21}$$

where q_s is the specific humidity of canopy air (kg kg^{-1}, section 5.3). Equations and are solved for c_s and e_s

$$c_s = c_a - 1.4 r_b P_{atm} A_n \tag{9.22}$$

$$e_s = \frac{e_a r_s + e_i r_b}{r_b + r_s} \tag{9.23}$$

Substitution of equation (9.23) into equation (9.1) gives an expression for stomatal resistance (r_s) as a function of photosynthesis (A_n), given here in terms of conductance with $g_s = 1/r_s$ and $g_b = 1/r_b$

$$g_s^2 + bg_s + c = 0 \tag{9.24}$$

where

$$b = 2(g_o * 10^{-6} + d) + \frac{(g_1 d)^2}{g_b * 10^{-6} D}$$
$$c = (g_o * 10^{-6})^2 + [2g_o * 10^{-6} + d\frac{1 - g_1^2}{D}]d \tag{9.25}$$

and

$$d = \frac{1.6 A_n}{c_s / P_{atm} * 10^6}$$
$$D = \frac{e_i - e_a}{1000} \tag{9.26}$$

Stomatal conductance, as solved by equation (9.24) (mol m $^{-2}$ s $^{-1}$), is the larger of the two roots that satisfy the quadratic equation. Values for c_i are given by

$$c_i = c_a - (1.4 r_b + 1.6 r_s) P_{atm} A_n \tag{9.27}$$

The equations for c_i , c_s , r_s , and A_n are solved iteratively until c_i converges. *Sun et al. (2012)* pointed out that the CLM4 numerical approach does not always converge. Therefore, the model uses a hybrid algorithm that combines the secant method and Brent's method to solve for c_i . The equation set is solved separately for sunlit (A_n^{sun} , r_s^{sun}) and shaded (A_n^{sha} , r_s^{sha}) leaves.

CHAPTER 10

PHOTOSYNTHETIC CAPACITY

The photosynthetic capacity is represented by two key parameters: 1) the maximum rate of carboxylation at 25 °C, $V_{c,max25}$; and 2) the maximum rate of electron transport at 25 °C, J_{max25} . They are predicted by a mechanistic model of leaf utilization of nitrogen for assimilation (LUNA V1.0) (*Ali et al. 2016*) based on an optimality hypothesis to nitrogen allocation among light capture, electron transport, carboxylation, respiration and storage. Specifically, the model allocates the nitrogen by maximizing the daily net photosynthetic carbon gain under following two key assumptions:

- nitrogen allocated for light capture, electron transport and carboxylation are co-limiting;

- respiratory nitrogen is allocated to maintain dark respiration determined by $V_{c,max}$.

Compared to traditional photosynthetic capacity models, a key advantage of LUNA is that the model is able to predict the potential acclimation of photosynthetic capacities at different environmental conditions as determined by temperature, radiation, CO_2 concentrations, day length, and humidity.

10.1 Model inputs and parameter estimations

The LUNA model includes the following four unitless parameters:

- J_{maxb0} , which specifies the baseline proportion of nitrogen allocated for electron transport;

- J_{maxb1} , which determines response of electron transport rate to light availability;

- $t_{c,j0}$, which defines the baseline ratio of Rubisco-limited rate to light-limited rate;

- H , which determines the response of electron transport rate to relative humidity.

The above four parameters are estimated by fitting the LUNA model to a global compilation of >800 obervations located at different biomes, canopy locations, and time of the year from 1993-2013 (Ali et al. 2015). The model inputs are area-based leaf nitrogen content, leaf mass per unit leaf area and the driving environmental conditions (average of past 10 days) including temperature, CO_2 concentrations, daily mean and maximum radiation, relative humidity and day length. The estimated values in CLM5 for the listed parameters are 0.0311, 0.1745, 0.8054, and 6.0999, repectively. In LUNA V1.0, the estimated parameter values are for C3 natural vegetations. In view that potentially large differences in photosythetic capacity could exist between crops and natural vegetations due to human selection and genetic modifications, in CLM5, the LUNA model are used only for C3 natural vegetations. The photosynthetic

capacity for crops and C4 plants are thus still kept the same as CLM4.5. Namely, it is estimated based on the leaf nitrogen content, fixed RUBISCO allocations for $V_{c\,\mathrm{max}\,25}$ and an adjusting factor to account for the impact of day length. In CLM5, the model simulates both sun-lit and shaded leaves; however, because the sun-lit and shaded leaves can changes through the day based on the sun angles, we do not differentiate the photosynthetic capacity difference for sun-lit or shaded leaves.

10.2 Model structure

10.2.1 Plant Nitrogen

The structure of the LUNA model is adapted from *Xu et al. (2012)*, where the plant nitrogen at the leaf level (LNC_a; gN/ m ^{2} leaf) is divided into four pools: structural nitrogen(N_{str}; gN/m ^{2} leaf), photosynthetic nitrogen (N_{psn}; gN/m ^{2} leaf), storage nitrogen(N_{store}; gN/m ^{2} leaf), and respiratory nitrogen (N_{resp}; gN/m ^{2} leaf). Namely,

$$\mathrm{LNC}_a = N_{\mathrm{psn}} + N_{\mathrm{str}} + N_{\mathrm{store}} + N_{\mathrm{resp}}. \qquad (10.1)$$

The photosynthetic nitrogen, N_{psn}, is further divided into nitrogen for light capture (N_{lc}; gN/m ^{2} leaf), nitrogen for electron transport (N_{et}; gN/m ^{2} leaf), and nitrogen for carboxylation (N_{cb}; gN/m ^{2} leaf). Namely,

$$N_{\mathrm{psn}} = N_{\mathrm{et}} + N_{\mathrm{cb}} + N_{\mathrm{lc}}. \qquad (10.2)$$

The structural nitrogen, N_{str}, is calculated as the multiplication of leaf mass per unit area (LMA; g biomass/m ^{2} leaf), and the structural nitrogen content (SNC; gN/g biomass). Namely,

$$N_{\mathrm{str}} = \mathrm{SNC} \cdot \mathrm{LMA} \qquad (10.3)$$

where SNC is set to be fixed at 0.002 (gN/g biomass), based on data on C:N ratio from dead wood (White etal.,2000), and LMA is the inverse of specific leaf area at the canopy top (SLA_0), a PFT-level parameter (Table 10.1).

Table 10.1: Plant functional type (PFT) leaf N parameters.

PFT	SLA_0	N_{cb}
NET Temperate	0.0100	0.0509
NET Boreal	0.0100	0.0466
NDT Boreal	0.0202	0.0546
BET Tropical	0.0190	0.0461
BET temperate	0.0190	0.0515
BDT tropical	0.0308	0.0716
BDT temperate	0.0308	0.1007
BDT boreal	0.0308	0.1007
BES temperate	0.0180	0.0517
BDS temperate	0.0307	0.0943
BDS boreal	0.0307	0.0943
C_3 arctic grass	0.0402	0.1365
C_3 grass	0.0402	0.1365
C_4 grass	0.0385	0.0900
Temperate Corn	0.0500	0.2930
Spring Wheat	0.0350	0.4102
Temperate Soybean	0.0350	0.4102
Cotton	0.0350	0.4102
Rice	0.0350	0.4102
Sugarcane	0.0500	0.2930
Tropical Corn	0.0500	0.2930
Tropical Soybean	0.0350	0.4102

Notes: SLA_0 is the specific leaf area at the canopy top (m ^{2} leaf/g biomass), and N_{cb} is the fraction of leaf nitrogen in Rubisco (g N in Rubisco g $^{-1}$ N)

We assume that plants optimize their nitrogen allocations (i.e., N_{store}, N_{resp}, N_{lc}, N_{et}, N_{cb}) to maximize the photosynthetic carbon gain, defined as the gross photosynthesis (A) minus the maintenance respiration for photosynthetic enzymes (R_{psn}), under specific environmental conditions and given plant's strategy of leaf nitrogen use. Namely, the solutions of nitrogen allocations { N_{store}, N_{resp}, N_{lc}, N_{et}, N_{cb} } can be estimated as follows,

$$\left\{ \hat{N}_{store}, \hat{N}_{resp}, \hat{N}_{lc}, \hat{N}_{et}, \hat{N}_{cb} \right\} = \underset{N_{store} + N_{resp} + N_{lc} + N_{et} + N_{cb} < FNC_a}{argmax} (A - R_{psn}), \tag{10.4}$$

where FNC_a is the functional nitrogen content defined as the total leaf nitrogen content (LNC_a) minus the structural nitrogen content (N_{str}).

The gross photosynthesis, A, was calculated with a coupled leaf gas exchange model based on the *Farquhar et al. (1980)* model of photosynthesis and Ball–Berry-type stomatal conductance model (Ball et al. 1987). The maintenance respiration for photosynthetic enzymes, R_{psn}, is calculated by the multiplication of total photosynthetic nitrogen (N_{psn}) and the maintenance respiration cost for photosynthetic enzymes.

10.2.2 Maximum electron transport rate

In the LUNA model, the maximum electron transport rate (J_{max}; μmol electron / m ^{2}/s) is simulated to have a baseline allocation of nitrogen and additional nitrogen allocation to change depending on the average daytime photosynthetic active radiation (PAR; μmol electron / m ^{2}/s), day length (hours) and air humidity. Specifically, the LUNA model has

$$J_{max} = J_{max0} + J_{maxb1} f \, (\text{day length}) \, f \, (\text{humidity}) \, \alpha PAR \tag{10.5}$$

The baseline electron transport rate, J_{max0}, is calculated as follows,

$$J_{max0} = J_{maxb0} FNC_a NUE_{J_{max}} \tag{10.6}$$

where J_{maxb0} (unitless) is the baseline proportion of nitrogen allocated for electron transport rate. $NUE_{J_{max}}$ (μmol electron /s/g N) is the nitrogen use efficiency of J_{max}. J_{maxb1} (unitless) is a coefficient determining the response of the electron transport rate to amount of absorbed light (i.e., αPAR). $f \, (\text{day length})$ is a function specifies the impact of day length (hours) on J_{max} in view that longer day length has been demonstrated by previous studies to alter V_{cmax25} and J_{max25} (Bauerle et al. 2012; Comstock and Ehleringer 1986) through photoperiod sensing and regulation (e.g., Song et al. 2013). Following Bauerle et al. (2012), $f \, (\text{day length})$ is simulated as follows,

$$f \, (\text{day length}) = \left(\frac{\text{day length}}{12} \right)^2 . \tag{10.7}$$

$f \, (\text{humidity})$ represents the impact of air humidity on J_{max}. We assume that higher humidity leads to higher J_{max} with less water limiation on stomta opening and that low relative humidity has a stronger impact on nitrogen allocation due to greater water limitation. When relative humidity (RH; unitless) is too low, we assume that plants are physiologically unable to reallocate nitrogen. We therefore assume that there exists a critical value of relative humidity ($RH_0 = 0.25$; unitless), below which there is no optimal nitrogen allocation. Based on the above assumptions, we have

$$f \, (\text{humidity}) = \left(1 - e^{\left(-H \frac{\max(RH - RH_0, 0)}{1 - RH_0} \right)} \right), \tag{10.8}$$

where H (unitless) specifies the impact of relative humidity on electron transport rate.

The efficiency of light energy absorption (unitless), α, is calculated depending on the amount of nitrogen allocated for light capture, N_{lc}. Following Niinemets and Tenhunen (1997), the LUNA model has,

$$\alpha = \frac{0.292}{1 + \frac{0.076}{N_{lc}C_b}} \tag{10.9}$$

where 0.292 is the conversion factor from photon to electron. C_b is the conversion factor (1.78) from nitrogen to chlorophyll. After we estimate $J_{\max}$, the actual electron transport rate with the daily maximum radiation (J_x) can be calculated using the empirical expression of leaf (1937),

$$J_x = \frac{\alpha \text{PAR}_{\max}}{\left(1 + \frac{\alpha^2 \text{PAR}_{\max}^2}{J_{\max}^2}\right)^{0.5}} \tag{10.10}$$

where $\text{PAR}_{\max}$ (μmol/m ^{2}/s) is the maximum photosynthetically active radiation during the day.

10.2.3 Maximum rate of carboxylation

The maximum rate of carboxylation at 25°C varies with foliage nitrogen concentration and specific leaf area and is calculated as in *Thornton and Zimmermann (2007)*. At 25°C,

$$V_{c\max 25} = N_{cb} NUE_{V_{c\max 25}} \tag{10.11}$$

where N_{cb} is nitrogen for carboxylation (g N m^{-2} leaf, Table 10.1), and $NUE_{V_{c\max 25}}$ = 47.3 x 6.25 and is the nitrogen use efficiency for $V_{c\max 25}$. The constant 47.3 is the specific Rubisco activity (μ mol CO$_2$ g^{-1} Rubisco s^{-1}) measured at 25°C, and the constant 6.25 is the nitrogen binding factor for Rubisco (g Rubisco g^{-1} N; *Rogers 2014*).

$V_{c\max 25}$ additionally varies with daylength (DYL) using the function $f(DYL)$, which introduces seasonal variation to $V_{c\max}$

$$f(DYL) = \frac{(DYL)^2}{(DYL_{\max})^2} \tag{10.12}$$

with $0.01 \leq f(DYL) \leq 1$. Daylength (seconds) is given by

$$DYL = 2 \times 13750.9871 \cos^{-1}\left[\frac{-\sin(lat)\sin(decl)}{\cos(lat)\cos(decl)}\right] \tag{10.13}$$

where lat (latitude) and $decl$ (declination angle) are from section 3.3. Maximum daylength ($DYL_{\max}$) is calculated similarly but using the maximum declination angle for present-day orbital geometry ($\pm$23.4667° [$\pm$0.409571 radians], positive for Northern Hemisphere latitudes and negative for Southern Hemisphere).

10.2.4 Implementation of Photosynthetic Capacity

Based on *Farquhar et al. (1980)* and Wullschleger (1993), we can calculate the electron-limited photosynthetic rate under daily maximum radiation (W_{jx}) and the Rubisco-limited photosynthetic rate (W_c) as follows,

$$W_{J_x} = K_j J_x, \tag{10.14}$$

$$W_c = K_c V_{c,\max}, \tag{10.15}$$

where K_j and K_c as the conversion factors for J_x and $V_{c,\max}$ ($V_{c,\max}$ to W_c and J_x to W_{J_x}), respectively. Based on *Xu et al. (2012)*, Maire et al. (2012) and Walker et al. (2014), we assume that W_c is proportional to W_{J_x}. Specifically, we have

$$W_c = t_\alpha t_{c,j0} W_{J_x} \tag{10.16}$$

where $t_{c,j0}$ is the baseline ratio of W_c to W_{J_x}. We recognize that this ratio may change depending on the nitrogen use efficiency of carboxylation and electron transport (Ainsworth and Rogers 2007), therefore the LUNA model has the modification factor, t_α, to adjust baseline the ratio depending on the nitrogen use efficiency for electron vs carboxylation (*Ali et al. 2016*).

10.2.5 Total Respiration

Following *Collatz et al. (1991)*, the total respiration (R_t) is calculated in proportion to $V_{c,max}$,

$$R_t = 0.015 V_{c,max}. \tag{10.17}$$

Accounting for the daytime and nighttime temperature, the daily respirations is calculated as follows,

$$R_{td} = R_t [D_{day} + D_{night} f_r(T_{night})/f_r(T_{day})], \tag{10.18}$$

where D_{day} and D_{night} are daytime and nighttime durations in seconds. $f_r(T_{night})$ and $f_r(T_{day})$ are the temperature response functions for respiration (see Appendix B in *Ali et al. (2016)* for details).

10.3 Numerical scheme

The LUNA model searches for the "optimal" nitrogen allocations for maximum net photosynthetic carbon gain by incrementally increase the nitrogen allocated for light capture (i.e., N_{lc}) (see *Ali et al. (2016)* for details). We assume that plants only optimize the nitrogen allocation when they can grow (i.e., GPP>0.0). If GPP become zero under stress, then the LUNA model assume a certain amount of enzyme will decay at daily rates of 0.1, in view that the half-life time for photosynthetic enzymes are short (~7 days) (Suzuki et al. 2001). To avoid unrealistic low values of photosynthetic capacity, the decay is only limited to 50 percent of the original enzyme levels.

CHAPTER 11

PLANT HYDRAULICS

11.1 Roots

11.1.1 Vertical Root Distribution

The root fraction r_i in each soil layer depends on the plant functional type

$$r_i = \left(\beta^{z_{h,\,i-1} \cdot 100} - \beta^{z_{h,\,i} \cdot 100} \right) \qquad \text{for } 1 \leq i \leq N_{levsoi} \tag{11.1}$$

where $z_{h,\,i}$ (m) is the depth from the soil surface to the interface between layers i and $i+1$ ($z_{h,\,0}$, the soil surface) (section 2.2), the factor of 100 converts from m to cm, and β is a plant-dependent root distribution parameter adopted from *Jackson et al. (1996)* (Table 11.1).

Table 11.1: Plant functional type root distribution parameters

Plant Functional Type	β
NET Temperate	0.976
NET Boreal	0.943
NDT Boreal	0.943
BET Tropical	0.993
BET temperate	0.966
BDT tropical	0.993
BDT temperate	0.966
BDT boreal	0.943
BES temperate	0.964
BDS temperate	0.964
BDS boreal	0.914
C_3 grass arctic	0.914
C_3 grass	0.943
C_4 grass	0.943
Crop R	0.943
Crop I	0.943
Corn R	0.943
Corn I	0.943
Temp Cereal R	0.943
Temp Cereal I	0.943
Winter Cereal R	0.943
Winter Cereal I	0.943
Soybean R	0.943
Soybean I	0.943

11.1.2 Root Spacing

To determine the conductance along the soil to root pathway (section 11.2.1) an estimate of the spacing between the roots within a soil layer is required. The distance between roots $dx_{root,i}$ (m) is calculated by assuming that roots are distributed uniformly throughout the soil (*Gardner 1960*)

$$dx_{root,i} = (\pi \cdot L_i)^{-\frac{1}{2}} \tag{11.2}$$

where L_i is the root length density (m m $^{-3}$)

$$L_i = \frac{B_{root,i}}{\rho_{root} C A_{root}}, \tag{11.3}$$

$B_{root,i}$ is the root biomass density (kg m $^{-3}$)

$$B_{root,i} = \frac{c\_to\_b \cdot C_{fineroot} \cdot r_i}{dz_i} \tag{11.4}$$

where $c\_to\_b = 2$ (kg biomass kg carbon $^{-1}$) and $C_{fineroot}$ is the amount of fine root carbon (kg m $^{-2}$).

ρ_{root} is the root density (kg m $^{-3}$), and CA_{root} is the fine root cross sectional area (m ^{2})

$$CA_{root} = \pi r_{root}^2 \tag{11.5}$$

where r_{root} is the root radius (m).

11.2 Plant Hydraulic Stress

The Plant Hydraulic Stress (PHS) routine explicitly models water transport through the vegetation according to a simple hydraulic framework following Darcy's Law for porous media flow equations influenced by *Bonan et al. (2014)*, *Chuang et al. (2006)*, *Sperry et al. (1998)*, *Sperry and Love (2015)*, *Williams et al (1996)*.

PHS solves for the vegetation water potential that matches water supply with transpiration demand. Water supply is modeled according to the circuit analog in Figure 11.1. Transpiration demand is modeled relative to maximum transpiration by a transpiration loss function dependent on leaf water potential.
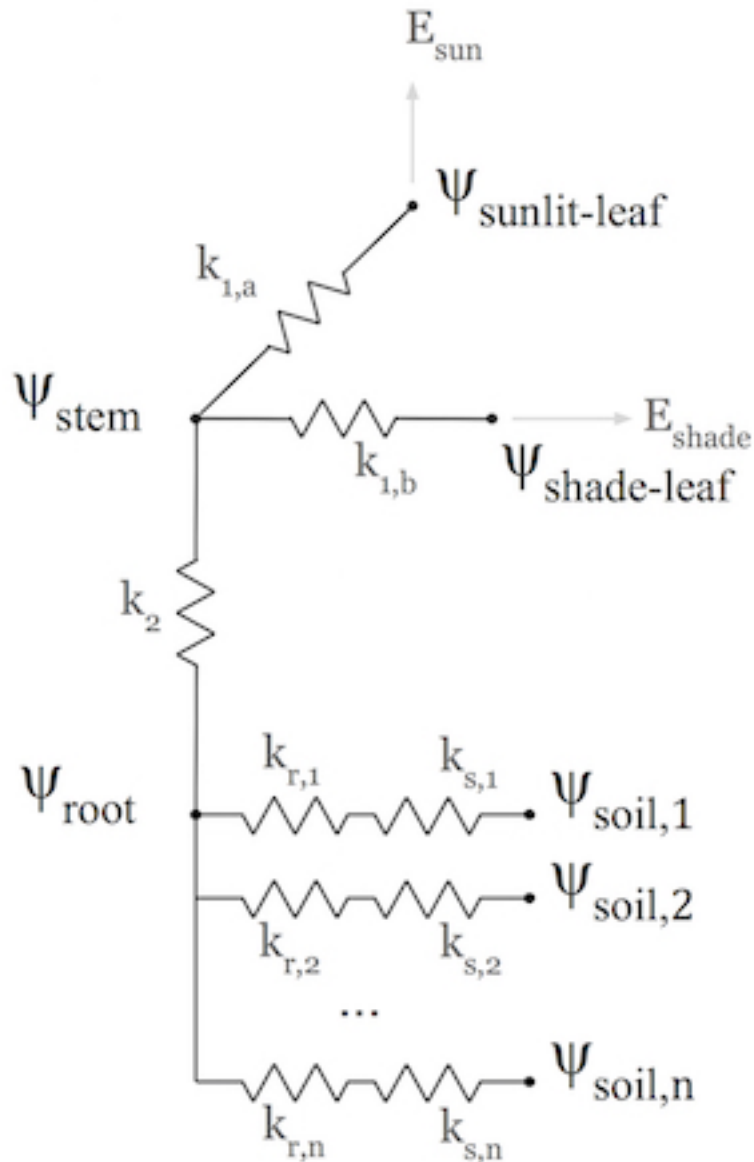
Figure 11.1: Circuit diagram of plant hydraulics scheme

11.2.1 Plant Water Supply

The supply equations are used to solve for vegetation water potential forced by transpiration demand and the set of layer-by-layer soil water potentials. The water supply is discretized into segments: soil-to-root, root-to-stem, and stem-to-leaf. There are typically several (1-49) soil-to-root flows operating in parallel, one per soil layer. There are two stem-to-leaf flows operating in parallel, corresponding to the sunlit and shaded "leaves".

In general the water fluxes (e.g. soil-to-root, root-to-stem, etc.) are modeled according to Darcy's Law for porous media flow as:

$$q = kA\left(\psi_1 - \psi_2\right) \tag{11.6}$$

q is the flux of water (mmH$_2$O/s) spanning the segment between ψ_1 and ψ_2

k is the hydraulic conductance (s^{-1})

A is the area basis (m^2/m^2) relating the conducting area basis to ground area

$\psi_1 - \psi_2$ is the gradient in water potential (mmH$_2$O) across the segment

The segments in Figure 11.1 have variable resistance, as the water potentials become lower, hydraulic conductance decreases. This is captured by multiplying the maximum segment conductance by a sigmoidal function capturing the percent loss of conductivity. The function uses two parameters to fit experimental vulnerability curves: the water potential at 50% loss of conductivity ($p50$) and a shape fitting parameter (c_k).

$$k = k_{max} \cdot 2^{-\left(\frac{\psi_1}{p50}\right)^{c_k}} \tag{11.7}$$

k_{max} is the maximum segment conductance (s^{-1})

$p50$ is the water potential at 50% loss of conductivity (mmH$_2$O)

ψ_1 is the water potential of the lower segment terminus (mmH$_2$O)

Stem-to-leaf

The area basis and conductance parameterization varies by segment. There are two stem-to-leaf fluxes in parallel, from stem to sunlit leaf and from stem to shaded leaf (q_{1a} and q_{1a}). The water flux from stem-to-leaf is the product of the segment conductance, the conducting area basis, and the water potential gradient from stem to leaf. Stem-to-leaf conductance is defined as the maximum conductance multiplied by the percent of maximum conductance, as calculated by the sigmoidal vulnerability curve. The maximum conductance is a PFT parameter representing the maximum conductance of water from stem to leaf per unit leaf area. This parameter can be defined separately for sunlit and shaded segments and should already include the appropriate length scaling (in other words this is a conductance, not conductivity). The water potential gradient is the difference between leaf water potential and stem water potential. There is no gravity term, assuming a negligible difference in height across the segment. The area basis is the leaf area index (either sunlit or shaded).

$$q_{1a} = k_{1a} \cdot \text{LAI}_{sun} \cdot \left(\psi_{stem} - \psi_{sunleaf}\right) \tag{11.8}$$

$$q_{1b} = k_{1b} \cdot \text{LAI}_{shade} \cdot \left(\psi_{stem} - \psi_{shadeleaf}\right) \tag{11.9}$$

$$k_{1a} = k_{1a,max} \cdot 2^{-\left(\frac{\psi_{stem}}{p50_1}\right)^{c_k}} \tag{11.10}$$

$$k_{1b} = k_{1b,max} \cdot 2^{-\left(\frac{\psi_{stem}}{p50_1}\right)^{c_k}} \tag{11.11}$$

Variables:

q_{1a} = flux of water (mmH$_2$O/s) from stem to sunlit leaf

q_{1b} = flux of water (mmH$_2$O/s) from stem to shaded leaf

LAI_{sun} = sunlit leaf area index (m2/m2)

LAI_{shade} = shaded leaf area index (m2/m2)

ψ_{stem} = stem water potential (mmH$_2$O)

$\psi_{sunleaf}$ = sunlit leaf water potential (mmH$_2$O)

$\psi_{shadeleaf}$ = shaded leaf water potential (mmH$_2$O)

Parameters:

$k_{1a,max}$ = maximum leaf conductance (s^{-1})

$k_{1b,max}$ = maximum leaf conductance (s^{-1})

$p50_1$ = water potential at 50% loss of conductance (mmH$_2$O)

c_k = vulnerability curve shape-fitting parameter (-)

Root-to-stem

There is one root-to-stem flux. This represents a flux from the root collar to the upper branch reaches. The water flux from root-to-stem is the product of the segment conductance, the conducting area basis, and the water potential gradient from root to stem. Root-to-stem conductance is defined as the maximum conductance multiplied by the percent of maximum conductance, as calculated by the sigmoidal vulnerability curve (two parameters). The maximum conductance is defined as the maximum root-to-stem conductivity per unit stem area (PFT parameter) divided by the length of the conducting path, which is taken to be the vegetation height. The area basis is the stem area index. The gradient in water potential is the difference between the root water potential and the stem water potential less the difference in gravitational potential.

$$q_2 = k_2 \cdot SAI \cdot (\psi_{root} - \psi_{stem} - \Delta\psi_z) \tag{11.12}$$

$$k_2 = \frac{k_{2,max}}{z_2} \cdot 2^{-\left(\frac{\psi_{root}}{p50_2}\right)^{c_k}} \tag{11.13}$$

Variables:

q_2 = flux of water (mmH$_2$O/s) from root to stem

SAI = stem area index (m2/m2)

$\Delta\psi_z$ = gravitational potential (mmH$_2$O)

ψ_{root} = root water potential (mmH$_2$O)

ψ_{stem} = stem water potential (mmH$_2$O)

Parameters:

$k_{2,max}$ = maximum stem conductivity (m/s)

$p50_2$ = water potential at 50% loss of conductivity (mmH$_2$O)

z_2 = vegetation height (m)

Soil-to-root

There are several soil-to-root fluxes operating in parallel (one for each root-containing soil layer). Each represents a flux from the given soil layer to the root collar. The water flux from soil-to-root is the product of the segment conductance, the conducting area basis, and the water potential gradient from soil to root. The area basis is a proxy for root area index, defined as the summed leaf and stem area index multiplied by the root-to-shoot ratio (PFT parameter) multiplied by the layer root fraction. The root fraction comes from an empirical root profile (section 11.1.1).

The gradient in water potential is the difference between the soil water potential and the root water potential less the difference in gravitational potential. There is only one root water potential to which all soil layers are connected in parallel. A soil-to-root flux can be either positive (vegetation water uptake) or negative (water deposition), depending on the relative values of the root and soil water potentials. This allows for the occurrence of hydraulic redistribution where water moves through vegetation tissue from one soil layer to another.

Soil-to-root conductance is the result of two resistances in series, first across the soil-root interface and then through the root tissue. The root tissue conductance is defined as the maximum conductance multiplied by the percent of maximum conductance, as calculated by the sigmoidal vulnerability curve. The maximum conductance is defined as the maximum root-tissue conductivity (PFT parameter) divided by the length of the conducting path, which is taken to be the soil layer depth plus lateral root length.

The soil-root interface conductance is defined as the soil conductivity divided by the conducting length from soil to root. The soil conductivity varies by soil layer and is calculated based on soil potential and soil properties, via the Brooks-Corey theory. The conducting length is determined from the characteristic root spacing (section 11.1.2).

$$q_{3,i} = k_{3,i} \cdot RAI \cdot (\psi_{soil,i} - \psi_{root} + \Delta\psi_{z,i}) \tag{11.14}$$

$$RAI = (LAI + SAI) \cdot r_i \cdot f_{root-leaf} \tag{11.15}$$

$$k_{3,i} = \frac{k_{r,i} \cdot k_{s,i}}{k_{r,i} + k_{s,i}} \tag{11.16}$$

$$k_{r,i} = \frac{k_{3,max}}{z_{3,i}} \cdot 2^{-\left(\frac{\psi_{soil,i}}{p50_3}\right)^{c_k}} \tag{11.17}$$

$$k_{s,i} = \frac{k_{soil,i}}{dx_{root,i}} \tag{11.18}$$

Variables:

$q_{3,i}$ = flux of water (mmH$_2$O/s) from soil layer i to root

$\Delta\psi_{z,i}$ = change in gravitational potential from soil layer i to surface (mmH$_2$O)

LAI = total leaf area index (m2/m2)

SAI = stem area index (m2/m2)

$\psi_{soil,i}$ = water potential in soil layer i (mmH$_2$O)

ψ_{root} = root water potential (mmH$_2$O)

$z_{3,i}$ = length of root tissue conducting path = soil layer depth + root lateral length (m)

r_i = root fraction in soil layer i (-)

$k_{soil,i}$ = Brooks-Corey soil conductivity in soil layer i (m/s)

Parameters:

$f_{root-leaf}$ = root-to-shoot ratio (-)

$p50_3$ = water potential at 50% loss of root tissue conductance (mmH$_2$O)

ck = shape-fitting parameter for vulnerability curve (-)

11.2.2 Plant Water Demand

Plant water demand depends on stomatal conductance, which is described in section 9.3. Here we describe the influence of PHS and the coupling of vegetation water demand and supply. PHS models vegetation water demand as transpiration attenuated by a transpiration loss function based on leaf water potential. Sunlit leaf transpiration is modeled as the maximum sunlit leaf transpiration multiplied by the percent of maximum transpiration as modeled by the sigmoidal loss function. The same follows for shaded leaf transpiration. Maximum stomatal conductance is calculated from the Medlyn model *(Medlyn et al. 2011)* absent water stress and used to calculate the maximum transpiration (see section 5.3). Water stress is calculated as the ratio of attenuated stomatal conductance to maximum stomatal conductance. Water stress is calculated with distinct values for sunlit and shaded leaves. Vegetation water stress is calculated based on leaf water potential and is used to attenuate photosynthesis (see section 9.4)

$$E_{sun} = E_{sun,max} \cdot 2^{-\left(\frac{\psi_{sunleaf}}{p50_e}\right)^{c_k}} \tag{11.19}$$

$$E_{shade} = E_{shade,max} \cdot 2^{-\left(\frac{\psi_{shadeleaf}}{p50_e}\right)^{c_k}} \tag{11.20}$$

$$\beta_{t,sun} = \frac{g_{s,sun}}{g_{s,sun,\beta_t=1}} \tag{11.21}$$

$$\beta_{t,shade} = \frac{g_{s,shade}}{g_{s,shade,\beta_t=1}} \tag{11.22}$$

E_{sun} = sunlit leaf transpiration (mm/s)

E_{shade} = shaded leaf transpiration (mm/s)

$E_{sun,max}$ = sunlit leaf transpiration absent water stress (mm/s)

$E_{shade,max}$ = shaded leaf transpiration absent water stress (mm/s)

$\psi_{sunleaf}$ = sunlit leaf water potential (mmH$_2$O)

$\psi_{shadeleaf}$ = shaded leaf water potential (mmH$_2$O)

$\beta_{t,sun}$ = sunlit transpiration water stress (-)

$\beta_{t,shade}$ = shaded transpiration water stress (-)

$g_{s,sun}$ = stomatal conductance of water corresponding to E_{sun}

$g_{s,shade}$ = stomatal conductance of water corresponding to E_{shade}

$g_{s,sun,max}$ = stomatal conductance of water corresponding to $E_{sun,max}$

$g_{s,shade,max}$ = stomatal conductance of water corresponding to $E_{shade,max}$

11.2.3 Vegetation Water Potential

Both plant water supply and demand are functions of vegetation water potential. PHS explicitly models root, stem, shaded leaf, and sunlit leaf water potential at each timestep. PHS iterates to find the vegetation water potential ψ (vector) that satisfies continuity between the non-linear vegetation water supply and demand (equations (11.8), (11.9), (11.12), (11.14), (11.19), (11.20)).

$$\psi = [\psi_{sunleaf}, \psi_{shadeleaf}, \psi_{stem}, \psi_{root}] \tag{11.23}$$

$$E_{sun} = q_{1a}$$
$$E_{shade} = q_{1b}$$
$$E_{sun} + E_{shade} = q_{1a} + q_{1b}$$
$$= q_2$$
$$= \sum_{i=1}^{nlevsoi} q_{3,i}$$

(11.24)

PHS finds the water potentials that match supply and demand. In the plant water transport equations (11.24), the demand terms (left-hand side) are decreasing functions of absolute leaf water potential. As absolute leaf water potential becomes larger, water stress increases, causing a decrease in transpiration demand. The supply terms (right-hand side) are increasing functions of absolute leaf water potential. As absolute leaf water potential becomes larger, the gradients in water potential increase, causing an increase in vegetation water supply. PHS takes a Newton's method approach to iteratively solve for the vegetation water potentials that satisfy continuity (11.24).

11.2.4 Numerical Implementation

The four plant water potential nodes are ($\psi_{root}, \psi_{xylem}, \psi_{shadeleaf}, \psi_{sunleaf}$). The fluxes between each pair of nodes are labeled in Figure 1. E_{sun} and E_{sha} are the transpiration from sunlit and shaded leaves, respectively. We use the circuit-analog model to calculate the vegetation water potential (ψ) for the four plant nodes, forced by soil matric potential and unstressed transpiration. The unstressed transpiration is acquired by running the photosynthesis model with $\beta_t = 1$. The unstressed transpiration flux is attenuated based on the leaf-level vegetation water potential. Using the attenuated transpiration, we solve for $g_{s,stressed}$ and output $\beta_t = \dfrac{g_{s,stressed}}{g_{s,unstressed}}$.

The continuity of water flow through the system yields four equations

$$E_{sun} = q_{1a}$$
$$E_{shade} = q_{1b}$$
$$q_{1a} + q_{1b} = q_2$$
$$q_2 = \sum_{i=1}^{nlevsoi} q_{3,i}$$

(11.25)

We seek the set of vegetation water potential values,

$$\psi = \begin{bmatrix} \psi_{sunleaf} \\ \psi_{shadeleaf} \\ \psi_{stem} \\ \psi_{root} \end{bmatrix}$$

(11.26)

that satisfies these equations, as forced by the soil moisture and atmospheric state. Each flux on the schematic can be represented in terms of the relevant water potentials. Defining the transpiration fluxes:

$$E_{sun} = E_{sun,max} \cdot 2^{-\left(\frac{\psi_{sunleaf}}{p50_e}\right)^{c_k}}$$
$$E_{shade} = E_{shade,max} \cdot 2^{-\left(\frac{\psi_{shadeleaf}}{p50_e}\right)^{c_k}}$$

(11.27)

Defining the water supply fluxes:

$$q_{1a} = k_{1a,max} \cdot 2^{-\left(\frac{\psi_{stem}}{p50_1}\right)^{c_k}} \cdot \text{LAI}_{sun} \cdot (\psi_{stem} - \psi_{sunleaf})$$

$$q_{1b} = k_{1b,max} \cdot 2^{-\left(\frac{\psi_{stem}}{p50_1}\right)^{c_k}} \cdot \text{LAI}_{shade} \cdot (\psi_{stem} - \psi_{shadeleaf})$$

$$q_2 = \frac{k_{2,max}}{z_2} \cdot 2^{-\left(\frac{\psi_{root}}{p50_2}\right)^{c_k}} \cdot SAI \cdot (\psi_{root} - \psi_{stem} - \Delta\psi_z)$$

$$q_{soil} = \sum_{i=1}^{nlevsoi} q_{3,i} = \sum_{i=1}^{nlevsoi} k_{3,i} \cdot RAI \cdot (\psi_{soil,i} - \psi_{root} + \Delta\psi_{z,i})$$

(11.28)

We're looking to find the vector ψ that fits with soil and atmospheric forcings while satisfying water flow continuity. Due to the model non-linearity, we use a linearized explicit approach, iterating with Newton's method. The initial guess is the solution for ψ (vector) from the previous time step. The general framework, from iteration *m* to *m+1* is:

$$q^{m+1} = q^m + \frac{\delta q}{\delta \psi}\Delta\psi$$

$$\psi^{m+1} = \psi^m + \Delta\psi$$

(11.29)

So for our first flux balance equation, at iteration *m+1*, we have:

$$E_{sun}^{m+1} = q_{1a}^{m+1}$$

(11.30)

Which can be linearized to:

$$E_{sun}^m + \frac{\delta E_{sun}}{\delta \psi}\Delta\psi = q_{1a}^m + \frac{\delta q_{1a}}{\delta \psi}\Delta\psi$$

(11.31)

And rearranged to be:

$$\frac{\delta q_{1a}}{\delta \psi}\Delta\psi - \frac{\delta E_{sun}}{\delta \psi}\Delta\psi = E_{sun}^m - q_{1a}^m$$

(11.32)

And for the other 3 flux balance equations:

$$\frac{\delta q_{1b}}{\delta \psi}\Delta\psi - \frac{\delta E_{sha}}{\delta \psi}\Delta\psi = E_{sha}^m - q_{1b}^m$$

$$\frac{\delta q_2}{\delta \psi}\Delta\psi - \frac{\delta q_{1a}}{\delta \psi}\Delta\psi - \frac{\delta q_{1b}}{\delta \psi}\Delta\psi = q_{1a}^m + q_{1b}^m - q_2^m$$

$$\frac{\delta q_{soil}}{\delta \psi}\Delta\psi - \frac{\delta q_2}{\delta \psi}\Delta\psi = q_2^m - q_{soil}^m$$

(11.33)

Putting all four together in matrix form:

$$\begin{bmatrix} \frac{\delta q_{1a}}{\delta \psi} - \frac{\delta E_{sun}}{\delta \psi} \\ \frac{\delta q_{1b}}{\delta \psi} - \frac{\delta E_{sha}}{\delta \psi} \\ \frac{\delta q_2}{\delta \psi} - \frac{\delta q_{1a}}{\delta \psi} - \frac{\delta q_{1b}}{\delta \psi} \\ \frac{\delta q_{soil}}{\delta \psi} - \frac{\delta q_2}{\delta \psi} \end{bmatrix} \Delta\psi = \begin{bmatrix} E_{sun}^m - q_{1a}^m \\ E_{sha}^m - q_{1b}^m \\ q_{1a}^m + q_{1b}^m - q_2^m \\ q_2^m - q_{soil}^m \end{bmatrix}$$

(11.34)

Now to expand the left-hand side, from generic ψ to all four plant water potential nodes, noting that many derivatives are zero (e.g. $\frac{\delta E_{sun}}{\delta \psi_{sha}} = 0$)

Introducing the notation: $A\Delta\psi = b$

$$\Delta\psi = \begin{bmatrix} \Delta\psi_{sunleaf} \\ \Delta\psi_{shadeleaf} \\ \Delta\psi_{stem} \\ \Delta\psi_{root} \end{bmatrix} \tag{11.35}$$

$$A = \begin{bmatrix} \dfrac{\delta q_{1a}}{\delta\psi_{sun}} - \dfrac{\delta E_{sun}}{\delta\psi_{sun}} & 0 & \dfrac{\delta q_{1a}}{\delta\psi_{stem}} & 0 \\[2ex] 0 & \dfrac{\delta q_{1b}}{\delta\psi_{sha}} - \dfrac{\delta E_{sha}}{\delta\psi_{sha}} & \dfrac{\delta q_{1b}}{\delta\psi_{stem}} & 0 \\[2ex] -\dfrac{\delta q_{1a}}{\delta\psi_{sun}} & -\dfrac{\delta q_{1b}}{\delta\psi_{sha}} & \dfrac{\delta q_2}{\delta\psi_{stem}} - \dfrac{\delta q_{1a}}{\delta\psi_{stem}} - \dfrac{\delta q_{1b}}{\delta\psi_{stem}} & \dfrac{\delta q_2}{\delta\psi_{root}} \\[2ex] 0 & 0 & -\dfrac{\delta q_2}{\delta\psi_{stem}} & \dfrac{\delta q_{soil}}{\delta\psi_{root}} - \dfrac{\delta q_2}{\delta\psi_{root}} \end{bmatrix} \tag{11.36}$$

$$b = \begin{bmatrix} E_{sun}^m - q_{b1}^m \\ E_{sha}^m - q_{b2}^m \\ q_{b1}^m + q_{b2}^m - q_{stem}^m \\ q_{stem}^m - q_{soil}^m \end{bmatrix} \tag{11.37}$$

Now we compute all the entries for A and b based on the soil moisture and maximum transpiration forcings and can solve to find:

$$\Delta\psi = A^{-1}b \tag{11.38}$$

$$\psi_{m+1} = \psi_m + \Delta\psi \tag{11.39}$$

We iterate until $b \to 0$, signifying water flux balance through the system. The result is a final set of water potentials (ψ_{root}, ψ_{xylem}, $\psi_{shadeleaf}$, $\psi_{sunleaf}$) satisfying non-divergent water flux through the system. The magnitude of the water flux is driven by soil matric potential and unstressed ($\beta_t = 1$) transpiration.

We use the transpiration solution (corresponding to the final solution for ψ) to compute stomatal conductance. The stomatal conductance is then used to compute β_t.

$$\beta_{t,sun} = \frac{g_{s,sun}}{g_{s,sun,\beta_t=1}} \tag{11.40}$$

$$\beta_{t,shade} = \frac{g_{s,shade}}{g_{s,shade,\beta_t=1}} \tag{11.41}$$

The β_t values are used in the Photosynthesis module (see section 9.4) to apply water stress. The solution for ψ is saved as a new variable (vegetation water potential) and is indicative of plant water status. The soil-to-root fluxes ($q_{3,1}, q_{3,2}, ..., q_{3,n}$) are used as the soil transpiration sink in the Richards' equation subsurface flow equations (see section 7.3).

11.2.5 Flow Diagram of Leaf Flux Calculations:

PHS runs nested in the loop that solves for sensible and latent heat fluxes and temperature for vegetated surfaces (see section 5.3). The scheme iterates for convergence of leaf temperature (T_l), transpiration water stress (β_t), and intercellular CO2 concentration (c_i). PHS is forced by maximum transpiration (absent water stress, $\beta_t = 1$), whereby we first solve for assimilation, stomatal conductance, and intercellular CO2 with $\beta_{t,sun}$ and $\beta_{t,shade}$ both set to 1. This involves iterating to convergence of c_i (see section 9.4).

Next, using the solutions for $E_{sun,max}$ and $E_{shade,max}$, PHS solves for ψ, $\beta_{t,sun}$, and $\beta_{t,shade}$. The values for $\beta_{t,sun}$, and $\beta_{t,shade}$ are inputs to the photosynthesis routine, which now solves for attenuated photosynthesis and stomatal conductance (reflecting water stress). Again this involves iterating to convergence of c_i. Non-linearities between β_t and transpiration require also iterating to convergence of β_t. The outermost level of iteration works towards convergence of leaf temperature, reflecting leaf surface energy balance.

Initial T_l →

Calculate metabolic parameters
(V_{cmax}, J_{max}, R_d, K_c, K_o, Γ_*)

Set $\beta_{t,sun}$ and $\beta_{t,shade}$ = 1

Calculate assimilation ($A_{n,max}$)
stomatal conductance ($g_{s,sun,max}$, $g_{s,shade,max}$)
transpiration ($E_{sun,max}$, $E_{shade,max}$)
[absent water stress]

Initial C_i →

Calculate C_i

c_i convergence?   No

Yes

PHS solves for ψ and β_t

Calculate assimilation (A_n)
stomatal conductance ($g_{s,sun}$, $g_{s,shade}$)
using β_t [includes water stress]

Initial C_i →

Calculate C_i

c_i convergence?   No

Yes

β_t convergence?   No

Yes

Calculate leaf temperature (T_l)
and fluxes (H_l, λE_l)

T_l convergence?   No

Yes

Figure 11.2: Flow diagram of leaf flux calculations

CHAPTER 12

LAKE MODEL

The lake model, denoted the *Lake, Ice, Snow, and Sediment Simulator* (LISSS), is from *Subin et al. (2012a)*. It includes extensive modifications to the lake code of *Zeng et al. (2002)* used in CLM versions 2 through 4, which utilized concepts from the lake models of *Bonan (1996)*, *Henderson-Sellers (1985)*, *Henderson-Sellers (1986)*, *Hostetler and Bartlein (1990)*, and the coupled lake-atmosphere model of *Hostetler et al. (1993)*, *Hostetler et al. (1993)*. Lakes have spatially variable depth prescribed in the surface data (section *External Data*); the surface data optionally includes lake optical extinction coeffient and horizontal fetch, currently only used for site simulations. Lake physics includes freezing and thawing in the lake body, resolved snow layers, and "soil" and bedrock layers below the lake body. Temperatures and ice fractions are simulated for $N_{levlak} = 10$ layers (for global simulations) or $N_{levlak} = 25$ (for site simulations) with discretization described in section 12.1. Lake albedo is described in section 12.3. Lake surface fluxes (section 12.4) generally follow the formulations for non-vegetated surfaces, including the calculations of aerodynamic resistances (section 5.2); however, the lake surface temperature T_g (representing an infinitesimal interface layer between the top resolved lake layer and the atmosphere) is solved for simultaneously with the surface fluxes. After surface fluxes are evaluated, temperatures are solved simultaneously in the resolved snow layers (if present), the lake body, and the soil and bedrock, using the ground heat flux G as a top boundary condition. Snow, soil, and bedrock models generally follow the formulations for non-vegetated surfaces (Chapter 6), with modifications described below.

12.1 Vertical Discretization

Currently, there is one lake modeled in each grid cell (with prescribed or assumed depth d, extinction coefficient η, and fetch f), although this could be modified with changes to the CLM subgrid decomposition algorithm in future model versions. As currently implemented, the lake consists of 0-5 snow layers; water and ice layers (10 for global simulations and 25 for site simulations) comprising the "lake body;" 10 "soil" layers; and 5 bedrock layers. Each lake body layer has a fixed water mass (set by the nominal layer thickness and the liquid density), with frozen mass-fraction I a state variable. Resolved snow layers are present if the snow thickness $z_{sno} \geq s_{\min}$, where $s_{\min}$ = 4 cm by default, and is adjusted for model timesteps other than 1800 s in order to maintain numerical stability (section 12.6.5). For global simulations with 10 body layers, the default (50 m lake) body layer thicknesses are given by: Δz_i of 0.1, 1, 2, 3, 4, 5, 7, 7, 10.45, and 10.45 m, with node depths z_i located at the center of each layer (i.e., 0.05, 0.6, 2.1, 4.6, 8.1, 12.6, 18.6, 25.6, 34.325, 44.775 m). For site simulations with 25 layers, the default thicknesses are (m): 0.1 for layer 1; 0.25 for layers 2-5; 0.5 for layers 6-9; 0.75 for layers 10-13; 2 for layers 14-15; 2.5 for layers 16-17; 3.5 for layers 18-21; and 5.225 for layers 22-25. For lakes with depth $d \neq 50$ m and $d \geq 1$ m, the top layer is kept at 10 cm and

the other 9 layer thicknesses are adjusted to maintain fixed proportions. For lakes with $d < 1$ m, all layers have equal thickness. Thicknesses of snow, soil, and bedrock layers follow the scheme used over non-vegetated surfaces (Chapter 6), with modifications to the snow layer thickness rules to keep snow layers at least as thick as $s_{\min}$ (section 12.6.5).

12.2 External Data

As discussed in *Subin et al. (2012a, b)*, the Global Lake and Wetland Database (*Lehner and Doll 2004*) is currently used to prescribe lake fraction in each land model grid cell, for a total of 2.3 million km^{-2}. As in *Subin et al. (2012a, b)*, the *Kourzeneva et al. (2012)* global gridded dataset is currently used to estimate a mean lake depth in each grid cell, based on interpolated compilations of geographic information.

12.3 Surface Albedo

For direct radiation, the albedo a for lakes with ground temperature T_g (K) above freezing is given by (*Pivovarov, 1972*)

$$a = \frac{0.5}{\cos z + 0.15} \tag{12.1}$$

where z is the zenith angle. For diffuse radiation, the expression in eq. is integrated over the full sky to yield $a = 0.10$.

For frozen lakes without resolved snow layers, the albedo at cold temperatures a_0 is 0.60 for visible and 0.40 for near infrared radiation. As the temperature at the ice surface, T_g, approaches freezing [T_f (K) (Table 2.7)], the albedo is relaxed towards 0.10 based on *Mironov et al. (2010)*:

$$a = a_0 \left(1 - x\right) + 0.10x, x = \exp\left(-95\frac{T_f - T_g}{T_f}\right) \tag{12.2}$$

where a is restricted to be no less than that given in (12.1).

For frozen lakes with resolved snow layers, the reflectance of the ice surface is fixed at a_0, and the snow reflectance is calculated as over non-vegetated surfaces (Chapter 3). These two reflectances are combined to obtain the snow-fraction-weighted albedo as in over non-vegetated surfaces (Chapter 3).

12.4 Surface Fluxes and Surface Temperature

12.4.1 Surface Properties

The fraction of shortwave radiation absorbed at the surface, β, depends on the lake state. If resolved snow layers are present, then β is set equal to the absorption fraction predicted by the snow-optics submodel (Chapter 3) for the top snow layer. Otherwise, β is set equal to the near infrared fraction of the shortwave radiation reaching the surface simulated by the atmospheric model or atmospheric data model used for offline simulations (Chapter 33). The remainder of the shortwave radiation fraction $(1 - \beta)$ is absorbed in the lake body or soil as described in section 12.5.5.

The surface roughnesses are functions of the lake state and atmospheric forcing. For frozen lakes ($T_g \leq T_f$) with resolved snow layers, the momentum roughness length $z_{0m} = 2.4 \times 10^{-3}$m (as over non-vegetated surfaces; Chapter 5), and the scalar roughness lengths (z_{0q} for latent heat; and z_{0h}, for sensible heat) are given by (*Zilitinkevich 1970*)

$$R_0 = \frac{z_{0m}u_*}{\nu}, \\ z_{0h} = z_{0q} = z_{0m} \exp\left\{-0.13R_0^{0.45}\right\} \tag{12.3}$$

where R_0 is the near-surface atmospheric roughness Reynolds number, z_{0h} is the roughness length for sensible heat, z_{0q} is the roughness length for latent heat, ν (m^2 s^{-1}) is the kinematic viscosity of air, and u (m s^{-1}) is the friction velocity in the atmospheric surface layer. For frozen lakes without resolved snow layers, $z_{0m} = 1 \times 10^{-3}$m (*Subin et al. (2012a)*), and the scalar roughness lengths are given by .

For unfrozen lakes, z_{0m} is given by (*Subin et al. (2012a)*)

$$z_{0m} = \max\left(\frac{\alpha\nu}{u_*}, C\frac{u_*^2}{g}\right) \tag{12.4}$$

where $\alpha = 0.1$, ν is the kinematic viscosity of air given below, C is the effective Charnock coefficient given below, and g is the acceleration of gravity (Table 2.7). The kinematic viscosity is given by

$$\nu = \nu_0 \left(\frac{T_g}{T_0}\right)^{1.5} \frac{P_0}{P_{ref}} \tag{12.5}$$

where $\nu_0 = 1.51 \times 10^{-5}\frac{m^2}{s}$, $T_0 = 293.15$ K, $P_0 = 1.013 \times 10^5$ Pa , and P_{ref} is the pressure at the atmospheric reference height. The Charnock coefficient C is a function of the lake fetch F (m), given in the surface data or set to 25 times the lake depth d by default:

$$\begin{aligned}
C &= C_{\min} + (C_{\max} - C_{\min}) \exp\{-\min(A, B)\} \\
A &= \left(\frac{Fg}{u^2}\right)^{1/3} \bigg/ f_c \\
B &= \varepsilon\frac{\sqrt{dg}}{u}
\end{aligned} \tag{12.6}$$

where A and B define the fetch- and depth-limitation, respectively; $C_{\min} = 0.01$, $C_{\max} = 0.01$, $\varepsilon = 1$, $f_c = 100$, and u (m s^{-1}) is the atmospheric forcing wind.

12.4.2 Surface Flux Solution

Conservation of energy at the lake surface requires

$$\beta\vec{S}_g - \vec{L}_g - H_g - \lambda E_g - G = 0 \tag{12.7}$$

where $\vec{S}_g$ is the absorbed solar radiation in the lake, β is the fraction absorbed at the surface, $\vec{L}_g$ is the net emitted longwave radiation (+ upwards), H_g is the sensible heat flux (+ upwards), E_g is the water vapor flux (+ upwards), and G is the ground heat flux (+ downwards). All of these fluxes depend implicitly on the temperature at the lake surface T_g. λ converts E_g to an energy flux based on

$$\lambda = \left\{\begin{array}{ll} \lambda_{sub} & T_g \leq T_f \\ \lambda_{vap} & T_g > T_f \end{array}\right\}. \tag{12.8}$$

The sensible heat flux (W m^{-2}) is

$$H_g = -\rho_{atm}C_p\frac{(\theta_{atm} - T_g)}{r_{ah}} \tag{12.9}$$

where ρ_{atm} is the density of moist air (kg m^{-3}) (Chapter 5), C_p is the specific heat capacity of air (J kg^{-1} K^{-1}) (Table 2.7), θ_{atm} is the atmospheric potential temperature (K) (Chapter 5), T_g is the lake surface temperature (K) (at an infinitesimal interface just above the top resolved model layer: snow, ice, or water), and r_{ah} is the aerodynamic resistance to sensible heat transfer (s m^{-1}) (section 5.1).

The water vapor flux (kg m^{-2} s^{-1}) is

$$E_g = -\frac{\rho_{atm}\left(q_{atm} - q_{sat}^{T_g}\right)}{r_{aw}} \tag{12.10}$$

where q_{atm} is the atmospheric specific humidity (kg kg^{-1}) (section 2.3.1), $q_{sat}^{T_g}$ is the saturated specific humidity (kg kg^{-1}) (section 5.5) at the lake surface temperature T_g, and r_{aw} is the aerodynamic resistance to water vapor transfer (s m^{-1}) (section 5.1).

The zonal and meridional momentum fluxes are

$$\tau_x = -\rho_{atm} \frac{u_{atm}}{r_{atm}} \tag{12.11}$$

$$\tau_y = -\rho_{atm} \frac{v_{atm}}{r_{atm}} \tag{12.12}$$

where u_{atm} and v_{atm} are the zonal and meridional atmospheric winds (m s^{-1}) (section 2.3.1), and r_{am} is the aerodynamic resistance for momentum (s m^{-1}) (section 5.1).

The heat flux into the lake surface G (W m^{-2}) is

$$G = \frac{2\lambda_T}{\Delta z_T} (T_g - T_T) \tag{12.13}$$

where λ_T is the thermal conductivity (W m^{-1} K^{-1}), Δz_T is the thickness (m), and T_T is the temperature (K) of the top resolved lake layer (snow, ice, or water). The top thermal conductivity λ_T of unfrozen lakes ($T_g > T_f$) includes conductivities due to molecular (λ_{liq}) and eddy (λ_K) diffusivities (section 12.5.4), as evaluated in the top lake layer at the previous timestep, where λ_{liq} is the thermal conductivity of water (Table 2.7). For frozen lakes without resolved snow layers, $\lambda_T = \lambda_{ice}$. When resolved snow layers are present, λ_T is calculated based on the water content, ice content, and thickness of the top snow layer, as for non-vegetated surfaces.

The absorbed solar radiation $\vec{S}_g$ is

$$\vec{S}_g = \sum_\Lambda S_{atm} \downarrow_\Lambda^\mu \left(1 - \alpha_{g,\Lambda}^\mu\right) + S_{atm} \downarrow_\Lambda (1 - \alpha_{g,\Lambda}) \tag{12.14}$$

where $S_{atm} \downarrow_\Lambda^\mu$ and $S_{atm} \downarrow_\Lambda$ are the incident direct beam and diffuse solar fluxes (W m^{-2}) and Λ denotes the visible ($< 0.7\mu$m) and near-infrared ($\geq 0.7\mu$m) wavebands (section 2.3.1), and $\alpha_{g,\Lambda}^\mu$ and $\alpha_{g,\mu}$ are the direct beam and diffuse lake albedos (section 12.3).

The net emitted longwave radiation is

$$\vec{L}_g = L_g \uparrow - L_{atm} \downarrow \tag{12.15}$$

where $L_g \uparrow$ is the upward longwave radiation from the surface, $L_{atm} \downarrow$ is the downward atmospheric longwave radiation (section 2.3.1). The upward longwave radiation from the surface is

$$L \uparrow = (1 - \varepsilon_g) L_{atm} \downarrow + \varepsilon_g \sigma \left(T_g^n\right)^4 + 4\varepsilon_g \sigma \left(T_g^n\right)^3 \left(T_g^{n+1} - T_g^n\right) \tag{12.16}$$

where $\varepsilon_g = 0.97$ is the lake surface emissivity, σ is the Stefan-Boltzmann constant (W m^{-2} K^{-4}) (Table 2.7), and $T_g^{n+1} - T_g^n$ is the difference in lake surface temperature between Newton-Raphson iterations (see below).

The sensible heat H_g, the water vapor flux E_g through its dependence on the saturated specific humidity, the net longwave radiation $\vec{L}_g$, and the ground heat flux G, all depend on the lake surface temperature T_g. Newton-Raphson iteration is applied to solve for T_g and the surface fluxes as

$$\Delta T_g = \frac{\beta \vec{S}_g - \vec{L}_g - H_g - \lambda E_g - G}{\frac{\partial \vec{L}_g}{\partial T_g} + \frac{\partial H_g}{\partial T_g} + \frac{\partial \lambda E_g}{\partial T_g} + \frac{\partial G}{\partial T_g}} \tag{12.17}$$

where $\Delta T_g = T_g^{n+1} - T_g^n$ and the subscript "n" indicates the iteration. Therefore, the surface temperature T_g^{n+1} can be written as

$$T_g^{n+1} = \frac{\beta \vec{S}_g - \vec{L}_g - H_g - \lambda E_g - G + T_g^n \left(\frac{\partial \vec{L}_g}{\partial T_g} + \frac{\partial H_g}{\partial T_g} + \frac{\partial \lambda E_g}{\partial T_g} + \frac{\partial G}{\partial T_g}\right)}{\frac{\partial \vec{L}_g}{\partial T_g} + \frac{\partial H_g}{\partial T_g} + \frac{\partial \lambda E_g}{\partial T_g} + \frac{\partial G}{\partial T_g}} \tag{12.18}$$

where the partial derivatives are

$$\frac{\partial \overrightarrow{L}_g}{\partial T_g} = 4\varepsilon_g \sigma \left(T_g^n\right)^3 , \tag{12.19}$$

$$\frac{\partial H_g}{\partial T_g} = \frac{\rho_{atm} C_p}{r_{ah}}, \tag{12.20}$$

$$\frac{\partial \lambda E_g}{\partial T_g} = \frac{\lambda \rho_{atm}}{r_{aw}} \frac{dq_{sat}^{T_g}}{dT_g}, \tag{12.21}$$

$$\frac{\partial G}{\partial T_g} = \frac{2\lambda_T}{\Delta z_T}. \tag{12.22}$$

The fluxes of momentum, sensible heat, and water vapor are solved for simultaneously with lake surface temperature as follows. The stability-related equations are the same as for non-vegetated surfaces (section 5.2), except that the surface roughnesses are here (weakly varying) functions of the friction velocity u. To begin, z_{0m} is set based on the value calculated for the last timestep (for $T_g > T_f$) or based on the values in section 12.4.1 (otherwise), and the scalar roughness lengths are set based on the relationships in section 12.4.1.

1. An initial guess for the wind speed V_a including the convective velocity U_c is obtained from (5.24) assuming an initial convective velocity $U_c = 0$ m s^{-1} for stable conditions ($\theta_{v, atm} - \theta_{v, s} \geq 0$ as evaluated from (5.50)) and $U_c = 0.5$ for unstable conditions ($\theta_{v, atm} - \theta_{v, s} < 0$).

2. An initial guess for the Monin-Obukhov length L is obtained from the bulk Richardson number using (5.46) and (5.48).

3. The following system of equations is iterated four times:

4. Heat of vaporization / sublimation λ ((12.8))

5. Thermal conductivity λ_T (above)

6. Friction velocity u ((5.32), (5.33), (5.34), (5.35))

7. Potential temperature scale θ ((5.37), (5.38), (5.39), (5.40))

8. Humidity scale q ((5.41), (5.42), (5.43), (5.44))

9. Aerodynamic resistances r_{am}, r_{ah}, and r_{aw} ((5.55), (5.56), (5.57))

10. Lake surface temperature T_g^{n+1} ((12.18))

11. Heat of vaporization / sublimation λ ((12.8))

12. Sensible heat flux H_g is updated for T_g^{n+1} ((12.9))

13. Water vapor flux E_g is updated for T_g^{n+1} as

$$E_g = -\frac{\rho_{atm}}{r_{aw}} \left[q_{atm} - q_{sat}^{T_g} - \frac{\partial q_{sat}^{T_g}}{\partial T_g} \left(T_g^{n+1} - T_g^n\right) \right] \tag{12.23}$$

where the last term on the right side of equation is the change in saturated specific humidity due to the change in T_g between iterations.

1. Saturated specific humidity $q_{sat}^{T_g}$ and its derivative $\frac{dq_{sat}^{T_g}}{dT_g}$ are updated for T_g^{n+1} (section 5.1).

2. Virtual potential temperature scale θ_v ((5.17))

3. Wind speed including the convective velocity, V_a ((5.24))

4. Monin-Obukhov length L ((5.49))

5. Roughness lengths ((12.3), (12.4)).

Once the four iterations for lake surface temperature have been yielded a tentative solution T'_g, several restrictions are imposed in order to maintain consistency with the top lake model layer temperature T_T (*Subin et al. (2012a)*).

$$
\begin{aligned}
&1)\ T_T \leq T_f < T'_g \Rightarrow T_g = T_f, \\
&2)\ T_T > T'_g > T_m \Rightarrow T_g = T_T, \\
&3)\ T_m > T'_g > T_T > T_f \Rightarrow T_g = T_T
\end{aligned}
\qquad (12.24)
$$

where T_m is the temperature of maximum liquid water density, 3.85º C (*Hostetler and Bartlein (1990)*). The first condition requires that, if there is any snow or ice present, the surface temperature is restricted to be less than or equal to freezing. The second and third conditions maintain convective stability in the top lake layer.

If eq. XXX is applied, the turbulent fluxes H_g and E_g are re-evaluated. The emitted longwave radiation and the momentum fluxes are re-evaluated in any case. The final ground heat flux G is calculated from the residual of the energy balance eq. XXX in order to precisely conserve energy. XXX This ground heat flux is taken as a prescribed flux boundary condition for the lake temperature solution (section 12.5.3). An energy balance check is included at each timestep to insure that eq. XXX is obeyed to within 0.1 W m⁻².

12.5 Lake Temperature

12.5.1 Introduction

The (optional-) snow, lake body (water and/or ice), soil, and bedrock system is unified for the lake temperature solution. The governing equation, similar to that for the snow-soil-bedrock system for vegetated land units (Chapter 6), is

$$
\tilde{c}_v \frac{\partial T}{\partial t} = \frac{\partial}{\partial z}\left(\tau \frac{\partial T}{\partial z} \right) - \frac{d\phi}{dz}
\qquad (12.25)
$$

where $\tilde{c}_v$ is the volumetric heat capacity (J m⁻³ K⁻¹), t is time (s), T is the temperature (K), τ is the thermal conductivity (W m⁻¹ K⁻¹), and ϕ is the solar radiation (W m⁻²) penetrating to depth z (m). The system is discretized into N layers, where

$$
N = n_{sno} + N_{levlak} + N_{levgrnd},
\qquad (12.26)
$$

n_{sno} is the number of actively modeled snow layers at the current timestep (Chapter 8), and $N_{levgrnd}$ is as for vegetated land units (Chapter 6). Energy is conserved as

$$
\frac{d}{dt} \sum_{j=1}^{N} \left[\tilde{c}_{v,j}(t)\left(T_j - T_f \right) + L_j(t) \right] \Delta z_j = G + (1 - \beta)\, \vec{S}_g
\qquad (12.27)
$$

where $\tilde{c}_{v,j}(t)$ is the volumetric heat capacity of the jth layer (section 12.5.5), $L_j(t)$ is the latent heat of fusion per unit volume of the jth layer (proportional to the mass of liquid water present), and the right-hand side represents the net influx of energy to the lake system. Note that $\tilde{c}_{v,j}(t)$ can only change due to phase change (except for changing snow layer mass, which, apart from energy required to melt snow, represents an untracked energy flux in the land model, along with advected energy associated with water flows in general), and this is restricted to occur at $T_j = T_f$ in the snow-lake-soil system, allowing eq. to be precisely enforced and justifying the exclusion of $c_{v,j}$ from the time derivative in eq. .

12.5.2 Overview of Changes from CLM4

Thermal conductivities include additional eddy diffusivity, beyond the *Hostetler and Bartlein (1990)* formulation, due to unresolved processes (*Fang and Stefan 1996*; *Subin et al. (2012a)*). Lake water is now allowed to freeze by an arbitrary fraction for each layer, which releases latent heat and changes thermal properties. Convective mixing occurs

for all lakes, even if frozen. Soil and bedrock are included beneath the lake. The full snow model is used if the snow thickness exceeds a threshold; if there are resolved snow layers, radiation transfer is predicted by the snow-optics submodel (Chapter 3), and the remaining radiation penetrating the bottom snow layer is absorbed in the top layer of lake ice; conversely, if there are no snow layers, the solar radiation penetrating the bottom lake layer is absorbed in the top soil layer. The lakes have variable depth, and all physics is assumed valid for arbitrary depth, except for a depth-dependent enhanced mixing (section 12.5.4). Finally, a previous sign error in the calculation of eddy diffusivity (specifically, the Brunt-Väisälä frequency term; eq.) was corrected.

12.5.3 Boundary Conditions

The top boundary condition, imposed at the top modeled layer $i = j_{top}$, where $j_{top} = -n_{sno} + 1$, is the downwards surface flux G defined by the energy flux residual during the surface temperature solution (section 12.5.3). The bottom boundary condition, imposed at $i = N_{levlak} + N_{levgrnd}$, is zero flux. The 2-m windspeed u_2 (m s^{-1}) is used in the calculation of eddy diffusivity:

$$u_2 = \frac{u_*}{k} \ln \left(\frac{2}{z_{0m}} \right) \geq 0.1.$$

(12.28)

where u_* is the friction velocity calculated in section 12.5.3 and k is the von Karman constant (Table 2.7).

12.5.4 Eddy Diffusivity and Thermal Conductivities

The total eddy diffusivity K_W (m^2 s^{-1}) for liquid water in the lake body is given by (*Subin et al. (2012a)*)

$$K_W = m_d \left(\kappa_e + K_{ed} + \kappa_m \right)$$

(12.29)

where κ_e is due to wind-driven eddies (*Hostetler and Bartlein (1990)*), K_{ed} is a modest enhanced diffusivity intended to represent unresolved mixing processes (*Fang and Stefan 1996*), $\kappa_m = \frac{\lambda_{liq}}{c_{liq}\rho_{liq}}$ is the molecular diffusivity of water (given by the ratio of its thermal conductivity (W m^{-1} K^{-1}) to the product of its heat capacity (J kg^{-1} K^{-1}) and density (kg m^{-3}), values given in Table 2.7), and m_d (unitless) is a factor which increases the overall diffusivity for large lakes, intended to represent 3-dimensional mixing processes such as caused by horizontal temperature gradients. As currently implemented,

$$m_d = \left\{ \begin{array}{ll} 1, & d < 25\mathrm{m} \\ 10, & d \geq 25\mathrm{m} \end{array} \right\}$$

(12.30)

where d is the lake depth.

The wind-driven eddy diffusion coefficient $\kappa_{e,\,i}$ (m^2 s^{-1}) for layers $1 \leq i \leq N_{levlak}$ is

$$\kappa_{e,\,i} = \left\{ \begin{array}{ll} \frac{kw^*z_i}{P_0(1+37Ri^2)} \exp\left(-k^*z_i\right) & T_g > T_f \\ 0 & T_g \leq T_f \end{array} \right\}$$

(12.31)

where $P_0 = 1$ is the neutral value of the turbulent Prandtl number, z_i is the node depth (m), the surface friction velocity (m s^{-1}) is $w^* = 0.0012u_2$, and k^* varies with latitude ϕ as $k^* = 6.6u_2^{-1.84}\sqrt{|\sin\phi|}$. For the bottom layer, $\kappa_{e,\,N_{levlak}} = \kappa_{e,\,N_{levlak}-1}$. As in *Hostetler and Bartlein (1990)*, the 2-m wind speed u_2 (m s^{-1}) (eq.) is used to evaluate w^* and k^* rather than the 10-m wind used by *Henderson-Sellers (1985)*.

The Richardson number is

$$R_i = \frac{-1 + \sqrt{1 + \frac{40N^2k^2z_i^2}{w^{*2}\exp(-2k^*z_i)}}}{20}$$

(12.32)

where

$$N^2 = \frac{g}{\rho_i} \frac{\partial \rho}{\partial z} \tag{12.33}$$

and g is the acceleration due to gravity (m s^{-2}) (Table 2.7), ρ_i is the density of water (kg m^{-3}), and $\frac{\partial \rho}{\partial z}$ is approximated as $\frac{\rho_{i+1} - \rho_i}{z_{i+1} - z_i}$. Note that because here, z is increasing downwards (unlike in *Hostetler and Bartlein (1990)*), eq. contains no negative sign; this is a correction from CLM4. The density of water is (*Hostetler and Bartlein (1990)*)

$$\rho_i = 1000 \left(1 - 1.9549 \times 10^{-5} \, |T_i - 277|^{1.68}\right). \tag{12.34}$$

The enhanced diffusivity K_{ed} is given by (*Fang and Stefan 1996*)

$$K_{ed} = 1.04 \times 10^{-8} \left(N^2\right)^{-0.43}, N^2 \geq 7.5 \times 10^{-5} \mathrm{s}^2 \tag{12.35}$$

where N^2 is calculated as in eq. except for the minimum value imposed in .

The thermal conductivity for the liquid water portion of lake body layer i, $\tau_{liq,i}$ (W m^{-1} K^{-1}) is given by

$$\tau_{liq,i} = K_W c_{liq} \rho_{liq}. \tag{12.36}$$

The thermal conductivity of the ice portion of lake body layer i, $\tau_{ice,eff}$ (W m^{-1} K^{-1}), is constant among layers, and is given by

$$\tau_{ice,eff} = \tau_{ice} \frac{\rho_{ice}}{\rho_{liq}} \tag{12.37}$$

where τ_{ice} (Table 2.7) is the nominal thermal conductivity of ice: $\tau_{ice,eff}$ is adjusted for the fact that the nominal model layer thicknesses remain constant even while the physical ice thickness exceeds the water thickness.

The overall thermal conductivity τ_i for layer i with ice mass-fraction I_i is the harmonic mean of the liquid and water fractions, assuming that they will be physically vertically stacked, and is given by

$$\tau_i = \frac{\tau_{ice,eff} \tau_{liq,i}}{\tau_{liq,i} I_i + \tau_{ice} \left(1 - I_i\right)}. \tag{12.38}$$

The thermal conductivity of snow, soil, and bedrock layers above and below the lake, respectively, are computed identically to those for vegetated land units (Chapter 6), except for the adjustment of thermal conductivity for frost heave or excess ice (*Subin et al., 2012a, Supporting Information*).

12.5.5 Radiation Penetration

If there are no resolved snow layers, the surface absorption fraction β is set according to the near-infrared fraction simulated by the atmospheric model. This is apportioned to the surface energy budget (section 12.4.1), and thus no additional radiation is absorbed in the top z_a (currently 0.6 m) of unfrozen lakes, for which the light extinction coefficient η (m^{-1}) varies between lake columns (eq.). For frozen lakes ($T_g \leq T_f$), the remaining $\left(1 - \beta\right) \vec{S}_g$ fraction of surface absorbed radiation that is not apportioned to the surface energy budget is absorbed in the top lake body layer. This is a simplification, as lake ice is partially transparent. If there are resolved snow layers, then the snow optics submodel (Chapter 3) is used to calculate the snow layer absorption (except for the absorption predicted for the top layer by the snow optics submodel, which is assigned to the surface energy budget), with the remainder penetrating snow layers absorbed in the top lake body ice layer.

For unfrozen lakes, the solar radiation remaining at depth $z > z_a$ in the lake body is given by

$$\phi = \left(1 - \beta \vec{S}_g\right) \exp\left\{-\eta \left(z - z_a\right)\right\}. \tag{12.39}$$

For all lake body layers, the flux absorbed by the layer i, ϕ_i , is

$$\phi_i = \left(1 - \beta \vec{S}_g\right) \left[\exp\left\{-\eta \left(z_i - \frac{\Delta z_i}{2} - z_a\right)\right\} - \exp\left\{-\eta \left(z_i + \frac{\Delta z_i}{2} - z_a\right)\right\}\right]. \tag{12.40}$$

The argument of each exponent is constrained to be non-negative (so $\phi_i = 0$ for layers contained within z_a). The remaining flux exiting the bottom of layer $i = N_{levlak}$ is absorbed in the top soil layer.

The light extinction coefficient η (m^{-1}), if not provided as external data, is a function of depth d (m) (*Subin et al. (2012a)*):

$$\eta = 1.1925 d^{-0.424}. \tag{12.41}$$

12.5.6 Heat Capacities

The vertically-integrated heat capacity for each lake layer, $c_{v,i}$ (J m^{-2}) is determined by the mass-weighted average over the heat capacities for the water and ice fractions:

$$c_{v,i} = \Delta z_i \rho_{liq} \left[c_{liq} \left(1 - I_i \right) + c_{ice} I_i \right]. \tag{12.42}$$

Note that the density of water is used for both ice and water fractions, as the thickness of the layer is fixed.

The total heat capacity $c_{v,i}$ for each soil, snow, and bedrock layer (J m^{-2}) is determined as for vegetated land units (Chapter 6), as the sum of the heat capacities for the water, ice, and mineral constituents.

12.5.7 Crank-Nicholson Solution

The solution method for thermal diffusion is similar to that used for soil (Chapter 6), except that the lake body layers are sandwiched between the snow and soil layers (section 12.5.1), and radiation flux is absorbed throughout the lake layers. Before solution, layer temperatures T_i (K), thermal conductivities τ_i (W m^{-1} K^{-1}), heat capacities $c_{v,i}$ (J m^{-2}), and layer and interface depths from all components are transformed into a uniform set of vectors with length $N = n_{sno} + N_{levlak} + N_{levgrnd}$ and consistent units to simplify the solution. Thermal conductivities at layer interfaces are calculated as the harmonic mean of the conductivities of the neighboring layers:

$$\lambda_i = \frac{\tau_i \tau_{i+1} \left(z_{i+1} - z_i \right)}{\tau_i \left(z_{i+1} - \hat{z}_i \right) + \tau_{i+1} \left(\hat{z}_i - z_i \right)}, \tag{12.43}$$

where λ_i is the conductivity at the interface between layer i and layer $i + 1$, z_i is the depth of the node of layer i, and $\hat{z}_i$ is the depth of the interface below layer i. Care is taken at the boundaries between snow and lake and between lake and soil. The governing equation is discretized for each layer as

$$\frac{c_{v,i}}{\Delta t} \left(T_i^{n+1} - T_i^n \right) = F_{i-1} - F_i + \phi_i \tag{12.44}$$

where superscripts $n + 1$ and n denote values at the end and beginning of the timestep Δt, respectively, F_i (W m^{-2}) is the downward heat flux at the bottom of layer i, and ϕ_i is the solar radiation absorbed in layer i.

Eq. is solved using the semi-implicit Crank-Nicholson Method, resulting in a tridiagonal system of equations:

$$\begin{aligned}
r_i &= a_i T_{i-1}^{n+1} + b_i T_i^{n+1} + c T_{i+1}^{n+1}, \\
a_i &= -0.5 \frac{\Delta t}{c_{v,i}} \frac{\partial F_{i-1}}{\partial T_{i-1}^n}, \\
b_i &= 1 + 0.5 \frac{\Delta t}{c_{v,i}} \left(\frac{\partial F_{i-1}}{\partial T_{i-1}^n} + \frac{\partial F_i}{\partial T_i^n} \right), \\
c_i &= -0.5 \frac{\Delta t}{c_{v,i}} \frac{\partial F_i}{\partial T_i^n}, \\
r_i &= T_i^n + 0.5 \frac{\Delta t}{c_{v,i}} \left(F_{i-1} - F_i \right) + \frac{\Delta t}{c_{v,i}} \phi_i.
\end{aligned} \tag{12.45}$$

The fluxes F_i are defined as follows: for the top layer, $F_{j_{top}-1} = 2G; a_{j_{top}} = 0$, where G is defined as in section 12.5.3 (the factor of 2 merely cancels out the Crank-Nicholson 0.5 in the equation for $r_{j_{top}}$). For the bottom layer, $F_{N_{levlak}+N_{levgrnd}} = 0$. For all other layers:

$$F_i = \lambda_i \frac{T_i^n - T_{i+1}^n}{z_{n+1} - z_n}. \tag{12.46}$$

12.5.8 Phase Change

Phase change in the lake, snow, and soil is done similarly to that done for the soil and snow for vegetated land units (Chapter 6), except without the allowance for freezing point depression in soil underlying lakes. After the heat diffusion is calculated, phase change occurs in a given layer if the temperature is below freezing and liquid water remains, or if the temperature is above freezing and ice remains.

If melting occurs, the available energy for melting, Q_{avail} (J m^{-2}), is computed as

$$Q_{avail} = (T_i - T_f) \, c_{v,i} \tag{12.47}$$

where T_i is the temperature of the layer after thermal diffusion (section 12.5.7), and $c_{v,i}$ is as calculated in section 12.5.6. The mass of melt in the layer M (kg m^{-2}) is given by

$$M = \min\left\{ M_{ice}, \frac{Q_{avail}}{H_{fus}} \right\} \tag{12.48}$$

where H_{fus} (J kg^{-1}) is the latent heat of fusion of water (Table 2.7), and M_{ice} is the mass of ice in the layer: $I_i \rho_{liq} \Delta z_i$ for a lake body layer, or simply the soil / snow ice content state variable (w_{ice}) for a soil / snow layer. The heat remainder, Q_{rem} is given by

$$Q_{rem} = Q_{avail} - M H_{fus}. \tag{12.49}$$

Finally, the mass of ice in the layer M_{ice} is adjusted downwards by M, and the temperature T_i of the layer is adjusted to

$$T_i = T_f + \frac{Q_{rem}}{c'_{v,i}} \tag{12.50}$$

where $c'_{v,i} = c_{v,i} + M (c_{liq} - c_{ice})$.

If freezing occurs, Q_{avail} is again given by but will be negative. The melt M, also negative, is given by

$$M = \max\left\{ -M_{liq}, \frac{Q_{avail}}{H_{fus}} \right\} \tag{12.51}$$

where M_{liq} is the mass of water in the layer: $(1 - I_i) \rho_{liq} \Delta z_i$ for a lake body layer, or the soil / snow water content state variable (w_{liq}). The heat remainder Q_{rem} is given by eq. and will be negative or zero. Finally, M_{liq} is adjusted downwards by $-M$ and the temperature is reset according to eq. .

In the presence of nonzero snow water W_{sno} without resolved snow layers over

an unfrozen top lake layer, the available energy in the top lake layer $(T_1 - T_f) \, c_{v,1}$ is used to melt the snow. Similar to above, W_{sno} is either completely melted and the remainder of heat returned to the top lake layer, or the available heat is exhausted and the top lake layer is set to freezing. The snow thickness is adjusted downwards in proportion to the amount of melt, maintaining constant density.

12.5.9 Convection

Convective mixing is based on *Hostetler et al.'s (1993, 1994)* coupled lake-atmosphere model, adjusting the lake temperature after diffusion and phase change to maintain a stable density profile. Unfrozen lakes overturn when $\rho_i > \rho_{i+1}$, in which case the layer thickness weighted average temperature for layers 1 to $i + 1$ is applied to layers 1 to $i + 1$ and the densities are updated. This scheme is applied iteratively to layers $1 \leq i < N_{levlak} - 1$. Unstable profiles occurring at the bottom of the lake (i.e., between layers $i = N_{levlak} - 1$ and $i = N_{levlak}$) are treated separately (*Subin et al. (2012a)*), as occasionally these can be induced by heat expelled from the sediments (not present in the original *Hostetler et al. (1994)* model). Mixing proceeds from the bottom upward in this case (i.e., first mixing layers

$i = N_{levlak} - 1$ and $i = N_{levlak}$, then checking $i = N_{levlak} - 2$ and $i = N_{levlak} - 1$ and mixing down to $i = N_{levlak}$ if needed, and on to the top), so as not to mix in with warmer over-lying layers.

For frozen lakes, this algorithm is generalized to conserve total enthalpy and ice content, and to maintain ice contiguous at the top of the lake. Thus, an additional mixing criterion is added: the presence of ice in a layer that is below a layer which is not completely frozen. When this occurs, these two lake layers and all those above mix. Total enthalpy Q is conserved as

$$Q = \sum_{j=1}^{i+1} \Delta z_j \rho_{liq} \left(T_j - T_f \right) \left[(1 - I_j) \, c_{liq} + I_j c_{ice} \right]. \tag{12.52}$$

Once the average ice fraction I_{av} is calculated from

$$\begin{aligned} I_{av} &= \frac{\sum_{j=1}^{i+1} I_j \Delta z_j}{Z_{i+1}}, \\ Z_{i+1} &= \sum_{j=1}^{i+1} \Delta z_j, \end{aligned} \tag{12.53}$$

the temperatures are calculated. A separate temperature is calculated for the frozen (T_{froz}) and unfrozen (T_{unfr}) fractions of the mixed layers. If the total heat content Q is positive (e.g. some layers will be above freezing), then the extra heat is all assigned to the unfrozen layers, while the fully frozen layers are kept at freezing. Conversely, if $Q < 0$, the heat deficit will all be assigned to the ice, and the liquid layers will be kept at freezing. For the layer that contains both ice and liquid (if present), a weighted average temperature will have to be calculated.

If $Q > 0$, then $T_{froz} = T_f$, and T_{unfr} is given by

$$T_{unfr} = \frac{Q}{\rho_{liq} Z_{i+1} \left[(1 - I_{av}) \, c_{liq} \right]} + T_f. \tag{12.54}$$

If $Q < 0$, then $T_{unfr} = T_f$, and T_{froz} is given by

$$T_{froz} = \frac{Q}{\rho_{liq} Z_{i+1} \left[I_{av} c_{ice} \right]} + T_f. \tag{12.55}$$

The ice is lumped together at the top. For each lake layer j from 1 to $i + 1$, the ice fraction and temperature are set as follows, where $Z_j = \sum_{m=1}^{j} \Delta z_m$:

1. If $Z_j \leq Z_{i+1} I_{av}$, then $I_j = 1$ and $T_j = T_{froz}$.

2. Otherwise, if $Z_{j-1} < Z_{i+1} I_{av}$, then the layer will contain both ice and water. The ice fraction is given by $I_j = \frac{Z_{i+1} I_{av} - Z_{j-1}}{\Delta z_j}$. The temperature is set to conserve the desired heat content that would be present if the layer could have two temperatures, and then dividing by the heat capacity of the layer to yield

$$T_j = \frac{T_{froz} I_j c_{ice} + T_{unfr} (1 - I_j) \, c_{liq}}{I_j c_{ice} + (1 - I_j) \, c_{liq}}. \tag{12.56}$$

3. Otherwise, $I_j = 0$ and $T_j = T_{unfr}$.

12.5.10 Energy Conservation

To check energy conservation, the left-hand side of eq. XXX is re-written to yield the total enthalpy of the lake system (J m^{-2}) H_{tot}:

$$H_{tot} = \sum_{i=j_{top}}^{N_{levlak}+N_{levgrnd}} \left[c_{v,i} \left(T_i - T_f \right) + M_{liq,i} H_{fus} \right] - W_{sno,bulk} H_{fus} \tag{12.57}$$

where $M_{liq,i}$ is the water mass of the ith layer (similar to section 12.5.8), and $W_{sno,bulk}$ is the mass of snow-ice not present in resolved snow layers. This expression is evaluated once at the beginning and once at the end of the timestep

(re-evaluating each $c_{v,i}$), and the change is compared with the net surface energy flux to yield the error flux E_{soi} (W m^{-2}):

$$E_{soi} = \frac{\Delta H_{tot}}{\Delta t} - G - \sum_{i=j_{top}}^{N_{levlak}+N_{levgrnd}} \phi_i \qquad (12.58)$$

If $|E_{soi}| < 0.1$W m^{-2}, it is subtracted from the sensible heat flux and added to G. Otherwise, the model is aborted.

12.6 Lake Hydrology

12.6.1 Overview

Hydrology is done similarly to other impervious non-vegetated columns (e.g., glaciers) where snow layers may be resolved but infiltration into the permanent ground is not allowed. The water mass of lake columns is currently maintained constant, aside from overlying snow. The water budget is balanced with q_{rgwl} (eq. ; kg m^{-2} s^{-1}), a generalized runoff term for impervious land units that may be negative.

There are some modifications to the soil and snow parameterizations as compared with the soil in vegetated land units, or the snow overlying other impervious columns. The soil can freeze or thaw, with the allowance for frost heave (or the initialization of excess ice) (sections 12.5.4 and 12.5.8), but no air-filled pore space is allowed in the soil. To preserve numerical stability in the lake model (which uses a slightly different surface flux algorithm than over other non-vegetated land units), two changes are made to the snow model. First, dew or frost is not allowed to be absorbed by a top snow layer which has become completely melted during the timestep. Second, because occasional instabilities occurred during model testing when the Courant–Friedrichs–Lewy (CFL) condition was violated, due to the explicit time-stepping integration of the surface flux solution, resolved snow layers must be a minimum of $s_{\min} = 4$ cm thick rather than 1 cm when the default timestep of 1800 s is used.

12.6.2 Water Balance

The total water balance of the system is given by

$$\Delta W_{sno} + \sum_{i=1}^{n_{levsoi}} \left(\Delta w_{liq,i} + \Delta w_{ice,i} \right) = \left(q_{rain} + q_{sno} - E_g - q_{rgwl} - q_{snwcp,\,ice} \right) \Delta t \qquad (12.59)$$

where W_{sno} (kg m^{-2}) is the total mass of snow (both liquid and ice, in resolved snow layers or bulk snow), $w_{liq,i}$ and $w_{ice,i}$ are the masses of water phases (kg m^{-2}) in soil layer i, q_{rain} and q_{sno} are the precipitation forcing from the atmosphere (kg m^{-2} s^{-1}), $q_{snwcp,\,ice}$ is the ice runoff associated with snow-capping (below), E_g is the ground evaporation (section 12.4.2), and n_{levsoi} is the number of hydrologically active soil layers (as opposed to dry bedrock layers).

12.6.3 Precipitation, Evaporation, and Runoff

All precipitation reaches the ground, as there is no vegetated fraction. As for other land types, incident snowfall accumulates (with ice mass W_{sno} and thickness z_{sno}) until its thickness exceeds a minimum thickness $s_{\min}$, at which point a resolved snow layer is initiated, with water, ice, dissolved aerosol, snow-grain radius, etc., state variables tracked by the Snow Hydrology submodel (Chapter 8). The density of fresh snow is assigned as for other land types (Chapter 8). Solid precipitation is added immediately to the snow, while liquid precipitation is added to snow layers, if they exist, after accounting for dew, frost, and sublimation (below). If z_{sno} exceeds $s_{\min}$ after solid precipitation is added but no snow layers are present, a new snow layer is initiated immediately, and then dew, frost, and sublimation are accounted for. Snow-capping is invoked if the snow depth $z_{sno} > 1000$m, in which case additional precipitation and frost deposition is added to $q_{snwcp,\,ice}$.

If there are resolved snow layers, the generalized "evaporation" E_g (i.e., evaporation, dew, frost, and sublimation) is treated as over other land units, except that the allowed evaporation from the ground is unlimited (though the top snow layer cannot lose more water mass than it contains). If there are no resolved snow layers but $W_{sno} > 0$ and $E_g > 0$, sublimation $q_{sub,sno}$ (kg m^{-2} s^{-1}) will be given by

$$q_{sub,sno} = \min\left\{ E_g, \frac{W_{sno}}{\Delta t} \right\}. \tag{12.60}$$

If $E_g < 0, T_g \leq T_f$, and there are no resolved snow layers or the top snow layer is not unfrozen, then the rate of frost production $q_{frost} = |E_g|$. If $E_g < 0$ but the top snow layer has completely thawed during the Phase Change step of the Lake Temperature solution (section 12.5.8), then frost (or dew) is not allowed to accumulate ($q_{frost} = 0$), to insure that the layer is eliminated by the Snow Hydrology (Chapter 8) code. (If $T_g > T_f$, then no snow is present (section 12.4.2), and evaporation or dew deposition is balanced by q_{rgwl}.) The snowpack is updated for frost and sublimation:

$$W_{sno} = W_{sno} + \Delta t \left(q_{frost} - q_{sub,sno} \right). \tag{12.61}$$

If there are resolved snow layers, then this update occurs using the Snow Hydrology submodel (Chapter 8). Otherwise, the snow ice mass is updated directly, and z_{sno} is adjusted by the same proportion as the snow ice (i.e., maintaining the same density), unless there was no snow before adding the frost, in which case the density is assumed to be 250 kg m^{-3}.

12.6.4 Soil Hydrology

The combined water and ice soil volume fraction in a soil layer θ_i is given by

$$\theta_i = \frac{1}{\Delta z_i} \left(\frac{w_{ice,i}}{\rho_{ice}} + \frac{w_{liq,i}}{\rho_{liq}} \right). \tag{12.62}$$

If $\theta_i < \theta_{sat,i}$, the pore volume fraction at saturation (as may occur when ice melts), then the liquid water mass is adjusted to

$$w_{liq,i} = \left(\theta_{sat,i} \Delta z_i - \frac{w_{ice,i}}{\rho_{ice}} \right) \rho_{liq}. \tag{12.63}$$

Otherwise, if excess ice is melting and $w_{liq,i} > \theta_{sat,i}\rho_{liq}\Delta z_i$, then the water in the layer is reset to

$$w_{liq,i} = \theta_{sat,i}\rho_{liq}\Delta z_i \tag{12.64}$$

This allows excess ice to be initialized (and begin to be lost only after the pore ice is melted, which is realistic if the excess ice is found in heterogeneous chunks) but irreversibly lost when melt occurs.

12.6.5 Modifications to Snow Layer Logic

A thickness difference $z_{lsa} = s_{\min} - \tilde{s}_{\min}$ adjusts the minimum resolved snow layer thickness for lake columns as compared to non-lake columns. The value of z_{lsa} is chosen to satisfy the CFL condition for the model timestep. By default, $\tilde{s}_{\min}$ = 1 cm and $s_{\min}$ = 4 cm. See *Subin et al. (2012a; including Supporting Information)* for further discussion.

The rules for combining and sub-dividing snow layers (section 8.7) are adjusted for lakes to maintain minimum thicknesses of $s_{\min}$ and to increase all target layer thicknesses by z_{lsa}. The rules for combining layers are modified by simply increasing layer thickness thresholds by z_{lsa}. The rules for dividing snow layers are contained in a separate subroutine that is modified for lakes, and is a function of the number of layers and the layer thicknesses. There are two types of operations: (a) subdividing layers in half, and (b) shifting some volume from higher layers to lower layers (without increasing the layer number). For subdivisions of type (a), the thickness thresholds triggering subdivision are

increased by $2z_{lsa}$ for lakes. For shifts of type (b), the thickness thresholds triggering the shifts are increased by z_{lsa} . At the end of the modified subroutine, a snow ice and liquid balance check are performed.

In rare instances, resolved snow layers may be present over an unfrozen top lake body layer. In this case, the snow layers may be eliminated if enough heat is present in the top layer to melt the snow: see *Subin et al. (2012a, Supporting Information)*.

CHAPTER 13

GLACIERS

This chapter describes features of CLM that are specific to coupling to an ice sheet model (in the CESM context, this is the CISM model; *Lipscomb and Sacks (2012)* provide documentation and user's guide for CISM). General information about glacier land units can be found elsewhere in this document (see Chapter 2 for an overview).

13.1 Summary of CLM5.0 updates relative to CLM4.5

Compared with CLM4.5 (*Oleson et al. 2013*), CLM5.0 contains substantial improvements in its capabilities for land-ice science. This section summarizes these improvements, and the following sections provide more details.

- All runs include multiple glacier elevation classes over Greenland and Antarctica and compute ice sheet surface mass balance in those regions.

- A number of namelist parameters offer fine-grained control over glacier behavior in different regions of the world (section 13.3). (The options used outside of Greenland and Antarctica reproduce the standard CLM4.5 glacier behavior.)

- CLM can now keep its glacier areas and elevations in sync with CISM when running with an evolving ice sheet. (However, in typical configurations, the ice sheet geometry still remains fixed throughout the run.)

- The downscaling to elevation classes now includes downwelling longwave radiation and partitioning of precipitation into rain vs. snow (section 13.4).

- Other land units within the CISM domain undergo the same downscaling as the glacier land unit, and surface mass balance is computed for the natural vegetated land unit. This allows CLM to produce glacial inception when running with an evolving ice sheet model.

- There have also been substantial improvements to CLM's snow physics, as described in other chapters of this document.

13.2 Overview

CLM is responsible for computing two quantities that are passed to the ice sheet model:

1. Surface mass balance (SMB) - the net annual accumulation/ablation of mass at the upper surface (section 13.5)

2. Ground surface temperature, which serves as an upper boundary condition for CISM's temperature calculation

The ice sheet model is typically run at much higher resolution than CLM (e.g., ~5 km rather than ~100 km). To improve the downscaling from CLM's grid to the ice sheet grid, the glaciated portion of each grid cell is divided into multiple elevation classes (section 13.4). The above quantities are computed separately in each elevation class. The CESM coupler then computes high-resolution quantities via horizontal and vertical interpolation, and passes these high-resolution quantities to CISM.

There are several reasons for computing the SMB in CLM rather than in CISM:

1. It is much cheaper to compute the SMB in CLM for ~10 elevation classes than in CISM. For example, suppose we are running CLM at a resolution of ~50 km and CISM at ~5 km. Greenland has dimensions of about 1000 x 2000 km. For CLM we would have 20 x 40 x 10 = 8,000 columns, whereas for CISM we would have 200 x 400 = 80,000 columns.

2. We can use the sophisticated snow physics parameterization already in CLM instead of implementing a separate scheme for CISM. Any improvements to CLM are applied to ice sheets automatically.

3. The atmosphere model can respond during runtime to ice-sheet surface changes (even in the absence of two-way feedbacks with CISM). As shown by *Pritchard et al. (2008)*, runtime albedo feedback from the ice sheet is critical for simulating ice-sheet retreat on paleoclimate time scales. Without this feedback the atmosphere warms much less, and the retreat is delayed.

4. The improved SMB is potentially available in CLM for all glaciated grid cells (e.g., in the Alps, Rockies, Andes, and Himalayas), not just those which are part of ice sheets.

In typical runs, CISM is not evolving; CLM computes the SMB and sends it to CISM, but CISM's ice sheet geometry remains fixed over the course of the run. In these runs, CISM serves two roles in the system:

1. Over the CISM domain (typically Greenland in CESM2), CISM dictates glacier areas and topographic elevations, overriding the values on CLM's surface dataset. CISM also dictates the elevation of non-glacier land units in its domain, and only in this domain are atmospheric fields downscaled to non-glacier land units. (So if you run with a stub glacier model - SGLC - then glacier areas and elevations will be taken entirely from CLM's surface dataset, and no downscaling will be done over non-glacier land units.)

2. CISM provides the grid onto which SMB is downscaled. (If you run with SGLC then SMB will still be computed in CLM, but it won't be downscaled to a high-resolution ice sheet grid.)

It is also possible to run CESM with an evolving ice sheet. In this case, CLM responds to CISM's evolution by adjusting the areas of the glacier land unit and each elevation class within this land unit, as well as the mean topographic heights of each elevation class. Thus, CLM's glacier areas and elevations remain in sync with CISM's. Conservation of mass and energy is done as for other landcover change (see Chapter 27).

13.3 Glacier regions and their behaviors

The world's glaciers and ice sheets are broken down into a number of different regions (four by default) that differ in three respects:

1. Whether the gridcell's glacier land unit contains:

   a. Multiple elevation classes (section 13.4)

   b. Multiple elevation classes plus virtual elevation classes

   c. Just a single elevation class whose elevation matches the atmosphere's topographic height (so there is no adjustment in atmospheric forcings due to downscaling).

2. Treatment of glacial melt water:

a. Glacial melt water runs off and is replaced by ice, thus keeping the column always frozen. In the absence of a dynamic ice sheet model, this behavior implicitly assumes an infinite store of glacial ice that can be melted (with appropriate adjustments made to ensure mass and energy conservation). This behavior is discussed in more detail in section 13.5.

b. Glacial melt water remains in place until it refreezes - possibly remaining in place indefinitely if the glacier column is in a warm climate. With this behavior, ice melt does not result in any runoff. Regions with this behavior cannot compute SMB, because negative SMB would be meaningless (due to the liquid water on top of the ice column). This behavior produces less realistic glacier physics. However, it avoids the negative ice runoff that is needed for the "replaced by ice" behavior to conserve mass and energy (as described in section 13.5). Thus, in regions where CLM has glaciers but the atmospheric forcings are too warm to sustain those glaciers, this behavior avoids persistent negative ice runoff. This situation can often occur for mountain glaciers, where topographic smoothing in the atmosphere results in a too-warm climate. There, avoiding persistent negative ice runoff can be more important than getting the right glacier ice physics.

3. Treatment of ice runoff from snow capping (as described in section 7.6). Note that this is irrelevant in regions with an evolving, two-way-coupled ice sheet (where the snow capping term is sent to CISM rather than running off):

   a. Ice runoff from snow capping remains ice. This is a crude parameterization of iceberg calving, and so is appropriate in regions where there is substantial iceberg calving in reality.

   b. Ice runoff from snow capping is melted (generating a negative sensible heat flux) and runs off as liquid. This matches the behavior for non-glacier columns. This is appropriate in regions that have little iceberg calving in reality. This can be important to avoid unrealistic cooling of the ocean and consequent runaway sea ice growth.

The default behaviors for the world's glacier and ice sheet regions are described in Table 13.1. Note that the standard CISM grid covers Greenland plus enough surrounding area to allow for ice sheet growth and to have a regular rectangular grid. We need to have the "replaced by ice" melt behavior within the CISM domain in order to compute SMB there, and we need virtual elevation classes in that domain in order to compute SMB for all elevation classes and to facilitate glacial advance and retreat in the two-way-coupled case. However, this domain is split into Greenland itself and areas outside Greenland so that ice runoff in the Canadian archipelago (which is inside the CISM domain) is melted before reaching the ocean, to avoid runaway sea ice growth in that region.

Table 13.1: Glacier region behaviors

Region	Elevation classes	Glacial melt	Ice runoff
Greenland	Virtual	Replaced by ice	Remains ice
Inside standard CISM grid but outside Greenland itself	Virtual	Replaced by ice	Melted
Antarctica	Multiple	Replaced by ice	Remains ice
All others	Single	Remains in place	Melted

Note: In regions that have both the `Glacial melt = Replaced by ice` and the `Ice runoff = Melted` behaviors (by default, this is just the region inside the standard CISM grid but outside Greenland itself): During periods of glacial melt, a negative ice runoff is generated (due to the `Glacial melt = Replaced by ice` behavior); this negative ice runoff is converted to a negative liquid runoff plus a positive sensible heat flux (due to the `Ice runoff = Melted` behavior). We recommend that you limit the portion of the globe with both of these behaviors combined, in order to avoid having too large of an impact of this non-physical behavior.

13.4 Multiple elevation class scheme

The glacier land unit contains multiple columns based on surface elevation. These are known as elevation classes, and the land unit is referred to as *glacier_mec*. (As described in section 13.3, some regions have only a single elevation class, but they are still referred to as *glacier_mec* land units.) The default is to have 10 elevation classes whose lower limits are 0, 200, 400, 700, 1000, 1300, 1600, 2000, 2500, and 3000 m. Each column is characterized by a fractional area and surface elevation that are read in during model initialization, and then possibly overridden by CISM as the run progresses. Each *glacier_mec* column within a grid cell has distinct ice and snow temperatures, snow water content, surface fluxes, and SMB.

The atmospheric surface temperature, potential temperature, specific humidity, density, and pressure are downscaled from the atmosphere's mean grid cell elevation to the *glacier_mec* column elevation using a specified lapse rate (typically 6.0 deg/km) and an assumption of uniform relative humidity. Longwave radiation is downscaled by assuming a linear decrease in downwelling longwave radiation with increasing elevation (0.032 W m^{-2} m^{-1}, limited to 0.5 - 1.5 times the gridcell mean value, then normalized to conserve gridcell total energy) *(Van Tricht et al., 2016)*. Total precipitation is partitioned into rain vs. snow as described in Chapter 2. The partitioning of precipitation is based on the downscaled temperature, allowing rain to fall at lower elevations while snow falls at higher elevations.

This downscaling allows lower-elevation columns to undergo surface melting while columns at higher elevations remain frozen. This gives a more accurate simulation of summer melting, which is a highly nonlinear function of air temperature.

Within the CISM domain, this same downscaling procedure is also applied to all non-urban land units. The elevation of non-glacier land units is taken from the mean elevation of ice-free grid cells in CISM. This is done in order to keep the glaciated and non-glaciated portions of the CISM domain as consistent as possible.

In contrast to most CLM subgrid units, glacier_mec columns can be active (i.e., have model calculations run there) even if their area is zero. These are known as "virtual" columns. This is done because the ice sheet model may require a SMB for some grid cells where CLM has zero glacier area in that elevation range. Virtual columns also facilitate glacial advance and retreat in the two-way coupled case. Virtual columns do not affect energy exchange between the land and the atmosphere.

13.5 Computation of the surface mass balance

This section describes the computation of surface mass balance and associated runoff terms. The description here only applies to regions where glacial melt runs off and is replaced by ice, not to regions where glacial melt remains in place. Thus, by default, this only applies to Greenland and Antarctica, not to mountain glaciers elsewhere in the world. (See also section 13.3.)

The SMB of a glacier or ice sheet is the net annual accumulation/ablation of mass at the upper surface. Ablation is defined as the mass of water that runs off to the ocean. Not all the surface meltwater runs off; some of the melt percolates into the snow and refreezes. Accumulation is primarily by snowfall and deposition, and ablation is primarily by melting and evaporation/sublimation. CLM uses a surface-energy-balance (SEB) scheme to compute the SMB. In this scheme, the melting depends on the sum of the radiative, turbulent, and conductive fluxes reaching the surface, as described elsewhere in this document.

Note that the SMB typically is defined as the total accumulation of ice and snow, minus the total ablation. The SMB flux passed to CISM is the mass balance for ice alone, not snow. We can think of CLM as owning the snow, whereas CISM owns the underlying ice. Fluctuations in snow depth between 0 and 10 m water equivalent are not reflected in the SMB passed to CISM. In transient runs, this can lead to delays of a few decades in the onset of accumulation or ablation in a given glacier column.

SMB is computed and sent to the CESM coupler regardless of whether and where CISM is operating. However, the effect of SMB terms on runoff fluxes differs depending on whether and where CISM is evolving in two-way-coupled mode. This is described by the variable *glc_dyn_runoff_routing*. (This is real-valued in the code to handle the edge

case where a CLM grid cell partially overlaps with the CISM grid, but we describe it as a logical variable here for simplicity.) In typical cases where CISM is not evolving, *glc_dyn_runoff_routing* will be false everywhere; in these cases, CISM's mass is not considered to be part of the coupled system. In cases where CISM is evolving and sending its own calving flux to the coupler, *glc_dyn_runoff_routing* will be true over the CISM domain and false elsewhere.

Any snow capping (section 7.6) is added to $q_{ice,frz}$. Any liquid water (i.e., melted ice) below the snow pack in the glacier column is added to $q_{ice,melt}$, then is converted back to ice to maintain a pure-ice column. Then the total SMB is given by $q_{ice,tot}$:

$$q_{ice,tot} = q_{ice,frz} - q_{ice,melt} \tag{13.1}$$

CLM is responsible for generating glacial surface melt, even when running with an evolving ice sheet. Thus, $q_{ice,melt}$ is always added to liquid runoff (q_{rgwl}), regardless of *glc_dyn_runoff_routing*. However, the ice runoff flux depends on *glc_dyn_runoff_routing*. If *glc_dyn_runoff_routing* is true, then CISM controls the fate of the snow capping mass in $q_{ice,frz}$ (e.g., eventually transporting it to lower elevations where it can be melted or calved). Since CISM will now own this mass, the snow capping flux does *not* contribute to any runoff fluxes generated by CLM in this case.

If *glc_dyn_runoff_routing* is false, then CLM sends the snow capping flux as runoff, as a crude representation of ice calving (see also sections 7.6 and 13.3). However, this ice runoff flux is reduced by $q_{ice,melt}$. This reduction is needed for conservation; its need is subtle, but can be understood with either of these explanations:

- When ice melts, we let the liquid run off and replace it with new ice. That new ice needs to come from somewhere to keep the coupled system in water balance. We "request" the new ice from the ocean by generating a negative ice runoff equivalent to the amount we have melted.

- Ice melt removes mass from the system, as it should. But the snow capping flux also removes mass from the system. The latter is a crude parameterization of calving, assuming steady state - i.e., all ice gain is balanced by ice loss. This removal of mass due to both accumulation and melt represents a double-counting. Each unit of melt indicates that one unit of accumulation should not have made it to the ocean as ice, but instead melted before it got there. So we need to correct for this double-counting by removing one unit of ice runoff for each unit of melt.

For a given point in space or time, this reduction can result in negative ice runoff. However, when integrated over space and time, for an ice sheet that is near equilibrium, this just serves to decrease the too-high positive ice runoff from snow capping. (The treatment of snow capping with *glc_dyn_runoff_routing* false is based on this near-equilibrium assumption - i.e., that ice accumulation is roughly balanced by $calving + melt$, integrated across space and time. For glaciers and ice sheets that violate this assumption, either because they are far out of equilibrium with the climate or because the model is being run for hundreds of years, there are two ways to avoid the unrealistic ice runoff from snow capping: by running with an evolving, two-way-coupled ice sheet or by changing a glacier region's ice runoff behavior as described in section 13.3.)

In regions where SMB is computed for glaciers, SMB is also computed for the natural vegetated land unit. Because there is no ice to melt in this land unit, it can only generate a zero or positive SMB. A positive SMB is generated once the snow pack reaches its maximum depth. When running with an evolving ice sheet, this condition triggers glacial inception.

CHAPTER 14

MODEL FOR SCALE ADAPTIVE RIVER TRANSPORT (MOSART)

14.1 Overview

MOSART is a river transport model designed for applications across local, regional and global scales *(Li et al., 2013b)*. A major purpose of MOSART is to provide freshwater input for the ocean model in coupled Earth System Models. MOSART also provides an effective way of evaluating and diagnosing the soil hydrology simulated by land surface models through direct comparison of the simulated river flow with observations of natural streamflow at gauging stations *(Li et al., 2015a)*. Moreover, MOSART provides a modeling framework for representing riverine transport and transformation of energy and biogeochemical fluxes under both natural and human-influenced conditions (*(Li et al., 2015b)*.

14.2 Routing Processes

MOSART divides each spatial unit such as a lat/lon grid or watershed into three categories of hydrologic units (as shown in Figure **??**): hillslopes that convert both surface and subsurface runoff into tributaries, tributaries that discharge into a single main channel, and the main channel that connects the local spatial unit with upstream/downstream units through the river network. MOSART assumes that all the tributaries within a spatial unit can be treated as a single hypothetical sub-network channel with a transport capacity equivalent to all the tributaries combined. Correspondingly, three routing processes are represented in MOSART: 1) hillslope routing: in each spatial unit, surface runoff is routed as overland flow into the sub-network channel, while subsurface runoff generated in the spatial unit directly enters the sub-network channel; 2) sub-network channel routing: the sub-network channel receives water from the hillslopes, routes water through the channel and discharges it into the main channel; 3) main channel routing: the main channel receives water from the sub-network channel and/or inflow, if any, from the upstream spatial units, and discharges the water to its downstream spatial unit or the ocean.

MOSART only routes positive runoff, although negative runoff can be generated occasionally by the land model (e.g., q_{gwl}). Negative runoff in any runoff component including q_{sur}, q_{sub}, q_{gwl} is not routed through MOSART, but instead is mapped directly from the spatial unit where it is generated at any time step to the coupler.
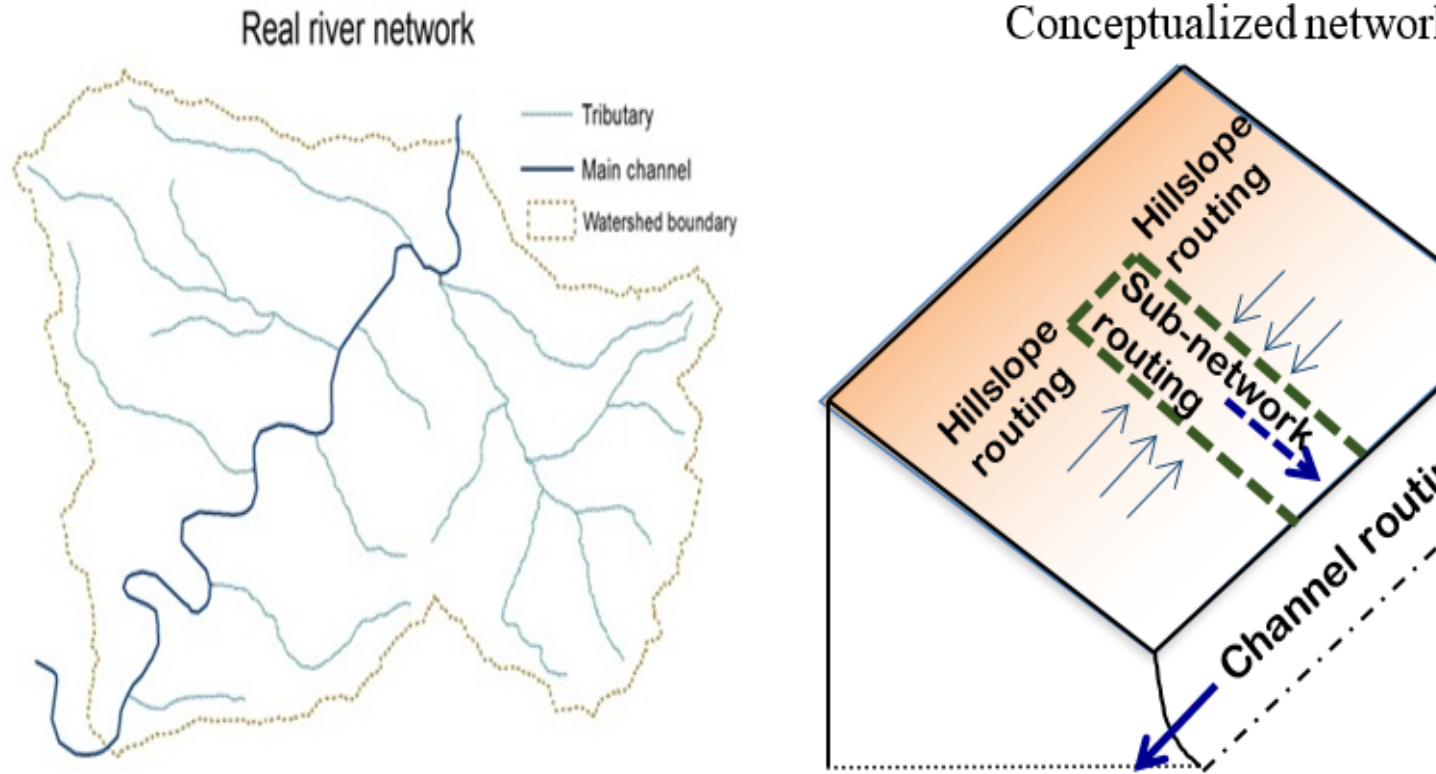
In MOSART, the travel velocities of water across hillslopes, sub-network and main channel are all estimated using Manning's equation with different levels of simplifications. Generally the Manning's equation is in the form of

$$V = \frac{R^{\frac{2}{3}} S_f}{n} \tag{14.1}$$

where V is the travel velocity (m s $^{-1}$), R is the hydraulic radius (m). S_f is the friction slope that accounts for the effects of gravity, friction, inertia and other forces on the water. If the channel slope is steep enough, the gravity force dominates over the others so one can approximate S_f by the channel bed slope S , which is the key assumption underpinning the kinematic wave method. n is the Manning's roughness coefficient, which is mainly controlled by surface roughness and sinuosity of the flow path.

If the water surface is sufficiently large or the water depth h is sufficiently shallow, the hydraulic radius can be approximated by the water depth. This is the case for both hillslope and sub-network channel routing.

$$R_h = h_h R_t = h_t \tag{14.2}$$

Here R_h (m) and R_t (m) are hydraulic radius for hillslope and sub-network channel routing respectively, and h_h (m) and h_t (m) are water depth during hillslope and sub-network channel routing respectively.

For the main channel, the hydraulic radius is given by

$$R_r = \frac{A_r}{P_r} \tag{14.3}$$

where A_r (m ^{2}) is the wetted area defined as the part of the channel cross-section area below the water surface, P_r (m) is the wetted perimeter, the perimeter confined in the wetted area.

For hillslopes, sub-network and main channels, a common continuity equation can be written as

$$\frac{dS}{dt} = Q_{in} - Q_{out} + R \tag{14.4}$$

where Q_{in} (m ^{3} s $^{-1}$) is the main channel flow from the upstream grid(s) into the main channel of the current grid, which is zero for hillslope and sub-network routing. Q_{out} (m ^{3} s $^{-1}$) is the outflow rate from hillslope into the sub-network, from the sub-network into the main channel, or from the current main channel to the main channel of its downstream grid (if not the outlet grid) or ocean (if the current grid is the basin outlet). R (m ^{3} s $^{-1}$) is a source term, which could be the surface runoff generation rate for hillslopes, or lateral inflow (from hillslopes) into sub-network channel or water-atmosphere exchange fluxes such as precipitation and evaporation. It is assumed that surface runoff is generated uniformly across all the hillslopes. Currently, MOSART does not exchange water with the atmosphere or return water to the land model so its function is strictly to transport water from runoff generation through the hillslope, tributaries, and main channels to the basin outlets.

14.3 Numerical Solution

The numerical implementation of MOSART is mainly based on a subcycling scheme and a local time-stepping algorithm. There are two levels of subcycling. For convenience, we denote T_{inputs} (s), T_{mosart} (s), $T_{hillslope}$ (s) and $T_{channel}$ (s) as the time steps of runoff inputs (from CLM to MOSART via the flux coupler), MOSART routing, hillslope routing, and channel routing, respectively. The first level of subcycling is between the runoff inputs and MOSART routing. If T_{inputs} is 10800s and T_{mosart} is 3600s, three MOSART time steps will be invoked each time the runoff inputs are updated. The second level of subcycling is between the hillslope routing and channel routing. This is to account for the fact that the travel velocity of water across hillslopes is usually much slower than that in the channels. $T_{hillslope}$ is usually set as the same as T_{mosart}, but within each time step of hillslope routing there are a few time steps for channel routing, i.e., $T_{hillslope} = D_{levelH2R} \cdot T_{channel}$. The local time-stepping algorithm is to account for the fact that the travel velocity of water is much faster in some river channels (e.g., with steeper bed slope, narrower channel width) than others. That is, for each channel (either a sub-network or main channel), the final time step of local channel routing is given as $T_{local} = T_{channel}/D_{local}$. D_{local} is currently estimated empirically as a function of local channel slope, width, length and upstream drainage area. If MOSART crashes due to a numerical issue, we recommend increasing $D_{levelH2R}$ and, if the issue remains, reducing T_{mosart}.

14.4 Parameters and Input Data

MOSART is supported by a comprehensive, global hydrography dataset at 0.5 ^{o} resolution. As such, the fundamental spatial unit of MOSART is a 0.5 ^{o} lat/lon grid. The topographic parameters (such as flow direction, channel length, topographic and channel slopes, etc.) were derived using the Dominant River Tracing (DRT) algorithm (*Wu et al., 2011* ; *Wu et al. 2012*). The DRT algorithm produces the topographic parameters in a scale-consistent way to preserve/upscale the key features of a baseline high-resolution hydrography dataset at multiple coarser spatial resolutions. Here the baseline high-resolution hydrography dataset is the 1km resolution Hydrological data and maps based on SHuttle Elevation Derivatives at multiple Scales (HydroSHEDS) (*Lehner and Döll, 2004* ; *Lehner et al., 2008*). The channel geometry parameters, e.g., bankfull width and depth, were estimated from empirical hydraulic geometry relationships as functions of the mean annual discharge. The Manning roughness coefficients for overland and channel flow were calculated as functions of landcover and water depth. For more details on the methodology to derive channel geometry and the Manning's roughness coefficients, please refer to *Getirana et al. (2012)* . The full list of parameters included in this global hydrography dataset is provided in Table 14.1. Evaluation of global simulations by MOSART using the aforementioned parameters is described in *Li et al. (2015b)* .

Table 14.1: List of parameters in the global hydrography dataset

Name	Unit	Description
F_{dir}	-	The D8 single flow direction for each coarse grid cell coded using 1 (E), 2 (SE), 4 (S), 8 (SW), 16 (W), 32 (NW), 64 (N), 128 (NE)
A_{total}	km^2	The upstream drainage area of each coarse grid cell
F_{dis}	m	The dominant river length for each coarse grid cell
$S_{channel}$	-	The average channel slope for each coarse grid cell
$S_{topographic}$	-	The average topographic slope (for overland flow routing) for each coarse grid cell
A_{local}	km^2	The surface area for each coarse grid cell
D_p	m^{-1}	Drainage density, calculated as the total channel length within each coarse grid cell divided by the local cell area
D_r	m	The bankfull depth of main channel
W_r	m	The bankfull width of main channel
D_t	m	The average bankfull depth of tributary channels
W_t	m	The average bankfull width of tributary channels
n_r	-	Manning's roughness coefficient for channel flow routing
n_h	-	Manning's roughness coefficient for overland flow routing

14.5 Difference between CLM5.0 and CLM4.5

1. Routing methods: RTM, a linear reservoir method, is used in CLM4.5 for river routing, whilst in CLM5.0, MOSART is an added option for river routing based on the more physically-based kinematic wave method.

2. Runoff treatment: In RTM runoff is routed regardless of its sign so negative streamflow can be simulated at times. MOSART routes only non-negative runoff and always produces positive streamflow, which is important for future extensions to model riverine heat and biogeochemical fluxes.

3. Input parameters: RTM in CLM4.5 only requires one layer of a spatially varying variable of channel velocity, whilst MOSART in CLM5.0 requires 13 parameters that are all available globally at 0.5 ° resolution.

4. Outputs: RTM only produces streamflow simulation, whilst MOSART additionally simulates the time-varying channel velocities, channel water depth, and channel surface water variations.

CHAPTER 15

URBAN MODEL (CLMU)

At the global scale, and at the coarse spatial resolution of current climate models, urbanization has negligible impact on climate. However, the urban parameterization (CLMU; *Oleson et al. (2008b)*; *Oleson et al. (2008c)*) allows simulation of the urban environment within a climate model, and particularly the temperature where people live. As such, the urban model allows scientific study of how climate change affects the urban heat island and possible urban planning and design strategies to mitigate warming (e.g., white roofs).

Urban areas in CLM are represented by up to three urban landunits per gridcell according to density class. The urban landunit is based on the "urban canyon" concept of *Oke (1987)* in which the canyon geometry is described by building height (H) and street width (W) (Figure 15.1). The canyon system consists of roofs, walls, and canyon floor. Walls are further divided into shaded and sunlit components. The canyon floor is divided into pervious (e.g., to represent residential lawns, parks) and impervious (e.g., to represent roads, parking lots, sidewalks) fractions. Vegetation is not explicitly modeled for the pervious fraction; instead evaporation is parameterized by a simplified bulk scheme.

Each of the five urban surfaces is treated as a column within the landunit (Figure 15.1). Radiation parameterizations account for trapping of solar and longwave radiation inside the canyon. Momentum fluxes are determined for the urban landunit using a roughness length and displacement height appropriate for the urban canyon and stability formulations from CLM. A one-dimensional heat conduction equation is solved numerically for a multiple-layer ($N_{levurb} = 10$) column to determine conduction fluxes into and out of canyon surfaces.

A new building energy model has been developed for CLM5.0. It accounts for the conduction of heat through interior surfaces (roof, sunlit and shaded walls, and floors), convection (sensible heat exchange) between interior surfaces and building air, longwave radiation exchange between interior surfaces, and ventilation (natural infiltration and exfiltration). Idealized HAC systems are assumed where the system capacity is infinite and the system supplies the amount of energy needed to keep the indoor air temperature (T_{iB}) within maximum and minimum emperatures ($T_{iB, \max}$, $T_{iB, \min}$), thus explicitly resolving space heating and air conditioning fluxes. Anthropogenic sources of waste heat ($Q_{H, waste}$) from HAC that account for inefficiencies in the heating and air conditioning equipment and from energy lost in the conversion of primary energy sources to end use energy are derived from *Sivak (2013)*. These sources of waste heat are incorporated as modifications to the canyon energy budget.

Turbulent [sensible heat ($Q_{H, u}$) and latent heat ($Q_{E, u}$)] and storage ($Q_{S, u}$) heat fluxes and surface ($T_{u, s}$) and internal ($T_{u, i=1, N_{levgrnd}}$) temperatures are determined for each urban surface u. Hydrology on the roof and canyon floor is simulated and walls are hydrologically inactive. A snowpack can form on the active surfaces. A certain amount of liquid water is allowed to pond on these surfaces which supports evaporation. Water in excess of the maximum ponding depth runs off (R_{roof}, $R_{imprvrd}$, R_{prvrd}).

The heat and moisture fluxes from each surface interact with each other through a bulk air mass that represents air in the urban canopy layer for which specific humidity (q_{ac}) and temperature (T_{ac}) are prognosed (Figure 15.2). The air temperature can be compared with that from surrounding vegetated/soil (rural) surfaces in the model to ascertain heat island characteristics. As with other landunits, the CLMU is forced either with output from a host atmospheric model (e.g., the Community Atmosphere Model (CAM)) or observed forcing (e.g., reanalysis or field observations). The urban model produces sensible, latent heat, and momentum fluxes, emitted longwave, and reflected solar radiation, which are area-averaged with fluxes from non-urban "landunits" (e.g., vegetation, lakes) to supply grid cell averaged fluxes to the atmospheric model.

Present day global urban extent and urban properties were developed by *Jackson et al. (2010)*. Urban extent, defined for four classes [tall building district (TBD), and high, medium, and low density (HD, MD, LD)], was derived from LandScan 2004, a population density dataset derived from census data, nighttime lights satellite observations, road proximity, and slope (*Dobson et al. 2000*). The urban extent data for TBD, HD, and MD classes are aggregated from the original 1 km resolution to both a 0.05º by 0.05º global grid for high-resolution studies or a 0.5º by 0.5º grid. For the current implementation, the LD class is not used because it is highly rural and better modeled as a vegetated/soil surface. Although the TBD, HD, and MD classes are represented as individual urban landunits, urban model history output is currently a weighted average of the output for individual classes.

For each of 33 distinct regions across the globe, thermal (e.g., heat capacity and thermal conductivity), radiative (e.g., albedo and emissivity) and morphological (e.g., height to width ratio, roof fraction, average building height, and pervious fraction of the canyon floor) properties are provided for each of the density classes. Building interior minimum and maximum temperatures are prescribed based on climate and socioeconomic considerations. The surface dataset creation routines (see CLM5.0 User's Guide) aggregate the data to the desired resolution.

An optional urban properties dataset, including a tool that allows for generating future urban development scenarios is also available (*Oleson and Feddema (2018)*). This will become the default dataset in future model versions. As described in *Oleson and Feddema (2018)* the urban properties dataset in *Jackson et al. (2010)* was modified with respect to wall and roof thermal properties to correct for biases in heat transfer due to layer and building type averaging. Further changes to the dataset reflect the need for scenario development, thus allowing for the creation of hypothetical wall types, and the easier interchange of wall facets. The new urban properties tool is available as part of the Toolbox for Human-Earth System Integration & Scaling (THESIS) tool set (http://www.cgd.ucar.edu/iam/projects/thesis/thesis-urbanproperties-tool.html; *Feddema and Kauffman (2016)*). The driver script (urban_prop.csh) specifies three input csv files (by default, mat_prop.csv, lam_spec.csv, and city_spec.csv; (Figure 15.3)) that describe the morphological, radiative, and thermal properties of urban areas, and generates a global dataset at 0.05° latitude by longitude in NetCDF format (urban_properties_data.05deg.nc). A standalone NCL routine (gen_data_clm.ncl) can be run separately after the mksurfdata_map tool creates the CLM surface dataset. This creates a supplementary streams file of setpoints for the maximum interior building temperature at yearly time resolution.

The urban model that was first released as a component of CLM4.0 is separately described in the urban technical note (*Oleson et al. (2010b)*). The main changes in the urban model from CLM4.0 to CLM4.5 were 1) an expansion of the single urban landunit to up to three landunits per grid cell stratified by urban density types, 2) the number of urban layers for roofs and walls was no longer constrained to be equal to the number of ground layers, 3) space heating and air conditioning wasteheat factors were set to zero by default so that the user could customize these factors for their own application, 4) the elevation threshold used to eliminate urban areas in the surface dataset creation routines was increased from 2200 meters to 2600 meters, 5) hydrologic and thermal calculations for the pervious road followed CLM4.5 parameterizations.

The main changes in the urban model from CLM4.5 to CLM5.0 are 1) a more sophisticated and realistic building space heating and air conditioning submodel that prognoses interior building air temperature and includes more realistic space heating and air conditioning wasteheat factors (see above), 2) the maximum building temperature (which determines air conditioning demand) is now read in from a namelist-defined file which allows for dynamic control of this input variable. The maximum building temperatures that are defined in *Jackson et al. (2010)* are implemented in year 1950 (thus air conditioning is off in prior years) and air conditioning is turned off in year 2100 (because the buildings are not suitable for air conditioning in some extreme global warming scenarios), 3) an optional updated urban properties dataset and new scenario tool. These features are described in more detail in *Oleson and Feddema (2018)*. In addition, a module of heat stress indices calculated online in the model that can be used to assess human
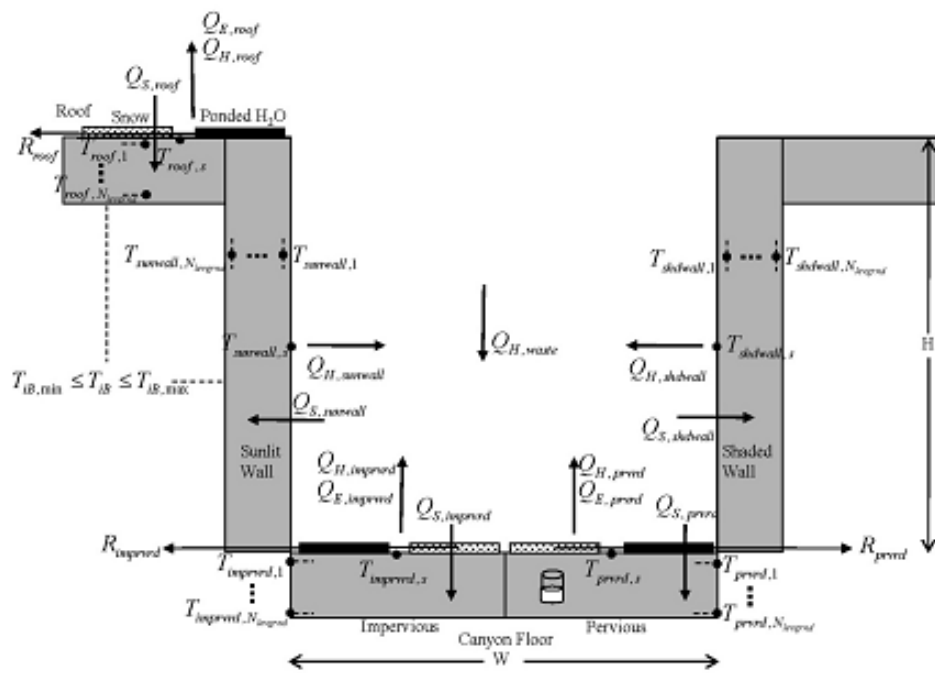
Figure 15.1: Schematic representation of the urban land unit. See the text for description of notation. Incident, reflected, and net solar and longwave radiation are calculated for each individual surface but are not shown for clarity.
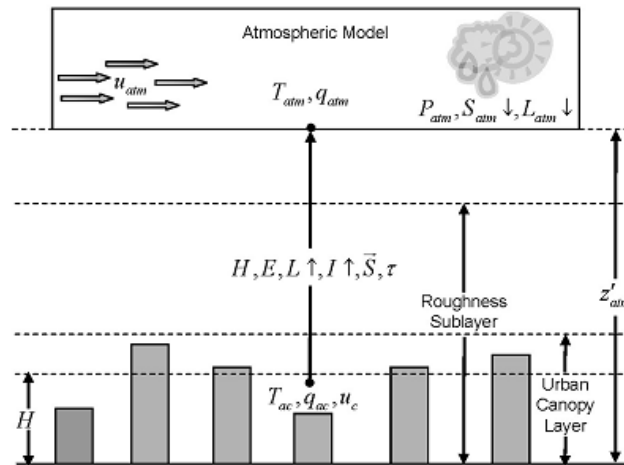
Figure 15.2: Schematic of urban and atmospheric model coupling. The urban model is forced by the atmospheric model wind (u_{atm}), temperature (T_{atm}), specific humidity (q_{atm}), precipitation (P_{atm}), solar ($S_{atm} \downarrow$) and long-wave ($L_{atm} \downarrow$) radiation at reference height z'_{atm} (section 2.3.1). Fluxes from the urban landunit to the atmosphere are turbulent sensible (H) and latent heat (λE), momentum (τ), albedo ($I \uparrow$), emitted longwave ($L \uparrow$), and absorbed shortwave ($\vec{S}$) radiation. Air temperature (T_{ac}), specific humidity (q_{ac}), and wind speed (u_c) within the urban canopy layer are diagnosed by the urban model. H is the average building height.

Figure 15.3: Schematic of THESIS urban properties tool. Executable scripts are in orange, input files are blue, and output files are green. Items within the black box outline are either read in as input, executed, or output by the driver script (urban_prop.csh).

thermal comfort for rural and urban areas has been added. This last development is described and evaluated by *Buzan et al. (2015)*.

CHAPTER 16

CN POOLS

16.1 Introduction

CLM includes a prognostic treatment of the terrestrial carbon and nitrogen cycles including natural vegetation, crops, and soil biogeochemistry. The model is fully prognostic with respect to all carbon and nitrogen state variables in the vegetation, litter, and soil organic matter. The seasonal timing of new vegetation growth and litterfall is also prognostic, responding to soil and air temperature, soil water availability, daylength, and crop management practices in varying degrees depending on a specified phenology type or management for each PFT (Chapter 20). The prognostic LAI, SAI, tissue stoichiometry, and vegetation heights are utilized by the biophysical model that couples carbon, water, and energy cycles.

Separate state variables for C and N are tracked for leaf, live stem, dead stem, live coarse root, dead coarse root, fine root, and grain pools (Figure 16.1). Each of these pools has two corresponding storage pools representing, respectively, short-term and long-term storage of non-structural carbohydrates and labile nitrogen. There are two additional carbon pools, one for the storage of growth respiration reserves, and another used to meet excess demand for maintenance respiration during periods with low photosynthesis. One additional nitrogen pool tracks retranslocated nitrogen, mobilized from leaf tissue prior to abscission and litterfall. Altogether there are 23 state variables for vegetation carbon, and 22 for vegetation nitrogen.

In addition to the vegetation pools, CLM includes a series of decomposing carbon and nitrogen pools as vegetation successively breaks down to CWD, and/or litter, and subsequently to soil organic matter. Discussion of the decomposition model, alternate specifications of decomposition rates, and methods to rapidly equilibrate the decomposition model, is in Chapter 21.

16.2 Tissue Stoichiometry

As of CLM5, vegetation tissues have a flexible stoichiometry, as described in *Ghimire et al. (2016)*. Each tissue has a target C:N ratio, with the target leaf C:N varying by plant functional type (see Table 16.1), and nitrogen is allocated at each timestep in order to allow the plant to best match the target stoichiometry. Nitrogen downregulation of productivity acts by increasing the C:N ratio of leaves when insufficient nitrogen is available to meet stoichiometric demands of leaf growth, thereby reducing the N available for photosynthesis and reducing the $V_{c,max25}$ and J_{max25} terms, as described in Chapter 10. Details of the flexible tissue stoichiometry are described in Chapter 19.
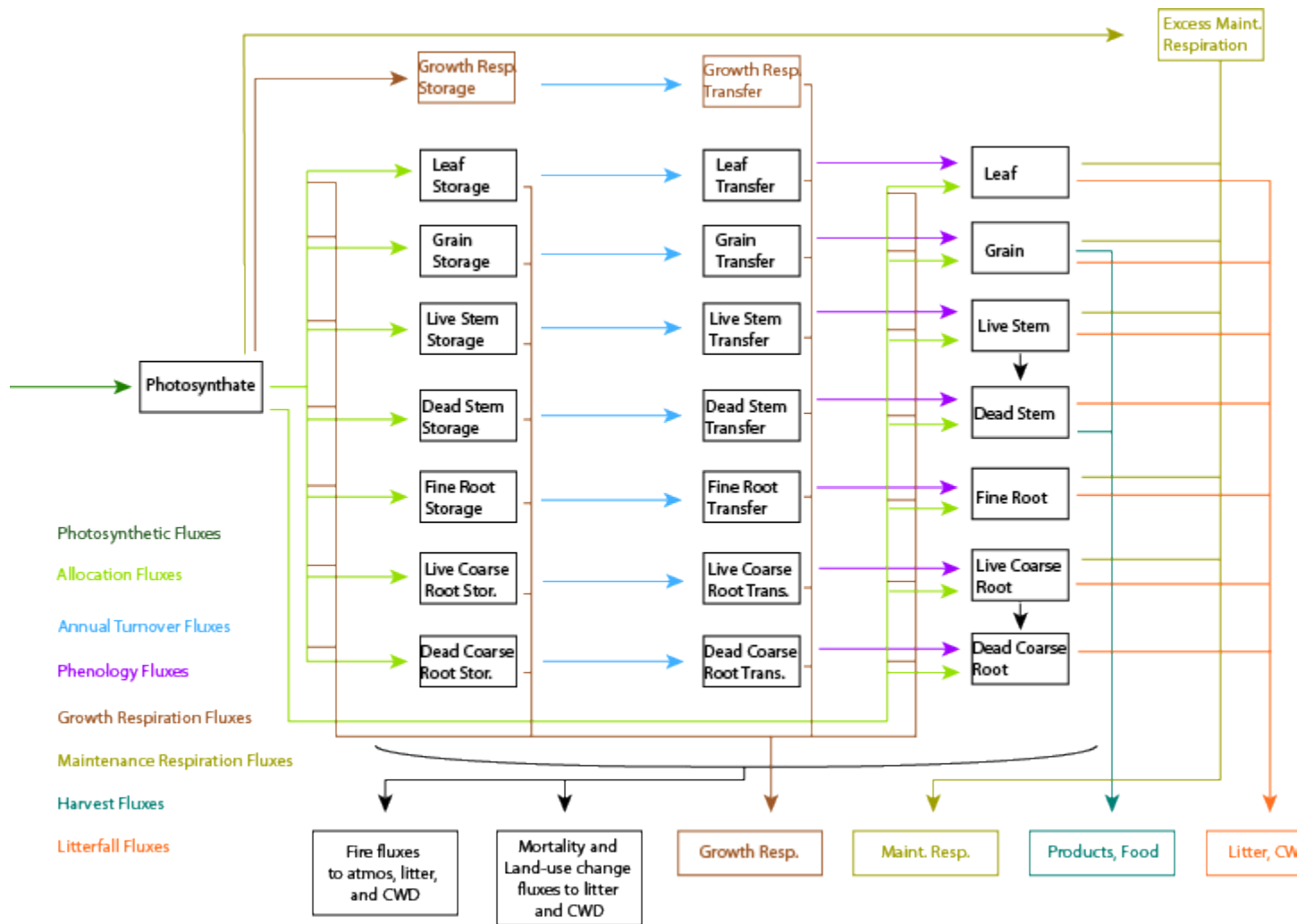
Figure 16.1: Vegetation fluxes and pools for carbon cycle in CLM5.

Table 16.1: Plant functional type (PFT) target C:N parameters.

PFT	target leaf C:N
NET Temperate	58.00
NET Boreal	58.00
NDT Boreal	25.81
BET Tropical	29.60
BET temperate	29.60
BDT tropical	23.45
BDT temperate	23.45
BDT boreal	23.45
BES temperate	36.42
BDS temperate	23.26
BDS boreal	23.26
C_3 arctic grass	28.03
C_3 grass	28.03
C_4 grass	35.36
Temperate Corn	25.00
Spring Wheat	20.00
Temperate Soybean	20.00
Cotton	20.00
Rice	20.00
Sugarcane	25.00
Tropical Corn	25.00
Tropical Soybean	20.00

CHAPTER 17

PLANT RESPIRATION

CLM5 includes changes to plant respiration including

- A new leaf respiration algorithm based on Atkin et al. (2016)
- A lower growth respiration coefficient, based on Atkin et al. (2017)

17.1 Autotrophic Respiration

The model treats maintenance and growth respiration fluxes separately, even though it is difficult to measure them as separate fluxes (Lavigne and Ryan, 1997; Sprugel et al., 1995). Maintenance respiration is defined as the carbon cost to support the metabolic activity of existing live tissue, while growth respiration is defined as the additional carbon cost for the synthesis of new growth.

17.1.1 Maintenance Respiration

Atkin et al. (2016) propose a model for leaf respiration that is based on the leaf nitrogen content per unit area (NS_{narea} (gN m ^{2} leaf), with an intercept parameter that is PFT dependant, and an acclimation term that depends upon the average temperature of the previous 10 day period $t_{2m,10days}$, in Celsius.

$$CF_{mr\_leaf} = i_{atkin,pft} + (NS_{narea}0.2061) - (0.0402(t_{2m,10days})) \qquad (17.1)$$

The temperature dependance of leaf maintenance (dark) respiration is described in Chapter 9.

$$CF_{mr\_livestem\_} = NS_{livestem}MR_{base}MR_{Q10}^{(T_{2m}-20)/10} \qquad (17.2)$$

$$CF_{mr\_livecroot\_} = NS_{livecroot}MR_{base}MR_{Q10}^{(T_{2m}-20)/10} \qquad (17.3)$$

$$CF_{mr\_froot\_} = \sum_{j=1}^{nlevsoi} NS_{froot}rootfr_jMR_{base}MR_{Q10}^{(Ts_j-20)/10} \qquad (17.4)$$

where MR_{q10} (= 2.0) is the temperature sensitivity for maintenance respiration, T_{2m} (ºC) is the air temperature at 2m height, Ts_jC) is the soil temperature at level j, and $rootfr_j$ is the fraction of fine roots distributed in soil level j.

Table 17.1: Atkin leaf respiration model intercept values.

Plant functional type	i_{atkin}
NET Temperate	1.499
NET Boreal	1.499
NDT Boreal	1.499
BET Tropical	1.756
BET temperate	1.756
BDT tropical	1.756
BDT temperate	1.756
BDT boreal	1.756
BES temperate	2.075
BDS temperate	2.075
BDS boreal	2.075
C_3 arctic grass	2.196
C_3 grass	2.196
C_4 grass	2.196

Note that, for woody vegetation, maintenance respiration costs are not calculated for the dead stem and dead coarse root components. These components are assumed to consist of dead xylem cells, with no metabolic function. By separating the small live component of the woody tissue (ray parenchyma, phloem, and sheathing lateral meristem cells) from the larger fraction of dead woody tissue, it is reasonable to assume a common base maintenance respiration rate for all live tissue types.

The total maintenance respiration cost is then given as:

$$CF_{mr} = CF_{mr\_leaf} + CF_{mr\_froot} + CF_{mr\_livestem} + CF_{mr\_livecroot}. \tag{17.5}$$

17.1.2 Growth Respiration

Growth respiration is calculated as a factor of 0.11 times the total carbon allocation to new growth (CF_{growth}, after allocating carbon for N acquisition, Chapter 18.) on a given timestep, based on construction costs for a range of woody and non-woody tissues, with estimates of the growth respiration flux revised downwards following (Atkin et al. 2017). For new carbon and nitrogen allocation that enters storage pools for subsequent display, it is not clear what fraction of the associated growth respiration should occur at the time of initial allocation, and what fraction should occur later, at the time of display of new growth from storage. Eddy covariance estimates of carbon fluxes in forest ecosystems suggest that the growth respiration associated with transfer of allocated carbon and nitrogen from storage into displayed tissue is not significant (Churkina et al., 2003), and so it is assumed in CLM that all of the growth respiration cost is incurred at the time of initial allocation, regardless of the fraction of allocation that is displayed immediately (i.e. regardless of the value of f_{cur}, section 13.5). This behavior is parameterized in such a way that if future research suggests that some fraction of the growth respiration cost should be incurred at the time of display from storage, a simple parameter modification will effect the change.[1]

---

[1] Parameter grpnow in routines CNGResp and CNAllocation, currently set to 1.0, could be changed to a smaller value to transfer some portion (1 - grpnow) of the growth respiration forward in time to occur at the time of growth display from storage.

CHAPTER 18

FIXATION AND UPTAKE OF NITROGEN (FUN)

18.1 Introduction

The Fixation and Uptake of Nitrogen model is based on work by *Fisher et al. (2010)*, *Brzostek et al. (2014)*, and *Shi et al. (2016)*. The concept of FUN is that in most cases, Nitrogen uptake requires the expenditure of energy in the form of carbon, and further, that there are numerous potential sources of Nitrogen in the environment which a plant may exchange for carbon. The ratio of carbon expended to Nitrogen acquired is referred to here as the cost, or exchange rate, of N acquisition (E_{nacq}, gC/gN)). There are eight pathways for N uptake:

1. Fixation by symbiotic bacteria in root nodules (for N fixing plants) ($_{fix}$)

2. Retranslocation of N from senescing tissues ($_{ret}$)

3. Active uptake of NH4 by arbuscular mycorrhizal plants ($_{active,nh4}$)

4. Active uptake of NH4 by ectomycorrhizal plants ($_{active,nh4}$)

5. Active uptake of NO3 by arbuscular mycorrhizal plants ($_{active,no3}$)

6. Active uptake of NO3 by ectomycorrhizal plants ($_{active,no3}$)

7. Nonmycorrhizal uptake of NH4 ($_{nonmyc,no3}$)

8. Nonmycorrhizal uptake of NO3 ($_{nonmyc,nh4}$)

The notation suffix for each pathway is given in parentheses here. At each timestep, each of these pathways is associated with a cost term ($N_{cost,x}$), a payment in carbon ($C_{nuptake,x}$), and an influx of Nitrogen ($N_{uptake,x}$) where x is one of the eight uptake streams listed above.

For each PFT, we define a fraction of the total C acquisition that can be used for N fixation (f_{fixers}), which is broadly equivalent to the fraction of a given PFT that is capable of fixing Nitrogen, and thus represents an upper limit on the amount to which fixation can be increased in low n conditions. For each PFT, the cost calculation is conducted twice. Once where fixation is possible and once where it is not. (f_{fixers})

For all of the active uptake pathways, whose cost depends on varying concentrations of N through the soil profile, the costs and fluxes are also determined by soil layer j.

18.2 Boundary conditions of FUN

18.2.1 Available Carbon

The carbon available for FUN, C_{avail} (gC m^{-2}) is the total canopy photosynthetic uptake (GPP), minus the maintenance respiration fluxes (m_r) and multiplied by the time step in seconds (δt). Thus, the remainder of this chapter considers fluxes per timestep, and integrates these fluxes as they are calculated.

$$C_{avail} = (GPP - m_r)\delta t$$

Growth respiration is thus only calculated on the part of the carbon uptake that remains after expenditure of C by the FUN module.

18.2.2 Available Soil Nitrogen

18.2.3 Cost of Nitrogen Fixation

The cost of fixation is derived from *Houlton et al. (2008)*.

$$N_{cost,fix} = -s_{fix}/(1.25e^{a_{fix}+b_{fix}.t_{soil}(1-0.5t_{soil}/c_{fix})})$$

Herein, a_{fix}, b_{fix} and c_{fix} are all parameters of the temperature response function of fixation reported by Houlton et al. (2008) ($exp[a + bT_s(1 - 0.5T_s/c)$). t_{soil} is the soil temperature in C. The values of these parameters are fitted to empirical data as a=-3.62 $\pm$ 0.52, b=0.27:math:*pm* 0.04 and c=25.15 $\pm$ 0.66. 1.25 converts from the temperature response function to a 0-1 limitation factor (as specifically employed by Houlton et al.). This function is a 'rate' of uptake for a given temperature. Here we assimilated the rate of fixation into the cost term by assuming that the rate is analagous to a conductance for N, and inverting the term to produce a cost/resistance analagoue. We then multiply this temperature term by the minimum cost at optimal temperature (s_{fix}) to give a temperature limited cost in terms of C to N ratios.

18.2.4 Cost of Active Uptake

The cost of N uptake from soil, for each layer j, is controlled by two uptake parameters that pertain respectively to the relationship between soil N content and N uptake, and root C density and N uptake.

For non-mycorrhizal uptake:

$$N_{cost,nonmyc,j} = \frac{k_{n,nonmyc}}{N_{smin,j}} + \frac{k_{c,nonmyc}}{c_{root,j}}$$

and for active uptake:

$$N_{cost,active,j} = \frac{k_{n,active}}{N_{smin,j}} + \frac{k_{c,active}}{c_{root,j}}$$

where $k_{n,active}$ varies according to whether we are considering ecto or arbuscular mycorrhizal uptake.

$$k_{n,active} = \left\{ \begin{array}{ll} k_{n,Eactive} & e = 1 \\ k_{n,Aactive} & e = 0 \end{array} \right\} \qquad (18.1)$$

where m=1 pertains to the fraction of the PFT that is ecotmycorrhizal, as opposed to arbuscular mycorrhizal.

18.3 Resolving N cost across simultaneous uptake streams

The total cost of N uptake is calculated based on the assumption that carbon is partitioned to each stream in proportion to the inverse of the cost of uptake. So, more expensive pathways receive less carbon. Earlier versions of FUN *(Fisher et al., 2010)*) utilized a scheme whereby plants only took up N from the cheapest pathway. *Brzostek et al. (2014)* introduced a scheme for the simultaneous uptake from different pathways. Here we calcualate a 'conductance' to N uptake (analagous to the inverse of the cost function conceptualized as a resistance term) $N_{conductance}$ (gN/gC) as:

$$N_{conductance,f} = \sum \left(1/N_{cost,x} \right)$$

From this, we then calculate the fraction of the carbon allocated to each pathway as

$$C_{frac,x} = \frac{1/N_{cost,x}}{N_{conductance}}$$

These fractions are used later, to calculate the carbon expended on different uptake pathways. Next, the N acquired from each uptake stream per unit C spent ($N_{exch,x}$, gN/gC) is determined as

$$N_{exch,x} = \frac{C_{frac,x}}{N_{cost,x}}$$

We then determine the total amount of N uptake per unit C spent ($N_{exch,tot}$, gN/gC) as the sum of all the uptake streams.

$$N_{exch,tot} = \sum N_{exch,x}$$

and thus the subsequent overall N cost is

$$N_{cost,tot} = 1/N_{exch,tot}$$

Retranslocation is determined via a different set of mechanisms, once the $N_{cost,tot}$ is known.

18.4 Nitrogen Retranslocation

The retranslocation uses an iterative algorithm to remove Nitrogen from each piece of falling litter. There are two pathways for this, 'free' uptake which removes the labile N pool, and 'paid-for' uptake which uses C to extract N from increasingly more recalcitrant pools.

At each timestep, the pool of carbon in falling leaves ($C_{fallingleaf}$, g m^{-2}) is generated from the quantity of litterfall on that day (see Phenology chapter for details). The amount of N in the litter pool ($N_{fallingleaf}$, g m^{-2}) is calculated as the total leaf N multiplied by the fraction of the leaf pool passed to litter that timestep.

$$N_{fallingleaf} = N_{leaf}.C_{fallingleaf}/C_{leaf}$$

The carbon available at the beginning of the iterative retranslocation calculation is equal to the C_{avail} input into FUN.

$$C_{avail,retrans,0} = C_{avail}$$

18.4.1 Free Retranslocation

Some part of the leaf Nitrogen pool is removed without the need for an C expenditure. This 'free' N uptake amount, ($N_{retrans,free}$, gN m^{-2}) is calculated as

$$N_{retrans,free} = max(N_{fallingleaf} - (C_{fallingleaf}/CN_{litter,min}), 0.0)$$

where $CN_{litter,min}$ is the minimum C:N ratio of the falling litter (currently set to 1.5 x the target C:N ratio).

The new $N_{fallingleaf}$ (gN m^{-2}) is then determined as

$$N_{fallingleaf} = N_{fallingleaf} - N_{retrans,free}$$

and the new litter C:N ratio as

$$CN_{fallingleaf} = C_{fallingleaf}/N_{fallingleaf}$$

18.4.2 Paid-for Retranslocation

The remaining calculations conduct an iterative calculation to determine the degree to which N retranslocation from leaves is paid for as C:N ratios and thus cost increase as N is extracted. The iteration continues until either

1. The cost of retranslocation ($cost_{retrans}$ increases beyond the cost of acquiring N from alternative pathways ($N_{cost,tot}$).

2. $CN_{fallingleaf}$ rises to a maximum level, after which no more extraction is possible (representing unavoidable N loss) or

3. There is no more carbon left to pay for extraction.

First we calculate the cost of extraction ($cost_{retrans}$, gC/gN) for the current leaf C:N ratio as

$$cost_{retrans} = k_{retrans}/(1/CN_{fallingleaf})^{1.3}$$

where $k_{retrans}$ is a parameter controlling the overall cost of resorption, which also increases exponentially as the C:N ratio increases

Next, we calculate the amount of C needed to be spent to increase the falling leaf C:N ratio by 1.0 in this iteration i ($C_{retrans_sper}$

$$C_{retrans,spent,i} = cost_{retrans}.(N_{fallingleaf} - C_{fallingleaf}/(CN_{fallingleaf} + 1.0))$$

(wherein the retranslocation cost is assumed to not change over the increment of 1.0 in C:N ratio). Next, we calculate whether this is larger than the remaining C available to spend.

$$C_{retrans,spent,i} = min(C_{retrans,spent,i}, C_{avail,retrans,i})$$

The amount of N retranslocated from the leaf in this iteration ($N_{retrans_paid,i}$, gN m^{-2}) is calculated, checking that it does not fall below zero:

$$N_{retrans,paid,i} = min(N_{fallingleaf}, C_{retrans,spent,i}/cost_{retrans})$$

The next step calculates the growth C which is accounted for by this amount of N extraction in this iteration ($C_{retrans,accounted,i}$). This is calculated using the current plant C:N ratio, and also for the additional C which will need to be spent on growth respiration to build this amount of new tissue.

$$C_{retrans,accounted,i} = N_{retrans,paid,i}.CN_{plant}.(1.0 + gr_{frac})$$

Then the falling leaf N is updated:

$$N_{fallingleaf} = N_{fallingleaf} - N_{ret,i}$$

and the $CN_{fallingleaf}$ and cost_{retrans} are updated. The amount of available carbon that is either unspent on N acquisition nor accounted for by N uptake is updated:

$$C_{avail,retrans,i+1} = C_{avail,retrans,i} - C_{retrans,spent,i} - C_{retrans,accounted,i}$$

18.4.3 Outputs of Retranslocation algorithm.

The final output of the retranslocation calculation are the retranslocated N ($N_{retrans}$, gN m^{-2}), C spent on retranslocation ($C_{retrans_paid}$, gC m^{-2}), and C accounted for by retranslocation ($C_{retrans_accounted}$, gC m^{-2}).

For paid-for uptake, we accumulate the total carbon spent on retranslocation ($C_{spent_retrans}$),

$$C_{retrans,spent} = \sum C_{retrans,i}$$

The total N acquired from retranslocation is

$$N_{retrans} = N_{retrans,paid} + N_{retrans,free}$$

where N acquired by paid-for retranslocation is

$$N_{retrans,paid} = \sum N_{retrans,paid,i}$$

The total carbon accounted for by retranslocation is the sum of the C accounted for by paid-for N uptake ($N_{retrans_paid}$) and by free N uptake ($N_{retrans_free}$).

$$C_{retrans,accounted} = \sum C_{retrans,accounted,i} + N_{retrans,free}.CN_{plant}.(1.0 + gr_{frac})$$

The total available carbon in FUN to spend on fixation and active uptake ($C_{tospend}$, gC m^{-2}) is calculated as the carbon available minus that account for by retranslocation:

$$C_{tospend} = C_{avail} - C_{retrans,accounted}$$

18.5 Carbon expenditure on fixation and active uptake.

At each model timestep, the overall cost of N uptake is calculated (see below) in terms of C:N ratios. The available carbon (C_{avail}, g m^{-2} s^{-1}) is then allocated to two alternative outcomes, payment for N uptake, or conservation for growth. For each carbon conserved for growth, a corresponding quantity of N must be made available. In the case where the plant target C:N ratio is fixed, the partitioning between carbon for growth (C_{growth}) and carbon for N uptake ($C_{nuptake}$) is calculated by solving a system of simultaneous equations. First, the carbon available must equal the carbon spent on N uptake plus that saved for growth.

$$C_{growth} + C_{nuptake} = C_{avail}$$

Second, the nitrogen acquired from expenditure of N (left hand side of term below) must equal the N that is required to match the growth carbon (right hand side of term below).

$$C_{nuptake}/N_{cost} = C_{growth}/CN_{target}$$

The solution to these two equated terms can be used to estimate the ideal $C_{nuptake}$ as follows,

$$C_{nuptake} = C_{tospend}/((1.0 + f_{gr} * (CN_{target}/N_{cost}) + 1).$$

and the other C and N fluxes can be determined following the logic above.

18.6 Modifications to allow variation in C:N ratios

The original FUN model as developed by *Fisher et al. (2010)* and *Brzostek et al. (2014)* assumes a fixed plant tissue C:N ratio. This means that in the case where N is especially limiting, all excess carbon will be utilized in an attempt to take up more Nitrogen. It has been repeatedly observed, however, that in these circumstances in real life, plants have some flexibility in the C:N stoichiometry of their tissues, and therefore, this assumption may not be realistic. However, the degree to which the C:N ratio varies with N availability is poorly documented, and existing global nitrogen models use a variety of heuristic methods by which to incorporate changing C:N ratios (Zaehle and Friend 2010; Ghimire et al. 2016). This algorithm exists as a placeholder to allow variable C:N ratios to occur, and to allow exploration of how much the parameters controlling their flexibility has on model outcomes. Incorporation of emerging understanding of the controls on tissue stoichiometry should ultimately replace this scheme.

Thus, in CLM5, we introduce the capacity for tissue C:N ratios to be prognostic, rather than static. Overall N and C availability (N_{uptake} and C_{growth}) and hence tissue C:N ratios, are both determined by FUN. Allocation to individual tissues is discussed in the allocation chapter

Here we introduce an algorithm which adjusts the C expenditure on uptake to allow varying tissue C:N ratios. Increasing C spent on uptake will directly reduce the C:N ratio, and reducing C spent on uptake (retaining more for tissue growth) will increase it. C spent on uptake is impacted by both the N cost in the environment, and the existing tissue C:N ratio of the plant. The output of this algorithm is γ_{FUN}, the fraction of the ideal $C_{nuptake}$ calculated from the FUN equation above

$$C_{nuptake} = C_{nuptake} \cdot \gamma_{FUN}$$

18.6.1 Response of C expenditure to Nitrogen uptake cost

The environmental cost of Nitrogen ($N_{cost,tot}$) is used to determine γ_{FUN}.

$$\gamma_{FUN} = max(0.0, 1.0 - (N_{cost,tot} - a_{cnflex})/b_{cnflex})$$

where a_{cnflex} and b_{cnflex} are parameters fitted to give flexible C:N ranges over the operating range of N costs of the model. Calibration of these parameters should be subject to future testing in idealized experimental settings; they are here intended as a placeholder to allow some flexible stoichiometry, in the absence of adequate understanding of this process. Here a_{cnflex} operates as the $N_{cost,tot}$ above which there is a modification in the C expenditure (to allow higher C:N ratios), and b_{cnflex} is the scalar which determines how much the C expenditure is modified for a given discrepancy between a_{cnflex} and the actual cost of uptake.

18.6.2 Response of C expenditure to plant C:N ratios

We first calculate a δ_{CN}, which is the difference between the target C:N ($target_{CN}$) a model parameter, and the existing C:N ratio (CN_{plant})

$$CN_{plant} = \frac{C_{leaf} + C_{leaf,storage}}{N_{leaf} + N_{leaf,storage})}$$

and

$$\delta_{CN} = CN_{plant} - target_{CN}$$

We then increase γ_{FUN} to account for situations where (even if N is expensive) plant C:N ratios have increased too far from the target. Where δ_{CN} is negative, we reduce C spent on N uptake and retain more C for growth

$$\gamma_{FUN} = \left\{ \begin{array}{ll} \gamma_{FUN} + 0.5.(delta_{CN}/c_{flexcn}) & delta_{CN} > 0 \\ \gamma_{FUN} + (1 - \gamma_{FUN}).min(1, \delta_{CN}/c_{flexcn}) & delta_{CN} < 0 \end{array} \right\}$$

We then restrict the degree to which C expenditure can be reduced (to prevent unrealistically high C:N ratios) as

$$\gamma_{FUN} = max(min(1.0, \gamma_{FUN}), 0.5)$$

18.7 Calculation of N uptake streams from active uptake and fixation

Once the final $C_{nuptake}$ is known, the fluxes of C to the individual pools can be derived as

$$C_{nuptake,x} = C_{frac,x}.C_{nuptake}$$

$$N_{uptake,x} = \frac{C_{nuptake}}{N_{cost}}$$

Following this, we determine whether the extraction estimates exceed the pool size for each source of N. Where $N_{active,no3} + N_{nonmyc,no3} > N_{avail,no3}$, we calculate the unmet uptake, $N_{unmet,no3}$

$$N_{unmet,no3} = N_{active,no3} + N_{nonmyc,no3} - N_{avail,no3}$$

then modify both fluxes to account

$$N_{active,no3} = N_{active,no3} + N_{unmet,no3}.\frac{N_{active,no3}}{N_{active,no3} + N_{nonmyc,no3}}$$

$$N_{nonmyc,no3} = N_{nonmyc,no3} + N_{unmet,no3}.\frac{N_{nonmyc,no3}}{N_{active,no3} + N_{nonmyc,no3}}$$

and similarly, for NH4, where $N_{active,nh4} + N_{nonmyc,nh4} > N_{avail,nh4}$, we calculate the unmet uptake, $N_{unmet,no3}$

$$N_{unmet,nh4} = N_{active,nh4} + N_{nonmyc,nh4} - N_{avail,nh4}$$

then modify both fluxes to account

$$N_{active,nh4} = N_{active,nh4} + N_{unmet,nh4}.\frac{N_{active,nh4}}{N_{active,nh4} + N_{nonmyc,nh4}}$$

$$N_{nonmyc,nh4} = N_{nonmyc,nh4} + N_{unmet,nh4}.\frac{N_{nonmyc,nh4}}{N_{active,nh4} + N_{nonmyc,nh4}}$$

and then update the C spent to account for hte new lower N acquisition in that layer/pool.

$$C_{active,nh4} = N_{active,nh4} \cdot N_{cost,active,nh4}$$
$$C_{active,no3} = N_{active,no3} \cdot N_{cost,active,no3}$$
$$C_{nonmyc,no3} = N_{nonmyc,no3} \cdot N_{cost,nonmyc,no3}$$
$$C_{nonmyc,no3} = N_{nonmyc,no3} \cdot N_{cost,nonmyc,no3}$$

Following this, we determine how much carbon is accounted for for each soil layer.

$$C_{accounted,x,j} = C_{spent,j,x} - (N_{acquired,j,x} \cdot CN_{plant} \cdot (1.0 + gr_{frac}))$$

CHAPTER 19

CARBON AND NITROGEN ALLOCATION

19.1 Introduction

The carbon and nitrogen allocation routines in CLM determine the fate of newly assimilated carbon, coming from the calculation of photosynthesis, and available mineral nitrogen, coming from plant uptake of mineral nitrogen in the soil or being drawn out of plant reserves. A significant change to CLM5 relative to prior versions is that allocation of carbon and nitrogen proceed independently rather than in a sequential manner.

19.2 Carbon Allocation for Maintenance Respiration Costs

Allocation of available carbon on each time step is prioritized, with first priority given to the demand for carbon to support maintenance respiration of live tissues (section 13.7). Second priority is to replenish the internal plant carbon pool that supports maintenance respiration during times when maintenance respiration exceeds photosynthesis (e.g. at night, during winter for perennial vegetation, or during periods of drought stress) (Sprugel et al., 1995). Third priority is to support growth of new tissues, including allocation to storage pools from which new growth will be displayed in subsequent time steps.

The total maintenance respiration demand (CF_{mr}, gC m^{-2} s^{-1}) is calculated as a function of tissue mass and nitrogen concentration, and temperature (section 13.7). The carbon supply to support this demand is composed of fluxes allocated from carbon assimilated in the current timestep ($CF_{GPP,mr}$, gC m^{-2} s^{-1}) and from a storage pool that is drawn down when total demand exceeds photosynthesis ($CF_{xs,mr}$, gC m^{-2} s^{-1}):

$$CF_{mr} = CF_{GPP,mr} + CF_{xs,mr} \tag{19.1}$$

$$CF_{GPP,mr} = -\begin{cases} CF_{mr} & \text{for } CF_{mr} \leq CF_{GPP} \\ CF_{GPP} & \text{for } CF_{mr} > CF_{GPP} \end{cases} \tag{19.2}$$

$$CF_{xs,mr} = -\begin{cases} 0 & \text{for } CF_{mr} \leq CF_{GPP} \\ CF_{mr} - CF_{GPP} & \text{for } CF_{mr} > CF_{GPP} \end{cases} \tag{19.3}$$

The storage pool that supplies carbon for maintenance respiration in excess of current CF_{GPP} (CS_{xs}, gC m^{-2}) is permitted to run a deficit (negative state), and the magnitude of this deficit determines an allocation demand which gradually replenishes CS_{xs}. The logic for allowing a negative state for this pool is to eliminate the need to know in

advance what the total maintenance respiration demand will be for a particular combination of climate and plant type. Using the deficit approach, the allocation to alleviate the deficit increases as the deficit increases, until the supply of carbon into the pool balances the demand for carbon leaving the pool in a quasi-steady state, with variability driven by the seasonal cycle, climate variation, disturbance, and internal dynamics of the plant-litter-soil system. In cases where the combination of climate and plant type are not suitable to sustained growth, the deficit in this pool increases until the available carbon is being allocated mostly to alleviate the deficit, and new growth approaches zero. The allocation flux to CS_{xs} ($CF_{GPP,xs}$, gC m^{-2} s^{-1}) is given as

$$CF_{GPP,xs,pot} = \begin{cases} 0 & \text{for } CS_{xs} \geq 0 \\ -CS_{xs}/(86400\tau_{xs}) & \text{for } CS_{xs} < 0 \end{cases} \tag{19.4}$$

$$CF_{GPP,xs} = \begin{cases} CF_{GPP,xs,pot} & \text{for } CF_{GPP,xs,pot} \leq CF_{GPP} - CF_{GPP,mr} \\ \max(CF_{GPP} - CF_{GPP,mr}, 0) & \text{for } CF_{GPP,xs,pot} > CF_{GPP} - CF_{GPP,mr} \end{cases} \tag{19.5}$$

where τ_{xs} is the time constant (currently set to 30 days) controlling the rate of replenishment of CS_{xs}.

Note that these two top-priority carbon allocation fluxes ($CF_{GPP,mr}$ and $CF_{GPP,xs}$) are not stoichiometrically associated with any nitrogen fluxes.

19.3 Carbon and Nitrogen Stoichiometry of New Growth

After accounting for the carbon cost of maintenance respiration, the remaining carbon flux from photosynthesis which can be allocated to new growth (CF_{avail}, gC m^{-2} s^{-1}) is

$$CF_{avail\_alloc} = CF_{GPP} - CF_{GPP,mr} - CF_{GPP,xs}. \tag{19.6}$$

Potential allocation to new growth is calculated for all of the plant carbon and nitrogen state variables based on specified C:N ratios for each tissue type and allometric parameters that relate allocation between various tissue types. The allometric parameters are defined as follows:

$$\begin{aligned} a_1 &= \text{ratio of new fine root : new leaf carbon allocation} \\ a_2 &= \text{ratio of new coarse root : new stem carbon allocation} \\ a_3 &= \text{ratio of new stem : new leaf carbon allocation} \\ a_4 &= \text{ratio new live wood : new total wood allocation} \\ g_1 &= \text{ratio of growth respiration carbon : new growth carbon.} \end{aligned} \tag{19.7}$$

Parameters a_1, a_2, and a_4 are defined as constants for a given PFT (Table 13.1), while $g_l = 0.3$ (unitless) is prescribed as a constant for all PFTs, based on construction costs for a range of woody and non-woody tissues (Larcher, 1995).

The model includes a dynamic allocation scheme for woody vegetation (parameter a_3 = -1, Table 19.1), in which case the ratio for carbon allocation between new stem and new leaf increases with increasing net primary production (NPP), as

$$a_3 = \frac{2.7}{1 + e^{-0.004NPP_{ann} - 300}} - 0.4 \tag{19.8}$$

where NPP_{ann} is the annual sum of NPP from the previous year. This mechanism has the effect of increasing woody allocation in favorable growth environments (Allen et al., 2005; Vanninen and Makela, 2005) and during the phase of stand growth prior to canopy closure (Axelsson and Axelsson, 1986).

Table 19.1: Allocation and target carbon:nitrogen ratio parameters

Plant functional type	a_1	a_2	a_3	a_4	$TargetCN_{leaf}$	$TargetCN_{fr}$	$TargetCN_{lw}$	$TargetCN_{dw}$
NET Temperate	1	0.3	-1	0.1	35	42	50	500
NET Boreal	1	0.3	-1	0.1	40	42	50	500
NDT Boreal	1	0.3	-1	0.1	25	42	50	500
BET Tropical	1	0.3	-1	0.1	30	42	50	500
BET temperate	1	0.3	-1	0.1	30	42	50	500
BDT tropical	1	0.3	-1	0.1	25	42	50	500
BDT temperate	1	0.3	-1	0.1	25	42	50	500
BDT boreal	1	0.3	-1	0.1	25	42	50	500
BES temperate	1	0.3	0.2	0.5	30	42	50	500
BDS temperate	1	0.3	0.2	0.5	25	42	50	500
BDS boreal C$_3$ arctic grass	1 1	0.3 0	0.2 0	0.1 0	25 25	42 42	50 0	500 0
C$_3$ grass	2	0	0	0	25	42	0	0
C$_4$ grass	2	0	0	0	25	42	0	0
Crop R	2	0	0	0	25	42	0	0
Crop I	2	0	0	0	25	42	0	0
Corn R	2	0	0	1	25	42	50	500
Corn I	2	0	0	1	25	42	50	500
Temp Cereal R	2	0	0	1	25	42	50	500
Temp Cereal I	2	0	0	1	25	42	50	500
Winter Cereal R	2	0	0	1	25	42	50	500
Winter Cereal I	2	0	0	1	25	42	50	500
Soybean R	2	0	0	1	25	42	50	500
Soybean I	2	0	0	1	25	42	50	500

Carbon to nitrogen ratios are defined for different tissue types as follows:

$$
\begin{aligned}
CN_{leaf} &= \_ \ \text{C : N for leaf} \\
CN_{fr} &= \_ \ \text{C : N for fine root} \\
CN_{lw} &= \_ \ \text{C : N for live wood (in stem and coarse root)} \\
CN_{dw} &= \_ \ \text{C : N for dead wood (in stem and coarse root)}
\end{aligned}
\tag{19.9}
$$

where all C:N parameters are defined as constants for a given PFT (Table 19.1).

Given values for the parameters in and , total carbon and nitrogen allocation to new growth (CF_{alloc}, gC m^{-2} s^{-1}, and NF_{alloc}, gN m^{-2} s^{-1}, respectively) can be expressed as functions of new leaf carbon allocation ($CF_{GPP,leaf}$, gC m^{-2} s^{-1}):

$$
\begin{aligned}
CF_{alloc} &= CF_{GPP,leaf} \, C_{allom} \\
NF_{alloc} &= CF_{GPP,leaf} \, N_{allom}
\end{aligned}
\tag{19.10}
$$

where

$$
C_{allom} = \begin{cases} (1 + g_1)\,(1 + a_1 + a_3\,(1 + a_2)) & \text{for woody PFT} \\ 1 + g_1 + a_1\,(1 + g_1) & \text{for non} - \text{woody PFT} \end{cases}
\tag{19.11}
$$

$$
N_{allom} = \begin{cases} \dfrac{1}{CN_{leaf}} + \dfrac{a_1}{CN_{fr}} + \dfrac{a_3 a_4 (1+a_2)}{CN_{lw}} + \\ \dfrac{a_3 (1 - a_4)(1 + a_2)}{CN_{dw}} & \text{for woody PFT} \\ \dfrac{1}{CN_{leaf}} + \dfrac{a_1}{CN_{fr}} & \text{for non} - \text{woody PFT.} \end{cases}
\tag{19.12}
$$

Since the C:N stoichiometry for new growth allocation is defined, from Eq. , as C_{allom}/ N_{allom}, the total carbon available for new growth allocation (CF_{avail_alloc}) can be used to calculate the total plant nitrogen demand for new

growth (NF_{plant_demand}, gN m^{-2} s^{-1}) as:

$$NF_{plant\_demand} = CF_{avail\_alloc} \frac{N_{allom}}{C_{allom}}.$$
(19.13)

19.4 Carbon Allocation to New Growth

There are two carbon pools associated with each plant tissue – one which represents the currently displayed tissue, and another which represents carbon stored for display in a subsequent growth period. The nitrogen pools follow this same organization. The model keeps track of stored carbon according to which tissue type it will eventually be displayed as, and the separation between display in the current timestep and storage for later display depends on the parameter f_{cur} (values 0 to 1). Given $CF_{alloc,leaf}$ and f_{cur}, the allocation fluxes of carbon to display and storage pools (where storage is indicated with _stor) for the various tissue types are given as:

$$CF_{alloc,leaf\_} = CF_{alloc,leaf\_tot} f_{cur}$$
(19.14)

$$CF_{alloc,leaf\_stor\_} = CF_{alloc,leaf\_tot} (1 - f_{cur})$$
(19.15)

$$CF_{alloc,froot\_} = CF_{alloc,leaf\_tot} a_1 f_{cur}$$
(19.16)

$$CF_{alloc,froot\_stor\_} = CF_{alloc,leaf\_tot} a_1 (1 - f_{cur})$$
(19.17)

$$CF_{alloc,livestem\_} = CF_{alloc,leaf\_tot} a_3 a_4 f_{cur}$$
(19.18)

$$CF_{alloc,livestem\_stor\_} = CF_{alloc,leaf\_tot} a_3 a_4 (1 - f_{cur})$$
(19.19)

$$CF_{alloc,deadstem\_} = CF_{alloc,leaf\_tot} a_3 (1 - a_4) f_{cur}$$
(19.20)

$$CF_{alloc,deadstem\_stor\_} = CF_{alloc,leaf\_tot} a_3 (1 - a_4) (1 - f_{cur})$$
(19.21)

$$CF_{alloc,livecroot\_} = CF_{alloc,leaf\_tot} a_2 a_3 a_4 f_{cur}$$
(19.22)

$$CF_{alloc,livecroot\_stor\_} = CF_{alloc,leaf\_tot} a_2 a_3 a_4 (1 - f_{cur})$$
(19.23)

$$CF_{alloc,deadcroot\_} = CF_{alloc,leaf\_tot} a_2 a_3 (1 - a_4) f_{cur}$$
(19.24)

$$CF_{alloc,deadcroot\_stor\_} = CF_{alloc,leaf\_tot} a_2 a_3 (1 - a_4) (1 - f_{cur}).$$
(19.25)

19.5 Nitrogen allocation

The total flux of nitrogen to be allocated is given by the FUN model (Chapter 18). This gives a total N to be allocated within a given timestep, N_{supply}. The total N allocated for a given tissue i is the minimum between the supply and the demand:

$$NF_{alloc,i} = min (NF_{demand,i}, NF_{supply,i})$$
(19.26)

The demand for each tissue, calculated for the tissue to remain on stoichiometry during growth, is:

$$NF_{demand,leaf\_} = \frac{CF_{alloc,leaf\_tot}}{CN_{leaf}} f_{cur}$$
(19.27)

$$NF_{demand,leaf\_stor\_} = \frac{CF_{alloc,leaf\_tot}}{CN_{leaf}} (1 - f_{cur})$$
(19.28)

$$NF_{demand,froot\_} = \frac{CF_{alloc,leaf\_tot}a_1}{CN_{fr}}f_{cur} \tag{19.29}$$

$$NF_{demand,froot\_stor\_} = \frac{CF_{alloc,leaf\_tot}a_1}{CN_{fr}}\left(1 - f_{cur}\right) \tag{19.30}$$

$$NF_{demand,livestem\_} = \frac{CF_{alloc,leaf\_tot}a_3 a_4}{CN_{lw}}f_{cur} \tag{19.31}$$

$$NF_{demand,livestem\_stor\_} = \frac{CF_{alloc,leaf\_tot}a_3 a_4}{CN_{lw}}\left(1 - f_{cur}\right) \tag{19.32}$$

$$NF_{demand,deadstem\_} = \frac{CF_{alloc,leaf\_tot}a_3\left(1 - a_4\right)}{CN_{dw}}f_{cur} \tag{19.33}$$

$$NF_{demand,deadstem\_stor\_} = \frac{CF_{alloc,leaf\_tot}a_3\left(1 - a_4\right)}{CN_{dw}}\left(1 - f_{cur}\right) \tag{19.34}$$

$$NF_{demand,livecroot\_} = \frac{CF_{alloc,leaf\_tot}a_2 a_3 a_4}{CN_{lw}}f_{cur} \tag{19.35}$$

$$NF_{demand,livecroot\_stor\_} = \frac{CF_{alloc,leaf\_tot}a_2 a_3 a_4}{CN_{lw}}\left(1 - f_{cur}\right) \tag{19.36}$$

$$NF_{demand,deadcroot\_} = \frac{CF_{alloc,leaf\_tot}a_2 a_3\left(1 - a_4\right)}{CN_{dw}}f_{cur} \tag{19.37}$$

$$NF_{demand,deadcroot\_stor\_} = \frac{CF_{alloc,leaf}a_2 a_3\left(1 - a_4\right)}{CN_{dw}}\left(1 - f_{cur}\right). \tag{19.38}$$

After each pool's demand is calculated, the total plant N demand is then the sum of each individual pool :math: *i* corresponding to each tissue:

$$NF_{demand,tot} = \sum_{i=tissues} NF_{demand,i} \tag{19.39}$$

and the total supply for each tissue :math: *i* is the product of the fractional demand and the total available N, calculated as the term :math: *N_{uptake}* equal to the sum of the eight N uptake streams described in the FUN model (Chapter 18).

$$NF_{alloc,i} = N_{uptake}NF_{demand,i}/NF_{demand,tot} \tag{19.40}$$

CHAPTER 20

VEGETATION PHENOLOGY AND TURNOVER

The CLM phenology model consists of several algorithms controlling the transfer of stored carbon and nitrogen out of storage pools for the display of new growth and into litter pools for losses of displayed growth. PFTs are classified into three distinct phenological types that are represented by separate algorithms: an evergreen type, for which some fraction of annual leaf growth persists in the displayed pool for longer than one year; a seasonal-deciduous type with a single growing season per year, controlled mainly by temperature and daylength; and a stress-deciduous type with the potential for multiple growing seasons per year, controlled by temperature and soil moisture conditions.

The three phenology types share a common set of control variables. The calculation of the phenology fluxes is generalized, operating identically for all three phenology types, given a specification of the common control variables. The following sections describe first the general flux parameterization, followed by the algorithms for setting the control parameters for the three phenology types.

20.1 General Phenology Flux Parameterization

Fluxes of carbon and nitrogen from storage pools and into displayed tissue pools pass through a special transfer pool (denoted _xfer), maintained as a separate state variable for each tissue type. Storage (_stor) and transfer (_xfer) pools are maintained separately to reduce the complexity of accounting for transfers into and out of storage over the course of a single growing season.

20.1.1 14.1.1 Onset Periods

The deciduous phenology algorithms specify the occurrence of onset growth periods (Figure 14.1). Carbon fluxes from the transfer pools into displayed growth are calculated during these periods as:

$$CF_{leaf\_xfer,leaf} = r_{xfer\_on} CS_{leaf\_xfer} \qquad (20.1)$$

$$CF_{froot\_xfer,froot} = r_{xfer\_on} CS_{froot\_xfer} \qquad (20.2)$$

$$CF_{livestem\_xfer,livestem} = r_{xfer\_on} CS_{livestem\_xfer} \qquad (20.3)$$
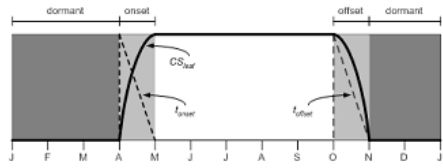
Figure 20.1: Example of annual phenology cycle for seasonal deciduous.

$$CF_{deadstem\_xfer,deadstem} = r_{xfer\_on} CS_{deadstem\_xfer} \qquad (20.4)$$

$$CF_{livecroot\_xfer,livecroot} = r_{xfer\_on} CS_{livecroot\_xfer} \qquad (20.5)$$

$$CF_{deadcroot\_xfer,deadcroot} = r_{xfer\_on} CS_{deadcroot\_xfer}, \qquad (20.6)$$

with corresponding nitrogen fluxes:

$$NF_{leaf\_xfer,leaf} = r_{xfer\_on} NS_{leaf\_xfer} \qquad (20.7)$$

$$NF_{froot\_xfer,froot} = r_{xfer\_on} NS_{froot\_xfer} \qquad (20.8)$$

$$NF_{livestem\_xfer,livestem} = r_{xfer\_on} NS_{livestem\_xfer} \qquad (20.9)$$

$$NF_{deadstem\_xfer,deadstem} = r_{xfer\_on} NS_{deadstem\_xfer} \qquad (20.10)$$

$$NF_{livecroot\_xfer,livecroot} = r_{xfer\_on} NS_{livecroot\_xfer} \qquad (20.11)$$

$$NF_{deadcroot\_xfer,deadcroot} = r_{xfer\_on} NS_{deadcroot\_xfer}, \qquad (20.12)$$

where CF is the carbon flux, CS is stored carbon, NF is the nitrogen flux, NS is stored nitrogen, r_{xfer_on} (s^{-1}) is a time-varying rate coefficient controlling flux out of the transfer pool:

$$r_{xfer\_on} = \begin{cases} 2/t_{onset} & \text{for } t_{onset} \neq \Delta t \\ 1/\Delta t & \text{for } t_{onset} = \Delta t \end{cases} \qquad (20.13)$$

and t_{onset} (s) is the number of seconds remaining in the current phenology onset growth period (Figure 14.1). The form of Eq. (20.13) produces a flux from the transfer pool which declines linearly over the onset growth period, approaching zero flux in the final timestep.

20.1.2 14.1.2 Offset Periods

The deciduous phenology algorithms also specify the occurrence of litterfall during offset periods. In contrast to the onset periods, only leaf and fine root state variables are subject to litterfall fluxes. Carbon fluxes from display pools into litter are calculated during these periods as:

$$CF_{leaf,litter}^{n} = \begin{cases} CF_{leaf,litter}^{n-1} + r_{xfer\_off}\left(CS_{leaf} - CF_{leaf,litter}^{n-1} t_{offset}\right) & \text{for } t_{offset} \neq \Delta t \\ (CS_{leaf}/\Delta t) + CF_{alloc,leaf} & \text{for } t_{offset} = \Delta t \end{cases} \qquad (20.14)$$

$$CF_{froot,litter}^{n} = \begin{cases} CF_{froot,litter}^{n-1} + r_{xfer\_off}\left(CS_{froot} - CF_{froot,litter}^{n-1} t_{offset}\right) & \text{for } t_{offset} \neq \Delta t \\ (CS_{froot}/\Delta t) + CF_{alloc,\,froot} & \text{for } t_{offset} = \Delta t \end{cases} \qquad (20.15)$$

$$r_{xfer\_off} = \frac{2\Delta t}{t_{offset}^2} \qquad (20.16)$$

where superscripts *n* and *n-1* refer to fluxes on the current and previous timesteps, respectively. The rate coefficient r_{xfer_off} varies with time to produce a linearly increasing litterfall rate throughout the offset period, and the special case for fluxes in the final litterfall timestep ($t_{offset} = \Delta t$) ensures that all of the displayed growth is sent to the litter pools for deciduous plant types.

Corresponding nitrogen fluxes during litterfall take into account retranslocation of nitrogen out of the displayed leaf pool prior to litterfall ($NF_{leaf,retrans}$, gN m^{-2} s^{-1}). Retranslocation of nitrogen out of fine roots is assumed to be negligible. The fluxes are:

$$NF_{leaf,litter} = CF_{leaf,litter}/CN_{leaf\_litter} \qquad (20.17)$$

$$NF_{froot,litter} = CF_{leaf,litter}/CN_{froot} \qquad (20.18)$$

$$NF_{leaf,retrans} = (CF_{leaf,litter}/CN_{leaf}) - NF_{leaf,litter}. \qquad (20.19)$$

where CN is C:N.

20.1.3 14.1.3 Background Onset Growth

The stress-deciduous phenology algorithm includes a provision for the case when stress signals are absent, and the vegetation shifts from a deciduous habit to an evergreen habit, until the next occurrence of an offset stress trigger . In that case, the regular onset flux mechanism is switched off and a background onset growth algorithm is invoked ($r_{bgtr} > 0$). During this period, small fluxes of carbon and nitrogen from the storage pools into the associated transfer pools are calculated on each time step, and the entire contents of the transfer pool are added to the associated displayed growth pool on each time step. The carbon fluxes from transfer to display pools under these conditions are:

$$CF_{leaf\_xfer,leaf} = CS_{leaf\_xfer}/\Delta t \tag{20.20}$$

$$CF_{froot\_xfer,froot} = CS_{froot\_xfer}/\Delta t \tag{20.21}$$

$$CF_{livestem\_xfer,livestem} = CS_{livestem\_xfer}/\Delta t \tag{20.22}$$

$$CF_{deadstem\_xfer,deadstem} = CS_{deadstem\_xfer}/\Delta t \tag{20.23}$$

$$CF_{livecroot\_xfer,livecroot} = CS_{livecroot\_xfer}/\Delta t \tag{20.24}$$

$$CF_{deadcroot\_xfer,deadcroot} = CS_{deadcroot\_xfer}/\Delta t, \tag{20.25}$$

and the corresponding nitrogen fluxes are:

$$NF_{leaf\_xfer,leaf} = NS_{leaf\_xfer}/\Delta t \tag{20.26}$$

$$NF_{froot\_xfer,froot} = NS_{froot\_xfer}/\Delta t \tag{20.27}$$

$$NF_{livestem\_xfer,livestem} = NS_{livestem\_xfer}/\Delta t \tag{20.28}$$

$$NF_{deadstem\_xfer,deadstem} = NS_{deadstem\_xfer}/\Delta t \tag{20.29}$$

$$NF_{livecroot\_xfer,livecroot} = NS_{livecroot\_xfer}/\Delta t \tag{20.30}$$

$$NF_{deadcroot\_xfer,deadcroot} = NS_{deadcroot\_xfer}/\Delta t. \tag{20.31}$$

20.1.4 14.1.4 Background Litterfall

Both evergreen and stress-deciduous phenology algorithms can specify a litterfall flux that is not associated with a specific offset period, but which occurs instead at a slow rate over an extended period of time, referred to as background litterfall. For evergreen types the background litterfall is the only litterfall flux. For stress-deciduous types either the offset period litterfall or the background litterfall mechanism may be active, but not both at once. Given a specification of the background litterfall rate (r_{bglf}, s^{-1}), litterfall carbon fluxes are calculated as

$$CF_{leaf,litter} = r_{bglf}CS_{leaf} \tag{20.32}$$

$$CS_{froot,litter} = r_{bglf}CS_{froot}, \tag{20.33}$$

with corresponding nitrogen litterfall and retranslocation fluxes:

$$NF_{leaf,litter} = CF_{leaf,litter}/CN_{leaf\_litter} \tag{20.34}$$

$$NF_{froot,litter} = CF_{froot,litter}/CN_{froot} \tag{20.35}$$

$$NF_{leaf,retrans} = (CF_{leaf,litter}/CN_{leaf}) - NF_{leaf,litter}. \tag{20.36}$$

20.1.5 14.1.5 Livewood Turnover

The conceptualization of live wood vs. dead wood fractions for stem and coarse root pools is intended to capture the difference in maintenance respiration rates between these two physiologically distinct tissue types. Unlike displayed pools for leaf and fine root, which are lost to litterfall, live wood cells reaching the end of their lifespan are retained as a part of the dead woody structure of stems and coarse roots. A mechanism is therefore included in the phenology routine to effect the transfer of live wood to dead wood pools, which also takes into account the different nitrogen concentrations typical of these tissue types.

A live wood turnover rate (r_{lwt}, s^{-1}) is defined as

$$r_{lwt} = p_{lwt}/(365 \cdot 86400) \tag{20.37}$$

where $p_{lwt} = 0.7$ is the assumed annual live wood turnover fraction. Carbon fluxes from live to dead wood pools are:

$$CF_{livestem,deadstem} = CS_{livestem}r_{lwt} \tag{20.38}$$

$$CF_{livecroot,deadcroot} = CS_{livecroot}r_{lwt}, \tag{20.39}$$

and the associated nitrogen fluxes, including retranslocation of nitrogen out of live wood during turnover, are:

$$NF_{livestem,deadstem} = CF_{livestem,deadstem}/CN_{dw} \tag{20.40}$$

$$NF_{livestem,retrans} = (CF_{livestem,deadstem}/CN_{lw}) - NF_{livestem,deadstem} \tag{20.41}$$

$$NF_{livecroot,deadcroot} = CF_{livecroot,deadcroot}/CN_{dw} \tag{20.42}$$

$$NF_{livecroot,retrans} = (CF_{livecroot,deadcroot}/CN_{lw}) - NF_{livecroot,deadcroot}. \tag{20.43}$$

20.2 Evergreen Phenology

The evergreen phenology algorithm is by far the simplest of the three possible types. It is assumed for all evergreen types that all carbon and nitrogen allocated for new growth in the current timestep goes immediately to the displayed growth pools (i.e. f$f_{cur} = 1.0$ (Chapter 13)). As such, there is never an accumulation of carbon or nitrogen in the storage or transfer pools, and so the onset growth and background onset growth mechanisms are never invoked for this type. Litterfall is specified to occur only through the background litterfall mechanism – there are no distinct periods of litterfall for evergreen types, but rather a continuous (slow) shedding of foliage and fine roots. This is an obvious area for potential improvements in the model, since it is known, at least for evergreen needleleaf trees in the temperate and boreal zones, that there are distinct periods of higher and lower leaf litterfall (Ferrari, 1999; Gholz et al., 1985). The rate of background litterfall (r_{bglf}, section 14.1.4) depends on the specified leaf longevity (τ_{leaf}, y), as

$$r_{bglf} = \frac{1}{\tau_{leaf} \cdot 365 \cdot 86400}. \tag{20.44}$$

20.3 Seasonal-Deciduous Phenology

The seasonal-deciduous phenology algorithm derives directly from the treatment used in the offline model Biome-BGC v. 4.1.2, (Thornton et al., 2002), which in turn is based on the parameterizations for leaf onset and offset for temperate deciduous broadleaf forest from White et al. (1997). Initiation of leaf onset is triggered when a common degree-day summation exceeds a critical value, and leaf litterfall is initiated when daylength is shorter than a critical value. Because of the dependence on daylength, the seasonal deciduous phenology algorithm is only valid for latitudes outside of the tropical zone, defined here as $|\text{latitude}| > 19.5°$. Neither the background onset nor background litterfall

mechanism is invoked for the seasonal-deciduous phenology algorithm. The algorithm allows a maximum of one onset period and one offset period each year.

The algorithms for initiation of onset and offset periods use the winter and summer solstices as coordination signals. The period between winter and summer solstice is identified as $dayl_n > dayl_{n-1}$, and the period between summer and winter solstice is identified as $dayl_n < dayl_{n-1}$, where $dayl_n$ and $dayl_{n-1}$ are the day length(s) calculated for the current and previous timesteps, respectively, using

$$dayl = 2 \cdot 13750.9871 \cdot acos \left(\frac{-\sin(lat)\sin(decl)}{\cos(lat)\cos(decl)} \right), \tag{20.45}$$

where *lat* and *decl* are the latitude and solar declination (radians), respectively, and the factor 13750.9871 is the number of seconds per radian of hour-angle.

20.3.1 14.3.1 Seasonal-Deciduous Onset Trigger

The onset trigger for the seasonal-deciduous phenology algorithm is based on an accumulated growing-degree-day approach (White et al., 1997). The growing-degree-day summation (GDD_{sum}) is initiated ($GDD_{sum} = 0$) when the phenological state is dormant and the model timestep crosses the winter solstice. Once these conditions are met, GDD_{sum} is updated on each timestep as

$$GDD^n_{sum} = \begin{cases} GDD^{n-1}_{sum} + (T_{s,3} - TKFRZ)\, f_{day} & \text{for } T_{s,3} > TKFRZ \\ GDD^{n-1}_{sum} & \text{for } T_{s,3} \leq TKFRZ \end{cases} \tag{20.46}$$

where $T_{s,3}$ (K) is the temperature of the third soil layer, and $f_{day} = \Delta t/86400$. The onset period is initiated if $GDD_{sum} > GDD_{sum\_crit}$, where

$$GDD_{sum\_crit} = \exp\left(4.8 + 0.13\left(T_{2m,ann\_avg} - TKFRZ\right)\right) \tag{20.47}$$

and where T_{2m,ann_avg} (K) is the annual average of the 2m air temperature, and TKFRZ is the freezing point of water (273.15 K). The following control variables are set when a new onset growth period is initiated:

$$GDD_{sum} = 0 \tag{20.48}$$

$$t_{onset} = 86400 \cdot n_{days\_on}, \tag{20.49}$$

where n_{days_on} is set to a constant value of 30 days. Fluxes from storage into transfer pools occur in the timestep when a new onset growth period is initiated. Carbon fluxes are:

$$CF_{leaf\_stor,leaf\_xfer} = f_{stor,xfer} CS_{leaf\_stor}/\Delta t \tag{20.50}$$

$$CF_{froot\_stor,froot\_xfer} = f_{stor,xfer} CS_{froot\_stor}/\Delta t \tag{20.51}$$

$$CF_{livestem\_stor,livestem\_xfer} = f_{stor,xfer} CS_{livestem\_stor}/\Delta t \tag{20.52}$$

$$CF_{deadstem\_stor,deadstem\_xfer} = f_{stor,xfer} CS_{deadstem\_stor}/\Delta t \tag{20.53}$$

$$CF_{livecroot\_stor,livecroot\_xfer} = f_{stor,xfer} CS_{livecroot\_stor}/\Delta t \tag{20.54}$$

$$CF_{deadcroot\_stor,deadcroot\_xfer} = f_{stor,xfer} CS_{deadcroot\_stor}/\Delta t \tag{20.55}$$

$$CF_{gresp\_stor,gresp\_xfer} = f_{stor,xfer} CS_{gresp\_stor}/\Delta t \tag{20.56}$$

and the associated nitrogen fluxes are:

$$NF_{leaf\_stor,leaf\_xfer} = f_{stor,xfer} NS_{leaf\_stor}/\Delta t \tag{20.57}$$

$$NF_{froot\_stor,froot\_xfer} = f_{stor,xfer} NS_{froot\_stor}/\Delta t \qquad (20.58)$$

$$NF_{livestem\_stor,livestem\_xfer} = f_{stor,xfer} NS_{livestem\_stor}/\Delta t \qquad (20.59)$$

$$NF_{deadstem\_stor,deadstem\_xfer} = f_{stor,xfer} NS_{deadstem\_stor}/\Delta t \qquad (20.60)$$

$$NF_{livecroot\_stor,livecroot\_xfer} = f_{stor,xfer} NS_{livecroot\_stor}/\Delta t \qquad (20.61)$$

$$NF_{deadcroot\_stor,deadcroot\_xfer} = f_{stor,xfer} NS_{deadcroot\_stor}/\Delta t \qquad (20.62)$$

where $f_{stor,xfer}$ is the fraction of current storage pool moved into the transfer pool for display over the incipient onset period. This fraction is set to 0.5, based on the observation that seasonal deciduous trees are capable of replacing their canopies from storage reserves in the event of a severe early-season disturbance such as frost damage or defoliation due to insect herbivory.

If the onset criterion ($GDD_{sum} > GDD_{sum\_crit}$) is not met before the summer solstice, then GDD_{sum} is set to 0.0 and the growing-degree-day accumulation will not start again until the following winter solstice. This mechanism prevents the initiation of very short growing seasons late in the summer in cold climates. The onset counter is decremented on each time step after initiation of the onset period, until it reaches zero, signaling the end of the onset period:

$$t_{onfset}^n = t_{onfset}^{n-1} - \Delta t \qquad (20.63)$$

20.3.2 14.3.2 Seasonal-Deciduous Offset Trigger

After the completion of an onset period, and once past the summer solstice, the offset (litterfall) period is triggered when daylength is shorter than 39300 s. The offset counter is set at the initiation of the offset period: $t_{offset} = 86400 \cdot n_{days\_off}$, where n_{days_off} is set to a constant value of 15 days. The offset counter is decremented on each time step after initiation of the offset period, until it reaches zero, signaling the end of the offset period:

$$t_{offset}^n = t_{offset}^{n-1} - \Delta t \qquad (20.64)$$

20.4 Stress-Deciduous Phenology

The stress-deciduous phenology algorithm was developed specifically for the CLM based in part on the grass phenology model proposed by White et al. (1997). The algorithm handles phenology for vegetation types such as grasses and tropical drought-deciduous trees that respond to both cold and drought-stress signals, and that can have multiple growing seasons per year. The algorithm also allows for the possibility that leaves might persist year-round in the absence of a suitable stress trigger. In that case the phenology switches to an evergreen habit, maintaining a marginally-deciduous leaf longevity (one year) until the occurrence of the next stress trigger.

20.4.1 14.4.1 Stress-Deciduous Onset Triggers

In climates that are warm year-round, onset triggering depends on soil water availability. At the beginning of a dormant period (end of previous offset period), an accumulated soil water index (SWI_{sum}, d) is initialized ($SWI_{sum} = 0$), with subsequent accumulation calculated as:

$$SWI_{sum}^n = \begin{cases} SWI_{sum}^{n-1} + f_{day} & \text{for } \Psi_{s,3} \geq \Psi_{onset} \\ SWI_{sum}^{n-1} & \text{for } \Psi_{s,3} < \Psi_{onset} \end{cases} \qquad (20.65)$$

where $\Psi_{s,3}$ is the soil water potential (MPa) in the third soil layer and $\Psi_{onset} = -0.6 MPa$ is the onset soil water potential threshold. Onset triggering is possible once $SWI_{sum} > 15$. To avoid spurious onset triggering due to soil moisture in the third soil layer exceeding the threshold due only to soil water suction of water from deeper in the

soil column, an additional precipitation trigger is included which requires at least 20 mm of rain over the previous 10 days *(Dahlin et al., 2015)*. If the cold climate growing degree-day accumulator is not active at the time when the soil moisture and precipitation thresholds are reached (see below), and if the daylength is greater than 6 hours, then onset is triggered. Except as noted below, SWI_{sum} continues to accumulate according to Eq. (20.65) during the dormant period if the daylength criterion prevents onset triggering, and onset is then triggered at the timestep when daylength exceeds 6 hours.

In climates with a cold season, onset triggering depends on both accumulated soil temperature summation and adequate soil moisture. At the beginning of a dormant period a freezing day accumulator (FD_{sum}, d) is initialized ($FD_{sum} = 0$), with subsequent accumulation calculated as:

$$FD_{sum}^n = \begin{cases} FD_{sum}^{n-1} + f_{day} & \text{for } T_{s,3} > TKFRZ \\ FD_{sum}^{n-1} & \text{for } T_{s,3} \leq TKFRZ \end{cases} . \tag{20.66}$$

If $FD_{sum} > 15$ during the dormant period, then a cold-climate onset triggering criterion is introduced, following exactly the growing degree-day summation (GDD_{sum}) logic of Eqs. (20.46) and (20.47). At that time SWI_{sum} is reset ($SWI_{sum} = 0$). Onset triggering under these conditions depends on meeting all three of the following criteria: $SWI_{sum} > 15$, $GDD_{sum} > GDD_{sum\_crit}$, and daylength greater than 6 hrs.

The following control variables are set when a new onset growth period is initiated: $SWI_{sum} = 0$, $FD_{sum} = 0$, $GDD_{sum} = 0$, $n_{days\_active} = 0$, and $t_{onset} = 86400 \cdot n_{days\_on}$, where n_{days_on} is set to a constant value of 30 days. Fluxes from storage into transfer pools occur in the timestep when a new onset growth period is initiated, and are handled identically to Eqs. (20.50) -(20.56) for carbon fluxes, and to Eqs. (20.57) - (20.62) for nitrogen fluxes. The onset counter is decremented on each time step after initiation of the onset period, until it reaches zero, signaling the end of the onset period:

$$t_{onfset}^n = t_{onfset}^{n-1} - \Delta t \tag{20.67}$$

20.4.2 14.4.2 Stress-Deciduous Offset Triggers

Any one of the following three conditions is sufficient to initiate an offset period for the stress-deciduous phenology algorithm: sustained period of dry soil, sustained period of cold temperature, or daylength shorter than 6 hours. Offset triggering due to dry soil or cold temperature conditions is only allowed once the most recent onset period is complete. Dry soil condition is evaluated with an offset soil water index accumulator ($OSWI_{sum}$, d). To test for a sustained period of dry soils, this control variable can increase or decrease, as follows:

$$OSWI_{sum}^n = \begin{cases} OSWI_{sum}^{n-1} + f_{day} & \text{for } \Psi_{s,3} \leq \Psi_{offset} \\ \max\left(OSWI_{sum}^{n-1} - f_{day}, 0\right) & \text{for } \Psi_{s,3} > \Psi_{onset} \end{cases} \tag{20.68}$$

where $\Psi_{offset} = -2 MPa$ is the offset soil water potential threshold. An offset period is triggered if the previous onset period is complete and $OSWI_{sum} \geq OSWI_{sum\_crit}$, where $OSWI_{sum\_crit} = 15$.

The cold temperature trigger is calculated with an offset freezing day accumulator (OFD_{sum}, d). To test for a sustained period of cold temperature, this variable can increase or decrease, as follows:

$$OFD_{sum}^n = \begin{cases} OFD_{sum}^{n-1} + f_{day} & \text{for } T_{s,3} \leq TKFRZ \\ \max\left(OFD_{sum}^{n-1} - f_{day}, 0\right) & \text{for } T_{s,3} > TKFRZ \end{cases} \tag{20.69}$$

An offset period is triggered if the previous onset period is complete and $OFD_{sum} > OFD_{sum\_crit}$, where $OFD_{sum\_crit} = 15$.

The offset counter is set at the initiation of the offset period: $t_{offset} = 86400 \cdot n_{days\_off}$, where n_{days_off} is set to a constant value of 15 days. The offset counter is decremented on each time step after initiation of the offset period, until it reaches zero, signaling the end of the offset period:

$$t_{offset}^n = t_{offset}^{n-1} - \Delta t \tag{20.70}$$

20.4.3 14.4.3 Stress-Deciduous: Long Growing Season

Under conditions when the stress-deciduous conditions triggering offset are not met for one year or longer, the stress-deciduous algorithm shifts toward the evergreen behavior. This can happen in cases where a stress-deciduous vegetation type is assigned in a climate where suitably strong stresses occur less frequently than once per year. This condition is evaluated by tracking the number of days since the beginning of the most recent onset period (n_{days_active}, d). At the end of an offset period n_{days_active} is reset to 0. A long growing season control variable (LGS, range 0 to 1) is calculated as:

$$LGS = \begin{cases} 0 & \text{for } n_{days\_active} < 365 \\ (n_{days\_active}/365) - 1 & \text{for } 365 \le n_{days\_active} < 730 \\ 1 & \text{for } n_{days\_active} \ge 730 \end{cases} . \tag{20.71}$$

The rate coefficient for background litterfall (r_{bglf}, s^{-1}) is calculated as a function of LGS:

$$r_{bglf} = \frac{LGS}{\tau_{leaf} \cdot 365 \cdot 86400} \tag{20.72}$$

where τ_{leaf} is the leaf longevity. The result is a shift to continuous litterfall as n_{days_active} increases from 365 to 730. When a new offset period is triggered r_{bglf} is set to 0.

The rate coefficient for background onset growth from the transfer pools (r_{bgtr}, s^{-1}) also depends on LGS, as:

$$r_{bgtr} = \frac{LGS}{365 \cdot 86400}. \tag{20.73}$$

On each timestep with $r_{bgtr} \ne 0$, carbon fluxes from storage to transfer pools are calculated as:

$$CF_{leaf\_stor,leaf\_xfer} = CS_{leaf\_stor} r_{bgtr} \tag{20.74}$$

$$CF_{froot\_stor,froot\_xfer} = CS_{froot\_stor} r_{bgtr} \tag{20.75}$$

$$CF_{livestem\_stor,livestem\_xfer} = CS_{livestem\_stor} r_{bgtr} \tag{20.76}$$

$$CF_{deadstem\_stor,deadstem\_xfer} = CS_{deadstem\_stor} r_{bgtr} \tag{20.77}$$

$$CF_{livecroot\_stor,livecroot\_xfer} = CS_{livecroot\_stor} r_{bgtr} \tag{20.78}$$

$$CF_{deadcroot\_stor,deadcroot\_xfer} = CS_{deadcroot\_stor} r_{bgtr}, \tag{20.79}$$

with corresponding nitrogen fluxes:

$$NF_{leaf\_stor,leaf\_xfer} = NS_{leaf\_stor} r_{bgtr} \tag{20.80}$$

$$NF_{froot\_stor,froot\_xfer} = NS_{froot\_stor} r_{bgtr} \tag{20.81}$$

$$NF_{livestem\_stor,livestem\_xfer} = NS_{livestem\_stor} r_{bgtr} \tag{20.82}$$

$$NF_{deadstem\_stor,deadstem\_xfer} = NS_{deadstem\_stor} r_{bgtr} \tag{20.83}$$

$$NF_{livecroot\_stor,livecroot\_xfer} = NS_{livecroot\_stor} r_{bgtr} \tag{20.84}$$

$$NF_{deadcroot\_stor,deadcroot\_xfer} = NS_{deadcroot\_stor} r_{bgtr}. \tag{20.85}$$

The result, in conjunction with the treatment of background onset growth, is a shift to continuous transfer from storage to display pools at a rate that would result in complete turnover of the storage pools in one year at steady state, once LGS reaches 1 (i.e. after two years without stress-deciduous offset conditions). If and when conditions cause stress-deciduous triggering again, r_{bgtr} is rest to 0.

20.5 Litterfall Fluxes Merged to the Column Level

CLM uses three litter pools, defined on the basis of commonly measured chemical fractionation of fresh litter into labile (LIT1 = hot water and alcohol soluble fraction), cellulose/hemicellulose (LIT2 = acid soluble fraction) and remaining material, referred to here for convenience as lignin (LIT3 = acid insoluble fraction) (Aber et al., 1990; Taylor et al., 1989). While multiple plant functional types can coexist on a single CLM soil column, each soil column includes a single instance of the litter pools. Fluxes entering the litter pools due to litterfall are calculated using a weighted average of the fluxes originating at the PFT level. Carbon fluxes are calculated as:

$$CF_{leaf,lit1} = \sum_{p=0}^{npfts} CF_{leaf,litter} f_{lab\_leaf,p} wcol_p \tag{20.86}$$

$$CF_{leaf,lit2} = \sum_{p=0}^{npfts} CF_{leaf,litter} f_{cel\_leaf,p} wcol_p \tag{20.87}$$

$$CF_{leaf,lit3} = \sum_{p=0}^{npfts} CF_{leaf,litter} f_{lig\_leaf,p} wcol_p \tag{20.88}$$

$$CF_{froot,lit1} = \sum_{p=0}^{npfts} CF_{froot,litter} f_{lab\_froot,p} wcol_p \tag{20.89}$$

$$CF_{froot,lit2} = \sum_{p=0}^{npfts} CF_{froot,litter} f_{cel\_froot,p} wcol_p \tag{20.90}$$

$$CF_{froot,lit3} = \sum_{p=0}^{npfts} CF_{froot,litter} f_{lig\_froot,p} wcol_p, \tag{20.91}$$

where $f_{lab\_leaf,p}$, $f_{cel\_leaf,p}$, and $f_{lig\_leaf,p}$ are the labile, cellulose/hemicellulose, and lignin fractions of leaf litter for PFT p, $f_{lab\_froot,p}$, $f_{cel\_froot,p}$, and $f_{lig\_froot,p}$ are the labile, cellulose/hemicellulose, and lignin fractions of fine root litter for PFT p, $wtcol_p$ is the weight relative to the column for PFT p, and p is an index through the plant functional types occurring on a column. Nitrogen fluxes to the litter pools are assumed to follow the C:N of the senescent tissue, and so are distributed using the same fractions used for carbon fluxes:

$$NF_{leaf,lit1} = \sum_{p=0}^{npfts} NF_{leaf,litter} f_{lab\_leaf,p} wcol_p \tag{20.92}$$

$$NF_{leaf,lit2} = \sum_{p=0}^{npfts} NF_{leaf,litter} f_{cel\_leaf,p} wcol_p \tag{20.93}$$

$$NF_{leaf,lit3} = \sum_{p=0}^{npfts} NF_{leaf,litter} f_{lig\_leaf,p} wcol_p \tag{20.94}$$

$$NF_{froot,lit1} = \sum_{p=0}^{npfts} NF_{froot,litter} f_{lab\_froot,p} wcol_p \tag{20.95}$$

$$NF_{froot,lit2} = \sum_{p=0}^{npfts} NF_{froot,litter} f_{cel\_froot,p} wcol_p \tag{20.96}$$

$$NF_{froot,lit3} = \sum_{p=0}^{npfts} NF_{froot,litter} f_{lig\_froot,p} wcol_p. \tag{20.97}$$

CHAPTER 21

DECOMPOSITION

Decomposition of fresh litter material into progressively more recalcitrant forms of soil organic matter is represented in CLM is defined as a cascade of k_{tras} transformations between m_{pool} decomposing coarse woody debris (CWD), litter, and soil organic matter (SOM) pools, each defined at n_{lev} vertical levels. CLM allows the user to define, at compile time, between 2 contrasting hypotheses of decomposition as embodied by two separate decomposition submodels: the CLM-CN pool structure used in CLM4.0, or a second pool structure, characterized by slower decomposition rates, based on the fCentury model (Parton et al. 1988). In addition, the user can choose, at compile time, whether to allow n_{lev} to equal 1, as in CLM4.0, or to equal the number of soil levels used for the soil hydrological and thermal calculations (see Section 2.2.1 for soil layering).

Model is structured to allow different representations of the soil C and N decomposition cascade, as well as a vertically-explicit treatment of soil biogeochemistry.

For the single-level model structure, the fundamental equation for carbon balance of the decomposing pools is:

$$\frac{\partial C_i}{\partial t} = R_i + \sum_{j \neq i} (i - r_j) \, T_{ji} k_j C_j - k_i C_i \tag{21.1}$$

where C_i is the carbon content of pool i, R_i are the carbon inputs from plant tissues directly to pool i (only non-zero for CWD and litter pools), k_i is the decay constant of pool i; T_{ji} is the fraction of carbon directed from pool j to pool i with fraction r_j lost as a respiration flux along the way.

Adding the vertical dimension to the decomposing pools changes the balance equation to the following:

$$\frac{\partial C_i(z)}{\partial t} = R_i(z) + \sum_{i \neq j} (1 - r_j) \, T_{ji} k_j(z) C_j(z) - k_i(z) C_i(z)$$
$$+ \frac{\partial}{\partial z} \left(D(z) \frac{\partial C_i}{\partial z} \right) + \frac{\partial}{\partial z} \left(A(z) C_i \right) \tag{21.2}$$

where C_i(z) is now defined at each model level, and in volumetric (gC m^{-3}) rather than areal (gC m^{-2}) units, along with R_i(z) and k_j(z). In addition, vertical transport is handled by the last two terms, for diffusive and advective transport. In the base model, advective transport is set to zero, leaving only a diffusive flux with diffusivity *D(z)* defined for all decomposing carbon and nitrogen pools. Further discussion of the vertical distribution of carbon inputs R_i(z), vertical turnover times k_j(z), and vertical transport *D(z)* is below. Discussion of the vertical model and analysis of both decomposition structures is in *Koven et al. (2013)*.
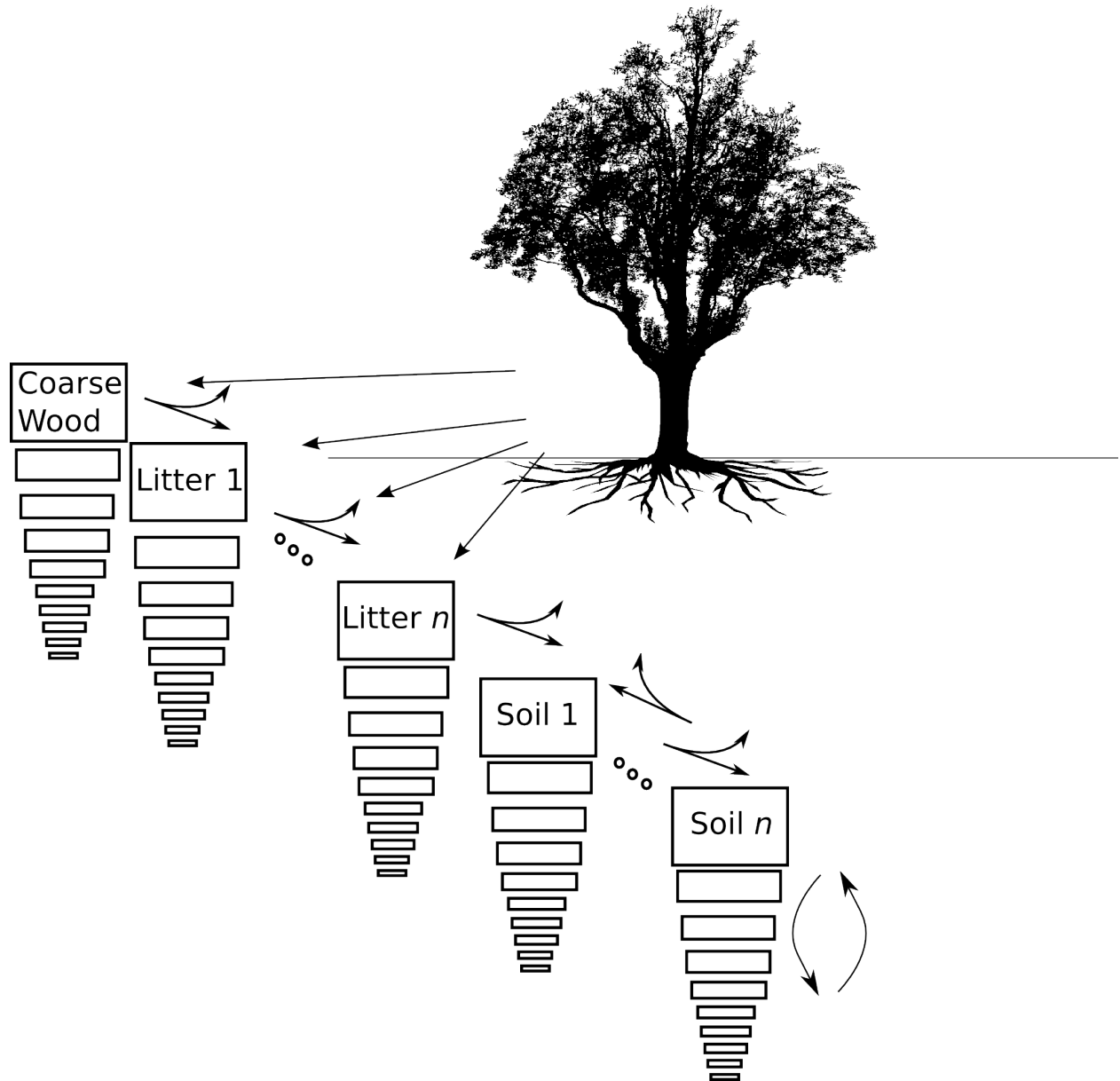
Figure 21.1: Schematic of decomposition model in CLM.

Century Soil C pool structure

CLM-CN Soil C pool structure
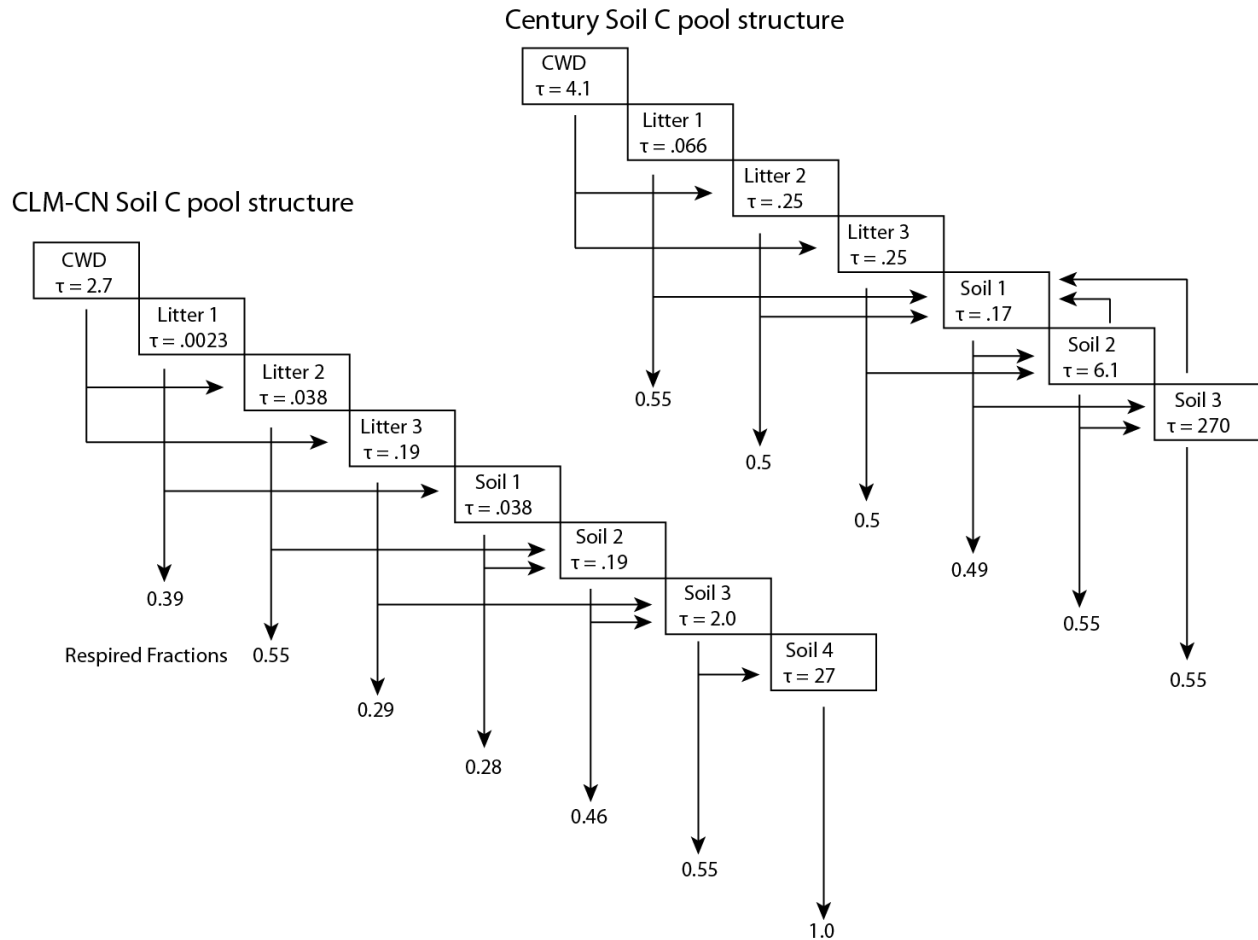
Figure 21.2: Pool structure, transitions, respired fractions (numbers at end of arrows), and turnover times (numbers in boxes) for the 2 alternate soil decomposition models included in CLM.

21.1 CLM-CN Pool Structure, Rate Constants and Parameters

The CLM-CN structure in CLM45 uses three state variables for fresh litter and four state variables for soil organic matter (SOM). The masses of carbon and nitrogen in the live microbial community are not modeled explicitly, but the activity of these organisms is represented by decomposition fluxes transferring mass between the litter and SOM pools, and heterotrophic respiration losses associated with these transformations. The litter and SOM pools in CLM-CN are arranged as a converging cascade (Figure 15.2), derived directly from the implementation in Biome-BGC v4.1.2 (Thornton et al. 2002; Thornton and Rosenbloom, 2005).

Model parameters are estimated based on a synthesis of microcosm decomposition studies using radio-labeled substrates (Degens and Sparling, 1996; Ladd et al. 1992; Martin et al. 1980; Mary et al. 1993; Saggar et al. 1994; Sørensen, 1981; van Veen et al. 1984). Multiple exponential models are fitted to data from the microcosm studies to estimate exponential decay rates and respiration fractions (Thornton, 1998). The microcosm experiments used for parameterization were all conducted at constant temperature and under moist conditions with relatively high mineral nitrogen concentrations, and so the resulting rate constants are assumed not limited by the availability of water or mineral nitrogen. Table 21.1 lists the base decomposition rates for each litter and SOM pool, as well as a base rate for physical fragmentation for the coarse woody debris pool (CWD).

Table 21.1: Decomposition rate constants for litter and SOM pools, C:N ratios, and acceleration parameters for the CLM-CN decomposition pool structure.

	Biome-BGC	CLM-CN		
	k_{disc1}(d^{-1})	k_{disc2} (hr^{-1})	C:N ratio	Acceleration term (a_i)
k_{Lit1}	0.7	0.04892	•	1
k_{Lit2}	0.07	0.00302	•	1
k_{Lit3}	0.014	0.00059	•	1
k_{SOM1}	0.07	0.00302	12	1
k_{SOM2}	0.014	0.00059	12	1
k_{SOM3}	0.0014	0.00006	10	5
k_{SOM4}	0.0001	0.000004	10	70
k_{CWD}	0.001	0.00004	•	1

The first column of Table 21.1 gives the rates as used for the Biome-BGC model, which uses a discrete-time model with a daily timestep. The second column of Table 21.1 shows the rates transformed for a one-hour discrete timestep typical of CLM-CN. The transformation is based on the conversion of the initial discrete-time value (k_{disc1}) first to a continuous time value (k_{cont}), then to the new discrete-time value with a different timestep (k_{disc2}) , following Olson (1963):

$$k_{cont} = -\log\left(1 - k_{disc1}\right) \tag{21.3}$$

$$k_{disc2} = 1 - \exp\left(-k_{cont}\frac{\Delta t_2}{\Delta t_1}\right) \tag{21.4}$$

where Δt_1 (s) and Δt_2 (s) are the time steps of the initial and new discrete-time models, respectively.

Respiration fractions are parameterized for decomposition fluxes out of each litter and SOM pool. The respiration fraction (*rf*, unitless) is the fraction of the decomposition carbon flux leaving one of the litter or SOM pools that is released as CO_2 due to heterotrophic respiration. Respiration fractions and exponential decay rates are estimated

simultaneously from the results of microcosm decomposition experiments (Thornton, 1998). The same values are used in CLM-CN and Biome-BGC (Table 21.2).

Table 21.2: Respiration fractions for litter and SOM pools

Pool	rf
rf_{Lit1}	0.39
rf_{Lit2}	0.55
rf_{Lit3}	0.29
rf_{SOM1}	0.28
rf_{SOM2}	0.46
rf_{SOM3}	0.55
rf_{SOM4}	1.0^a

[a] The respiration fraction for pool SOM4 is 1.0 by definition: since there is no pool downstream of SOM4, the entire carbon flux leaving this pool is assumed to be respired as CO_2.

21.2 Century-based Pool Structure, Rate Constants and Parameters

The Century-based decomposition cascade is, like CLM-CN, a first-order decay model; the two structures differ in the number of pools, the connections between those pools, the turnover times of the pools, and the respired fraction during each transition (Figure 15.2). The turnover times are different for the Century-based pool structure, following those described in Parton et al. (1988) (Table 21.3).

Table 21.3: Turnover times, C:N ratios, and acceleration parameters for the Century-based decomposition cascade.

	Turnover time (year)	C:N ratio	Acceleration term (a_i)
CWD	4.1	·	1
Litter 1	0.066	·	1
Litter 2	0.25	·	1
Litter 3	0.25	·	1
SOM 1	0.17	8	1
SOM 2	6.1	11	15
SOM 3	270	11	675

Likewise, values for the respiration fraction of Century-based structure are in Table 21.4.

Table 21.4: Respiration fractions for litter and SOM pools for Century-based structure

Pool	rf
rf_{Lit1}	0.55
rf_{Lit2}	0.5
rf_{Lit3}	0.5
rf_{SOM1}	f(txt)
rf_{SOM2}	0.55
rf_{SOM3}	0.55

21.3 Environmental modifiers on decomposition rate

These base rates are modified on each timestep by functions of the current soil environment. For the single-level model, there are two rate modifiers, temperature (r_{tsoil}, unitless) and moisture (r_{water}, unitless), both of which are calculated using the average environmental conditions of the top five model levels (top 29 cm of soil column). For the vertically-resolved model, two additional environmental modifiers are calculated beyond the temperature and moisture limitations: an oxygen scalar (r_{oxygen}, unitless), and a depth scalar (r_{depth}, unitless).

The Temperature scalar r_{tsoil} is calculated in CLM using a Q_{10} approach, with $Q_{10} = 1.5$.

$$r_{tsoil} = Q_{10}^{\left(\frac{T_{soil,\,j} - T_{ref}}{10} \right)} \tag{21.5}$$

where j is the soil layer index, $T_{soil,j}$ (K) is the temperature of soil level j. The reference temperature T_{ref} = 25C.

The rate scalar for soil water potential (r_{water}, unitless) is calculated using a relationship from Andrén and Paustian (1987) and supported by additional data in Orchard and Cook (1983):

$$r_{water} = \sum_{j=1}^{5} \left\{ \begin{array}{ll} 0 & \text{for } \Psi_j < \Psi_{\min} \\ \frac{\log(\Psi_{\min}/\Psi_j)}{\log(\Psi_{\min}/\Psi_{\max})} w_{soil,\,j} & \text{for } \Psi_{\min} \leq \Psi_j \leq \Psi_{\max} \\ 1 & \text{for } \Psi_j > \Psi_{\max} \end{array} \right\} \tag{21.6}$$

where Ψ_j is the soil water potential in layer j, Ψ_{min} is a lower limit for soil water potential control on decomposition rate (in CLM5, this was changed from a default value of -10 MPa used in CLM4.5 and earlier to a default value of -2.5 MPa). $\Psi_{max,j}$ (MPa) is the soil moisture at which decomposition proceeds at a moisture-unlimited rate. The default value of $\Psi_{max,j}$ for CLM5 is updated from a saturated value used in CLM4.5 and earlier, to a value nominally at field capacity, with a value of -0.002 MPa

For frozen soils, the bulk of the rapid dropoff in decomposition with decreasing temperature is due to the moisture limitation, since matric potential is limited by temperature in the supercooled water formulation of Niu and Yang (2006),

$$\psi\left(T\right) = -\frac{L_f\left(T - T_f\right)}{10^3 T} \tag{21.7}$$

An additional frozen decomposition limitation can be specified using a 'frozen Q_{10}' following *Koven et al. (2011)*, however the default value of this is the same as the unfrozen Q_{10} value, and therefore the basic hypothesis is that frozen respiration is limited by liquid water availability, and can be modeled following the same approach as thawed but dry soils.

An additional rate scalar, r_{oxygen} is enabled when the CH_4 submodel is used (set equal to 1 for the single layer model or when the CH_4 submodel is disabled). This limits decomposition when there is insufficient molecular oxygen to satisfy stoichiometric demand (1 mol O_2 consumed per mol CO_2 produced) from heterotrophic decomposers, and supply from diffusion through soil layers (unsaturated and saturated) or aerenchyma (Chapter 19). A minimum value of r_{oxygen} is set at 0.2, with the assumption that oxygen within organic tissues can supply the necessary stoichiometric demand at this rate. This value lies between estimates of 0.025–0.1 (Frolking et al. 2001), and 0.35 (Wania et al. 2009); the large range of these estimates poses a large unresolved uncertainty.

Lastly, a possible explicit depth dependence, r_{depth}, (set equal to 1 for the single layer model) can be applied to soil C decomposition rates to account for processes other than temperature, moisture, and anoxia that can limit decomposition. This depth dependence of decomposition was shown by Jenkinson and Coleman (2008) to be an important term in fitting total C and 14C profiles, and implies that unresolved processes, such as priming effects, microscale anoxia, soil mineral surface and/or aggregate stabilization may be important in controlling the fate of carbon at depth *Koven et al. (2013)*. CLM includes these unresolved depth controls via an exponential decrease in the soil turnover time with depth:

$$r_{depth} = \exp\left(-\frac{z}{z_\tau}\right) \tag{21.8}$$

where z_τ is the e-folding depth for decomposition. For CLM4.5, the default value of this was 0.5m. For CLM5, this has been changed to a default value of 10m, which effectively means that intrinsic decomposition rates may proceed as quickly at depth as at the surface.

The combined decomposition rate scalar (r_{total},unitless) is:

$$r_{total} = r_{tsoil} r_{water} r_{oxygen} r_{depth}. \tag{21.9}$$

21.4 N-limitation of Decomposition Fluxes

Decomposition rates can also be limited by the availability of mineral nitrogen, but calculation of this limitation depends on first estimating the potential rates of decomposition, assuming an unlimited mineral nitrogen supply. The general case is described here first, referring to a generic decomposition flux from an "upstream" pool (u) to a "downstream" pool (d), with an intervening loss due to respiration. The potential carbon flux out of the upstream pool ($CF_{pot,u}$, gC m^{-2} s^{-1}) is:

$$CF_{pot,\,u} = CS_u k_u \tag{21.10}$$

where CS_u (gC m^{-2}) is the initial mass in the upstream pool and k_u is the decay rate constant (s:sup:-1) for the upstream pool, adjusted for temperature and moisture conditions. Depending on the C:N ratios of the upstream and downstream pools and the amount of carbon lost in the transformation due to respiration (the respiration fraction), the execution of this potential carbon flux can generate either a source or a sink of new mineral nitrogen ($NF_{pot\_min,u \to d}$, gN m^{-2} s^{-1}). The governing equation (Thornton and Rosenbloom, 2005) is:

$$NF_{pot\_min,\,u \to d} = \frac{CF_{pot,\,u}\left(1 - rf_u - \frac{CN_d}{CN_u}\right)}{CN_d} \tag{21.11}$$

where rf_u is the respiration fraction for fluxes leaving the upstream pool, CN_u and CN_d are the C:N ratios for upstream and downstream pools, respectively. Negative values of $NF_{pot\_min,u \to d}$ indicate that the decomposition flux results in a source of new mineral nitrogen, while positive values indicate that the potential decomposition flux results in a sink (demand) for mineral nitrogen.

Following from the general case, potential carbon fluxes leaving individual pools in the decomposition cascade, for the example of the CLM-CN pool structure, are given as:

$$CF_{pot,\,Lit1} = CS_{Lit1} k_{Lit1} r_{total}/\Delta t \tag{21.12}$$

$$CF_{pot,\,Lit2} = CS_{Lit2} k_{Lit2} r_{total}/\Delta t \tag{21.13}$$

$$CF_{pot,\,Lit3} = CS_{Lit3} k_{Lit3} r_{total}/\Delta t \tag{21.14}$$

$$CF_{pot,\,SOM1} = CS_{SOM1} k_{SOM1} r_{total}/\Delta t \tag{21.15}$$

$$CF_{pot,\,SOM2} = CS_{SOM2} k_{SOM2} r_{total}/\Delta t \tag{21.16}$$

$$CF_{pot,\,SOM3} = CS_{SOM3} k_{SOM3} r_{total}/\Delta t \tag{21.17}$$

$$CF_{pot,\,SOM4} = CS_{SOM4} k_{SOM4} r_{total}/\Delta t \tag{21.18}$$

where the factor ($1/\Delta t$) is included because the rate constant is calculated for the entire timestep (Eqs. and), but the convention is to express all fluxes on a per-second basis. Potential mineral nitrogen fluxes associated with these decomposition steps are, again for the example of the CLM-CN pool structure (the CENTURY structure will be similar but without the different terminal step):

$$NF_{pot\_min,\,Lit1 \to SOM1} = CF_{pot,\,Lit1}\left(1 - rf_{Lit1} - \frac{CN_{SOM1}}{CN_{Lit1}}\right)\Big/CN_{SOM1} \tag{21.19}$$

$$NF_{pot\_min,\,Lit2 \to SOM2} = CF_{pot,\,Lit2} \left(1 - rf_{Lit2} - \frac{CN_{SOM2}}{CN_{Lit2}}\right) \Big/ CN_{SOM2} \tag{21.20}$$

$$NF_{pot\_min,\,Lit3 \to SOM3} = CF_{pot,\,Lit3} \left(1 - rf_{Lit3} - \frac{CN_{SOM3}}{CN_{Lit3}}\right) \Big/ CN_{SOM3} \tag{21.21}$$

$$NF_{pot\_min,\,SOM1 \to SOM2} = CF_{pot,\,SOM1} \left(1 - rf_{SOM1} - \frac{CN_{SOM2}}{CN_{SOM1}}\right) \Big/ CN_{SOM2} \tag{21.22}$$

$$NF_{pot\_min,\,SOM2 \to SOM3} = CF_{pot,\,SOM2} \left(1 - rf_{SOM2} - \frac{CN_{SOM3}}{CN_{SOM2}}\right) \Big/ CN_{SOM3} \tag{21.23}$$

$$NF_{pot\_min,\,SOM3 \to SOM4} = CF_{pot,\,SOM3} \left(1 - rf_{SOM3} - \frac{CN_{SOM4}}{CN_{SOM3}}\right) \Big/ CN_{SOM4} \tag{21.24}$$

$$NF_{pot\_min,\,SOM4} = -CF_{pot,\,SOM4}/CN_{SOM4} \tag{21.25}$$

where the special form of Eq. arises because there is no SOM pool downstream of SOM4 in the converging cascade: all carbon fluxes leaving that pool are assumed to be in the form of respired CO_2, and all nitrogen fluxes leaving that pool are assumed to be sources of new mineral nitrogen.

Steps in the decomposition cascade that result in release of new mineral nitrogen (mineralization fluxes) are allowed to proceed at their potential rates, without modification for nitrogen availability. Steps that result in an uptake of mineral nitrogen (immobilization fluxes) are subject to rate limitation, depending on the availability of mineral nitrogen, the total immobilization demand, and the total demand for soil mineral nitrogen to support new plant growth. The potential mineral nitrogen fluxes from Eqs. - are evaluated, summing all the positive fluxes to generate the total potential nitrogen immobilization flux (NF_{immob_demand}, gN m^{-2} s^{-1}), and summing absolute values of all the negative fluxes to generate the total nitrogen mineralization flux (NF_{gross_nmin}, gN m^{-2} s^{-1}). Since NF_{griss_nmin} is a source of new mineral nitrogen to the soil mineral nitrogen pool it is not limited by the availability of soil mineral nitrogen, and is therefore an actual as opposed to a potential flux.

21.5 N Competition between plant uptake and soil immobilization fluxes

Once NF_{immob_demand} and NF_{nit_demand} for each layer j are known, the competition between plant and microbial nitrogen demand can be resolved. Mineral nitrogen in the soil pool (NS_{sminn}, gN m^{-2}) at the beginning of the timestep is considered the available supply.

Here, the NF_{plant_demand} is the theoretical maximum demand for nitrogen by plants to meet the entire carbon uptake given an N cost of zero (and therefore represents the upper bound on N requirements). N uptake costs that are > 0 imply that the plant will take up less N that it demands, ultimately. However, given the heuristic nature of the N competition algorithm, this discrepancy is not explicitly resolved here.

The hypothetical plant nitrogen demand from the soil mineral pool is distributed between layers in proportion to the profile of available mineral N:

$$NF_{plant\_demand,j} = NF_{plant\_demand} NS_{sminn\_j} \Big/ \sum_{j=1}^{nj} NS_{sminn,j} \tag{21.26}$$

Plants first compete for ammonia (NH4). For each soil layer (j), we calculate the total NH4 demand as:

$$NF_{total\_demand_{nh4},j} = NF_{immob\_demand,j} + NF_{immob\_demand,j} + NF_{nit\_demand,j} \tag{21.27}$$

where If $NF_{total\_demand,j}\Delta t < NS_{sminn,j}$, then the available pool is large enough to meet both the maximum plant and microbial demand, then immobilization proceeds at the maximum rate.

$$f_{immob\_demand,j} = 1.0 \tag{21.28}$$

where $f_{immob\_demand,j}$ is the fraction of potential immobilization demand that can be met given current supply of mineral nitrogen in this layer. We also set the actual nitrification flux to be the same as the potential flux (NF_{nit} = NF_{nit_demand}).

If $NF_{total\_demand,j}\Delta t \geq NS_{sminn,j}$, then there is not enough mineral nitrogen to meet the combined demands for plant growth and heterotrophic immobilization, immobilization is reduced proportional to the discrepancy, by $f_{immob\_demand,j}$, where

$$f_{immob\_demand,j} = \frac{NS_{sminn,j}}{\Delta t \, NF_{total\_demand,j}} \tag{21.29}$$

The N available to the FUN model for plant uptake ($NF_{plant\_avail\_sminn}$ (gN m^{-2}), which determines both the cost of N uptake, and the absolute limit on the N which is available for acquisition, is calculated as the total mineralized pool minus the actual immobilized flux:

$$NF_{plant\_avail\_sminn,j} = NS_{sminn,j} - f_{immob\_demand}NF_{immob\_demand,j} \tag{21.30}$$

This treatment of competition for nitrogen as a limiting resource is referred to a demand-based competition, where the fraction of the available resource that eventually flows to a particular process depends on the demand from that process in comparison to the total demand from all processes. Processes expressing a greater demand acquire a larger vfraction of the available resource.

21.6 Final Decomposition Fluxes

With f_{immob_demand} known, final decomposition fluxes can be calculated. Actual carbon fluxes leaving the individual litter and SOM pools, again for the example of the CLM-CN pool structure (the CENTURY structure will be similar but, again without the different terminal step), are calculated as:

$$CF_{Lit1} = \left\{ \begin{array}{ll} CF_{pot,\,Lit1}f_{immob\_demand} & \text{for } NF_{pot\_min,\,Lit1\rightarrow SOM1} > 0 \\ CF_{pot,\,Lit1} & \text{for } NF_{pot\_min,\,Lit1\rightarrow SOM1} \leq 0 \end{array} \right\} \tag{21.31}$$

$$CF_{Lit2} = \left\{ \begin{array}{ll} CF_{pot,\,Lit2}f_{immob\_demand} & \text{for } NF_{pot\_min,\,Lit2\rightarrow SOM2} > 0 \\ CF_{pot,\,Lit2} & \text{for } NF_{pot\_min,\,Lit2\rightarrow SOM2} \leq 0 \end{array} \right\} \tag{21.32}$$

$$CF_{Lit3} = \left\{ \begin{array}{ll} CF_{pot,\,Lit3}f_{immob\_demand} & \text{for } NF_{pot\_min,\,Lit3\rightarrow SOM3} > 0 \\ CF_{pot,\,Lit3} & \text{for } NF_{pot\_min,\,Lit3\rightarrow SOM3} \leq 0 \end{array} \right\} \tag{21.33}$$

$$CF_{SOM1} = \left\{ \begin{array}{ll} CF_{pot,\,SOM1}f_{immob\_demand} & \text{for } NF_{pot\_min,\,SOM1\rightarrow SOM2} > 0 \\ CF_{pot,\,SOM1} & \text{for } NF_{pot\_min,\,SOM1\rightarrow SOM2} \leq 0 \end{array} \right\} \tag{21.34}$$

$$CF_{SOM2} = \left\{ \begin{array}{ll} CF_{pot,\,SOM2}f_{immob\_demand} & \text{for } NF_{pot\_min,\,SOM2\rightarrow SOM3} > 0 \\ CF_{pot,\,SOM2} & \text{for } NF_{pot\_min,\,SOM2\rightarrow SOM3} \leq 0 \end{array} \right\} \tag{21.35}$$

$$CF_{SOM3} = \left\{ \begin{array}{ll} CF_{pot,\,SOM3}f_{immob\_demand} & \text{for } NF_{pot\_min,\,SOM3\rightarrow SOM4} > 0 \\ CF_{pot,\,SOM3} & \text{for } NF_{pot\_min,\,SOM3\rightarrow SOM4} \leq 0 \end{array} \right\} \tag{21.36}$$

$$CF_{SOM4} = CF_{pot,\,SOM4} \tag{21.37}$$

Heterotrophic respiration fluxes (losses of carbon as CO$_2$ to the atmosphere) are:

$$CF_{Lit1,\,HR} = CF_{Lit1}rf_{Lit1} \tag{21.38}$$

$$CF_{Lit2,\,HR} = CF_{Lit2}rf_{Lit2} \tag{21.39}$$

$$CF_{Lit3,\,HR} = CF_{Lit3}rf_{Lit3} \tag{21.40}$$

$$CF_{SOM1,\,HR} = CF_{SOM1}rf_{SOM1} \tag{21.41}$$

$$CF_{SOM2, HR} = CF_{SOM2} r f_{SOM2} \tag{21.42}$$

$$CF_{SOM3, HR} = CF_{SOM3} r f_{SOM3} \tag{21.43}$$

$$CF_{SOM4, HR} = CF_{SOM4} r f_{SOM4} \tag{21.44}$$

Transfers of carbon from upstream to downstream pools in the decomposition cascade are given as:

$$CF_{Lit1, SOM1} = CF_{Lit1} \left(1 - r f_{Lit1}\right) \tag{21.45}$$

$$CF_{Lit2, SOM2} = CF_{Lit2} \left(1 - r f_{Lit2}\right) \tag{21.46}$$

$$CF_{Lit3, SOM3} = CF_{Lit3} \left(1 - r f_{Lit3}\right) \tag{21.47}$$

$$CF_{SOM1, SOM2} = CF_{SOM1} \left(1 - r f_{SOM1}\right) \tag{21.48}$$

$$CF_{SOM2, SOM3} = CF_{SOM2} \left(1 - r f_{SOM2}\right) \tag{21.49}$$

$$CF_{SOM3, SOM4} = CF_{SOM3} \left(1 - r f_{SOM3}\right) \tag{21.50}$$

In accounting for the fluxes of nitrogen between pools in the decomposition cascade and associated fluxes to or from the soil mineral nitrogen pool, the model first calculates a flux of nitrogen from an upstream pool to a downstream pool, then calculates a flux either from the soil mineral nitrogen pool to the downstream pool (immobilization) or from the downstream pool to the soil mineral nitrogen pool (mineralization). Transfers of nitrogen from upstream to downstream pools in the decomposition cascade are given as:

$$NF_{Lit1, SOM1} = CF_{Lit1}/CN_{Lit1} \tag{21.51}$$

$$NF_{Lit2, SOM2} = CF_{Lit2}/CN_{Lit2} \tag{21.52}$$

$$NF_{Lit3, SOM3} = CF_{Lit3}/CN_{Lit3} \tag{21.53}$$

$$NF_{SOM1, SOM2} = CF_{SOM1}/CN_{SOM1} \tag{21.54}$$

$$NF_{SOM2, SOM3} = CF_{SOM2}/CN_{SOM2} \tag{21.55}$$

$$NF_{SOM3, SOM4} = CF_{SOM3}/CN_{SOM3} \tag{21.56}$$

Corresponding fluxes to or from the soil mineral nitrogen pool depend on whether the decomposition step is an immobilization flux or a mineralization flux:

$$NF_{sminn, Lit1 \to SOM1} = \left\{ \begin{array}{ll} NF_{pot\_min, Lit1 \to SOM1} f_{immob\_demand} & \text{for } NF_{pot\_min, Lit1 \to SOM1} > 0 \\ NF_{pot\_min, Lit1 \to SOM1} & \text{for } NF_{pot\_min, Lit1 \to SOM1} \leq 0 \end{array} \right\} \tag{21.57}$$

$$NF_{sminn, Lit2 \to SOM2} = \left\{ \begin{array}{ll} NF_{pot\_min, Lit2 \to SOM2} f_{immob\_demand} & \text{for } NF_{pot\_min, Lit2 \to SOM2} > 0 \\ NF_{pot\_min, Lit2 \to SOM2} & \text{for } NF_{pot\_min, Lit2 \to SOM2} \leq 0 \end{array} \right\} \tag{21.58}$$

$$NF_{sminn, Lit3 \to SOM3} = \left\{ \begin{array}{ll} NF_{pot\_min, Lit3 \to SOM3} f_{immob\_demand} & \text{for } NF_{pot\_min, Lit3 \to SOM3} > 0 \\ NF_{pot\_min, Lit3 \to SOM3} & \text{for } NF_{pot\_min, Lit3 \to SOM3} \leq 0 \end{array} \right\} \tag{21.59}$$

$$NF_{sminn, SOM1 \to SOM2} = \left\{ \begin{array}{ll} NF_{pot\_min, SOM1 \to SOM2} f_{immob\_demand} & \text{for } NF_{pot\_min, SOM1 \to SOM2} > 0 \\ NF_{pot\_min, SOM1 \to SOM2} & \text{for } NF_{pot\_min, SOM1 \to SOM2} \leq 0 \end{array} \right\} \tag{21.60}$$

$$NF_{sminn, SOM2 \to SOM3} = \left\{ \begin{array}{ll} NF_{pot\_min, SOM2 \to SOM3} f_{immob\_demand} & \text{for } NF_{pot\_min, SOM2 \to SOM3} > 0 \\ NF_{pot\_min, SOM2 \to SOM3} & \text{for } NF_{pot\_min, SOM2 \to SOM3} \leq 0 \end{array} \right\} \tag{21.61}$$

$$NF_{sminn, SOM3 \to SOM4} = \left\{ \begin{array}{ll} NF_{pot\_min, SOM3 \to SOM4} f_{immob\_demand} & \text{for } NF_{pot\_min, SOM3 \to SOM4} > 0 \\ NF_{pot\_min, SOM3 \to SOM4} & \text{for } NF_{pot\_min, SOM3 \to SOM4} \leq 0 \end{array} \right\} \tag{21.62}$$

$$NF_{sminn, SOM4} = NF_{pot\_min, SOM4} \tag{21.63}$$

21.7 Vertical Distribution and Transport of Decomposing C and N pools

Additional terms are needed to calculate the vertically-resolved soil C and N budget: the initial vertical distribution of C and N from PFTs delivered to the litter and CWD pools, and the vertical transport of C and N pools.

For initial vertical inputs, CLM uses separate profiles for aboveground (leaf, stem) and belowground (root) inputs. Aboveground inputs are given a single exponential with default e-folding depth = 0.1m. Belowground inputs are distributed according to rooting profiles with default values based on the Jackson et al. (1996) exponential parameterization.

Vertical mixing is accomplished by an advection-diffusion equation. The goal of this is to consider slow, soild- and adsorbed-phase transport due to bioturbation, cryoturbation, and erosion. Faster aqueous-phase transport is not included in CLM, but has been developed as part of the CLM-BeTR suite of parameterizations (Tang and Riley 2013). The default value of the advection term is 0 cm/yr, such that transport is purely diffusive. Diffusive transport differs in rate between permafrost soils (where cryoturbation is the dominant transport term) and non-permafrost soils (where bioturbation dominates). For permafrost soils, a parameterization based on that of *Koven et al. (2009)* is used: the diffusivity parameter is constant through the active layer, and decreases linearly from the base of the active layer to zero at a set depth (default 3m); the default permafrost diffusivity is 5 cm^2/yr. For non-permafrost soils, the default diffusivity is 1 cm^2/yr.

21.8 Model Equilibration and its Acceleration

For transient experiments, it is usually assumed that the carbon cycle is starting from a point of relatively close equilibrium, i.e. that productivity is balanced by ecosystem carbon losses through respiratory and disturbance pathways. In order to satisfy this assumption, the model is generally run until the productivity and loss terms find a stable long-term equilibrium; at this point the model is considered 'spun up'.

Because of the coupling between the slowest SOM pools and productivity through N downregulation of photosynthesis, equilibration of the model for initialization purposes will take an extremely long time in the standard mode. This is particularly true for the CENTURY-based decomposition cascade, which includes a passive pool. In order to rapidly equilibrate the model, a modified version of the "accelerated decomposition" *(Thornton and Rosenbloon, 2005)* is used. The fundamental idea of this approach is to allow fluxes between the various pools (both turnover-defined and vertically-defined fluxes) adjust rapidly, while keeping the pool sizes themselves small so that they can fill quickly. To do this, the base decomposition rate k_i for each pool i is accelerated by a term a_i such that the slow pools are collapsed onto an approximately annual timescale *Koven et al. (2013)*. Accelerating the pools beyond this timescale distorts the seasonal and/or diurnal cycles of decomposition and N mineralization, thus leading to a substantially different ecosystem productivity than the full model. For the vertical model, the vertical transport terms are also accelerated by the same term a_i, as is the radioactive decay when ^{14}C is enabled, following the same principle of keeping fluxes between pools (or fluxes lost to decay) close to the full model while keeping the pools sizes small. When leaving the accelerated decomposition mode, the concentration of C and N in pools that had been accelerated are multiplied by the same term a_i, to bring the model into approximate equilibrium. Note that in CLM, the model can also transition into accelerated decomposition mode from the standard mode (by dividing the pools by a_i), and that the transitions into and out of accelerated decomposition mode are handled automatically by CLM upon loading from restart files (which preserve information about the mode of the model when restart files were written).

The base acceleration terms for the two decomposition cascades are shown in Tables 15.1 and 15.3. In addition to the base terms, CLM5 also includes a geographic term to the acceleration in order to apply larger values to high-latitude systems, where decomposition rates are particularly slow and thus equilibration can take significantly longer than in temperate or tropical climates. This geographic term takes the form of a logistic equation, where a_i is equal to the product of the base acceleration term and a_l below:

$$a_l = 1 + 50/\left(1 + exp\left(-0.1 * \left(abs(latitude) - 60\right)\right)\right) \tag{21.64}$$

CHAPTER 22

EXTERNAL NITROGEN CYCLE

22.1 Summary of CLM5.0 updates relative to CLM4.5

We describe external inputs to the nitrogen cycle in CLM5.0. Much of the following information appeared in the CLM4.5 Technical Note (*Oleson et al. 2013*) as well as *Koven et al. (2013)*.

CLM5.0 includes the following changes to terrestrial nitrogen inputs:

- Time varrying deposition of reactive nitrogen. In off-line runs this changes monthly. In coupled simulations N deposition is passed at the coupling timestep (e.g., half-hourly).

- Asymbiotic (or free living) N fixation is a function of evapotranspiration and is added to the inorganic nitrogen (NH_4^+) pool (described below).

- Symbiotic N fixation is handled by the FUN model (chapter 18) and is passed straight to the plant, not the mineral nitrogen pool.

22.2 Overview

In addition to the relatively rapid cycling of nitrogen within the plant – litter – soil organic matter system, CLM also represents several processes which couple the internal nitrogen cycle to external sources and sinks. Inputs of new mineral nitrogen are from atmospheric deposition and biological nitrogen fixation. Losses of mineral nitrogen are due to nitrification, denitrification, leaching, and losses in fire. While the short-term dynamics of nitrogen limitation depend on the behavior of the internal nitrogen cycle, establishment of total ecosystem nitrogen stocks depends on the balance between sources and sinks in the external nitrogen cycle (*Thomas et al. 2015*).

As with CLM4.5, CLM5.0 represents inorganic N transformations based on the Century N-gas model; this includes separate NH_4^+ and NO_3^- pools, as well as environmentally controlled nitrification and denitrification rates that is described below.

22.3 Atmospheric Nitrogen Deposition

CLM uses a single variable to represent the total deposition of mineral nitrogen onto the land surface, combining wet and dry deposition of NO_y and NH_x as a single flux (NF_{ndep_sminn}, gN m^{-2} s^{-1}). This flux is intended to represent total reactive nitrogen deposited to the land surface which originates from the following natural and anthropogenic sources (Galloway et al. 2004): formation of NO_x during lightning, NO_x and NH_3 emission from wildfire, NO_x emission from natural soils, NH_3 emission from natural soils, vegetation, and wild animals, NO_x and NH_3 emission during fossil fuel combustion (both thermal and fuel NO_x production), NO_x and NH_3 emission from other industrial processes, NO_x and NH_3 emission from fire associated with deforestation, NO_x and NH_3 emission from agricultural burning, NO_x emission from agricultural soils, NH_3 emission from agricultural crops, NH_3 emission from agricultural animal waste, and NH_3 emission from human waste and waste water. The deposition flux is provided as a spatially and (potentially) temporally varying dataset (see section 2.3.1 for a description of the default input dataset).

The nitrogen deposition flux is assumed to enter the NH_4^+ pool, and is vertically distributed throughout the soil profile. Although N deposition inputs include both oxidized and reduced forms, CLM5 only reads in total N deposition. This approach is held over from CLM4.0, which only represented a single mineral nitrogen pool, however, real pathways for wet and dry nitrogen deposition can be more complex than currently represented in the CLM5.0, including release from melting snowpack and direct foliar uptake of deposited NO_y (*Tye et al. 2005*; *Vallano and Sparks, 2007*).

In offline (uncoupled) CLM5.0 simulations monthly estimates of N deposition are provided, as opposed to decadal files supplied with previous versions of the model. In coupled simulations, N depositions fluxes are passed to the land model at the frequency of the time step (every half hour) through the coupler.

22.4 Biological Nitrogen Fixation

The fixation of new reactive nitrogen from atmospheric N_2 by soil microorganisms is an important component of both preindustrial and modern-day nitrogen budgets, but a mechanistic understanding of global-scale controls on biological nitrogen fixation (BNF) is still only poorly developed (*Cleveland et al. 1999*; *Galloway et al. 2004*). CLM5.0 uses the FUN model (chapter 18) to calculate the carbon cost and nitrogen acquired through symbotic nitrogen fixation. This nitrogen is immediately available to plants.

Cleveland et al. (1999) suggested an empirical relationships that predicts BNF as a function of either evapotranspiration rate or net primary productivity for natural vegetation. CLM5.0 adopts the evapotranspiration approach to calculate asymbiotic, or free-living, N fixation. This function has been modified from the *Cleveland et al. (1999)* estimates to provide lower estimate of free-living nitrogen fixation in CLM5.0 (CF_{ann_ET}, mm yr^{-1}). This moves away from the NPP approach used in CLM4.0 and 4.5 and avoids unrealistically increasing freeliving rates of N fixation under global change scenarios (*Wieder et al. 2015* The expression used is:

$$NF_{nfix,sminn} = 0.0006\,(0.0117 + CF_{ann\_ET})\,/\,(86400 \cdot 365) \tag{22.1}$$

Where $NF_{nfix,sminn}$ (gN m^{-2} s^{-1}) is the rate of free-living nitrogen fixation in Figure 22.1.

As with Atmospheric N deposition, free-living N inputs are added directly to the NH_4^+ pool.

22.5 Nitrification and Denitrification Losses of Nitrogen

Nitrification is an autotrophic process that converts less mobile ammonium ions into nitrate, that can more easily be lost from soil systems by leaching or denitrification. The process catalyzed by ammonia oxidizing archaea and bacteria that convert ammonium (NH_4^+) into nitrite, which is subsequently oxidized into nitrate (NO_3^-). Conditions favoring nitrification include high NH_4^+ concentrations, well aerated soils, a neutral pH and warmer temperatures.

Under aerobic conditions in the soil oxygen is the preferred electron acceptor supporting the metabolism of heterotrophs, but anaerobic conditions favor the activity of soil heterotrophs which use nitrate as an electron acceptor
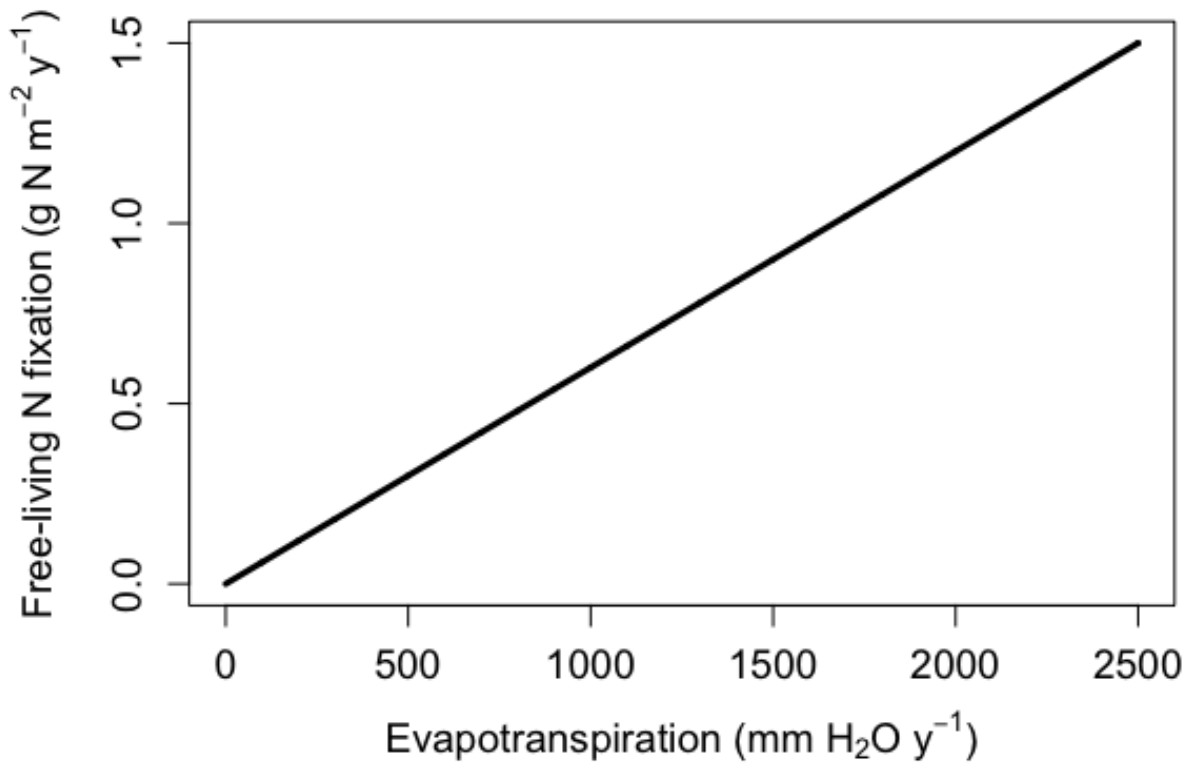
Figure 22.1: Free-living nitrogen fixation as a function of annual evapotranspiration. Results here show annual N inputs from free-living N fixations, but the model actually calculates inputs on a per second basis.

(e.g. *Pseudomonas* and *Clostridium*) supporting respiration. This process, known as denitrification, results in the transformation of nitrate to gaseous N_2, with smaller associated production of NO_x and N_2O. It is typically assumed that nitrogen fixation and denitrification were approximately balanced in the preindustrial biosphere (*Galloway et al. 2004*). It is likely that denitrification can occur within anaerobic microsites within an otherwise aerobic soil environment, leading to large global denitrification fluxes even when fluxes per unit area are rather low (*Galloway et al. 2004*).

CLM includes a detailed representation of nitrification and denitrification based on the Century N model (*Parton et al. 1996*, *2001*; *del Grosso et al. 2000*). In this approach, nitrification of NH_4^+ to NO_3^- is a function of temperature, moisture, and pH:

$$f_{nitr,p} = [NH_4] \, k_{nitr} f(T) \, f(H_2O) \, f(pH) \tag{22.2}$$

where $f_{nitr,p}$ is the potential nitrification rate (prior to competition for NH_4^+ by plant uptake and N immobilization), k_{nitr} is the maximum nitrification rate (10 % day-1, (*Parton et al. 2001*), and *f(T)* and *f(H)$_2$O* are rate modifiers for temperature and moisture content. CLM uses the same rate modifiers as are used in the decomposition routine. *f(pH)* is a rate modifier for pH; however, because CLM does not calculate pH, instead a fixed pH value of 6.5 is used in the pH function of *Parton et al. (1996)*.

The potential denitrification rate is co-limited by NO^{-3} concentration and C consumption rates, and occurs only in the anoxic fraction of soils:

$$f_{denitr,p} = \min \left(f(decomp), f\left(\left[NO_3^- \right] \right) \right) frac_{anox} \tag{22.3}$$

where $f_{denitr,p}$ is the potential denitrification rate and *f(decomp)* and *f([NO3$^-$])* are the carbon- and nitrate- limited denitrification rate functions, respectively, (*del Grosso et al. 2000*). Because the modified CLM includes explicit treatment of soil biogeochemical vertical profiles, including diffusion of the trace gases O_2 and CH_4 (*Riley et al. 2011a*), the calculation of anoxic fraction $frac_{anox}$ uses this information following the anoxic microsite formulation of *Arah and Vinten (1995)*.

$$frac_{anox} = \exp \left(-a R_{\psi}^{-\alpha} V^{-\beta} C^{\gamma} \left[\theta + \chi \varepsilon \right]^{\delta} \right) \tag{22.4}$$

where a, α, β, γ, and δ are constants (equal to 1.5x10^{-10}, 1.26, 0.6, 0.6, and 0.85, respectively), R_{ψ} is the radius of a typical pore space at moisture content ψ, V is the O_2 consumption rate, C is the O_2 concentration, θ is the water-filled pore space, χ is the ratio of diffusivity of oxygen in water to that in air, and ϵ is the air-filled pore space (*Arah and Vinten (1995)*). These parameters are all calculated separately at each layer to define a profile of anoxic porespace fraction in the soil.

The nitrification/denitrification models used here also predict fluxes of N_2O via a "hole-in-the-pipe" approach (*Firestone and Davidson, 1989*). A constant fraction (6 * 10^{-4}, *Li et al. 2000*) of the nitrification flux is assumed to be N_2O, while the fraction of denitrification going to N_2O, $P_{N2:N2O}$, is variable, following the Century (*del Grosso et al. 2000*) approach:

$$P_{N_2:N_2O} = \max \left(0.16 k_1, k_1 \exp \left(-0.8 P_{NO_3:CO_2} \right) \right) f_{WFPS} \tag{22.5}$$

where $P_{NO3:CO2}$ is the ratio of CO_2 production in a given soil layer to the NO_3^- concentration, k_1 is a function of d_g, the gas diffusivity through the soil matrix:

$$k_1 = \max \left(1.7, 38.4 - 350 * d_g \right) \tag{22.6}$$

and f_{WFPS} is a function of the water filled pore space *WFPS:*

$$f_{WFPS} = \max \left(0.1, 0.015 \times WFPS - 0.32 \right) \tag{22.7}$$

22.6 Leaching Losses of Nitrogen

Soil mineral nitrogen remaining after plant uptake, immobilization, and denitrification is subject to loss as a dissolved component of hydrologic outflow from the soil column (leaching). This leaching loss ($NF_{leached}$, gN m^{-2} s^{-1}) depends on the concentration of dissolved mineral (inorganic) nitrogen in soil water solution (DIN, gN kgH$_2$O), and the rate of hydrologic discharge from the soil column to streamflow (Q_{dis}, kgH$_2$O m^{-2} s^{-1}, section 7.5), as

$$NF_{leached} = DIN \cdot Q_{dis}. \tag{22.8}$$

DIN is calculated assuming that a constant fraction (sf, proportion) of the remaining soil mineral N pool is in soluble form, and that this entire fraction is dissolved in the total soil water. For the Century- based formulation in CLM5.0, the leaching acts only on the NO$_3^{-'}$ pool (which is assumed to be 100% soluble), while the NH$_4^+$ pool is assumed to be 100% adsorbed onto mineral surfaces and unaffected by leaching. DIN is then given as

$$DIN = \frac{NS_{sminn}sf}{WS_{tot\_soil}} \tag{22.9}$$

where WS_{tot_soil} (kgH:sub:2O m^{-2}) is the total mass of soil water content integrated over the column. The total mineral nitrogen leaching flux is limited on each time step to not exceed the soluble fraction of NS_{sminn}

$$NF_{leached} = \min\left(NF_{leached}, \frac{NS_{sminn}sf}{\Delta t}\right). \tag{22.10}$$

22.7 Losses of Nitrogen Due to Fire

The final pathway for nitrogen loss is through combustion, also known as pyrodenitrification. Detailed equations are provided, together with the effects of fire on the carbon budget, in Chapter 24). It is assumed in CLM-CN that losses of N due to fire are restricted to vegetation and litter pools (including coarse woody debris). Loss rates of N are determined by the fraction of biomass lost to combustion, assuming that most of the nitrogen in the burned biomass is lost to the atmosphere (*Schlesinger, 1997*; *Smith et al. 2005*). It is assumed that soil organic matter pools of carbon and nitrogen are not directly affected by fire (*Neff et al. 2005*).

CHAPTER 23

PLANT MORTALITY

Plant mortality as described here applies to perennial vegetation types, and is intended to represent the death of individuals from a stand of plants due to the aggregate of processes such as wind throw, insect attack, disease, extreme temperatures or drought, and age-related decline in vigor. These processes are referred to in aggregate as "gap-phase" mortality. Mortality due to fire and anthropogenic land cover change are treated separately (see Chapters 24 and 27, respectively).

23.1 Mortality Fluxes Leaving Vegetation Pools

Whole-plant mortality is parameterized very simply, assuming a mortality rate of 2% yr^{-1} for all vegetation types. This is clearly a gross oversimplification of an important process, and additional work is required to better constrain this process in different climate zones (*Keller et al. 2004*; *Sollins 1982*), for different species mixtures (*Gomes et al. 2003*), and for different size and age classes (*Busing 2005*; *Law et al. 2003*). Literature values for forest mortality rates range from at least 0.7% to 3.0% yr^{-1}. Taking the annual rate of mortality (*am*, proportion yr^{-1}) as 0.02, a mortality rate per second (*m*) is calculated as $m = am/(365 \cdot 86400)$. All vegetation carbon and nitrogen pools for display, storage, and transfer are affected at rate *m*, with mortality fluxes out of vegetation pools eventually merged to the column level and deposited in litter pools. Mortality (*mort*) fluxes out of displayed vegetation carbon and nitrogen pools are

$$CF_{leaf\_mort} = CS_{leaf}m \tag{23.1}$$

$$CF_{froot\_mort} = CS_{froot}m \tag{23.2}$$

$$CF_{livestem\_mort} = CS_{livestem}m \tag{23.3}$$

$$CF_{deadstem\_mort} = CS_{deadstem}m \tag{23.4}$$

$$CF_{livecroot\_mort} = CS_{livecroot}m \tag{23.5}$$

$$CF_{deadcroot\_mort} = CS_{deadcroot}m \tag{23.6}$$

$$NF_{leaf\_mort} = NS_{leaf}m \tag{23.7}$$

$$NF_{froot\_mort} = NS_{froot}m \tag{23.8}$$

$$NF_{livestem\_mort} = NS_{livestem}m \tag{23.9}$$

$$NF_{deadstem\_mort} = NS_{deadstem}m \tag{23.10}$$

$$NF_{livecroot\_mort} = NS_{livecroot}m \tag{23.11}$$

$$NF_{deadcroot\_mort} = NS_{deadcroot}m \tag{23.12}$$

$$NF_{retrans\_mort} = NS_{retrans}m. \tag{23.13}$$

where CF are carbon fluxes, CS is carbon storage, NF are nitrogen fluxes, NS is nitrogen storage, *croot* refers to coarse roots, *froot* refers to fine roots, and *retrans* refers to retranslocated.

Mortality fluxes out of carbon and nitrogen storage (*stor)* pools are

$$CF_{leaf\_stor\_mort} = CS_{leaf\_stor}m \tag{23.14}$$

$$CF_{froot\_stor\_mort} = CS_{froot\_stor}m \tag{23.15}$$

$$CF_{livestem\_stor\_mort} = CS_{livestem\_stor}m \tag{23.16}$$

$$CF_{deadstem\_stor\_mort} = CS_{deadstem\_stor}m \tag{23.17}$$

$$CF_{livecroot\_stor\_mort} = CS_{livecroot\_stor}m \tag{23.18}$$

$$CF_{deadcroot\_stor\_mort} = CS_{deadcroot\_stor}m \tag{23.19}$$

$$CF_{gresp\_stor\_mort} = CS_{gresp\_stor}m \tag{23.20}$$

$$NF_{leaf\_stor\_mort} = NS_{leaf\_stor}m \tag{23.21}$$

$$NF_{froot\_stor\_mort} = NS_{froot\_stor}m \tag{23.22}$$

$$NF_{livestem\_stor\_mort} = NS_{livestem\_stor}m \tag{23.23}$$

$$NF_{deadstem\_stor\_mort} = NS_{deadstem\_stor}m \tag{23.24}$$

$$NF_{livecroot\_stor\_mort} = NS_{livecroot\_stor}m \tag{23.25}$$

$$NF_{deadcroot\_stor\_mort} = NS_{deadcroot\_stor}m \tag{23.26}$$

where *gresp* refers to growth respiration.

Mortality fluxes out of carbon and nitrogen transfer (*xfer)* growth pools are

$$CF_{leaf\_xfer\_mort} = CS_{leaf\_xfer}m \tag{23.27}$$

$$CF_{froot\_xfer\_mort} = CS_{froot\_xfer}m \tag{23.28}$$

$$CF_{livestem\_xfer\_mort} = CS_{livestem\_xfer}m \tag{23.29}$$

$$CF_{deadstem\_xfer\_mort} = CS_{deadstem\_xfer}m \tag{23.30}$$

$$CF_{livecroot\_xfer\_mort} = CS_{livecroot\_xfer}m \tag{23.31}$$

$$CF_{deadcroot\_xfer\_mort} = CS_{deadcroot\_xfer}m \tag{23.32}$$

$$CF_{gresp\_xfer\_mort} = CS_{gresp\_xfer}m \tag{23.33}$$

$$NF_{leaf\_xfer\_mort} = NS_{leaf\_xfer}m \tag{23.34}$$

$$NF_{froot\_xfer\_mort} = NS_{froot\_xfer}m \tag{23.35}$$

$$NF_{livestem\_xfer\_mort} = NS_{livestem\_xfer}m \tag{23.36}$$

$$NF_{deadstem\_xfer\_mort} = NS_{deadstem\_xfer}m \tag{23.37}$$

$$NF_{livecroot\_xfer\_mort} = NS_{livecroot\_xfer}m \tag{23.38}$$

$$NF_{deadcroot\_xfer\_mort} = NS_{deadcroot\_xfer}m \tag{23.39}$$

23.2 Mortality Fluxes Merged to the Column Level

Analogous to the treatment of litterfall fluxes, mortality fluxes leaving the vegetation pools are merged to the column level according to the weighted distribution of PFTs on the column ($wcol_p$), and deposited in litter and coarse woody debris pools, which are defined at the column level. Carbon and nitrogen fluxes from mortality of displayed leaf and fine root into litter pools are calculated as

$$CF_{leaf\_mort,lit1} = \sum_{p=0}^{npfts} CF_{leaf\_mort} f_{lab\_leaf,p} wcol_p \tag{23.40}$$

$$CF_{leaf\_mort,lit2} = \sum_{p=0}^{npfts} CF_{leaf\_mort} f_{cel\_leaf,p} wcol_p \tag{23.41}$$

$$CF_{leaf\_mort,lit3} = \sum_{p=0}^{npfts} CF_{leaf\_mort} f_{lig\_leaf,p} wcol_p \tag{23.42}$$

$$CF_{froot\_mort,lit1} = \sum_{p=0}^{npfts} CF_{froot\_mort} f_{lab\_froot,p} wcol_p \tag{23.43}$$

$$CF_{froot\_mort,lit2} = \sum_{p=0}^{npfts} CF_{froot\_mort} f_{cel\_froot,p} wcol_p \tag{23.44}$$

$$CF_{froot\_mort,lit3} = \sum_{p=0}^{npfts} CF_{froot\_mort} f_{lig\_froot,p} wcol_p \tag{23.45}$$

$$NF_{leaf\_mort,lit1} = \sum_{p=0}^{npfts} NF_{leaf\_mort} f_{lab\_leaf,p} wcol_p \tag{23.46}$$

$$NF_{leaf\_mort,lit2} = \sum_{p=0}^{npfts} NF_{leaf\_mort} f_{cel\_leaf,p} wcol_p \tag{23.47}$$

$$NF_{leaf\_mort,lit3} = \sum_{p=0}^{npfts} NF_{leaf\_mort} f_{lig\_leaf,p} wcol_p \tag{23.48}$$

$$NF_{froot\_mort,lit1} = \sum_{p=0}^{npfts} NF_{froot\_mort} f_{lab\_froot,p} wcol_p \tag{23.49}$$

$$NF_{froot\_mort,lit2} = \sum_{p=0}^{npfts} NF_{froot\_mort} f_{cel\_froot,p} wcol_p \tag{23.50}$$

$$NF_{froot\_mort,lit3} = \sum_{p=0}^{npfts} NF_{froot\_mort} f_{lig\_froot,p} wcol_p. \tag{23.51}$$

where *lab* refers to labile, *cel* refers to cellulose, and *lig* refers to lignin. Carbon and nitrogen mortality fluxes from displayed live and dead stem and coarse root pools are merged to the column level and deposited in the coarse woody debris (*cwd*) pools:

$$CF_{livestem\_mort,cwd} = \sum_{p=0}^{npfts} CF_{livestem\_mort} wcol_p \tag{23.52}$$

$$CF_{deadstem\_mort,cwd} = \sum_{p=0}^{npfts} CF_{deadstem\_mort} wcol_p \tag{23.53}$$

$$CF_{livecroot\_mort,cwd} = \sum_{p=0}^{npfts} CF_{livecroot\_mort} wcol_p \tag{23.54}$$

$$CF_{deadcroot\_mort,cwd} = \sum_{p=0}^{npfts} CF_{deadcroot\_mort} wcol_p \tag{23.55}$$

$$NF_{livestem\_mort,cwd} = \sum_{p=0}^{npfts} NF_{livestem\_mort} wcol_p \tag{23.56}$$

$$NF_{deadstem\_mort,cwd} = \sum_{p=0}^{npfts} NF_{deadstem\_mort} wcol_p \tag{23.57}$$

$$NF_{livecroot\_mort,cwd} = \sum_{p=0}^{npfts} NF_{livecroot\_mort} wcol_p \tag{23.58}$$

$$NF_{deadcroot\_mort,cwd} = \sum_{p=0}^{npfts} NF_{deadcroot\_mort} wcol_p \tag{23.59}$$

All vegetation storage and transfer pools for carbon and nitrogen are assumed to exist as labile pools within the plant (e.g. as carbohydrate stores, in the case of carbon pools). This assumption applies to storage and transfer pools for both non-woody and woody tissues. The mortality fluxes from these pools are therefore assumed to be deposited in the labile litter pools (CS_{lit1}, NS_{lit1}), after being merged to the column level. Carbon mortality fluxes out of storage and transfer pools are:

$$CF_{leaf\_stor\_mort,lit1} = \sum_{p=0}^{npfts} CF_{leaf\_stor\_mort} wcol_p \tag{23.60}$$

$$CF_{froot\_stor\_mort,lit1} = \sum_{p=0}^{npfts} CF_{froot\_stor\_mort} wcol_p \tag{23.61}$$

$$CF_{livestem\_stor\_mort,lit1} = \sum_{p=0}^{npfts} CF_{livestem\_stor\_mort} wcol_p \tag{23.62}$$

$$CF_{deadstem\_stor\_mort,lit1} = \sum_{p=0}^{npfts} CF_{deadstem\_stor\_mort} wcol_p \tag{23.63}$$

$$CF_{livecroot\_stor\_mort,lit1} = \sum_{p=0}^{npfts} CF_{livecroot\_stor\_mort} wcol_p \tag{23.64}$$

$$CF_{deadcroot\_stor\_mort,lit1} = \sum_{p=0}^{npfts} CF_{deadcroot\_stor\_mort} wcol_p \tag{23.65}$$

$$CF_{gresp\_stor\_mort,lit1} = \sum_{p=0}^{npfts} CF_{gresp\_stor\_mort} wcol_p \tag{23.66}$$

$$CF_{leaf\_xfer\_mort,lit1} = \sum_{p=0}^{npfts} CF_{leaf\_xfer\_mort} wcol_p \tag{23.67}$$

$$CF_{froot\_xfer\_mort,lit1} = \sum_{p=0}^{npfts} CF_{froot\_xfer\_mort} wcol_p \qquad (23.68)$$

$$CF_{livestem\_xfer\_mort,lit1} = \sum_{p=0}^{npfts} CF_{livestem\_xfer\_mort} wcol_p \qquad (23.69)$$

$$CF_{deadstem\_xfer\_mort,lit1} = \sum_{p=0}^{npfts} CF_{deadstem\_xfer\_mort} wcol_p \qquad (23.70)$$

$$CF_{livecroot\_xfer\_mort,lit1} = \sum_{p=0}^{npfts} CF_{livecroot\_xfer\_mort} wcol_p \qquad (23.71)$$

$$CF_{deadcroot\_xfer\_mort,lit1} = \sum_{p=0}^{npfts} CF_{deadcroot\_xfer\_mort} wcol_p \qquad (23.72)$$

$$CF_{gresp\_xfer\_mort,lit1} = \sum_{p=0}^{npfts} CF_{gresp\_xfer\_mort} wcol_p. \qquad (23.73)$$

Nitrogen mortality fluxes out of storage and transfer pools, including the storage pool for retranslocated nitrogen, are calculated as:

$$NF_{leaf\_stor\_mort,lit1} = \sum_{p=0}^{npfts} NF_{leaf\_stor\_mort} wcol_p \qquad (23.74)$$

$$NF_{froot\_stor\_mort,lit1} = \sum_{p=0}^{npfts} NF_{froot\_stor\_mort} wcol_p \qquad (23.75)$$

$$NF_{livestem\_stor\_mort,lit1} = \sum_{p=0}^{npfts} NF_{livestem\_stor\_mort} wcol_p \qquad (23.76)$$

$$NF_{deadstem\_stor\_mort,lit1} = \sum_{p=0}^{npfts} NF_{deadstem\_stor\_mort} wcol_p \qquad (23.77)$$

$$NF_{livecroot\_stor\_mort,lit1} = \sum_{p=0}^{npfts} NF_{livecroot\_stor\_mort} wcol_p \qquad (23.78)$$

$$NF_{deadcroot\_stor\_mort,lit1} = \sum_{p=0}^{npfts} NF_{deadcroot\_stor\_mort} wcol_p \qquad (23.79)$$

$$NF_{retrans\_mort,lit1} = \sum_{p=0}^{npfts} NF_{retrans\_mort} wcol_p \qquad (23.80)$$

$$NF_{leaf\_xfer\_mort,lit1} = \sum_{p=0}^{npfts} NF_{leaf\_xfer\_mort} wcol_p \qquad (23.81)$$

$$NF_{froot\_xfer\_mort,lit1} = \sum_{p=0}^{npfts} NF_{froot\_xfer\_mort} wcol_p \qquad (23.82)$$

$$NF_{livestem\_xfer\_mort,lit1} = \sum_{p=0}^{npfts} NF_{livestem\_xfer\_mort} wcol_p \qquad (23.83)$$

$$NF_{deadstem\_xfer\_mort,lit1} = \sum_{p=0}^{npfts} NF_{deadstem\_xfer\_mort} wcol_p \qquad (23.84)$$

$$NF_{livecroot\_xfer\_mort,lit1} = \sum_{p=0}^{npfts} NF_{livecroot\_xfer\_mort} wcol_p \qquad (23.85)$$

$$NF_{deadcroot\_xfer\_mort,lit1} = \sum_{p=0}^{npfts} NF_{deadcroot\_xfer\_mort} wcol_p. \qquad (23.86)$$

CHAPTER 24

FIRE

The fire parameterization in CLM contains four components: non-peat fires outside cropland and tropical closed forests, agricultural fires in cropland, deforestation fires in the tropical closed forests, and peat fires (see *Li et al. 2012a*, *Li et al. 2012b*, *Li et al. 2013*, *Li and Lawrence 2017* for details). In this fire parameterization, burned area is affected by climate and weather conditions, vegetation composition and structure, and human activities. After burned area is calculated, we estimate the fire impact, including biomass and peat burning, fire-induced vegetation mortality, adjustment of the carbon and nitrogen (C/N) pools, and fire emissions.

24.1 Non-peat fires outside cropland and tropical closed forest

Burned area in a grid cell, A_b (km^2 s^{-1}), is determined by

$$A_b = N_f a \tag{24.1}$$

where N_f (count s^{-1}) is fire counts in the grid cell; a (km^2) is average fire spread area of a fire.

24.1.1 Fire counts

Fire counts N_f is taken as

$$N_f = N_i f_b f_m f_{se,o} \tag{24.2}$$

where N_i (count s^{-1}) is the number of ignition sources due to natural causes and human activities; f_b and f_m (fractions) represent the availability and combustibility of fuel, respectively; $f_{se,o}$ is the fraction of anthropogenic and natural fires unsuppressed by humans and related to the socioeconomic conditions.

N_i (count s^{-1}) is given as

$$N_i = (I_n + I_a) A_g \tag{24.3}$$

where I_n (count km^{-2} s^{-1}) and I_a (count km^{-2} s^{-1}) are the number of natural and anthropogenic ignitions per km^2, respectively; A_g is the area of the grid cell (km^2). I_n is estimated by

$$I_n = \gamma \psi I_l \tag{24.4}$$

where γ =0.22 is ignition efficiency of cloud-to-ground lightning; $\psi = \frac{1}{5.16 + 2.16\cos[3min(60,\lambda)]}$ is the cloud-to-ground lightning fraction and depends on the latitude λ (degrees) ; I_l (flash km^{-2} s^{-1}) is the total lightning flashes. I_a is modeled as a monotonic increasing function of population density:

$$I_a = \frac{\alpha D_P k(D_P)}{n} \tag{24.5}$$

where $\alpha = 0.01$ (count person^{-1} mon^{-1}) is the number of potential ignition sources by a person per month; D_P (person km^{-2}) is the population density; $k(D_P) = 6.8 D_P^{-0.6}$ represents anthropogenic ignition potential as a function of human population density D_P ; n is the seconds in a month.

Fuel availability f_b is given as

$$f_b = \left\{ \begin{array}{ll} 0 & B_{ag} < B_{low} \\ \frac{B_{ag} - B_{low}}{B_{up} - B_{low}} & B_{low} \leq B_{ag} \leq B_{up} \\ 1 & B_{ag} > B_{up} \end{array} \right\} , \tag{24.6}$$

where B_{ag} (g C m^{-2}) is the biomass of combined leaf, stem, litter, and woody debris pools; B_{low} = 105 g C m^{-2} is the lower fuel threshold below which fire does not occur; B_{up} = 1050 g C m^{-2} is the upper fuel threshold above which fire occurrence is not limited by fuel availability.

Fuel combustibility f_m is estimated by

$$f_m = f_{RH} f_\beta, \qquad T_{17cm} > T_f \tag{24.7}$$

where f_{RH} and f_β represent the dependence of fuel combustibility on relative humidity RH (%) and root-zone soil moisture limitation β (fraction); T_{17cm} is the temperature of the top 17 cm of soil (K) and T_f is the freezing temperature. f_{RH} is a weighted average of real time RH (RH_0) and 30-day running mean RH (RH_{30d}):

$$f_{RH} = (1 - w)l_{RH_0} + wl_{RH_{30d}} \tag{24.8}$$

where weight $w = \max[0, \min(1, \frac{B_{ag} - 2500}{2500})]$, $l_{RH_0} = 1 - \max[0, \min(1, \frac{RH_0 - 30}{80 - 30})]$, and $l_{RH_{30d}} = 1 - \max[0.75, \min(1, \frac{RH_{30d}}{90})]$. f_β is given by

$$f_\beta = \left\{ \begin{array}{ll} 1 & \beta \leq \beta_{low} \\ \frac{\beta_{up} - \beta}{\beta_{up} - \beta_{low}} & \beta_{low} < \beta < \beta_{up} \\ 0 & \beta \geq \beta_{up} \end{array} \right\} , \tag{24.9}$$

where β_{low} =0.85 and β_{up} =0.98 are the lower and upper thresholds, respectively.

For scarcely populated regions ($D_p \leq 0.1$ person km^{-2}), we assume that anthropogenic suppression on fire occurrence is negligible, i.e., $f_{se,o} = 1.0$. In regions of $D_p > 0.1$ person km^{-2}, we parameterize the fraction of anthropogenic and natural fires unsuppressed by human activities as

$$f_{se,o} = f_d f_e \tag{24.10}$$

where f_d and f_e are the effects of the demographic and economic conditions on fire occurrence. The demographic influence on fire occurrence is

$$f_d = 0.01 + 0.98 \exp(-0.025 D_P). \tag{24.11}$$

For shrub and grass PFTs, the economic influence on fire occurrence is parameterized as a function of Gross Domestic Product GDP (k 1995US\$ capita^{-1}):

$$f_e = 0.1 + 0.9 \times \exp[-\pi(\frac{GDP}{8})^{0.5}] \tag{24.12}$$

which captures 73% of the observed MODIS fire counts with variable GDP in regions where shrub and grass PFTs are dominant (fractional coverage of shrub and grass PFTs > 50%). In regions outside tropical closed forests and dominated by trees (fractional coverage of tree PFTs > 50%), we use

$$f_e = \left\{ \begin{array}{ll} 0.39 & GDP > 20 \\ 0.79 & 8 < GDP \leq 20 \\ 1 & GDP \leq 8 \end{array} \right\}, \tag{24.13}$$

to reproduce the relationship between MODIS fire counts and GDP.

24.1.2 Average spread area of a fire

Fire fighting capacity depends on socioeconomic conditions and affects fire spread area. Due to a lack of observations, we consider the socioeconomic impact on the average burned area rather than separately on fire spread rate and fire duration:

$$a = a^* F_{se} \tag{24.14}$$

where a^* is the average burned area of a fire without anthropogenic suppression and F_{se} is the socioeconomic effect on fire spread area.

Average burned area of a fire without anthropogenic suppression is assumed elliptical in shape with the wind direction along the major axis and the point of ignition at one of the foci. According to the area formula for an ellipse, average burned area of a fire can be represented as:

$$a^* = \pi \frac{l}{2} \frac{w}{2} \times 10^{-6} = \frac{\pi u_p^2 \tau^2}{4 L_B} (1 + \frac{1}{H_B})^2 \times 10^{-6} \tag{24.15}$$

where u_p (m s^{-1}) is the fire spread rate in the downwind direction; τ (s) is average fire duration; L_B and H_B are length-to-breadth ratio and head-to-back ratio of the ellipse; 10^{-6} converts m^2 to km^2.

According to *Arora and Boer (2005)*,

$$L_B = 1.0 + 10.0[1 - \exp(-0.06W)] \tag{24.16}$$

where W(m s^{-1}) is the wind speed. According to the mathematical properties of the ellipse, the head-to-back ratio H_B is

$$H_B = \frac{u_p}{u_b} = \frac{L_B + (L_B^2 - 1)^{0.5}}{L_B - (L_B^2 - 1)^{0.5}}. \tag{24.17}$$

The fire spread rate in the downwind direction is represented as

$$u_p = u_{\max} C_m g(W) \tag{24.18}$$

(*Arora and Boer, 2005*), where $u_{\max}$ (m s^{-1}) is the PFT-dependent average maximum fire spread rate in natural vegetation regions; $C_m = \sqrt{f_m}$ and $g(W)$ represent the dependence of u_p on fuel wetness and wind speed W, respectively. $u_{\max}$ is set to 0.33 m s^{-1} for grass PFTs, 0.28 m s^{-1} for shrub PFTs, 0.26 m s^{-1} for needleleaf tree PFTs, and 0.25 m s^{-1} for other tree PFTs. $g(W)$ is derived from the mathematical properties of the ellipse and equation (24.16) and (24.17).

$$g(W) = \frac{2L_B}{1 + \frac{1}{H_B}} g(0). \tag{24.19}$$

Since g(W)=1.0, and L_B and H_B are at their maxima $L_B^{\max} = 11.0$ and $H_B^{\max} = 482.0$ when $W \to \infty$, g(0) can be derived as

$$g(0) = \frac{1 + \frac{1}{H_B^{\max}}}{2L_B^{\max}} = 0.05. \tag{24.20}$$

In the absence of globally gridded data on barriers to fire (e.g. rivers, lakes, roads, firebreaks) and human fire-fighting efforts, average fire duration is simply assumed equal to 1 which is the observed 2001–2004 mean persistence of most fires in the world (*Giglio et al. 2006*).

As with the socioeconomic influence on fire occurrence, we assume that the socioeconomic influence on fire spreading is negligible in regions of $D_p \leq 0.1$ person km^{-2}, i.e., $F_{se} = 1.0$. In regions of $D_p > 0.1$ person km^{-2}, we parameterize such socioeconomic influence as:

$$F_{se} = F_d F_e \tag{24.21}$$

where F_d and F_e are effects of the demographic and economic conditions on the average spread area of a fire, and are identified by maximizing the explained variability of the GFED3 burned area fraction with both socioeconomic indices in grid cells with various dominant vegetation types. For shrub and grass PFTs, the demographic impact factor is

$$F_d = 0.2 + 0.8 \times \exp[-\pi(\frac{D_p}{450})^{0.5}] \tag{24.22}$$

and the economic impact factor is

$$F_e = 0.2 + 0.8 \times \exp(-\pi\frac{GDP}{7}). \tag{24.23}$$

For tree PFTs outside tropical closed forests, the demographic and economic impact factors are given as

$$F_d = 0.4 + 0.6 \times \exp(-\pi\frac{D_p}{125}) \tag{24.24}$$

and

$$F_e = \begin{cases} 0.62, & GDP > 20 \\ 0.83, & 8 < GDP \leq 20 \\ 1, & GDP \leq 8 \end{cases} . \tag{24.25}$$

Equations (24.22) - (24.25) reflect that more developed and more densely populated regions have a higher fire fighting capability.

24.1.3 Fire impact

In post-fire regions, we calculate PFT-level fire carbon emissions from biomass burning of the jth PFT, ϕ_j (g C s^{-1}), as

$$\phi_j = A_{b,j} \mathbf{C}_j \bullet \mathbf{CC}_j \tag{24.26}$$

where $A_{b,j}$ (km^2 s^{-1}) is burned area for the jth PFT; $\mathbf{C_j} = (C_{leaf}, C_{stem}, C_{root}, C_{ts})$ is a vector with carbon density (g C km^{-2}) for leaf, stem (live and dead stem), root (fine, live coarse and dead coarse root), and transfer and storage carbon pools as elements; $\mathbf{CC}_j = (\mathbf{CC}_{leaf}, \mathbf{CC}_{stem}, \mathbf{CC}_{root}, \mathbf{CC}_{ts})$ is the corresponding combustion completeness factor vector (Table 24.1). Moreover, we assume that 50% and 28% of column-level litter and coarse woody debris are burned and the corresponding carbon is transferred to atmosphere.

Tissue mortality due to fire leads to carbon transfers in two ways. First, carbon from uncombusted leaf, live stem, dead stem, root, and transfer and storage pools $\mathbf{C'_{j1}}$ $=$ $(C_{leaf}(1 - CC_{leaf}), C_{livestem}(1 - CC_{stem}), C_{deadstem}(1 - CC_{stem}), C_{root}(1 - CC_{root}), C_{ts}(1 - CC_{ts}))_j$ (g C km^{-2}) is transferred to litter as

$$\Psi_{j1} = \frac{A_{b,j}}{f_j A_g} \mathbf{C'_{j1}} \bullet M_{j1} \tag{24.27}$$

where $M_{j1} = (M_{leaf}, M_{livestem,1}, M_{deadstem}, M_{root}, M_{ts})_j$ is the corresponding mortality factor vector (Table 24.1). Second, carbon from uncombusted live stems is transferred to dead stems as:

$$\Psi_{j2} = \frac{A_{b,j}}{f_j A_g} C_{livestem}(1 - CC_{stem})M_{livestem,2} \tag{24.28}$$

where $M_{livestem,2}$ is the corresponding mortality factor (Table 24.1).

Fire nitrogen emissions and nitrogen transfers due to fire-induced mortality are calculated the same way as for carbon, using the same values for combustion completeness and mortality factors. With CLM's dynamic vegetation option enabled, the number of tree PFT individuals killed by fire per km^2 (individual km^{-2} s^{-1}) is given by

$$P_{disturb,j} = \frac{A_{b,j}}{f_j A_g} P_j \xi_j \tag{24.29}$$

where P_j (individual km^{-2}) is the population density for the j th tree PFT and ξ_j is the whole-plant mortality factor (Table 24.1).

24.2 Agricultural fires

The burned area of cropland (km^2 s^{-1}) is taken as A_b:

$$A_b = a_1 f_{se} f_t f_{crop} A_g \tag{24.30}$$

where a_1 (s^{-1}) is a constant; f_{se} represents the socioeconomic effect on fires; f_t determines the seasonality of agricultural fires; f_{crop} is the fractional coverage of cropland. $a_1 = 1.6\times10^{-4}$ hr^{-1} is estimated using an inverse method, by matching 1997-2004 simulations to the analysis of *van der Werf et al. (2010)* that shows the 2001-2009 average contribution of cropland fires is 4.7% of the total global burned area.

The socioeconomic factor f_{se} is given as follows:

$$f_{se} = f_d f_e. \tag{24.31}$$

Here

$$f_d = 0.04 + 0.96 \times \exp[-\pi(\frac{D_p}{350})^{0.5}] \tag{24.32}$$

and

$$f_e = 0.01 + 0.99 \times \exp(-\pi\frac{GDP}{10}) \tag{24.33}$$

are the effects of population density and GDP on burned area, derived in a similar way to equation (24.32) and (24.33). f_t is set to 1 at the first time step during the climatological peak month for agricultural fires (*van der Werf et al. 2010*); f_t is set to 0 otherwise. Peak month in this dataset correlates with the month after harvesting or the month before planting. In CLM we use this dataset the same way whether the CROP option is active or not, without regard to the CROP option's simulated planting and harvesting dates.

In the post-fire region, fire impact is parameterized similar to section 24.1.3 but with combustion completeness factors and tissue mortality factors for crop PFTs (Table 24.1).

24.3 Deforestation fires

CLM focuses on deforestation fires in tropical closed forests. Tropical closed forests are defined as grid cells with tropical tree (BET and BDT tropical) coverage > 60% according to the FAO classification. Deforestation fires are

defined as fires caused by deforestation, including escaped deforestation fires, termed degradation fires. Deforestation and degradation fires are assumed to occur outside of cropland areas in these grid cells. Burned area is controlled by the deforestation rate and climate:

$$A_b = b \, f_{lu} f_{cli,d} f_b A_g \tag{24.34}$$

where b (s^{-1}) is a global constant; f_{lu} (fraction) represents the effect of decreasing fractional coverage of tree PFTs derived from land use data; $f_{cli,d}$ (fraction) represents the effect of climate conditions on the burned area.

Constants b and f_{lu} are calibrated based on observations and reanalysis datasets in the Amazon rainforest (tropical closed forests within 15.5 º S - 10.5 º N, 30.5 º W - 91 º W). $b = 0.033$ d^{-1} and f_{lu} is defined as

$$f_{lu} = \max(0.0005, 0.19D - 0.001) \tag{24.35}$$

where D (yr^{-1}) is the annual loss of tree cover based on CLM land use and land cover change data.

The effect of climate on deforestation fires is parameterized as:

$$
\begin{aligned}
f_{cli,d} \quad = \quad & \max\left[0, \min(1, \tfrac{b_2 - P_{60d}}{b_2})\right]^{0.5} \times \\
& \max\left[0, \min(1, \tfrac{b_3 - P_{10d}}{b_3})\right]^{0.5} \times \\
& \max\left[0, \min(1, \tfrac{0.25 - P}{0.25})\right]
\end{aligned}
\tag{24.36}
$$

where P (mm d^{-1}) is instantaneous precipitation, while P_{60d} (mm d^{-1}) and P_{10d} (mm d^{-1}) are 60-day and 10-day running means of precipitation, respectively; b_2 (mm d^{-1}) and b_3 (mm d^{-1}) are the grid-cell dependent thresholds of P_{60d} and P_{10d}; 0.25 mm d^{-1} is the maximum precipitation rate for drizzle. *Le Page et al. (2010)* analyzed the relationship between large-scale deforestation fire counts and precipitation during 2003 -2006 in southern Amazonia where tropical evergreen trees (BET Tropical) are dominant. Figure 2 in *Le Page et al. (2010)* showed that fires generally occurred if both P_{60d} and P_{10d} were less than about 4.0 mm d^{-1}, and fires occurred more frequently in a drier environment. Based on the 30-yr (1985 to 2004) precipitation data in *Qian et al. (2006)*. The climatological precipitation of dry months (P < 4.0 mm d^{-1}) in a year over tropical deciduous tree (BDT Tropical) dominated regions is 46% of that over BET Tropical dominated regions, so we set the PFT-dependent thresholds of P_{60d} and P_{10d} as 4.0 mm d^{-1} for BET Tropical and 1.8 mm d^{-1} (= 4.0 mm d^{-1} × 46%) for BDT Tropical, and b_2 and b_3 are the average of thresholds of BET Tropical and BDT Tropical weighted bytheir coverage.

The post-fire area due to deforestation is not limited to land-type conversion regions. In the tree-reduced region, the maximum fire carbon emissions are assumed to be 80% of the total conversion flux. According to the fraction of conversion flux for tropical trees in the tree-reduced region (60%) assigned by CLM4-CN, to reach the maximum fire carbon emissions in a conversion region requires burning this region about twice when we set PFT-dependent combustion completeness factors to about 0.3 for stem [the mean of 0.2−0.4 used in *van der Werf et al. (2010)*. Therefore, when the burned area calculated from equation (24.36) is no more than twice the tree-reduced area, we assume no escaped fires outside the land-type conversion region, and the fire-related fraction of the total conversion flux is estimated as $\frac{A_b/A_g}{2D}$. Otherwise, 80% of the total conversion flux is assumed to be fire carbon emissions, and the biomass combustion and vegetation mortality outside the tree-reduced regions with an area fraction of $\frac{A_b}{A_g} - 2D$ are set as in section 24.1.3.

24.4 Peat fires

The burned area due to peat fires is given as A_b:

$$A_b = c \, f_{cli,p} f_{peat} (1 - f_{sat}) A_g \tag{24.37}$$

where c (s^{-1}) is a constant; $f_{cli,p}$ represents the effect of climate on the burned area; f_{peat} is the fractional coverage of peatland in the grid cell; and f_{sat} is the fraction of the grid cell with a water table at the surface or higher. $c = 0.17 \times$

10^{-3} hr^{-1} for tropical peat fires and $c = 0.9 \times 10^{-5}$ hr^{-1} for boreal peat fires are derived using an inverse method, by matching simulations to earlier studies: about 2.4 Mha peatland was burned over Indonesia in 1997 (*Page et al. 2002*) and the average burned area of peat fires in Western Canada was 0.2 Mha yr^{-1} for 1980-1999 (*Turetsky et al. 2004*).

For tropical peat fires, $f_{cli,p}$ is set as a function of long-term precipitation P_{60d} :

$$f_{cli,p} = max \left[0, \min \left(1, \frac{4 - P_{60d}}{4} \right) \right]^2 .$$ (24.38)

For boreal peat fires, $f_{cli,p}$ is set to

$$f_{cli,p} = \exp(-\pi \frac{\theta_{17cm}}{0.3}) \cdot \max[0, \min(1, \frac{T_{17cm} - T_f}{10})]$$ (24.39)

where θ_{17cm} is the wetness of the top 17 cm of soil.

Peat fires lead to peat burning and the combustion and mortality of vegetation over peatlands. For tropical peat fires, based on *Page et al. (2002)*, about 6% of the peat carbon loss from stored carbon is caused by 33.9% of the peatland burned. Carbon emissions due to peat burning (g C m^{-2} s^{-1}) are therefore set as the product of 6%/33.9%, burned area fraction of peat fire (s^{-1}), and soil organic carbon (g C m^{-2}). For boreal peat fires, the carbon emissions due to peat burning are set as 2.2 kg C m^{-2} peat fire area (*Turetsky et al. 2002*). Biomass combustion and vegetation mortality in post-fire peatlands are set the same as section 24.1.3 for non-crop PFTs and as section 24.2 for crops PFTs.

24.5 Fire trace gas and aerosol emissions

CESM2 is the first Earth system model that can model the full coupling among fire, fire emissions, land, and atmosphere. CLM5, as the land component of CESM2, calculates the surface trace gas and aerosol emissions due to fire and fire emission heights, as the inputs of atmospheric chemistry model and aerosol model.

Emissions for trace gas and aerosol species x and the j-th PFT, $E_{x,j}$ (g species s^{-1}), are given by

$$E_{x,j} = EF_{x,j} \frac{\phi_j}{[C]} .$$ (24.40)

Here, $EF_{x,j}$ (g species (g dm)$^{-1}$) is PFT-dependent emission factor scaled from biome-level values (Li et al., in prep, also used for FireMIP fire emissions data) by Dr. Val Martin and Dr. Li. $[C] = 0.5$ (g C (g dm)$^{-1}$) is a conversion factor from dry matter to carbon.

Emission height is PFT-dependent: 4.3 km for needleleaf tree PFTs, 3 km for other boreal and temperate tree PFTs, 2.5 km for tropical tree PFTs, 2 km for shrub PFTs, and 1 km for grass and crop PFTs. These values are compiled from earlier studies by Dr. Val Martin.

Table 24.1: PFT-specific combustion completeness and fire mortality factors.

PFT	CC_{leaf}	CC_{stem}	CC_{root}	CC_{ts}	M_{leaf}	$M_{livestem,1}$	$M_{deadstem}$	M_{root}	M_{ts}	$M_{livestem,2}$	ξ_j
NET Temperate	0.80	0.30	0.00	0.50	0.80	0.15	0.15	0.15	0.50	0.35	0.15
NET Boreal	0.80	0.30	0.00	0.50	0.80	0.15	0.15	0.15	0.50	0.35	0.15
NDT Boreal	0.80	0.30	0.00	0.50	0.80	0.15	0.15	0.15	0.50	0.35	0.15
BET Tropical	0.80	0.27	0.00	0.45	0.80	0.13	0.13	0.13	0.45	0.32	0.13
BET Temperate	0.80	0.27	0.00	0.45	0.80	0.13	0.13	0.13	0.45	0.32	0.13
BDT Tropical	0.80	0.27	0.00	0.45	0.80	0.10	0.10	0.10	0.35	0.25	0.10
BDT Temperate	0.80	0.27	0.00	0.45	0.80	0.10	0.10	0.10	0.35	0.25	0.10
BDT Boreal	0.80	0.27	0.00	0.45	0.80	0.13	0.13	0.13	0.45	0.32	0.13
BES Temperate	0.80	0.35	0.00	0.55	0.80	0.17	0.17	0.17	0.55	0.38	0.17
BDS Temperate	0.80	0.35	0.00	0.55	0.80	0.17	0.17	0.17	0.55	0.38	0.17
BDS Boreal	0.80	0.35	0.00	0.55	0.80	0.17	0.17	0.17	0.55	0.38	0.17
C_3 Grass Arctic	0.80	0.80	0.00	0.80	0.80	0.20	0.20	0.20	0.80	0.60	0.20
C_3 Grass	0.80	0.80	0.00	0.80	0.80	0.20	0.20	0.20	0.80	0.60	0.20
C_4 Grass	0.80	0.80	0.00	0.80	0.80	0.20	0.20	0.20	0.80	0.60	0.20
Crop	0.80	0.80	0.00	0.80	0.80	0.20	0.20	0.20	0.80	0.60	0.20

Leaves (CC_{leaf}), stems (CC_{stem}), roots (CC_{root}), and transfer and storage carbon (CC_{ts}); mortality factors for leaves (M_{leaf}), live stems ($M_{livestem,1}$), dead stems ($M_{deadstem}$), roots (M_{root}), and transfer and storage carbon (M_{ts}) related to the carbon transfers from these pools to litter pool; mortality factors for live stems ($M_{livestem,2}$) related to the carbon transfer from live stems to dead stems; whole-plant mortality factor (ξ_j).

CHAPTER 25

METHANE MODEL

The representation of processes in the methane biogeochemical model integrated in CLM [CLM4Me; (*Riley et al. 2011a*)] is based on several previously published models (*Cao et al. 1996*; *Petrescu et al. 2010*; *Tianet al. 2010*; *Walter et al. 2001*; *Wania et al. 2010*; *Zhang et al. 2002*; *Zhuang et al. 2004*). Although the model has similarities with these precursor models, a number of new process representations and parameterization have been integrated into CLM.

Mechanistically modeling net surface CH_4 emissions requires representing a complex and interacting series of processes. We first (section 25.1) describe the overall model structure and flow of information in the CH_4 model, then describe the methods used to represent: CH_4 mass balance; CH_4 production; ebullition; aerenchyma transport; CH_4 oxidation; reactive transport solution, including boundary conditions, numerical solution, water table interface, etc.; seasonal inundation effects; and impact of seasonal inundation on CH_4 production.

25.1 Methane Model Structure and Flow

The driver routine for the methane biogeochemistry calculations (ch4, in ch4Mod.F) controls the initialization of boundary conditions, inundation, and impact of redox conditions; calls to routines to calculate CH_4 production, oxidation, transport through aerenchyma, ebullition, and the overall mass balance (for unsaturated and saturated soils and, if desired, lakes); resolves changes to CH_4 calculations associated with a changing inundated fraction; performs a mass balance check; and calculates the average gridcell CH_4 production, oxidation, and exchanges with the atmosphere.

25.2 Governing Mass-Balance Relationship

The model (Figure 25.1) accounts for CH_4 production in the anaerobic fraction of soil (P, mol m^{-3} s^{-1}), ebullition (E, mol m^{-3} s^{-1}), aerenchyma transport (A, mol m^{-3} s^{-1}), aqueous and gaseous diffusion (F_D, mol m^{-2} s^{-1}), and oxidation (O, mol m^{-3} s^{-1}) via a transient reaction diffusion equation:

$$\frac{\partial (RC)}{\partial t} = \frac{\partial F_D}{\partial z} + P(z,t) - E(z,t) - A(z,t) - O(z,t) \tag{25.1}$$

Here z (m) represents the vertical dimension, t (s) is time, and R accounts for gas in both the aqueous and gaseous phases:$R = \epsilon_a + K_H \epsilon_w$, with ϵ_a, ϵ_w, and K_H (-) the air-filled porosity, water-filled porosity, and partitioning coeffi-

cient for the species of interest, respectively, and C represents CH_4 or O_2 concentration with respect to water volume (mol m^{-3}).

An analogous version of equation is concurrently solved for O_2, but with the following differences relative to CH_4: $P = E = 0$ (i.e., no production or ebullition), and the oxidation sink includes the O_2 demanded by methanotrophs, heterotroph decomposers, nitrifiers, and autotrophic root respiration.

As currently implemented, each gridcell contains an inundated and a non-inundated fraction. Therefore, equation is solved four times for each gridcell and time step: in the inundated and non-inundated fractions, and for CH_4 and O_2. If desired, the CH_4 and O_2 mass balance equation is solved again for lakes (Chapter 9). For non-inundated areas, the water table interface is defined at the deepest transition from greater than 95% saturated to less than 95% saturated that occurs above frozen soil layers. The inundated fraction is allowed to change at each time step, and the total soil CH_4 quantity is conserved by evolving CH_4 to the atmosphere when the inundated fraction decreases, and averaging a portion of the non-inundated concentration into the inundated concentration when the inundated fraction increases.
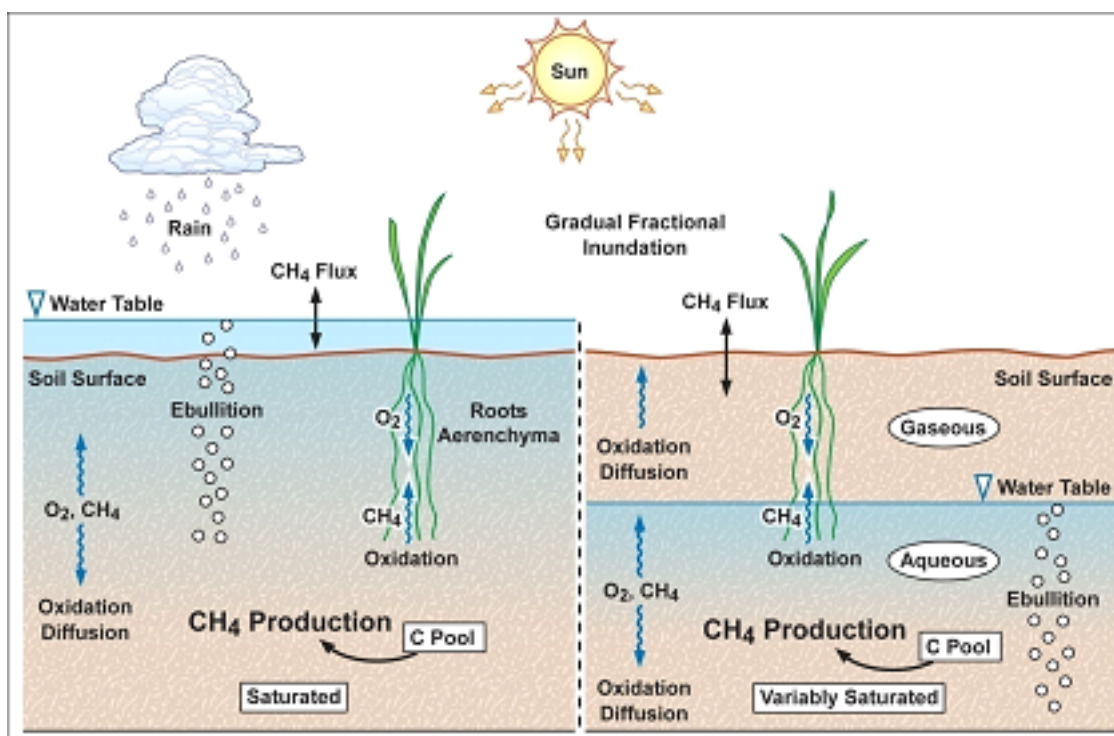
Figure 25.1: Schematic representation of biological and physical processes integrated in CLM that affect the net CH_4 surface flux (*Riley et al. 2011a*). (left) Fully inundated portion of a CLM gridcell and (right) variably saturated portion of a gridcell.

25.3 CH$_4$ Production

Because CLM does not currently specifically represent wetland plant functional types or soil biogeochemical processes, we used gridcell-averaged decomposition rates as proxies. Thus, the upland (default) heterotrophic respiration is used to estimate the wetland decomposition rate after first dividing off the O_2 limitation. The O_2 consumption associated with anaerobic decomposition is then set to the unlimited version so that it will be reduced appropriately during O_2 competition. CH_4 production at each soil level in the anaerobic portion (i.e., below the water table) of the column is related to the gridcell estimate of heterotrophic respiration from soil and litter (R_H; mol C m^{-2} s^{-1}) corrected for its soil temperature (T_s) dependence, soil temperature through a A_{10} factor (f_T), pH (f_{pH}), redox potential (f_{pE}), and a

factor accounting for the seasonal inundation fraction (*S*, described below):

$$P = R_H f_{CH_4} f_T f_{pH} f_{pE} S. \tag{25.2}$$

Here, f_{CH_4} is the baseline ratio between CO_2 and CH_4 production (all parameters values are given in Table 25.1). Currently, f_{CH_4} is modified to account for our assumptions that methanogens may have a higher Q_{10} than aerobic decomposers; are not N limited; and do not have a low-moisture limitation.

When the single BGC soil level is used in CLM (Chapter 21), the temperature factor, f_T, is set to 0 for temperatures equal to or below freezing, even though CLM allows heterotrophic respiration below freezing. However, if the vertically resolved BGC soil column is used, CH_4 production continues below freezing because liquid water stress limits decomposition. The base temperature for the Q_{10} factor, T_B, is 22° C and effectively modified the base f_{CH_4} value.

For the single-layer BGC version, R_H is distributed among soil levels by assuming that 50% is associated with the roots (using the CLM PFT-specific rooting distribution) and the rest is evenly divided among the top 0.28 m of soil (to be consistent with CLM's soil decomposition algorithm). For the vertically resolved BGC version, the prognosed distribution of R_H is used to estimate CH_4 production.

The factor f_{pH} is nominally set to 1, although a static spatial map of *pH* can be used to determine this factor (*Dunfield et al. 1993*) by applying:

$$f_{pH} = 10^{-0.2235pH^2 + 2.7727pH - 8.6}. \tag{25.3}$$

The f_{pE} factor assumes that alternative electron acceptors are reduced with an e-folding time of 30 days after inundation. The default version of the model applies this factor to horizontal changes in inundated area but not to vertical changes in the water table depth in the upland fraction of the gridcell. We consider both f_{pH} and f_{pE} to be poorly constrained in the model and identify these controllers as important areas for model improvement.

As a non-default option to account for CH_4 production in anoxic microsites above the water table, we apply the Arah and Stephen (1998) estimate of anaerobic fraction:

$$\varphi = \frac{1}{1 + \eta C_{O_2}}. \tag{25.4}$$

Here, ϕ is the factor by which production is inhibited above the water table (compared to production as calculated in equation , C_{O_2} (mol m^{-3}) is the bulk soil oxygen concentration, and η = 400 mol m^{-3}.

The O_2 required to facilitate the vertically resolved heterotrophic decomposition and root respiration is estimated assuming 1 mol O_2 is required per mol CO_2 produced. The model also calculates the O_2 required during nitrification, and the total O_2 demand is used in the O_2 mass balance solution.

Table 25.1: Parameter descriptions and sensitivity analysis ranges applied in the methane model

Mechanism	Parameter	Baseline Value	Range for Sensitivity Analysis	Units	Description
Production	Q_{10}	2	$1.5 - 4$	•	CH_4 production Q_{10}
	f_{pH}	1	On, off	•	Impact of pH on CH_4 production
	f_{pE}	1	On, off	•	Impact of redox potential on CH_4 production
	S	Varies	NA	•	Seasonal inundation factor
	β	0.2	NA	•	Effect of anoxia on decomposition rate (used to calculate S only)
	f_{CH_4}	0.2	NA	•	Ratio between CH_4 and CO_2 production below the water table
Ebullition	$C_{e,max}$	0.15	NA	mol m^{-3}	CH_4 concentration to start ebullition
	$C_{e,min}$	0.15	NA	•	CH_4 concentration to end ebullition
Diffusion	f_{D_0}	1	1, 10	m^2 s^{-1}	Diffusion coefficient multiplier (Table 24.2)
Aerenchyma	p	0.3	NA	•	Grass aerenchyma porosity
	R	2.9×10^{-3} m	NA	m	Aerenchyma radius
	r_L	3	NA	•	Root length to depth ratio
	F_a	1	$0.5 - 1.5$	•	Aerenchyma conductance multiplier
Oxidation	K_{CH_4}	5 x 10^{-3}	5×10^{-4}-5×10^{-2}	mol m^{-3}	CH_4 half-saturation oxidation coefficient (wetlands)
	K_{O_2}	2 x 10^{-2}	2×10^{-3} - 2×10^{-1}	mol m^{-3}	O_2 half-saturation oxidation coefficient
	$R_{o,\max}$	1.25 x 10^{-5}	1.25×10^{-6} - 1.25×10^{-4}	mol m	dation rate (wetlands)

25.4 Ebullition

Briefly, the simulated aqueous CH_4 concentration in each soil level is used to estimate the expected equilibrium gaseous partial pressure (C_e), as a function of temperature and depth below the water table, by first estimating the Henry's law partitioning coefficient (k_h^C) by the method described in *Wania et al. (2010)*:

$$\log\left(\frac{1}{k_H}\right) = \log k_H^s - \frac{1}{C_H}\left(\frac{1}{T} - \frac{1}{T^s}\right) \tag{25.5}$$

$$k_h^C = T k_H R_g \tag{25.6}$$

$$C_e = \frac{C_w R_g T}{\theta_s k_H^C p} \tag{25.7}$$

where C_H is a constant, R_g is the universal gas constant, k_H^s is Henry's law partitioning coefficient at standard temperature (T^s), C_w is local aqueous CH_4 concentration, and p is pressure.

The local pressure is calculated as the sum of the ambient pressure, water pressure down to the local depth, and pressure from surface ponding (if applicable). When the CH_4 partial pressure exceeds 15% of the local pressure (Baird et al. 2004; Strack et al. 2006; Wania et al. 2010), bubbling occurs to remove CH_4 to below this value, modified by the fraction of CH_4 in the bubbles [taken as 57%; (*Kellner et al. 2006*; *Wania et al. 2010*)]. Bubbles are immediately added to the surface flux for saturated columns and are placed immediately above the water table interface in unsaturated columns.

25.5 Aerenchyma Transport

Aerenchyma transport is modeled in CLM as gaseous diffusion driven by a concentration gradient between the specific soil layer and the atmosphere and, if specified, by vertical advection with the transpiration stream. There is evidence that pressure driven flow can also occur, but we did not include that mechanism in the current model.

The diffusive transport through aerenchyma (A, mol m^{-2} s^{-1}) from each soil layer is represented in the model as:

$$A = \frac{C(z) - C_a}{r_L z/D + r_a} p T \rho_r, \tag{25.8}$$

where D is the free-air gas diffusion coefficient (m:sup:2 s^{-1}); $C(z)$ (mol m^{-3}) is the gaseous concentration at depth z (m); r_L is the ratio of root length to depth; p is the porosity (-); T is specific aerenchyma area (m:sup:2 m^{-2}); r_a is the aerodynamic resistance between the surface and the atmospheric reference height (s m:sup:-1); and ρ_r is the rooting density as a function of depth (-). The gaseous concentration is calculated with Henry's law as described in equation .

Based on the ranges reported in *Colmer (2003)*, we have chosen baseline aerenchyma porosity values of 0.3 for grass and crop PFTs and 0.1 for tree and shrub PFTs:

$$T = \frac{4 f_N N_a}{0.22} \pi R^2. \tag{25.9}$$

Here N_a is annual net primary production (NPP, mol m^{-2} s^{-1}); R is the aerenchyma radius (2.9 $\times 10^{-3}$ m); f_N is the belowground fraction of annual NPP; and the 0.22 factor represents the amount of C per tiller. O_2 can also diffuse in from the atmosphere to the soil layer via the reverse of the same pathway, with the same representation as Equation but with the gas diffusivity of oxygen.

CLM also simulates the direct emission of CH_4 from leaves to the atmosphere via transpiration of dissolved methane. We calculate this flux (F_{CH_4-T} ; mol m^{-2} s^{-1}) using the simulated soil water methane concentration ($C_{CH_4,j}$ (mol m^{-3})) in each soil layer j and the CLM predicted transpiration (F_T) for each PFT, assuming that no methane was oxidized inside the plant tissue:

$$F_{CH_4-T} = \sum_j \rho_{r,j} F_T C_{CH_4,j}. \tag{25.10}$$

25.6 CH$_4$ Oxidation

CLM represents CH$_4$ oxidation with double Michaelis-Menten kinetics (*Arah and Stephen 1998*; *Segers 1998*), dependent on both the gaseous CH$_4$ and O$_2$ concentrations:

$$R_{oxic} = R_{o,\max} \left[\frac{C_{CH_4}}{K_{CH_4} + C_{CH_4}} \right] \left[\frac{C_{O_2}}{K_{O_2} + C_{O_2}} \right] Q_{10} F_{\vartheta} \tag{25.11}$$

where K_{CH_4} and K_{O_2} are the half saturation coefficients (mol m^{-3}) with respect to CH$_4$ and O$_2$ concentrations, respectively; $R_{o,\max}$ is the maximum oxidation rate (mol m^{-3} s^{-1}); and Q_{10} specifies the temperature dependence of the reaction with a base temperature set to 12 $^{\circ}$ C. The soil moisture limitation factor F_{θ} is applied above the water table to represent water stress for methanotrophs. Based on the data in *Schnell and King (1996)*, we take $F_{\theta} = e^{-P/P_c}$, where P is the soil moisture potential and $P_c = -2.4 \times 10^5$ mm.

25.7 Reactive Transport Solution

The solution to equation is solved in several sequential steps: resolve competition for CH$_4$ and O$_2$ (section 25.7.1); add the ebullition flux into the layer directly above the water table or into the atmosphere; calculate the overall CH$_4$ or O$_2$ source term based on production, aerenchyma transport, ebullition, and oxidation; establish boundary conditions, including surface conductance to account for snow, ponding, and turbulent conductances and bottom flux condition (section 25.7.2); calculate diffusivity (section 25.7.3); and solve the resulting mass balance using a tridiagonal solver (section 25.7.5).

25.7.1 Competition for CH$_4$ and O$_2$

For each time step, the unlimited CH$_4$ and O$_2$ demands in each model depth interval are computed. If the total demand over a time step for one of the species exceeds the amount available in a particular control volume, the demand from each process associated with the sink is scaled by the fraction required to ensure non-negative concentrations. Since the methanotrophs are limited by both CH$_4$ and O$_2$, the stricter limitation is applied to methanotroph oxidation, and then the limitations are scaled back for the other processes. The competition is designed so that the sinks must not exceed the available concentration over the time step, and if any limitation exists, the sinks must sum to this value. Because the sinks are calculated explicitly while the transport is semi-implicit, negative concentrations can occur after the tridiagonal solution. When this condition occurs for O$_2$, the concentrations are reset to zero; if it occurs for CH$_4$, the surface flux is adjusted and the concentration is set to zero if the adjustment is not too large.

25.7.2 CH$_4$ and O$_2$ Source Terms

The overall CH$_4$ net source term consists of production, oxidation at the base of aerenchyma, transport through aerenchyma, methanotrophic oxidation, and ebullition (either to the control volume above the water table if unsaturated or directly to the atmosphere if saturated). For O$_2$ below the top control volume, the net source term consists of O$_2$ losses from methanotrophy, SOM decomposition, and autotrophic respiration, and an O$_2$ source through aerenchyma.

25.7.3 Aqueous and Gaseous Diffusion

For gaseous diffusion, we adopted the temperature dependence of molecular free-air diffusion coefficients (D_0) (m:sup:2 s^{-1})) as described by *Lerman (1979)* and applied by *Wania et al. (2010)* (Table 25.2).

Table 25.2: Temperature dependence of aqueous and gaseous diffusion coefficients for CH_4 and O_2

D_0 (m² s⁻¹)	CH_4	O_2
Aqueous	$0.9798 + 0.02986T + 0.0004381T^2$	$1.172 + 0.03443T + 0.0005048T^2$
Gaseous	$0.1875 + 0.0013T$	$0.1759 + 0.0011T$

Gaseous diffusivity in soils also depends on the molecular diffusivity, soil structure, porosity, and organic matter content. *Moldrup et al. (2003)*, using observations across a range of unsaturated mineral soils, showed that the relationship between effective diffusivity (D_e (m:sup:2 s⁻¹)) and soil properties can be represented as:

$$D_e = D_0 \theta_a^2 \left(\frac{\theta_a}{\theta_s} \right)^{3/b},$$

(25.12)

where θ_a and θ_s are the air-filled and total (saturated water-filled) porosities (-), respectively, and b is the slope of the water retention curve (-). However, *Iiyama and Hasegawa (2005)* have shown that the original Millington-Quirk (*Millington and Quirk 1961*) relationship matched measurements more closely in unsaturated peat soils:

$$D_e = D_0 \frac{\theta_a^{10/3}}{\theta_s^2}$$

(25.13)

In CLM, we applied equation for soils with zero organic matter content and equation for soils with more than 130 kg m⁻³ organic matter content. A linear interpolation between these two limits is applied for soils with SOM content below 130 kg m⁻³. For aqueous diffusion in the saturated part of the soil column, we applied (*Moldrup et al. (2003)*):

$$D_e = D_0 \theta_s^2.$$

(25.14)

To simplify the solution, we assumed that gaseous diffusion dominates above the water table interface and aqueous diffusion below the water table interface. Descriptions, baseline values, and dimensions for parameters specific to the CH_4 model are given in Table 25.1. For freezing or frozen soils below the water table, diffusion is limited to the remaining liquid (CLM allows for some freezing point depression), and the diffusion coefficients are scaled by the volume-fraction of liquid. For unsaturated soils, Henry's law equilibrium is assumed at the interface with the water table.

25.7.4 Boundary Conditions

We assume the CH_4 and O_2 surface fluxes can be calculated from an effective conductance and a gaseous concentration gradient between the atmospheric concentration and either the gaseous concentration in the first soil layer (unsaturated soils) or in equilibrium with the water (saturated soil $w (C_1^n - C_a)$ and $w (C_1^{n+1} - C_a)$ for the fully explicit and fully implicit cases, respectively (however, see *Tang and Riley (2013)* for a more complete representation of this process). Here, w is the surface boundary layer conductance as calculated in the existing CLM surface latent heat calculations. If the top layer is not fully saturated, the $\frac{D_{m1}}{\Delta x_{m1}}$ term is replaced with a series combination: $\left[\frac{1}{w} + \frac{\Delta x_1}{D_1} \right]^{-1}$, and if the top layer is saturated, this term is replaced with $\left[\frac{K_H}{w} + \frac{\frac{1}{2}\Delta x_1}{D_1} \right]^{-1}$, where K_H is the Henry's law equilibrium constant.

When snow is present, a resistance is added to account for diffusion through the snow based on the Millington-Quirk expression (25.13) and CLM's prediction of the liquid water, ice, and air fractions of each snow layer. When the soil is ponded, the diffusivity is assumed to be that of methane in pure water, and the resistance as the ratio of the ponding depth to diffusivity. The overall conductance is taken as the series combination of surface, snow, and ponding resistances. We assume a zero flux gradient at the bottom of the soil column.

25.7.5 Crank-Nicholson Solution

Equation is solved using a Crank-Nicholson solution (*Press et al. 1992*), which combines fully explicit and implicit representations of the mass balance. The fully explicit decomposition of equation can be written as

$$\frac{R_j^{n+1} C_j^{n+1} - R_j^n C_j^n}{\Delta t} = \frac{1}{\Delta x_j} \left[\frac{D_{p1}^n}{\Delta x_{p1}} \left(C_{j+1}^n - C_j^n \right) - \frac{D_{m1}^n}{\Delta x_{m1}} \left(C_j^n - C_{j-1}^n \right) \right] + S_j^n, \tag{25.15}$$

where j refers to the cell in the vertically discretized soil column (increasing downward), n refers to the current time step, Δt is the time step (s), $p1$ is $j+\frac{1}{2}$, $m1$ is $j-\frac{1}{2}$, and S_j^n is the net source at time step n and position j, i.e., $S_j^n = P(j,n) - E(j,n) - A(j,n) - O(j,n)$. The diffusivity coefficients are calculated as harmonic means of values from the adjacent cells. Equation is solved for gaseous and aqueous concentrations above and below the water table, respectively. The R term ensure the total mass balance in both phases is properly accounted for. An analogous relationship can be generated for the fully implicit case by replacing n by $n+1$ on the C and S terms of equation . Using an average of the fully implicit and fully explicit relationships gives:

$$-\frac{1}{2\Delta x_j} \frac{D_{m1}}{\Delta x_{m1}} C_{j-1}^{n+1} + \left[\frac{R_j^{n+1}}{\Delta t} + \frac{1}{2\Delta x_j} \left(\frac{D_{p1}}{\Delta x_{p1}} + \frac{D_{m1}}{\Delta x_{m1}} \right) \right] C_j^{n+1} - \frac{1}{2\Delta x_j} \frac{D_{p1}}{\Delta x_{p1}} C_{j+1}^{n+1} =$$
$$\frac{R_j^n}{\Delta t} + \frac{1}{2\Delta x_j} \left[\frac{D_{p1}}{\Delta x_{p1}} \left(C_{j+1}^n - C_j^n \right) - \frac{D_{m1}}{\Delta x_{m1}} \left(C_j^n - C_{j-1}^n \right) \right] + \frac{1}{2} \left[S_j^n + S_j^{n+1} \right] \tag{25.16}$$

Equation is solved with a standard tridiagonal solver, i.e.:

$$a C_{j-1}^{n+1} + b C_j^{n+1} + c C_{j+1}^{n+1} = r, \tag{25.17}$$

with coefficients specified in equation .

Two methane balance checks are performed at each timestep to insure that the diffusion solution and the time-varying aggregation over inundated and non-inundated areas strictly conserves methane molecules (except for production minus consumption) and carbon atoms.

25.7.6 Interface between water table and unsaturated zone

We assume Henry's Law equilibrium at the interface between the saturated and unsaturated zone and constant flux from the soil element below the interface to the center of the soil element above the interface. In this case, the coefficients are the same as described above, except for the soil element above the interface:

$$\frac{D_{p1}}{\Delta x_{p1}} = \left[K_H \frac{\Delta x_j}{2D_j} + \frac{\Delta x_{j+1}}{2D_{j+1}} \right]^{-1}$$

$$b = \left[\frac{R_j^{n+1}}{\Delta t} + \frac{1}{2\Delta x_j} \left(K_H \frac{D_{p1}}{\Delta x_{p1}} + \frac{D_{m1}}{\Delta x_{m1}} \right) \right]$$

$$r = \frac{R_j^n}{\Delta t} C_j^n + \frac{1}{2\Delta x_j} \left[\frac{D_{p1}}{\Delta x_{p1}} \left(C_{j+1}^n - K_H C_j^n \right) - \frac{D_{m1}}{\Delta x_{m1}} \left(C_j^n - C_{j-1}^n \right) \right] + \frac{1}{2} \left[S_j^n + S_j^{n+1} \right] \tag{25.18}$$

and the soil element below the interface:

$$\frac{D_{m1}}{\Delta x_{m1}} = \left[K_H \frac{\Delta x_{j-1}}{2D_{j-1}} + \frac{\Delta x_j}{2D_j} \right]^{-1}$$

$$a = -K_H \frac{1}{2\Delta x_j} \frac{D_{m1}}{\Delta x_{m1}}$$

$$r = \frac{R_j^n}{\Delta t} + C_j^n + \frac{1}{2\Delta x_j} \left[\frac{D_{p1}}{\Delta x_{p1}} \left(C_{j+1}^n - C_j^n \right) - \frac{D_{m1}}{\Delta x_{m1}} \left(C_j^n - K_H C_{j-1}^n \right) \right] + \frac{1}{2} \left[S_j^n + S_j^{n+1} \right] \tag{25.19}$$

25.8 Inundated Fraction Prediction

A simplified dynamic representation of spatial inundation based on recent work by *Prigent et al. (2007)* is used. Prigent et al. (2007) described a multi-satellite approach to estimate the global monthly inundated fraction (F_i) over an equal area grid (0.25 ∘ ×0.25∘ at the equator) from 1993 - 2000. They suggested that the IGBP estimate for inundation could be used as a measure of sensitivity of their detection approach at low inundation. We therefore used the sum of their satellite-derived F_i and the constant IGBP estimate when it was less than 10% to perform a simple inversion for the inundated fraction for methane production (f_s). The method optimized two parameters (fws_{slope} and $fws_{intercept}$) for each grid cell in a simple model based on simulated total water storage (TWS):

$$f_s = fws_{slope}TWS + fws_{intercept}. \tag{25.20}$$

These parameters were evaluated at the 0.5° resolution, and aggregated for coarser simulations. Ongoing work in the hydrology submodel of CLM may alleviate the need for this crude simplification of inundated fraction in future model versions.

25.9 Seasonal Inundation

A simple scaling factor is used to mimic the impact of seasonal inundation on CH_4 production (see appendix B in *Riley et al. (2011a)* for a discussion of this simplified expression):

$$S = \frac{\beta \left(f - \bar{f} \right) + \bar{f}}{f}, S \leq 1. \tag{25.21}$$

Here, f is the instantaneous inundated fraction, $\bar{f}$ is the annual average inundated fraction (evaluated for the previous calendar year) weighted by heterotrophic respiration, and β is the anoxia factor that relates the fully anoxic decomposition rate to the fully oxygen-unlimited decomposition rate, all other conditions being equal.

CHAPTER 26

CROPS AND IRRIGATION

26.1 Summary of CLM5.0 updates relative to the CLM4.5

We describe here the complete crop and irrigation parameterizations that appear in CLM5.0. Corresponding information for CLM4.5 appeared in the CLM4.5 Technical Note (*Oleson et al. 2013*).

CLM5.0 includes the following new updates to the CROP option, where CROP refers to the interactive crop management model and is included as an option with the BGC configuration:

- New crop functional types

- All crop areas are actively managed

- Fertilization rates updated based on crop type and geographic region

- New Irrigation triggers

- Phenological triggers vary by latitude for some crop types

- Ability to simulate transient crop management

- Adjustments to allocation and phenological parameters

- Crops reaching their maximum LAI triggers the grain fill phase

- Grain C and N pools are included in a 1-year product pool

- C for annual crop seeding comes from the grain C pool

- Initial seed C for planting is increased from 1 to 3 g C/m^2

These updates appear in detail in the sections below. Many also appear in *Levis et al. (2016)*.

26.2 The crop model

26.2.1 Introduction

Groups developing Earth System Models generally account for the human footprint on the landscape in simulations of historical and future climates. Traditionally we have represented this footprint with natural vegetation types and particularly grasses because they resemble many common crops. Most modeling efforts have not incorporated more explicit representations of land management such as crop type, planting, harvesting, tillage, fertilization, and irrigation, because global scale datasets of these factors have lagged behind vegetation mapping. As this begins to change, we increasingly find models that will simulate the biogeophysical and biogeochemical effects not only of natural but also human-managed land cover.

AgroIBIS is a state-of-the-art land surface model with options to simulate dynamic vegetation (*Kucharik et al. 2000*) and interactive crop management (*Kucharik and Brye 2003*). The interactive crop management parameterizations from AgroIBIS (March 2003 version) were coupled as a proof-of-concept to the Community Land Model version 3 [CLM3.0, *Oleson et al. (2004)*] (not published), then coupled to the CLM3.5 (*Levis et al. 2009*) and later released to the community with CLM4CN (*Levis et al. 2012*), and CLM4.5BGC. Additional updates after the release of CLM4.5 were available by request (*Levis et al. 2016*), and those are now incorporated into CLM5.

With interactive crop management and, therefore, a more accurate representation of agricultural landscapes, we hope to improve the CLM's simulated biogeophysics and biogeochemistry. These advances may improve fully coupled simulations with the Community Earth System Model (CESM), while helping human societies answer questions about changing food, energy, and water resources in response to climate, environmental, land use, and land management change (e.g., *Kucharik and Brye 2003*; *Lobell et al. 2006*). As implemented here, the crop model uses the same physiology as the natural vegetation, though uses different crop-specific parameter values, phenology, and allocation, as well as fertilizer and irrigation management.

26.2.2 Crop plant functional types

To allow crops to coexist with natural vegetation in a grid cell, the vegetated land unit is separated into a naturally vegetated land unit and a managed crop land unit. Unlike the plant functional types (pfts) in the naturally vegetated land unit, the managed crop pfts in the managed crop land unit do not share soil columns and thus permit for differences in the land management between crops. Each crop type has a rainfed and an irrigated pft that are on independent soil columns. Crop grid cell coverage is assigned from satellite data (similar to all natural pfts), and the managed crop type proportions within the crop area is based on the dataset created by *Portmann et al. (2010)* for present day. New in CLM5, crop area is extrapolated through time using the dataset provided by Land Use Model Intercomparison Project (LUMIP), which is part of CMIP6 Land use timeseries (*Lawrence et al. 2016*). For more details about how crop distributions are determined, see Chapter 27.

CLM5 includes eight actively managed crop types (temperate soybean, tropical soybean, temperate corn, tropical corn, spring wheat, cotton, rice, and sugarcane) that are chosen based on the availability of corresponding algorithms in AgroIBIS and as developed by *Badger and Dirmeyer (2015)* and described by *Levis et al. (2016)*. The representations of sugarcane, rice, cotton, tropical corn, and tropical soy are new in CLM5. Sugarcane and tropical corn are both C4 plants and are therefore represented using the temperate corn functional form. Tropical soybean uses the temperate soybean functional form, while rice and cotton use the wheat functional form. In tropical regions, parameter values were developed for the Amazon Basin, and planting date window is shifted by six months relative to the Northern Hemisphere.

In addition, CLM's default list of plant functional types (pfts) includes an irrigated and unirrigated unmanaged C3 crop (Table 26.1) treated as a second C3 grass. The unmanaged C3 crop is only used when the crop model is not active and has grid cell coverage assigned from satellite data, and the unmanaged C3 irrigated crop type is currently not used since irrigation requires the crop model to be active. The default list of pfts also includes twenty-three inactive crop pfts that do not yet have associated parameters required for active management. Each of the inactive crop types is simulated using the parameters of the spatially closest associated crop type that is most similar to the functional

type (e.g., C3 or C4), which is required to maintain similar phenological parameters based on temperature thresholds. Information detailing which parameters are used for each crop type is included in Table 26.1. It should be noted that pft-level history output merges all crop types into the actively managed crop type, so analysis of crop-specific output will require use of the land surface dataset to remap the yields of each actively and inactively managed crop type. Otherwise, the actively managed crop type will include yields for that crop type and all inactively managed crop types that are using the same parameter set.

Table 26.1: Crop plant functional types (pfts) included in CLM5BGCCROP.

ITV	Plant function types (PFTs)	Management Class	Crop Parameters Used
15	c3 unmanaged rainfed crop	none	not applicable
16	c3 unmanaged irrigated crop	none	not applicable
17	rainfed temperate corn	active	rainfed temperate corn
18	irrigated temperate corn	active	irrigated temperate corn
19	rainfed spring wheat	active	rainfed spring wheat
20	irrigated spring wheat	active	irrigated spring wheat
21	rainfed winter wheat	inactive	rainfed spring wheat
22	irrigated winter wheat	inactive	irrigated spring wheat
23	rainfed temperate soybean	active	rainfed temperate soybean
24	irrigated temperate soybean	active	irrigated temperate soybean
25	rainfed barley	inactive	rainfed spring wheat
26	irrigated barley	inactive	irrigated spring wheat
27	rainfed winter barley	inactive	rainfed spring wheat
28	irrigated winter barley	inactive	irrigated spring wheat
29	rainfed rye	inactive	rainfed spring wheat
30	irrigated rye	inactive	irrigated spring wheat
31	rainfed winter rye	inactive	rainfed spring wheat
32	irrigated winter rye	inactive	irrigated spring wheat
33	rainfed cassava	inactive	rainfed rice
34	irrigated cassava	inactive	irrigated rice
35	rainfed citrus	inactive	rainfed spring wheat
36	irrigated citrus	inactive	irrigated spring wheat
37	rainfed cocoa	inactive	rainfed rice
38	irrigated cocoa	inactive	irrigated rice
39	rainfed coffee	inactive	rainfed rice
40	irrigated coffee	inactive	irrigated rice
41	rainfed cotton	active	rainfed cotton
42	irrigated cotton	active	irrigated cotton
43	rainfed datepalm	inactive	rainfed cotton
44	irrigated datepalm	inactive	irrigated cotton
45	rainfed foddergrass	inactive	rainfed spring wheat
46	irrigated foddergrass	inactive	irrigated spring wheat
47	rainfed grapes	inactive	rainfed spring wheat
48	irrigated grapes	inactive	irrigated spring wheat
49	rainfed groundnuts	inactive	rainfed rice
50	irrigated groundnuts	inactive	irrigated rice
51	rainfed millet	inactive	rainfed tropical corn
52	irrigated millet	inactive	irrigated tropical corn
53	rainfed oilpalm	inactive	rainfed rice
54	irrigated oilpalm	inactive	irrigated rice
55	rainfed potatoes	inactive	rainfed spring wheat

Table 26.1 – continued from previous page

ITV	Plant function types (PFTs)	Management Class	Crop Parameters Used
56	irrigated potatoes	inactive	irrigated spring wheat
57	rainfed pulses	inactive	rainfed spring wheat
58	irrigated pulses	inactive	irrigated spring wheat
59	rainfed rapeseed	inactive	rainfed spring wheat
60	irrigated rapeseed	inactive	irrigated spring wheat
61	rainfed rice	active	rainfed rice
62	irrigated rice	active	irrigated rice
63	rainfed sorghum	inactive	rainfed tropical corn
64	irrigated sorghum	inactive	irrigated tropical corn
65	rainfed sugarbeet	inactive	rainfed spring wheat
66	irrigated sugarbeet	inactive	irrigated spring wheat
67	rainfed sugarcane	active	rainfed sugarcane
68	irrigated sugarcane	active	irrigated sugarcane
69	rainfed sunflower	inactive	rainfed spring wheat
70	irrigated sunflower	inactive	irrigated spring wheat
71	rainfed miscanthus	inactive	rainfed tropical corn
72	irrigated miscanthus	inactive	irrigated tropical corn
73	rainfed switchgrass	inactive	rainfed tropical corn
74	irrigated switchgrass	inactive	irrigated tropical corn
75	rainfed tropical corn	active	rainfed tropical corn
76	irrigated tropical corn	active	irrigated tropical corn
77	rainfed tropical soybean	active	rainfed tropical soybean
78	irrigated tropical soybean	active	irrigated tropical soybean

26.2.3 Phenology

CLM5-BGC includes evergreen, seasonally deciduous (responding to changes in day length), and stress deciduous (responding to changes in temperature and/or soil moisture) phenology algorithms (Chapter 20). CLM5-BGC-crop uses the AgroIBIS crop phenology algorithm, consisting of three distinct phases.

Phase 1 starts at planting and ends with leaf emergence, phase 2 continues from leaf emergence to the beginning of grain fill, and phase 3 starts from the beginning of grain fill and ends with physiological maturity and harvest.

Planting

All crops must meet the following requirements between the minimum planting date and the maximum planting date (for the northern hemisphere) in Table 26.2:

$$
\begin{aligned}
T_{10d} &> T_p \\
T_{10d}^{\min} &> T_p^{\min} \\
GDD_8 &\geq GDD_{\min}
\end{aligned}
\tag{26.1}
$$

where T_{10d} is the 10-day running mean of T_{2m}, (the simulated 2-m air temperature during each model time step) and $T_{10d}^{\min}$ is the 10-day running mean of $T_{2m}^{\min}$ (the daily minimum of T_{2m}). T_p and $T_p^{\min}$ are crop-specific coldest planting temperatures (Table 26.2), GDD_8 is the 20-year running mean growing degree-days (units are degree-days or ^{o} days) tracked from April through September (NH) above 8° C with maximum daily increments of 30° days (see equation (26.3)), and GDD_{min} is the minimum growing degree day requirement (Table 26.2). GDD_8 does not change as quickly as T_{10d} and $T_{10d}^{\min}$, so it determines whether it is warm enough for the crop to be planted in a grid cell, while the 2-m air temperature variables determine the day when the crop may be planted if the GDD_8 threshold is met. If the requirements in equation (26.1) are not met by the maximum planting date, crops are still planted on the maximum planting date as long as $GDD_8 > 0$. In the southern hemisphere (SH) the NH requirements apply 6 months later.

At planting, each crop seed pool is assigned 3 gC m^{-2} from its grain product pool. The seed carbon is transferred to the leaves upon leaf emergence. An equivalent amount of seed leaf N is assigned given the pft's C to N ratio for leaves (CN_{leaf} in Table 26.3; this differs from AgroIBIS, which uses a seed leaf area index instead of seed C). The model updates the average growing degree-days necessary for the crop to reach vegetative and physiological maturity, GDD_{mat}, according to the following AgroIBIS rules:

$$
\begin{aligned}
GDD_{\text{mat}}^{\text{corn,sugarcane}} &= 0.85 GDD_8 & \text{and} && 950 < GDD_{\text{mat}}^{\text{corn,sugarcane}} < 1850°\text{days} \\
GDD_{\text{mat}}^{\text{spring wheat,cotton}} &= GDD_0 & \text{and} && GDD_{\text{mat}}^{\text{spring wheat,cotton}} < 1700°\text{days} \\
GDD_{\text{mat}}^{\text{temp.soy}} &= GDD_{10} & \text{and} && GDD_{\text{mat}}^{\text{temp.soy}} < 1900°\text{days} \\
GDD_{\text{mat}}^{\text{rice}} &= GDD_0 & \text{and} && GDD_{\text{mat}}^{\text{rice}} < 2100°\text{days} \\
GDD_{\text{mat}}^{\text{trop.soy}} &= GDD_{10} & \text{and} && GDD_{\text{mat}}^{\text{trop.soy}} < 2100°\text{days}
\end{aligned} \tag{26.2}
$$

where GDD_0, GDD_8, and GDD_{10} are the 20-year running mean growing degree-days tracked from April through September (NH) over 0ºC, 8ºC, and 10ºC, respectively, with maximum daily increments of 26º days (for GDD_0) or 30º days (for GDD_8 and GDD_{10}). Equation (26.3) shows how we calculate GDD_0, GDD_8, and GDD_{10} for each model timestep:

$$
\begin{aligned}
GDD_0 &= GDD_0 + T_{2m} - T_f & \text{where} && 0 \leq T_{2m} - T_f \leq 26°\text{days} \\
GDD_8 &= GDD_8 + T_{2m} - T_f - 8 & \text{where} && 0 \leq T_{2m} - T_f - 8 \leq 30°\text{days} \\
GDD_{10} &= GDD_{10} + T_{2m} - T_f - 10 & \text{where} && 0 \leq T_{2m} - T_f - 10 \leq 30°\text{days}
\end{aligned} \tag{26.3}
$$

where, if T_{2m} - T_f takes on values outside the above ranges within a day, then it equals the minimum or maximum value in the range for that day. T_f is the freezing temperature of water and equals 273.15 K, T_{2m} is the 2-m air temperature in units of K, and GDD is in units of ºdays.

Leaf emergence

According to AgroIBIS, leaves may emerge when the growing degree-days of soil temperature to 0.05 m depth ($GDD_{T_{soi}}$), which is tracked since planting, reaches 1 to 5% of GDD_{mat} (see Phase 2 % GDD_{mat} in Table 26.2). The base temperature threshold values for $GDD_{T_{soi}}$ are listed in Table 26.2 (the same base temperature threshold values are also used for $GDD_{T_{2m}}$ in section 26.2.3), and leaf emergence (crop phenology phase 2) starts when this threshold is met. Leaf onset occurs in the first time step of phase 2, at which moment all seed C is transferred to leaf C. Subsequently, the leaf area index generally increases throughout phase 2 until it reaches a predetermined maximum value. Stem and root C also increase throughout phase 2 based on the carbon allocation algorithm in section 26.2.4.

Grain fill

The grain fill phase (phase 3) begins in one of two ways. The first potential trigger is based on temperature, similar to phase 2. A variable tracked since planting, similar to $GDD_{T_{soi}}$ but for 2-m air temperature, $GDD_{T_{2m}}$, must reach a heat unit threshold, h, of of 40 to 65% of GDD_{mat} (see Phase 3 % GDD_{mat} in Table 26.2). For crops with the C4 photosynthetic pathway (temperate and tropical corn, sugarcane), the GDD_{mat} is based on an empirical function and ranges between 950 and 1850. The second potential trigger for phase 3 is based on leaf area index. When the maximum value of leaf area index is reached in phase 2 (Table 26.3), phase 3 begins. In phase 3, the leaf area index begins to decline in response to a background litterfall rate calculated as the inverse of leaf longevity for the pft as done in the BGC part of the model.

Harvest

Harvest is assumed to occur as soon as the crop reaches maturity. When $GDD_{T_{2m}}$ reaches 100% of GDD_{mat} or the number of days past planting reaches a crop-specific maximum (Table 26.2), then the crop is harvested. Harvest occurs in one time step using the BGC leaf offset algorithm.

Table 26.2: Crop phenology and morphology parameters for the active crop plant functional types (pfts) in CLM5BGCCROP. Numbers in the first row correspond to the list of pfts in Table 26.1.

	temperate corn	spring wheat	temperatue soybean	cotton	rice	sugarcane	tropical corn	tropical soybean
IVT	17, 18	19, 20	23, 24	41, 42	61, 62	67, 68	75, 76	77, 78
$Date_{planting}^{min}$	April 1	April 1	May 1	April 1	January 1	January 1	March 20	April 15
$Date_{planting}^{max}$	June 15	June 15	June 15	May 31	Feburary 28	March 31	April 15	June 31
T_p(K)	283.15	280.15	286.15	294.15	294.15	294.15	294.15	294.15
T_p^{min}(K)	279.15	272.15	279.15	283.15	283.15	283.15	283.15	283.15
GDD_{min}(°days)	50	50	50	50	50	50	50	50
base temperature for GDD (°C)	8	0	10	10	10	10	10	10
GDD_{mat}(°days)	950-1850	≤1700	≤1900	≤1700	≤2100	950-1850	950-1850	≤2100
Phase 2 % GDD_{mat}	0.03	0.05	0.03	0.03	0.01	0.03	0.03	0.03
Phase 3 % GDD_{mat}	0.65	0.6	0.5	0.5	0.4	0.65	0.5	0.5
Harvest: days past planting	≤165	≤150	≤150	≤160	≤150	≤300	≤160	≤150
z_{top}^{max} (m)	2.5	1.2	0.75	1.5	1.8	4	2.5	1
SLA (m^2 leaf g^{-1} C)	0.05	0.035	0.035	0.035	0.035	0.05	0.05	0.035
χ_L index	-0.5	-0.5	-0.5	-0.5	-0.5	-0.5	-0.5	-0.5
grperc	0.11	0.11	0.11	0.11	0.11	0.11	0.11	0.11
flnr	0.293	0.41	0.41	0.41	0.41	0.293	0.293	0.41
fcur	1	1	1	1	1	1	1	1

Notes: $Date_{planting}^{min}$ and $Date_{planting}^{max}$ are the minimum and maximum planting date in the Northern Hemisphere, the corresponding dates in the Southern Hemisphere apply 6 months later. T_p and T_p^{min} are crop-specific average and coldest planting temperatures, respectively. GDD_{min} is the lowest (for planting) 20-year running mean growing degree-days based on the base temperature threshold in the 7th row, tracked from April to September (NH). GDD_{mat} is a crop's 20-year running mean growing degree-days needed for vegetative and physiological maturity. Harvest occurs at $100\%GDD_{mat}$ or when the days past planting reach the number in the 11th row. Crop growth phases are described in the text. z_{top}^{max} is the maximum top-of-canopy height of a crop, SLA is specific leaf area. χ_L is the leaf orientation index, equals -1 for vertical, 0 for random, and 1 for horizontal leaf orientation. grperc is the growth respiration factor. flnr is the fraction of leaf N in the Rubisco enzyme. fcur is the fraction of allocation that goes to currently displayed growth.

26.2.4 Allocation

Allocation changes based on the crop phenology phases phenology (section 26.2.3). Simulated C assimilation begins every year upon leaf emergence in phase 2 and ends with harvest at the end of phase 3; therefore, so does the allocation of such C to the crop's leaf, live stem, fine root, and reproductive pools.

Typically, C:N ratios in plant tissue vary throughout the growing season and tend to be lower during early growth stages and higher in later growth stages. In order to account for this seasonal change, two sets of C:N ratios are established in CLM for the leaf, stem, and fine root of crops: one during the leaf emergence phase (phenology phase 2), and a second during grain fill phase (phenology phase 3). This modified C:N ratio approach accounts for the nitrogen retranslocation that occurs during the grain fill phase (phase 3) of crop growth. Leaf, stem, and root C:N ratios for phase 2 are calculated using the new CLM5 carbon and nitrogen allocation scheme (Chapter 19), which provides a target C:N value (Table 26.3) and allows C:N to vary through time. During grain fill (phase 3) of the crop growth cycle, a portion of the nitrogen in the plant tissues is moved to a storage pool to fulfill nitrogen demands of organ (reproductive pool) development, such that the resulting C:N ratio of the plant tissue is reflective of measurements at harvest. All C:N ratios were determined by calibration process, through comparisons of model output versus observations of plant carbon throughout the growing season.

The BGC part of the model keeps track of a term representing excess maintenance respiration, which supplies the carbon required for maintenance respiration during periods of low photosynthesis (Chapter 17). Carbon supply for excess maintenance respiration cannot continue to happen after harvest for annual crops, so at harvest the excess respiration pool is turned into a flux that extracts CO_2 directly from the atmosphere. This way any excess maintenance respiration remaining at harvest is eliminated as if such respiration had not taken place.

Leaf emergence

During phase 2, the allocation coefficients (fraction of available C) to each C pool are defined as:

$$
\begin{aligned}
a_{repr} &= 0 \\
a_{froot} &= a^i_{froot} - (a^i_{froot} - a^f_{froot})\frac{GDD_{T2m}}{GDD_{mat}} \quad \text{where} \quad \frac{GDD_{T2m}}{GDD_{mat}} \leq 1 \\
a_{leaf} &= (1 - a_{froot}) \cdot \frac{a^i_{leaf}(e^{-b} - e^{-b\frac{GDD_{T2m}}{h}})}{e^{-b} - 1} \quad \text{where} \quad b = 0.1 \\
a_{livestem} &= 1 - a_{repr} - a_{froot} - a_{leaf}
\end{aligned}
\tag{26.4}
$$

where a^i_{leaf}, a^i_{froot}, and a^f_{froot} are initial and final values of these coefficients (Table 26.3), and h is a heat unit threshold defined in section 26.2.3. At a crop-specific maximum leaf area index, L_{max} (Table 26.3), carbon allocation is directed exclusively to the fine roots.

Grain fill

The calculation of a_{froot} remains the same from phase 2 to phase 3. During grain fill (phase 3), other allocation coefficients change to:

$$
\begin{aligned}
a_{leaf} &= a^{i,3}_{leaf} & &\text{when} \quad a^{i,3}_{leaf} \leq a^f_{leaf} \quad \text{else} \\
a_{leaf} &= a_{leaf}\left(1 - \frac{GDD_{T2m} - h}{GDD_{mat}d_L - h}\right)^{d^{leaf}_{alloc}} \geq a^f_{leaf} & &\text{where} \quad \frac{GDD_{T2m} - h}{GDD_{mat}d_L - h} \leq 1 \\[6pt]
a_{livestem} &= a^{i,3}_{livestem} & &\text{when} \quad a^{i,3}_{livestem} \leq a^f_{livestem} \quad \text{else} \\
a_{livestem} &= a_{livestem}\left(1 - \frac{GDD_{T2m} - h}{GDD_{mat}d_L - h}\right)^{d^{stem}_{alloc}} \geq a^f_{livestem} & &\text{where} \quad \frac{GDD_{T2m} - h}{GDD_{mat}d_L - h} \leq 1 \\[6pt]
a_{repr} &= 1 - a_{froot} - a_{livestem} - a_{leaf}
\end{aligned}
\tag{26.5}
$$

where $a^{i,3}_{leaf}$ and $a^{i,3}_{livestem}$ (initial values) equal the last a_{leaf} and $a_{livestem}$ calculated in phase 2, d_L, d^{leaf}_{alloc} and d^{stem}_{alloc} are leaf area index and leaf and stem allocation decline factors, and a^f_{leaf} and $a^f_{livestem}$ are final values of these allocation coefficients (Table 26.3).

Nitrogen retranslocation for crops

Nitrogen retranslocation in crops occurs when nitrogen that was used for tissue growth of leaves, stems, and fine roots during the early growth season is remobilized and used for grain development (*Pollmer et al. 1979*, *Crawford et al. 1982*, *Simpson et al. 1983*, *Ta and Weiland 1992*, *Barbottin et al. 2005*, *Gallais et al. 2006*, *Gallais et al. 2007*). Nitrogen allocation for crops follows that of natural vegetation, is supplied in CLM by the soil mineral nitrogen pool, and depends on C:N ratios for leaves, stems, roots, and organs. Nitrogen demand during organ development is fulfilled through retranslocation from leaves, stems, and roots. Nitrogen retranslocation is initiated at the beginning of the grain fill stage for all crops except soybean, for which retranslocation is after LAI decline. Nitrogen stored in the leaf and stem is moved into a storage retranslocation pool for all crops, and for wheat and rice, nitrogen in roots is also released into the retranslocation storage pool. The quantity of nitrogen mobilized depends on the C:N ratio of the plant tissue, and is calculated as

$$leaf\_to\_retransn = N_{leaf} - \frac{C_{leaf}}{CN^f_{leaf}} \tag{26.6}$$

$$stemn\_to\_retransn = N_{stem} - \frac{C_{stem}}{CN^f_{stem}} \tag{26.7}$$

$$frootn\_to\_retransn = N_{froot} - \frac{C_{froot}}{CN^f_{froot}} \tag{26.8}$$

where C_{leaf}, C_{stem}, and C_{froot} is the carbon in the plant leaf, stem, and fine root, respectively, N_{leaf}, N_{stem}, and N_{froot} is the nitrogen in the plant leaf, stem, and fine root, respectively, and CN^f_{leaf}, CN^f_{stem}, and CN^f_{froot} is the post-grain fill C:N ratio of the leaf, stem, and fine root respectively (Table 26.3). Since C:N measurements are often taken from mature crops, pre-grain development C:N ratios for leaves, stems, and roots in the model are optimized to allow maximum nitrogen accumulation for later use during organ development, and post-grain fill C:N ratios are assigned the same as crop residue. After nitrogen is moved into the retranslocated pool, the nitrogen in this pool is used to meet plant nitrogen demand by assigning the available nitrogen from the retranslocated pool equal to the plant nitrogen demand for each organ ($CN^f_{[organ]}$ in Table 26.3). Once the retranslocation pool is depleted, soil mineral nitrogen pool is used to fulfill plant nitrogen demands.

Harvest

Variables track the flow of grain C and N to food and of all other plant pools, including live stem C and N, to litter. Putting live stem C and N into the litter pool is in contrast to the approach for unmanaged PFTs which puts live stem C and N into dead stem pools first. Leaf and root C and N pools are routed to the litter pools in the same manner as natural vegetation. Whereas food C and N was formerly transferred to the litter pool, CLM5 routes food C and N to a grain product pool where the C and N decay to the atmosphere over one year, similar in structure to the wood product pools. Additionally, CLM5 accounts for the C and N required for crop seeding by removing the seed C and N from the grain product pool during harvest. The crop seed pool is then used to seed crops in the subsequent year. Calcuating the crop yields (Equation (26.9)) requires that you sum the GRAINC_TO_FOOD variable for each year, and must account for the proportion of C in the dry crop weight. Here, we assume that grain C is 45% of the total dry weight. Additionally, harvest is not typically 100% efficient, so analysis needs to assume that harvest efficiency is less. We assume a harvest efficiency of 85%.

$$Grain\ yield(g.m^{-2}) = \frac{\sum(GRAINC\_TO\_FOOD) * 0.85}{0.45} \tag{26.9}$$

Table 26.3: Crop allocation parameters for the active crop plant functional types (pfts) in CLM5BGCCROP. Numbers in the first row correspond to the list of pfts in Table 26.1.

	temperate corn	spring wheat	temperatue soybean	cotton	rice	sugarcane	tropical corn	tropical soybean
IVT	17, 18	19, 20	23, 24	41, 42	61, 62	67, 68	75, 76	77, 78
a_{leaf}^i	0.6	0.9	0.85	0.85	0.75	0.6	0.6	0.85
L_{max} (m ^{2} m $^{-2}$)	5	7	6	6	7	5	5	6
a_{froot}^i	0.1	0.05	0.2	0.2	0.1	0.1	0.1	0.2
a_{froot}^f	0.05	0	0.2	0.2	0	0.05	0.05	0.2
a_{leaf}^f	0	0	0	0	0	0	0	0
$a_{livestem}^f$	0	0.05	0.3	0.3	0.05	0	0	0.3
d_L	1.05	1.05	1.05	1.05	1.05	1.05	1.05	1.05
d_{alloc}^{stem}	2	1	5	5	1	2	2	5
d_{alloc}^{leaf}	5	3	2	2	3	5	5	2
CN_{leaf}	25	20	20	20	20	25	25	20
CN_{stem}	50	50	50	50	50	50	50	50
CN_{froot}	42	42	42	42	42	42	42	42
CN_{leaf}^f	65	65	65	65	65	65	65	65
CN_{stem}^f	120	100	130	130	100	120	120	130
CN_{froot}^f	0	40	0	0	40	0	0	0
CN_{grain}	50	50	50	50	50	50	50	50

Notes: Crop growth phases and corresponding variables are described throughout the text. CN_{leaf}, CN_{stem}, and CN_{froot} are the target C:N ratios used during the leaf emergence phase (phase 2).

26.2.5 Other Features

Physical Crop Characteristics

Leaf area index (L) is calculated as a function of specific leaf area (SLA, Table 26.2) and leaf C. Stem area index (S) is equal to $0.1L$ for temperate and tropical corn and sugarcane and $0.2L$ for other crops, as in AgroIBIS. All live C and N pools go to 0 after crop harvest, but the S is kept at 0.25 to simulate a post-harvest "stubble" on the ground.

Crop heights at the top and bottom of the canopy, z_{top} and z_{bot} (m), come from the AgroIBIS formulation:

$$z_{top} = z_{top}^{\max} \left(\frac{L}{L_{\max}-1} \right)^2 \geq 0.05 \text{ where } \frac{L}{L_{\max}-1} \leq 1 \tag{26.10}$$
$$z_{bot} = 0.02\text{m}$$

where $z_{top}^{\max}$ is the maximum top-of-canopy height of the crop (Table 26.2) and $L_{\max}$ is the maximum leaf area index (Table 26.3).

Interactive Fertilization

CLM simulates fertilization by adding nitrogen directly to the soil mineral nitrogen pool to meet crop nitrogen demands using both industrial fertilizer and manure application. CLM's separate crop land unit ensures that natural vegetation will not access the fertilizer applied to crops. Fertilizer in CLM5BGCCROP is prescribed by crop functional types and varies spatially for each year based on the LUMIP land use and land cover change time series (LUH2 for historical and

SSPs for future) (*Lawrence et al. 2016*). One of two fields is used to prescribe industrial fertilizer based on the type of simulation. For non-transient simulations, annual fertilizer application in g N/m^2/yr is specified on the land surface data set by the field CONST_FERTNITRO_CFT. In transient simulations, annual fertilizer application is specified on the land use time series file by the field FERTNITRO_CFT, which is also in g N/m^2/yr. The values for both of these fields come from the LUMIP time series for each year. In addition to the industrial fertilizer, background manure fertilizer is specified on the parameter file by the field 'manunitro'. For the current CLM5BGCCROP, manure N is applied at a rate of 0.002 kg N/m^2/yr. Because previous versions of CLM (e.g., CLM4) had rapid denitrification rates, fertilizer is applied slowly to minimize N loss (primarily through denitrification) and maximize plant uptake. The current implementation of CLM5 inherits this legacy, although denitrification rates are slower in the current version of the model (*Koven et al. 2013*). As such, fertilizer application begins during the leaf emergence phase of crop development (phase 2) and continues for 20 days, which helps reduce large losses of nitrogen from leaching and denitrification during the early stage of crop development. The 20-day period is chosen as an optimization to limit fertilizer application to the emergence stage. A fertilizer counter in seconds, *f*, is set as soon as the leaf emergence phase for crops initiates:

$$f = n \times 86400 \tag{26.11}$$

where *n* is set to 20 fertilizer application days and 86400 is the number of seconds per day. When the crop enters phase 2 (leaf emergence) of its growth cycle, fertilizer application begins by initializing fertilizer amount to the total fertilizer at each column within the grid cell divided by the initialized *f*. Fertilizer is applied and *f* is decremented each time step until a zero balance on the counter is reached.

Biological nitrogen fixation for soybeans

Biological N fixation for soybeans is calculated by the fixation and uptake of nitrogen module (Chapter 18) and is the same as N fixation in natural vegetation. Unlike natural vegetation, where a fraction of each pft are N fixers, all soybeans are treated as N fixers.

Latitudinal variation in base growth tempereature

For most crops, $GDD_{T_{2m}}$ (growing degree days since planting) is the same in all locations. However, the for both rainfed and irrigated spring wheat and sugarcane, the calculation of $GDD_{T_{2m}}$ allows for latitudinal variation:

$$latitudinal\ variation\ in\ base\ T = \left\{ \begin{array}{ll} baset + 12 - 0.4 \times latitude & 0 \leq latitude \leq 30 \\ baset + 12 + 0.4 \times latitude & -30 \leq latitude \leq 0 \end{array} \right\} \tag{26.12}$$

where *baset* is the *base temperature for GDD* (7th row) in Table 26.2. Such latitudinal variation in base growth temperature could increase the base temperature, slow down $GDD_{T_{2m}}$ accumulation, and extend the growing season for regions within 30ºS to 30ºN for spring wheat and sugarcane.

Separate reproductive pool

One notable difference between natural vegetation and crops is the presence of reproductive carbon and nitrogen pools. Accounting for the reproductive pools helps determine whether crops are performing reasonably through yield calculations. The reproductive pool is maintained similarly to the leaf, stem, and fine root pools, but allocation of carbon and nitrogen does not begin until the grain fill stage of crop development. Equation (26.5) describes the carbon and nitrogen allocation coefficients to the reproductive pool. In CLM5BGCCROP, as allocation declines in stem, leaf, and root pools (see section 26.2.4) during the grain fill stage of growth, increasing amounts of carbon and nitrogen are available for grain development.

26.3 The irrigation model

The CLM includes the option to irrigate cropland areas that are equipped for irrigation. The application of irrigation responds dynamically to the soil moisture conditions simulated by the CLM. This irrigation algorithm is based loosely on the implementation of *Ozdogan et al. (2010)*.

When irrigation is enabled, the crop areas of each grid cell are divided into irrigated and rainfed fractions according to a dataset of areas equipped for irrigation (*Portmann et al. 2010*). Irrigated and rainfed crops are placed on separate soil columns, so that irrigation is only applied to the soil beneath irrigated crops.

In irrigated croplands, a check is made once per day to determine whether irrigation is required on that day. This check is made in the first time step after 6 AM local time. Irrigation is required if crop leaf area > 0, and the available soil water is below a specified threshold.

The soil moisture deficit D_{irrig} is

$$D_{irrig} = \left\{ \begin{array}{ll} w_{thresh} - w_{avail} & w_{thresh} > w_{avail} \\ 0 & w_{thresh} \leq w_{avail} \end{array} \right\} \tag{26.13}$$

where w_{thresh} is the irrigation moisture threshold (mm) and w_{avail} is the available moisture (mm). The moisture threshold is

$$w_{thresh} = f_{thresh} \left(w_{target} - w_{wilt} \right) + w_{wilt} \tag{26.14}$$

where w_{target} is the irrigation target soil moisture (mm)

$$w_{target} = \sum_{j=1}^{N_{irr}} \theta_{target} \Delta z_j , \tag{26.15}$$

w_{wilt} is the wilting point soil moisture (mm)

$$w_{wilt} = \sum_{j=1}^{N_{irr}} \theta_{wilt} \Delta z_j , \tag{26.16}$$

and f_{thresh} is a tuning parameter. The available moisture in the soil is

$$w_{avail} = \sum_{j=1}^{N_{irr}} \theta_j \Delta z_j , \tag{26.17}$$

N_{irr} is the index of the soil layer corresponding to a specified depth z_{irrig} (Table 26.4) and Δz_j is the thickness of the soil layer in layer j (section 2.2). θ_j is the volumetric soil moisture in layer j (section 7.3). θ_{target} and θ_{wilt} are the target and wilting point volumetric soil moisture values, respectively, and are determined by inverting (7.53) using soil matric potential parameters Ψ_{target} and Ψ_{wilt} (Table 26.4). After the soil moisture deficit D_{irrig} is calculated, irrigation in an amount equal to $\frac{D_{irrig}}{T_{irrig}}$ (mm/s) is applied uniformly over the irrigation period T_{irrig} (s). Irrigation water is applied directly to the ground surface, bypassing canopy interception (i.e., added to $q_{grnd,liq}$: section 7.1).

To conserve mass, irrigation is removed from river water storage (Chapter 14). When river water storage is inadequate to meet irrigation demand, there are two options: 1) the additional water can be removed from the ocean model, or 2) the irrigation demand can be reduced such that river water storage is maintained above a specified threshold.

Table 26.4: Irrigation parameters

Parameter	
f_{thresh}	1.0
z_{irrig} (m)	0.6
Ψ_{target} (mm)	-3400
Ψ_{wilt} (mm)	-150000

CHAPTER 27

TRANSIENT LAND USE AND LAND COVER CHANGE

CLM includes a treatment of mass and energy fluxes associated with prescribed temporal land use and land cover change (LULCC). The model uses an annual time series of the spatial distribution of the natural and crop land units of each grid cell, in combination with the distribution of PFTs and CFTs that exist in those land units. Additional land use is prescribed through annual crop-specific management of nitrogen fertilizer and irrigation (described further in 26), and through wood harvest on tree PFTs. For changes in the distributions of natural and crop vegetation, CLM diagnoses the change in area of the PFTs and CFTs on January 1 of each model year and then performs mass and energy balance accounting necessary to represent the expansion and contraction of the PFT and CFT areas. The biogeophysical impacts of LULCC are simulated through changes in surface properties which in turn impact the surface albedo, hydrology, and roughness which then impact fluxes of energy, moisture and momentum to the atmosphere under the altered properties. Additionally, changes in energy and moisture associated with changes in the natural and crop vegetation distribution are accounted for through small fluxes to the river and atmosphere. The biogeochemical impacts of LULCC are simulated through changes in CLM carbon pools and fluxes (see also Chapter 16).

CLM can also respond to changes in ice sheet areas and elevations when it is coupled to an evolving ice sheet model (in the CESM context, this is the Community Ice Sheet Model, CISM; see also Chapter 13). Conservation of water, energy, carbon and nitrogen is handled similarly for glacier-vegetation transitions as for natural vegetation-crop transitions.

27.1 Annual Transient Land Use and Land Cover Data

The changes in area over time associated with changes in natural and crop vegetation and the land use on that vegetation are prescribed through a forcing dataset, referred to here as the *landuse.timeseries* dataset. The *landuse.timeseries* dataset consists of an annual time series of global grids, where each annual time slice describes the fractional area occupied by all PFTs and CFTs along with the nitrogen fertilizer and irrigation fraction of each crop CFT, and the annual wood harvest applied to tree PFTs. Changes in area of PFTs and CFTs are performed annually on the first time step of January 1 of the year. Wood harvest for each PFT is also performed on the first time step of the year. Fertilizer application and irrigation for each CFT are performed at each model time step depending on rules from the crop model. Fertilizer application rates are set annually. The irrigation fraction is also set annually; irrigated crops are placed on separate columns from their unirrigated counterparts, so changes in irrigated fraction triggers the changes in subgrid areas discussed below (sections 27.2 and 27.3).

As a special case, when the time dimension of the *landuse.timeseries* dataset starts at a later year than the current model time step, the first time slice from the *landuse.timeseries* dataset is used to represent the current time step PFT and CFT fractional area distributions. Similarly, when the time dimension of the *landuse.timeseries* dataset stops at an earlier year than the current model time step, the last time slice of the *landuse.timeseries* dataset is used. Thus, the simulation will have invariant representations of PFT and CFT distributions through time for the periods prior to and following the time duration of the *landuse.timeseries* dataset, with transient PFT and CFT distributions during the period covered by the *landuse.timeseries* dataset.

27.2 Reconciling Changes in Area

In the first time step of January 1, changes in land unit weights can potentially come from two sources: Changes in the area of the crop land unit come from the *landuse.timeseries* dataset (section 27.1), and changes in the area of the glacier land unit come from the ice sheet model. The areas of other land units are then adjusted so that the total land unit area remains 100%.

If the total land unit area of glaciers and crops has decreased, then the natural vegetated landunit is increased to fill in the abandoned land. If the total land unit area of glaciers and crops has increased, then other land unit areas are decreased in a specified order until the total is once again 100%. The order of decrease is: natural vegetation, crop, urban medium density, urban high density, urban tall building district, wetland, lake.

These rules have two important implications:

1. We always match CISM's glacier areas exactly, even if that means a disagreement with prescribed crop areas. This is needed for conservation when CISM is evolving in two-way-coupled mode.

2. For land units other than crop, glacier and natural vegetation, their areas can decrease (due to encroaching crops or glaciers), but can never increase. So, for example, if a grid cell starts as 5% lake, crops expand to fill the entire grid cell, then later crop area decreases, the lake area will not return: instead, the abandoned cropland will become entirely natural vegetation.

For all levels of the subgrid hierarchy (land unit, column and patch), we only track net changes in area, not gross transitions. So, for example, if part of a gridcell experiences an increase in glacier area while another part of that gridcell experiences an equal decrease in glacier area (in the same glacier elevation class), CLM acts as if there were no changes. As another example, consider a gridcell containing natural vegetation, crop and glacier. If there is a decrease in glacier area and an equal increase in crop area, CLM will assume that the crop expands into the old glacier area, and nothing happened to the natural vegetation area. A more realistic alternative would be that the crop expanded into natural vegetation, and natural vegetation expanded into glacier. The final areas will be correct in these cases, but the adjustments of carbon and nitrogen states (section 27.3.2) will be less accurate than what would be obtained with a full tracking of gross transitions.

27.3 Mass and Energy Conservation

27.3.1 Water and Energy Conservation

When subgrid areas change, the water and energy states remain unchanged on a per-area basis. This can lead to changes in the total gridcell water and energy content.

For example, consider a gridcell with two columns: column 1 has a water mass of 1 kg m^{-2} and column 2 has a water mass of 2 kg m^{-2} for a given water state variable, where these are expressed per unit column area. If column 1 increases in area at the expense of column 2, then column 1 will still have a water mass of 1 kg m^{-2}, but now expressed over the new column area. This results in a decrease in the total gridcell water content.

Water and energy are conserved by summing up the total water and energy content of each gridcell before and after a change in area. Differences in liquid and ice water content are balanced by liquid and ice runoff terms, which can

be either positive or negative. (Negative runoff is effectively a withdrawal of water from the ocean.) Differences in energy content are balanced by a sensible heat flux term, which again can be either positive or negative. These balancing fluxes are spread evenly throughout the following year.

There is a special case when a given crop column type newly comes into existence - for example, when temperate corn first comes into existence in a gridcell. In this case, the column's below-ground temperature and water states are copied from the natural vegetated column in its gridcell, so that these state variables begin in a close-to-spun-up state. Other state variables (most of which spin up relatively quickly) begin at their cold start initialization values. This initialization is not necessary for the two other land unit types that currently can grow - natural vegetation and glacier: Those land unit types are always active, even when they have zero area on the gridcell, so their state variables will be spun up immediately when they come into existence. After this initialization, the conservation code described above takes effect.

27.3.2 Carbon and Nitrogen Conservation

Because of the long timescales involved with below-ground carbon and nitrogen dynamics, it is more important that these state variables be adjusted properly when subgrid areas change. Carbon and nitrogen variables are adjusted with the following three-step process:

(1) Patch-level (i.e., vegetation) state variables are adjusted for any changes in patch areas; this may lead to fluxes into column-level (i.e., soil) state variables

(2) Column-level (i.e., soil) state variables are updated based on the fluxes generated in (1)

(3) Column-level (i.e., soil) state variables are adjusted for any changes in column areas

First, patch-level (i.e., vegetation) state variables are adjusted for any changes in patch areas. This includes changes in column or land unit areas, even if the relative proportions of each patch remain constant: the relevant quantities are the patch weights relative to the gridcell.

For a patch that decreases in area, the carbon and nitrogen density on the remaining patch area remains the same as before (i.e., expressed as g per m^2 patch area). Because the area has decreased, this represents a decrease in total carbon or nitrogen mass (i.e., expressed as g per m^2 gridcell area). The lost mass meets a variety of fates: some is immediately lost to the atmosphere, some is sent to product pools (which are lost to the atmosphere over longer time scales), and some is sent to litter pools.

For a patch that increases in area, the carbon and nitrogen density on the new patch area is decreased in order to conserve mass. This decrease is basically proportional to the relative increase in patch area. However, a small amount of seed carbon and nitrogen is added to the leaf and dead stem pools in the new patch area.

Next, column-level (i.e., soil) state variables are updated based on any fluxes to soil pools due to decreases in patch areas. This step is needed so that any lost vegetation carbon and nitrogen is conserved when column areas are changing.

Finally, column-level state variables are adjusted for any changes in column areas. Similarly to patches, for a column that decreases in area, the carbon and nitrogen density on the remaining column area remains the same as before (i.e., expressed as g per m^2 column area). This represents a decrease in total carbon or nitrogen mass on the gridcell, and this lost mass is tracked for each gridcell. After these mass losses are summed for all shrinking columns, they are distributed amongst the growing columns in order to conserve mass. Thus, a growing column's new carbon density will be a weighted sum of its original carbon density and the carbon densities of all shrinking columns in its gridcell.

This operation makes some simplifying assumptions. First, as described in section 27.2, we only track net area changes, not gross changes. Second, we assume that growing columns all grow proportionally into each of the shrinking columns.

Non-vegetated land units (e.g., glacier) do not typically track soil carbon and nitrogen. When columns from these land units initially shrink, they are assumed to contribute zero carbon and nitrogen. However, when they grow into previously-vegetated areas, they store any pre-existing soil carbon and nitrogen from the shrinking columns. This stored carbon and nitrogen will remain unchanged until the column later shrinks, at which point it will contribute to the carbon and nitrogen in the growing columns (exactly as would happen for a vegetated column).

In contrast to water and energy (section 27.3.1), no special treatment is needed for carbon and nitrogen states in columns that newly come into existence. The state of a new column is derived from a weighted average of the states of shrinking columns. This behavior falls out from the above general rules.

27.4 Annual Transient Land Cover Dataset Development

This section describes the development of the *landuse.timeseries* dataset. Development of this dataset involves the translation of harmonized datasets of LULCC for the historical period and for the different Shared Socioeconomic Pathway (SSP) - Representative Concentration Pathway (RCP) scenarios. Additionally, LULCC time series are to be generated for the Last Millennium and the extension beyond 2100 experiments of CMIP6.

27.4.1 LUH2 Transient Land Use and Land Cover Change Dataset

To coordinate the processing and consistency of LULCC data between the historical period (1850-2015) and the six SSP-RCP (2016-2100) scenarios derived from Integrated Assessment Models (IAM), the University of Maryland and the University of New Hampshire research groups (Louise Chini, George Hurtt, Steve Frolking and Ritvik Sahajpal; luh.umd.edu) produced a new version of the Land Use Harmonized version 2 (LUH2) transient datasets for use with Earth System Model simulations. The new data sets are the product of the Land Use Model Intercomparison Project (LUMIP; https://cmip.ucar.edu/lumip) as part of the Coupled Model Intercomparison Project 6 (CMIP6). The historical component of the transient LULCC dataset has agriculture and urban land use based on HYDE 3.2 with wood harvest based on FAO, Landsat and other sources, for the period 850-2015. The SSP-RCP transient LULCC components (2015-2100) are referred to as the LUH2 Future Scenario datasets. The LULCC information is provided at 0.25 degree grid resolution and includes fractional grid cell coverage by the 12 land units of:

Primary Forest, Secondary Forest, Primary Non-Forest, Secondary Non-Forest,

Pasture, Rangeland, Urban,

C3 Annual Crop, C4 Annual Crop, C3 Perennial Crop, C4 Perennial Crop, and C3 Nitrogen Fixing Crop.

The new land unit format is an improvement on the CMIP5 LULCC datasets as they: provide Forest and Non Forest information in combination with Primary and Secondary land; differentiate between Pasture and Rangelands for grazing livestock; and specify annual details on the types of Crops grown and management practices applied in each grid cell. Like the CMIP5 LULCC datasets Primary vegetation represents the fractional area of a grid cell with vegetation undisturbed by human activities. Secondary vegetation represents vegetated areas that have recovered from some human disturbance; this could include re-vegetation of pasture and crop areas as well as primary vegetation areas that have been logged. In this manner the land units can change through deforestation from Forested to Non Forested land and in the opposite direction from Non Forested to Forested land through reforestation or afforestation without going through the Crop, Pasture or Rangeland states.

The LUH2 dataset provides a time series of land cover states as well as a transition matrices that describes the annual fraction of land that is transformed from one land unit category to another (e.g. Primary Forest to C3 Annual Crop, Pasture to C3 Perrenial Crop, etc.; Lawrence et al. 2016). Included in these transition matrices is the total conversion of one land cover type to another referred to as Gross LULCC. This value can be larger than the sum of the changes in the state of a land unit from one time period to the next known as the Net LULCC. This difference is possible as land unit changes can occur both from the land unit and to the land unit at the same time. An example of this difference occurs with shifting cultivation where Secondary Forest can be converted to C3 Annual Crop at the same time as C3 Annual Crop is abandoned to Secondary Forest.

The transition matrices also provide harmonized prescriptions of wood harvest both in area of the grid cell harvested and in the amount of biomass carbon harvested. The wood harvest biomass amount includes a 30% slash component inline with the CMIP5 LULCC data described in (Hurtt et al. 2011). The harvest area and carbon amounts are prescribed for the five classes of: Primary Forest, Primary Non-Forest, Secondary Mature Forest, Secondary Young Forest, and Secondary Non-Forest.

Additional land use management is prescribed on the Crop land units for nitrogen fertilization and irrigation equipped land. The fertilizer application and the the irrigation fraction is prescribed for each Crop land unit in a grid cell individually for each year of the time series. The wood harvest and crop management are both prescribed spatially on the same 0.25 degree grid as the land use class transitions.

27.4.2 Representing LUH2 Land Use and Land Cover Change in CLM5

To represent the LUH2 transient LULCC dataset in CLM5, the annual fractional composition of the twelve land units specified in the dataset needs to be faithfully represented with a corresponding PFT and CFT mosaics of CLM. CLM5 represents the land surface as a hierarchy of sub-grid types: glacier; lake; urban; vegetated land; and crop land. The vegetated land is further divided into a mosaic of Plant Functional Types (PFTs), while the crop land is divided into a mosaic of Crop Functional Types (CFTs).

To support this translation task the CLM5 Land Use Data tool has been built that extends the methods described in Lawrence et al (2012) to include all the new functionality of CMIP6 and CLM5 LULCC. The tool translates each of the LUH2 land units for a given year into fractional PFT and CFT values based on the current day CLM5 data for the land unit in that grid cell. The current day land unit descriptions are generated from from 1km resolution MODIS, MIRCA2000, ICESAT, AVHRR, SRTM, and CRU climate data products combined with reference year LUH2 land unit data, usually set to 2005. Where the land unit does not exist in a grid cell for the current day, the land unit description is generated from nearest neighbors with an inverse distance weighted search algorithm.

The Land Use Data tool produces raw vegetation, crop, and management data files which are combined with other raw land surface data to produce the CLM5 initial surface dataset and the dynamic *landuse.timeseries* dataset with the CLM5 mksurfdata_map tool. The schematic of this entire process from LUH2 time series and high resolution current day data to the output of CLM5 surface datasets from the mksurfdata_map tool is shown in Figure 21.2.

The methodology for creating the CLM5 transient PFT and CFT dataset is based on four steps which are applied across all of the historical and future time series. The first step involves generating the current day descriptions of natural and managed vegetation PFTs at 1km resolution from the global source datasets, and the current day description of crop CFTs at the 10km resolution from the MIRCA 2000 datasets. The second step combines the current day (2005) LUH2 land units with the current day CLM5 PFT and CFT distributions to get CLM5 land unit descriptions in either PFTs or CFTs at the LUH2 resolution of 0.25 degrees. The third step involves combining the LUH2 land unit time series with the CLM5 PFT and CFT descriptions for that land unit to generate the CLM5 raw PFT and CFT time series in the *landuse.timeseries* file. At this point in the process management information in terms of fertilizer, irrigation and wood harvest are added to the CLM5 PFT and CFT data to complete the CLM5 raw PFT and CFT files. The final step is to combine these files with the other raw CLM5 surface data files in the mksurfdata_map tool.
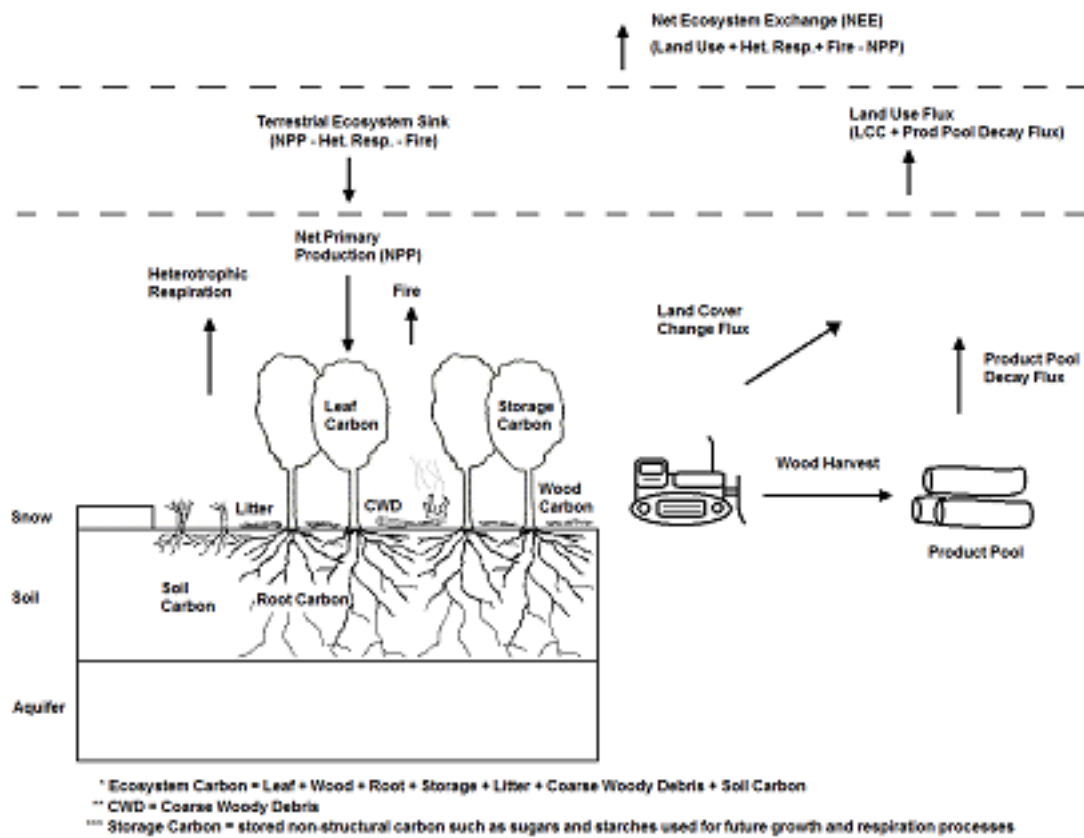
Figure 27.1: Schematic of land cover change impacts on CLM carbon pools and fluxes.
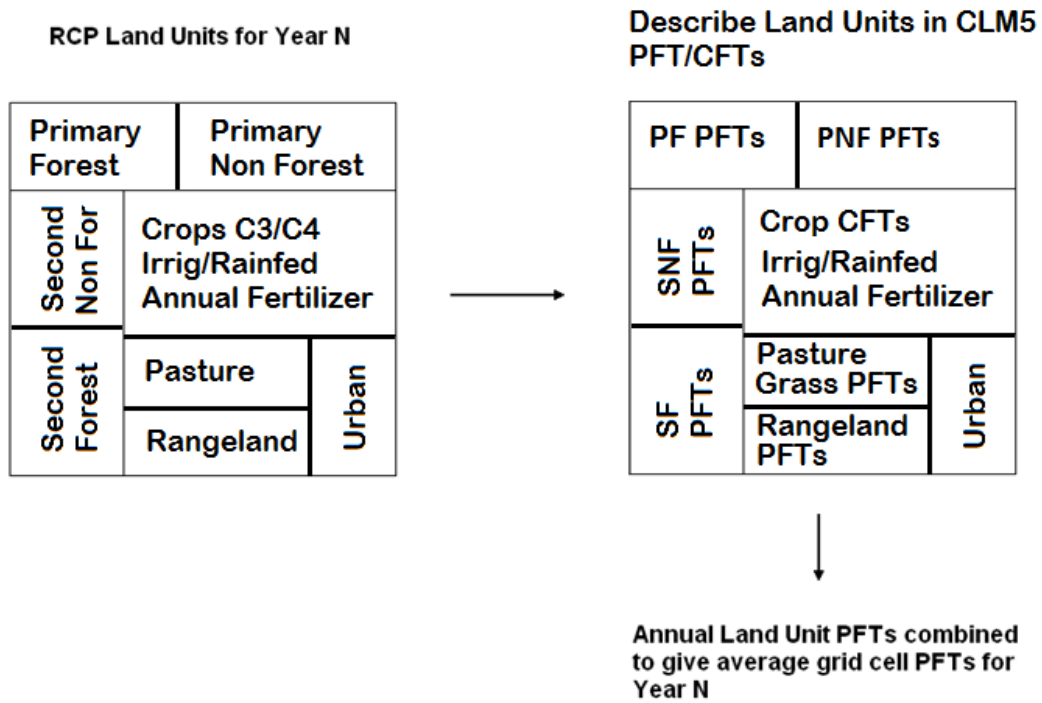
Figure 27.2: Schematic of translation of annual LUH2 land units to CLM5 plant and crop functional types.
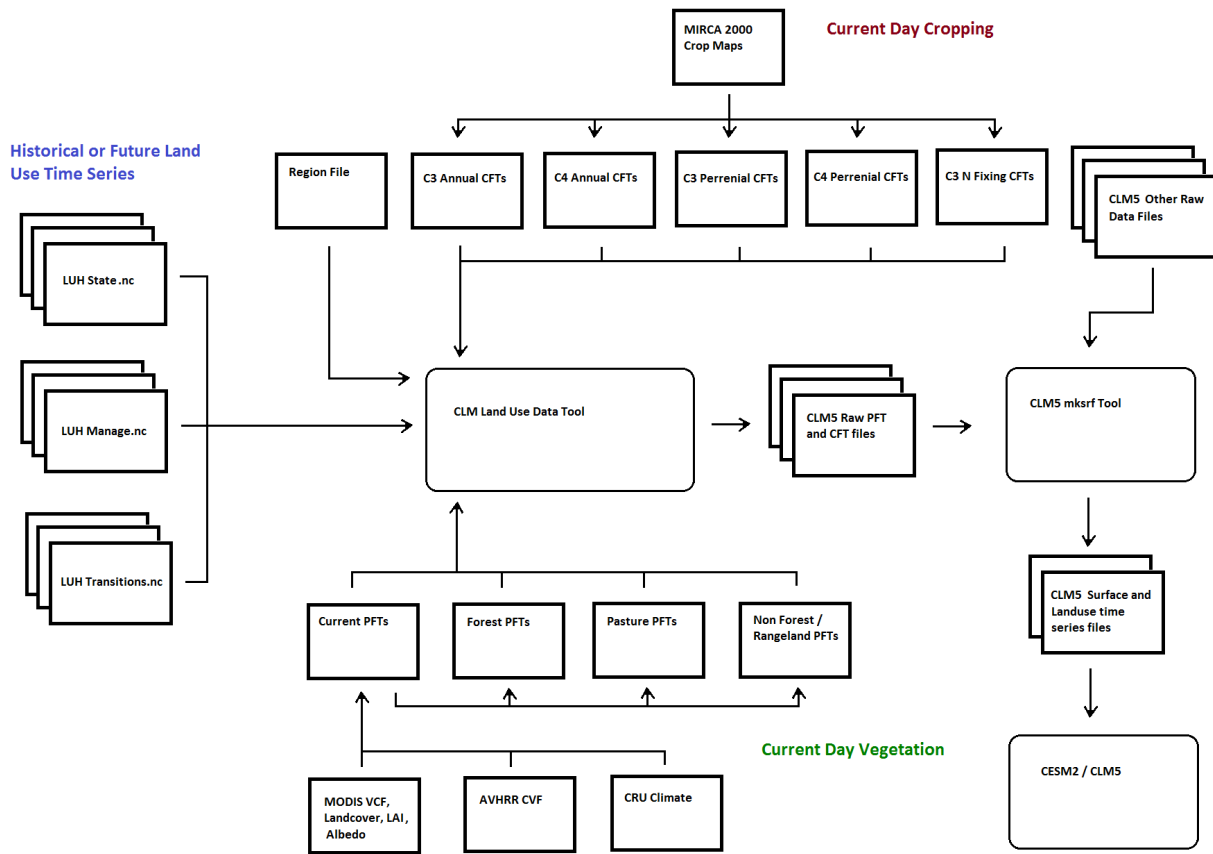
Figure 27.3: Workflow of CLM5 Land Use Data Tool and Mksurfdata_map Tool

CHAPTER 28

DYNAMIC GLOBAL VEGETATION

28.1 What has changed

- Deprecation of the dynamic global vegetation model (DGVM): The CLM5.0 model contains the legacy 'CNDV' code, which runs the CLM biogeochemistry model in combination with the LPJ-derived dynamics vegetation model introduced in CLM3. While this capacity has not technically been removed from the model, the DGVM has not been tested in the development of CLM5 and is no longer scientifically supported.

- Introduction of FATES: The Functionally Assembled Terrestrial Ecosystem Simulator (FATES) is the actively developed DGVM for the CLM5.

CHAPTER 29

TECHNICAL DOCUMENTATION FOR FATES

FATES is the "Functionally Assembled Terrestrial Ecosystem Simulator". It is an external module which can run within a given "Host Land Model" (HLM). Currently (November 2017) implementations are supported in both the Community Land Model(CLM) and in the land model of the E3SM Dept. of Energy Earth System Model.

FATES was derived from the CLM Ecosystem Demography model (CLM(ED)), which was documented in:

Fisher, R. A., Muszala, S., Verteinstein, M., Lawrence, P., Xu, C., McDowell, N. G., Knox, R. G., Koven, C., Holm, J., Rogers, B. M., Spessa, A., Lawrence, D., and Bonan, G.: Taking off the training wheels: the properties of a dynamic vegetation model without climate envelopes, CLM4.5(ED), Geosci. Model Dev., 8, 3593-3619, https://doi.org/10.5194/gmd-8-3593-2015, 2015.

and this technical note was first published as an appendix to that paper.

https://pdfs.semanticscholar.org/396c/b9f172cb681421ed78325a2237bfb428eece.pdf

29.1 Introduction

The Ecosystem Demography ('ED'), concept within FATES is derived from the work of *Moorcroft et al. (2001)*

and is a cohort model of vegetation competition and co-existence, allowing a representation of the biosphere which accounts for the division of the land surface into successional stages, and for competition for light between height structured cohorts of representative trees of various plant functional types.

The implementation of the Ecosystem Demography concept within FATES links the surface flux and canopy physiology concepts in the CLM/E3SM with numerous additional developments necessary to accommodate the new model also documented here. These include a version of the SPITFIRE (Spread and InTensity of Fire) model of *Thonicke et al. (2010)*, and an adoption of the concept of *Perfect Plasticity Approximation* approach of *Purves et al. 2008*, *Lichstein et al. 2011* and *Weng et al. 2014*, in accounting for the spatial arrangement of crowns. Novel algorithms accounting for the fragmentation of coarse woody debris into chemical litter streams, for the physiological optimisation of canopy thickness, for the accumulation of seeds in the seed bank, for multi-layer multi-PFT radiation transfer, for drought-deciduous and cold-deciduous phenology, for carbon storage allocation, and for tree mortality under carbon stress, are also included and presented here.
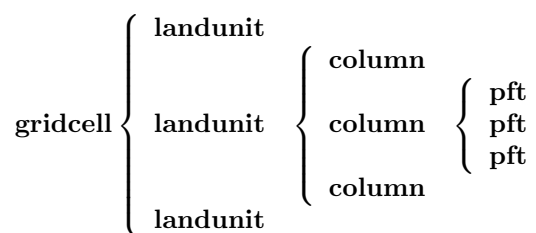
Numerous other implementations of the Ecosystem Demography concept exist (See *Fisher et al. (2018)* for a review of these) Therefore, to avoid confusion between the concept of 'Ecosystem Demography' and the implementation of this concept in different models, the CLM(ED) implementation described by *Fisher et al. (2015)* will hereafter be called 'FATES' (the Functionally Assembled Terrestrial Ecosystem Simulator).

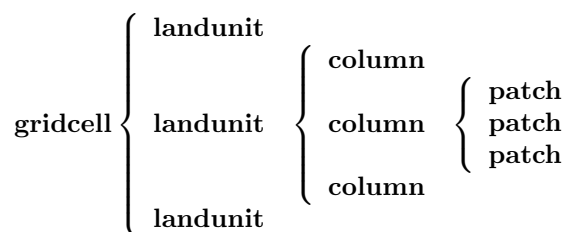## 29.2 The representation of ecosystem heterogeneity in FATES

The terrestrial surface of the Earth is heterogeneous for many reasons, driven by variations in climate, edaphic history, ecological variability, geological forcing and human interventions. Land surface models represent this variability first by introducing a grid structure to the land surface, allowing different atmospheric forcings to operate in each grid cell, and subsequently by representing 'sub-grid' variability in the surface properties. In the CLM, the land surface is divided into numerous 'landunits' corresponding to the underlying condition of the surface (e.g. soils, ice, lakes, bare ground) and then 'columns' referring to elements of the surface that share below ground resources (water & nutrients). Within the soil landunit, for example, there are separate columns for crops, and for natural vegetation, as these are assumed to use separate resource pools. The FATES model at present only operates on the naturally vegetated column. The soil column is sub-divided into numerous tiles, that correspond to statistical fractions of the potentially vegetated land area. In the CLM 4.5 (and all previous versions of the model), sub-grid tiling operates on the basis of plant functional types (PFTs). That is, each piece of land is assumed to be occupied by only one plant functional type, with multiple PFT-specific tiles sharing a common soil water and nutrient pool. This PFT-based tiling structure is the standard method used by most land surface models deployed in climate prediction.

The introduction of the Ecosystem Demography concept introduces significant alterations to the representation of the land surface in the CLM. In FATES, the tiling structure represents the disturbance history of the ecosystem. Thus, some fraction of the land surface is characterized as 'recently disturbed', some fraction has escaped disturbance for a long time, and other areas will have intermediate disturbances. Thus the ED concept essentially discretizes the trajectory of succession from disturbed ground to 'mature' ecosystems. Within FATES, each "disturbance history class" is referred to as a 'patch'. The word "patch" has many possible interpretations, so it is important to note that: **there is no spatial location associated with the concept of a 'patch' . It refers to a fraction of the potential vegetated area consisting of all parts of the ecosystem with similar disturbance history.**

The 'patch' organizational structure in CLM thus replaces the previous 'PFT' structure in the organization heirarchy. The original hierarchical land surface organizational structure of CLM as described in *Oleson et al. 2013* may be depicted as:

$$
\text{gridcell}
\begin{cases}
\text{landunit} \\[4pt]
\text{landunit}
\begin{cases}
\text{column} \\[4pt]
\text{column}
\begin{cases}
\text{pft} \\
\text{pft} \\
\text{pft}
\end{cases} \\[4pt]
\text{column}
\end{cases} \\[4pt]
\text{landunit}
\end{cases}
$$

and the new structure is altered to the following:

$$
\text{gridcell}
\begin{cases}
\text{landunit} \\[4pt]
\text{landunit}
\begin{cases}
\text{column} \\[4pt]
\text{column}
\begin{cases}
\text{patch} \\
\text{patch} \\
\text{patch}
\end{cases} \\[4pt]
\text{column}
\end{cases} \\[4pt]
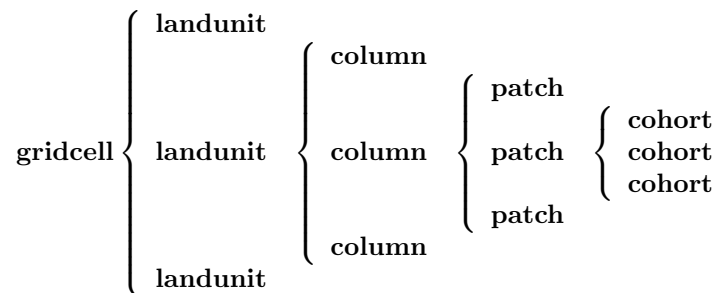\text{landunit}
\end{cases}
$$

Thus, each gridcell becomes a matrix of 'patches' that are conceptualized by their 'age since disturbance' in years. This is the equivalent of grouping together all those areas of a gridcell that are 'canopy gaps', into a single entity, and all those areas that are 'mature forest' into a single entity.

29.2.1 Cohortized representation of tree populations

Each common-disturbance-history patch is a notional ecosystem that might in reality contain numerous individual plants which vary in their physiological attributes, in height and in spatial position. One way of addressing this heterogeneity is to simulate a forest of specific individuals, and to monitor their behavior through time. This is the approach taken by "gap" and individual-based models (*Smith et al. 2001*, *Sato et al. 2007*, *Uriarte et al. 2009*, *Fyllas et al. 2014*). The depiction of individuals typically implies that the outcome of the model is stochastic. This is because we lack the necessary detailed knowledge to simulate the individual plant's fates. Thus gap models imply both stochastic locations and mortality of plants. Thus, (with a genuinely random seed) each model outcome is different, and an ensemble of model runs is required to generate an average representative solution. Because the random death of large individual trees can cause significant deviations from the mean trajectory for a small plot (a typical simulated plot size is 30m x 30 m) the number of runs required to minimize these deviations is large and computationally expensive. For this reason, models that resolve individual trees typically use a physiological timestep of one day or longer (e.g. *Smith et al. 2001*, *Xiaidong et al. 2005*, *Sato et al. 2007*

The approach introduced by the Ecosystem Demography model *Moorcroft et al. 2001* is to group the hypothetical population of plants into "cohorts". In the notional ecosystem, after the land-surface is divided into common-disturbance-history patches, the population in each patch is divided first into plant functional types (the standard approach to representing plant diversity in large scale vegetation models), and then each plant type is represented as numerous height classes. Importantly, **for each PFT/height class bin, we model *one* representative individual plant, which tracks the average properties of this 'cohort' of individual plants.** Thus, each common-disturbance-history patch is typically occupied by a set of cohorts of different plant functional types, and different height classes within those plant functional types. Each cohort is associated with a number of identical trees, n_{coh} (where coh denotes the identification or index number for a given cohort)..

The complete hierarchy of elements in FATES is therefore now described as follows:

$$
\text{gridcell} \begin{cases} \text{landunit} \\ \\ \text{landunit} \begin{cases} \text{column} \\ \\ \text{column} \begin{cases} \text{patch} \\ \\ \text{patch} \begin{cases} \text{cohort} \\ \text{cohort} \\ \text{cohort} \end{cases} \\ \text{patch} \end{cases} \\ \\ \text{column} \end{cases} \\ \\ \text{landunit} \end{cases}
$$

29.2.2 Discretization of cohorts and patches

Newly disturbed land and newly recruited seedlings can in theory be generated at each new model timestep as the result of germination and disturbance processes. If the new patches and cohorts established at *every* timestep were tracked by the model structure, the computational load would of course be extremely high (and thus equivalent to an individual-based approach). A signature feature of the ED model is the system by which *functionally equivalent* patches and cohorts are fused into single model entities to save memory and computational time.

This functionality requires that criteria are established for the meaning of *functional equivalence*, which are by necessity slightly subjective, as they represent ways of abstracting reality into a more tractable mathematical representation. As an example of this, for height-structured cohorts, we calculate the relativized differences in height (h_{coh}, m) between two cohorts of the same pft, p and q as

$$d_{hite,p,q} = \frac{\text{abs.}(h_p - h_q)}{\frac{1}{2}(h_p + h_q)}$$

If $d_{hite,p,q}$ is smaller than some threshold t_{ch}, and they are of the same plant functional type, the two cohorts are considered equivalent and merged to form a third cohort r, with the properties of cohort p and q averaged such that

they conserve mass. The model parameter t_{ch} can be adjusted to adjust the trade-off between simulation accuracy and computational load. There is no theoretical optimal value for this threshold but it may be altered to have finer or coarser model resolutions as needed.

Similarly, for common-disturbance-history patches, we again assign a threshold criteria, which is then compared to the difference between patches m and n, and if the difference is less than some threshold value (t_p) then patches are merged together, otherwise they are kept separate. However, in contrast with height-structured cohorts, where the meaning of the difference criteria is relatively clear, how the landscape should be divided into common-disturbance-history units is less clear. Several alternative criteria are possible, including Leaf Area Index, total biomass and total stem basal area.

In this implementation of FATES we assess the amount of above-ground biomass in each PFT/plant diameter bin. Biomass is first grouped into fixed diameter bins for each PFT (ft) and a significant difference in any bin will cause patches to remain separated. This means that if two patches have similar total biomass, but differ in the distribution of that biomass between diameter classes or plant types, they remain as separate entities. Thus

$$B_{profile,m,dc,ft} = \sum_{d_{c,min}}^{d_{c,max}} (B_{ag,coh} n_{coh})$$

$B_{profile,m,dc,ft}$ is the binned above-ground biomass profile for patch m,d_c is the diameter class. $d_{c,min}$ and $d_{c,max}$ are the lower and upper boundaries for the d_c diameter class. $B_{ag,coh}$ and n_{coh} depict the biomass (KgC m^{-2}) and the number of individuals of each cohort respectively. A difference matrix between patches m and n is thus calculated as

$$d_{biomass,mn,dc,ft} = \frac{\mathrm{abs}(B_{profile,m,hc,ft} - B_{profile,n,hc,ft})}{\frac{1}{2}(B_{profile,m,hc,ft} + B_{profile,n,hc,ft})}$$

If all the values of $d_{biomass,mn,hc,ft}$ are smaller than the threshold, t_p, then the patches m and n are fused together to form a new patch o.

To increase computational efficiency and to simplify the coding structure of the model, the maximum number of patches is capped at $P_{no,max}$. To force the fusion of patches down to this number, the simulation begins with a relatively sensitive discretization of patches ($t_p = 0.2$) but if the patch number exceeds the maximum, the fusion routine is repeated iteratively until the two most similar patches reach their fusion threshold. This approach maintains an even discretization along the biomass gradient, in contrast to, for example, simply fusing the oldest or youngest patches together.

The area of the new patch ($A_{patch,o}$, m^2) is the sum of the area of the two existing patches,

$$A_{patch,o} = A_{patch,n} + A_{patch,m}$$

and the cohorts 'belonging' to patches m and n now co-occupy patch o. The state properties of m and n (litter, seed pools, etc.) are also averaged in accordance with mass conservation .

29.2.3 Linked Lists: the general code structure of FATES

The number of patches in each natural vegetation column and the number of cohorts in any given patch are variable through time because they are re-calculated for each daily timestep of the model. The more complex an ecosystem, the larger the number of patches and cohorts. For a slowly growing ecosystem, where maximum cohort size achieved between disturbance intervals is low, the number of cohorts is also low. For fast-growing ecosystems where many plant types are viable and maximum heights are large, more cohorts are required to represent the ecosystem with adequate complexity.

In terms of variable structure, the creation of an array whose size could accommodate every possible cohort would mean defining the maximum potential number of cohorts for every potential patch, which would result in very large amounts of wasted allocated memory, on account of the heterogeneity in the number of cohorts between complex and simple ecosystems (n.b. this does still happen for some variables at restart timesteps). To resolve this, the cohort

structure in FATES model does not use an array system for internal calculations. Instead it uses a system of *linked lists* where each cohort structure is linked to the cohorts larger than and smaller than itself using a system of pointers. The shortest cohort in each patch has a 'shorter' pointer that points to the *null* value, and the tallest cohort has a 'taller' pointer that points to the null value.

Instead of iterating along a vector indexed by *coh*, the code structures typically begin at the tallest cohort in a given patch, and iterate until a null pointer is encountered.

Using this structure, it is therefore possible to have an unbounded upper limit on cohort number, and also to easily alter the ordering of cohorts if, for example, a cohort of one functional type begins to grow faster than a competitor of another functional type, and the cohort list can easily be re-ordered by altering the pointer structure. Each cohort has *pointers* indicating to which patch and gridcell it belongs. The patch system is analogous to the cohort system, except that patches are ordered in terms of their relative age, with pointers to older and younger patches where cp_1 is the oldest:

29.2.4 Indices used in FATES

Some of the indices used in FATES are similar to those used in the standard CLM4.5 model; column (c), land unit(l), grid cell(g) and soil layer (j). On account of the additional complexity of the new representation of plant function, several additional indices are introduced that describe the discritization of plant type, fuel type, litter type, plant height, canopy identity, leaf vertical structure and fuel moisture characteristics. To provide a reference with which to interpret the equations that follow, they are listed here.

Table 29.1: Table of subscripts used in this document

Parameter Symbol	Parameter Name
ft	Plant Functional Type
fc	Fuel Class
lsc	Litter Size Class
coh	Cohort Index
patch	Patch Index
Cl	Canopy Layer
z	Leaf Layer
mc	Moisture Class

29.2.5 Cohort State Variables

The unit of allometry in the ED model is the cohort. Each cohort represents a group of plants with similar functional types and heights that occupy portions of column with similar disturbance histories. The state variables of each cohort therefore consist of several pieces of information that fully describe the growth status of the plant and its position in the ecosystem structure, and from which the model can be restarted. The state variables of a cohort are as follows:

Table 29.2: State Variables of 'cohort' sructure

Quantity	Variable name	Units	Notes
Plant Functional Type	ft_{coh}	integer	
Number of Individuals	n_{coh}	n per 10000m:math:` ^{-2}``	
Height	h_{coh}	m	
Diameter	dbh_{coh}	cm	
Structural Biomass	$b_{struc,coh}$	KgC plant^{-1}	Stem wood (above and below ground)
Alive Biomass	$b_{alive,coh}$	KgC plant^{-1}	Leaf, fine root and sapwood
Stored Biomass	$b_{store,coh}$	KgC plant^{-1}	Labile carbon reserve
Leaf memory	$l_{memory,coh}$	KgC plant^{-1}	Leaf mass when leaves are dropped
Canopy Layer	$C_{l,coh}$	integer	1 = top layer
Phenological Status	$S_{phen,coh}$	integer	1=leaves off. 2=leaves on
Canopy trimming	$C_{trim,coh}$	fraction	1.0=max leaf area
Patch Index	p_{coh}	integer	To which patch does this cohort belong?

29.2.6 Patch State Variables

A patch, as discuss earlier, is a fraction of the landscape which contains ecosystems with similar structure and disturbance history. A patch has no spatial location. The state variables, which are 'ecosystem' rather than 'tree' scale properties, from which the model can be restarted, are as follows

Table 29.3: State variables of 'patch' structure

Quantity	Variable name	Units	Indexed By	
Area	A_{patch}	m^2	•	
Age	age_{patch}	years	•	
Seed	$seed_{patch}$	KgC m^{-2}	ft	
Leaf Litter	$l_{litter,patch}$	KgC m^{-2}	ft	
Root Litter	$r_{litter,patch}$	KgC m^{-2}	ft	
AG Coarse Woody Debris	:math:` {CWD}_{AG,patch}``	KgC m^{-2}	Size Class (lsc)	
BG Coarse Woody Debris	:math:` {CWD}_{BG,patch}``	KgC m^{-2}	Size Class (lsc)	
Canopy Spread	$S_{c,patch}$	•	Canopy Layer	
Column Index	l_{patch}	integer	•	

29.2.7 Model Structure

Code concerned with the Ecosystem Demography model interfaces with the CLM model in four ways: i) During initialization, ii) During the calculation of surface processes (albedo, radiation absorption, canopy fluxes) each model time step (typically half-hourly), iii) During the main invokation of the ED model code at the end of each day. Daily cohort-level NPP is used to grow plants and alter the cohort structures, disturbance processes (fire and mortality) operate to alter the patch structures, and all fragmenting carbon pool dynamics are calculated. iv) during restart

reading and writing. The net assimilation (NPP) fluxes attributed to each cohort are accumulated throughout each daily cycle and passed into the ED code as the major driver of vegetation dynamics.

29.3 Initialization of vegetation from bare ground

If the model is restarted from a bare ground state (as opposed to a pre-existing vegetation state), the state variables above are initialized as follows. First, the number of plants per PFT is allocated according to the initial seeding density (S_{init}, individuals per m^2) and the area of the patch A_{patch}, which in the first timestep is the same as the area of the notional ecosystem A_{tot}. The model has no meaningful spatial dimension, but we assign a notional area such that the values of 'n_{coh}' can be attributed. The default value of A_{tot} is one hectare (10,000 m^2), but the model will behave identically irrepective of the value of this parameter.

$$n_{coh,0} = S_{init}A_{patch}$$

Each cohort is initialized at the minimum canopy height $h_{min,ft}$, which is specified as a parameter for each plant functional type and denotes the smallest size of plant which is tracked by the model. Smaller plants are not considered, and their emergence from the recruitment processes is unresolved and therefore implicitly parameterized in the seedling establishment model.. The diameter of each cohort is then specified using the log-linear allometry between stem diameter and canopy height

$$dbh_{coh} = 10^{\frac{\log_{10}(h_{coh})-c_{allom}}{m_{allom}}}$$

where the slope of the log-log relationship, m_{allom} is 0.64 and the intercept c_{allom} is 0.37. The structural biomass associated with a plant of this diameter and height is given (as a function of wood density, ρ, g cm^{-3})

$$b_{struc,coh} = c_{str}h_{coh}^{e_{str,hite}}dbh_{coh}^{e_{str,dbh}}\rho_{ft}^{e_{str,dens}}$$

taken from the original ED1.0 allometry *Moorcroft et al. 2001* (values of the allometric constants in Table *[table:allom]*. The maximum amount of leaf biomass associated with this diameter of tree is calculated according to the following allometry

$$b_{max,leaf,coh} = c_{leaf}dbh_{coh}^{e_{leaf,dbh}}\rho_{ft}^{e_{leaf,dens}}$$

from this quantity, we calculate the active/fine root biomass $b_{root,coh}$ as

$$b_{root,coh} = b_{max,leaf,coh} \cdot f_{frla}$$

where f_{frla} is the fraction of fine root biomass to leaf biomass, assigned per PFT

Table 29.4: Parameters needed for model initialization.

Parameter Symbol	Parameter Name	Units	Default Value
h_{min}	Minimum plant height	m	1.5
S_{init}	Initial Planting density	Individuals m^{-2}	
A_{tot}	Model area	m^2	10,000

[table:init]

29.4 Allocation of biomass

Total live biomass b_{alive} is the state variable of the model that describes the sum of the three live biomass pools leaf b_{leaf}, root b_{root} and sapwood b_{sw} (all in kGC individual^{-1}). The quantities are constrained by the following

$$b_{alive} = b_{leaf} + b_{root} + b_{sw}$$

Sapwood volume is a function of tree height and leaf biomass

$$b_{sw} = b_{leaf} \cdot h_{coh} \cdot f_{swh}$$

where f_{swh} is the ratio of sapwood mass (kgC) to leaf mass per unit tree height (m). Also, root mass is a function of leaf mass

$$b_{root} = b_{leaf} \cdot f_{swh}$$

Thus

$$b_{alive} = b_{leaf} + b_{leaf} \cdot f_{frla} + b_{leaf} \cdot h_{coh} \cdot f_{swh}$$

Rearranging gives the fraction of biomass in the leaf pool f_{leaf} as

$$f_{leaf} = \frac{1}{1 + h_{coh} \cdot f_{swh} + f_{frla}}$$

Thus, we can determine the leaf fraction from the height at the tissue ratios, and the phenological status of the cohort $S_{phen,coh}$.

$$b_{leaf} = b_{alive} \cdot l_{frac}$$

To divide the live biomass pool at restart, or whenever it is recalculated, into its consituent parts, we first

$$b_{leaf} = \begin{cases} b_{alive} \cdot l_{frac} & \text{for } S_{phen,coh} = 1 \\ \\ 0 & \text{for } S_{phen,coh} = 0 \end{cases}$$

Because sometimes the leaves are dropped, using leaf biomass as a predictor of root and sapwood would produce zero live biomass in the winter. To account for this, we add the LAI memory variable l_{memory} to the live biomass pool to account for the need to maintain root biomass when leaf biomass is zero. Thus, to calculated the root biomass, we use

$$b_{root} = (b_{alive} + l_{memory}) \cdot l_{frac} \cdot f_{frla}$$

To calculated the sapwood biomass, we use

$$b_{sw} = (b_{alive} + l_{memory}) \cdot l_{frac} \cdot f_{swh} \cdot h_{coh}$$

Table 29.5: Allometric Constants

Parameter Symbol	Parameter Name	Units	Default Value
c_{allom}	Allometry intercept		0.37
m_{allom}	Allometry slope		0.64
c_{str}	Structural biomass multiplier		0.06896
$e_{str,dbh}$	Structural Biomass dbh exponent		1.94
$e_{str,hite}$	Structural Biomass height exponent		0.572
$e_{str,dens}$	Structural Biomass density exponent		0.931
c_{leaf}	Leaf biomass multiplier		0.0419
$e_{leaf,dbh}$	Leaf biomass dbh exponent		1.56
$e_{leaf,dens}$	Leaf biomass density exponent		0.55
f_{swh}	Ratio of sapwood mass to height	m^{-1}	
f_{frla}	Ratio of fine root mass to leaf mass	•	1.0

[table:allom]

29.5 Canopy Structure and the Perfect Plasticity Approximation

During initialization and every subsequent daily ED timestep, the canopy structure model is called to determine how the leaf area of the different cohorts is arranged relative to the incoming radiation, which will then be used to drive the radiation and photosynthesis calculations. This task requires that some assumptions are made about 1) the shape and depth of the canopy within which the plant leaves are arranged and 2) how the leaves of different cohorts are arranged relative to each other. This set of assumptions are critical to model performance in ED-like cohort based models, since they determine how light resources are partitioned between competing plants of varying heights, which has a very significant impact on how vegetation distribution emerges from competition *Fisher et al. 2010*.

The standard ED1.0 model makes a simple 'flat disk' assumption, that the leaf area of each cohort is spread in an homogenous layer at one exact height across entire the ground area represented by each patch. FATES has diverged from this representation due to (at least) two problematic emergent properties that we identified as generating unrealistic behaviours espetially for large-area patches.

1. Over-estimation of light competition . The vertical stacking of cohorts which have all their leaf area at the same nominal height means that when one cohort is only very slightly taller than it's competitor, it is completely shaded by it. This means that any small advantage in terms of height growth translates into a large advantage in terms of light competition, even at the seedling stage. This property of the model artificially exaggerates the process of light competition. In reality, trees do not compete for light until their canopies begin to overlap and canopy closure is approached.

2. Unrealistic over-crowding. The 'flat-disk' assumption has no consideration of the spatial extent of tree crowns. Therefore it has no control on the packing density of plants in the model. Given a mismatch between production and mortality, entirely unrealistic tree densities are thus possible for some combinations of recruitment, growth and mortality rates.

To account for the filling of space in three dimensions using the one-dimensional representation of the canopy employed by CLM, we implement a new scheme derived from that of *Purves et al. 2008*. Their argument follows the development of an individual-based variant of the SORTIE model, called SHELL, which allows the location of

individual plant crowns to be highly flexible in space. Ultimately, the solutions of this model possess an emergent property whereby the crowns of the plants simply fill all of the available space in the canopy before forming a distinct understorey.

Purves et al. developed a model that uses this feature, called the 'perfect plasticity approximation', which assumes the plants are able to perfectly fill all of the available canopy space. That is, at canopy closure, all of the available horizontal space is filled, with negligible gaps, owing to lateral tree growth and the ability of tree canopies to grow into the available gaps (this is of course, an over-simplified but potential useful ecosystem property). The 'perfect plasticity approximation' (PPA) implies that the community of trees is subdivided into discrete canopy layers, and by extension, each cohort represented by FATES model is assigned a canopy layer status flag, C_L. In this version, we set the maximum number of canopy layers at 2 for simplicity, although is possible to have a larger number of layers in theory. $C_{L,coh} = 1$ means that all the trees of cohort coh are in the upper canopy (overstory), and $C_{L,coh} = 2$ means that all the trees of cohort coh are in the understorey.

In this model, all the trees in the canopy experience full light on their uppermost leaf layer, and all trees in the understorey experience the same light (full sunlight attenuated by the average LAI of the upper canopy) on their uppermost leaves, as described in the radiation transfer section (more nuanced versions of this approach may be investigated in future model versions). The canopy is assumed to be cylindrical, the lower layers of which experience self-shading by the upper layers.

To determine whether a second canopy layer is required, the model needs to know the spatial extent of tree crowns. Crown area, A_{crown}, m^2, is defined as

$$A_{crown,coh} = \pi (dbh_{coh} S_{c,patch,Cl})^{1.56}$$

where A_{crown} is the crown area of a single tree canopy (m:math:^{-2}) and $S_{c,patch,Cl}$ is the 'canopy spread' parameter (m cm^-1) of this canopy layer, which is assigned as a function of canopy space filling, discussed below. In contrast to *Purves et al. 2008* , we use an exponent, identical to that for leaf biomass, of 1.56, not 2.0, such that tree leaf area index does not change as a function of diameter.

To determine whether the canopy is closed, we calculate the total canopy area as:

$$A_{canopy} = \sum_{coh=1}^{nc,patch} A_{crown,coh} . n_{coh}$$

where nc_{patch} is the number of cohorts in a given patch. If the area of all crowns A_{canopy} (m:math:^{-2}) is larger than the total ground area of a patch (A_{patch}), then some fraction of each cohort is demoted to the understorey.

Under these circumstances, the *extra* crown area A_{loss} (i.e., A_{canopy} - A_p) is moved into the understorey. For each cohort already in the canopy, we determine a fraction of trees that are moved from the canopy (L_c) to the understorey. L_c is calculated as *Fisher et al. 2010*

$$L_c = \frac{A_{loss,patch} w_{coh}}{\sum_{coh=1}^{nc,patch} w_{coh}},$$

where w_{coh} is a weighting of each cohort determined by basal diameter dbh (cm) and the competitive exclusion coefficient C_e

$$w_{coh} = dbh_{coh} C_e.$$

The higher the value of C_e the greater the impact of tree diameter on the probability of a given tree obtaining a position in the canopy layer. That is, for high C_e values, competition is highly deterministic. The smaller the value of C_e, the greater the influence of random factors on the competitive exclusion process, and the higher the probability that slower growing trees will get into the canopy. Appropriate values of C_e are poorly constrained but alter the outcome of competitive processes.

The process by which trees are moved between canopy layers is complex because 1) the crown area predicted for a cohort to lose may be larger than the total crown area of the cohort, which requires iterative solutions, and 2) on some

occasions (e.g. after fire), the canopy may open up and require 'promotion' of cohorts from the understorey, and 3) canopy area may change due to the variations of canopy spread values ($S_{c,patch,Cl}$, see the section below for details) when fractions of cohorts are demoted or promoted. Further details can be found in the code references in the footnote.

29.5.1 Horizontal Canopy Spread

Purves et al. 2008 estimated the ratio between canopy and stem diameter c_p as 0.1 m cm^{-1} for canopy trees in North American forests, but this estimate was made on trees in closed canopies, whose shape is subject to space competition from other individuals. Sapling trees have no constraints in their horizontal spatial structure, and as such, are more likely to display their leaves to full sunlight. Also, prior to canopy closure, light interception by leaves on the sides of the canopy is also higher than it would be in a closed canopy forest. If the 'canopy spread' parameter is constant for all trees, then we simulate high levels of self-shading for plants in unclosed canopies, which is arguably unrealistic and can lower the productivity of trees in areas of unclosed canopy (e.g. low productivity areas of boreal or semi-arid regions where LAI and canopy cover might naturally be low). We here interpret the degree of canopy spread, S_c as a function of how much tree crowns interfere with each other in space, or the total canopy area A_{canopy}. However A_{canopy} itself is a function of S_c, leading to a circularity. S_c is thus solved iteratively through time.

Each daily model step, A_{canopy} and the fraction of the gridcell occupied by tree canopies in each canopy layer ($A_{f,Cl}$ = $A_{canopy,Cl}/A_{patch}$) is calculated based on S_c from the previous timestep. If A_f is greater than a threshold value A_t, S_c is increased by a small increment i. The threshold A_t is, hypothetically, the canopy fraction at which light competition begins to impact on tree growth. This is less than 1.0 owing to the non-perfect spatial spacing of tree canopies. If $A_{f,Cl}$ is greater than A_t, then S_c is reduced by an increment i, to reduce the spatial extent of the canopy, thus.

$$S_{c,patch,Cl,t+1} = \begin{cases} S_{c,patch,Cl,t} + i & \text{for } A_{f,Cl} < A_t \\ S_{c,patch,Cl,t} - i & \text{for } A_{f,Cl} > A_t \end{cases}$$

The values of S_c are bounded to upper and lower limits. The lower limit corresponds to the observed canopy spread parameter for canopy trees $S_{c,min}$ and the upper limit corresponds to the largest canopy extent $S_{c,max}$

$$S_{c,patch,Cl} = \begin{cases} S_{c,min} & \text{for } S_{c,patch,Cl} < S_{c,\min} \\ S_{c,max} & \text{for } S_{c,patch,Cl} > S_{c,\max} \end{cases}$$

This iterative scheme requires two additional parameters (i and A_t). i affects the speed with which canopy spread (and hence leaf are index) increase as canopy closure is neared. However, the model is relatively insensitive to the choice of either i or A_t.

29.5.2 Definition of Leaf and Stem Area Profile

Within each patch, the model defines and tracks cohorts of multiple plant functional types that exist either in the canopy or understorey. Light on the top leaf surface of each cohort in the canopy is the same, and the rate of decay through the canopy is also the same for each PFT. Therefore, we accumulate all the cohorts of a given PFT together for the sake of the radiation and photosynthesis calculations (to avoid separate calculations for every cohort).

Therefore, the leaf area index for each patch is defined as a three-dimensional array $lai_{Cl,ft,z}$ where C_l is the canopy layer, ft is the functional type and z is the leaf layer within each canopy. This three-dimensional structure is the basis of the radiation and photosynthetic models. In addition to a leaf area profile matrix, we also define, for each patch, the area which is covered by leaves at each layer as $carea_{Cl,ft,z}$.

Each plant cohort is already defined as a member of a single canopy layer and functional type. This means that to generate the $x_{Cl,ft,z}$ matrix, it only remains to divide the leaf area of each cohort into leaf layers. First, we determine

how many leaf layers are occupied by a single cohort, by calculating the 'tree LAI' as the total leaf area of each cohort divided by its crown area (both in m^2)

$$tree_{lai,coh} = \frac{b_{leaf,coh} \cdot \text{sla}_{ft}}{A_{crown,coh}}$$

where sla_{ft} is the specific leaf area in m^2 KgC^{-1} and b_{leaf} is in kGC per plant.

Stem area index (SAI) is ratio of the total area of all woody stems on a plant to the area of ground covered by the plant. During winter in deciduous areas, the extra absorption by woody stems can have a significant impact on the surface energy budget. However, in previous *big leaf* versions of the CLM, computing the circumstances under which stem area was visible in the absence of leaves was difficult and the algorithm was largely heuristic as a result. Given the multi-layer canopy introduced for FATES, we can determine the leaves in the higher canopy layers will likely shade stem area in the lower layers when leaves are on, and therefore stem area index can be calculated as a function of woody biomass directly.

Literature on stem area index is particularly poor, as it's estimation is complex and not particularly amenable to the use of, for example, assumptions of random distribution in space that are typically used to calculate leaf area from light interception. *Kucharik et al. 1998* estimated that SAI visible from an LAI2000 sensor was around 0.5 m^2 m^-2. Low et al. 2001 estimate that the wood area index for Ponderosa Pine forest is 0.27-0.33. The existing CLM(CN) algorithm sets the minimum SAI at 0.25 to match MODIS observations, but then allows SAI to rise as a function of the LAI lost, meaning than in some places, predicted SAI can reach value of 8 or more. Clearly, greater scientific input on this quantity is badly needed. Here we determine that SAI is a linear function of woody biomass, to at very least provide a mechanistic link between the existence of wood and radiation absorbed by it. The non-linearity between how much woody area exists and how much radiation is absorbed is provided by the radiation absorption algorithm. Specifically, the SAI of an individual cohort ($tree_{sai,coh}$, m^2 m^{-2}) is calculated as follows,

$$tree_{sai,coh} = k_{sai} \cdot b_{struc,coh},$$

where k_{sai} is the coefficient linking structural biomass to SAI. The number of occupied leaf layers for cohort *coh* ($n_{z,coh}$) is then equal to the rounded up integer value of the tree SAI ($tree_{sai,coh}$) and LAI ($tree_{lai,coh}$) divided by the layer thickness (i.e., the resolution of the canopy layer model, in units of vegetation index ($lai+sai$) with a default value of 1.0, δ_{vai}),

$$n_{z,coh} = \frac{tree_{lai,coh} + tree_{sai,coh}}{\delta_{vai}}.$$

The fraction of each layer that is leaf (as opposed to stem) can then be calculated as

$$f_{leaf,coh} = \frac{tree_{lai,coh}}{tree_{sai,coh} + tree_{lai,coh}}.$$

Finally, the leaf area in each leaf layer pertaining to this cohort is thus

$$lai_{z,coh} = \begin{cases} \delta_{vai} \cdot f_{leaf,coh} \frac{A_{canopy,coh}}{A_{canopy,patch}} & \text{for } i = 1, ..., i = n_{z,coh} - 1 \\ \delta_{vai} \cdot f_{leaf,coh} \frac{A_{canopy,coh}}{A_{canopy,patch}} \cdot r_{vai} & \text{for } i = n_{z,coh} \end{cases}$$

and the stem area index is

$$sai_{z,coh} = \begin{cases} \delta_{vai} \cdot (1 - f_{leaf,coh}) \frac{A_{canopy,coh}}{A_{canopy,patch}} & \text{for } i = 1, ..., i = n_{z,coh} - 1 \\ \delta_{vai} \cdot (1 - f_{leaf,coh}) \frac{A_{canopy,coh}}{A_{canopy,patch}} \cdot r_{vai} & \text{for } i = n_{z,coh} \end{cases}$$

where r_{vai} is the remainder of the canopy that is below the last full leaf layer

$$r_{vai} = (tree_{lai,coh} + tree_{sai,coh}) - (\delta_{vai} \cdot (n_{z,coh} - 1)).$$

$A_{canopy,patch}$ is the total canopy area occupied by plants in a given patch (m:math:`^{2}`) and is calculated as follows,

$$A_{canopy,patch} = \min \left(\sum_{coh=1}^{coh=ncoh} A_{canopy,coh}, A_{patch} \right).$$

The canopy is conceived as a cylinder, although this assumption could be altered given sufficient evidence that canopy shape was an important determinant of competitive outcomes, and the area of ground covered by each leaf layer is the same through the cohort canopy. With the calculated SAI and LAI, we are able to calculate the complete canopy profile. Specifically, the relative canopy area for the cohort coh is calculated as

$$area_{1:nz,coh} = \frac{A_{crown,coh}}{A_{canopy,patch}}.$$

The total occupied canopy area for each canopy layer (Cl), plant functional type (ft) and leaf layer (z) bin is thus

$$c_{area,Cl,ft,z} = \sum_{coh=1}^{coh=ncoh} area_{1:nz,coh}$$

where $ft_{coh} = ft$ and $Cl_{coh} = Cl$.

All of these quantities are summed across cohorts to give the complete leaf and stem area profiles,

$$lai_{Cl,ft,z} = \sum_{coh=1}^{coh=ncoh} lai_{z,coh}$$

$$sai_{Cl,ft,z} = \sum_{coh=1}^{coh=ncoh} sai_{z,coh}$$

29.5.3 Burial of leaf area by snow

The calculations above all pertain to the total leaf and stem area indices which charecterize the vegetation structure. In addition, the model must know when the vegetation is covered by snow, and by how much, so that the albedo and energy balance calculations can be adjusted accordingly. Therefore, we calculated a 'total' and 'exposed' lai and sai profile using a representation of the bottom and top canopy heights, and the depth of the average snow pack. For each leaf layer z of each cohort, we calculate an 'exposed fraction $f_{exp,z}$ via consideration of the top and bottom heights of that layer $h_{top,z}$ and $h_{bot,z}$ (m),

$$h_{top,z} = h_{coh} - h_{coh} \cdot f_{crown,ft} \cdot \frac{z}{n_{z,coh}}$$

$$h_{bot,z} = h_{coh} - h_{coh} \cdot f_{crown,ft} \cdot \frac{z+1}{n_{z,coh}}$$

where $f_{crown,ft}$ is the plant functional type (ft) specific fraction of the cohort height that is occupied by the crown. Specifically, the 'exposed fraction $f_{exp,z}$ is calculated as follows,

$$f_{exp,z} \begin{cases} = 1.0 & h_{bot,z} > d_{snow} \\ = \frac{d_{snow} - h_{bot,z}}{h_{top,z} - h_{bot,z}} & h_{top,z} > d_{snow}, h_{bot,z} < d_{snow} \\ = 0.0 & h_{top,z} < d_{snow} \end{cases}$$

The resulting exposed ($elai, esai$) and total ($tlai, tsai$) leaf and stem area indicies are calculated as

$$\begin{aligned} elai_{Cl,ft,z} &= lai_{Cl,ft,z} \cdot f_{exp,z} \\ esai_{Cl,ft,z} &= sai_{Cl,ft,z} \cdot f_{exp,z} \\ tlai_{Cl,ft,z} &= lai_{Cl,ft,z} \\ tsai_{Cl,ft,z} &= sai_{Cl,ft,z} \end{aligned},$$

and are used in the radiation interception and photosynthesis algorithms described later.

Parameter Symbol	Parameter Name	Units	Notes	Indexed by
:math:' delta_ {vai}'	Thickness of single canopy layer	m^{-2}m: math:^{-2}		
C_e	Competitive Exclusion Parameter	none		
$c_{p,min}$	Minimum canopy spread	m^2 cm:math:' ^{-1}'		
$c_{p,max}$	Competitive Exclusion Parameter	m^2 cm:math:' ^{-1}'		
i	Incremental change in c_p	m^2 cm:math:' ^{-1}' y^{-1}		
A_t	Threshold canopy closure	none		
$f_{crown,ft}$	Crown fraction	none		ft
k_{sai}	Stem area per unit woody biomass	m^2 KgC^-1		

29.6 Radiation Transfer

29.6.1 Fundamental Radiation Transfer Theory

The first interaction of the land surface with the properties of vegetation concerns the partitioning of energy into that which is absorbed by vegetation, reflected back into the atmosphere, and absorbed by the ground surface. Older versions of the CLM have utilized a "two-stream" approximation *Sellers 1985*, *Sellers et al. 1986* that provided an empirical solution for the radiation partitioning of a multi-layer canopy for two streams, of diffuse and direct light. However, implementation of the Ecosystem Demography model requires a) the adoption of an explicit multiple layer canopy b) the implementation of a multiple plant type canopy and c) the distinction of canopy and under-storey layers, in-between which the radiation streams are fully mixed. The radiation mixing between canopy layers is necessary as the position of different plants in the under-storey is not defined spatially or relative to the canopy trees above. In this new scheme, we thus implemented a one-dimensional scheme that traces the absorption, transmittance and reflectance of each canopy layer and the soil, iterating the upwards and downwards passes of radiation through the canopy until a pre-defined accuracy tolerance is reached. This approach is based on the work of *Norman 1979*.

Here we describe the basic theory of the radiation transfer model for the case of a single homogenous canopy, and in the next section we discuss how this is applied to the multi layer multi PFT canopy in the FATES implementation. The code considers the fractions of a single unit of incoming direct and a single unit of incoming diffuse light, that are absorbed at each layer of the canopy for a given solar angle (α_s, radians). Direct radiation is extinguished through the canopy according to the coefficient k_{dir} that is calculated from the incoming solar angle and the dimensionless leaf angle distribution parameter (χ) as

$$k_{dir} = g_{dir}/\sin(\alpha_s)$$

where

$$g_{dir} = \phi_1 + \phi_2 \cdot \sin(\alpha_s)$$

and

$$\phi_1 = 0.5 - 0.633\chi_l - 0.33\chi_l^2$$
$$\phi_2 = 0.877(1 - 2\phi_1)$$

The leaf angle distribution is a descriptor of how leaf surfaces are arranged in space. Values approaching 1.0 indicate that (on average) the majority of leaves are horizontally arranged with respect to the ground. Values approaching -1.0 indicate that leaves are mostly vertically arranged, and a value of 0.0 denotes a canopy where leaf angle is random (a 'spherical' distribution).

According to Beer's Law, the fraction of light that is transferred through a single layer of vegetation (leaves or stems) of thickness δ_{vai}, without being intercepted by any surface, is

$$tr_{dir} = e^{-k_{dir}\delta_{vai}}$$

and the incident direct radiation transmitted to each layer of the canopy ($dir_{tr,z}$) is thus calculated from the cumulative leaf area (L_{above}) shading each layer (z):

$$dir_{tr,z} = e^{-k_{dir}L_{above,z}}$$

The fraction of the leaves f_{sun} that are exposed to direct light is also calculated from the decay coefficient k_{dir}.

$$f_{sun,z} = e^{-k_{dir}L_{above,z}}$$
and
$$f_{shade,z} = 1 - f_{sun,z}$$

where $f_{shade,z}$ is the fraction of leaves that are shaded from direct radiation and only receive diffuse light.

Diffuse radiation, by definition, enters the canopy from a spectrum of potential incident directions, therefore the unintercepted transfer (tr_{dif}) through a leaf layer of thickness δ_l is calculated as the mean of the transfer rate from each of 9 different incident light directions (α_s) between 0 and 180 degrees to the horizontal.

$$tr_{dif} = \frac{1}{9}\sum_{\alpha_s=5\pi/180}^{\alpha_s=85\pi/180} e^{-k_{dir,l}\delta_{vai}}$$

$$tr_{dif} = \frac{1}{9}\pi\sum_{\alpha s=0}^{\pi/2} \frac{e^{-gdir}\alpha_s}{\delta_{vai}\cdot\sin(\alpha_s)\sin(\alpha_s)\cos(\alpha_s)}$$

The fraction (1-tr_{dif}) of the diffuse radiation is intercepted by leaves as it passes through each leaf layer. Of this, some fraction is reflected by the leaf surfaces and some is transmitted through. The fractions of diffuse radiation reflected from ($refl_{dif}$) and transmitted though ($tran_{dif}$) each layer of leaves are thus, respectively

$$refl_{dif} = (1 - tr_{dif})\rho_{l,ft}$$
$$tran_{dif} = (1 - tr_{dif})\tau_{l,ft} + tr_{dif}$$

where $\rho_{l,ft}$ and $\tau_{l,ft}$ are the fractions of incident light reflected and transmitted by individual leaf surfaces.

Once we know the fractions of light that are transmitted and reflected by each leaf layer, we begin the process of distributing light through the canopy. Starting with the first leaf layer (z=1), where the incident downwards diffuse radiation (dif_{down}) is 1.0, we work downwards for n_z layers, calculating the radiation in the next layer down ($z + 1$) as:

$$dif_{down,z+1} = \frac{dif_{down,z}tran_{dif}}{1 - r_{z+1}refl_{dif}}$$

Here, $dif_{down,z}tran_{dif}$ calculates the fraction of incoming energy transmitted downwards onto layer $z + 1$. This flux is then increased by the additional radiation r_z that is reflected upwards from further down in the canopy to layer z, and then is reflected back downwards according to the reflected fraction $refl_{dif}$. The more radiation in $r_{z+1}refl_{dif}$, the smaller the denominator and the larger the downwards flux. r is also calculated sequentially, starting this time at the soil surface layer (where $z = n_z + 1$)

$$r_{nz+1} = alb_s$$

where alb_s is the soil albedo characteristic. The upwards reflected fraction r_z for each leaf layer, moving upwards, is then *Norman 1979*

$$r_z = \frac{r_{z+1} \times tran_{dif}^2}{(1 - r_{z+1}refl_{dif}) + refl_{dif}}.$$

The corresponding upwards diffuse radiation flux is therefore the fraction of downwards radiation that is incident on a particular layer, multiplied by the fraction that is reflected from all the lower layers:

$$dif_{up,z} = r_z \, dif_{down,z+1}$$

Now we have initial conditions for the upwards and downwards diffuse fluxes, these must be modified to account for the fact that, on interception with leaves, direct radiation is transformed into diffuse radiation. In addition, the initial solutions to the upwards and downwards radiation only allow a single 'bounce' of radiation through the canopy, so some radiation which might be intercepted by leaves higher up is potentially lost. Therefore, the solution to this model is iterative. The iterative solution has upwards and a downwards components that calculate the upwards and downwards fluxes of total radiation at each leaf layer ($rad_{dn,z}$ and $rad_{up,z}$) . The downwards component begins at the top canopy layer ($z = 1$). Here we define the incoming solar diffuse and direct radiation ($solar_{dir}$ and $solar_{dir}$ respectively).

$$dif_{dn,1} = solar_{dif}$$
$$rad_{dn,z+1} = dif_{dn,z} \cdot tran_{dif} + dif_{up,z+1} \cdot refl_{dif} + solar_{dir} \cdot dir_{tr,z}(1 - tr_{dir})\tau_l.$$

The first term of the right-hand side deals with the diffuse radiation transmitted downwards, the second with the diffuse radiation travelling upwards, and the third with the direct radiation incoming at each layer ($dir_{tr,z}$) that is intercepted by leaves ($1 - tr_{dir}$) and then transmitted through through the leaf matrix as diffuse radiation (τ_l). At the bottom of the canopy, the light reflected off the soil surface is calculated as

$$rad_{up,nz} = dif_{\mathrm{down,z}} \cdot \mathrm{salb_{dif}} + solar_{dir} \cdot dir_{tr,z} salb_{dir}.$$

The upwards propagation of the reflected radiation is then

$$rad_{up,z} = dif_{up,z+1} \cdot tran_{dif} + dif_{dn,z} \cdot refl_{dif} + solar_{dir} \cdot dir_{tr,z}(1 - tr_{dir})\rho_l.$$

Here the first two terms deal with the diffuse downwards and upwards fluxes, as before, and the third deals direct beam light that is intercepted by leaves and reflected upwards. These upwards and downwards fluxes are computed for multiple iterations, and at each iteration, $rad_{up,z}$ and $rad_{down,z}$ are compared to their values in the previous iteration. The iteration scheme stops once the differences between iterations for all layers is below a predefined tolerance factor, (set here at 10^{-4}). Subsequently, the fractions of absorbed direct ($abs_{dir,z}$) and diffuse ($abs_{dif,z}$) radiation for each leaf layer then

$$abs_{dir,z} = solar_{dir} \cdot dir_{tr,z} \cdot (1 - tr_{dir}) \cdot (1 - \rho_l - \tau_l)$$

$$abs_{dif,z} = (dif_{dn,z} + dif_{up,z+1}) \cdot (1 - tr_{dif}) \cdot (1 - \rho_l - \tau_l).$$

and, the radiation energy absorbed by the soil for the diffuse and direct streams is is calculated as

$$abs_{soil} = dif_{down,nz+1} \cdot (1 - salb_{dif}) + solar_{dir} \cdot dir_{tr,nz+1} \cdot (1 - salb_{dir}).$$

Canopy level albedo is denoted as the upwards flux from the top leaf layer

$$alb_{canopy} = \frac{dif_{up,z+1}}{solar_{dir} + solar_{dif}}$$

and the division of absorbed energy into sunlit and shaded leaf fractions, (required by the photosynthesis calculations), is

$$abs_{sha,z} = abs_{dif,z} \cdot f_{sha}$$

$$abs_{sun,z} = abs_{dif,z} \cdot f_{sun} + abs_{dir,z}$$

29.6.2 Resolution of radiation transfer theory within the FATES canopy structure

The radiation transfer theory above, was described with reference to a single canopy of one plant functional type, for the sake of clarity of explanation. The FATES model, however, calculates radiative and photosynthetic fluxes for a more complex hierarchical structure within each patch/time-since-disturbance class, as described in the leaf area profile section. Firstly, we denote two or more canopy layers (denoted C_l). The concept of a 'canopy layer' refers to the idea that plants are organized into discrete over and under-stories, as predicted by the Perfect Plasticity Approximation (*Purves et al. 2008*, *Fisher et al. 2010*). Within each canopy layer there potentially exist multiple cohorts of different plant functional types and heights. Within each canopy layer, C_l, and functional type, ft, the model resolves numerous leaf layers z, and, for some processes, notably photosynthesis, each leaf layer is split into a fraction of sun and shade leaves, f_{sun} and f_{sha}, respectively.

The radiation scheme described in Section is solved explicitly for this structure, for both the visible and near-infrared wavebands, according to the following assumptions.

- A *canopy layer* (C_L) refers to either the over or understorey
- A *leaf layer* (z) refers to the discretization of the LAI within the canopy of a given plant functional type.
- All PFTs in the same canopy layer have the same solar radiation incident on the top layer of the canopy
- Light is transmitted through the canopy of each plant functional type independently
- Between canopy layers, the light streams from different plant functional types are mixed, such that the (undefined) spatial location of plants in lower canopy layers does not impact the amount of light received.
- Where understorey layers fill less area than the overstorey layers, radiation is directly transferred to the soil surface.
- All these calculations pertain to a single patch, so we omit the *patch* subscript for simplicity in the following discussion.

Within this framework, the majority of the terms in the radiative transfer scheme are calculated with indices of C_L, ft and z. In the following text, we revisit the simplified version of the radiation model described above, and explain how it is modified to account for the more complex canopy structure used by FATES.

Firstly, the light penetration functions, k_{dir} and g_{dir} are described as functions of ft, because the leaf angle distribution, χ_l, is a pft-specific parameter. Thus, the diffuse irradiance transfer rate, tr_{dif} is also ft specific because g_{dir}, on which it depends, is a function of χ_l.

The amount of direct light reaching each leaf layer is a function of the leaves existing above the layer in question. If a leaf layer 'z' is in the top canopy layer (the over-storey), it is only shaded by leaves of the same PFT so k_{dir} is unchanged from equation. If there is more than one canopy layer ($C_{l,max} > 1$), then the amount of direct light reaching the top leaf surfaces of the second/lower layer is the weighted average of the light attenuated by all the parallel tree canopies in the canopy layer above, thus.

$$dir_{tr,Cl,:,1} = \sum_{ft=1}^{npft} (dir_{tr,Cl,ft,z_{max}} \cdot c_{area,Cl-1,ft,z_{max}})$$

where pft_{wt} is the areal fraction of each canopy layer occupied by each functional type and z_{max} is the index of the bottom canopy layer of each pft in each canopy layer (the subscripts C_l and ft are implied but omitted from all z_{max} references to avoid additional complications)

Similarly, the sunlit fraction for a leaf layer 'z' in the second canopy layer (where $C_l > 1$) is

$$f_{sun,Cl,ft,z} = W_{sun,Cl} \cdot e^{k_{dir,ft,laic,z}}$$

where $W_{sun,Cl}$ is the weighted average sunlit fraction in the bottom layer of a given canopy layer.

$$W_{sun,Cl} = \sum_{ft=1}^{npft} (f_{sun,Cl-1,ft,zmax} \cdot c_{area,Cl-1,ft,zmax})$$

Following through the sequence of equations for the simple single pft and canopy layer approach above, the $refl_{dif}$ and $tran_{dif}$ fluxes are also indexed by C_l, ft, and z. The diffuse radiation reflectance ratio r_z is also calculated in a manner that homogenizes fluxes between canopy layers. For the canopy layer nearest the soil ($C_l = C_{l,max}$). For the top canopy layer (C_l=1), a weighted average reflectance from the lower layers is used as the baseline, in lieu of the soil albedo. Thus:

$$r_{z,Cl,:,1} = \sum_{ft=1}^{npft} \left(r_{z,Cl-1,ft,1} pft_{wt,Cl-1,ft,1} \right)$$

For the iterative flux resolution, the upwards and downwards fluxes are also averaged between canopy layers, thus where $C_l > 1$

$$rad_{dn,Cl,ft,1} = \sum_{ft=1}^{npft} \left(rad_{dn,Cl-1,ft,zmax} \cdot pft_{wt,Cl-1,ft,zmax} \right)$$

and where C_l =1, and $C_{l,max} > 1$

$$rad_{up,Cl,ft,zmax} = \sum_{ft=1}^{npft} \left(rad_{up,Cl+1,ft,1} \cdot pft_{wt,Cl+1,ft,1} \right)$$

The remaining terms in the radiation calculations are all also indexed by C_l, ft and z so that the fraction of absorbed radiation outputs are termed $abs_{dir,Cl,ft,z}$ and $abs_{dif,Cl,ft,z}$. The sunlit and shaded absorption rates are therefore

$$abs_{sha,Cl,ft,z} = abs_{dif,Cl,ft,z} \cdot f_{sha,Cl,ft,z}$$

and

$$abs_{sun,Cl,ft,z} = abs_{dif,Cl,ft,z} \cdot f_{sun,Cl,ft,z} + abs_{dir,Cl,ft,z}$$

The albedo of the mixed pft canopy is calculated as the weighted average of the upwards radiation from the top leaf layer of each pft where C_l=1:

$$alb_{canopy} = \sum_{ft=1}^{npft} \frac{dif_{up,1,ft,1} pft_{wt,1,ft,1}}{solar_{dir} + solar_{dif}}$$

The radiation absorbed by the soil after passing through through under-storey vegetation is:

$$abs_{soil} = \sum_{ft=1}^{npft} pft_{wt,1,ft,1} \left(dif_{down,nz+1} (1 - salb_{dif}) + solar_{dir} dir_{tr,nz+1}(1 - salb_{dir}) \right)$$

to which is added the diffuse flux coming directly from the upper canopy and hitting no understorey vegetation.

$$abs_{soil} = abs_{soil} + dif_{dn,2,1} (1 - \sum_{ft=1}^{npft} pft_{wt,1,ft,1})(1 - salb_{dif})$$

and the direct flux coming directly from the upper canopy and hitting no understorey vegetation.

$$abs_{soil} = abs_{soil} + solar_{dir} dir_{tr,2,1} (1 - \sum_{ft=1}^{npft} pft_{wt,1,ft,1})(1 - salb_{dir})$$

These changes to the radiation code are designed to be structurally flexible, and the scheme may be collapsed down to only include on canopy layer, functional type and pft for testing if necessary.

Table 29.6: Parameters needed for radiation transfer model.

Parameter Symbol	Parameter Name	Units	indexed by
χ	Leaf angle distribution parameter	none	ft
ρ_l	Fraction of light reflected by leaf surface	none	ft
τ_l	Fraction of light transmitted by leaf surface	none	ft
alb_s	Fraction of light reflected by soil	none	direct vs diffuse

29.7 Photosynthesis

29.7.1 Fundamental photosynthetic physiology theory

In this section we describe the physiological basis of the photosynthesis model before describing its application to the FATES canopy structure. This description in this section is largely repeated from the Oleson et al. CLM4.5 technical note but included here for comparison with its implementation in FATES. Photosynthesis in C3 plants is based on the model of *Farquhar 1980* as modified by *Collatz et al. (1991)*. Photosynthetic assimilation in C4 plants is based on the model of *Collatz et al. (1991)*. In both models, leaf photosynthesis, gpp (μmol CO_2 m^{-2} s^{-1}) is calculated as the minimum of three potentially limiting fluxes, described below:

$$\text{gpp} = \min(w_j, w_c, w_p).$$

The RuBP carboxylase (Rubisco) limited rate of carboxylation w_c (μmol CO_2 m^{-2} s^{-1}) is determined as

$$w_c = \begin{cases} \frac{V_{c,max}(c_i - \Gamma_*)}{ci + K_c(1 + o_i/K_o)} & \text{for } C_3 \text{ plants} \\ \\ V_{c,max} & \text{for } C_4 \text{ plants} \end{cases} \qquad c_i - \Gamma_* \geq 0$$

where c_i is the internal leaf CO_2 partial pressure (Pa) and $o_i(0.209P_{atm})$ is the O_2 partial pressure (Pa). K_c and K_o are the Michaelis-Menten constants (Pa) for CO_2 and O_2. These vary with vegetation temperature T_v (^{o}C) according to an Arrhenious function described in *Oleson et al. 2013*. $V_{c,max}$ is the leaf layer photosynthetic capacity (μ mol CO_2 m^{-2} s^{-1}).

The maximum rate of carboxylation allowed by the capacity to regenerate RuBP (i.e., the light-limited rate) w_j (μmol CO_2 m^{-2} s^{-1}) is

$$w_j = \begin{cases} \frac{J(c_i - \Gamma_*)}{4ci + 8\Gamma_*} & \text{for C}_3 \text{ plants} \\ \\ 4.6\phi\alpha & \text{for C}_4 \text{ plants} \end{cases} \qquad c_i - \Gamma_* \geq 0$$

To find J, the electron transport rate (μ mol CO_2 m^{-2} s^{-1}), we solve the following quadratic term and take its smaller root,

$$\Theta_{psII}J^2 - (I_{psII} + J_{max})J + I_{psII}J_{max} = 0$$

where J_{max} is the maximum potential rate of electron transport (μmol m^{-2} s^{-1}), I_{PSII} is the is the light utilized in electron transport by photosystem II (μmol m^{-2} s^{-1}) and Θ_{PSII} is is curvature parameter. I_{PSII} is determined as

$$I_{PSII} = 0.5\Phi_{PSII}(4.6\phi)$$

where ϕ is the absorbed photosynthetically active radiation (Wm:math:^{-2}) for either sunlit or shaded leaves (abs_{sun} and abs_{sha}). ϕ is converted to photosynthetic photon flux assuming 4.6 μmol photons per joule. Parameter values are $\Phi_{PSII} = 0.7$ for C3 and $\Phi_{PSII} = 0.85$ for C4 plants.

The export limited rate of carboxylation for C3 plants and the PEP carboxylase limited rate of carboxylation for C4 plants w_e (also in μmol CO_2 m^{-2} s^{-1}) is

$$w_e = \begin{cases} 3T_{p,0} & \text{for } C_3 \text{ plants} \\ \\ k_p \frac{c_i}{P_{atm}} & \text{for } C_4 \text{ plants.} \end{cases}$$

T_p is the triose-phosphate limited rate of photosynthesis, which is equal to $0.167V_{c,max0}$. k_p is the initial slope of C4 CO_2 response curve. The Michaelis-Menten constants K_c and K_o are modeled as follows,

$$K_c = K_{c,25}(a_{kc})^{\frac{T_v - 25}{10}},$$

$$K_o = K_{o,25}(a_{ko})^{\frac{T_v - 25}{10}},$$

where $K_{c,25}$ = 30.0 and $K_{o,25}$ = 30000.0 are values (Pa) at 25 ^oC, and a_{kc} = 2.1 and a_{ko} =1.2 are the relative changes in $K_{c,25}$ and $K_{o,25}$ respectively, for a 10°C change in temperature. The CO_2 compensation point Γ_* (Pa) is

$$\Gamma_* = \frac{1}{2}\frac{K_c}{K_o}0.21o_i$$

where the term 0.21 represents the ratio of maximum rates of oxygenation to carboxylation, which is virtually constant with temperature *Farquhar, 1980*.

29.7.2 Resolution of the photosynthesis theory within the FATES canopy structure.

The photosynthesis scheme is modified from the CLM4.5 model to give estimates of photosynthesis, respiration and stomatal conductance for a three dimenstional matrix indexed by canopy level (C_l), plant functional type (ft) and leaf layer (z). We conduct the photosynthesis calculations at each layer for both sunlit and shaded leaves. Thus, the model also generates estimates of w_c, w_j and w_e indexed in the same three dimensional matrix. In this implementation, some properties (stomatal conductance parameters, top-of-canopy photosynthetic capacity) vary with plant functional type, and some vary with both functional type and canopy depth (absorbed photosynthetically active radiation, nitrogen-based variation in photosynthetic properties). The remaining drivers of photosynthesis (P_{atm}, K_c, o_i, K_o, temperature, atmospheric CO_2) remain the same throughout the canopy. The rate of gross photosynthesis ($gpp_{Cl,ft,z}$)is the smoothed minimum of the three potentially limiting processes (carboxylation, electron transport, export limitation), but calculated independently for each leaf layer:

$$\text{gpp}_{Cl,ft,z} = \min(\text{w}_{c,Cl,ft,z}, \text{w}_{j,Cl,ft,z}, \text{w}_{e,Cl,ft,z}).$$

For $w_{c,Cl,ft,z}$,, we use

$$w_{c,Cl,ft,z} = \begin{cases} \frac{V_{c,max,Cl,ft,z}(c_{i,Cl,ft,z}-\Gamma_*)}{c_{i,Cl,ft,z}+K_c(1+o_i/K_o)} & \text{for } C_3 \text{ plants} \\ \\ V_{c,max,Cl,ft,z} & \text{for } C_4 \text{ plants} \end{cases} \quad c_{i,Cl,ft,z} - \Gamma_* \geq 0$$

where $V_{c,max}$ now varies with PFT, canopy depth and layer (see below). Internal leaf CO_2 ($c_{i,Cl,ft,z}$) is tracked seperately for each leaf layer. For the light limited rate w_j, we use

$$w_j = \begin{cases} \frac{J(c_i-\Gamma_*)4.6\phi\alpha}{4ci+8\Gamma_*} & \text{for } C_3 \text{ plants} \\ \\ 4.6\phi\alpha & \text{for } C_4 \text{ plants} \end{cases}$$

where J is calculated as above but based on the absorbed photosynthetically active radiation($\phi_{Cl,ft,z}$) for either sunlit or shaded leaves in Wm^{-2}. Specifically,

$$\phi_{Cl,ft,z} = \begin{cases} abs_{sun,Cl,ft,z} & \text{for sunlit leaves} \\ \\ abs_{sha,Cl,ft,z} & \text{for shaded leaves} \end{cases}$$

The export limited rate of carboxylation for C3 plants and the PEP carboxylase limited rate of carboxylation for C4 plants w_c (also in μmol CO_2 m^{-2} s^{-1}) is calculated in a similar fashion,

$$w_{e,Cl,ft,z} = \begin{cases} 0.5 V_{c,max,Cl,ft,z} & \text{for } C_3 \text{ plants} \\ 4000 V_{c,max,Cl,ft,z} \frac{c_{i,Cl,ft,z}}{P_{atm}} & \text{for } C_4 \text{ plants.} \end{cases}$$

29.7.3 Variation in plant physiology with canopy depth

Both $V_{c,max}$ and J_{max} vary with vertical depth in the canopy on account of the well-documented reduction in canopy nitrogen through the leaf profile, see *Bonan et al. 2012* for details). Thus, both $V_{c,max}$ and J_{max} are indexed by by C_l, ft and z according to the nitrogen decay coefficient K_n and the amount of vegetation area shading each leaf layer V_{above},

$$\begin{aligned} V_{c,max,Cl,ft,z} &= V_{c,max0,ft} e^{-K_{n,ft} V_{above,Cl,ft,z}}, \\ J_{max,Cl,ft,z} &= J_{max0,ft} e^{-K_{n,ft} V_{above,Cl,ft,z}}, \end{aligned}$$

where $V_{c,max,0}$ and $J_{max,0}$ are the top-of-canopy photosynthetic rates. V_{above} is the sum of exposed leaf area index (elai$_{Cl,ft,z}$) and the exposed stem area index (esai$_{Cl,ft,z}$)(m^2 m^{-2}). Namely,

$$V_{Cl,ft,z} = \text{elai}_{Cl,ft,z} + \text{esai}_{Cl,ft,z}.$$

The vegetation index shading a particular leaf layer in the top canopy layer is equal to

$$V_{above,Cl,ft,z} = \sum_1^z V_{Cl,ft,z} \quad \text{for } Cl = 1.$$

For lower canopy layers, the weighted average vegetation index of the canopy layer above (V_{canopy}) is added to this within-canopy shading. Thus,

$$V_{above,Cl,ft,z} = \sum_1^z V_{Cl,ft,z} + V_{canopy,Cl-1} \quad \text{for } Cl > 1,$$

where V_{canopy} is calculated as

$$V_{canopy,Cl} = \sum_{ft=1}^{npft} \sum_{z=1}^{nz(ft)} \left(V_{Cl,ft,z} \cdot pft_{wt,Cl,ft,1} \right).$$

K_n is the coefficient of nitrogen decay with canopy depth. The value of this parameter is taken from the work of *Lloyd et al. 2010* who determined, from 204 vertical profiles of leaf traits, that the decay rate of N through canopies of tropical rainforests was a function of the V_{cmax} at the top of the canopy. They obtain the following term to predict K_n,

$$K_{n,ft} = e^{0.00963 V_{c,max0,ft} - 2.43},$$

where V_{cmax} is again in μmol CO_2 m^{-2} s^{-1}.

29.7.4 Water Stress on gas exchange

The top of canopy leaf photosynthetic capacity, $V_{c,max0}$, is also adjusted for the availability of water to plants as

$$V_{c,max0,25} = V_{c,max0,25} \beta_{sw},$$

where the adjusting factor β_{sw} ranges from one when the soil is wet to zero when the soil is dry. It depends on the soil water potential of each soil layer, the root distribution of the plant functional type, and a plant-dependent response to soil water stress,

$$\beta_{sw} = \sum_{j=1}^{nj} w_j r_j,$$

where w_j is a plant wilting factor for layer j and r_j is the fraction of roots in layer j. The plant wilting factor w_j is

$$w_j = \begin{cases} \frac{\psi_c - \psi_j}{\psi_c - \psi_o}\left(\frac{\theta_{sat,j} - \theta_{ice,j}}{\theta_{sat,j}}\right) & \text{for } T_i > \text{-2C} \\ 0 & \text{for } T_j \geq \text{-2C} \end{cases}$$

where ψ_i is the soil water matric potential (mm) and ψ_c and ψ_o are the soil water potential (mm) when stomata are fully closed or fully open, respectively. The term in brackets scales w_i the ratio of the effective porosity (after accounting for the ice fraction) relative to the total porosity. $w_i = 0$ when the temperature of the soil layer (T_i) is below some threshold (-2:math:`^{o}`C) or when there is no liquid water in the soil layer ($\theta_{liq,i} \leq 0$). For more details on the calculation of soil matric potential, see the CLM4.5 technical note.

Variation of water stress and water uptake within tiles

The remaining drivers of the photosynthesis model remain constant (atmospheric CO_2 and O^2 and canopy temperature) throughout the canopy, except for the water stress index β_{sw}. β_{sw} must be indexed by ft, because plants of differing functional types have the capacity to have varying root depth, and thus access different soil moisture profile and experience differing stress functions. Thus, the water stress function applied to gas exchange calculation is now calculated as

$$\beta_{sw,ft} = \sum_{j=1}^{nj} w_{j,ft} r_{j,ft},$$

where w_j is the water stress at each soil layer j and $r_{j,ft}$ is the root fraction of each PFT's root mass in layer j. Note that this alteration of the β_{sw} parameter also necessitates recalculation of the vertical water extraction profiles. In the original model, the fraction of extraction from each layer ($r_{e,j,patch}$) is the product of a single root distribution, because each patch only has one plant functional type. In FATES, we need to calculate a new weighted patch effective rooting depth profile $r_{e,j,patch}$ as the weighted average of the functional-type level stress functions and their relative contributions to canopy conductance. Thus for each layer j, the extraction fraction is summed over all PFTs as

$$r_{e,j,patch} = \sum_{ft=1}^{ft=npft} \frac{w_{j,ft}}{\sum_{j=1}^{=nj} w_{j,ft}} \frac{G_{s,ft}}{G_{s,canopy}},$$

where nj is the number of soil layers, $G_{s,canopy}$ is the total canopy (see section 9 for details) and $G_{s,ft}$ is the canopy conductance for plant functional type ft,

$$G_{s,ft} = \sum_1 w_{ncoh,ft} gs_{can,coh} n_{coh}.$$

29.7.5 Aggregation of assimilated carbon into cohorts

The derivation of photosynthetic rates per leaf layer, as above, give us the estimated rate of assimilation for a unit area of leaf at a given point in the canopy in μmol CO_2 m^{-2} s$_{-1}$. To allow the integration of these rates into fluxes per individual tree, or cohort of trees (gCO:math:`_2` tree^{-1} s^{-1}), they must be multiplied by the amount of leaf area placed in each layer by each cohort. Each cohort is described by a single functional type, ft and canopy layer C_l flag, so the problem is constrained to integrating these fluxes through the vertical profile (z).

We fist make a weighted average of photosynthesis rates from sun (gpp$_{sun}$, μmol CO_2 m^{-2} s^{-1}) and shade leaves (gpp$_{shade}$, μmol CO_2 m^{-2} s^{-1}) as

$$\text{gpp}_{Cl,ft,z} = \text{gpp}_{sun,Cl,ft,z} f_{sun,Cl,ft,z} + \text{gpp}_{sha,Cl,ft,z}(1 - f_{sun,Cl,ft,z}).$$

The assimilation per leaf layer is then accumulated across all the leaf layers in a given cohort (*coh*) to give the cohort-specific gross primary productivity (GPP_{coh}),

$$GPP_{coh} = 12 \times 10^{-9} \sum_{z=1}^{nz(coh)} gpp_{Cl,ft,z} A_{crown,coh} \text{elai}_{Cl,ft,z}$$

The $\text{elai}_{l,Cl,ft,z}$ is the exposed leaf area which is present in each leaf layer in $m^2\ m^{-2}$. (For all the leaf layers that are completely occupied by a cohort, this is the same as the leaf fraction of δ_{vai}). The fluxes are converted from μmol into mol and then multiplied by 12 (the molecular weight of carbon) to give units for GPP_{coh} of KgC cohort^{-1} s^{-1}. These are integrated for each timestep to give KgC cohort^{-1} day^{-1}

Table 29.7: Parameters needed for photosynthesis model.

Parameter Symbol	Parameter Name	Units	indexed by
$V_{c,max0}$	Maximum carboxylation capacity	μ mol CO$_2$ m^{-2} s^{-1}	ft
r_b	Base Rate of Respiration	gC gN^{-1}s^{-1})	
q_{10}	Temp. Response of stem and root respiration		
$R_{cn,leaf,ft}$	CN ratio of leaf matter	gC/gN	ft
$R_{cn,root,ft}$	CN ratio of root matter	gC/gN	ft
f_{gr}	Growth Respiration Fraction	none	
ψ_c	Water content when stomata close	Pa	ft
ψ_o	Water content above which stomata are open	Pa	ft

29.8 Plant respiration

Plant respiration per individual $R_{plant,coh}$ (KgC individual $^{-1}$ s^{-1}) is the sum of two terms, growth and maintenance respiration $R_{g,coh}$ and $R_{m,coh}$

$$R_{plant} = R_{g,coh} + R_{m,coh}$$

Maintenance respiration is the sum of the respiration terms from four different plant tissues, leaf, $R_{m,leaf,coh}$, fine root $R_{m,froot,coh}$, coarse root $R_{m,croot,coh}$ and stem $R_{m,stem,coh}$, all also in (KgC individual $^{-1}$ s^{-1}) .

$$R_{m,coh} = R_{m,leaf,coh} + R_{m,froot,coh} + R_{m,croot,coh} + R_{m,stem,coh}$$

To calculate canopy leaf respiration, which varies through we canopy, we first determine the top-of-canopy leaf respiration rate ($r_{m,leaf,ft,0}$, gC s^{-1} m^{-2}) is calculated from a base rate of respiration per unit leaf nitrogen derived from *Ryan et al. 1991*. The base rate for leaf respiration (r_b) is 2.525 gC/gN s^{-1},

$$r_{m,leaf,ft,0} = r_b N_{a,ft} (1.5^{(25-20)/10})$$

where r_b is the base rate of metabolism (2.525 x 10^6 gC/gN s^{-1}. This base rate is adjusted assuming a Q$_{10}$ of 1.5 to scale from the baseline of 20C to the CLM default base rate temperature of 25C. For use in the calculations of net photosynthesis and stomatal conductance, leaf respiration is converted from gC s^{-1} m^{-2}, into μmol CO$_2$ m^{-2} s^{-1} (/$12 \cdot 10^{-6}$).

This top-of-canopy flux is scaled to account for variation in N_a through the vertical canopy, in the same manner as the $V_{c,max}$ values are scaled using V_{above}.

$$r_{leaf,Cl,ft,z} = r_{m,leaf,ft,0} e^{-K_{n,ft} V_{above,Cl,ft,z}} \beta_{ft} f(t)$$

Leaf respiration is also adjusted such that it is reduced by drought stress, β_{ft}, and canopy temperature, $f(t_{veg})$. For details of the temperature functions affecting leaf respiration see the CLM4 technical note, Section 8, Equations 8.13 and 8.14. The adjusted leaf level fluxes are scaled to individual-level (gC individual $^{-1}$ s^{-1}) in the same fashion as the GPP_{coh} calculations

$$\text{R}_{\text{m,leaf,coh}} = 12 \times 10^{-9} \sum_{z=1}^{\text{nz(coh)}} \text{r}_{\text{leaf,Cl,ft,z}} \text{A}_{\text{crown}} \text{elai}_{\text{Cl,ft,z}}$$

The stem and the coarse-root respiration terms are derived using the same base rate of respiration per unit of tissue Nitrogen.

$$R_{m,croot,coh} = 10^{-3} r_b t_c \beta_{ft} N_{\text{livecroot,coh}}$$

$$R_{m,stem,coh} = 10^{-3} r_b t_c \beta_{ft} N_{\text{stem,coh}}$$

Here, t_c is a temperature relationship based on a q_{10} value of 1.5, where t_v is the vegetation temperature. We use a base rate of 20 here as, again, this is the baseline temperature used by *Ryan et al. 1991*. The 10^{-3} converts from gC invididual^{-1} s^{-1} to KgC invididual^{-1} s^{-1}

$$t_c = q_{10}^{(t_v - 20)/10}$$

The tissue N contents for live sapwood are derived from the leaf CN ratios, and for fine roots from the root CN ratio as:

$$N_{\text{stem,coh}} = \frac{B_{\text{sapwood,coh}}}{R_{cn,leaf,ft}}$$

and

$$N_{\text{livecroot,coh}} = \frac{B_{\text{root,coh}} w_{frac,ft}}{R_{cn,root,ft}}$$

where $B_{\text{sapwood,coh}}$ and $B_{\text{root,coh}}$ are the biomass pools of sapwood and live root biomass respectively (KgC individual) and $w_{frac,ft}$ is the fraction of coarse root tissue in the root pool (0.5 for woody plants, 0.0 for grasses and crops). We assume here that stem CN ratio is the same as the leaf C:N ratio, for simplicity. The final maintenance respiration term is derived from the fine root respiration, which accounts for gradients of temperature in the soil profile and thus calculated for each soil layer j as follows:

$$R_{m,froot,j} = \frac{(1 - w_{frac,ft}) B_{\text{root,coh}} b_r \beta_{ft}}{10^3 R_{cn,leaf,ft}} \sum_{j=1}^{nj} t_{c,soi,j} r_{i,ft,j}$$

$t_{c,soi}$ is a function of soil temperature in layer j that has the same form as that for stem respiration, but uses vertically resolved soil temperature instead of canopy temperature. In the CLM4.5, only coarse and not fine root respriation varies as a function of soil depth, and we maintain this assumption here, although it may be altered in later versions. The growth respiration, $R_{g,coh}$ is a fixed fraction f_{gr} of the carbon remaining after maintenance respiration has occurred.

$$R_{g,coh} = \max(0, GPP_{g,coh} - R_{\text{m,coh}}) \text{f}_{\text{gr}}$$

Table 29.8: Parameters needed for plant respiration model.

Parameter Symbol	Parameter Name	Units	indexed by
$-K_{n,ft}$	Rate of reduction of N through the canopy	none	•
r_b	Base Rate of Respiration	gC gN^{-1}s^{-1})	
q_{10}	Temp. Response of stem and root respiration		
$R_{cn,leaf,ft}$	CN ratio of leaf matter	gC/gN	ft
$R_{cn,root,ft}$	CN ratio of root matter	gC/gN	ft
f_{gr}	Growth Respiration Fraction	none	

29.9 Stomatal Conductance

29.9.1 Fundamental stomatal conductance theory

Stomatal conductance is unchanged in concept from the CLM4.5 approach. Leaf stomatal resistance is calculated from the Ball-Berry conductance model as described by *Collatz et al. (1991)* and implemented in a global climate model by *Sellers et al. 1996*. The model relates stomatal conductance (i.e., the inverse of resistance) to net leaf photosynthesis, scaled by the relative humidity at the leaf surface and the CO_2 concentration at the leaf surface. The primary difference between the CLM implementation and that used by *Collatz et al. (1991)* and *Sellers et al. (1996)* is that they used net photosynthesis (i.e., leaf photosynthesis minus leaf respiration) instead of gross photosynthesis. As implemented here, stomatal conductance equals the minimum conductance (b) when gross photosynthesis (A) is zero. Leaf stomatal resistance is

$$\frac{1}{r_s} = m_{ft}\frac{A}{c_s}\frac{e_s}{e_i}P_{atm} + b_{ft}\beta_{sw}$$

where r_s is leaf stomatal resistance (s m^2 μmol^{-1}), b_{ft} is a plant functional type dependent parameter equivalent to g_0 in the Ball-Berry model literature. This parameter is also scaled by the water stress index β_{sw}. Similarly, m_{ft} is the slope of the relationship between the assimilation, c_s and humidty dependant term and the stomatal conductance, and so is equivalent to the g_1 term in the stomatal literature. A is leaf photosynthesis (μmol CO_2 m^{-2} s^{-1}), c_s is the CO_2 partial pressure at the leaf surface (Pa), e_s is the vapor pressure at the leaf surface (Pa), e_i is the saturation vapor pressure (Pa) inside the leaf at the vegetation temperature conductance (μmol m^{-2} s^{-1}) when $A = 0$. Typical values are $m_{ft} = 9$ for C$_3$ plants and $m_{ft} = 4$ for C$_4$ plants (*Collatz et al. 1991*, *Collatz, 1992*, *Sellers et al 1996*). *Sellers et al. 1996* used $b = 10000$ for C$_3$ plants and $b = 40000$ for C$_4$ plants. Here, b was chosen to give a maximum stomatal resistance of 20000 s m^{-1}. These terms are nevertheless plant strategy dependent, and have been found to vary widely with plant type *Medlyn et al. 2011*.

Resistance is converted from units of s m$^2\mu$ mol^{-1} to s m^{-1} as: 1 s m^{-1} = 1×10^{-9}R$_{gas}\theta_{atm}P_{atm}$ (μmol^{-1} m^2 s), where R$_{gas}$ is the universal gas constant (J K^{-1} kmol^{-1}) and θ_{atm} is the atmospheric potential temperature (K).

29.9.2 Resolution of stomatal conductance theory in the FATES canopy structure

The stomatal conductance is calculated, as with photosynthesis, for each canopy, PFT and leaf layer. The CLM code requires a single canopy conductance estimate to be generated from the multi-layer multi-PFT array. In previous iterations of the CLM, sun and shade-leaf specific values have been reported and then averaged by their respective leaf areas. In this version, the total canopy condutance $G_{s,canopy}$, is calculated as the sum of the cohort-level conductance values.

$$G_{s,canopy} = \sum \frac{gs_{can,coh}n_{coh}}{A_{patch}}$$

Cohort conductance is the sum of the inverse of the leaf resistances at each canopy layer ($r_{s,z}$) multipled by the area of each cohort.

$$gs_{can,coh} = \sum_{z=1}^{z=nv,coh} \frac{A_{crown,coh}}{r_{s,cl,ft,z} + r_b}$$

Table 29.9: Parameters needed for stomatal conductance model.

Parameter Symbol	Parameter Name	Units	indexed by
b_{ft}	Slope of Ball-Berry term	none	ft
m_{ft}	Slope of Ball-Berry term	none	ft

29.10 Allocation and Growth

Total assimilation carbon enters the ED model each day as a cohort-specific Net Primary Productivity NPP_{coh}, which is calculated as

$$NPP_{coh} = GPP_{coh} - R_{plant,coh}$$

This flux of carbon is allocated between the demands of tissue turnover, of carbohydrate storage and of growth (increase in size of one or many plant organs). Priority is explicitly given to maintenance respiration, followed by tissue maintenance and storage, then allocation to live biomass and then to the expansion of structural and live biomass pools. All fluxes here are first converted into in KgC individual^{-1} year^{-1} and ultimately integrated using a timesteps of 1/365 years for each day.

29.10.1 Tissue maintenance demand

We calculate a 'tissue maintenance' flux. The magnitude of this flux is such that the quantity of biomass in each pool will remain constant, given background turnover rates. For roots, this maintenenace demand is simply

$$r_{md,coh} = b_{root} \cdot \alpha_{root,ft}$$

Where $\alpha_{root,ft}$ is the root turnover rate in y^-1. Given that, for deciduous trees, loss of leaves is assumed to happen only one per growing season, the algorithm is dependent on phenological habit (whether or not this PFT is evergreen), thus

$$l_{md,coh} = \begin{cases} b_{leaf} \cdot \alpha_{leaf,ft} & \text{for } P_{evergreen} = 1 \\ \\ 0 & \text{for } P_{evergreen} = 0 \end{cases}$$

Leaf litter resulting from deciduous senescence is handled in the phenology section. The total quantity of maintenance demand ($t_{md,coh}$. KgC individual y^{-1}) is therefore

$$t_{md,coh} = l_{md,coh} + r_{md,coh}$$

29.10.2 Allocation to storage and turnover

The model must now determine whether the NPP input is sufficient to meet the maintenance demand and keep tissue levels constant. To determine this, we introduce the idea of 'carbon balance' $C_{bal,coh}$ (KgC individual^{-1}) where

$$C_{bal,coh} = NPP_{coh} - t_{md,coh} \cdot f_{md,min,ft}$$

where $f_{md,min,ft}$ is the minimum fraction of the maintenance demand that the plant must meet each timestep, which is indexed by *ft* and represents a life-history-strategy decision concerning whether leaves should remain on in the case of low carbon uptake (a risky strategy) or not be replaced (a conservative strategy). Subsequently, we determine a flux to the storage pool, where the flux into the pool, as a fraction of $C_{bal,coh}$, is proportional to the discrepancy between the target pool size and the actual pool size f_{tstore} where

$$f_{tstore} = \max\left(0, \frac{b_{store}}{b_{leaf} \cdot S_{cushion}}\right)$$

The allocation to storage is a fourth power function of f_{tstore} to mimic the qualitative behaviour found for carbon allocation in arabidopsis by *Smith et al. 2007*.

$$\frac{\delta b_{store}}{\delta t} = \begin{cases} C_{bal,coh} \cdot e^{-f_{tstore}^4} & \text{for } C_{bal,coh} > 0 \\ \\ C_{bal,coh} & \text{for } C_{bal,coh} \le 0 \end{cases}$$

If the carbon remaining after the storage and minimum turnover fluxes have been met, the next priority is the remaining flux to leaves $t_{md} \cdot (1 - f_{md,min})$. If the quantity of carbon left $(C_{bal,coh} - \frac{\delta b_{store}}{\delta t})$ is insufficient to supply this amount of carbon, then the store of alive carbon is depleted (to represent those leaves that have fallen off and not been replaced)

$$\frac{\delta b_{alive}}{\delta t} = \begin{cases} 0 & \text{for } (C_{bal,coh} - \frac{\delta b_{store}}{\delta t}) > t_{md} \cdot (1 - f_{md,min}) \\ \\ t_{md} \cdot (1 - f_{md,min}) - \left(C_{bal,coh} - \frac{\delta b_{store}}{\delta t}\right) & \text{for } (C_{bal,coh} - \frac{\delta b_{store}}{\delta t}) \le t_{md} \cdot (1 - f_{md,min}) \end{cases}$$

correspondingly, the carbon left over for growth (C_{growth}: (KgC individual^{-1} year^{-1}) is therefore

$$C_{growth} = \begin{cases} C_{bal,coh} - \frac{\delta b_{store}}{\delta t} & \text{for } (C_{bal,coh} - \frac{\delta b_{store}}{\delta t}) > 0 \\ \\ 0 & \text{for } (C_{bal,coh} - \frac{\delta b_{store}}{\delta t}) \le 0 \end{cases}$$

to allocate the remaining carbon (if there is any), we first ascertain whether the live biomass pool is at its target, or whether is has been depleted by previous low carbon timesteps. Thus

$$\begin{aligned} b_{alive,target} &= b_{leaf,target}(1 + f_{frla} + f_{swh}h_{coh}) && \text{for } S_{phen,coh} = 2 \\ b_{alive,target} &= b_{leaf,target}(f_{frla} + f_{swh}h_{coh}) && \text{for } S_{phen,coh} = 1 \end{aligned}$$

where the target leaf biomass $b_{leaf.target}$ ((Kg C individual^{-1})) is the allometric relationship between dbh and leaf biomass, ameliorated by the leaf trimming fraction (see 'control of leaf area' below)

$$b_{leaf.target} = c_{leaf} \cdot dbh_{coh}^{e_{leaf,dbh}} \rho_{ft}^{e_{leaf,dens}} \cdot C_{trim,coh}$$

ρ_{ft} is the wood density, in g cm^3.

29.10.3 Allocation to Seeds

The fraction remaining for growth (expansion of live and structural tissues) f_{growth} is 1 minus that allocated to seeds.

$$f_{growth,coh} = 1 - f_{seed,coh}$$

Allocation to seeds only occurs if the alive biomass is not below its target, and then is a predefined fixed fraction of the carbon remaining for growth. Allocation to clonal reproduction (primarily for grasses) occurs when max$_{dbh}$ is achieved.

$$f_{seed,coh} = \begin{cases} R_{frac,ft} & \text{for max}_{dbh} < dbh_{coh} \\ \\ (R_{frac,ft} + C_{frac,ft}) & \text{for max}_{dbh} \ge dbh_{coh} \end{cases}$$

the total amount allocated to seed production ($p_{seed,coh}$ in KgC individual $^{-1}$ y^{-1}) is thus

$$p_{seed,coh} = C_{growth} \cdot f_{seed,coh}$$

29.10.4 Allocation to growing pools

The carbon is then partitioned into carbon available to grow the b_{alive} and b_{struc} pools. A fraction v_a is available to live biomass pools, and a fraction v_s is available to structural pools.

$$\frac{\delta b_{alive}}{\delta t} = C_{growth} \cdot f_{growth} v_a$$

$$\frac{\delta b_{struc}}{\delta t} = C_{growth} \cdot f_{growth} v_s$$

If the alive biomass is lower than its ideal target, all of the available carbon is directed into that pool. Thus:

$$v_a = \begin{cases} \frac{1}{1+u} & \text{for } b_{alive} \geq b_{alive,target} \\ 1.0 & \text{for } b_{alive} < b_{alive,target} \end{cases}$$

$$v_s = \begin{cases} \frac{u}{1+u} & \text{for } b_{alive} \geq b_{alive,target} \\ 0.0 & \text{for } b_{alive} < b_{alive,target} \end{cases}$$

In this case, the division of carbon between the live and structural pools u is derived as the inverse of the sum of the rates of change in live biomass with respect to structural:

$$u = \frac{1}{\frac{\delta b_{leaf}}{\delta b_{struc}} + \frac{\delta b_{root}}{\delta b_{struc}} + \frac{\delta b_{sw}}{\delta b_{struc}}}$$

To calculate all these differentials, we first start with $\delta b_{leaf}/\delta b_{struc}$, where

$$\frac{\delta b_{leaf}}{\delta b_{struc}} = \frac{\frac{\delta \text{dbh}}{\delta b_{struc}}}{\frac{\delta \text{dbh}}{\delta b_{leaf}}}$$

The rates of change of dbh with respect to leaf and structural biomass are the differentials of the allometric equations linking these terms to each other. Hence,

$$\frac{\delta \text{dbh}}{\delta b_{leaf}} = \frac{1}{b_{trim,coh}} \cdot (e_{leaf,dbh} - 1) \exp \left(c_{leaf} \text{dbh}^{(e_{leaf,dbh})-1} \rho_{ft}^{e_{leaf,dens}} \right)$$

and where $\text{dbh}_{coh} > \text{dbh}_{max}$

$$\frac{\delta b_{struc}}{\delta \text{dbh}} = e_{str,dbh} \cdot c_{str} \cdot e_{str,hite} h_{coh}^{e_{str,dbh}-1} \text{dbh}_{coh}^{e_{str,dbh}} \rho_{ft}^{e_{str,dens}}$$

If $\text{dbh}_{coh} \leq \text{dbh}_{max}$ then we must also account for allocation for growing taller as:

$$\frac{\delta b_{struc}}{\delta \text{dbh}} = \frac{\delta b_{struc}}{\delta \text{dbh}} + \frac{\delta h}{\delta \text{dbh}} \cdot \frac{\delta b_{struc}}{\delta \text{dbh}}$$

where

$$\frac{\delta h}{\delta \text{dbh}} = 1.4976 \text{dbh}_{coh}^{m_{allom}-1}$$

$$\frac{\delta \text{dbh}}{\delta b_{struc}} = \frac{1}{\frac{\delta b_{struc}}{\delta \text{dbh}}}$$

Once we have the $\delta b_{leaf}/\delta b_{struc}$, we calculate $\delta b_{root}/\delta b_{struc}$ as

$$\frac{\delta b_{root}}{\delta b_{struc}} = \frac{\delta b_{leaf}}{\delta b_{struc}} \cdot f_{frla}$$

and the sapwood differential as

$$\frac{\delta b_{sw}}{\delta b_{struc}} = f_{swh} \left(h_{coh} \frac{\delta b_{leaf}}{\delta b_{struc}} + b_{leaf,coh} \frac{\delta h}{\delta b_{struc}} \right)$$

where

$$\frac{\delta h}{\delta b_{struc}} = \frac{1}{c_{str} \times e_{str,hite} h_{coh}^{e_{str,dbh}-1} \mathrm{dbh}_{coh}^{e_{str,dbh}} \rho_{ft}^{e_{str,dens}}}$$

In all of the above terms, height in in m, dbh is in cm, and all biomass pools are in KgCm^{-2}. The allometric terms for the growth trajectory are all taken from the ED1.0 model, but could in theory be altered to accomodate alternative allometric relationships. Critically, the non-linear relationships between live and structural biomass pools are maintained in this algorithm, which diverges from the methodology currently deployed in the CLM4.5.

29.10.5 Integration of allocated fluxes

All of the flux calculations generate differential of the biomass state variables against time (in years). To integrate these differential rates into changes in the state variables, we use a simple simple forward Euler integration. Other methods exist (e.g. ODEINT solvers, Runge Kutta methods etc.), but they are more prone to errors that become difficult to diagnose, and the typically slow rates of change of carbon pools mean that these are less important than they might be in strongly non-linear systems (soil drainage, energy balance, etc.)

$$b_{alive,t+1} = \min \left(0, b_{alive,t} + \frac{\delta b_{alive}}{\delta t} \delta t \right)$$

$$b_{struc,t+1} = \min \left(0, b_{struc,t} + \frac{\delta b_{struc}}{\delta t} \delta t \right)$$

$$b_{store,t+1} = \min \left(0, b_{store,t} + \frac{\delta b_{store}}{\delta t} \delta t \right)$$

In this case, δt is set to be one day ($\frac{1}{365}$ years).

Table 29.10: Parameters needed for allocation model.

Parameter Symbol	Parameter Name	Units	indexed by
S	Target stored biomass as fraction of b_{leaf}	none	*ft*
f	Minimum fraction of turnover that must be met	none	*ft*
R	Fraction allocated to seeds	none	*ft*
C	Fraction allocated to clonal reproduction	none	*ft*
$\max_{dbh}$	Diameter at which maximum height is achieved	m	*ft*
P	Does this cohort have an evergreen phenological habit?	1=yes, 0=no	*ft*

29.11 Control of Leaf Area Index

The leaf area A_{leaf} (m:math:^{-2}) of each cohort is calculated from leaf biomass $b_{leaf,coh}$ (kgC individual^{-1}) and specific leaf area (SLA, m^2 kg C^{-1})

$$A_{leaf,coh} = b_{leaf,coh} \cdot SLA_{ft}$$

For a given tree allometry, leaf biomass is determined from basal area using the function used by *Moorcroft et al. 2001* where d_w is wood density in g cm^{-3}.

$$b_{leaf,coh} = c_{leaf} \cdot dbh_{coh}^{e_{leaf,dbh}} \rho_{ft}^{e_{leaf,dens}}$$

However, using this model, where leaf area and crown area are both functions of diameter, the leaf area index of each tree in a closed canopy forest is always the same (where $S_{c,patch} = S_{c,min}$, irrespective of the growth conditions. To allow greater plasticity in tree canopy structure, and for tree leaf area index to adapt to prevailing conditions, we implemented a methodology for removing those leaves in the canopy that exist in negative carbon balance. That is, their total annual assimilation rate is insufficient to pay for the turnover and maintenance costs associated with their supportive root and stem tissue, plus the costs of growing the leaf. The tissue turnover maintenance cost (KgC m$^{-2}y^{-1}$ of leaf is the total maintenance demand divided by the leaf area:

$$L_{cost,coh} = \frac{t_{md,coh}}{b_{leaf,coh} \cdot \text{SLA}}$$

The net uptake for each leaf layer $U_{net,z}$ in (KgC m^{-2} year^{-1}) is

$$U_{net,coh,z} = g_{coh,z} - r_{m,leaf,coh,z}$$

where g_z is the GPP of each layer of leaves in each tree (KgC m^{-2} year^{-1}), $r_{m,leaf,z}$ is the rate of leaf dark respiration (also KgC m^{-2} year^{-1}). We use an iterative scheme to define the cohort specific canopy trimming fraction $C_{trim,coh}$, on an annual time-step, where

$$b_{leaf,coh} = C_{trim} \times 0.0419 dbh_{coh}^{1.56} d_w^{0.55}$$

If the annual maintenance cost of the bottom layer of leaves (KgC m-2 year-1) is less than then the canopy is trimmed by an increment $\iota_l(0.01)$, which is applied until the end of next calander year. Because this is an optimality model, there is an issue of the timescale over which net assimilation is evaluated, the timescale of response, and the plasticity of plants to respond to these pressures. These properties should be investigated further in future efforts.

$$C_{trim,y+1} = \begin{cases} \max(C_{trim,y} - \iota_l, 1.0) & \text{for}(L_{cost,coh} > U_{net,coh,nz}) \\ \\ \min(C_{trim,y} + \iota_l, L_{trim,min}) & \text{for}(L_{cost,coh} < U_{net,coh,nz}) \end{cases}$$

We impose an arbitrary minimum value on the scope of canopy trimming of $L_{trim,min}$ (0.5). If plants are able simply to drop all of their canopy in times of stress, with no consequences, then tree mortality from carbon starvation is much less likely to occur because of the greatly reduced maintenance and turnover requirements.

Table 29.11: Parameters needed for leaf area control model.

Parameter Symbol	Parameter Name	Units	indexed by
ι_l	Fraction by which leaf mass is reduced next year	none	•
$L_{trim,min}$	Minimum fraction to which leaf mass can be reduced	•	

29.12 Phenology

29.12.1 Cold Deciduous Phenology

Cold Leaf-out timing

The phenology model of *Botta et al. 2000* is used in FATES to determine the leaf-on timing. The Botta et al. model was verified against satellite data and is one of the only globally verified and published models of leaf-out phenology. This model differs from the phenology model in the CLM4.5. The model simulates leaf-on date as a function of the number of growing degree days (GDD), defined by the sum of mean daily temperatures (T_{day} ^oC) above a given threshold T_g (0 ^oC).

$$GDD = \sum \max(T_{day} - T_g, 0)$$

Budburst occurs when GDD exceeds a threshold (GDD_{crit}). The threshold is modulated by the number of chilling days experienced (NCD) where the mean daily temperature falls below a threshold determined by *Botta et al. 2000<botta2000>* as 5^oC. A greater number of chilling days means that fewer growing degree days are required before budburst:

$$GDD_{crit} = a + be^{c.NCD}$$

where a = -68, b= 638 and c=-0.01 *Botta et al. 2000<botta2000>*. In the Northern Hemisphere, counting of degree days begins on 1st January, and of chilling days on 1st November. The calendar opposite of these dates is used for points in the Southern Hemisphere.

If the growing degree days exceed the critical threshold, leaf-on is triggered by a change in the gridcell phenology status flag $S_{phen,grid}$ where '2' indicates that leaves should come on and '1' indicates that they should fall.

$$S_{phen,grid} = 2 \quad \text{if } S_{phen,grid} = 1 \text{ and } GDD_{grid} \geq GDD_{crit}$$

Cold Leaf-off timing

The leaf-off model is taken from the Sheffield Dynamic Vegetation Model (SDGVM) and is similar to that for LPJ *Sitch et al. 2003* and IBIS *Foley et al. 1996* models. The average daily temperatures of the previous 10 day period are stored. Senescence is triggered when the number of days with an average temperature below 7.5^o ($n_{colddays}$) rises above a threshold values $n_{crit,cold}$, set at 5 days.

$$S_{phen,grid} = 1 \quad \text{if } S_{phen,grid} = 2 \text{ and } n_{colddays} \geq n_{crit,cold}$$

Global implementation modifications

Because of the global implementation of the cold-deciduous phenology scheme, adjustments must be made to account for the possibility of cold-deciduous plants experiencing situations where no chilling period triggering leaf-off ever happens. If left unaccounted for, these leaves will last indefinitely, resulting in highly unrealistic behaviour. Therefore, we implement two additional rules. Firstly, if the number of days since the last senescence event was triggered is larger than 364, then leaf-off is triggered on that day. Secondly, if no chilling days have occured during the winter accumulation period, then leaf-on is not triggered. This means that in effect, where there are no cold periods, leaves will fall off and not come back on, meaning that cold-deciduous plants can only grow in places where there is a cold season.

Further to this rule, we introduce a 'buffer' time periods after leaf-on of 30 days, so that cold-snap periods in the spring cannot trigger a leaf senescence. The 30 day limit is an arbitrary limit. In addition, we constrain growing degree day accumulation to the second half of the year (Jult onwards in the Northern hemisphere, or Jan-June in the Southern) and only allow GDD accumulation while the leaves are off.

29.12.2 Drought-deciduous Phenology: TBD

In the current version of the model, a drought deciduous algorithm exists, but is not yet operational, due to issue detected in the existing CN and soil moisture modules, which also affect the behaviour of the native ED drought deciduous model. This is a priority to address before the science tag is released.

29.12.3 Carbon Dynamics of deciduous plants

In the present version, leaf expansion and senescence happen over the course of a single day. This is clearly not an empirically robust representation of leaf behaviour, whereby leaf expansion occurs over a period of 10-14 days, and senescence over a similar period. This will be incorporated in later versions. When the cold or drought phenological status of the gridcell status changes ($S_{phen,grid}$) from '2' to '1', and the leaves are still on ($S_{phen,coh}$ =2), the leaf biomass at this timestep is 'remembered' by the model state variable $l_{memory,coh}$. This provides a 'target' biomass for leaf onset at the beginning of the next growing season (it is a target, since depletion of stored carbon in the off season may render achieving the target impossible).

$$l_{memory,coh} = b_{leaf,coh}$$

Leaf carbon is then added to the leaf litter flux $l_{leaf,coh}$ (KgC individual^{-1})

$$l_{leaf,coh} = b_{leaf,coh}$$

The alive biomass is depleted by the quantity of leaf mass lost, and the leaf biomass is set to zero

$$b_{alive,coh} = b_{alive,coh} - b_{leaf,coh}$$

$$b_{leaf,coh} = 0$$

Finally, the status $S_{phen,coh}$ is set to 1, indicating that the leaves have fallen off.

For bud burst, or leaf-on, the same occurs in reverse. If the leaves are off ($S_{phen,coh}$=1) and the phenological status triggers budburst ($S_{phen,grid}$=2) then the leaf mass is set the maximum of the leaf memory and the available store

$$b_{leaf,coh} = \max \left(l_{memory,coh}, b_{store,coh} \right)$$

this amount of carbon is removed from the store

$$b_{store,coh} = b_{store,coh} - b_{leaf,coh}$$

and the new leaf biomass is added to the alive pool

$$b_{alive,coh} = b_{alive,coh} + b_{leaf,coh}$$

Lastly, the leaf memory variable is set to zero and the phenological status of the cohort back to '2'. No parameters are currently required for this carbon accounting scheme.

Table 29.12: Parameters needed for phenology model.

Parameter Symbol	Parameter Name	Units	indexed by
$n_{crit,cold}$	Threshold of cold days for senescence	none	•
T_g	Threshold for counting growing degree days	^oC	

29.13 Seed Dynamics and Recruitment

The production of seeds and their subsequent germination is a process that must be captured explicitly or implicitly in vegetation models. FATES contains a seed bank model designed to allow the dynamics of seed production and germination to be simulated independently. In the ED1.0 model, seed recruitment occurs in the same timestep as allocation to seeds, which prohibits the survival of a viable seed bank through a period of disturbance or low productivity (winter, drought). In FATES, a plant functional type specific seed bank is tracked in each patch ($Seeds_{patch}$ KgC m^{-2}), whose rate of change (KgC m^{-2} y^{-1}) is the balance of inputs, germination and decay:

$$\frac{\delta Seeds_{FT}}{\delta t} = Seed_{in,ft} - Seed_{germ,ft} - Seed_{decay,ft}$$

where $Seed_{in}$, $Seed_{germ}$ and $Seed_{decay}$ are the production, germination and decay (or onset of inviability) of seeds, all in KgC m^{-2} year^{-1}.

Seeds are assumed to be distributed evenly across the site (in this version of the model), so the total input to the seed pool is therefore the sum of all of the reproductive output of all the cohorts in each patch of the correct PFT type.

$$Seed_{in,ft} = \frac{\sum_{p=1}^{n_{patch}} \sum_{i=1}^{n_{coh}} p_{seed,i}.n_{coh}}{area_{site}}$$

Seed decay is the sum of all the processes that reduce the number of seeds, taken from *Lischke et al. 2006*. Firstly, the rate at which seeds become inviable is described as a constant rate ϕ (y:math:^{-1}) which is set to 0.51, the mean of the parameters used by *Lischke et al. 2006*.

$$Seed_{decay,ft} = Seeds_{FT}.\phi$$

The seed germination flux is also prescribed as a fraction of the existing pool (α_{sgerm}), but with a cap on maximum germination rate β_{sgerm}, to prevent excessive dominance of one plant functional type over the seed pool.

$$Seed_{germ,ft} = \max(Seeds_{FT} \cdot \alpha_{sgerm}, \beta_{sgerm})$$

Table 29.13: Parameters needed for seed model.

Parameter Symbol	Parameter Name	Units	indexed by
K_s	Maximum seed mass	kgC m^{-2}	
α_{sgerm}	Proportional germination rate	•	
β_{sgerm}	Maximum germination rate	KgC m^{-2} y^{-1}	
ϕ	Decay rate of viable seeds	none	FT
$R_{frac,ft}$	Fraction of C_{bal} devoted to reproduction	none	FT

29.14 Litter Production and Fragmentation

The original CLM4.5 model contains streams of carbon pertaining to different chemical properties of litter (lignin, cellulose and labile streams, specifically). In FATES model, the fire simulation scheme in the SPITFIRE model requires that the model tracks the pools of litter pools that differ with respect to their propensity to burn (surface

area-volume ratio, bulk density etc.). Therefore, this model contains more complexity in the representation of coarse woody debris. We also introduce the concept of 'fragmenting' pools, which are pools that can be burned, but are not available for decomposition or respiration. In this way, we can both maintain above-ground pools that affect the rate of burning, and the lag between tree mortality and availability of woody material for decomposition.

FATES recognizes four classes of litter. Above- and below-ground coarse woody debris (CWD_{AG}, CWD_{BG}) and leaf litter (l_{leaf} and fine root litter l_{root}). All pools are represented per patch, and with units of kGC m^{-}2. Further to this, CWD_{AG}, CWD_{BG} are split into four litter size classes (lsc) for the purposes of proscribing this to the SPITFIRE fire model (seed 'Fuel Load' section for more detail. 1-hour (twigs), 10-hour (small branches), 100-hour (large branches) and 1000-hour(boles or trunks). 4.5 %, 7.5%, 21 % and 67% of the woody biomass ($b_{store,coh} + b_{sw,coh}$) is partitioned into each class, respectively.

l_{leaf} and l_{root} are indexed by plant functional type (ft). The rational for indexing leaf and fine root by PFT is that leaf and fine root matter typically vary in their carbon:nitrogen ratio, whereas woody pools typically do not.

Rates of change of litter, all in kGC m^{-}2 year^{-1}, are calculated as

$$\frac{\delta CWD_{AG,out,lsc}}{\delta t} = CWD_{AG,in,lsc} - CWD_{AG,out,lsc}$$

$$\frac{\delta CWD_{BG,out,lsc}}{\delta t} = CWD_{BG,in,lsc} - CWD_{BG,in,lsc}$$

$$\frac{\delta l_{leaf,out,ft}}{\delta t} = l_{leaf,in,ft} - l_{leaf,out,ft}$$

$$\frac{\delta l_{root,out,ft}}{\delta t} = l_{root,in,ft} - l_{root,out,ft}$$

29.14.1 Litter Inputs

Inputs into the litter pools come from tissue turnover, mortality of canopy trees, mortality of understorey trees, mortality of seeds, and leaf senescence of deciduous plants.

$$l_{leaf,in,ft} = \left(\sum_{i=1}^{n_{coh,ft}} n_{coh}(l_{md,coh} + l_{leaf,coh}) + M_{t,coh}.b_{leaf,coh} \right) / \sum_{p=1}^{n_{pat}} A_{patch}$$

where $l_{md,coh}$ is the leaf turnover rate for evergreen trees and $l_{leaf,coh}$ is the leaf loss from phenology in that timestep (KgC m^{-2}. $M_{t,coh}$ is the total mortality flux in that timestep (in individuals). For fine root input. $n_{coh,ft}$ is the number of cohorts of functional type 'FT' in the current patch.

$$l_{root,in,ft} = \left(\sum_{i=1}^{n_{coh,ft}} n_{coh}(r_{md,coh}) + M_{t,coh}.b_{root,coh} \right) / \sum_{p=1}^{n_{pat}} A_{p}$$

where $r_{md,coh}$ is the root turnover rate. For coarse woody debris input ($CWD_{AG,in,lsc}$, we first calculate the sum of the mortality $M_{t,coh}.(b_{struc,coh} + b_{sw,coh})$ and turnover $n_{coh}(w_{md,coh})$ fluxes, then separate these into size classes and above/below ground fractions using the fixed fractions assigned to each (f_{lsc} and f_{ag})

$$CWD_{AG,in,lsc} = \left(f_{lsc}.f_{ag} \sum_{i=1}^{n_{coh,ft}} n_{coh}w_{md,coh} + M_{t,coh}.(b_{struc,coh} + b_{sw,coh}) \right) / \sum_{p=1}^{n_{pat}} A_{p}$$

$$CWD_{BG,in,lsc} = \left(f_{lsc}.(1 - f_{ag}) \sum_{i=1}^{n_{coh,ft}} n_{coh}w_{md,coh} + M_{t,coh}.(b_{struc,coh} + b_{sw,coh}) \right) / \sum_{p=1}^{n_{pat}} A_{p}$$

29.14.2 Litter Outputs

The fragmenting litter pool is available for burning but not for respiration or decomposition. Fragmentation rates are calculated according to a maximum fragmentation rate ($\alpha_{cwd,lsc}$ or α_{litter}) which is ameliorated by a temperature and water dependent scalar S_{tw}. The form of the temperature scalar is taken from the existing CLM4.5BGC decomposition cascade calculations). The water scaler is equal to the water limitation on photosynthesis (since the CLM4.5BGC water scaler pertains to the water potential of individual soil layers, which it is difficult to meaningfully average, given the non-linearities in the impact of soil moisture). The scaler code is modular, and new functions may be implemented trivially. Rate constants for the decay of the litter pools are extremely uncertain in literature, as few studies either separate litter into size classes, nor examine its decomposition under non-limiting moisture and temperature conditions. Thus, these parameters should be considered as part of sensitivity analyses of the model outputs.

$$CWD_{AG,out,lsc} = CWD_{AG,lsc}.\alpha_{cwd,lsc}.S_{tw}$$

$$CWD_{BG,out,lsc} = CWD_{BG,lsc}.\alpha_{cwd,lsc}.S_{tw}$$

$$l_{leaf,out,ft} = l_{leaf,ft}.\alpha_{litter}.S_{tw}$$

$$l_{root,out,ft} = l_{root,ft}.\alpha_{root,ft}.S_{tw}$$

29.14.3 Flux into decompsition cascade

Upon fragmentation and release from the litter pool, carbon is transferred into the labile, lignin and cellulose decomposition pools. These pools are vertically resolved in the biogeochemistry model. The movement of carbon into each vertical layer is obviously different for above- and below-ground fragmenting pools. For each layer z and chemical litter type i, we derive a flux from ED into the decomposition cascade as $ED_{lit,i,z}$ (kGC m^{-2} s^{-1})

where t_c is the time conversion factor from years to seconds, $f_{lab,l}$, $f_{cel,l}$ and $f_{lig,l}$ are the fractions of labile, cellulose and lignin in leaf litter, and $f_{lab,r}$, $f_{cel,r}$ and $f_{lig,r}$ are their counterparts for root matter. Similarly, l_{prof}, $r_{f,prof}$ and $r_{c,prof}$ are the fractions of leaf, coarse root and fine root matter that are passed into each vertical soil layer z, derived from the CLM(BGC) model.

Table 29.14: Parameters needed for litter model.

Parameter Symbol	Parameter Name	Units	indexed by
$\alpha_{cwd,lsc}$	Maximum fragmentation rate of CWD	y^{-1}	
α_{litter}	Maximum fragmentation rate of leaf litter	y^{-1}	
α_{root}	Maximum fragmentation rate of fine root litter	y^{-1}	
$f_{lab,l}$	Fraction of leaf mass in labile carbon pool	none	
$f_{cel,l}$	Fraction of leaf mass in cellulose carbon pool	none	
$f_{lig,l}$	Fraction of leaf mass in lignin carbon pool	none	
$f_{lab,r}$	Fraction of root mass in labile carbon pool	none	
$f_{cel,r}$	Fraction of root mass in cellulose carbon pool	none	
$f_{lig,r}$	Fraction of root mass in lignin carbon pool	none	
$l_{prof,z}$	Fraction of leaf matter directed to soil layer z	none	soil layer
$r_{c,prof,z}$	Fraction of coarse root matter directed to soil layer z	none	soil layer
$r_{f,prof,z}$	Fraction of fine root matter directed to soil layer z	none	soil layer

29.15 Plant Mortality

Total plant mortality per cohort $M_{t,coh}$, (fraction year^{-1}) is simulated as the sum of four additive terms,

$$M_{t,coh} = M_{b,coh} + M_{cs,coh} + M_{hf,coh} + M_{f,coh},$$

where M_b is the background mortality that is unaccounted by any of the other mortality rates and is fixed at 0.014. M_{cs} is the carbon starvation derived mortality, which is a function of the non-structural carbon storage term $b_{store,coh}$ and the PFT-specific 'target' carbon storage, $l_{targ,ft}$, as follows:

$$M_{cs,coh} = \max \left(0.0, S_{m,ft} \left(0.5 - \frac{b_{store,coh}}{l_{targ,ft} b_{leaf}} \right) \right)$$

where $S_{m,ft}$ is the *stress mortality* parameter, or the fraction of trees in a landscape that die when the mean condition of a given cohort triggers mortality. This parameter is needed to scale from individual-level mortality simulation to grid-cell average conditions.

Mechanistic simulation of hydraulic failure is not undertaken on account of it's mechanistic complexity (see *McDowell et al. 2013* for details). Instead, we use a proxy for hydraulic failure induced mortality ($M_{hf,coh}$) that uses a water potential threshold beyond mortality is triggered, such that the tolerance of low water potentials is a function of plant functional type (as expressed via the ψ_c parameter). For each day that the aggregate water potential falls below a threshold value, a set fraction of the trees are killed. The aggregation of soil moisture potential across the root zone is expressed using the β function. We thus determine plant mortality caused by extremely low water potentials as

$$M_{hf,coh} = \begin{cases} S_{m,ft} & \text{for } \beta_{ft} < 10^{-6} \\ \\ 0.0 & \text{for } \beta_{ft} >= 10^{-6}. \end{cases}$$

The threshold value of 10^{-6} represents a state where the average soil moisture potential is within 10^{-6} of the wilting point (a PFT specific parameter $\theta_{w,ft}$).

$M_{hf,coh}$ is the fire-induced mortality, as described in the fire modelling section.

Table 29.15: Parameters needed for mortality model.

Parameter Symbol	Parameter Name	Units	indexed by
$S_{m,ft}$	Stress Mortality Scaler	none	
$l_{targ,ft}$	Target carbon storage fraction	none	ft

29.16 Fire (SPITFIRE)

The influence of fire on vegetation is estimated using the SPITFIRE model, which has been modified for use in ED following it's original implementation in the LPJ-SPITFIRE model (*Thonicke et al. 2010, Pfeiffer et al. 2013*). This model as described is substantially different from the existing CLM4.5 fire model *Li et al. 2012*, however, further developments are intended to increase the merging of SPITFIRE's natural vegetation fire scheme with the fire suppression, forest-clearing and peat fire estimations in the existing model. The coupling to the ED model allows fires to interact with vegetation in a size-structured manner, so small fires can burn only understorey vegetation. Also, the patch structure and representation of succession in the ED model allows the model to track the impacts of fire on different forest stands, therefore removing the problem of area-averaging implicit in area-based DGVMs. The SPITFIRE approach has also been coupled to the LPJ-GUESS individual-based model (Forrest et al. in prep) and so this is not the only implementation of this type of scheme in existence.

The SPITFIRE model operates at a daily timestep and at the patch level, meaning that different litter pools and vegetation charecteristics of open and closed forests can be represented effectively (we omit the *patch* subscript throughout for simplicity).

29.16.1 Properties of fuel load

Many fire processes are impacted by the properties of the litter pool in the SPITFIRE model. There are one live (live grasses) and five dead fuel categories (dead leaf litter and four pools of coarse woody debris). Coarse woody debris is classified into 1h, 10h, 100h, and 1000h fuels, defined by the order of magnitude of time required for fuel to lose (or gain) 63% of the difference between its current moisture content and the equilibrium moisture content under defined atmospheric conditions. *Thonicke et al. 2010*. For the purposes of describing the behaviour of fire, we introduce a new index 'fuel class' *fc*, the values of which correspond to each of the six possible fuel categories as follows.

fc index	Fuel type	Drying Time
1	dead grass	n/a
2	twigs	1h fuels
3	small branches	10h fuel
4	large branches	100h fuel
5	stems and trunks	1000h fuel
6	live grasses	n/a

29.16.2 Nesterov Index

Dead fuel moisture ($moist_{df,fc}$), and several other properties of fire behaviour, are a function of the 'Nesterov Index' (N_I) which is an accumulation over time of a function of temperature and humidity (Eqn 5, *Thonicke et al. 2010*),

$$N_I = \sum \max(T_d(T_d - D), 0)$$

where T_d is the daily mean temperature in $^\circ$C and D is the dew point calculated as .

$$\upsilon = \frac{17.27 T_d}{237.70 + T_d} + \log(RH/100)$$

$$D = \frac{237.70\upsilon}{17.27 - \upsilon}$$

where RH is the relative humidity (%).

On days when the total precipitation exceeds 3.0mm, the Nesterov index accumulator is reset back to zero.

29.16.3 Fuel properties

Total fuel load $F_{tot,patch}$ for a given patch is the sum of the above ground coarse woody debris and the leaf litter, plus the alive grass leaf biomass $b_{l,grass}$ multiplied by the non-mineral fraction (1-M_f).

$$F_{tot,patch} = \left(\sum_{fc=1}^{fc=5} CWD_{AG,fc} + l_{litter} + b_{l,grass} \right) (1 - M_f)$$

Many of the model behaviours are affected by the patch-level weighted average properties of the fuel load. Typically, these are calculated in the absence of 1000-h fuels because these do not contribute greatly to fire spread properties.

Dead Fuel Moisture Content

Dead fuel moisture is calculated as

$$moist_{df,fc} = e^{-\alpha_{fmc,fc} N_I}$$

where $\alpha_{fmc,fc}$ is a parameter defining how fuel moisture content varies between the first four dead fuel classes.

Live grass moisture Content

The live grass fractional moisture content($moist_{lg}$) is a function of the soil moisture content. (Equation B2 in *Thonicke et al. 2010*)

$$moist_{lg} = \max(0.0, \frac{10}{9}\theta_{30} - \frac{1}{9})$$

where θ_{30} is the fractional moisture content of the top 30cm of soil.

Patch Fuel Moisture

The total patch fuel moisture is based on the weighted average of the different moisture contents associated with each of the different live grass and dead fuel types available (except 1000-h fuels).

$$F_{m,patch} = \sum_{fc=1}^{fc=4} \frac{F_{fc}}{F_{tot}} moist_{df,fc} + \frac{b_{l,grass}}{F_{tot}} moist_{lg}$$

Effective Fuel Moisture Content

Effective Fuel Moisture Content is used for calculations of fuel consumed, and is a function of the ratio of dead fuel moisture content $M_{df,fc}$ and the moisture of extinction factor, $m_{ef,fc}$

$$E_{moist,fc} = \frac{moist_{fc}}{m_{ef,fc}}$$

where the m_{ef} is a function of surface-area to volume ratio.

$$m_{ef,fc} = 0.524 - 0.066 \log_{10} \sigma_{fc}$$

Patch Fuel Moisture of Extinction

The patch 'moisture of extinction' factor (F_{mef}) is the weighted average of the m_{ef} of the different fuel classes

$$F_{mef,patch} = \sum_{fc=1}^{fc=5} \frac{F_{fc}}{F_{tot}} m_{ef,fc} + \frac{b_{l,grass}}{F_{tot}} m_{ef,grass}$$

Patch Fuel Bulk Density

The patch fuel bulk density is the weighted average of the bulk density of the different fuel classes (except 1000-h fuels).

$$F_{bd,patch} = \sum_{fc=1}^{fc=4} \frac{F_{fc}}{F_{tot}} \beta_{fuel,fc} + \frac{b_{l,grass}}{F_{tot}} \beta_{fuel,lgrass}$$

where $\beta_{fuel,fc}$ is the bulk density of each fuel size class (kG m^{-3})

Patch Fuel Surface Area to Volume

The patch surface area to volume ratio (F_σ) is the weighted average of the surface area to volume ratios (σ_{fuel}) of the different fuel classes (except 1000-h fuels).

$$F_\sigma = \sum_{fc=1}^{fc=4} \frac{F_{fc}}{F_{tot}} \sigma_{fuel,fc} + \frac{b_{l,grass}}{F_{tot}} \sigma_{fuel,grass}$$

29.16.4 Forward rate of spread

For each patch and each day, we calculate the rate of forward spread of the fire ros_f (nominally in the direction of the wind).

$$ros_f = \frac{i_r x_i (1 + \phi_w)}{F_{bd,patch} e_{ps} q_{ig}}$$

e_{ps} is the effective heating number ($e^{\frac{-4.528}{F_{\sigma,patch}}}$). q_{ig} is the heat of pre-ignition ($581 + 2594 F_m$). x_i is the propagating flux calculated as (see *Thonicke et al. 2010* Appendix A).

$$x_i = \frac{e^{0.792 + 3.7597 F_{\sigma,patch}^{0.5} \left(\frac{F_{bd,patch}}{p_d} + 0.1 \right)}}{192 + 7.9095 F_{\sigma,patch}}$$

ϕ_w is the influence of windspeed on rate of spread.

$$\phi_w = c b_w^b . \beta^{-e}$$

Where b, c and e are all functions of surface-area-volume ratio $F_{\sigma,patch}$: $b = 0.15988 F_{\sigma,patch}^{0.54}$, $c = 7.47 e^{-0.8711 F_{\sigma,patch}^{0.55}}$, $e = 0.715 e^{-0.01094 F_{\sigma,patch}}$. $b_w = 196.86 W$ where W is the the windspeed in ms^{-1}, and $\beta = \frac{F_{bd}/p_d}{0.200395 F_{\sigma,patch}^{-0.8189}}$ where p_d is the particle density (513).

i_r is the reaction intensity, calculated using the following set of expressions (from *Thonicke et al. 2010* Appendix A).:

$$i_r = \Gamma_{opt} F_{tot} H d_{moist} d_{miner}$$
$$d_{moist} = \max\left(0.0, (1 - 2.59 m_w + 5.11 m_w^2 - 3.52 m_w^3)\right)$$
$$m_w = \frac{F_{m,patch}}{F_{mef,patch}}$$
$$\Gamma_{opt} = \Gamma_{max} \beta^a \lambda$$
$$\Gamma_{max} = \frac{1}{0.0591 + 2.926 F_{\sigma,patch}^{-1.5}}$$
$$\lambda = e^{a(1-\beta)}$$
$$a = 8.9033 F_{\sigma,patch}^{-0.7913}$$

Γ_{opt} is the residence time of the fire, and d_{miner} is the mineral damping coefficient (=0.174:math:S_e^{-0.19} , where S_e is 0.01 and so = d_{miner} 0.41739).

29.16.5 Fuel Consumption

The fuel consumption (fraction of biomass pools) of each dead biomass pool in the area affected by fire on a given day ($f_{c,dead,fc}$) is a function of effective fuel moisture $E_{moist,fc}$ and size class fc (Eqn B1, B4 and B5, *Thonicke et*

al. 2010). The fraction of each fuel class that is consumed decreases as its moisture content relative to its moisture of extinction ($E_{moist,fc}$) increases.

$$f_{cdead,fc} = \max\left(0, \min(1, m_{int,mc,fc} - m_{slope,mc,fc}E_{moist,fc})\right)$$

m_{int} and m_{slope} are parameters, the value of which is modulated by both size class fc and by the effective fuel moisture class mc, defined by $E_{moist,fc}$. m_{int} and m_{slope} are defined for low-, mid-, and high-moisture conditions, the boundaries of which are also functions of the litter size class following *Peterson and Ryan 1986* (page 802). The fuel burned, $f_{cground,fc}$ (Kg m^{-2} day^{-1}) iscalculated from $f_{cdead,fc}$ for each fuel class:

$$f_{cground,fc} = f_{c,dead,fc}(1 - M_f)\frac{F_{fc}}{0.45}$$

Where 0.45 converts from carbon to biomass. The total fuel consumption, $f_{ctot,patch}$(Kg m^{-2}), used to calculate fire intensity, is then given by

$$f_{ctot,patch} = \sum_{fc=1}^{fc=4} f_{c,ground,fc} + f_{c,ground,lgrass}$$

There is no contribution from the 1000 hour fuels to the patch-level $f_{ctot,patch}$ used in the fire intensity calculation.

29.16.6 Fire Intensity

Fire intensity at the front of the burning area ($I_{surface}$, kW m^{-2}) is a function of the total fuel consumed ($f_{ctot,patch}$) and the rate of spread at the front of the fire, ros_f (m min^{-1}) (Eqn 15 *Thonicke et al. 2010*)

$$I_{surface} = \frac{0.001}{60}f_{energy}f_{ctot,patch}ros_f$$

where f_{energy} is the energy content of fuel (Kj/Kg - the same, 18000 Kj/Kg for all fuel classes). Fire intensity is used to define whether an ignition is successful. If the fire intensity is greater than 50Kw/m then the ignition is successful.

29.16.7 Fire Duration

Fire duration is a function of the fire danger index with a maximum length of $F_{dur,max}$ (240 minutes in *Thonicke et al. 2010* Eqn 14, derived from Canadian Forest Fire Behaviour Predictions Systems)

$$D_f = \min\left(F_{dur,max}, \frac{F_{dur,max}}{1 + F_{dur,max}e^{-11.06fdi}}\right)$$

29.16.8 Fire Danger Index

Fire danger index (*fdi*) is a representation of the effect of meteorological conditions on the likelihood of a fire. It is calculated for each gridcell as a function of the Nesterov Index . *fdi* is calculated from NI as

$$fdi = 1 - e^{\alpha N_I}$$

where α = 0.00037 following *Venevsky et al. 2002*.

29.16.9 Area Burned

Total area burnt is assumed to be in the shape of an ellipse, whose major axis f_{length} (m) is determined by the forward and backward rates of spread (ros_f and ros_b respectively).

$$f_{length} = F_d(ros_b + ros_f)$$

ros_b is a function of ros_f and windspeed (Eqn 10 *Thonicke et al. 2010*)

$$ros_b = ros_f e^{-0.012W}$$

The minor axis to major axis ratio l_b of the ellipse is determined by the windspeed. If the windspeed (W) is less than 16.67 ms^{-1} then $l_b = 1$. Otherwise (Eqn 12 and 13, *Thonicke et al. 2010*)

$$l_b = \min\left(8, f_{tree}(1.0 + 8.729(1.0 - e^{-0.108W})^{2.155}) + (f_{grass}(1.1 + 3.6W^{0.0464}))\right)$$

f_{grass} and f_{tree} are the fractions of the patch surface covered by grass and trees respectively.

The total area burned (A_{burn} in m^2) is therefore (Eqn 11, *Thonicke et al. 2010*)

$$A_{burn} = \frac{n_f \frac{3.1416}{4l_b}(f_{length}^2)}{10000}$$

where n_f is the number of fires.

29.16.10 Crown Damage

c_k is the fraction of the crown which is consumed by the fire. This is calculated from scorch height H_s, tree height h and the crown fraction parameter F_{crown} (Eqn 17 *Thonicke et al. 2010*):

$$c_k = \begin{cases} 0 & \text{for } H_s < (h - hF_{crown}) \\ 1 - \frac{h - H_s}{h - F_{crown}} & \text{for } h > H_s > (h - hF_{crown}) \\ 1 & \text{for } H_s > h \end{cases}$$

The scorch height H_s (m) is a function of the fire intensity, following *Byram, 1959*, and is proportional to a plant functional type specific parameter $\alpha_{s,ft}$ (Eqn 16 *Thonicke et al. 2010*):

$$H_s = \sum_{FT=1}^{NPFT} \alpha_{s,p} \cdot f_{biomass,ft} I_{surface}^{0.667}$$

where $f_{biomass,ft}$ is the fraction of the above-ground biomass in each plant functional type.

29.16.11 Cambial Damage and Kill

The cambial kill is a function of the fuel consumed $f_{c,tot}$, the bark thickness t_b, and τ_l, the duration of cambial heating (minutes) (Eqn 8, *Peterson and Ryan 1986*):

$$\tau_l = \sum_{fc=1}^{fc=5} 39.4 F_{p,c} \frac{10000}{0.45}(1 - (1 - f_{c,dead,fc})^{0.5})$$

Bark thickness is a linear function of tree diameter dbh_{coh}, defined by PFT-specific parameters $\beta_{1,bt}$ and $\beta_{2,bt}$ (Eqn 21 *Thonicke et al. 2010*):

$$t_{b,coh} = \beta_{1,bt,ft} + \beta_{2,bt,ft} dbh_{coh}$$

The critical time for cambial kill, τ_c (minutes) is given as (Eqn 20 *Thonicke et al. 2010*):

$$\tau_c = 2.9t_b^2$$

The mortality rate caused by cambial heating τ_{pm} of trees within the area affected by fire is a function of the ratio between τ_l and τ_c (Eqn 19, *Thonicke et al. 2010*):

$$\tau_{pm} = \begin{cases} 1.0 & \text{for } \tau_1/\tau_c \geq 2.0 \\ 0.563(\tau_l/\tau_c)) - 0.125 & \text{for } 2.0 > \tau_1/\tau_c \geq 0.22 \\ 0.0 & \text{for } \tau_1/\tau_c < 0.22 \end{cases}$$

Table 29.16: Parameters needed for fire model.

Parameter Symbol	Parameter Name	Units	indexed by
$\beta_{1,bt}$	Intercept of bark thickness function	mm	*FT*
$\beta_{2,bt}$	Slope of bark thickness function	mm cm^{-1}	*FT*
F_{crown}	Ratio of crown height to total height	none	*FT*
α_{fmc}	Fuel moisture parameter	^{o}C $^{-2}$	*fc*
β_{fuel}	Fuel Bulk Density	kG m^{-3}	*fc*
$\sigma_{fuel,fc}$	Surface area to volume ratio	cm $^{-1}$	*fc*
m_{int}	Intercept of fuel burned	none	*fc*, moisture class
m_{slope}	Slope of fuel burned	none	*fc*, moisture class
M_f	Fuel Mineral Fraction		
$F_{dur,max}$	Maximum Duration of Fire	Minutes	
f_{energy}	Energy content of fuel	kJ/kG	
α_s	Flame height parameter		*FT*

CHAPTER 30

BIOGENIC VOLATILE ORGANIC COMPOUNDS (BVOCS)

This chapter briefly describes the biogenic volatile organic compound (BVOC) emissions model implemented in CLM. The CLM3 version (Levis et al. 2003; Oleson et al. 2004) was based on Guenther et al. (1995). Heald et al. (2008) updated this scheme in CLM4 based on Guenther et al. (2006). The current version was implemented in CLM4.5 and is based on MEGAN2.1 discussed in detail in Guenther et al. (2012). This update of MEGAN incorporates four main features: 1) expansion to 147 chemical compounds, 2) the treatment of the light-dependent fraction (LDF) for each compound, 3) inclusion of the inhibition of isoprene emission by atmospheric CO_2 and 4) emission factors mapped to the specific PFTs of the CLM.

MEGAN2.1 now describes the emissions of speciated monoterpenes, sesquiterpenes, oxygenated VOCs as well as iso-prene. A flexible scheme has been implemented in the CLM to specify a subset of emissions. This allows for additional flexibility in grouping chemical compounds to form the lumped species frequently used in atmospheric chemistry. The mapping or grouping is therefore defined through a namelist parameter in drv_flds_in, e.g. megan_specifier = 'ISOP = isoprene', 'BIGALK = pentane + hexane + heptane + tricyclene'.

Terrestrial BVOC emissions from plants to the atmosphere are expressed as a flux, F_i (μ g C m^{-2} ground area h^{-1}), for emission of chemical compound i

$$F_i = \gamma_i \rho \sum_j \varepsilon_{i,j} \left(wt\right)_j \tag{30.1}$$

where γ_i is the emission activity factor accounting for responses to meteorological and phenological conditions, ρ is the canopy loss and production factor also known as escape efficiency (set to 1), and $\varepsilon_{i,j}$ (μ g C m^{-2} ground area h^{-1}) is the emission factor at standard conditions of light, temperature, and leaf area for plant functional type j with fractional coverage $(wt)_j$ (Guenther et al. 2012). The emission activity factor γ_i depends on plant functional type, temperature, LAI, leaf age, and soil moisture (Guenther et al. 2012). For isoprene only, the effect of CO_2 inhibition is now included as described by Heald et al. (2009). Previously, only isoprene was treated as a light-dependent emission. In MEGAN2.1, each chemical compound is assigned a LDF (ranging from 1.0 for isoprene to 0.2 for some monoterpenes, VOCs and acetone). The activity factor for the light response of emissions is therefore estimated as:

$$\gamma_{P,i} = (1 - LDF_i) + \gamma_{P\_LDF} LDF_i \tag{30.2}$$

where the LDF activity factor (γ_{P_LDF}) is specified as a function of PAR as in previous versions of MEGAN.

The values for each emission factor $\epsilon_{i,j}$ are now available for each of the plant functional types in the CLM and each chemical compound. This information is distributed through an external file, allowing for more frequent and easier updates.

CHAPTER 31

DUST MODEL

Atmospheric dust is mobilized from the land by wind in the CLM. The most important factors determining soil erodibility and dust emission include the wind friction speed, the vegetation cover, and the soil moisture. The CLM dust mobilization scheme (*Mahowald et al. 2006*) accounts for these factors based on the DEAD (Dust Entrainment and Deposition) model of *Zender et al. (2003)*. Please refer to the *Zender et al. (2003)* article for additional information regarding the equations presented in this section.

The total vertical mass flux of dust, F_j (kg m^{-2} s^{-1}), from the ground into transport bin j is given by

$$F_j = TSf_m\alpha Q_s \sum_{i=1}^{I} M_{i,j} \tag{31.1}$$

where T is a global factor that compensates for the DEAD model's sensitivity to horizontal and temporal resolution and equals 5 x 10^{-4} in the CLM instead of 7 x 10^{-4} in *Zender et al. (2003)*. S is the source erodibility factor set to 1 in the CLM and serves as a place holder at this time.

The grid cell fraction of exposed bare soil suitable for dust mobilization f_m is given by

$$f_m = (1 - f_{lake})(1 - f_{sno})(1 - f_v)\frac{w_{liq,1}}{w_{liq,1} + w_{ice,1}} \tag{31.2}$$

where f_{lake} and f_{sno} are the CLM grid cell fractions of lake (section 2.3.3) and snow cover (section 8.1), all ranging from zero to one. Not mentioned by *Zender et al. (2003)*, $w_{liq,1}$ and $w_{ice,1}$ are the CLM top soil layer liquid water and ice contents (mm) entered as a ratio expressing the decreasing ability of dust to mobilize from increasingly frozen soil. The grid cell fraction of vegetation cover, f_v, is defined as

$$0 \le f_v = \frac{L + S}{(L + S)_t} \le 1 \quad \text{where } (L + S)_t = 0.3 \text{ m}^2\text{m}^{-2} \tag{31.3}$$

where equation applies only for dust mobilization and is not related to the plant functional type fractions prescribed from the CLM input data or simulated by the CLM dynamic vegetation model (Chapter 22). L and S are the CLM leaf and stem area index values (m^2 m^{-2}) averaged at the land unit level so as to include all the pfts and the bare ground present in a vegetated land unit. L and S may be prescribed from the CLM input data (section 2.1.4) or simulated by the CLM biogeochemistry model (Chapter 20).

The sandblasting mass efficiency α (m^{-1}) is calculated as

$$\alpha = 100e^{(13.4M_{clay}-6.0)\ln 10} \begin{cases} M_{clay} = \%clay \times 0.01 & 0 \le \%clay \le 20 \\ M_{clay} = 20 \times 0.01 & 20 < \%clay \le 100 \end{cases} \tag{31.4}$$

where M_{clay} is the mass fraction of clay particles in the soil and %clay is determined from the surface dataset (section 2.3.3). $M_{clay} = 0$ corresponds to sand and $M_{clay} = 0.2$ to sandy loam.

Q_s is the total horizontally saltating mass flux (kg m^{-1} s^{-1}) of "large" particles (Table 31.1), also referred to as the vertically integrated streamwise mass flux

$$Q_s = \begin{cases} \frac{c_s \rho_{atm} u_{*s}^3}{g} \left(1 - \frac{u_{*t}}{u_{*s}}\right) \left(1 + \frac{u_{*t}}{u_{*s}}\right)^2 & \text{for } u_{*t} < u_{*s} \\ 0 & \text{for } u_{*t} \geq u_{*s} \end{cases} \tag{31.5}$$

where the saltation constant c_s equals 2.61 and ρ_{atm} is the atmospheric density (kg m^{-3}) (Table 2.4), g the acceleration of gravity (m s^{-2}) (Table 2.7). The threshold wind friction speed for saltation u_{*t} (m s^{-1}) is

$$u_{*t} = f_z \left[Re_{*t}^f \rho_{osp} g D_{osp} \left(1 + \frac{6 \times 10^{-7}}{\rho_{osp} g D_{osp}^{2.5}}\right) \right]^{\frac{1}{2}} \rho_{atm}^{-\frac{1}{2}} f_w \tag{31.6}$$

where f_z is a factor dependent on surface roughness but set to 1 as a place holder for now, ρ_{osp} and D_{osp} are the density (2650 kg m^{-3}) and diameter (75 x 10^{-6} m) of optimal saltation particles, and f_w is a factor dependent on soil moisture:

$$f_w = \begin{cases} 1 & \text{for } w \leq w_t \\ \sqrt{1 + 1.21 \left[100 \left(w - w_t\right)\right]^{0.68}} & \text{for } w > w_t \end{cases} \tag{31.7}$$

where

$$w_t = a \left(0.17 M_{clay} + 0.14 M_{clay}^2\right) \qquad 0 \leq M_{clay} = \%clay \times 0.01 \leq 1 \tag{31.8}$$

and

$$w = \frac{\theta_1 \rho_{liq}}{\rho_{d,1}} \tag{31.9}$$

where $a = M_{clay}^{-1}$ for tuning purposes, θ_1 is the volumetric soil moisture in the top soil layer (m ^{3}m^{-3}) (section 7.3), ρ_{liq} is the density of liquid water (kg m^{-3}) (Table 2.7), and $\rho_{d,1}$ is the bulk density of soil in the top soil layer (kg m^{-3}) defined as in section 6.3 rather than as in *Zender et al. (2003)*. Re_{*t}^f from equation is the threshold friction Reynolds factor

$$Re_{*t}^f = \begin{cases} \frac{0.1291^2}{-1 + 1.928 Re_{*t}} & \text{for } 0.03 \leq Re_{*t} \leq 10 \\ 0.12^2 \left(1 - 0.0858 e^{-0.0617(Re_{*t} - 10)}\right)^2 & \text{for } Re_{*t} > 10 \end{cases} \tag{31.10}$$

and Re_{*t} is the threshold friction Reynolds number approximation for optimally sized particles

$$Re_{*t} = 0.38 + 1331 \left(100 D_{osp}\right)^{1.56} \tag{31.11}$$

In (31.5), u_{*s} is defined as the wind friction speed (m s^{-1}) accounting for the Owen effect (*Owen 1964*)

$$u_s = \begin{cases} u & \text{for } U_{10} < U_{10,t} \\ u_* + 0.003 \left(U_{10} - U_{10,t}\right)^2 & \text{for } U_{10} \geq U_{10,t} \end{cases} \tag{31.12}$$

where u_* is the CLM wind friction speed (m s^{-1}), also known as friction velocity (section 5.1), U_{10} is the 10-m wind speed (m s^{-1}) calculated as the wind speed at the top of the canopy in section 4.3 of *Bonan (1996)* but here for 10 m above the ground, and $U_{10,t}$ is the threshold wind speed at 10 m (m s^{-1})

$$U_{10,t} = u_{*t} \frac{U_{10}}{u_*} \tag{31.13}$$

In equation we sum $M_{i,j}$ over $I = 3$ source modes i where $M_{i,j}$ is the mass fraction of each source mode i carried in each of *:math:'J=4'* transport bins j

$$M_{i,j} = \frac{m_i}{2} \left[\text{erf} \left(\frac{\ln \frac{D_{j,\max}}{\tilde{D}_{v,i}}}{\sqrt{2} \ln \sigma_{g,i}} \right) - \text{erf} \left(\frac{\ln \frac{D_{j,\min}}{\tilde{D}_{v,i}}}{\sqrt{2} \ln \sigma_{g,i}} \right) \right] \qquad (31.14)$$

where m_i , $\tilde{D}_{v,i}$, and $\sigma_{g,i}$ are the mass fraction, mass median diameter, and geometric standard deviation assigned to each particle source mode i (Table 31.1), while $D_{j,\min}$ and $D_{j,\max}$ are the minimum and maximum diameters (m) in each transport bin j (Table 31.2).

Table 31.1: Mass fraction m_i , mass median diameter $\tilde{D}_{v,i}$, and geometric standard deviation $\sigma_{g,i}$, per dust source mode i

i	m_i (fraction)	$\tilde{D}_{v,i}$ (m)	$\sigma_{g,i}$
1	0.036	0.832 x 10^{-6}	2.1
2	0.957	4.820 x 10^{-6}	1.9
3	0.007	19.38 x 10^{-6}	1.6

Table 31.2: Minimum and maximum particle diameters in each dust transport bin j

j	$D_{j,\min}$ (m)	$D_{j,\max}$ (m)
1	0.1 x 10^{-6}	1.0 x 10^{-6}
2	1.0 x 10^{-6}	2.5 x 10^{-6}
3	2.5 x 10^{-6}	5.0 x 10^{-6}
4	5.0 x 10^{-6}	10.0 x 10^{-6}

CHAPTER 32

CARBON ISOTOPES

CLM includes a fully prognostic representation of the fluxes, storage, and isotopic discrimination of the carbon isotopes ^{13}C and ^{14}C. The implementation of the C isotopes capability takes advantage of the CLM hierarchical data structures, replicating the carbon state and flux variable structures at the column and PFT level to track total carbon and both C isotopes separately (see description of data structure hierarchy in Chapter 2). For the most part, fluxes and associated updates to carbon state variables for ^{13}C are calculated directly from the corresponding total C fluxes. Separate calculations are required in a few special cases, such as where isotopic discrimination occurs, or where the necessary isotopic ratios are undefined. The general approach for ^{13}C flux and state variable calculation is described here, followed by a description of all the places where special calculations are required.

32.1 General Form for Calculating ^{13}C and ^{14}C Flux

In general, the flux of ^{13}C and corresponding to a given flux of total C (CF_{13C} and CF_{totC}, respectively) is determined by CF_{totC}, the masses of ^{13}C and total C in the upstream pools (CS_{13C_up} and CS_{totC_up}, respectively, i.e. the pools *from which* the fluxes of ^{13}C and total C originate), and a fractionation factor, f_{frac}:

$$CF_{13C} = \left\{ \begin{array}{ll} CF_{totC}\frac{CS_{13C\_up}}{CS_{totC\_up}}f_{frac} & \text{for } CS_{totC} \neq 0 \\ 0 & \text{for } CS_{totC} = 0 \end{array} \right\} \tag{32.1}$$

If the f_{frac} = 1.0 (no fractionation), then the fluxes CF_{13C} and CF_{totC} will be in simple proportion to the masses CS_{13C_up} and CS_{totC_up}. Values of $f_{frac} < 1.0$ indicate a discrimination against the heavier isotope (^{13}C) in the flux-generating process, while $f_{frac} > 1.0$ would indicate a preference for the heavier isotope. Currently, in all cases where Eq. is used to calculate a ^{13}C flux, f_{frac} is set to 1.0.

For ^{14}C, no fractionation is used in either the initial photosynthetic step, nor in subsequent fluxes from upstream to downstream pools; as discussed below, this is because observations of ^{14}C are typically described in units that implicitly correct out the fractionation of ^{14}C by referencing them to ^{13}C ratios.

32.2 Isotope Symbols, Units, and Reference Standards

Carbon has two primary stable isotopes, ^{12}C and ^{13}C. ^{12}C is the most abundant, comprising about 99% of all carbon. The isotope ratio of a compound, R_A, is the mass ratio of the rare isotope to the abundant isotope

$$R_A = \frac{^{13}C_A}{^{12}C_A}. \tag{32.2}$$

Carbon isotope ratios are often expressed using delta notation, δ. The δ^{13}C value of a compound A, $\delta^{13}C_A$, is the difference between the isotope ratio of the compound, R_A, and that of the Pee Dee Belemnite standard, R_{PDB}, in parts per thousand

$$\delta^{13}C_A = \left(\frac{R_A}{R_{PDB}} - 1 \right) \times 1000 \tag{32.3}$$

where R_{PDB} = 0.0112372, and units of δ are per mil (‰).

Isotopic fractionation can be expressed in several ways. One expression of the fractionation factor is with alpha (α) notation. For example, the equilibrium fractionation between two reservoirs A and B can be written as:

$$\alpha_{A-B} = \frac{R_A}{R_B} = \frac{\delta_A + 1000}{\delta_B + 1000}. \tag{32.4}$$

This can also be expressed using epsilon notation (ϵ), where

$$\alpha_{A-B} = \frac{\varepsilon_{A-B}}{1000} + 1 \tag{32.5}$$

In other words, if $\epsilon_{A-B} = 4.4\,‰$, then $\alpha_{A-B} = 1.0044$.

In addition to the stable isotopes ^{12}C and ^{13}C, the unstable isotope ^{14}C is included in CLM. ^{14}C can also be described using the delta notation:

$$\delta^{14}C = \left(\frac{A_s}{A_{abs}} - 1 \right) \times 1000 \tag{32.6}$$

However, observations of ^{14}C are typically fractionation-corrected using the following notation:

$$\Delta^{14}C = 1000 \times \left(\left(1 + \frac{\delta^{14}C}{1000} \right) \frac{0.975^2}{\left(1 + \frac{\delta^{13}C}{1000} \right)^2} - 1 \right) \tag{32.7}$$

where δ^{14}C is the measured isotopic fraction and Δ^{14}C corrects for mass-dependent isotopic fractionation processes (assumed to be 0.975 for fractionation of ^{13}C by photosynthesis). CLM assumes a background preindustrial atmospheric ^{14}C /C ratio of 10^{-12}, which is used for A:sub::*abs*. For the reference standard A$_{abs}$, which is a plant tissue and has a δ^{13}C value is -25 ‰ due to photosynthetic discrimination, δ^{14}C = Δ^{14}C. For CLM, in order to use the ^{14}C model independently of the ^{13}C model, for the ^{14}C calculations, this fractionation is set to zero, such that the 0.975 term becomes 1, the δ^{13}C term (for the calculation of δ^{14}C only) becomes 0, and thus δ^{14}C = Δ^{14}C.

32.3 Carbon Isotope Discrimination During Photosynthesis

Photosynthesis is modeled in CLM as a two-step process: diffusion of CO_2 into the stomatal cavity, followed by enzymatic fixation (Chapter 9). Each step is associated with a kinetic isotope effect. The kinetic isotope effect during diffusion of CO_2 through the stomatal opening is 4.4‰. The kinetic isotope effect during fixation of CO_2 with Rubisco is ∼30‰; however, since about 5-10% of carbon in C3 plants reacts with phosphoenolpyruvate carboxylase (PEPC) (Melzer and O'Leary, 1987), the net kinetic isotope effect during fixation is ∼27‰ for C3 plants. In C4 plant

photosynthesis, only the diffusion effect is important. The fractionation factor equations for C3 and C4 plants are given below:

For C4 plants,

$$\alpha_{psn} = 1 + \frac{4.4}{1000} \tag{32.8}$$

For C3 plants,

$$\alpha_{psn} = 1 + \frac{4.4 + 22.6\frac{c_i^*}{pCO_2}}{1000} \tag{32.9}$$

where α_{psn} is the fractionation factor, and c_i^* and pCO_2 are the revised intracellular and atmospheric CO_2 partial pressure, respectively.

As can be seen from the above equation, kinetic isotope effect during fixation of CO_2 is dependent on the intracellular CO_2 concentration, which in turn depends on the net carbon assimilation. That is calculated during the photosynthesis calculation as follows:

$$c_i = pCO_2 - a_n p\frac{(1.4g_s) + (1.6g_b)}{g_b g_s} \tag{32.10}$$

where a_n is net carbon assimilation during photosynthesis, p is atmospheric pressure, g_b is leaf boundary layer conductance, and g_s is leaf stomatal conductance.

Isotopic fractionation code is compatible with multi-layered canopy parameterization; i.e., it is possible to calculate varying discrimination rates for each layer of a multi-layered canopy. However, as with the rest of the photosynthesis model, the number of canopy layers is currently set to one by default.

32.4 ^{14}C radioactive decay and historical atmospheric ^{14}C and ^{13}C concentrations

In the preindustrial biosphere, radioactive decay of ^{14}C in carbon pools allows dating of long-term age since photosynthetic uptake; while over the 20th century, radiocarbon in the atmosphere was first diluted by radiocarbon-free fossil fuels and then enriched by aboveground thermonuclear testing to approximately double its long-term mean concentration. CLM includes both of these processes to allow comparison of carbon that may vary on multiple timescales with observed values.

For radioactive decay, at each timestep all ^{14}C pools are reduced at a rate of $-\log/\tau$, where τ is the half-life (Libby half-life value of 5568 years). In order to rapidly equilibrate the long-lived pools during accelerated decomposition spinup, the radioactive decay of the accelerated pools is also accelerated by the same degree as the decomposition, such that the ^{14}C value of these pools is in equilibrium when taken out of the spinup mode.

For variation of atmospheric ^{14}C and ^{13}C over the historical period, Δ^{14}C and Δ:sup:13C values can be set to either fixed concentrations or time-varying concentrations read in from a file. A default file is provided that spans the historical period (*Graven et al., 2017*). For Δ^{14}C, values are provided and read in for three latitude bands (30 ºN-90 ºN, 30 ºS-30 ºN, and 30 ºS-90 ºS).

CHAPTER 33

LAND-ONLY MODE

In land-only mode (uncoupled to an atmospheric model), the atmospheric forcing required by CLM (Table 2.4) is supplied by observed datasets. The standard forcing provided with the model is a 110-year (1901-2010) dataset provided by the Global Soil Wetness Project (GSWP3; NEED A REFERENCE). The GSWP3 dataset has a spatial resolution of 0.5º X 0.5º and a temporal resolution of three hours.

An alternative forcing dataset is also available, CRUNCEP, a 110-year (1901-2010) dataset (CRUNCEP; *Viovy 2011*) that is a combination of two existing datasets; the CRU TS3.2 0.5º X 0.5º monthly data covering the period 1901 to 2002 (*Mitchell and Jones 2005*) and the NCEP reanalysis 2.5º X 2.5º 6-hourly data covering the period 1948 to 2010. The CRUNCEP dataset has been used to force CLM for studies of vegetation growth, evapotranspiration, and gross primary production (*Mao et al. 2012*, *Mao et al. 2013*, *Shi et al. 2013*) and for the TRENDY (trends in net land-atmosphere carbon exchange over the period 1980-2010) project (*Piao et al. 2012*). Version 7 is available here (*Viovy 2011*).

Here, the GSWP3 dataset, which does not include data for particular fields over oceans, lakes, and Antarctica is modified. This missing data is filled with *Qian et al. (2006)* data from 1948 that is interpolated by the data atmosphere model to the 0.5º GSWP3 grid. This allows the model to be run over Antarctica and ensures data is available along coastlines regardless of model resolution.

The forcing data is ingested into a data atmosphere model in three "streams"; precipitation (P) (mm s^{-1}), solar radiation (S_{atm}) (W m^{-2}), and four other fields [atmospheric pressure P_{atm} (Pa), atmospheric specific humidity q_{atm} (kg kg^{-1}), atmospheric temperature T_{atm} (K), and atmospheric wind W_{atm} (m s^{-1})]. These are separate streams because they are handled differently according to the type of field. In the GSWP3 dataset, the precipitation stream is provided at three hour intervals and the data atmosphere model prescribes the same precipitation rate for each model time step within the three hour period. The four fields that are grouped together in another stream (pressure, humidity, temperature, and wind) are provided at three hour intervals and the data atmosphere model linearly interpolates these fields to the time step of the model.

The total solar radiation is also provided at three hour intervals. The data is fit to the model time step using a diurnal function that depends on the cosine of the solar zenith angle μ to provide a smoother diurnal cycle of solar radiation and to ensure that all of the solar radiation supplied by the three-hourly forcing data is actually used. The solar radiation at model time step t_M is

$$
\begin{aligned}
S_{atm}\left(t_M\right) &= \frac{\frac{\Delta t_{FD}}{\Delta t_M} S_{atm}(t_{FD})\mu(t_M)}{\sum_{i=1}^{\frac{\Delta t_{FD}}{\Delta t_M}} \mu\left(t_{M_i}\right)} && \text{for } \mu\left(t_M\right) > 0.001 \\
S_{atm}\left(t_M\right) &= 0 && \text{for } \mu\left(t_M\right) \leq 0.001
\end{aligned}
\tag{33.1}
$$

where Δt_{FD} is the time step of the forcing data (3 hours × 3600 seconds hour^{-1} = 10800 seconds), Δt_M is the model time step (seconds), $S_{atm}(t_{FD})$ is the three-hourly solar radiation from the forcing data (W m^{-2}), and $\mu(t_M)$ is the cosine of the solar zenith angle at model time step t_M (section 3.3). The term in the denominator of equation (1) is the sum of the cosine of the solar zenith angle for each model time step falling within the three hour period. For numerical purposes, $\mu(t_{M_i}) \geq 0.001$.

The total incident solar radiation S_{atm} at the model time step t_M is then split into near-infrared and visible radiation and partitioned into direct and diffuse according to factors derived from one year's worth of hourly CAM output from CAM version cam3_5_55 as

$$S_{atm} \downarrow_{vis}^{\mu} = R_{vis}(\alpha S_{atm}) \tag{33.2}$$

$$S_{atm} \downarrow_{nir}^{\mu} = R_{nir}[(1 - \alpha) S_{atm}] \tag{33.3}$$

$$S_{atm} \downarrow_{vis} = (1 - R_{vis})(\alpha S_{atm}) \tag{33.4}$$

$$S_{atm} \downarrow_{nir} = (1 - R_{nir})[(1 - \alpha) S_{atm}]. \tag{33.5}$$

where α, the ratio of visible to total incident solar radiation, is assumed to be

$$\alpha = \frac{S_{atm} \downarrow_{vis}^{\mu} + S_{atm} \downarrow_{vis}}{S_{atm}} = 0.5. \tag{33.6}$$

The ratio of direct to total incident radiation in the visible R_{vis} is

$$R_{vis} = a_0 + a_1 \times \alpha S_{atm} + a_2 \times (\alpha S_{atm})^2 + a_3 \times (\alpha S_{atm})^3 \qquad 0.01 \leq R_{vis} \leq 0.99 \tag{33.7}$$

and in the near-infrared R_{nir} is

$$R_{nir} = b_0 + b_1 \times (1 - \alpha) S_{atm} + b_2 \times [(1 - \alpha) S_{atm}]^2 + b_3 \times [(1 - \alpha) S_{atm}]^3 \qquad 0.01 \leq R_{nir} \leq 0.99 \tag{33.8}$$

where $a_0 = 0.17639$, $a_1 = 0.00380$, $a_2 = -9.0039 \times 10^{-6}$, $a_3 = 8.1351 \times 10^{-9}$ and $b_0 = 0.29548$, $b_1 = 0.00504$, $b_2 = -1.4957 \times 10^{-5}$, $b_3 = 1.4881 \times 10^{-8}$ are coefficients from polynomial fits to the CAM data.

The additional atmospheric forcing variables required by Table 2.4 are derived as follows. The atmospheric reference height z'_{atm} (m) is set to 30 m. The directional wind components are derived as $u_{atm} = v_{atm} = W_{atm}/\sqrt{2}$. The potential temperature $\overline{\theta_{atm}}$ (K) is set to the atmospheric temperature T_{atm}. The atmospheric longwave radiation $L_{atm} \downarrow$ (W m^{-2}) is derived from the atmospheric vapor pressure e_{atm} and temperature T_{atm} (*Idso 1981*) as

$$L_{atm} \downarrow = \left[0.70 + 5.95 \times 10^{-5} \times 0.01 e_{atm} \exp\left(\frac{1500}{T_{atm}}\right) \right] \sigma T_{atm}^4 \tag{33.9}$$

where

$$e_{atm} = \frac{P_{atm} q_{atm}}{0.622 + 0.378 q_{atm}} \tag{33.10}$$

and σ is the Stefan-Boltzmann constant (W m^{-2} K^{-4}) (Table 2.7). The fraction of precipitation P (mm s^{-1}) falling as rain and/or snow is

$$q_{rain} = P(f_P), \tag{33.11}$$

$$q_{snow} = P(1 - f_P) \tag{33.12}$$

where

$$f_P = 0 < 0.5(T_{atm} - T_f) < 1. \tag{33.13}$$

The aerosol deposition rates D_{sp} (14 rates as described in Table 2.4) are provided by a time-varying, globally-gridded aerosol deposition file developed by *Lamarque et al. (2010)*.

If the user wishes to provide atmospheric forcing data from another source, the data format outlined above will need to be followed with the following exceptions. The data atmosphere model will accept a user-supplied relative humidity RH (%) and derive specific humidity q_{atm} (kg kg^{-1}) from

$$q_{atm} = \frac{0.622e_{atm}}{P_{atm} - 0.378e_{atm}} \tag{33.14}$$

where the atmospheric vapor pressure e_{atm} (Pa) is derived from the water ($T_{atm} > T_f$) or ice ($T_{atm} \leq T_f$) saturation vapor pressure $e_{sat}^{T_{atm}}$ as $e_{atm} = \frac{RH}{100}e_{sat}^{T_{atm}}$ where T_f is the freezing temperature of water (K) (Table 2.7), and P_{atm} is the pressure at height z_{atm} (Pa). The data atmosphere model will also accept a user-supplied dew point temperature T_{dew} (K) and derive specific humidity q_{atm} from

$$q_{atm} = \frac{0.622e_{sat}^{T_{dew}}}{P_{atm} - 0.378e_{sat}^{T_{dew}}}. \tag{33.15}$$

Here, e_{sat}^T, the saturation vapor pressure as a function of temperature, is derived from *Lowe's (1977)* polynomials. If not provided by the user, the atmospheric pressure P_{atm} (Pa) is set equal to the standard atmospheric pressure $P_{std} = 101325$ Pa, and surface pressure P_{srf} (Pa) is set equal to P_{atm}.

The user may provide the total direct and diffuse solar radiation, $S_{atm} \downarrow^{\mu}$ and $S_{atm} \downarrow$. These will be time-interpolated using the procedure described above and then each term equally apportioned into the visible and near-infrared wavebands (e.g., $S_{atm} \downarrow_{vis}^{\mu} = 0.5 S_{atm} \downarrow^{\mu}$, $S_{atm} \downarrow_{nir}^{\mu} = 0.5 S_{atm} \downarrow^{\mu}$).

33.1 Anomaly Forcing

The 'Anomaly Forcing' atmospheric forcing mode provides a means to drive CLM with projections of future climate conditions without the need for large, high-frequency datasets. From an existing climate simulation spanning both the historical and future time periods, a set of anomalies are created by removing a climatological seasonal cycle based on the end of the historical period from each year of the future time period of the simulation. These anomalies can then be applied to a repeating high-frequency forcing dataset of finite duration (e.g. 10 years). State and flux forcing variables are adjusted using additive and multiplicative anomalies, respectively:

$$\begin{aligned} S' &= S + k_{anomaly} & \text{state variable} \\ F' &= f \times k_{anomaly} & \text{flux variable} \end{aligned} \tag{33.16}$$

where S' is the adjusted atmospheric state variable, S is the state variable from the high-frequency reference atmospheric forcing dataset, and $k_{anomaly}$ is an additive anomaly. Similarly, F' is the adjusted atmospheric flux variable, F is the flux variable from the high-frequency reference atmospheric forcing dataset, and $k_{anomaly}$ is a multiplicative anomaly. State variables are temperature T_{atm}, pressure P_{atm}, humidity q_{atm}, and wind W_{atm}. Flux variables are precipitation P, atmospheric shortwave radiation $S_{atm} \downarrow$, and atmospheric longwave radiation $L_{atm} \downarrow$.

CHAPTER 34

REFERENCES

Aber, J.D., Melillo, J.M. and McClaugherty, C.A., 1990. Predicting long-term patterns of mass loss, nitrogen dynamics, and soil organic matter formation from initial fime litter chemistry in temperate forest ecosystems. Canadian Journal of Botany, 68: 2201-2208.

Aber, J.D., Goodale, C.L., Ollinger, S.V., Smith, M.-L., Magill, A.H., Martin, M.E., Hallett, R.A., and Stoddard, J.L. 2003. Is nitrogen deposition altering the nitrogen status of northeastern forests? BioScience 53:375-389.

Ali, A. A., C. Xu, A. Rogers, R. A. Fisher, S. D. Wullschleger, E. Massoud, J. A. Vrugt, J. D. Muss, N. McDowell, and J. Fisher, 2016: A global scale mechanistic model of photosynthetic capacity (LUNA V1. 0). Geosci. Mod. Dev., 9:587-606.

Allen, C.B., Will, R.E., and Jacobson, M.A. 2005. Production efficiency and radiation use efficiency of four tree species receiving irrigation and fertilization. Forest Science 51:556-569.

Anderson, E.A. 1976. A point energy and mass balance model of a snow cover. NOAA Technical Report NWS 19, Office of Hydrology, National Weather Service, Silver Spring, MD.

André, J.-C., Goutorbe, J.-P., and Perrier, A. 1986. HAPEX-MOBILHY: A hydrologic atmosphere experiment for the study of water budget and evaporation flux at the climatic scale. Bull. Amer. Meteor. Soc. 67:138-144.

Andrén, O. and Paustian, K., 1987. Barley straw decomposition in the field: a comparison of models. Ecology 68:1190-1200.

Arah, J.R.M. and Stephen, K.D., 1998. A model of the processes leading to methane emission from peatland. Atmos. Environ. 32:3257-3264.

Arah, J. and Vinten, A., 1995. Simplified models of anoxia and denitrification in aggregated and simple-structured soils. European Journal of Soil Science 46:507-517.

Arendt, A., et al. 2012. Randolph Glacier Inventory: A Dataset of Global Glacier Outlines Version: 1.0, Global Land Ice Measurements from Space, Boulder Colorado, USA. Digital Media.

Arora, V.K. and Boer, G.J. 2005. Fire as an interactive component of dynamic vegetation models. J. Geophys. Res. 110:G02008. DOI:10.1029/2005JG000042.

Arya, S.P. 2001. Introduction to Meteorology. Academic Press, San Diego, CA.

Asner, G.P., Wessman, C.A., Schimel, D.S., and Archer, S. 1998. Variability in leaf and litter optical properties: implications for BRDF model inversions using AVHRR, MODIS, and MISR. Remote Sens. Environ. 63:243-257.

Axelsson, E., and Axelsson, B. 1986. Changes in carbon allocation patterns in spruce and pine trees following irrigation and fertilization. Tree Phys. 2:189-204.

Atkin OK, Bloomfield KJ, Reich PB, Tjoelker MG, Asner GP, Bonal D et al (2015) Global variability in leaf respiration in relation to climate, plant functional types and leaf traits. New Phytologist 206:614–636

Leaf Respiration in Terrestrial Biosphere Models. In Plant Respiration: Metabolic Fluxes and Carbon Balance, Advances in Photosynthesis and Respiration 43, G. Tcherkez, J. Ghashghaie (eds.) Springer International Publishing AG 2017

Badger, A.M., and Dirmeyer, P.A., 2015. Climate response to Amazon forest replacement by heterogeneous crop cover. Hydrol. Earth. Syst. Sci. 19:4547- 4557.

Baird, A.J., Beckwith, C.W., Waldron, S. and Waddington, J.M., 2004. Ebullition of methane-containing gas bubbles from near-surface Sphagnum peat. Geophys. Res. Lett. 31. DOI:10.1029/2004GL021157.

Baldocchi, D., et al. 2001. FLUXNET: A new tool to study the temporal and spatial variability of ecosystem-scale carbon dioxide, water vapor, and energy flux densities. Bull. Amer. Meteor. Soc. 82:2415-2433.

Barbottin, A., Lecomte, C., Bouchard, C., and Jeuffroy, M.-H. 2005. Nitrogen remobilization during grain filling in wheat: Genotypic and environmental effects. Crop Sci. 45:1141-1150.

Batjes, N.H., 2006. ISRIC-WISE derived soil properties on a 5 by 5 arc-minutes global grid. Report 2006/02 (available through : http://www.isric.org)

Berger, A.L. 1978a. Long-term variations of daily insolation and quaternary climatic changes. J. Atmos. Sci. 35:2362-2367.

Berger, A.L. 1978b. A simple algorithm to compute long-term variations of daily or monthly insolation. Contribution de l'Institut d'Astronomie et de Géophysique, Université Catholique de Louvain, Louvain-la-Neuve, No. 18.

Berger, A., Loutre, M.-F., and Tricot, C. 1993. Insolation and Earth's orbital periods. J. Geophys. Res. 98:10341-10362.

Berkowitz, B., and Balberg, I. 1992. Percolation approach to the problem of hydraulic conductivity in porous media. Transport in Porous Media 9:275–286.

Beven, K.J., and Kirkby, M.J. 1979. A physically based variable contributing area model of basin hydrology. Hydrol. Sci. Bull. 24:43-69.

Bohren, C. F., and Huffman, D. R. 1983. Absorption and scattering of light by small particles. John Wiley & Sons, New York, NY.

Bonan, G.B. 1996. A land surface model (LSM version 1.0) for ecological, hydrological, and atmospheric studies: Technical description and user's guide. NCAR Technical Note NCAR/TN-417+STR, National Center for Atmospheric Research, Boulder, CO, 150 pp.

Bonan, G.B. 1998. The land surface climatology of the NCAR Land Surface Model coupled to the NCAR Community Climate Model. J. Climate 11:1307-1326.

Bonan, G.B. 2002. Ecological Climatology: Concepts and Applications. Cambridge University Press.

Bonan, G.B., Oleson, K.W., Vertenstein, M., Levis, S., Zeng, X., Dai, Y., Dickinson, R.E., and Yang, Z.-L. 2002a. The land surface climatology of the Community Land Model coupled to the NCAR Community Climate Model. J. Climate 15: 3123-3149.

Bonan, G.B., Levis, S., Kergoat, L., and Oleson, K.W. 2002b. Landscapes as patches of plant functional types: An integrating concept for climate and ecosystem models. Global Biogeochem. Cycles 16: 5.1-5.23.

Bonan, G.B., and Levis, S. 2006. Evaluating aspects of the Community Land and Atmosphere Models (CLM3 and CAM3) using a dynamic global vegetation model. J. Climate 19:2290-2301.

Bonan, G.B., Lawrence P.J., Oleson K.W., Levis S., Jung M., Reichstein M., Lawrence, D.M., and Swenson, S.C. 2011. Improving canopy processes in the Community Land Model (CLM4) using global flux fields empirically inferred from FLUXNET data. J. Geophys. Res. 116, G02014. DOI:10.1029/2010JG001593.

Bonan, G. B., Oleson, K.W., Fisher, R.A., Lasslop, G., and Reichstein, M. 2012. Reconciling leaf physiological traits and canopy flux data: Use of the TRY and FLUXNET databases in the Community Land Model version 4, J. Geophys. Res., 117, G02026. DOI:10.1029/2011JG001913.

Bonan, G.B., Williams, M., Fisher, R.A., and Oleson, K.W. 2014. Modeling stomatal conductance in the earth system: linking leaf water-use efficiency and water transport along the soil–plant–atmosphere continuum, Geosci. Model Dev., 7, 2193-2222, doi:10.5194/gmd-7-2193-2014.

Botta, A et al., 2000. A global prognostic scheme of leaf onset using satellite data. Global Change Biology 6.7, pp. 709-725.

Brun, E. 1989. Investigation of wet-snow metamorphism in respect of liquid water content. Ann. Glaciol. 13:22-26.

Brunke, M. A., P. Broxton, J. Pelletier, D. Gochis, P. Hazenberg, D. M. Lawrence, L. R. Leung, G.-Y. Niu, P. A. Troch, and X. Zeng, 2016: Implementing and Evaluating Variable Soil Thickness in the Community Land Model, Version 4.5 (CLM4.5). J. Clim. 29:3441-3461.

Brzostek, E. R., J. B. Fisher, and R. P. Phillips, 2014. Modeling the carbon cost of plant nitrogen acquisition: Mycorrhizal trade-offs and multipath resistance uptake improve predictions of retranslocation. J. Geophys. Res. Biogeosci., 119, 1684–1697, doi:10.1002/2014JG002660.

Bugmann, H., and Solomon, A.M. 2000. Explaining forest composition and biomass across multiple biogeographical regions. Ecol. Appl. 10:95-114.

Busing, R.T. 2005. Tree mortality, canopy turnover, and woody detritus in old cove forests of the southern Appalachians. Ecology 86:73-84.

Buzan, J.R., Oleson, K., and Huber, M. 2015: Implementation and comparison of a suite of heat stress metrics within the Community Land Model version 4.5, Geosci. Model Dev., 8, 151-170, doi:10.5194/gmd-8-151-2015.

Byram, G.M., 1959. Combustion of forest fuels. In Forest fire: control and use.(Ed. KP Davis) pp. 61-89.

Campbell, G.S., and Norman, J.M. 1998. An Introduction to Environmental Biophysics (2:math:*{}^{nd}* edition). Springer-Verlag, New York.

Castillo, G., Kendra, C., Levis, S., and Thornton, P. 2012. Evaluation of the new CNDV option of the Community Land Model: effects of dynamic vegetation and interactive nitrogen on CLM4 means and variability. J. Climate 25:3702–3714.

Cao, M., Marshall, S. and Gregson, K., 1996. Global carbon exchange and methane emissions from natural wetlands: Application of a process-based model. J. Geophys. Res. 101(D9):14,399-14,414.

Chuang Y.L., Oren R., Bertozzi A.L, Phillips N., Katul G.G. 2006. The porous media model for the hydraulic system of a conifer tree: Linking sap flux data to transpiration rate, Ecological Modelling, 191, 447-468, doi:10.1016/j.ecolmodel.2005.03.027.

Churkina, G. et al., 2003. Analyzing the ecosystem carbon dynamics of four European coniferous forests using a biogeochemistry model. Ecosystems, 6: 168-184.

CIESIN: Gridded population of the world version 3 (GPWv3), 2005. Population density grids, Technical report, Socioeconomic Data and Applications Center (SEDAC), Columbia University, Palisades, New York, USA.

Clapp, R.B., and Hornberger, G.M. 1978. Empirical equations for some soil hydraulic properties. Water Resour. Res. 14:601-604.

Clauser, C., and Huenges, E. 1995. Thermal conductivity of rocks and minerals. pp. 105-126. In: T. J. Ahrens (editor) Rock Physics and Phase Relations: A Handbook of Physical Constants. Washington, D.C.

Cleveland, C.C., Townsend, A.R., Schimel, D.S., Fisher, H., Howarth, R.W., Hedin, L.O., Perakis, S.S., Latty, E.F., Von Fischer, J.C., Elseroad, A., and Wasson, M.F. 1999. Global patterns of terrestrial biological nitrogen (N2) fixation in natural ecosystems. Global Biogeochem. Cycles 13:623-645.

Collatz, G.J., Ball, J.T., Grivet, C., and Berry, J.A. 1991. Physiological and environmental regulation of stomatal conductance, photosynthesis, and transpiration: A model that includes a laminar boundary layer. Agric. For. Meteor. 54:107-136.

Collatz, G.J., Ribas-Carbo, M., and Berry, J.A. 1992. Coupled photosynthesis-stomatal conductance model for leaves of C_4 plants. Aust. J. Plant Physiol. 19:519-538.

Colmer, T.D., 2003. Long-distance transport of gases in plants: a perspective on internal aeration and radial oxygen loss from roots. Plant Cell and Environment 26:17-36.

Conway, H., Gades, A., and Raymond, C.F. 1996. Albedo of dirty snow during conditions of melt. Water Resour. Res. 32:1713-1718.

Cosby, B.J., Hornberger, G.M., Clapp, R.B., and Ginn, T.R. 1984. A statistical exploration of the relationships of soil moisture characteristics to the physical properties of soils. Water Resour. Res. 20:682-690.

Crawford, T. W., Rendig, V. V., and Broadent, F. E. 1982. Sources, fluxes, and sinks of nitrogen during early reproductive growth of maize (Zea mays L.). Plant Physiol. 70:1645-1660.

Dahlin, K., R. Fisher, and P. Lawrence, 2015: Environmental drivers of drought deciduous phenology in the Community Land Model. Biogeosciences, 12:5061-5074.

Dai, Y., and Zeng, Q. 1997. A land surface model (IAP94) for climate studies. Part I: formulation and validation in off-line experiments. Adv. Atmos. Sci. 14:433-460.

Dai, Y., et al. 2001. Common Land Model: Technical documentation and user's guide [Available online at http://climate.eas.gatech.edu/dai/clmdoc.pdf].

Dai, Y., Zeng, X., Dickinson, R.E., Baker, I., Bonan, G.B., Bosilovich, M.G., Denning, A.S., Dirmeyer, P.A., Houser, P.R., Niu, G., Oleson, K.W., Schlosser, C.A., and Yang, Z.-L. 2003. The Common Land Model. Bull. Amer. Meteor. Soc. 84:1013-1023.

Dai, Y., Dickinson, R.E., and Wang, Y.-P. 2004. A two-big-leaf model for canopy temperature, photosynthesis, and stomatal conductance. J. Climate 17:2281-2299.

Dai, A., and Trenberth, K.E. 2002. Estimates of freshwater discharge from continents: Latitudinal and seasonal variations. J. Hydrometeor. 3:660-687.

DeFries, R.S., Hansen, M.C., Townshend, J.R.G., Janetos, A.C., and Loveland, T.R. 2000. A new global 1-km dataset of percentage tree cover derived from remote sensing. Global Change Biol. 6:247-254.

Degens, B. and Sparling, G., 1996. Changes in aggregation do not correspond with changes in labile organic C fractions in soil amended with ^{14}C-glucose. Soil Biology and Biochemistry, 28(4/5): 453-462.

de Kauwe, D.A., Kala, J., Lin, Y.-S., Pitman, A.J., Medlyn, B.E., Duursma, R.A., Abramowitz, G., Wang, Y.-P., Miralles, D.G. 2015. A test of an optimal stomatal conductance scheme within the CABLE land surface model. Geosci. Model Dev. 8(2):431-452.

de Vries, D.A. 1963. Thermal Properties of Soils. In: W.R. van Wijk (editor) Physics of the Plant Environment. North-Holland, Amsterdam.

Dickinson, R.E. 1983. Land surface processes and climate-surface albedos and energy balance. Adv. Geophys. 25:305-353.

Dickinson, R.E., Henderson-Sellers, A., and Kennedy, P.J. 1993. Biosphere-Atmosphere Transfer Scheme (BATS) version 1e as coupled to the NCAR Community Climate Model. NCAR Technical Note NCAR/TN-387+STR. National Center for Atmospheric Research, Boulder, CO.

Dickinson, R.E., Oleson, K.W., Bonan, G., Hoffman, F., Thornton, P., Vertenstein, M., Yang, Z.-L., and Zeng, X. 2006. The Community Land Model and its climate statistics as a component of the Community Climate System Model. J. Climate 19:2302-2324.

Dingman, S.L. 2002. Physical Hydrology. Second Edition. Prentice Hall, NJ.

Dirmeyer, P.A., Dolman, A.J., and Sato, N. 1999. The pilot phase of the Global Soil Wetness Project. Bull. Amer. Meteor. Soc. 80:851-878.

Dobson, J.E., Bright, E.A., Coleman, P.R., Durfee, R.C., and Worley, B.A. 2000. LandScan: A global population database for estimating populations at risk. Photogramm. Eng. Rem. Sens. 66:849-857.

Dorman, J.L., and Sellers, P.J. 1989. A global climatology of albedo, roughness length and stomatal resistance for atmospheric general circulation models as represented by the simple biosphere model (SiB). J. Appl. Meteor. 28:833-855.

Dougherty, R.L., Bradford, J.A., Coyne, P.I., and Sims, P.L. 1994. Applying an empirical model of stomatal conductance to three C4 grasses. Agric. For. Meteor. 67:269-290.

Drewniak, B., Song, J., Prell, J., Kotamarthi, V.R., and Jacob, R. 2013. Modeling agriculture in the Community Land Model. Geosci. Model Dev. 6:495-515. DOI:10.5194/gmd-6-495-2013.

Dunfield, P., Knowles, R., Dumont, R. and Moore, T.R., 1993. Methane Production and Consumption in Temperate and Sub-Arctic Peat Soils - Response to Temperature and Ph. Soil Biology & Biochemistry 25:321-326.

Entekhabi, D., and Eagleson, P.S. 1989. Land surface hydrology parameterization for atmospheric general circulation models including subgrid scale spatial variability. J. Climate 2:816-831.

Fang, X. and Stefan, H.G., 1996. Long-term lake water temperature and ice cover simulations/measurements. Cold Regions Science and Technology 24:289-304.

Farouki, O.T. 1981. The thermal properties of soils in cold regions. Cold Regions Sci. and Tech. 5:67-75.

Farquhar, G.D., von Caemmerer, S., and Berry, J.A. 1980. A biochemical model of photosynthetic CO_2 assimilation in leaves of C_3 species. Planta 149:78-90.

Farquhar, G.D., and von Caemmerer, S. 1982. Modeling of photosynthetic response to environmental conditions. pp. 549-587. In: O.L. Lange, P.S. Nobel, C.B. Osmond, and H. Zeigler (editors) Encyclopedia of Plant Physiology. Vol. 12B. Physiological Plant Ecology. II. Water Relations and Carbon Assimilation. Springer-Verlag, New York.

Feddema, J., Kauffman, B. 2016. Urban Properties Tool (Version 1.2). NCAR THESIS Tools Library. Retrieved from: https://svn-iam-thesis-release.cgd.ucar.edu/urban_properties/. doi:10.5065/D6R78CMT.

Ferrari, J.B., 1999. Fine-scale patterns of leaf litterfall and nitrogen cycling in an old-growth forest. Canadian Journal of Forest Research, 29: 291-302.

Firestone, M.K. and Davidson, E.A. 1989. Exchange of Trace Gases between Terrestrial Ecosystems and the Atmosphere. In: M.O. Andreae and D.S. Schimel (Editors). John Wiley and Sons, pp. 7-21.

Fisher, J. B., S. Sitch, Y. Malhi, R. A. Fisher, C. Huntingford, and S.-Y. Tan, 2010. Carbon cost of plant nitrogen acquisition: A mechanistic, globally applicable model of plant nitrogen uptake, retranslocation, and fixation. Global Biogeochem. Cycles, 24, GB1014, doi:10.1029/2009GB003621.

Fisher, R. A., S. Muszala, M. Verteinstein, P. Lawrence, C. Xu, N. G. McDowell, R. G. Knox, C. Koven, J. Holm, B. M. Rogers, A. Spessa, D. Lawrence, and G. Bonan, 2015: Taking off the training wheels: the properties of a dynamic vegetation model without climate envelopes, CLM4.5(ED). Geosci. Model Dev., 8: 3593-3619, doi:10.5194/gmd-8-3593-2015.

Fisher, R.A., C.D. Koven, W.R.L. Anderegg, et al., 2018: Vegetation demographics in Earth System Models: A review of progress and priorities. Glob Change Biol. 2018;24:35–54. https://doi.org/10.1111/gcb.13910

Flanner, M.G., and Zender. C.S. 2005. Snowpack radiative heating: Influence on Tibetan Plateau climate. Geophys. Res. Lett. 32:L06501. DOI:10.1029/2004GL022076.

Flanner, M.G., and Zender, C.S. 2006. Linking snowpack microphysics and albedo evolution. J. Geophys. Res. 111:D12208. DOI:10.1029/2005JD006834.

Flanner, M.G., Zender, C.S., Randerson, J.T., and Rasch, P.J. 2007. Present day climate forcing and response from black carbon in snow. J. Geophys. Res. 112:D11202. DOI:10.1029/2006JD008003.

Flatau, P.J., Walko, R.L., and Cotton, W.R. 1992. Polynomial fits to saturation vapor pressure. J. Appl. Meteor. 31:1507-1513.

Foley, J.A. et al., 1996. An integrated biosphere model of land surface processes, terrestrial carbon balance, and vegetation dynamics. Global Biogeochemical Cycles 10.4, pp. 603-628.

Friedl, M.A., McIver, D.K., Hodges, J.C.F., Zhang, X.Y., Muchoney, D., Strahler, A.H., Woodcock, C.E., Gopal, S., Schneider, A., Cooper, A., Baccini, A., Gao, F., and Schaaf, C. 2002. Global land cover mapping from MODIS: algorithms and early results. Remote Sens. Environ. 83:287-302.

Frolking, S., et al. 2001. Modeling Northern Peatland Decomposition and Peat Accumulation. Ecosystems. 4:479-498.

Fyllas, N.M. et al., 2014. Analysing Amazonian forest productivity using a new individual and trait- based model (TFS v. 1). Geoscientific Model Development 7.4, pp. 1251-1269.

Gallais, A., Coque, M. Quillere, I., Prioul, J., and Hirel, B. 2006. Modeling postsilking nitrogen fluxes in maize (Zea mays) using 15N-labeling field experiments. New Phytologist 172:696-707.

Gallais, A., Coque, M., Gouis, J. L., Prioul, J. L., Hirel, B., and Quillere, I. 2007. Estimating the proportion of nitrogen remobilization and of postsilking nitrogen uptake allocated to maize kernels by Nitrogen-15 labeling. Crop Sci. 47:685-693.

Galloway, J.N., et al. 2004. Nitrogen cycles: past, present, and future. Biogeochem. 70:153-226.

Garcia, R.L., Kanemasu, E.T., Blad, B.L., Bauer, A., Hatfield, J.L., Major, D.A., Reginato, R.J., and Hubbard, K.G. 1988. Interception and use efficiency of light in winter wheat under different nitrogen regimes. Agric. For. Meteor. 44:175-186.

Gardner, W. R. 1960. Dynamic aspects of water availability to plants, Soil Sci., 89, 63–73.

Gash, J.H.C., Nobre, C.A., Roberts, J.M., and Victoria, R.L. 1996. An overview of ABRACOS. pp. 1-14. In: J.H.C. Gash, C.A. Nobre, J.M. Roberts, and R.L. Victoria (editors) Amazonian Deforestation and Climate. John Wiley and Sons, Chichester, England.

Getirana, A. C. V., A. Boone, D. Yamazaki, B. Decharme, F. Papa, and N. Mognard. 2012. The hydrological modeling and analysis platform (HyMAP): Evaluation in the Amazon basin, J. Hydrometeorol., 13, 1641-1665.

Ghimire, B., W. J. Riley, C. D. Koven, M. Mu, and J. T. Randerson, 2016: Representing leaf and root physiological traits in CLM improves global carbon and nitrogen cycling predictions. J. Adv. Mod. Earth Sys. 8: 598-613.

Gholz, H.L., Perry, C.S., Cropper, W.P., Jr. and Hendry, L.C., 1985. Litterfall, decomposition, and nitrogen and phosphorous dynamics in a chronosequence of slash pine (*Pinus elliottii*) plantations. Forest Science, 31: 463-478.

Giglio, L., Csiszar, I., and Justice, C.O. 2006. Global distribution and seasonality of active fires as observed with the Terra and Aqua Moderate Resolution Imaging Spectroradiometer (MODIS) sensors. J. Geophys. Res. 111:G02016. DOI:10.1029/2005JG000142.

Global Soil Data Task 2000. Global soil data products CD-ROM (IGBP-DIS). International Geosphere-Biosphere Programme-Data and Information Available Services [Available online at http://www.daac.ornl.gov].

Gomes, E.P.C., Mantovani, W., and Kageyama, P.Y. 2003. Mortality and recruitment of trees in a secondary montane rain forest in southeastern Brazil. Brazilian Journal of Biology 63:47-60.

Gosz, J.R., Likens, G.E., and Bormann, F.H. 1973. Nutrient release from decomposing leaf and branch litter in the Hubbard Brook Forest, New Hampshire. Ecological Monographs 43:173-191.

Gotangco Castillo C., Levis S., and Thornton P. 2012. Evaluation of the new CNDV option of the Community Land Model: Effects of dynamic vegetation and interactive nitrogen on CLM4 means and variability. J. Climate 25:3702-3714. DOI:10.1175/JCLID-11-00372.1.

Graham, S.T., Famiglietti, J.S., and Maidment, D.R. 1999. Five-minute, 1/2°, and 1° data sets of continental watersheds and river networks for use in regional and global hydrologic and climate system modeling studies. Water Resour. Res. 35:583-587.

Graven, H., C. E. Allison, D. M. Etheridge, S. Hammer, R. F. Keeling, I. Levin, H. A. J. Meijer, M. Rubino, P. P. Tans, C. M. Trudinger, B. H. Vaughn and J. W. C. White, 2017. Compiled records of carbon isotopes in atmospheric CO2 for historical simulations in CMIP6, Geoscientific Model Development, in review. doi: 10.5194/gmd-2017-166.

Grenfell, T.C., and Warren, S.G. 1999. Representation of a nonspherical ice particle by a collection of independent spheres for scattering and absorption of radiation. J. Geophys. Res. 104(D24):37697-37709.

del Grosso, S.J., et al. 2000. General model for N2O and N2 gas emissions from soils due to dentrification. Global Biogeochem. Cycles 14:1045-1060.

Guenther, A., Hewitt, C.N., Erickson, D., Fall, R., Geron, C., Graedel, T., Harley, P., Klinger, L., Lerdau, M., McKay, W.A., Pierce, T., Scholes, B., Steinbrecher, R., Tallamraju, R., Taylor, J., and Zimmerman, P. 1995. A global model of natural volatile organic compound emissions. J. Geophys. Res. 100:8873-8892.

Guenther, A., Karl, T., Harley, P., Wiedinmyer, C., Palmer. P.I., and Geron, C. 2006. Estimates of global terrestrial isoprene emissions using MEGAN (Model of Emissions of Gases and Aerosols from Nature). Atmos. Chem. Phys. 6:3181–3210.

Guenther, A. B., Jiang, X., Heald, C. L., Sakulyanontvittaya, T., Duhl, T., Emmons, L. K., & Wang, X., 2012. The Model of Emissions of Gases and Aerosols from Nature version 2.1 (MEGAN2.1): an extended and updated framework for modeling biogenic emissions, Geosci. Model Dev., 5, 1471–1492. DOI:10.5194.

Hack, J.J., Caron, J.M., Yeager, S.G., Oleson, K.W., Holland, M.M., Truesdale, J.E., and Rasch, P.J. 2006. Simulation of the global hydrological cycle in the CCSM Community Atmosphere Model version 3 (CAM3): mean features. J. Climate 19:2199-2221.

Hansen, M., DeFries, R.S., Townshend, J.R.G., Carroll, M., Dimiceli, C., and Sohlberg, R.A. 2003. Global percent tree cover at a spatial resolution of 500 meters: first results of the MODIS vegetation continuous fields algorithm. Earth Interactions 7:1-15.

Hastings, D.A., Dunbar, P.K., Elphingstone, G.M., Bootz, M., Murakami, H., Maruyama, H., Masaharu, H., Holland, P., Payne, J., Bryant, N.A., Logan, T.L., Muller, J.-P., Schreier, G., and MacDonald, J.S., eds., 1999. The Global Land One-kilometer Base Elevation (GLOBE) Digital Elevation Model, Version 1.0. National Oceanic and Atmospheric Administration, National Geophysical Data Center, 325 Broadway, Boulder, Colorado 80305-3328, U.S.A.

Heald, C.L., Henze, D.K., Horowitz, L.W., Feddema, J., Lamarque, J.-F., Guenther, A., Hess, P.G., Vitt, F., Seinfeld, J.H., Goldstein, A.H., and Fung, I. 2008. Predicted change in global secondary organic aerosol concentrations in response to future climate, emissions, and land use change. J. Geophys. Res. 113:D05211. DOI:10.1029/2007JD009092.

Heald, C.L., Wilkinson, M.J., Monson, R.K., Alo, C.A., Wang, G.L., and Guenther, A. 2009. Response of isoprene emission to ambient CO_2 changes and implications for global budgets. Global Change Biol. 15:1127-1140. DOI:10.1111/j.1365-2486.2008.01802.x

Henderson-Sellers, B. 1985. New formulation of eddy diffusion thermocline models. Appl. Math. Modelling 9:441-446.

Henderson-Sellers, B. 1986. Calculating the surface energy balance for lake and reservoir modeling: A review. Rev. Geophys. 24:625-649.

Henderson-Sellers, A., Yang, Z.-L., and Dickinson, R.E. 1993. The project for intercomparison of land-surface parameterization schemes. Bull. Amer. Meteor. Soc. 74: 1335-1349.

Hostetler, S.W., and Bartlein, P.J. 1990. Simulation of lake evaporation with application to modeling lake level variations of Harney-Malheur Lake, Oregon. Water Resour. Res. 26:2603-2612.

Hostetler, S.W., Bates, G.T., and Giorgi, F. 1993. Interactive coupling of a lake thermal model with a regional climate model. J. Geophys. Res. 98:5045-5057.

Hostetler, S.W., Giorgi, F., Bates, G.T., and Bartlein, P.J. 1994. Lake-atmosphere feedbacks associated with paleolakes Bonneville and Lahontan. Science 263:665-668.

Hou, Z., Huang, M., Leung, L.R., Lin, G., and Ricciuto, D.M. 2012. Sensitivity of surface flux simulations to hydrologic parameters based on an uncertainty quantification framework applied to the Community Land Model. J. Geophys. Res. 117:D15108.

Houlton, B.Z., Wang, Y.P., Vitousek, P.M. and Field, C.B., 2008. A unifying framework for dinitrogen fixation in the terrestrial biosphere. Nature, 454(7202), p.327.

Huang, M., and Liang, X. 2006. On the assessment of the impact of reducing parameters and identification of parameter uncertainties for a hydrologic model with applications to ungauged basins. J. Hydrol. 320:37-61.

Hugelius, G., C. Tarnocai, G. Broll, J.G. Canadell, P. Kuhry, adn D.K. Swanson, 2012. The Northern Circumpolar Soil Carbon Database: spatially distributed datasets of soil coverage and soil carbon storage in the northern permafrost regions. Earth Syst. Sci. Data Discuss., 5, 707-733 (available online at (http://dev1.geo.su.se/bbcc/dev/ncscd/).

Hunt, H.W., Ingham, E.R., Coleman, D.C., Elliott, E.T., and Reid, C.P.P. 1988. Nitrogen limitation of production and decomposition in prairie, mountain meadow, and pine forest. Ecology 69:1009-1016.

Hunt, E.R., Jr. and Running, S.W., 1992. Simulated dry matter yields for aspen and spruce stands in the north american boreal forest. Canadian Journal of Remote Sensing, 18: 126-133.

Hunt, E.R., Jr. et al., 1996. Global net carbon exchange and intra-annual atmospheric CO_2 concentrations predicted by an ecosystem process model and three-dimensional atmospheric transport model. Global Biogeochemical Cycles, 10: 431-456.

Hurtt, G.C., Frolking, S., Fearon, M.G., Moore, B., Shevliakova, E., Malyshev, S., Pacala, S.W., and Houghton, R.A. 2006. The underpinnings of land-use history: three centuries of global gridded land-use transitions, wood-harvest activity, and resulting secondary lands. Global Change Biol. 12:1208-1229.

Hurtt, G.C., et al. 2011. Harmonization of land-use scenarios for the period 1500-2100: 600 years of global gridded annual land-use transitions, wood harvest, and resulting secondary lands. Climatic Change 109:117-161. DOI:10.1007/s10584-011-0153-2.

Idso, S.B. 1981. A set of equations for full spectrum and 8- to 14-μ m and 10.5- to 12.5-μ m thermal radiation from cloudless skies. Water Resour. Res. 17:295-304.

Iiyama, I. and Hasegawa, S., 2005. Gas diffusion coefficient of undisturbed peat soils. Soil Science and Plant Nutrition 51:431-435.

Jacksonetal1996: E., and Schulze, E. D. 1996. A global analysis of root distributions for terrestrial biomes Oecologia 108:389–411. DOI:10.1007/BF00333714.

Jackson, T.L., Feddema, J.J., Oleson, K.W., Bonan, G.B., and Bauer, J.T. 2010. Parameterization of urban characteristics for global climate modeling. Annals of the Association of American Geographers. 100:848-865.

Jenkinson, D. and Coleman, K. 2008. The turnover of organic carbon in subsoils. Part 2. Modelling carbon turnover. European Journal of Soil Science 59:400-413.

Jordan, R. 1991. A One-dimensional Temperature Model for a Snow Cover: Technical Documentation for SNTHERM.89. U.S. Army Cold Regions Research and Engineering Laboratory, Special Report 91-16.

Kattge, J., and Knorr, W. 2007. Temperature acclimation in a biochemical model of photosynthesis: a reanalysis of data from 36 species. Plant Cell Environ. 30:1176-1190. DOI:10.1111/j.1365-3040.2007.01690.x.

Kattge, J., Knorr, W., Raddatz, T., and Wirth C. 2009: Quantifying photosynthetic capacity and its relationship to leaf nitrogen content for global–scale terrestrial biosphere models. Global Change Biol. 15:976–991.

Kavetski, D., Binning, P. and Sloan, S.W., 2002. Noniterative time stepping schemes with adaptive truncation error control for the solution of Richards equation. Water Resources Research, 38(10).

Keller, M., Palace, M., Asner, G.P., Pereira, R., Jr. and Silva, J.N.M., 2004. Coarse woody debris in undisturbed and logged forests in the eastern Brazilian Amazon. Global Change Biology, 10: 784-795.

Kellner, E., Baird, A.J., Oosterwoud, M., Harrison, K. and Waddington, J.M., 2006. Effect of temperature and atmospheric pressure on methane (CH4) ebullition from near-surface peats. Geophys. Res. Lett. 33. DOI:10.1029/2006GL027509.

Kimball, J.S., Thornton, P.E., White, M.A. and Running, S.W. 1997. Simulating forest productivity and surface-atmosphere exchange in the BOREAS study region. Tree Physiology 17:589-599.

Kohyama, T., Suzuki, E., Partomihardjo, T., and Yamada, T. 2001. Dynamic steady state of patch-mosaic tree size structure of a mixed diptocarp forest regulated by local crowding. Ecological Research 16:85-98.

Kourzeneva, E., 2009. Global dataset for the parameterization of lakes in Numerical Weather Prediction and Climate modeling. ALADIN Newsletter, No 37, July-December, 2009, F. Bouttier and C. Fischer, Eds., Meteo-France, Toulouse, France, 46-53.

Kourzeneva, E., 2010: External data for lake parameterization in Numerical Weather Prediction and climate modeling. Boreal Environment Research, 15, 165-177.

Kourzeneva, E., Asensio, H., Martin, E. and Faroux, S., 2012. Global gridded dataset of lake coverage and lake depth for use in numerical weather prediction and climate modelling. Tellus A 64.

Koven, C., et al. 2009. On the formation of high-latitude soil carbon stocks: The effects of cryoturbation and insulation by organic matter in a land surface model. Geophys. Res. Lett. 36: L21501.

Koven, C.D., et al. 2011. Permafrost carbon-climate feedbacks accelerate global warming. Proceedings of the National Academy of Sciences 108:14769-14774.

Koven, C.D. et al. 2013. The effect of vertically-resolved soil biogeochemistry and alternate soil C and N models on C dynamics of CLM4. Biogeosciences Discussions 10:7201-7256.

Koven, C.D. et al. 2015. Permafrost carbon-climate feedback is sensitive to deep soil carbon decomposability but not deep soil nitrogen dynamics. Proceedings of the National Academies of Science, 112, 12, 3752-3757, doi:10.1073/pnas.1415123112

Koven, C.D., G. Hugelius, D.M. Lawrence, and W.R. Wieder, 2017: Higher climatological temperature sensitivity of soil carbon in cold than warm climates. Nature Clim. Change, 7, doi:10.1038/nclimate3421.

Kucharik, C.J., J.M. Norman, and S.T. Gower, 1998. Measurements of branch area and adjusting leaf area index indirect measurements. Agricultural and Forest Meteorology 91.1, pp. 69-88.

Kucharik, C.J., Foley, J.A., Delire, C., Fisher, V.A., Coe, M.T., Lenters, J.D., Young-Molling, C., and Ramankutty, N. 2000. Testing the performance of a dynamic global ecosystem model: water balance, carbon balance, and vegetation structure. Global Biogeochem. Cycles 14: 795–825.

Kucharik, C.J., and Brye, K.R. 2003. Integrated BIosphere Simulator (IBIS) yield and nitrate loss predictions for Wisconsin maize receiving varied amounts of nitrogen fertilizer. Journal of Environmental Quality 32: 247–268.

Ladd, J.N., Jocteur-Monrozier, L. and Amato, M., 1992. Carbon turnover and nitrogen transformations in an alfisol and vertisol amended with [U-^{14}C] glucose and [^{15}N] ammonium sulfate. Soil Biology and Biochemistry, 24: 359-371.

Lamarque, J.-F., et al. 2010. Historical (1850-2000) gridded anthropogenic and biomass burning emissions of reactive gases and aerosols: methodology and application. Atmos. Chem. Phys. Discuss. 10:4963-5019. DOI:10.5194/acpd-10-4963-2010.

Larcher, W. 1995. Physiological Plant Ecology, Springer-Verlag, Berlin Heidelberg.

Lavigne, M.B., and Ryan, M.G. 1997. Growth and maintenance respiration rates of aspen, black spruce, and jack pine stems at northern and southern BOREAS sites. Tree Phys. 17:543-551.

Law, B.E., Sun, O.J., Campbell, J., Van Tuyl, S. and Thornton, P.E. 2003. Changes in carbon storage and fluxes in a chronosequence of ponderosa pine. Global Change Biology, 9: 510-514.

Lawrence, D.M., Thornton, P.E., Oleson, K.W., and Bonan, G.B. 2007. The partitioning of evapotranspiration into transpiration, soil evaporation, and canopy evaporation in a GCM: Impacts on land-atmosphere interaction. J. Hydrometeor. 8:862-880.

Lawrence, D.M., and Slater, A.G. 2008. Incorporating organic soil into a global climate model. Clim. Dyn. 30. DOI:10.1007/s00382-007-0278-1.

Lawrence, D.M., Slater, A.G., Romanovsky, V.E., and Nicolsky, D.J. 2008. The sensitivity of a model projection of near-surface permafrost degradation to soil column depth and inclusion of soil organic matter. J. Geophys. Res. 113:F02011. DOI:10.1029/2007JF000883.

Lawrence, D.M., K.W. Oleson, M.G. Flanner, P.E. Thornton, S.C. Swenson, P.J. Lawrence, X. Zeng, Z.-L. Yang, S. Levis, K. Sakaguchi, G.B. Bonan, and A.G. Slater, 2011. Parameterization improvements and functional and structural advances in version 4 of the Community Land Model. J. Adv. Model. Earth Sys. 3. DOI:10.1029/2011MS000045.

Lawrence, D.M., Hurtt, G.C., Arneth, A., Brovkin, V., Calvin, K.V., Jones, A.D., Jones, C.D., Lawrence, P.J., de Noblet-Ducoudré, N., Pongratz, J., Seneviratne, S.I., and Shevliakova, E. 2016. The Land Use Model Intercomparison Project (LUMIP) contribution to CMIP6: rationale and experimental design. Geosci. Model Dev. 9:2973-2998. DOI:10.5194/gmd-9-2973-2016.

Lawrence, P.J., and Chase, T.N. 2007. Representing a MODIS consistent land surface in the Community Land Model (CLM 3.0). J. Geophys. Res. 112:G01023. DOI:10.1029/2006JG000168.

Lawrence, P.J., and Chase, T.N. 2010. Investigating the climate impacts of global land cover change in the Community Climate System Model. Int. J. Climatol. 30:2066-2087. DOI:10.1002/joc.2061.

Lawrence, P.J., et al. 2012. Simulating the biogeochemical and biogeophysical impacts of transient land cover change and wood harvest in the Community Climate System Model (CCSM4) from 1850 to 2100. J. Climate 25:3071-3095. DOI:10.1175/JCLI-D-11-00256.1.

Lehner, B. and Döll, P., 2004. Development and validation of a global database of lakes, reservoirs and wetlands, J. Hydrol., 296, 1–22.

Lehner, B., Verdin, K. and Jarvis, A., 2008. New global hydrograhy derived from spaceborne elevation data. Eos Trans., AGU, 89, 93 – 94.

Le Page, Y., van der Werf, G.R., Morton, D.C., and Pereira, J.M.C. 2010. Modeling fire-driven deforestation potential in Amazonia under current and projected climate conditions. J. Geophys. Res. 115:G03012. DOI:10.1029/2009JG001190.

Lerman, A., 1979. Geochemical processes: Water and sediment environments. John Wiley and Sons, New York, N.Y.

Letts, M.G., Roulet, N.T., Comer, N.T., Skarupa, M.R., and Verseghy, D.L. 2000. Parametrization of peatland hydraulic properties for the Canadian Land Surface Scheme. Atmos.-Ocean 38:141-160.

Levis, S., Wiedinmyer, C., Bonan, G.B., and Guenther, A. 2003. Simulating biogenic volatile organic compound emissions in the Community Climate System Model. J. Geophys. Res. 108:4659. DOI:10.1029/2002JD003203.

Levis, S., Bonan, G.B., Vertenstein, M., and Oleson, K.W. 2004. The community land model's dynamic global vegetation model (CLM-DGVM): technical description and user's guide. NCAR Technical Note NCAR/TN-459+STR. National Center for Atmospheric Research, Boulder, Colorado. 50 pp.

Levis, S., Thornton, P., Bonan, G., and Kucharik, C. 2009. Modeling land use and land management with the Community Land Model. iLeaps newsletter, No. 7.

Levis, S., Bonan, G., Kluzek, E., Thornton, P., Jones, A., Sacks, W., and Kucharik, C 2012. Interactive crop management in the Community Earth System Model (CESM1): Seasonal influences on land-atmosphere fluxes. J. Climate 25: 4839-4859. DOI:10.1175/JCLI-D-11-00446.1.

Levis, S., Badger, A., Drewniak, B., Nevison, C., Ren, X. 2016. CLMcrop yields and water requirements: avoided impacts by choosing RCP 4.5 over 8.5. Climatic Change. DOI:10.1007/s10584-016-1654-9.

Li, C., Aber, J., Stange, F., Butterbach-Bahl, K. and Papen, H. 2000. A process-oriented model of N2O and NO emissions from forest soils: 1. Model development. J. Geophys. Res. 105(D4):4369-4384.

Li, F., Zeng, X.-D., and Levis, S. 2012a. A process-based fire parameterization of intermediate complexity in a Dynamic Global Vegetation Model. Biogeosciences 9:2761-2780.

Li, F., Zeng, X. D., and Levis, S. 2012b. Corrigendum to "A process-based fire parameterization of intermediate complexity in a Dynamic Global Vegetation Model" published in Biogeosciences, 9, 2761–2780, 2012". Biogeosciences 9: 4771-4772.

Li, F., Levis, S., and Ward, D. S. 2013a. Quantifying the role of fire in the Earth system – Part 1: Improved global fire modeling in the Community Earth System Model (CESM1). Biogeosciences 10:2293-2314.

Li, F., and Lawrence, D. 2017. Role of fire in the global land water budget during the 20th century through changing ecosystems. J. Clim. 30: 1894-1908.

Li, H.-Y., Huang, M., Tesfa, T., Ke, Y., Sun, Y., Liu, Y., and Leung, L. R. 2013b. A subbasin-based framework to represent land surface processes in an Earth System Model, Geosci. Model Dev. Discuss. 6:2699-2730. DOI:10.5194/gmdd-6-2699-2013.

Li, H., Huang, M., Wigmosta, M.S., Ke, Y., Coleman, A.M., Leung, L.R., Wang, A., and Ricciuto, D.M. 2011. Evaluating runoff simulations from the Community Land Model 4.0 using observations from flux towers and a mountainous watershed. J. Geophys. Res. 116:D24120. DOI:10.1029/2011JD016276.

Li, H., L. Leung, A. Getirana, M. Huang, H. Wu, Y. Xu, J. Guo and N. Voisin. 2015a. Evaluating global streamflow simulations by a physically-based routing model coupled with the Community Land Model, J. of Hydromet., 16(2):948-971, doi: 10.1175/JHM-D-14-0079.1

Li, H., L. Leung, T. Tesfa, N. Voisin, M. Hejazi, L. Liu, Y. Liu, J. Rice, H. Wu, and X. Yang. 2015. Modeling stream temperature in the Anthropocene: An earth system modeling approach, J. Adv. Model. Earth Syst., 7, doi:10.1002/2015MS000471.

Liang, X., Lettenmaier, D.P., Wood, E.F., and Burges, S.J. 1994. A simple hydrologically based model of land surface water and energy fluxes for GSMs. J. Geophys. Res. 99(D7):14,415–14,428.

Lichstein, J.W. and S.W. Pacala, 2011. Local diversity in heterogeneous landscapes: quantitative assessment with a height-structured forest metacommunity model'. Theoretical Ecology 4.2, pp. 269-281.

Lipscomb, W., and Sacks, W. 2012. The CESM land ice model documentation and user's guide. 46 pp. [Available online at http://www.cesm.ucar.edu/models/cesm1.1/cism/].

Lischke, H. et al., 2006. TreeMig: a forest-landscape model for simulating spatio-temporal patterns from stand to landscape scale. Ecological Modelling 199.4, pp. 409-420. 41

Lloyd, J. and Taylor, J.A., 1994. On the temperature dependence of soil respiration. Functional Ecology, 8: 315-323.

Lloyd, J., et al. 2010. Optimisation of photosynthetic carbon gain and within-canopy gradients of associated foliar traits for Amazon forest trees. Biogeosci. 7:1833-1859. DOI:10.5194/bg-7-1833-2010.

Lobell, D.B., Bala, G., and Duffy, P.B. 2006. Biogeophysical impacts of cropland management changes on climate. Geophys. Res. Lett. 33:L06708. DOI:10.1029/2005GL025492.

Lombardozzi, D.L., Bonan, G.B., Smith, N.G., Dukes, J.S. 2015. Temperature acclimation of photosynthesis and respiration: A key uncertainty in the carbon cycle-climate feedback. Geophys. Res. Lett. 42:8624-8631.

Loveland, T.R., Reed, B.C., Brown, J.F., Ohlen, D.O., Zhu, Z., Yang, L., and Merchant, J.W. 2000. Development of a global land cover characteristics database and IGBP DISCover from 1 km AVHRR data. Int. J. Remote Sens. 21:1303-1330.

Lowe, P.R. 1977. An approximating polynomial for the computation of saturation vapor pressure. J. Appl. Meteor. 16:100-103.

Luo, Y., Hui, D., and Zhang, D. 2006. Elevated CO2 stimulates net accumulations of carbon and nitrogen in land ecosystems: a meta-analysis. Ecology 87:53-63.

Magill, A.H. et al., 1997. Biogeochemical response of forest ecosystems to simulated chronic nitrogen deposition. Ecological Applications, 7: 402-415.

Mahowald, N.M., Muhs, D.R., Levis, S., Rasch, P.J., Yoshioka, M., Zender, C.S., and Luo, C. 2006. Change in atmospheric mineral aerosols in response to climate: last glacial period, pre-industrial, modern and doubled CO_2 climates. J. Geophys. Res. 111:D10202. DOI:10.1029/2005JD006653.

Makela, A. 2002. Derivation of stem taper from the pipe model theory in a carbon balance framework. Tree Phys. 22:891-905.

Mao, J., Thornton, P.E., Shi, X., Zhao, M., and Post, W.M. 2012. Remote sensing evaluation of CLM4 GPP for the period 2000 to 2009. J. Climate 25:5327-5342.

Mao, J., Shi, X., Thornton, P.E., Hoffman, F.M., Zhu, Z., and Ranga B. Myneni, R.B. 2013. Global latitudinal-asymmetric vegetation growth trends and their driving mechanisms: 1982-2009. Remote Sensing 5:1484-1497.

Martin, J.P., Haider, K. and Kassim, G., 1980. Biodegradation and stabilization after 2 years of specific crop, lignin, and polysaccharide carbons in soils. Soil Science Society of America Journal 44:1250-1255.

Mary, B., Fresneau, C., Morel, J.L. and Mariotti, A., 1993. C and N cycling during decomposition of root mucilage, roots and glucose in soil. Soil Biology and Biochemistry 25:1005-1014.

McDowell, N.G. et al., 2013. Evaluating theories of drought-induced vegetation mortality using a multimodel experiment framework. New Phytologist 200.2, pp. 304-321.

McGuire, A.D., Melillo, J.M., Joyce, L.A., Kicklighter, D.W., Grace, A.L., Moore III, B., and Vorosmarty, C.J. 1992. Interactions between carbon and nitrogen dynamics in estimating net primary productivity for potential vegetation in North America. Global Biogeochem. Cycles 6:101-124.

Medlyn, B.E., Duursma, R.A., Eamus, D., Ellsworth, D.S., Prentice, I.C., Barton, C.V.M., Crous, K.Y., De Angelis, P., Freeman, M., and Wingate, L., 2011. Reconciling the optimal and empirical approaches to modelling stomatal conductance. Global Change Biology, 17: 2134–2144. doi:10.1111/j.1365-2486.2010.02375.x

Melzer, E., and O'Leary, M.H. 1987. Anapleurotic CO2 Fixation by Phosphoenolpyruvate Carboxylase in C3 Plants. Plant. Physiol. 84:58.

Miller, J.R., Russell, G.L., and Caliri, G. 1994. Continental-scale river flow in climate models. J. Climate 7:914-928.

Millington, R. and Quirk, J.P., 1961. Permeability of Porous Solids. Transactions of the Faraday Society 57:1200-1207.

Mironov, D. et al., 2010. Implementation of the lake parameterisation scheme FLake into the numerical weather prediction model COSMO. Boreal Environment Research 15:218-230.

Mitchell, T.D., and Jones, P.D. 2005. An improved method of constructing a database of monthly climate observations and associated high-resolution grids. Int. J. Climatol. 25:693-712.

Moldrup, P. et al. 2003. Modeling diffusion and reaction in soils: X. A unifying model for solute and gas diffusivity in unsaturated soil. Soil Science 168:321-337.

Moorcroft, P.R., G.C. Hurtt, and S.W. Pacala, 2001. A method for scaling vegetation dynamics: the ecosystem demography model ED. Ecological monographs 71.4, pp. 557-586.

Myneni, R.B., et al. 2002. Global products of vegetation leaf area and fraction absorbed PAR from year one of MODIS data. Remote Sens. Environ. 83:214-231.

Neff, J.C., Harden, J.W. and Gleixner, G. 2005. Fire effects on soil organic matter content, composition, and nutrients in boreal interior Alaska. Canadian Journal of Forest Research-Revue Canadienne De Recherche Forestiere 35:2178-2187.

Neitsch, S.L., Arnold, J.G., Kiniry, J.R., and Williams J.R. 2005. Soil and Water Assessment Tool, Theoretical Documentation: Version 2005. Temple, TX. USDA Agricultural Research Service and Texas A&M Blackland Research Center.

Negron-Juarez, R. Koven, C.D., Riley, W.J., Knox, R.G., Chambers, J.Q. 2015. Environmental Research Letters 10:064017. DOI:10.1088/1748-9326/10/6/064017.

Nemani, R.R., and Running, S.W. 1996. Implementation of a hierarchical global vegetation classification in ecosystem function models. J. Veg. Sci. 7:337-346.

Niinemets, U., Kull, O., and Tenhunen, J.D. 1998. An analysis of light effects on foliar morphology, physiology, and light interception in temperate deciduous woody species of contrasting shade tolerance. Tree Phys. 18:681-696.

Niu, G.-Y., Yang, Z.-L., Dickinson, R.E., and Gulden, L.E. 2005. A simple TOPMODEL-based runoff parameterization (SIMTOP) for use in global climate models. J. Geophys. Res. 110:D21106. DOI:10.1029/2005JD006111.

Niu, G.-Y., and Yang, Z.-L. 2006. Effects of frozen soil on snowmelt runoff and soil water storage at a continental scale. J. Hydrometeor. 7:937-952.

Niu, G.-Y., Yang, Z.-L., Dickinson, R.E., Gulden, L.E., and Su, H. 2007. Development of a simple groundwater model for use in climate models and evaluation with Gravity Recovery and Climate Experiment data. J. Geophys. Res. 112:D07103. DOI:10.1029/2006JD007522.

Niu, G.-Y., and Yang, Z.-L. 2007. An observation-based formulation of snow cover fraction and its evaluation over large North American river basins. J. Geophys. Res. 112:D21101. DOI:10.1029/2007JD008674.

Norman, J.M., 1979. Modeling the complete crop canopy. Modification of the Aerial Environment of Crops, pp. 249-280.

Oikawa, S., Hikosaka, K. and Hirose, T., 2005. Dynamics of leaf area and nitrogen in the canopy of an annual herb, Xanthium canadense. Oecologia, 143: 517-526.

Oke, T. 1987. Boundary Layer Climates (2:math:*{}^{nd}* edition). Routledge, London and New York.

Oleson, K.W., and Bonan, G.B. 2000. The effects of remotely-sensed plant functional type and leaf area index on simulations of boreal forest surface fluxes by the NCAR land surface model. J. Hydrometeor. 1:431-446.

Oleson, K.W., Dai, Y., Bonan, G., Bosilovich, M., Dickinson, R., Dirmeyer, P., Hoffman, F., Houser, P., Levis, S., Niu, G.-Y., Thornton, P., Vertenstein, M., Yang, Z.-L., and Zeng. X. 2004. Technical description of the Community Land Model (CLM). NCAR Technical Note NCAR/TN-461+STR. National Center for Atmospheric Research, Boulder, Colorado. 173 pp.

Oleson, K.W., Niu, G.-Y., Yang, Z.-L., Lawrence, D.M., Thornton, P.E., Lawrence, P.J., Stöckli, R., Dickinson, R.E., Bonan, G.B., Levis, S., Dai, A., and Qian, T. 2008a. Improvements to the Community Land Model and their impact on the hydrological cycle. J. Geophys. Res. 113:G01021. DOI:10.1029/2007JG000563.

Oleson, K.W., Bonan, G.B., Feddema, J., Vertenstein, M., and Grimmond, C.S.B. 2008b. An urban parameterization for a global climate model. 1. Formulation and evaluation for two cities. J. Appl. Meteor. Clim. 47:1038-1060.

Oleson, K.W., Bonan, G.B., Feddema, J., and Vertenstein, M. 2008c. An urban parameterization for a global climate model. 2. Sensitivity to input parameters and the simulated urban heat island in offline simulations. J. Appl. Meteor. Clim. 47:1061-1076.

Oleson, K.W., et al. 2010a. Technical description of version 4.0 of the Community Land model (CLM). NCAR Technical Note NCAR/TN-478+STR, National Center for Atmospheric Research, Boulder, CO, 257 pp.

Oleson, K.W., Bonan, G.B., Feddema, J., Vertenstein, M., and Kluzek, E. 2010b. Technical description of an urban parameterization for the Community Land Model (CLMU). NCAR Technical Note NCAR/TN-480+STR, National Center for Atmospheric Research, Boulder, CO, 169 pp.

Oleson, K.W., et al. 2013. Technical description of version 4.5 of the Community Land Model (CLM). NCAR Technical Note NCAR/TN-503+STR, National Center for Atmospheric Research, Boulder, CO, 420 pp.

Oleson, K.W., and Feddema, J. 2018. Parameterization and surface data improvements and new capabilities for the Community Land Model Urban (CLMU). JAMES, submitted.

Olson, J.S., 1963. Energy storage and the balance of producers and decomposers in ecological systems. Ecology 44:322-331.

Olson, D.M., Dinerstein, E., Wikramanayake, E.D., Burgess, N.D., Powell, G.V.N., Underwood, E.C., D'Amico, J.A., Itoua, I., Strand, H. E., Morrison, J. C., Loucks, C. J., Allnutt, T. F., Ricketts, T. H., Kura, Y., Lamoreux, J. F., Wettengel, W. W., Heda, P., and Kassem, K. R., 2001. Terrestrial ecoregions of the world a new map of life on earth, Bioscience, 51, 933–938.

Orchard, V.A. and Cook, F.J., 1983. Relationship between soil respiration and soil moisture. Soil Biology and Biochemistry, 15: 447-453.

Owen, P.R. 1964. Saltation of uniform grains in air. J. Fluid Mech. 20:225-242.

Ozdogan, M., Rodell, M., Beaudoing, H.K., and Toll, D.L. 2010. Simulating the effects of irrigation over the United States in a land surface model based on satellite-derived agricultural data. Journal of Hydrometeorology 11:171-184.

Page, S.E., Siegert, F., Rieley, J.O., Boehm, H-D.V., Jaya, A., and Limin, S. 2002. The amount of carbon released from peat and forest fires in Indonesia in 1997. Nature 420:61-65.

Panofsky, H.A., and Dutton, J.A. 1984. Atmospheric Turbulence: Models and Methods for Engineering Applications. John Wiley and Sons, New York.

Parton, W., Stewart, J. and Cole, C., 1988. Dynamics of C, N, P And S in Grassland Soils - A Model. Biogeochemistry 5:109-131.

Parton, W.J., et al. 1993. Observations and modeling of biomass and soil organic matter dynamics for the grassland biome worlwide. Global Biogeochemical Cycles 7:785-809.

Parton, W. et al. 1996. Generalized model for N2 and N2O production from nitrification and denitrification. Global Biogeochemical Cycles 10:401-412.

Parton, W.J. et al. 2001. Generalized model for NOx and N2O emissions from soils. J. Geophys. Res. 106(D15):17403-17419.

Paterson, W.S.B., 1994. The Physics of Glaciers. Elsevier Science Inc., New York, 480 pp.

Pelletier, J. D., P. D. Broxton, P. Hazenberg, X. Zeng, P. A. Troch, G. Y. Niu, Z. Williams, M. A. Brunke, and D. Gochis, 2016: A gridded global data set of soil, intact regolith, and sedimentary deposit thicknesses for regional and global land surface modeling. J. Adv. Mod. Earth Sys. 8:41-65.

Peterson, D.L. and K.C. Ryan, 1986. Modeling postfire conifer mortality for long-range planning. Environmental Management 10.6, pp. 797-808.

Petrescu, A.M.R. et al. 2010. Modeling regional to global CH4 emissions of boreal and arctic wetlands. Global Biogeochemical Cycles, 24(GB4009).

Pfeiffer, M., A. Spessa, and J.O. Kaplan, 2013. A model for global biomass burning in preindustrial time: LPJ-LMfire (v1. 0). Geoscientific Model Development 6.3, pp. 643-685.

Philip, J.R. 1957. Evaporation, and moisture and heat fields in the soil. J. Meteor. 14:354-366.

Piao, S.L., et al. 2012. The carbon budget of terrestrial ecosystems in East Asia over the last two decades. Biogeosciences 9:3571-3586.

Pivovarov, A.A., 1972. Thermal Conditions in Freezing Lakes and Reservoirs. John Wiley, New York.

Pollmer, W.G., Eberhard, D., Klein, D., and Dhillon, B.S. 1979. Genetic control of nitrogen uptake and translocation in maize. Crop Sci. 19:82-86.

Pomeroy, J. W., D. M. Gray, K. R. Shook, B. Toth, R. L. H. Essery, A. Pietroniro, and N. Hedstrom. 1998. An evaluation of snow accumulation and ablation processes for land surface modelling. Hydrol. Process. 12:2339–2367.

Portmann, F.T., Siebert, S., and Döll, P. 2010. MIRCA2000 - Global monthly irrigated and rainfed crop areas around the year 2000: A new high-resolution data set for agricultural and hydrological modeling. Global Biogeochem. Cycles. 24, GB1011. DOI:10.1029/2008GB003435.

Press, W.H., Teukolsky, S.A., Vetterling, W.T., and Flannery, B.P. 1992. Numerical Recipes in FORTRAN: The Art of Scientific Computing. Cambridge University Press, New York.

Prigent, C., Papa, F., Aires, F., Rossow, W.B. and Matthews, E. 2007. Global inundation dynamics inferred from multiple satellite observations, 1993-2000. J. Geophys. Res. 112(D12).

Pritchard, M.S., Bush, A.B.G., and Marshall, S.J. 2008. Neglecting ice-atmosphere interactions underestimates ice sheet melt in millennial-scale deglaciation simulations. Geophys. Res. Lett. ** 35:L01503. DOI:10.1029/2007GL031738.

Purves, D.W. et al., 2008. Predicting and understanding forest dynamics using a simple tractable model. Proceedings of the National Academy of Sciences 105.44, pp. 17018-17022.

Qian, T et al., 2006. Simulation of global land surface conditions from 1948 to 2004: Part I: Forcing data and evaluations. J. Hydrometeorology 7, pp. 953-975.

Ramankutty, N., and Foley, J. A., 1998. Characterizing patterns of global land use: An analysis of global croplands data. Global Biogeochemical Cycles, 12, 667-685.

Ramankutty, N., Evan, A., Monfreda, C., and Foley, J.A. 2008. Farming the Planet. Part 1: The Geographic Distribution of Global Agricultural Lands in the Year 2000. Global Biogeochem. Cycles. 22:GB1003. DOI:10.1029/2007GB002952.

Randlett, D.L., Zak, D.R., Pregitzer, K.S., and Curtis, P.S. 1996. Elevated atmospheric carbon dioxide and leaf litter chemistry: Influences on microbial respiration and net nitrogen mineralization. Soil Sci. Soc. Am. J. 60:1571-1577.

Rastetter, E.B., Ryan, M.G., Shaver, G.R., Melillo, J.M., Nadelhoffer, K.J., Hobbie, J.E., and Aber, J.D. 1991. A general biogeochemical model describing the responses of the C and N cycles in terrestrial ecosystems to changes in CO2, climate and N deposition. Tree Phys. 9:101-126.

Rastner, P., Bolch, T., Mölg, N., Machguth, H., and Paul, F., 2012. The first complete glacier inventory for the whole of Greenland, The Cryosphere Discuss., 6, 2399-2436, 10.5194/tcd-6-2399-2012.

Riley, W. J., Z. M. Subin, D. M. Lawrence, S. C. Swenson, M. S. Torn, L. Meng, N. Mahowald, and P. Hess, 2011a. Barriers to predicting global terrestrial methane fluxes: Analyses using a methane biogeochemistry model integrated in CESM. Biogeosciences, 8, 1925–1953. DOI:10.5194/bg-8-1925-2011.

Riley, W.J. et al. 2011b. CLM4Me, a Methane Biogeochemistry Model Integrated in CESM, Land and Biogeochemistry Model Working Group Meeting, Boulder, CO.

Roesch, A., M. Wild, H. Gilgen, and A. Ohmura. 2001. A new snow cover fraction parametrization for the ECHAM4 GCM, Clim. Dyn., 17:933–946.

Rogers, A., 2014: The use and misuse of Vcmax in Earth system models. Photosynt. Res., 119:1-15.

Rogers, A., B. E. Medlyn, J. S. Dukes, G. Bonan, S. Caemmerer, M. C. Dietze, J. Kattge, A. D. Leakey, L. M. Mercado, and U. Niinemets, 2017: A roadmap for improving the representation of photosynthesis in Earth system models. New Phytologist, 213:22-42.

Ryan, M. G. 1991. A simple method for estimating gross carbon budgets for vegetation in forest ecosystems. Tree Phys. 9:255-266.

Running, S.W. and Coughlan, J.C., 1988. A general model of forest ecosystem processes for regional applications. I. Hydrological balance, canopy gas exchange and primary production processes. Ecological Modelling, 42: 125-154.

Running, S.W. et al., 1989. Mapping regional forest evapotranspiration and photosynthesis by coupling satellite data with ecosystem simlation. Ecology, 70: 1090-1101.

Running, S.W. and Gower, S.T., 1991. FOREST BGC, A general model of forest ecosystem processes for regional applications. II. Dynamic carbon allocation and nitrogen budgets. Tree Physiology, 9: 147-160.

Running, S.W. and Hunt, E.R., Jr., 1993. Generalization of a forest ecosystem process model for other biomes, BIOME-BGC, and an applicationfor global-scale models. In: J.R. Ehleringer and C. Field (Editors), Scaling Physiological Processes: Leaf to Globe. Academic Press, San Diego, CA, pp. 141-158.

Sacks, W. J., Cook, B. I., Buenning, N., Levis, S., and Helkowski, J. H. 2009. Effects of global irrigation on the near-surface climate. Climate Dyn., 33, 159–175. DOI:10.1007/s00382-008-0445-z.

Saggar, S., Tate, K.R., Feltham, C.W., Childs, C.W. and Parshotam, A., 1994. Carbon turnover in a range of allophanic soils amended with ^{14}C-labelled glucose. Soil Biology and Biochemistry, 26: 1263-1271.

Sakaguchi, K., and Zeng, X. 2009. Effects of soil wetness, plant litter, and under-canopy atmospheric stability on ground evaporation in the Community Land Model (CLM3.5). J. Geophys. Res. 114:D01107. DOI:10.1029/2008JD010834.

Sato, H., A. Itoh, and T. Kohyama, 2007. SEIB-DGVM: A new Dynamic Global Vegetation Model using a spatially explicit individual-based approach. Ecological Modelling 200.3, pp. 2793307.

Schaaf, C.B., Gao, F., Strahler, A.H., Lucht, W., Li, X., Tsang, T., Strugnell, N.C., Zhang, X., Jin, Y., and Muller, J.-P. 2002. First operational BRDF, albedo nadir reflectance products from MODIS. Remote Sens. Environ. 83:135-148.

Schlesinger, W.H., 1997. Biogeochemistry: an analysis of global change. Academic Press, London, 588 pp.

Schnell, S. and King, G.M., 1996. Responses of methanotrophic activity in soils and cultures to water stress. Applied and Environmental Microbiology 62:3203-3209.

Segers, R., 1998. Methane production and methane consumption: a review of processes underlying wetland methane fluxes. Biogeochemistry 41:23-51.

Sellers, P.J. 1985. Canopy reflectance, photosynthesis and transpiration. Int. J. Remote Sens. 6:1335-1372.

Sellers, P.J., Mintz, Y., Sud, Y.C., and Dalcher, A. 1986. A simple biosphere model (SiB) for use within general circulation models. J. Atmos. Sci. 43:505-531.

Sellers, P.J., Hall, F.G., Asrar, G., Strebel, D.E., and Murphy, R.E. 1988. The First ISLSCP Field Experiment (FIFE). Bull. Amer. Meteor. Soc. 69:22-27.

Sellers, P.J., Berry, J.A., Collatz, G.J., Field, C.B., and Hall, F.G. 1992. Canopy reflectance, photosynthesis, and transpiration. III. A reanalysis using improved leaf models and a new canopy integration scheme. Remote Sens. Environ. 42:187-216.

Sellers, P.J., et al. 1995. The Boreal Ecosystem-Atmosphere Study (BOREAS): An overview and early results from the 1994 field year. Bull. Amer. Meteor. Soc. 76:1549-1577.

Sellers, P.J., Randall, D.A., Collatz, G.J., Berry, J.A., Field, C.B., Dazlich, D.A., Zhang, C., Collelo, G.D., and Bounoua, L. 1996. A revised land surface parameterization (SiB2) for atmospheric GCMs. Part I: Model formulation. J. Climate 9:676-705.

Sellers, Piers J et al. (1996). A revised land surface parameterization (SiB2) for atmospheric GCMs. Part II: The generation of global fields of terrestrial biophysical parameters from satellite data. Journal of climate 9.4, pp. 706-737.

Shi, X., Mao, J., Thornton, P.E., and Huang, M. 2013. Spatiotemporal patterns of evapotranspiration in response to multiple environmental factors simulated by the Community Land Model. Environ. Res. Lett. 8:024012.

Shi, M., J. B. Fisher, E. R. Brzostek, and R. P. Phillips, 2016: Carbon cost of plant nitrogen acquisition: global carbon cycle impact from an improved plant nitrogen cycle in the Community Land Model. Glob. Change Biol., 22:1299-1314.

Shiklomanov, I.A. 2000. Appraisal and assessment of world water resources. Water International 25:11-32.

Siebert, S., Döll, P., Hoogeveen, J., Faures, J.M., Frenken, K., Feick, S., 2005. Development and validation of the global map of irrigation areas. Hydrol Earth Syst Sc 9:535–547

Simard, M., Pinto, N., Fisher, J.B., and Baccini, A. (2011), Mapping forest canopy height globally with spaceborne lidar. J. Geophys. Res., 116, G04021, doi:10.1029/2011JG001708.

Simpson, R.J., Lambers, H., and Dalling, M.J. 1983. Nitrogen redistribution during grain growth in wheat (Triticum avestivum L.). Plant Physiol. 71:7-14.

Sitch, S et al. (2003). Evaluation of ecosystem dynamics, plant geography and terrestrial carbon cycling in the LPJ dynamic global vegetation model. Global Change Biology 9.2, pp. 161-185.

Sivak, M. 2013. Air conditioning versus heating: climate control is more energy demanding in Minneapolis than in Miami. Environ. Res. Lett., 8, doi:10.1088/1748-9326/8/1/014050.

Smith, B., I.C. Prentice, and M.T. Sykes, 2001. Representation of vegetation dynamics in the modelling of terrestrial ecosystems: comparing two contrasting approaches within European climate space. Global Ecology and Biogeography 10.6, pp. 621-637.

Smith, A.M.S., Wooster, M.J., Drake, N.A., Dipotso, F.M. and Perry, G.L.W., 2005. Fire in African savanna: Testing the impact of incomplete combustion on pyrogenic emissions estimates. Ecological Applications, 15: 1074-1082.

Smith, A.M. and M. Stitt, 2007. Coordination of carbon supply and plant growth. Plant, cell & environment 30.9, pp. 1126-1149.

Sollins, P., 1982. Input and decay of coarse woody debris in coniferous stands in western Oregon and Washington. Canadian Journal of Forest Research, 12: 18-28.

Son, Y. and Gower, S.T., 1991. Aboveground nitrogen and phosphorus use by five plantation-grown trees with different leaf longevities. Biogeochemistry, 14: 167-191.

Sørensen, L.H., 1981. Carbon-nitrogen relationships during the humification of cellulose in soils containing different amounts of clay. Soil Biology and Biochemistry, 13: 313-321.

Sperry, J.S., Adler, F.R., Campbell, G.S. and Comstock, J.P. 1998. Limitation of plant water use by rhizosphere and xylem conductance: results from a model. Plant, Cell & Environment, 21: 347–359. doi:10.1046/j.1365-3040.1998.00287.x

Sperry, J.S. and Love, D.M. 2015. What plant hydraulics can tell us about responses to climate-change droughts. New Phytol, 207: 14–27. doi:10.1111/nph.13354

Sprugel, D.G., Ryan, M.G., Brooks, J.R., Vogt, K.A., and Martin, T.A. 1995. Respiration from the organ level to stand level. pp. 255-299. In: W. K. Smith and T. M. Hinkley (editors) Resource Physiology of Conifers. Academic Press, San Diego,CA.

Stauffer, D., and Aharony, A. 1994. Introduction to Percolation Theory. Taylor and Francis, London.

Still, C.J., Berry, J.A., Collatz, G.J., and DeFries, R.S. 2003. Global distribution of C3 and C4 vegetation: carbon cycle implications. Global Biogeochem. Cycles 17:1006. DOI:10.1029/2001GB001807.

Stöckli, R., Lawrence, D.M., Niu, G.-Y., Oleson, K.W., Thornton, P.E., Yang, Z.-L., Bonan, G.B., Denning, A.S., and Running, S.W. 2008. Use of FLUXNET in the Community Land Model development. J. Geophys. Res. 113:G01025. DOI:10.1029/2007JG000562.

Strack, M., Kellner, E. and Waddington, J.M., 2006. Effect of entrapped gas on peatland surface level fluctuations. Hydrological Processes 20:3611-3622.

Strahler, A.H., Muchoney, D., Borak, J., Friedl, M., Gopal, S., Lambin, E., and Moody. A. 1999. MODIS Land Cover Product: Algorithm Theoretical Basis Document (Version 5.0). Boston University, Boston.

Stull, R.B. 1988. An Introduction to Boundary Layer Meteorology. Kluwer Academic Publishers, Dordrecht.

Subin, Z.M., Riley, W.J. and Mironov, D. 2012a. Improved lake model for climate simulations, J. Adv. Model. Earth Syst., 4, M02001. DOI:10.1029/2011MS000072.

Subin, Z.M., Murphy, L.N., Li, F., Bonfils, C. and Riley, W.J., 2012b. Boreal lakes moderate seasonal and diurnal temperature variation and perturb atmospheric circulation: analyses in the Community Earth System Model 1 (CESM1). Tellus A, North America, 64.

Sun, Y., Gu, L., and Dickinson, R. E. 2012. A numerical issue in calculating the coupled carbon and water fluxes in a climate model, J. Geophys. Res., 117, D22103. DOI:10.1029/2012JD018059.

Swenson, S.C., Lawrence, D.M., and Lee, H. 2012. Improved Simulation of the Terrestrial Hydrological Cycle in Permafrost Regions by the Community Land Model. JAMES, 4, M08002. DOI:10.1029/2012MS000165.

Swenson, S.C. and Lawrence, D.M. 2012. A New Fractional Snow Covered Area Parameterization for the Community Land Model and its Effect on the Surface Energy Balance. JGR, 117, D21107. DOI:10.1029/2012JD018178.

Swenson, S.C., and D. M. Lawrence. 2014. Assessing a dry surface layer-based soil resistance parameterization for the Community Land Model using GRACE and FLUXNET-MTE data. JGR, 119, 10, 299–10,312, DOI:10.1002/2014JD022314.

Swenson, S.C., and D. M. Lawrence. 2015. A GRACE-based assessment of interannual groundwater dynamics in the Community Land Model. WRR, 51, doi:10.1002/2015WR017582.

Ta, C.T. and Weiland, R.T. 1992. Nitrogen partitioning in maize during ear development. Crop Sci. 32:443-451.

Tang, J.Y. and Riley, W.J. 2013. A new top boundary condition for modeling surface diffusive exchange of a generic volatile tracer: Theoretical analysis and application to soil evaporation. Hydrol. Earth Syst. Sci. 17:873-893.

Tarnocai, C., Kettles, I. M., and Lacelle, B., 2011. Peatlands of Canada, Geological Survey of Canada, Open File 6561, CD-ROM. DOI:10.495/288786.

Taylor, B.R., Parkinson, D. and Parsons, W.F.J., 1989. Nitrogen and lignin content as predictors of litter decay rates: A microcosm test. Ecology, 70: 97-104.

Thomas R.Q., Brookshire E.N., Gerber S. 2015. Nitrogen limitation on land: how can it occur in Earth system models? Global Change Biology, 21, 1777-1793, doi:10.1111/gcb.12813.

Thonicke, K., Venevsky, S., Sitch, S., and Cramer, W. 2001. The role of fire disturbance for global vegetation dynamics: coupling fire into a Dynamic Global Vegetation Model. Global Ecology and Biogeography 10:661-667.

Thonicke, K. et al., 2010. The influence of vegetation, fire spread and fire behaviour on biomass burning and trace gas emissions: results from a process-based model. Biogeosciences 7.6, pp. 1991-2011.

Thornton, P.E., 1998. Regional ecosystem simulation: combining surface- and satellite-based observations to study linkages between terrestrial energy and mass budgets. Ph.D. Thesis, The University of Montana, Missoula, 280 pp.

Thornton, P.E., Law, B.E., Gholz, H.L., Clark, K.L., Falge, E., Ellsworth, D.S., Goldstein, A.H., Monson, R.K., Hollinger, D., Falk, M., Chen, J., and Sparks, J.P. 2002. Modeling and measuring the effects of disturbance history and climate on carbon and water budgets in evergreen needleleaf forests. Agric. For. Meteor. 113:185-222.

Thornton, P.E., and Rosenbloom, N.A. 2005. Ecosystem model spin-up: estimating steady state conditions in a coupled terrestrial carbon and nitrogen cycle model. Ecological Modelling 189:25-48.

Thornton, P.E., and Zimmermann, N.E. 2007. An improved canopy integration scheme for a land surface model with prognostic canopy structure. J. Climate 20:3902-3923.

Thornton, P.E., Lamarque, J.-F., Rosenbloom, N.A., and Mahowald, N.M. 2007. Influence of carbon-nitrogen cycle coupling on land model response to CO_2 fertilization and climate variability. Global Biogeochem. Cycles 21:GB4018.

Thornton, P.E., Doney, S.C., Lindsay, K., Moore, J.K., Mahowald, N., Randerson, J.T., Fung, I., Lamarque, J.F., Feddema, J.J., and Lee, Y.H. 2009. Carbon-nitrogen interactions regulate climate-carbon cycle feedbacks: results from an atmosphere-ocean general circulation model. Biogeosci. 6:2099-2120.

Tian, H. et al. 2010. Spatial and temporal patterns of CH4 and N2O fluxes in terrestrial ecosystems of North America during 1979-2008: application of a global biogeochemistry model. Biogeosciences 7:2673-2694.

Toon, O.B., McKay, C.P., Ackerman, T.P., and Santhanam, K. 1989. Rapid calculation of radiative heating rates and photodissociation rates in inhomogeneous multiple scattering atmospheres. J. Geophys. Res. 94(D13):16,287-16,301.

Turetsky, M.R., Wieder, R.K., Halsey, L.A., and Vitt, D.H. 2002. Current disturbance and the diminishing peatland carbon sink. Geophys. Res. Lett. 29:1526. DOI:10.1029/2001GL014000.

Turetsky, M.R., Amiro, B.D., Bosch, E., and Bhatti, J.S. 2004. Historical burn area in western Canadian peatlands and its relationship to fire weather indices. Global Biogeochem. Cycles 18:GB4014. DOI:10.1029/2004GB002222.

Tye, A.M., et al. 2005. The fate of N-15 added to high Arctic tundra to mimic increased inputs of atmospheric nitrogen released from a melting snowpack. Global Change Biology 11:1640-1654.

Unland, H.E., Houser, P.R., Shuttleworth, W.J., and Yang, Z.-L. 1996. Surface flux measurement and modeling at a semi-arid Sonoran Desert site. Agric. For. Meteor. 82:119-153.

UNSTAT, 2005. National Accounts Main Aggregates Database, United Nations Statistics Division.

Uriarte, M. et al., 2009. Natural disturbance and human land use as determinants of tropical forest dynamics: results from a forest simulator. Ecological Monographs 79.3, pp. 423-443.

Vallano, D.M. and Sparks, J.P. 2007. Quantifying foliar uptake of gaseous itrogen dioxide using enriched foliar δ^{15}N values. New Phytologist 177:946-955.

van der Werf, G.R., Randerson, J.T., Giglio, L., Collatz, G.J., Mu, M., Kasibhatla, S.P., Morton, D.C., DeFries, R.S., Jin, Y., van Leeuwen, T.T. 2010. Global fire emissions and the contribution of deforestation, savanna, forest, agricultural, and peat fires (1997-2009) Atmos. Chem. Phys. 10:11707-11735.

van Veen, J.A., Ladd, J.N. and Frissel, M.J., 1984. Modelling C and N turnover through the microbial biomass in soil. Plant and Soil, 76: 257-274.

van Kampenhout, L., J.T.M. Lenaerts, W.H. Lipscomb, W.J. Sacks, D.M. Lawrence, A.G. Slater, and M.R. van den Broeke, 2017. Improving the Representation of Polar Snow and Firn in the Community Earth System Model. Journal of Advances in Modeling Earth Systems 9, no. 7: 2583–2600. https://doi.org/10.1002/2017MS000988.

Van Tricht, K., Lhermitte, S., Gorodetskaya, I.V. and van Lipzig, N.P.M., 2016. Improving satellite-retrieved surface radiative fluxes in polar regions using a smart sampling approach. The Cryosphere 10:2379-2397. doi:10.5194/tc-10-2379-2016

Van Vuuren, D.P., Lucas, P.S., and Hilderink, H.B.M., 2006. Downscaling drivers of global environmental change: enabling use of global SRES scenarios at the national and grid levels, Report 550025001, Netherlands Environmental Assessment Agency, 45 pp.

Vanninen, P., and Makela, A. 2005. Carbon budget for Scots pine trees: effects of size, competition and site fertility on growth allocation and production. Tree Phys. 25:17-30.

Venevsky, S. et al., 2002. Simulating fire regimes in human-dominated ecosystems: Iberian Peninsula case study. Global Change Biology 8.10, pp. 984-998.

Verdin, K. L., and S. K. Greenlee, 1996. Development of continental scale digital elevation models and extraction of hydrographic features, paper presented at the Third International Conference/Workshop on Integrating GIS and Environmental Modeling, Santa Fe, New Mexico, 21–26 January, Natl. Cent. for Geogr. Inf. and Anal., Santa Barbara, Calif.

Vionnet, V., E. Brun, S. Morin, A. Boone, S. Faroux, P. Le Moigne, E. Martin, and J.-M. Willemet. The Detailed Snowpack Scheme Crocus and Its Implementation in SURFEX v7.2. GMD 5, no. 3 (May 24, 2012): 773-91. https://doi.org/10.5194/gmd-5-773-2012.

Viovy, N. 2011. CRUNCEP dataset. [Description available at http://dods.extra.cea.fr/data/p529viov/cruncep/readme.htm. Data available at http://dods.extra.cea.fr/store/p529viov/cruncep/V4_1901_2011/].

Vitousek, P.M., and Howarth, R.W. 1991. Nitrogen limitation on land and in the sea: How can it occur? Biogeochem. 13:87-115.

Walter, B.P., Heimann, M. and Matthews, E., 2001. Modeling modern methane emissions from natural wetlands 1. Model description and results. J. Geophys. Res. 106(D24):34189-34206.

Wania, R., Ross, I. and Prentice, I.C. 2009. Integrating peatlands and permafrost into a dynamic global vegetation model: 2. Evaluation and sensitivity of vegetation and carbon cycle processes. Global Biogeochem. Cycles 23.

Wania, R., Ross, I. and Prentice, I.C. 2010. Implementation and evaluation of a new methane model within a dynamic global vegetation model LPJ-WHyMe v1.3. Geoscientific Model Development Discussions 3:1-59.

Wang, A., and Zeng, X. 2009. Improving the treatment of vertical snow burial fraction over short vegetation in the NCAR CLM3. Adv. Atmos. Sci. 26:877-886. DOI:10.1007/s00376-009-8098-3.

Weng, E.S. et al., 2014. Scaling from individuals to ecosystems in an Earth System Model using a mathematically tractable model of height-structured competition for light. Biogeosciences Discussions 11.12, pp. 17757-17860.

White, M.A., Thornton, P.E., and Running, S.W. 1997. A continental phenology model for monitoring vegetation responses to interannual climatic variability. Global Biogeochem. Cycles 11:217-234.

White, M.A., Thornton, P.E., Running, S.W., and Nemani, R.R. 2000. Parameterization and sensitivity analysis of the Biome-BGC terrestrial ecosystem model: net primary production controls. Earth Interactions 4:1-85.

Wieder, W. R., Cleveland, C. C., Lawrence, D. M., and Bonan, G. B. 2015. Effects of model structural uncertainty on carbon cycle projections: biological nitrogen fixation as a case study. Environmental Research Letters, 10(4), 044016.

Williams, M., Rastetter, E.B., Fernandes, D.N., Goulden, M.L., Wofsy, S.C., Shaver, G.R., Melillo, J.M., Munger, J.W., Fan, S.M. and Nadelhoffer, K.J. 1996. Modelling the soil-plant-atmosphere continuum in a Quercus–Acer stand at Harvard Forest: the regulation of stomatal conductance by light, nitrogen and soil/plant hydraulic properties. Plant, Cell & Environment, 19: 911–927. doi:10.1111/j.1365-3040.1996.tb00456.x

Wiscombe, W.J., and Warren, S.G. 1980. A model for the spectral albedo of snow. I. Pure snow. J. Atmos. Sci. 37:2712-2733.

Wood, E.F., Lettenmaier, D.P., and Zartarian, V.G. 1992. A land-surface hydrology parameterization with subgrid variability for general circulation models. J. Geophys. Res. 97(D3):2717–2728. DOI:10.1029/91JD01786.

World Bank, 2004. World development indicators 2004, Oxford University Press, New York, 416 pp.

Wu, H., J. S. Kimball, N. Mantua, and J. Stanford, 2011: Automated upscaling of river networks for macroscale hydrological modeling. Water Resour. Res., 47, W03517, doi:10.1029/2009WR008871.

Wu, H., J. S. Kimball, H. Li, M. Huang, L. R. Leung, and R. F. Adler, 2012. A New Global River Network Database for Macroscale Hydrologic modeling, Water Resour. Res., 48, W09701, doi:10.1029/2012WR012313.

Xiaodong, Y. and H.H. Shugart, 2005. FAREAST: a forest gap model to simulate dynamics and patterns of eastern Eurasian forests. Journal of Biogeography 32.9, pp. 1641-1658.

Xu, C., R. Fisher, S. D. Wullschleger, C. J. Wilson, M. Cai, and N. G. McDowell, 2012: Toward a mechanistic modeling of nitrogen limitation on vegetation dynamics. PloS one, 7:e37914.

Yang, Z.-L. 1998. Technical note of a 10-layer soil moisture and temperature model. Unpublished manuscript.

Zender, C.S., Bian, H., and Newman, D. 2003. Mineral dust entrainment and deposition (DEAD) model: Description and 1990s dust climatology. ** J. Geophys. Res. 108(D14):4416. DOI:10.1029/2002JD002775.

Zeng, X., and Dickinson, R.E. 1998. Effect of surface sublayer on surface skin temperature and fluxes. J.Climate 11:537-550.

Zeng, X., Zhao, M., and Dickinson, R.E. 1998. Intercomparison of bulk aerodynamic algorithms for the computation of sea surface fluxes using the TOGA COARE and TAO data. J. Climate 11:2628-2644.

Zeng, X. 2001. Global vegetation root distribution for land modeling. J. Hydrometeor. 2:525-530.

Zeng, X., Shaikh, M., Dai, Y., Dickinson, R.E., and Myneni, R. 2002. Coupling of the Common Land Model to the NCAR Community Climate Model. J. Climate 15:1832-1854.

Zeng, X., Dickinson, R.E., Barlage, M., Dai, Y., Wang, G., and Oleson, K. 2005. Treatment of under-canopy turbulence in land models. J. Climate 18:5086-5094.

Zeng, X., and Wang, A. 2007. Consistent parameterization of roughness length and displacement height for sparse and dense canopies in land models. J. Hydrometeor. 8:730-737.

Zeng, X., and Decker, M. 2009. Improving the numerical solution of soil moisture-based Richards equation for land models with a deep or shallow water table. J. Hydrometeor. 10:308-319.

Zeng, X., Zeng, X., and Barlage, M. 2008. Growing temperate shrubs over arid and semiarid regions in the Community Land Model - Dynamic Global Vegetation Model. Global Biogeochem. Cycles 22:GB3003. DOI:10.1029/2007GB003014.

Zhang, Y., Li, C.S., Trettin, C.C., Li, H. and Sun, G., 2002. An integrated model of soil, hydrology, and vegetation for carbon dynamics in wetland ecosystems. Global Biogeochemical Cycles 16. DOI:10.1029/2001GB001838.

Zhuang, Q., et al. 2004. Methane fluxes between terrestrial ecosystems and the atmosphere at northern high latitudes during the past century: A retrospective analysis with a process-based biogeochemistry model. Global Biogeochemical Cycles 18. DOI:10.1029/2004GB002239.

Zilitinkevich, S.S. 1970. Dynamics of the Atmospheric Boundary Layer. Leningrad Gidrometeor.